C55.2.C61/2/984

Proceedings of the Ninth Annual Climate Diagnostics Workshop

Dept. of Atmospheric Sciences
Oregon State University
Corvallis, Oregon

October 22-26, 1984

U.S. DEPARTMENT OF COMMERCE
National Oceanic and Atmospheric Administration

Publications listed below are available in both hard copy and microfiche form from the National Technical Information Service, U.S. Department of Commerce, Sills Building, 5285 Port Royal Road, Springfield, VA 22161. Prices on request. Order by accession number (given in parentheses).

Proceedings of the First Climate Diagnostics Workshop (PB264993)

Proceedings of the Second Climate Diagnostics Workshop (PB282151)

Proceedings of the Third Climate Diagnostics Workshop (PB298355)

Proceedings of the Fourth Climate Diagnostics Workshop (PB80-201130)

Proceedings of the Fifth Climate Diagnostics Workshop (PB81-222200)

Proceedings of the Sixth Climate Diagnostics Workshop (PB82-219486)

Proceedings of the Seventh Climate Diagnostics Workshop (PB83-208033)

Proceedings of the Eighth Climate Diagnostics Workshop (PB84-192418)

When articles in any of the workshops are referenced, please include the appropriate number at the end of the reference. This allows various journals to accept these references more readily.

Proceedings of the Ninth Annual Climate Diagnostics Workshop

Held at the

Dept. of Atmospheric Sciences
Oregon State University
Corvallis, Oregon

October 22-26, 1984

March 1985

U. S. DEPARTMENT OF COMMERCE
Malcolm Baldrige, Secretary

National Oceanic and Atmospheric Administration
Anthony J. Calio, Deputy Administrator

PREFACE

The Ninth Annual Climate Diagnostics Workshop was hosted by the Department of Atmospheric Sciences, Oregon State University in Corvallis, Oregon. The success of the Workshop was in no small way due to the work of Larry Gates and the OSU Organizing Committee, who jointly shared with the Climate Analysis Center in the planning and organization of the Workshop. The local arrangements, hospitality, and excellent facilities made the Workshop a pleasant experience for all participants. Gail Lucas and Rod Quiroz of the CAC contributed immeasurably in preparations for the Workshop. Luke Mannello has done his usual excellent job in preparing these Proceedings for publication. Session Chairmen--William Bonner, Allan Murphy, Eugene Rasmusson, William Quinn, Steven Esbenson, Jay Winston, Donald Gilman, Hualu Pan, and Kelly Redmond--are commended for their effective and enthusiastic management of the sessions.

The purpose of these Proceedings is to provide synopses of the presentations at the Workshop and all of the papers that were presented are included here. The Workshop opened with the same format as previous years, with a session devoted to a review of climate fluctuations for the period September 1983 to August 1984. This was followed by sessions on climate diagnostics, ENSO, intraseasonal oscillations, climate variability of the west coast of the Americas, modeling, diagnostics: monsoons and rainfall predictions and specification, special topics and data sets.

I would finally like to thank all attendees for their contributions and participation in a most successful Workshop. We look forward to next year's international Workshop with great anticipation.

William D. Bonner
March 1985

Ninth Climate Diagnostics Workshop
Corvallis, Oregon
October 22-26, 1984

List of Participants

Phillip A. Arkin	NOAA/NWS/CAC
Ferdinand Baer	University of Maryland
Timothy P. Barnett	Scripps Institution of Oceanography, Univ. of Calif.
Anthony G. Barnston	NOAA/NWS/CAC
Kenneth H. Bergman	NOAA/NWS/CAC
George J. Boer	Canadian Climate Center, Atmospheric Environment Serv.
William D. Bonner	NOAA/NWS/NMC
Reid A. Bryson	University of Washington
Wayne V. Burt	Oregon State University
Daniel Cayan	Scripps Institution of Oceanography, Univ. of Calif.
Fong-Chiau Chang	University of Washington
Wen-Yuan Chen	NOAA/NWS/CAC
Pao-Shin Chu	Oregon State University
Angel Cornejo	Scripps Institution of Oceanography, Univ. of Calif.
Robert R. Dickson	NOAA/NWS/CAC
Arthur V. Douglas	Creighton University
Brigitte Doring	Haenkel KGaA, Duesseldorf
Richard F. Eibert	Entropy, Ltd.
David B. Enfield	Oregon State University
Edward S. Epstein	NOAA/NWS/CAC
Steven K. Esbensen	Oregon State University
C. K. Folland	British Meteorological Office
W. Lawrence Gates	Oregon State University
Joyce Gavin	Lamont-Doherty Geological Observatory, Columbia Univ.
John E. Geisler	University of Utah
Donald L. Gilman	NOAA/NWS/CAC
H. B. Gordon	Australian Numerical Meteorology Research Ctr.
David S. Gutzler	Massachusetts Institute of Technology
Robert P. Harnack	Rutgers University, Cook College
John E. Hay	University of British Columbia
John D. Horel	Scripps Institute of Oceanography, Univ. of Calif.
Huang-Hsiung Hsu	University of Washington
Thomas R. Karl	NOAA/NESDIS
Richard W. Katz	National Center for Atmospheric Research
Richard A. Keen	University of Colorado
James L. Kinter III	NASA/GSFC
William H. Klein	University of Maryland
George J. Kukla	Lamont-Doherty Geol. Observatory of Columbia Univ.
John E. Kutzbach	University of Wisconsin
Peter J. Lamb	Illinois State Water Survey Div.
W. Ka-Ming Lau	NASA/GSFC
John A. Laurmann	Gas Research Institute, Chicago
Robert E. Livezey	NOAA/NWS/CAC
G. Robert Lofgren	University of Arizona
Roland A. Madden	National Center for Atmospheric Research
Larry Mahrt	Oregon State University
G.A. McBean	Institute of Ocean Sciencies

James P. McGuirk	Texas A&M University
Todd P. Mitchell	University of Washington
Christopher N.K. Mooers	Naval Postgraduate School
Ullrich Mueller	Haenkel KGaA, Duesseldorf
Takio Murakami	University of Hawaii
Robert Mureau	Netherlands Meteorological Institute
Tom Murphree	University of California, Davis
Allan H. Murphy	Oregon State University
Antonio Navarra	NOAA/GFDL
Victor T. Neal	Oregon State University
Sharon E. Nicholson	Clark University
Sumant Nigam	Massachusetts Institute of Technology
Hau-Lu Pan	Oregon State University
Philip A. Peck	NOAA/NWS Forecast Office, Portland
William H. Quinn	Oregon State University
Roderick S. Quiroz	NOAA/NWS/CAC
Uwe Radok	University of Colorado
Colin S. Ramage	University of Hawaii
Eugene M. Rasmusson	NOAA/NWS/CAC
Kelly Redmond	Oregon State University
Richard W. Reynolds	NOAA/NWS/CAC
John O. Roads	Scripps Institution of Oceanography, Univ. of Calif.
Alan D. Robock	University of Maryland
David R. Rodenhuis	University of Maryland
Chester F. Ropelewski	NOAA/NWS/CAC
Richard D. Rosen	Atmospheric and Environmental Research
James C. Sadler	University of Hawaii
B. Santer	University of East Anglia
Michael E. Schlesinger	Oregon State University
Thomas A. Schroeder	University of Hawaii
Rennie Selkirk	Masssachusetts Institute of Technology
Amir Shabbar	Canadian Climate Centre
James J. Simpson	Scripps Institution of Oceanography, Univ. of Calif.
Joseph Sirutis	NOAA/GFDL
Ralph J. Slutz	University of Colorado
Robert L. Smith	Oregon State University
William A. Sprigg	NOAA/NCPO
James W. Tauss	University of Maryland
Edward Tollerud	University of Colorado
Sushel Unninayar	WMO
Huug van den Dool	University of Maryland
Hassan Virji	National Science Foundation
A. James Wagner	NOAA/NWS/CAC
John M. Wallace	University of Washington
John E. Walsh	University of Illinois
Bryan C. Weare	University of California
Klaus W. Weickmann	University of Wisconsin
Jay S. Winston	University of Maryland
Peter B. Wright	University of Washington
Brent Yarnal	Colorado State University

TABLE OF CONTENTS

Page

Preface iii

List of Participants v

Workshop Program vii

SESSION 1: The 1983-84 Climate

Global surface air temperature variations: 1983-84. . . . . P. D. Jones, P. M. Kelly, and B. Santer 1

Monitoring climate in real time: An application of the Climate Anomaly Monitoring System (CAMS). . . . . .C. F. Ropelewski 11

Review of the climate of Fall 1983 and Winter 1983-84 . . . . . K. H. Bergman and R. S. Quiroz 21

Some empirical evidence for the influence of snow cover on temperature and precipitation . . . . . J. Namias (Presented by D. Cayan) 32

Blocking as an explanation of the severe cold of winter 1983-84 . . . . . R. S. Quiroz 44

Circulation and weather for MAM and JJA 1984. . . . . A. J. Wagner and C.F. Ropelewski 50

SESSION II: Climate Diagnostics: Temperature

On the relationship between North Atlantic SST anomalies with U.S. surface temperature anomalies . . . . . D. R. Cayan 60

Worldwide marine temperature fluctuations on the season-to-century time scale . . . . . .C. K. Folland, D. E. Parker, and M. Newman 70

Recent unusual mean winter temperatures across the contiguous U.S . . . . . T. R. Karl, R. Livezey, and E. Epstein 86

Towards understanding the geographical distribution and seasonality in persistence of monthly mean surface air temperature over the U.S.A. . . . . H. M. van den Dool and W. H. Klein 91

Temperature and precipitation trends in North America. . . . . G. Kukla, J. Gavin, and T. Karl 96

SESSION III: ENSO and Intraseasonal Oscillations

Recent long-term climatic change over the eastern tropical and sub-tropical Pacific and its ramifications. . . . W. H. Quinn and V.T. Neal 101

SESSION III: ENSO and Intraseasonal Oscillations (Con.)

Global relationships with the Southern Oscillation. . . . . .P. B. Wright, T.P. Mitchell, and J. M. Wallace 110

Time series modeling of the Southern Oscillation. . . . . P.-S. Chu and R. Katz 114

Satellite observations of a large-amplitude 40-50 day oscillation in upper tropospheric temperature over the equatorial Pacific Ocean during the 1982-83 ENSO event. . . . . E. Tollerud 115

Subseasonal and interannual variations of tropical convection and the El Niño/Southern Oscillation. . . . . W. K.-M. Lau and P. H. Chan 119

The annual variation in the vertical structure of the 40-50 day tropical oscillation . . . . . R. A. Madden 123

Life cycle of a 28-72 day atmospheric oscillation during northern winter . . . . . K. Weickmann and J. Kutzbach 128

SESSION IV: West Coast Atmosphere-Ocean Climate Variability

The distribution of rainfall along the coast of northern Peru during 1982-83. . . . . .J.D. Horel and A. Cornejo-Garrido 141

Peru coastal winds during 1982-83. . . D. B. Enfield and P.A. Newberger 147

Climatic events of the west coast of southern Africa. . . . . S. E. Nicholson and D. Entekhabi 157

Several aspects of interannual variability in the California current system. . . . . C.N.K. Mooers and L. C. Breaker 166

Warm and cold episodes in the California current: A case for large-scale mid-latitude atmospheric forcing. . . . . J. J. Simpson 173

Relationships between Pacific Northwest coast climate and ENSO events . . . . . B. Yarnal 185

Evidence of an 18-year cycle in Pacific Northwest precipitation data . . . . . P. A. Peck and V. C. Bissell 193

SESSION V: Modeling

Time-averaging the flux-profile relationship. . . . . L. Mahrt, , C. Berthou, P. Marquet and J.-C. Andre 199

Atmospheric general circulation model simulations of the modern Antarctic climate. . . . . M. Schlesinger 201

SESSION V: Modeling (Con.)

Atmospheric response to an equatorial Pacific sea surface temperature anomaly: The effects of orography . . . . . M. L. Blackmon, G. T. Bates, and J.E. Geisler 211

Horizontal fluxes in real and model atmospheres. . . . . G. J. Boer 218

The impact of heat sources on the atmospheric circulation . . . . . R. Mureau, J. D. Opsteegh, and J. S. Winston 225

The effect of anomalous snow cover on the general circulation of the atmosphere using a simple climate model. . . . A. Robock and J.W. Tauss 231

Interannual climate variability in low vertical resolution spectral atmospheric model. . . . . H. B. Gordon 238

Variability simulations with a steady, linearized primitive equation model. . . . . J. L. Kinter, III and S. Nigam 246

Understanding El Niño events using a simple dynamical atmospheric model . . . . . B. C. Weare 250

Anomaly general circulation models . . . . . A. Navarra and K. Miyakoda 257

SESSION VI: Climate Diagnostics: Monsoons and Rainfall

Transition from the Southern to the Northern Hemisphere summer monsoon . . . . . T. Murakami 262

Large-scale variability in Indian monsoon rainfall inferred from satellite data. . . . . P. A. Arkin, J. Janowiak, and W. Replane 265

Tropospheric static stability and central North American summer rainfall during 1979. . . . . P. J. Lamb and R. A. Peppler 274

Meteorological conditions during drought episodes in the U.S. Great Plains. . . . . F.-C. Chang and J. M. Wallace 284

SESSION VII. Prediction and Specification

Monthly forecast experiments with sea surface temperature anomaly forcings and envelope mountains: Preliminary results . . . . . J. Sirutis, K. Miyakoda, Y.-H. Lu, J. Ploshay, and R. Reynolds 292

Spectral statistical forecasts of the 500 mb height field . . . . . J. O. Roads and T. P. Barnett 296

Prediction of monthly 700-mb heights using antecedent and simulated prognostic height predictors. . .R. Harnack, C. Kleupfel and R. Livezey 305

SESSION VII: Prediction and Specification (Con.)

Specification of mean surface temperature anomalies in Europe and Asia during the Fall months . . . . . W. H. Klein and R. Yang 317

Land surface fluctuations and associated climatic variability . . . . . J. Walsh and W. Jasperson 326

Concurrent and lagged relationships between precipitation frequency and 700-mb heights. . . . . A. V. Douglas and P. J. Englehart 331

SESSION VIII: Special Topics

Tropical convection and North American cyclones during the 1982-83 El Niño . . . . . R. A. Keen 341

An observational study of the vertical structure of interannual wind fluctuations in the tropics . . . . . D. S. Gutzler 346

Low-frequency baroclinic features observed in the lee of major mountain ranges. . . . . H. H. Hsu and J. M. Wallace 352

Slow fluctuations of the tropical circulation during the FGGE-year. . . . . R. Selkirk 360

Very anomalous behavior of outgoing longwave radiation in the tropics in 1983-84: Aftermath of ENSO? . . . . . J. S. Winston 373

SESSION IX: Data Sets

Climate System Fluctuations, Monitoring. . . . . S. Unninayar 384

The status of the NOAA/NESDIS radiation budget data set. . . A. Gruber 398

A sea surface temperature analysis based on in situ and satellite data. . . . . R. W. Reynolds and W. H. Gemmill 408

Effect of initialization on diagnoses of large-scale circulation statistics from NMC analyses. . . . . R.D. Rosen and D.A. Salstein 417

Observing the eastern Pacific Hadley circulation. . . . . J.P. McGuirk, A.H. Thompson, and N.R. Smith 429

Global Surface Air Temperature Variations: 1983-1984

P.D.Jones, P.M.Kelly and B.Santer

Climatic Research Unit
School of Environmental Sciences
University of East Anglia
Norwich NR4 7TJ
United Kingdom

We discuss global surface air temperature anomaly data for the period September 1983 to August 1984 and place them in their long-term context. The values are drawn from the gridded data set described by Jones et al. (Monthly Weather Review, 101, 59-70, 1982), updated globally using data from stations reporting on the CLIMAT network. The information is largely for the landmasses of the Northern Hemisphere and of the Southern Hemisphere north of 45°S. Data are also presented for Antarctica (Raper et al., Monthly Weather Review, 112, 1341-1353, 1984).

Annual data for the Northern Hemisphere, the Arctic (65-85°N) and the Antarctic (65-90°S) for the period 1881 to 1983 are presented in Figure 1. The data are expressed as departures from the reference period 1961-1975. Over the Northern Hemisphere, 1983 was the fourth warmest year during the 103-year record. 1981 was the warmest year (the second and third warmest were 1938 and 1953, respectively) and 1980-1984 promises to be the warmest 5-year period in the record. The recent warming is close to rivalling that of the 1920s and 1930s, but is different in character. It is most noticeable in middle latitudes, whereas the earlier warming was more pronounced at high latitudes (see Figure 1). The Antarctic warmth of the 1970s has continued into the 1980s.

Monthly mean estimates for the three regions for the period January 1979 to August 1984 are shown in Figure 2. We have already noted the warmth of 1983 over the Northern Hemisphere. November 1983 was the warmest this century. January 1984 was particularly warm over the Arctic, in contrast to April. Autumn (SH) 1984 was the warmest in the Antarctic record. It was 0.43 C warmer than the previous warmest, 1975. Of course, given the shortness of the Antarctic data set, records are likely to be broken fairly frequently.

Maps of surface air temperature anomalies over the major landmasses of both hemispheres for the months of September 1983 to August 1984 are presented in Figures 3 to 14. The data in these charts are expressed as departures from the reference period 1961-1975. The hatching indicates anomalies of magnitude greater than 2 or 4°C depending on the month. The maximum departures experienced in each region are indicated. We discuss the main features of the large-scale spatial patterns rather than regional detail. Further information concerning the latter can be found in Climate Monitor, the bulletin of the Climatic Research Unit.

The main features of the Northern Hemisphere temperature patterns are:

- the warmth of western Siberia (and, to a lesser extent, parts of North America) throughout much of the 12-month period;
- the coldness of the Davis Strait region; and
- abrupt transitions between various months.

The warmth of western Siberia and adjacent regions can be seen in all months except April, although the precise area affected varied from month to month. It was most notable in November (+11°C), January (+11°C) and February (+10°C). At many stations in western Siberia, the only warmer November-February average on record was 1943/44. Positive temperature departures also affected North America in many months, but the region affected shifted considerably at different times of the year.

Remarkably low temperatures have occurred frequently in the Davis Strait region in recent years and they have been accompanied by extreme sea-ice conditions. This was also a characteristic of the present study period. January to June 1984 were notably cold at western Greenland stations such as Egedesminde and Godthaab. The record coldness of the 1982/83 winter (the coldest since 1866) was broken during the 1983/84 season. From February 1982 to June 1984, every monthly mean temperature at Egedesminde and Godthaab has been below the appropriate 1961-1975 reference period mean!

Two marked transitions are apparent during the study period. First, a shift from warm, to cold, then back to warm conditions occurred over Siberia during spring 1984. The other major transition affected North America. During November/December, the region switched from being generally warm to notably cold. By January, warmth had become reestablished and, with regional variations (particularly cooling in the east), warmth characterised much of the remainder of the study period.

The lack of land in the Southern Hemisphere means that it is impossible to discuss large-scale patterns of temperature anomalies. Outside of Antarctica, anomalies in excess of two degrees C occurred over South America in September (negative), December (positive) and all months between May and August (negative) and over Australia in January (negative).

This work was supported by US Department of Energy contracts DE-AC02-79EV10098 and DE-AC02-81EV10739.

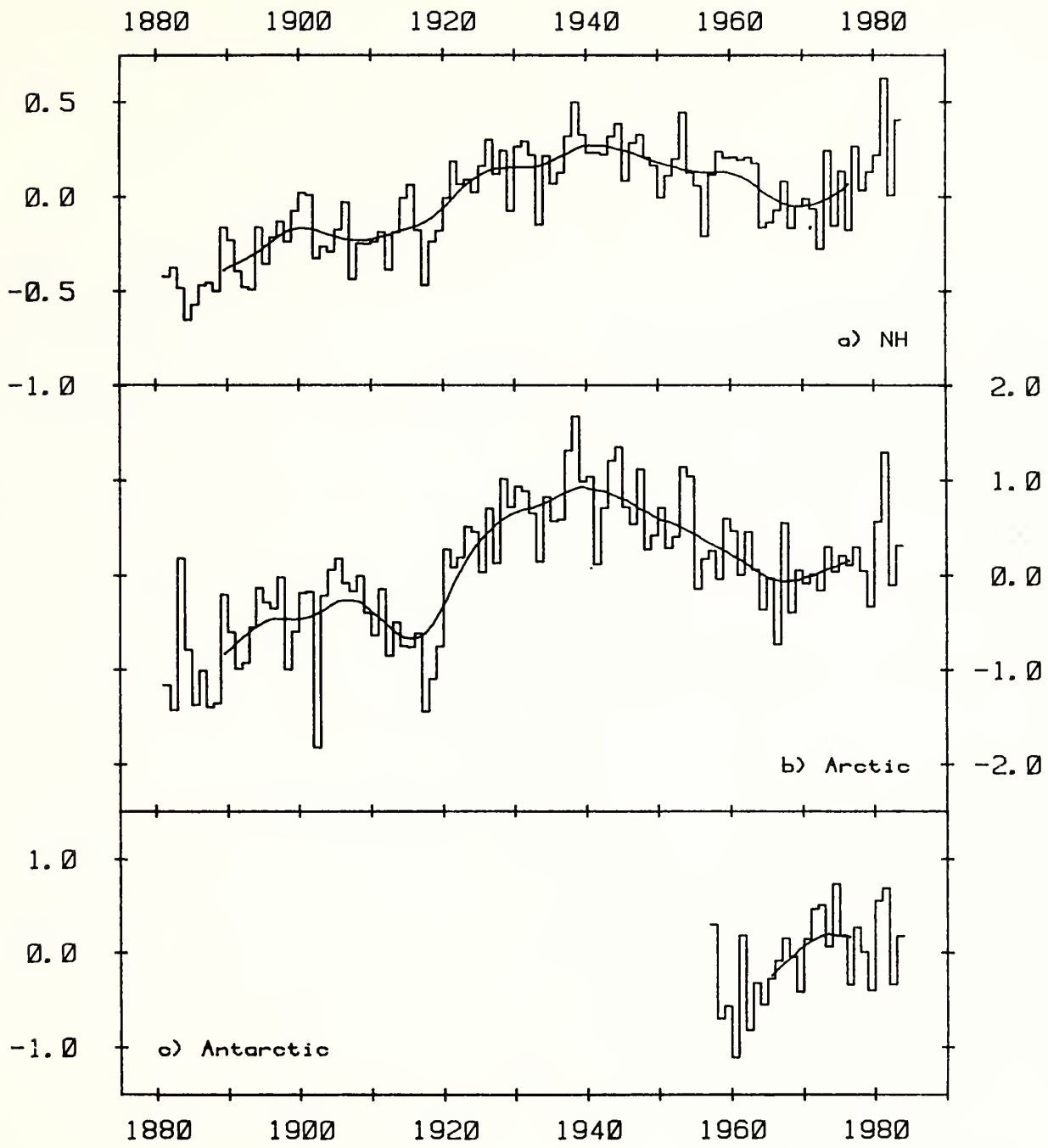

Figure 1: Annual surface air temperature for (a) the Northern Hemisphere (0-85° N); (b) Arctic regions (65-85°N); and (c) the Antarctic (65-90°S). Data are expressed as departures, in degrees Celsius, from the 1961-1975 reference period mean. The curve shows the data after application of a binomial filter designed to reduce the amplitude of fluctuations on time scales less than 20 years by 50% or more.

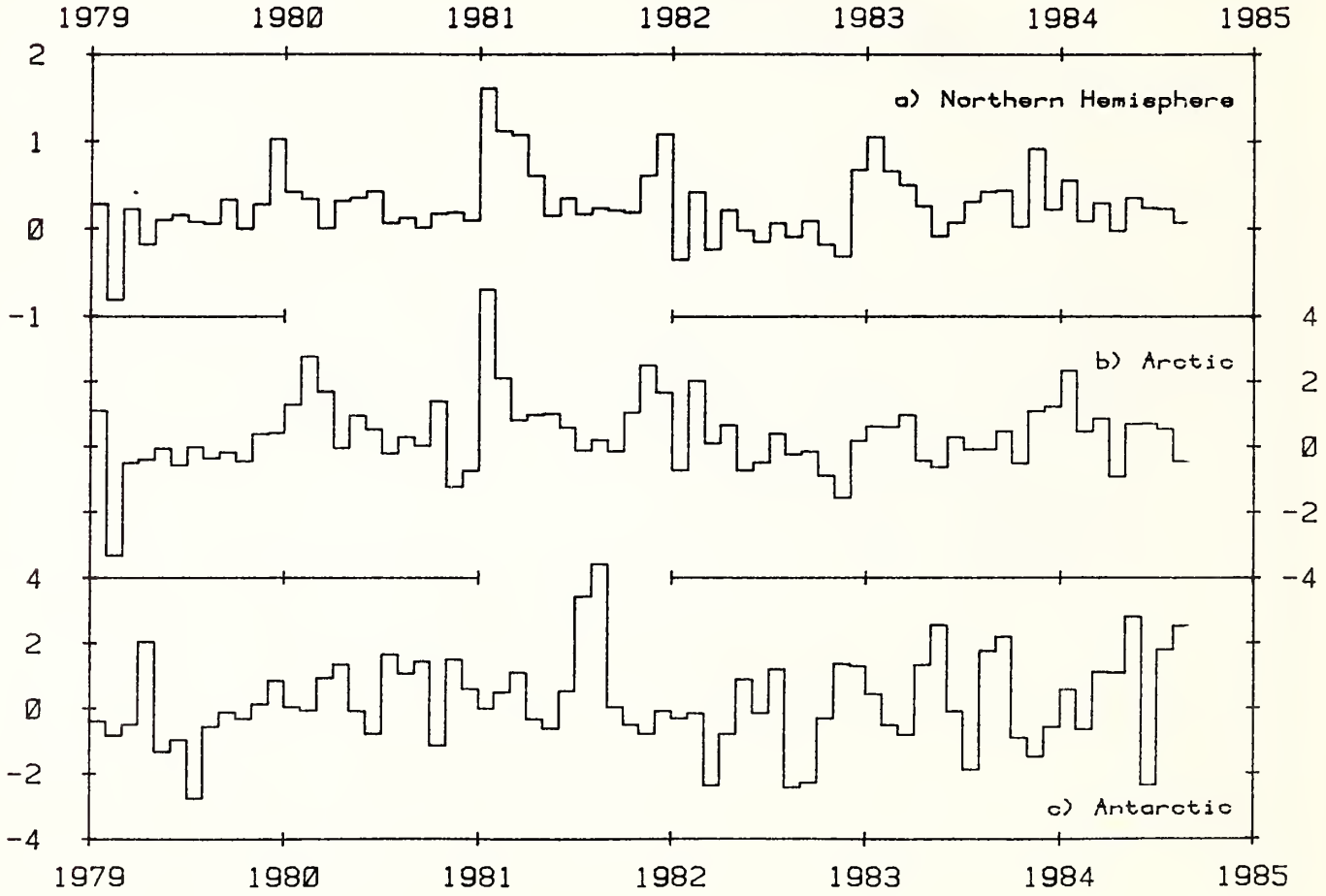

Figure 2: Monthly surface air temperature for the period January 1979 to August 1984: (a) the Northern Hemisphere; (b) Arctic regions; and (c) the Antarctic. Data are expressed as departures, in degrees Celsius, from the appropriate 1961-1975 reference period monthly mean.

Figure 3: Surface air temperature for September 1983. The data are expressed as departures, in degrees Celsius, from the mean for the reference period 1961-1975. Shading indicates departures greater than two degrees Celsius in magnitude.

Figure 4: Surface air temperature for October 1983. The data are expressed as departures, in degrees Celsius, from the mean for the reference period 1961-1975. Shading indicates departures greater than two degrees Celsius in magnitude.

Figure 5: Surface air temperature for November 1983. The data are expressed as departures, in degrees Celsius, from the mean for the reference period 1961-1975. Shading indicates departures greater than two degrees Celsius in magnitude over the Southern Hemisphere and four degrees Celsius over the Northern Hemisphere.

Figure 6: Surface air temperature for December 1983. The data are expressed as departures, in degrees Celsius, from the mean for the reference period 1961-1975. Shading indicates departures greater than two degrees Celsius in magnitude over the Southern Hemisphere and four degrees Celsius over the Northern Hemisphere.

Figure 7: Surface air temperature for January 1984. The data are expressed as departures, in degrees Celsius, from the mean for the reference period 1961-1975. Shading indicates departures greater than two degrees Celsius in magnitude over the Southern Hemisphere and four degrees Celsius over the Northern Hemisphere.

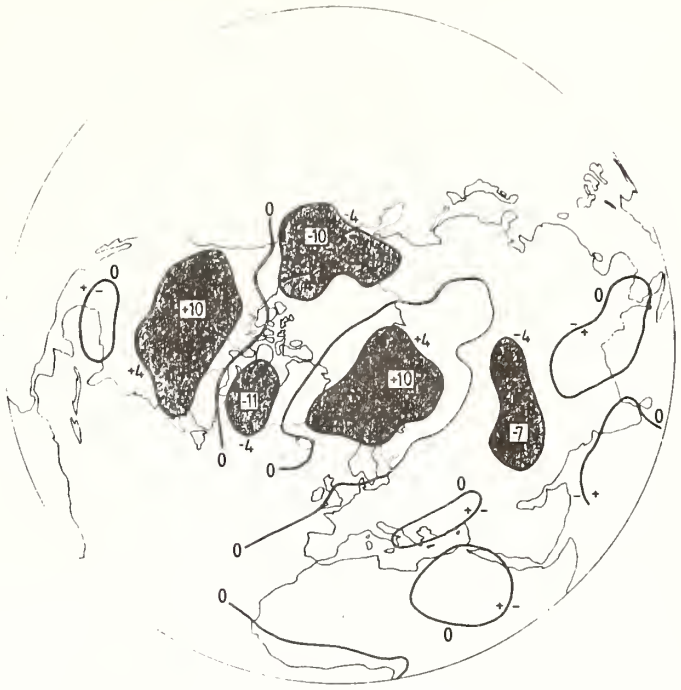

Figure 8: Surface air temperature for February 1984. The data are expressed as departures, in degrees Celsius, from the mean for the reference period 1961-1975. Shading indicates departures greater than two degrees Celsius in magnitude over the Southern Hemisphere and four degrees Celsius over the Northern Hemisphere.

Figure 9: Surface air temperature for March 1984. The data are expressed as departures, in degrees Celsius, from the mean for the reference period 1961-1975. Shading indicates departures greater than two degrees Celsius in magnitude over the Southern Hemisphere and four degrees Celsius over the Northern Hemisphere.

Figure 10: Surface air temperature for April 1984. The data are expressed as departures, in degrees Celsius, from the mean for the reference period 1961-1975. Shading indicates departures greater than two degrees Celsius in magnitude.

Figure 11: Surface air temperature for May 1984. The data are expressed as departures, in degrees Celsius, from the mean for the reference period 1961-1975. Shading indicates departures greater than two degrees Celsius in magnitude.

Figure 12: Surface air temperature for June 1984. The data are expressed as departures, in degrees Celsius, from the mean for the reference period 1961-1975. Shading indicates departures greater than two degrees Celsius in magnitude.

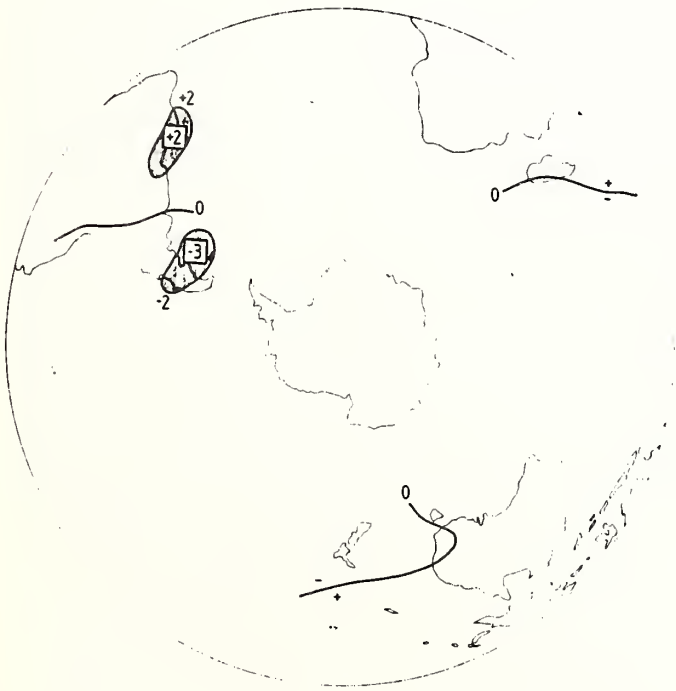

Figure 13: Surface air temperature for July 1984. The data are expressed as departures, in degrees Celsius, from the mean for the reference period 1961-1975. Shading indicates departures greater than two degrees Celsius in magnitude.

Figure 14: Surface air temperature for August 1984. The data are expressed as departures, in degrees Celsius, from the mean for the reference period 1961-1975. Shading indicates departures greater than two degrees Celsius in magnitude.

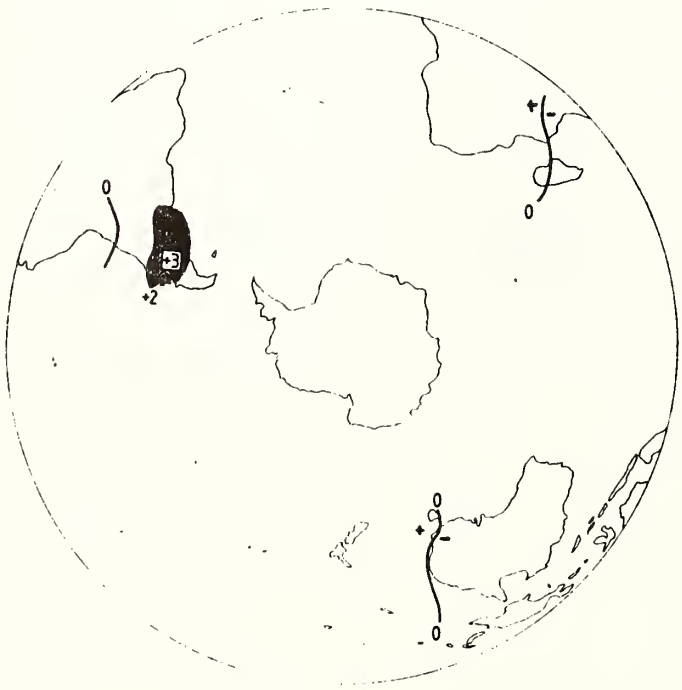

Monitoring Climate in Real Time: An Application of The Climate Anomaly Monitoring System (CAMS)

by

C. F. Ropelewski
Climate Analysis Center
National Meteorological Center
NWS/NOAA
Washington, D. C. 20233

I. Introduction

The purpose of this paper is to describe the structure and current operations of the Climate Anomaly Monitoring System (CAMS).

CAMS is the culmination of a series of Climate Analysis Center (CAC) projects which were designed to examine anomalies in surface parameters. The specific goal of CAMS is "to identify and describe in near real time the initiation and evolution of significant anomalies in temperature and precipitation over the land surface of the earth." Implicit in this definition is the concern with surface anomalies that have monthly to seasonal temporal scales and spatial scales that cover significant geographical areas.

Two rather stringent data requirements had to be met in order to satisfy these goals and make CAMS a reality. The first requirement was for high quality, reliable, "near real time" surface data. To meet this requirement CAMS drew heavily on the resources and previous developments of CAC's Analysis and Information Branch (AIB). The second requirement was for sufficiently long data records (i.e. 30 yrs. or more) to form reasonable statistics for identification and measurement of "anomalous conditions" at several locations around the world. To meet this second requirement CAMS drew heavily on historical records obtained from the National Center for Atmospheric Research (NCAR) and other sources.

II. Data

A. Real-time data.

The CAC summarizes daily surface weather data received over the Global Telecommunications System (GTS) into several data files; among these is a monthly summary file. This file contains monthly mean temperatures and precipitation amounts for several thousand stations globally. The number of stations received for a test period from Nov. 1982 to Mar. 1983 is given in Table I. Their typical distribution is given in Fig. 1.

While between 7400 and 7500 monthly station summaries are compiled, not all of these summaries are based on a complete month's data. The column labeled 90% in Table I shows the number of stations that had three days or less of missing data over the testing period. Since part of the CAMS philosophy is to work with only highly reliable data, strict limitations are placed on the amount of missing data. The definitions of the restrictions were tempered somewhat by the pragmatic requirement for having as much

global data as possible. For temperature data, no more than 3 daily mean temperatures may be missing from the monthly summary file for the station to be included in that month's CAMS data. For precipitation, only one day of missing data per month is permitted. CAMS data will thus at times, underestimate the actual precipitation amounts.

Shortly after the tenth of the month CLIMAT data for the previous month become available. The CLIMAT reports are monthly summaries compiled at the observing stations and transmitted over the GTS. Barring coding and transmission errors these are the same data that are published after several months lag in the "Monthly Climatic Data for the World". Typically over 900 CLIMAT reports are received monthly. These reports are used to supplement and replace data in the CAMS files. The CLIMAT reports fill in missing data in the CAMS files and replace the preliminary data in most cases.

The CLIMAT data at some stations are susceptible to errors in placing the decimal point. Therefore, before the CLIMAT values are accepted they are compared to the preliminary estimates. If a CLIMAT value falls within a prescribed range of the preliminary estimate, then the CLIMAT value is accepted; otherwise it is rejected. In the first year of CAMS operation no more then 1 or 2 CLIMAT reports failed to meet the criteria each month. A sample of the typical geographical distribution of CLIMAT reports, Fig. 2, shows that there are considerably fewer CLIMAT stations than the stations received over the GTS and used in CAMS. The number and density of CLIMAT stations would have to be increased dramatically to meet the minimum requirements for climate monitoring (Jenne, 1982) with CLIMAT data alone.

B. Historical data.

The need for historical data in the CAMS context is twofold. First, sufficiently long records are required in order to compute basic statistical quantities. These statistics form the framework within which CAMS is able to "identify and describe" surface anomalies. Second, the historical base is necessary for diagnostic comparisons of similar or related occurrences. Data from several sources are incorporated into the CAMS files but the most data, by far, came from the NCAR set provided by the CAMS stations with 30y or more of data are illustrated in Fig. 3.

III. CAMS Analysis

The thrust of the CAMS analysis scheme is to provide some statistical measure of the magnitudes of climate anomalies. Thus while actual data values or departures (e.g. Fig. 4) can be plotted and analyzed, the main emphasis has been on the display and analysis of temperature and precipitation anomalies in terms of their appropriate statistical distributions.

We assume that temperature departures are normally distributed, i.e. that they have a "Gaussian" distribution, and display temperature anomalies as percentiles of this distribution (e.g. Fig. 5). Anomalies and precipitation amounts are more difficult to characterize since precipitation amounts are not "normally" distributed. While definition of the correct distibution for precipitation may be subject to some debate, it is clear that some skewed distribution is best suited. In CAMS, we make use of the Gamma distribution because of its relative simplicity and ease of use. The parameters of the Gamma distribution are computed from the available data using

the maximum likelihood method (Thom, 1955). The parameters of the Gamma and the mean monthly precipitation amounts are computed for each month/season. The smaller the value of the "shape" parameter, the more skewed is the distribution. Values of this parameter of 50 or more imply that the distribution is near Gaussian. The second parameter of the Gamma distribution is a "scale" factor and carries the units (mm in CAMS). The parameter of the Gamma distribution is computed from the non-zero precipitation amounts in the historical record. In application of the Gamma distribution the number or zero's in the record must be considered. The number of months with precipitation observations of zero can be deduced from information in CAMS files, since the product of the shape and scale parameters is the mean of the non-zero precipitation values in the record, and the straight arithmetic mean and the length of record are available. An illustration of the practical use of the Gamma distribution may be found in Ropelewski and Jalickee (1983). Once the parameters of the distribution have been determined, the field of precipitation percentiles can be analyzed (e.g. Fig. 6).

IV. Summary

The data synthesis and analysis outlined here is an attempt to realistically characterize monthly and seasonal climate anomalies in real time. The system has several potential sources of uncertainty. The realiance on unvalidated data transmitted over the GTS will undoubtedly introduce some errors. The computation of the standard deviations for temperature and parameters of the Gamma distribution for precipitation based on only 30 years of data also introduces uncertainties. Finally the isopleth analyses, a modified Cressman scheme, may give rise to errors where the data density is low and or sharp gradients exist. While these limitations must be kept in mind there is little doubt that CAMS has the capability of providing a "first look" at surface climate anomalies on monthly to seasonal temporal scales and quantifying these anomalies in terms of their statistical significance.

References

Ropelewski C. F., and J. Jalickee, 1983: Estimating the Significance of Seasonal Precipitation Amounts Using Approximations of the Inverse Gamma Function over an Extended Range, Eighth Conference on Probability and Statistics in Atmospheric Sciences, November 16-18, 1983, Hot Springs, Arkansas. Preprint Volume, pp. 125-129.

Thom, H.C.S., 1955: A note on the Gamma distribution, Mon. Wea. Rev., 86, 117-122.

Jenne, R.L., 1982: "Planning Guidance for the World Climate Data System", WCP-19, 134pp. World Climate Program Office, WMO, Geneva, Switzerland.

TABLE I - SUMMARY OF STATIONS RECEIVED (MONTHLY)

Month	No. of Stations Received	90%
8211	7429	5279
12	7451	5149
83 1	7394	5224
2	7439	5234
3	7476	5250

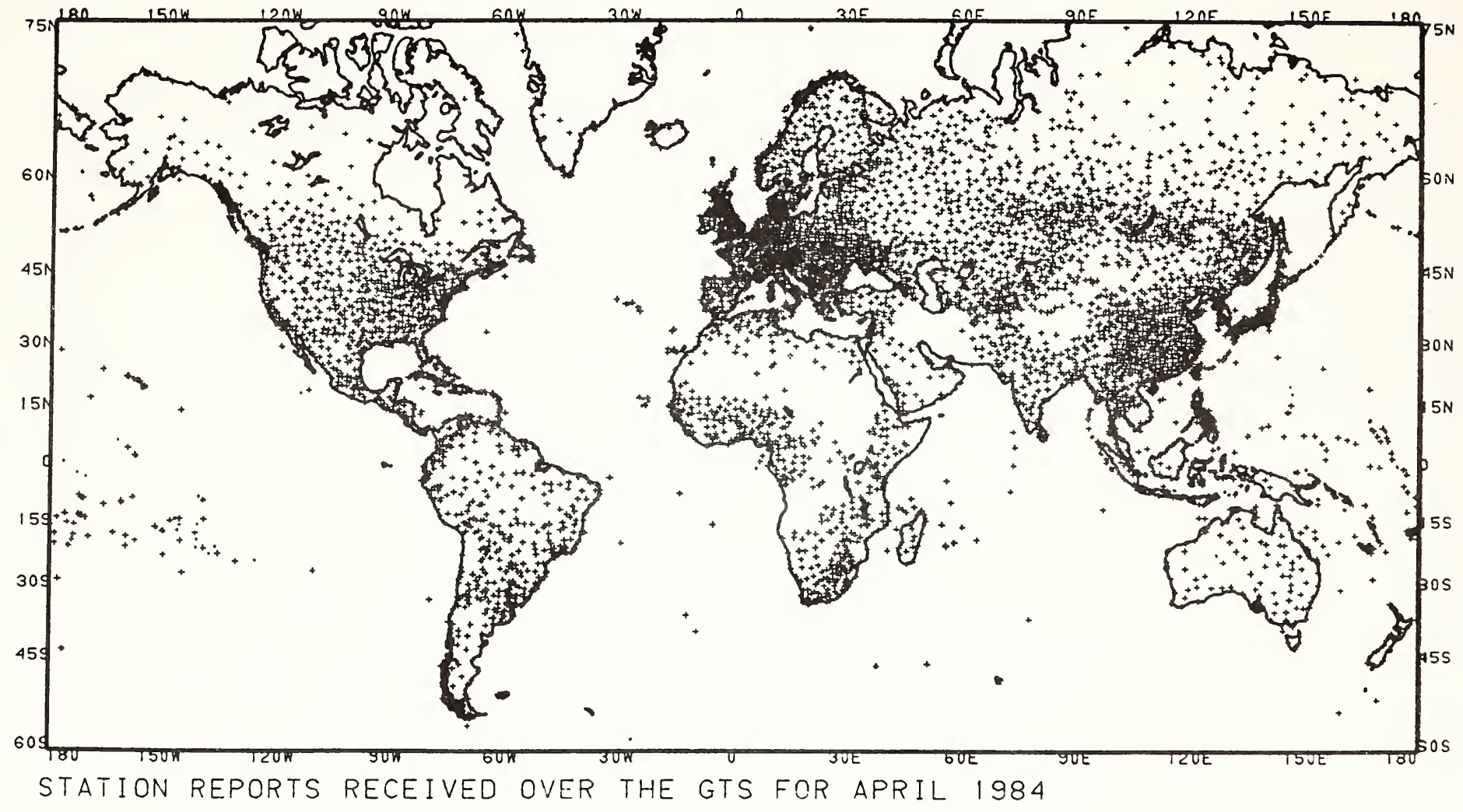

Fig. 1. The locations of GTS station reports received for April 1984 indicated by a "+".

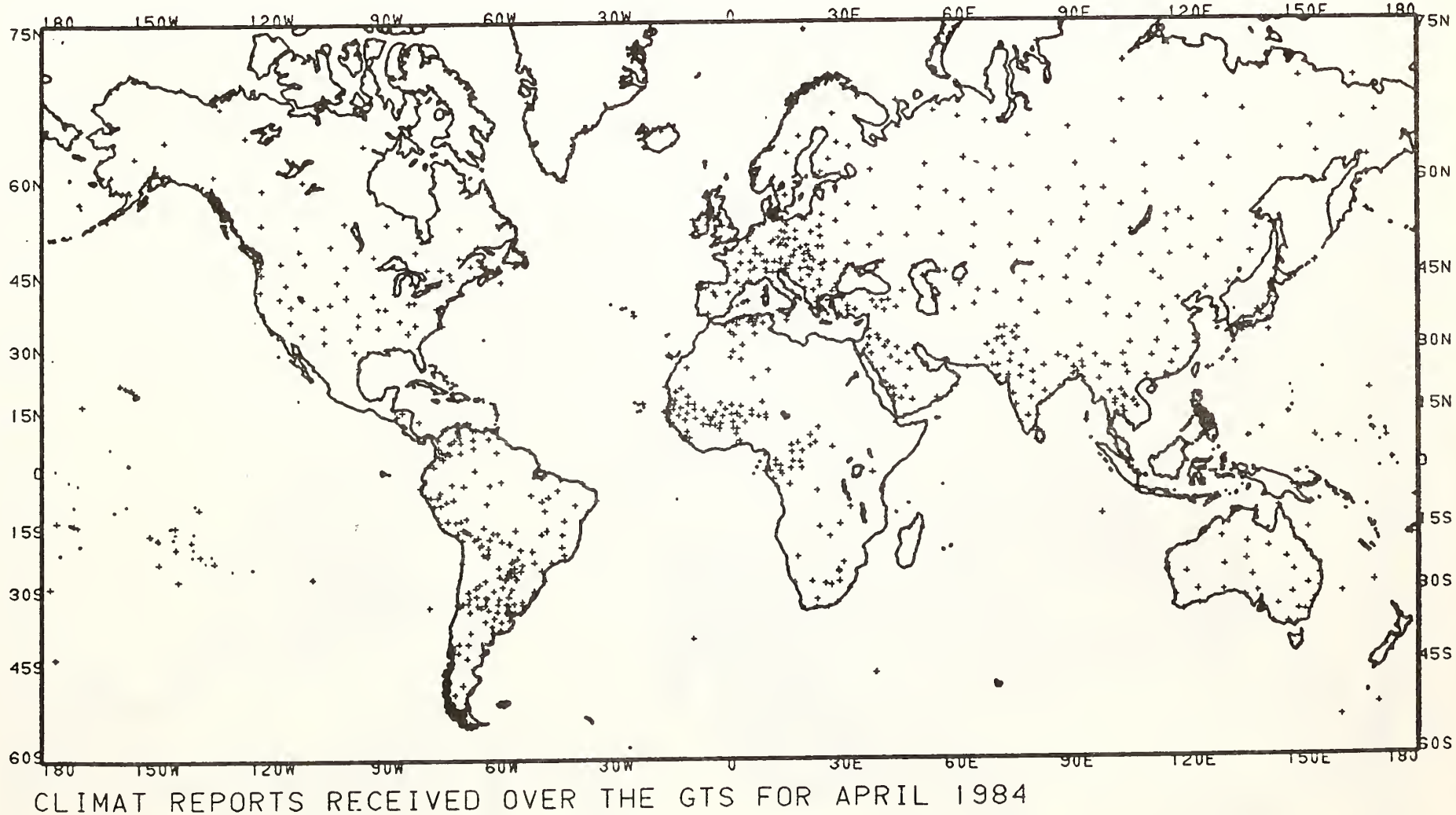

Fig. 2. The locations of CLIMAT reports received over the GTS for April, 1984.

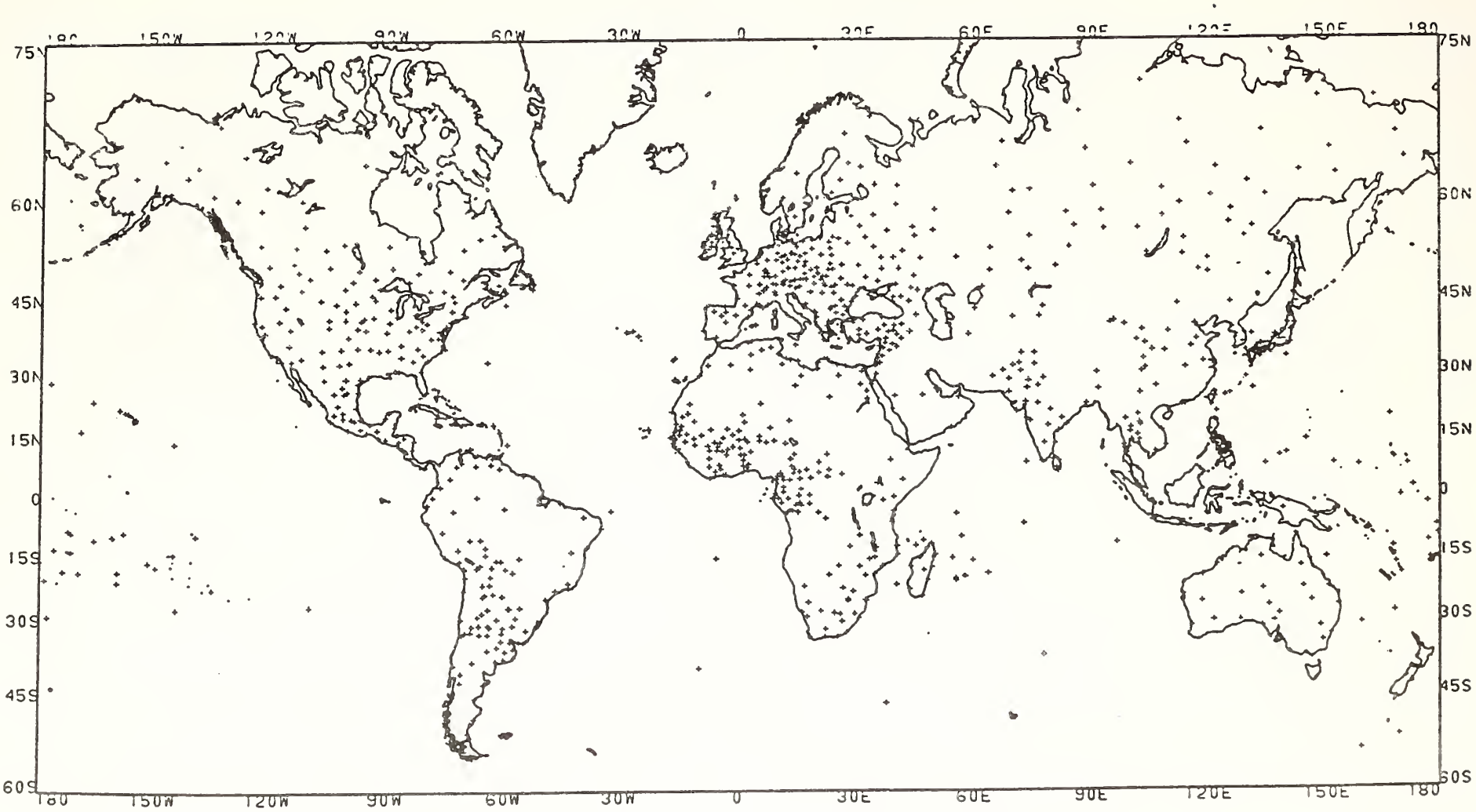

Fig. 3. The locations of CAMS stations with 30 years or more of data.

Fig. 4. Southern Hemisphere Surface Temperature Anomaly. Analysis based on station data over land and sea surface temperature (CAC analysis) over the water. The small plus sign indicates the location of data over land. Some ambiguities in the anomaly field are to be pected in coastal regions particularly where tight gradients exist. The solid line around the Antarctic represents the northern limit of sea ice. The dashed line around the Antarctic represents the 1973-82 base period mean sea ice position.

Fig. 5. Northern Hemisphere Surface Temperature Anomalies expressed as Percentiles of the Normal (Gaussian) Distribution. E.g., the "10 percentile" implies that the temperature was in the lowest ten percent of the historical record under the assumption that temperatures are normally distributed.

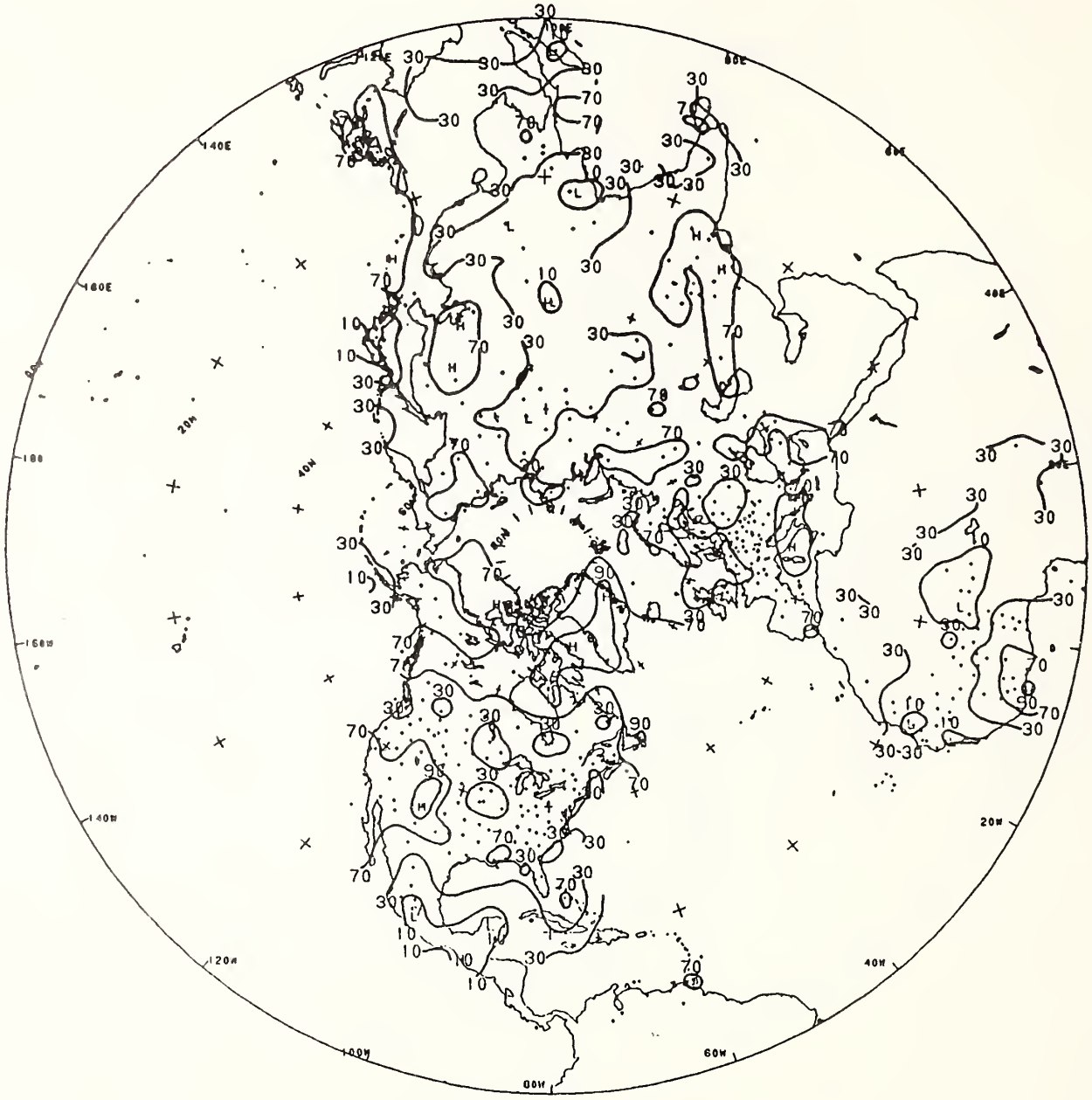

PRECIPITATION PERCENTILES AUGUST 1984

Fig. 6. Northern Hemisphere Precipitation Anomalies expressed as Percentiles of the Gamma Distribution. E.g., the "10 percentile" implies that the precipitation was in the lowest ten percent of the historical record under the assumption that the probability distribution of precipitation is described by a Gamma distribution function.

REVIEW OF THE CLIMATE OF FALL 1983 AND WINTER 1983-84

K. Bergman and R. Quiroz
Climate Analysis Center
NMC, NWS, NOAA Washington, D.C. 20233

Introduction:

This review covers the major climatic events of the period September 1983 thru February 1984. Further details are given by Bergman (1984, hereafter referred to as B) for September through November, 1983, and by Quiroz (1984, hereafter referred to as Q) for December 1983 through February 1984. The first part of this summary covers tropical circulation and climatic statistics, with the main emphasis on the tropical Pacific area. We note especially the aftermath of the record El Nino event of 1982-3. In the second part, we discuss the Northern Hemisphere circulation and its climatic effects, and in the last part we focus on conditions in the U.S., where the winter season was characterized by severe cold and wide swings in temperature.

Tropical Circulation and Climate:

Recent trends in three significant equatorial Pacific indicators monitored by the CAC are shown in Fig. 1. The top graph shows that the SOI as defined by Tahiti SLP minus Darwin SLP had returned to near-normal values by September after the marked negative departure of early 1983. Similarly, the 200 mb westerly wind anomaly averaged over an equatorial strip shows slightly positive values after the marked negative (easterly) anomalous winds of early 1983. Finally, outgoing long-wave radiation anomalies in the equatorial mid-Pacific switched from negative values (above normal precipitation) to positive values (below normal precipitation) in September. All these graphs indicate that the marked negative ENSO phase ended around September, to be suceeded by a weakly positive phase.

A Hovmoller diagram (Fig. 2) of equatorial sea surface temperature (SST) anomalies shows a return to near-normal conditions by the end of the period. Note that anomalously warm temperatures disappeared first from the central Pacific and lingered longest along the west coast of South America, in marked contrast to the history of other recent El Nino events. A similar Hovmoller diagram (Fig. 3) for the anomalous zonal component of the 850 mb wind shows a rapid changeover from anomalous westerly flow to anomalous easterly flow during summer 1983 in the central Pacific. During fall and winter, the trade winds became increasingly strong in the central part of the Pacific. By early spring 1984, the easterly anomaly at 160E was nearly as strong as the westerly anomaly at 160W in winter-spring of 1983. The diagram suggests two other features:

(a) A rough periodicity of about one year between changeovers.

(b) A slow progression of major anomalies from west to east across the Pacific.

Since less than two complete "cycles" are shown, these features are highly speculative.

The stronger than normal trades were associated with development of colder than normal SST's across parts of the central Pacific. By November 1983 (See B, Fig. 6), slight cold anomalies were present along the equator in the eastern Pacific, while a belt of warmer-than-normal temperatures appeared at about 10S latitude. During the fall, temperatures 1 to 2C above normal occurred along part of the west coast of North America. This phenomenon, referred to as the "little El-Nino", was not obviously linked to events that occurred farther south. By February 1984 (See Q, Fig. 3b) a marked cold SST anomaly had developed in the central Pacific near the date-line. Both satellite and ship data confirm this as a real feature, probably a result of the anomalously strong easterlies centered at 160E and the creation of a region of anomalous divergence to the east of this wind maximum.

A Hovmoller diagram (Fig. 4) of anomalous outgoing longwave radiation (OLR) shows a reversal from the dry west--wet east pattern of early 1983 to one of dry east of 140E but wet west of 140E by winter 1983-4. Compare this diagram with Figs. 2 and 3. The OLR anomaly maps of fall and winter 1983-4 (See B, Fig. 12 and Q, Fig. 5B) show the development of this pattern. During the fall, a marked negative anomaly existed off the west coast of Central America and was associated with above-normal tropical cyclone development. In both fall and winter, a negative anomaly extended from the extreme western Pacific westward to the northern Indian Ocean, where precipitation in Sri Lanka, Malaysia, and much of Indonesia was well above normal.

A quick look at the high tropospheric flow, as shown by 200 mb stream-function analyses (Fig. 5) indicates the relatively normal pattern of winter. The highly anomalous nature of the 1982-3 winter compared to 1983-4 is also shown by the departure from normal of mean tropospheric zonal kinetic energy for the Northern Hemisphere (Fig. 6).

Northern Hemisphere Circulation:

The 700 mb mean heights and departures from normal for fall 1983 are shown in Fig. 7a. The most marked feature is the negative anomaly (-91 meters) just east of Finland. This anomaly is nearly -2.5 standard deviations (sigmas). Other seasonal anomalies were comparatively weak. Note, however, the positive anomalies and southerly anomalous flow over much of Siberia. A several-month period of persistent above-normal temperatures over much of Siberia began in October.

The temperature percentiles for Fall 1983 (Fig. 7b) show temperatures exceeding the 90th percentile over much of eastern Siberia. In the United States Fall was above normal nearly everywhere, as expected with the low-amplitude mean pattern across the country. Note the very warm temperatures in Southern and Baja California in connection with the previously mentioned above normal (by 1 to 2 C) SST's along the coast.

The corresponding precipitation map (Fig. 7c) shows a comparatively wet autumn for North America and a comparatively dry one in central Europe. Note the low percentiles in the Sahel region of northwest Africa, where the southwest monsoon retreated earlier than normal. In India, a close-to-normal summer monsoon season ended about on schedule.

The 700 mb chart for winter Fig. 8a) shows the following main features:

(a) A negative anomaly in the north-central Pacific, but not nearly so marked as in winter 1982-3.
(b) A very fast zonal flow across the north-central Atlantic sandwiched between anomalies of +2.7 and -2.2 standard deviations, resulting in the strongest mean jet-level winds at 50-60 N in at least the last 10 years.
(c) An anomaly of +2.9 standard deviations centered north of the Caspian Sea. Positive anomalies covered most of the Soviet Union and led to well-above normal winter temperatures there.
(d) A moderately stronger ridge-and-trough pattern over North America than normal. The effects of this pattern on the climate of the United States are discussed in the next section.

The temperature map (Fig. 8b) for winter shows:

(a) A large warm area greater than the 90th percentile in western Siberia.
(b) Colder than normal temperatures to the south over Pakistan, Tibet, etc. This combination of anomalies was associated with the occurrence of a blocking pattern during part of the season.
(c) Much of the United States below normal, with the south-central states colder than the 10th percentile.
(d) Much above normal temperatures continuing along the California coast.

The precipitation map (Fig. 8c) shows:

(a) Very wet conditions in Northern Europe associated with the frequent passage of storms off the North Atlantic in the fast zonal flow.
(b) An unusual amount of winter rain in penninsular India.
(c) Relatively close-to-normal precipitation across the United States, although very dry conditions developed in February from California through the Southwest to Texas.

Winter in the United States:

The atmospheric circulation and resulting climatic conditions in the United States varied markedly during the course of the winter season. Extreme cold in December over the central part of the country gave way to comparative warmth in February (Fig. 9). The mean 700 mb chart for December (Fig. 11a) shows a high latitude blocking pattern with a geopotential height anomaly of +3.1 standard deviations over Alaska coupled with a strong flow from the Arctic southward into the central United States. (See the paper by R. Quiroz in this volume on the evolution of this blocking pattern.) December 1983 was the coldest month of that name for the 48 contiguous states on an area-weighted basis in at least the last 53 years. It averaged only 1.9C warmer than the coldest month of record (January 1979) in the 53 year period of comparative records. Thirty-nine U.S. cities, located mostly in the Great Plains and Mississippi Valley, experienced their coldest December of record, with some records going back more than 100 years.

After a mixed regime in January that featured zonal circulation early in the month but a resumption of blocking near the West Coast around the middle of the month, a markedly zonal flow prevailed across the continent in February (Fig. 11b) Note that a negative 700 mb height anomaly has replaced the December positive anomaly over Alaska and the Gulf of Alaska. February proved to be the seventh warmest such month in the last 54 years of records. The cold pocket in the northern Great Basin (Fig. 9d) was associated with the presence of stagnant air masses over a continuous snow cover, leading to marked radiational cooling. Winter temperatures in this region are often inversely correlated with surface temperatures elsewhere in the western states.

Normalized snow cover in North America (Fig. 10) shows a trend that parallels the mean temperatures, with a marked decrease in coverage from December to February. However, any cause-and-effect relationships are problematical. The cold December temperatures in the southern United States were clearly advectional, since significant snow cover did not extend much south of Kansas. However, the presence of a greater-than-normal snow cover farther north may have contributed to the extreme severity of the late December cold wave.

Conclusion:

The September 1983 through February 1984 period was characterized by two noteworthy climatic events. One was the end of the strong El Nino event that dominated early 1983. By February 1984, some key equatorial Pacific inidcators suggested that "anti-El Nino" conditions had in fact developed. The 850 mb winds and the precipitation distribution evolved into patterns almost exactly out-of-phase with conditions in early 1983.

The other noteworthy climatic event was the development of frequent blocking in the Northern Hemispheric winter circulation, resulting in highly anomalous winter temperatures in both North America and Eurasia for at least part of the season. In December 1983, negative temperature anomalies in the United States were of record magnitudes.

Acknowledgements:

The tropical climatic analyses were provided by members of the Diagnostics Branch, CAC, and the Northern Hemispheric circulation charts by Prediction Branch, CAC. Charts showing Northern Hemispheric percentiles of temperature and precipitation are courtesy of C. Ropelewski, CAC. (See his article in this volume.) Ropelewski also contributed Fig. 9 and the statistics on the temperatures of winter months compared to previous winters. Fig. 6 was provided by A. J. Miller of CAC.

References:

Bergman, K. H., 1984: The climate of autumn 1983 - Featuring the conclusion of a major El Nino event. Monthly Weather Review, 112, pp. 1441-1456.

Quiroz, R. S., 1984: The climate of the 1983-4 winter - A season of strong blocking and severe cold in North America. Monthly Weather Review, 112, pp. 1894-1912.

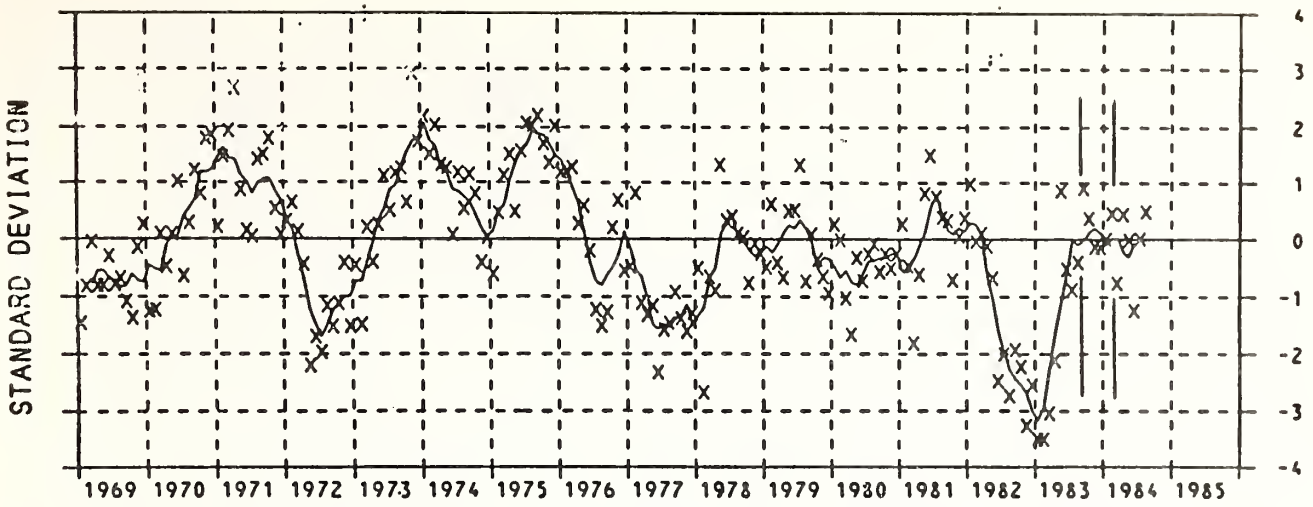

FIG. 1a Five-month running mean of the difference between the standardized sea level pressure anomalies at Tahiti and Darwin (Tahiti-Darwin). Values are standardized by the standard deviation of the appropriate monthly mean. Crosses are individual monthly means.

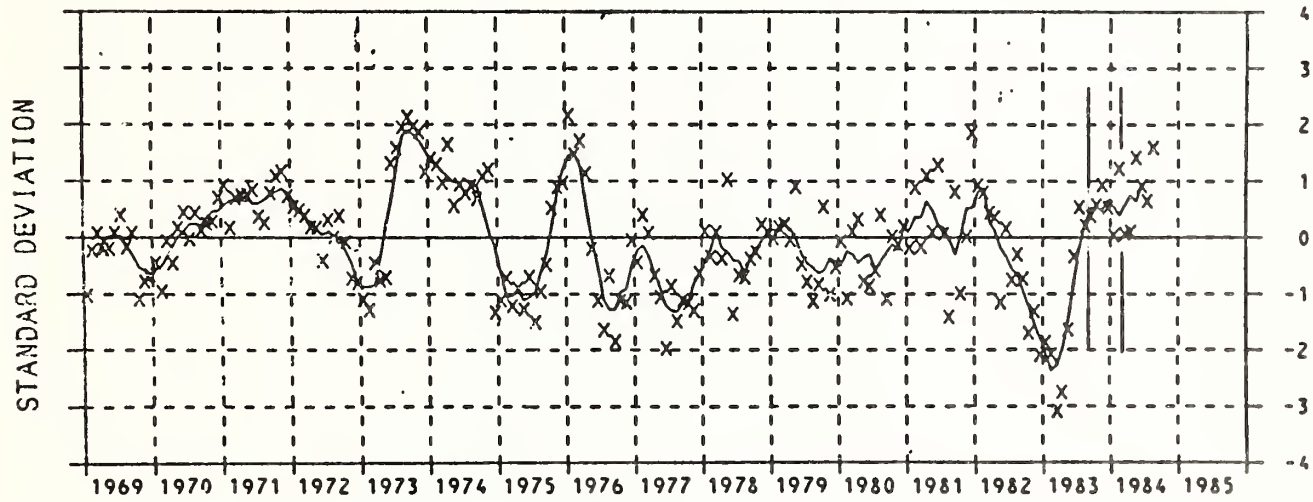

FIG. 1b Five month running mean of the standardized monthly 200 mb westerly wind anomaly averaged over the area 5°N-5°S, 165°W-110°W. Values are standardized by the standard deviation of the appropriate monthly mean. Crosses are individual monthly means.

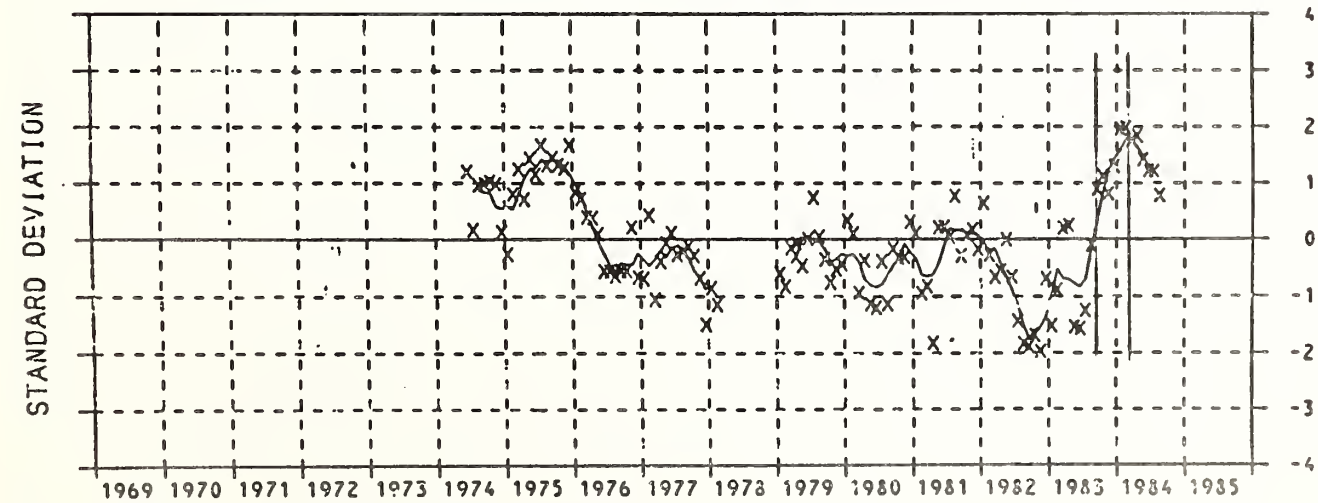

FIG. 1c As in Fig. 1b, except for the standardized monthly anomaly in outgoing longwave radiation over the area 5°N-5°S, 160°E-160°W.

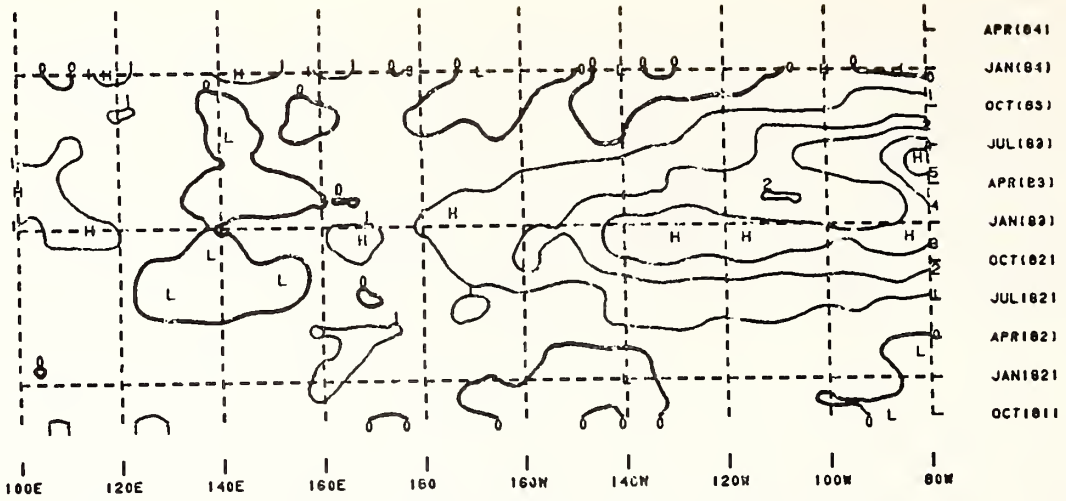

FIG. 2 SST ANOMALY (5N-5S)

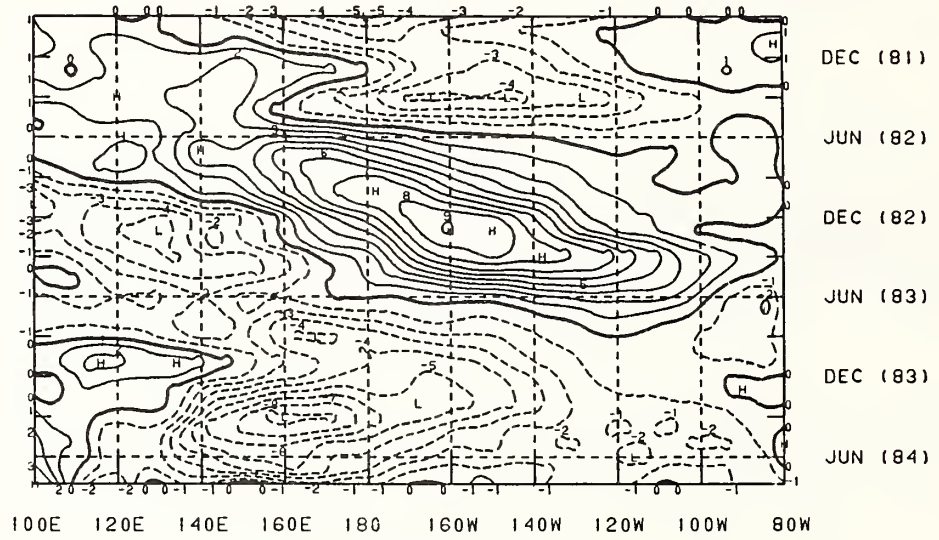

FIG. 3

(5N-5S) 850 MB U COMP WIND ANOMALY

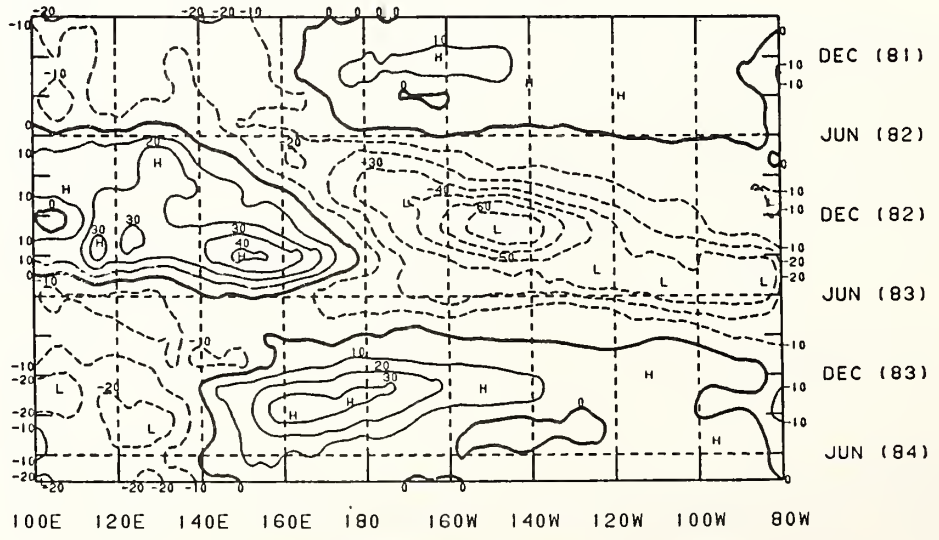

FIG. 4

(5N-5S) ANOMALY OLR

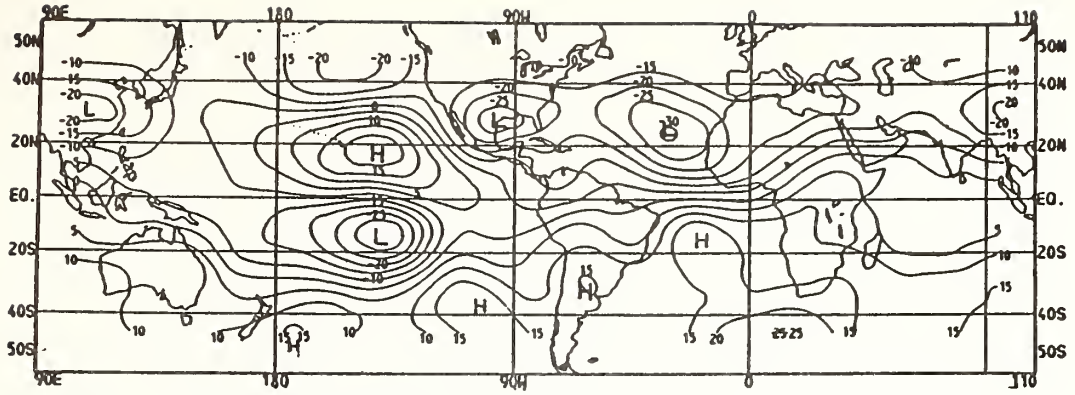

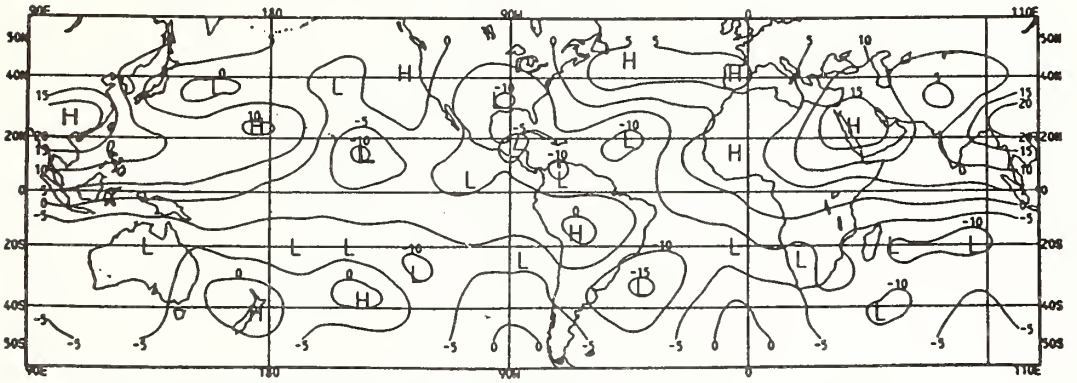

FIG. 5

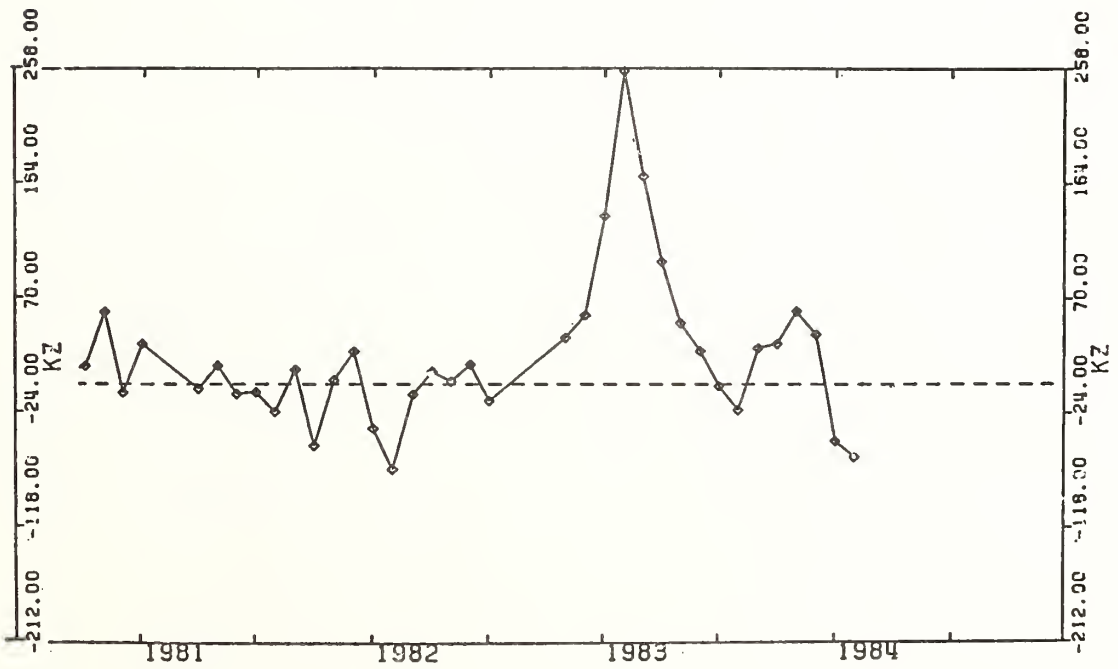

MEAN ZONAL KINETIC ENERGY, SURFACE TO 100 MB

FIG. 6

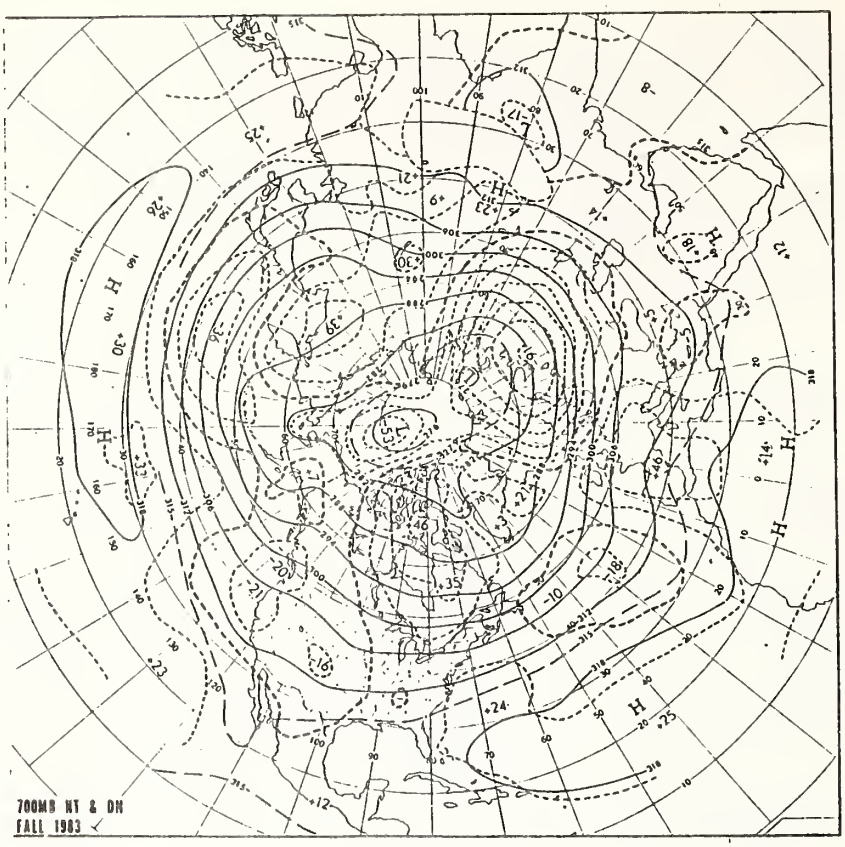

FIG. 7a

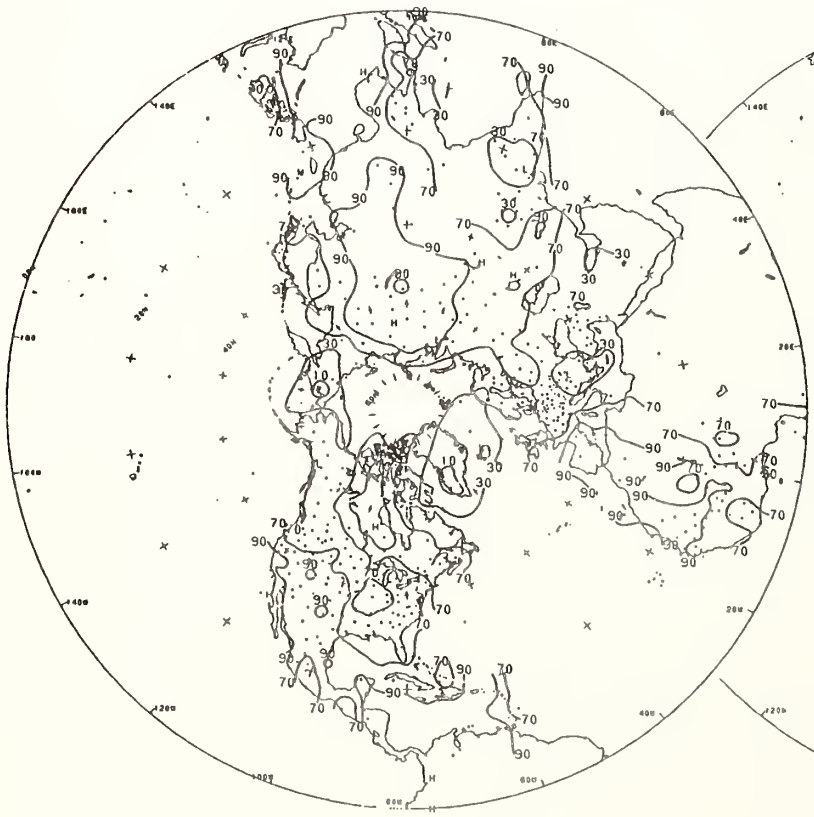

TEMPERATURE PERCENTILES FALL 1983

FIG. 7b

PRECIPITATION PERCENTILES FALL 1983

FIG. 7c

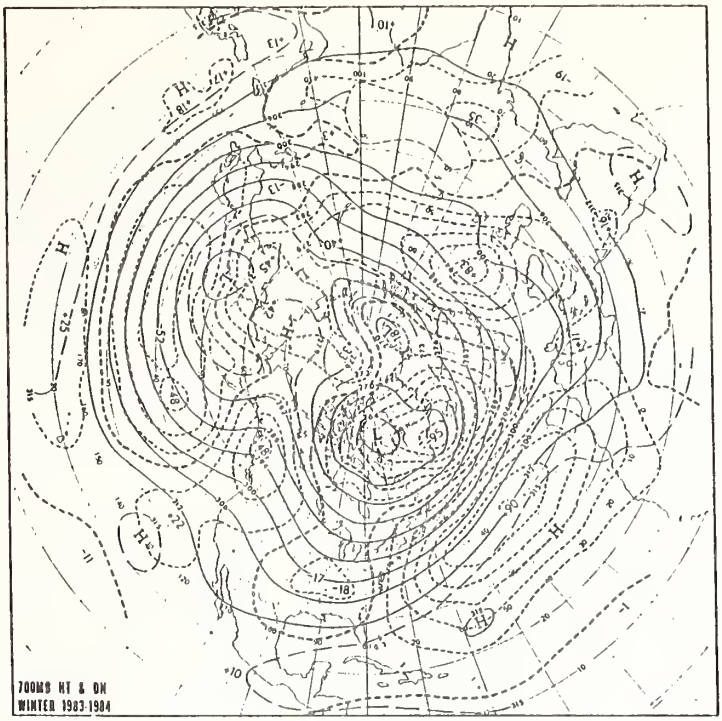

FIG. 8a

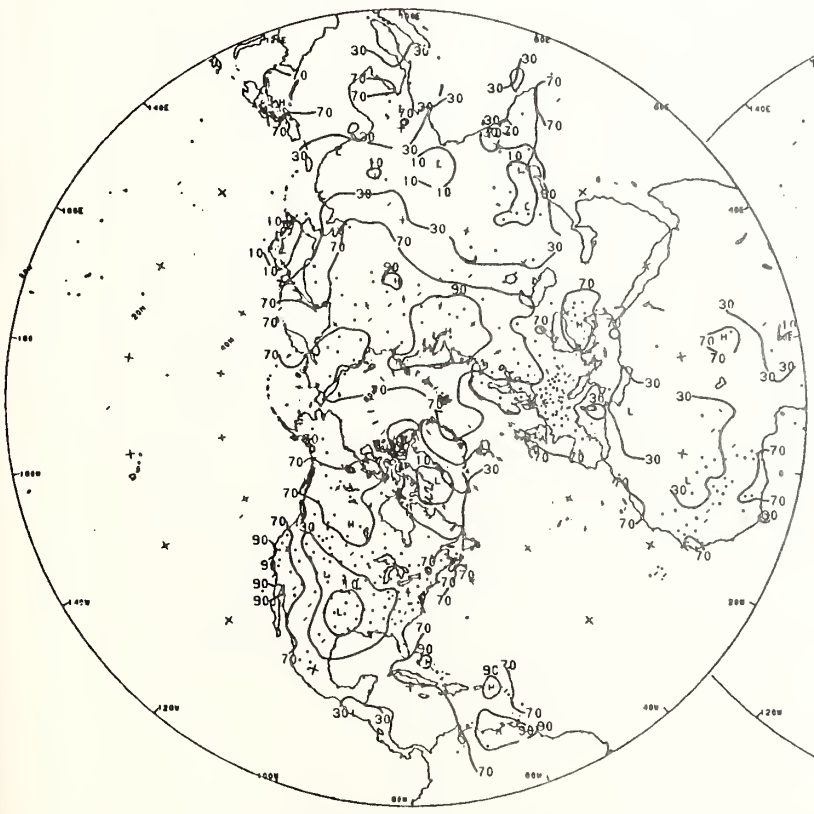

TEMPERATURE PERCENTILES WINTER 1983-1984

FIG. 8b

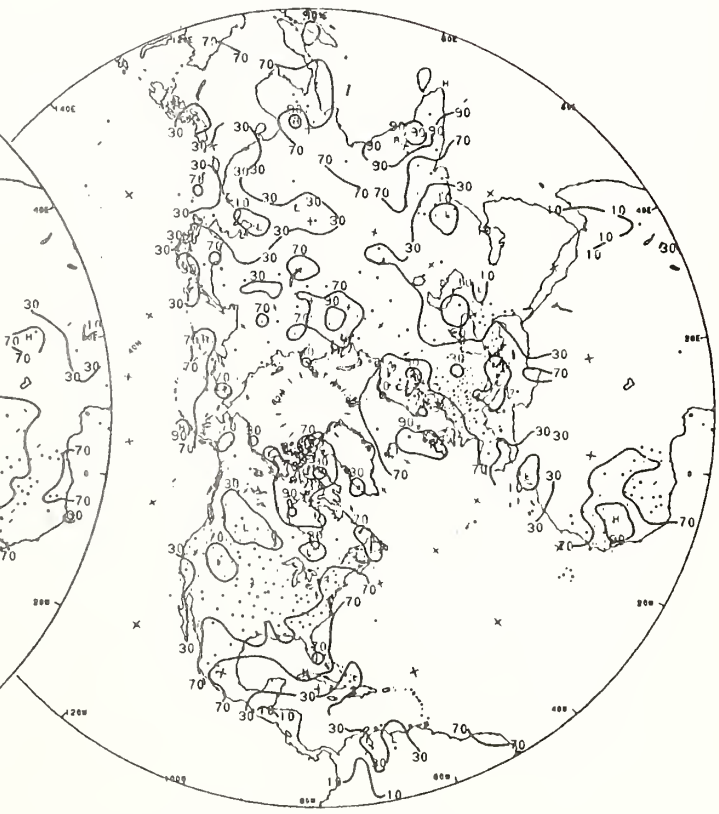

PRECIPITATION PERCENTILES WINTER 1983-1984

FIG. 8c

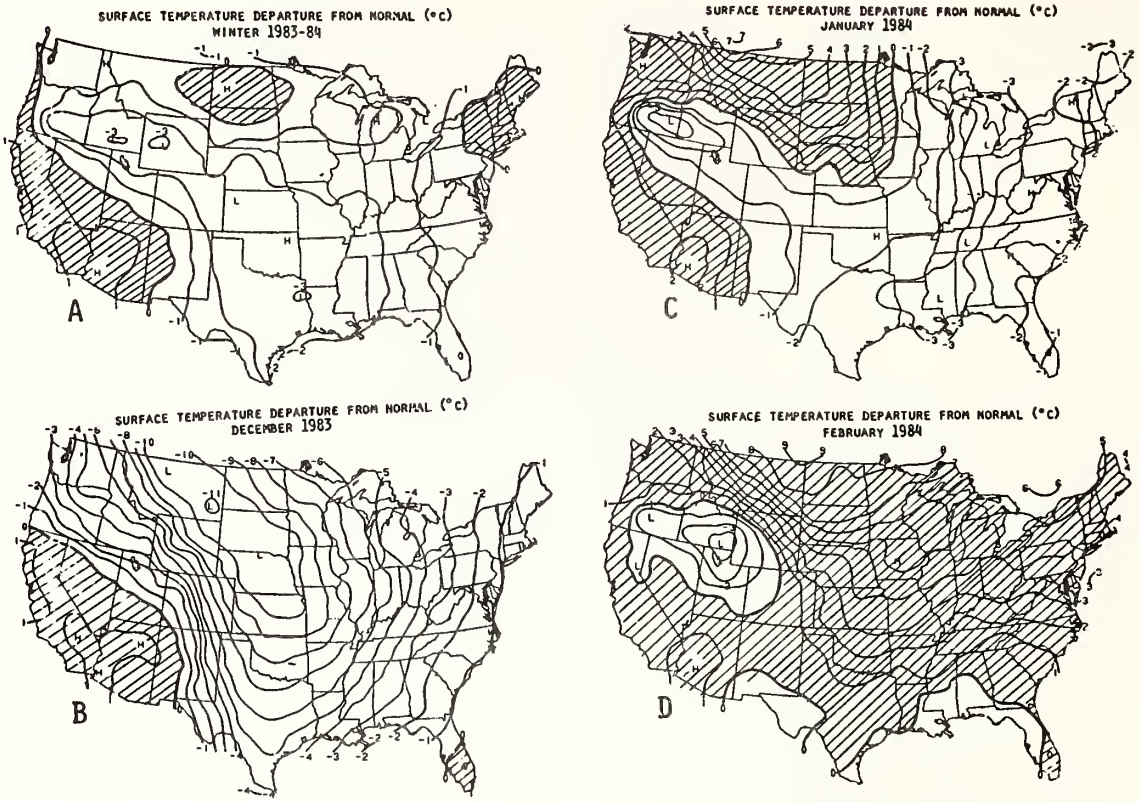
SURFACE TEMPERATURE DEPARTURE FROM NORMAL (°C)
WINTER 1983-84
A
SURFACE TEMPERATURE DEPARTURE FROM NORMAL (°C)
JANUARY 1984
C
SURFACE TEMPERATURE DEPARTURE FROM NORMAL (°C)
DECEMBER 1983
B
SURFACE TEMPERATURE DEPARTURE FROM NORMAL (°C)
FEBRUARY 1984
D

FIG. 9

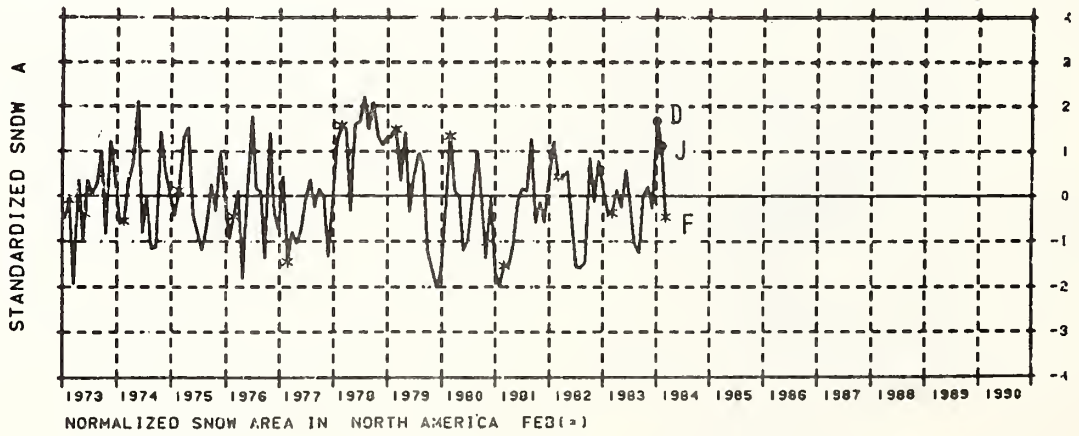
STANDARDIZED SNOW A
D
J
F
1973 1974 1975 1976 1977 1978 1979 1980 1981 1982 1983 1984 1985 1986 1987 1988 1989 1990
NORMALIZED SNOW AREA IN NORTH AMERICA FEB(a)

FIG. 10

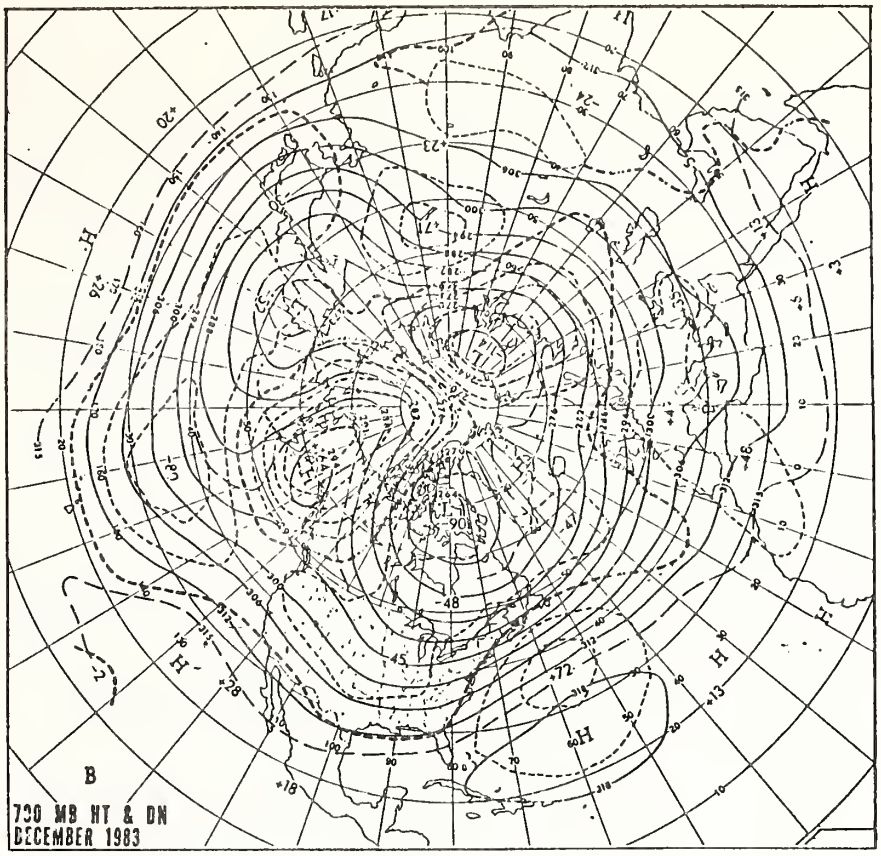

FIG. 11a

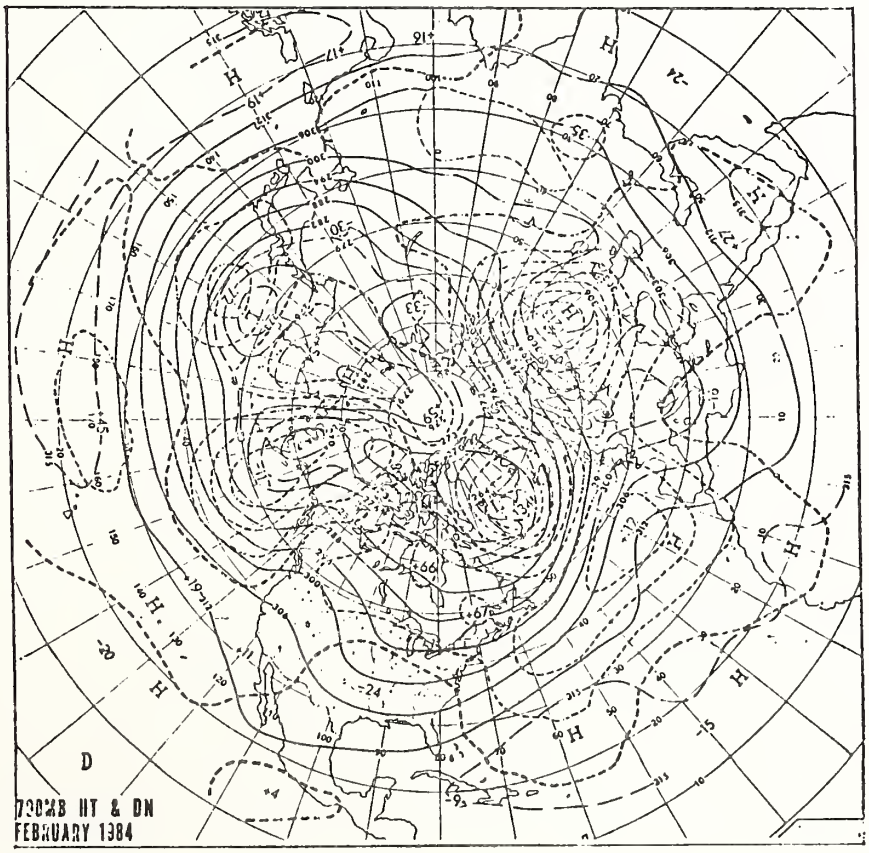

FIG. 11b

Some Empirical Evidence for the Influence of Snow Cover on Temperature and Precipitation

Jerome Namias
Scripps Institution of Oceanography
University of California San Diego
La Jolla, California 92093

The essence of this paper is that the thermodynamic effects of variable snow cover during a given winter can alter temperature anomalies and precipitation patterns over the contiguous United States. This background acts to modulate conditions imposed by the concomitant general circulation which deploys different air masses with variable static stability. The lower tropospheric stability is responsive to the presence or absence of snow which effects the albedo and sensible heat exchange. In turn, stability alterations affect the ease with which clouds and precipitation are formed, again feeding back to alter back radiation. The winter months of 1983-'84 offer some remarkable illustrations of these effects because December and January were characterized by persistent and recurrent snows over much of the eastern half of the country, while an abrupt change from a low to a high index regime at the end of January led to dramatic snow melt over this area.

The observed changes in temperature anomaly and snow pattern are shown in Figure 1 by the middle and lower sets of charts. The temperature pattern change from January to February was responsible for the appreciable diminution in mid-western snow cover. This change in snow cover probably had a substantial effect in modulating the circulation influences on both surface temperatures and precipitation fields. The precipitation fields for January and February are shown by tercile classes in Figure 2 and by amounts in Figure 4. Obviously January was abnormally cool and dry over the Midwest while February was warm and wet.

The influence of the snow, or lack of it, on the temperature of the overlying air is suggested by Figure 1. This shows (lower panel) the dramatic snow melt in February after a snow-laden January over much of the Midwest, and indicates the abnormality by comparison with the median position of the snow line (broken). The observed temperature anomalies (middle) show remarkable warming over much of the eastern half of the country which qualitatively suggests

some association with the reduction in snow. However, thanks to Klein's work on specification of temperature from 700mb circulation it is now possbile to compute the probable temperature anomaly patterns associated with observed mean circulations. The performance of these specification equations is in general very good, so that large errors may be attributed to factors not included in the equations, in this case a boundary influence such as snow cover. Thus, while the specifications made for February (top right of Figure 1) were quite good (about average as these specifications go) the one made for January (upper top left panel) was poor in the East, failing to estimate the below normal temperatures over much of the area by as much as two tercile classes. This failure suggests that the extensive eastern snow cover in January inhibited the warming which the circulation was attempting to impose over the eastern region. The errors of the specifications (deg. F.) are shown in Figure 3 where the values were large in January but small in February (lower panel).

The nature of the warming in February as a partial response to the mean circulation is clarified by Figures 5,6 and 7. Here the very cold December and the heavy snows are indicated by the anomalously strong trough over central U.S. and the exceptionally strong ridge over Alaska. This ridge recurrently deployed Arctic air into the trough which in turn contributed to frequent and persistent snows. By January the Alaskan ridge had disappeared (Figure 7) and much of U.S. was flooded with mild Pacific air rather than cold Arctic air. Consequently anomalous warming took place in the Northern Plains, a warming which often spreads eastward through the Midwest. Some of this sequence of events is shown by the charts in Figure 1 (central panels). The failure of the warming to proceed eastward was probably due to the presence of the snow cover described earlier (Figure 1, lowest panel). However, after much of the snow melted, beginning the first week in February, the warming apparently proceeded in its normal fashion since the agreement between specified and observed patterns was very good in February (top and middle right panels of Figure 1).

Upper air characteristics of these developments are shown in Figures 8 and 9, from which it is seen that much of the temperature change between months was confined to the layer of air below 850mb with little change above this level - another fact which hints of the effects of snow cover. Note the stronger stability of the lower air layer in December and January when snow was dominant over the Midwest where these soundings were taken. The general conditions of stability indicated in Figures 8 and 9 were coherent over a large area as demonstrated in the panels for various levels depicted in Figure 10. It is concluded from the above material that the January snow field had a strong influence over a large area of the eastern half of the

United states, keeping the near surface air cold but not materially influencing the layers above 850mb. December was a month of great weekly change at the beginning and middle of the month when conditions favored the development of snow producing storms. We shall now discuss possible effects on the precipitations fields.

INFLUENCE ON PRECIPITATION FIELDS

The United States precipitation patterns for January and February were strikingly different as shown by Figure 2 and also by Figure 4. The large area of dryness over the Midwest in January gave way to moderate or heavy precipitation in February. In terms of departures from normal or actual amounts (Figure 4), February was appreciably wetter than January, having more than twice as much precipitation than January in many Midwest areas despite the lesser number of days in February.

It is of course possible that this difference in precipitation between the two months can be entirely accounted for by the anomalies of the circulation; This might be tested by statistical means, such as Klein's specification methods were designed to do for temperature patterns. Unfortunately, such equations are not yet available, so that at present only experienced synoptic judgement can be used to translate the observed circulations into associated precipitation patterns. Thus, January (Figure 6) might be expected to be dryer than February (Figure 7) but this author does not believe that the extensive and extreme area of dryness of January can be adequately explained by the circulation alone. On the other hand, a wet Midwest would be suggested by the upper air mean trough observed in February. At any rate it is possible if not probable that important clues to this pattern difference can be found in some of the elements used to explain the temperature pattern differences - especially the snow cover effects on static stability. It will be remembered that the static stability in the layers below 850mb over the Midwest was very pronounced in December and January but much less so in February (Figures 8,9 and 10). There are also substantial dew point differences in the surface layer, also seen in these figures. Thus it is hypothesized that the extensive and persistent snow cover in January may have inhibited precipitation over much of the Midwest and East during January. Further, the snow melt and surface warming may have helped to facilitate the formation of precipitation in February - particularly rain over much of the snow free areas.

Quantitative specification methods (now being developed by Klein) should clarify this matter. Obviously these arguments, while plausible, require more quantitative research - preferably testing with realistic dynamic numerical models.

Legends to Figures

1. Observed temperature classes (terciles expressed as above normal, (A), near normal, (N), and below normal, (B).) shown in middle panels, and the anomalies specifed from observed 700mb mean charts using Klein's method (top panels). Lower panels show snow boundary at ends of months (as indicated).

2. Precipitation patterns (expressed in three equally likely classes) for January and February, 1984. L stands for light, M for moderate and H for heavy. Note marked change in East from January to February.

3. Error of Klein specifications for January and for February 1984 as computed from the data of charts shown in Figure 1. Note the large errors (specifications too warm) in January, much smaller errors in February after removal of anomalous snow over much of the east.

4. Total precipitation (top panels) and percent of normal (bottom) in January and February 1984. Note contrast in east after the disappearance of the anomalous snows.

5. 700mb Heights (solid) and anomalies (broken) for December, 2 1984.

6. Same as Figure 5 but for January, 1984.

7. Same as Figures 5 and 6 but for February, 1984. Note strong changes between months in Figures 5, 6 and 7.

8. Mean lapse rates (solid) against the normal (broken) for December, 1983, January and the first half of February, 1984, and the corresponding dew points (triangles). All values represent a point in the Midwest - 40 N, 85 W.

9. Same as Figure 8 but for 35 N, 85 W. Note in Figures 8 and 9 the marked stability in the layer below 850mb in December and January and the relative diminution in stability in February as the abnormal snows disappeared.

10. Fields of temperature anomalies at four different levels for December 1983, January and February 1984. Zero isopleth is drawn heavy, positive anomalies are shown as solid lines drawn for every degree C. and negative values as broken lines, also drawn for every degree C. Note that the fields are coherent over large areas and that the major changes in stability occurred in the layer below 850mb due to the influence of the presence or absence of snow.

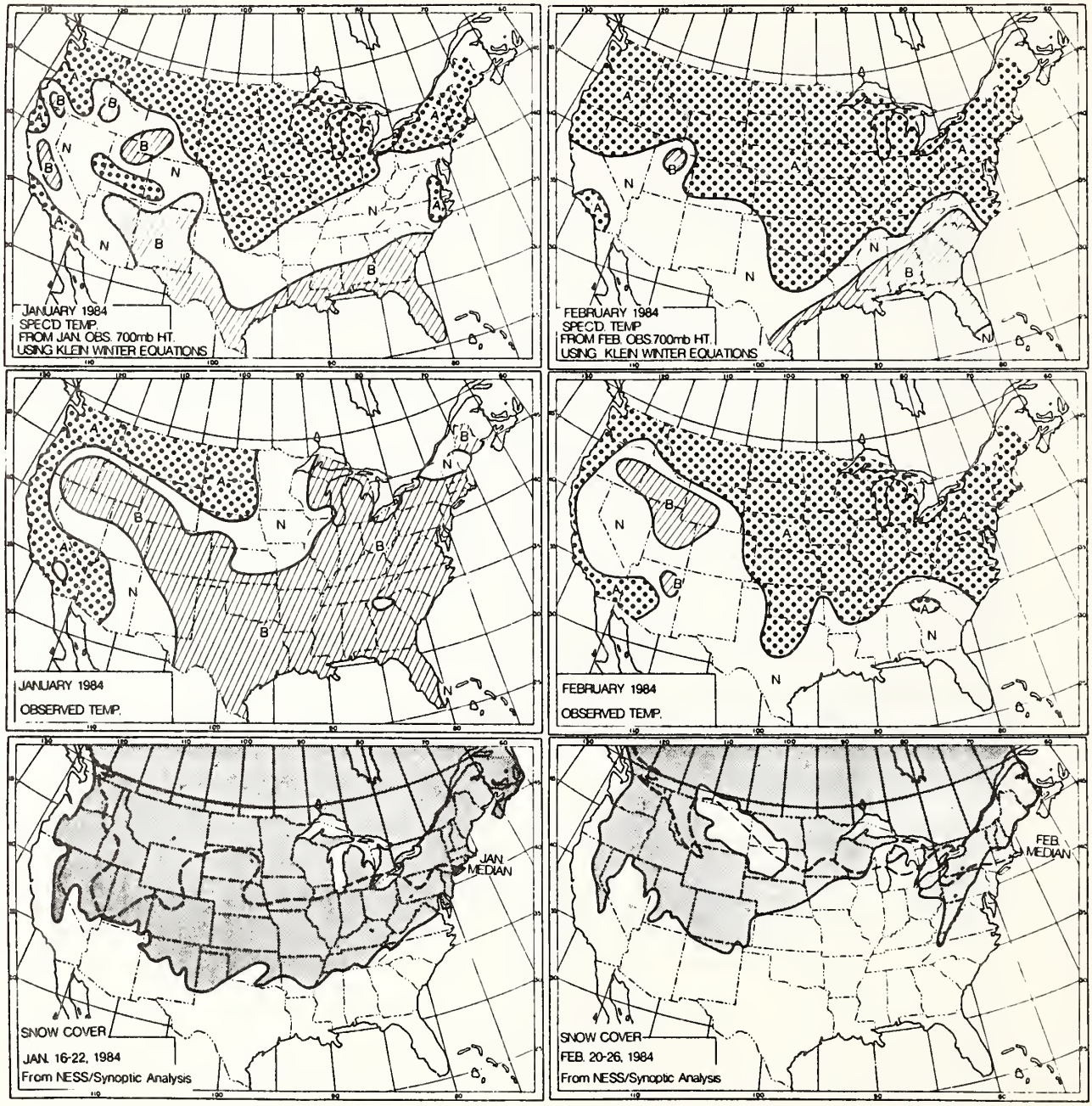
JANUARY 1984
SPEC'D TEMP.
FROM JAN. OBS. 700mb HT.
USING KLEIN WINTER EQUATIONS
FEBRUARY 1984
SPEC'D. TEMP
FROM FEB. OBS.700mb HT.
USING KLEIN WINTER EQUATIONS
JANUARY 1984
OBSERVED TEMP.
FEBRUARY 1984
OBSERVED TEMP.
JAN.
MEDIAN
FEB.
MEDIAN
SNOW COVER
JAN. 16-22, 1984
From NESS/Synoptic Analysis
SNOW COVER
FEB. 20-26, 1984
From NESS/Synoptic Analysis

1

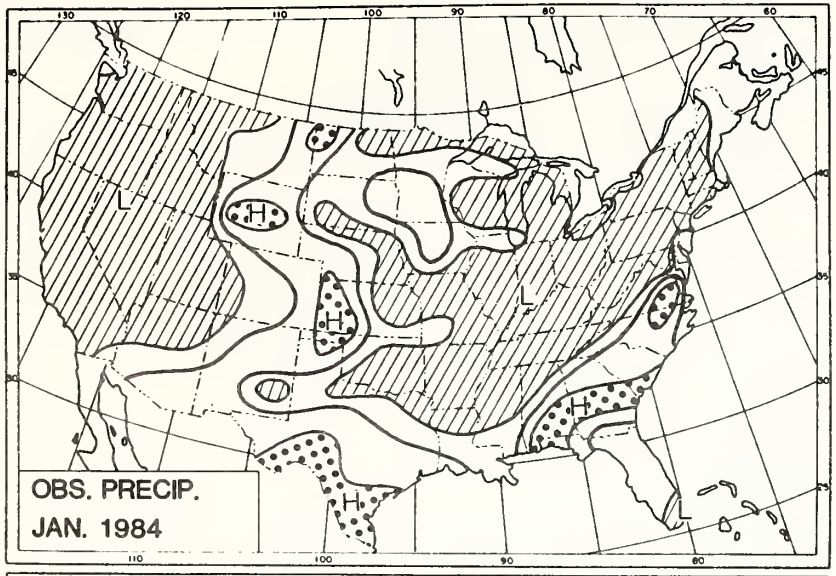
OBS. PRECIP.
JAN. 1984

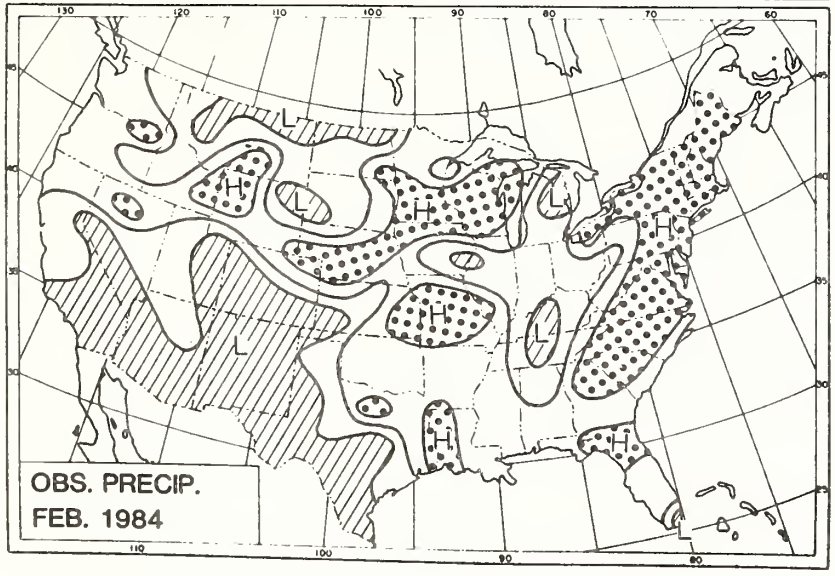
OBS. PRECIP.
FEB. 1984

2

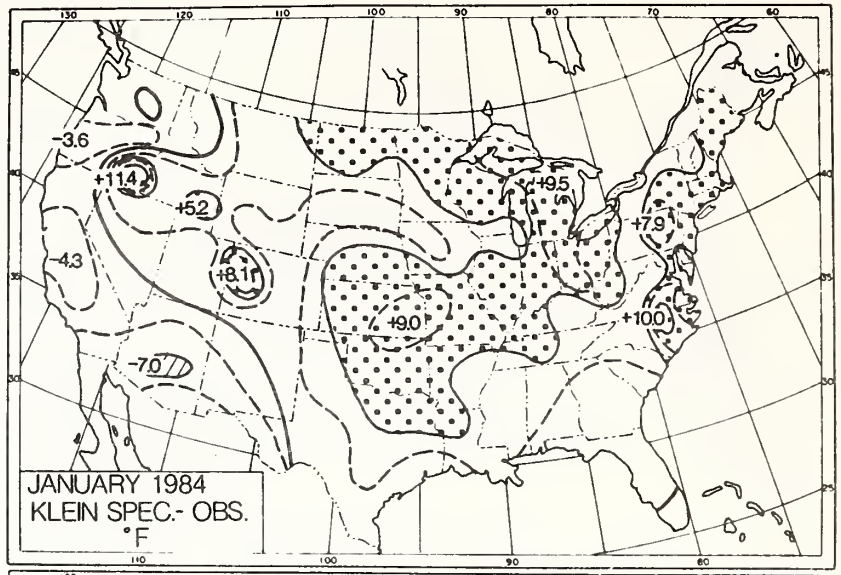
-3.6
+11.4
+5.2
-4.3
+8.1
-7.0
+9.5
+7.9
+9.0
+10.0
JANUARY 1984
KLEIN SPEC.- OBS.
°F

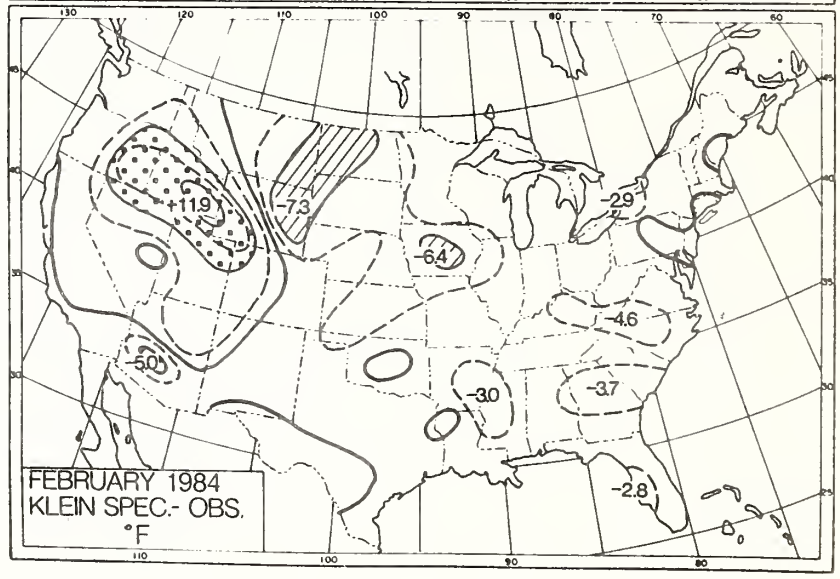
+11.9
-7.3
-6.4
-5.0
-3.0
-2.9
-4.6
-3.7
-2.8
FEBRUARY 1984
KLEIN SPEC.- OBS.
°F

3

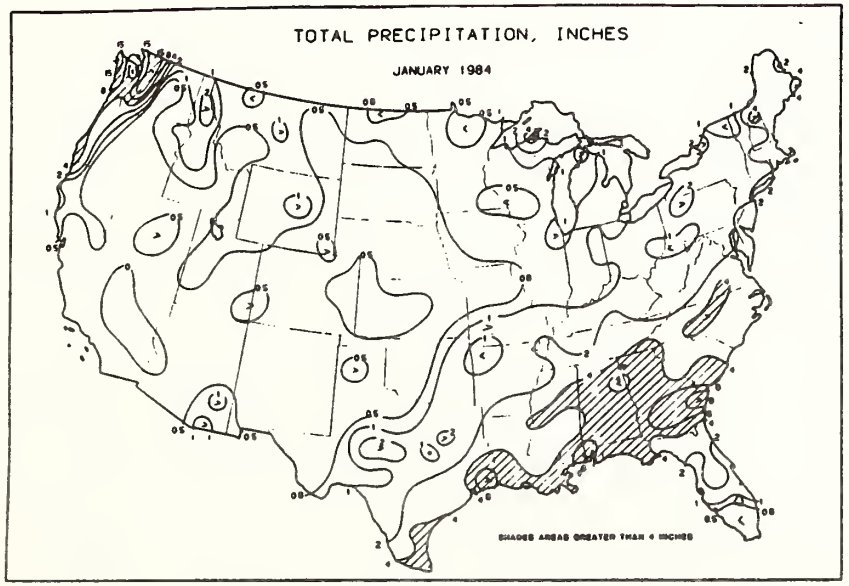
TOTAL PRECIPITATION, INCHES
JANUARY 1984

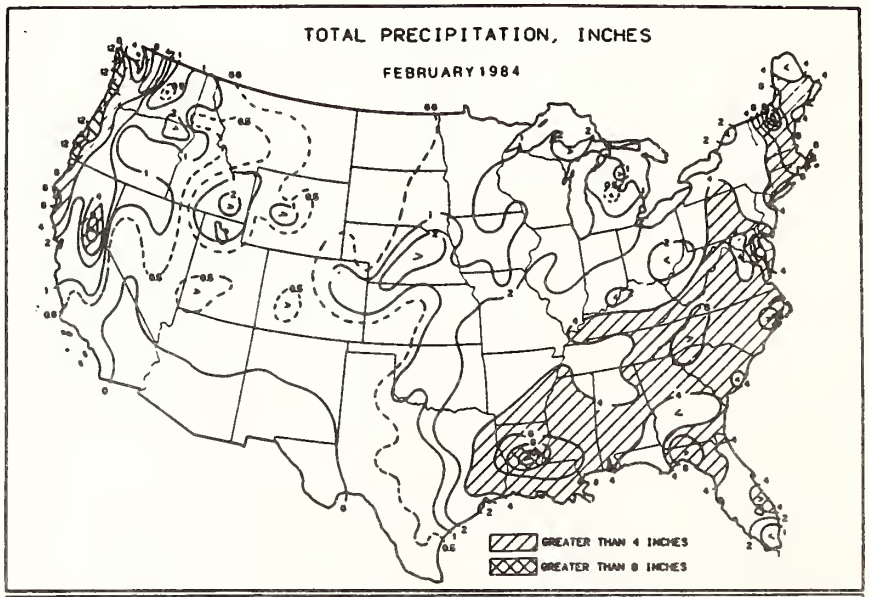
TOTAL PRECIPITATION, INCHES
FEBRUARY 1984
GREATER THAN 4 INCHES
GREATER THAN 8 INCHES

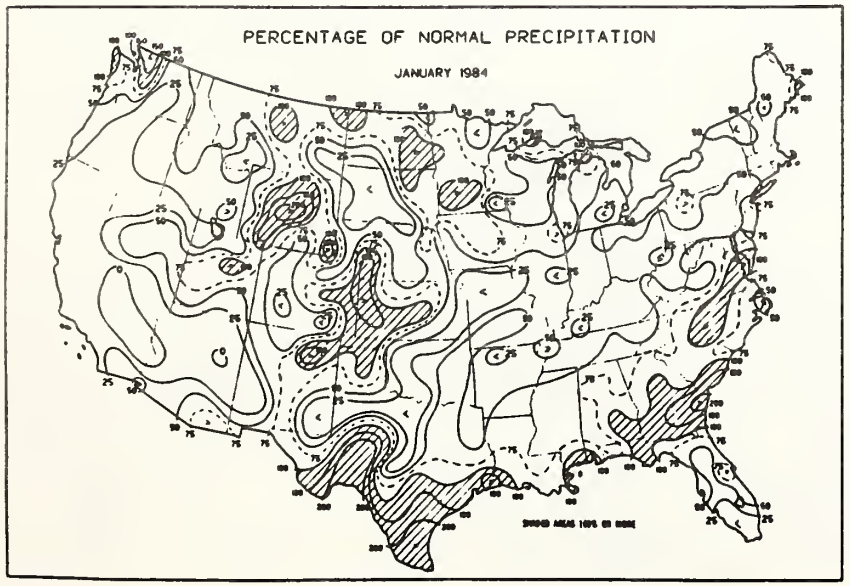
PERCENTAGE OF NORMAL PRECIPITATION
JANUARY 1984

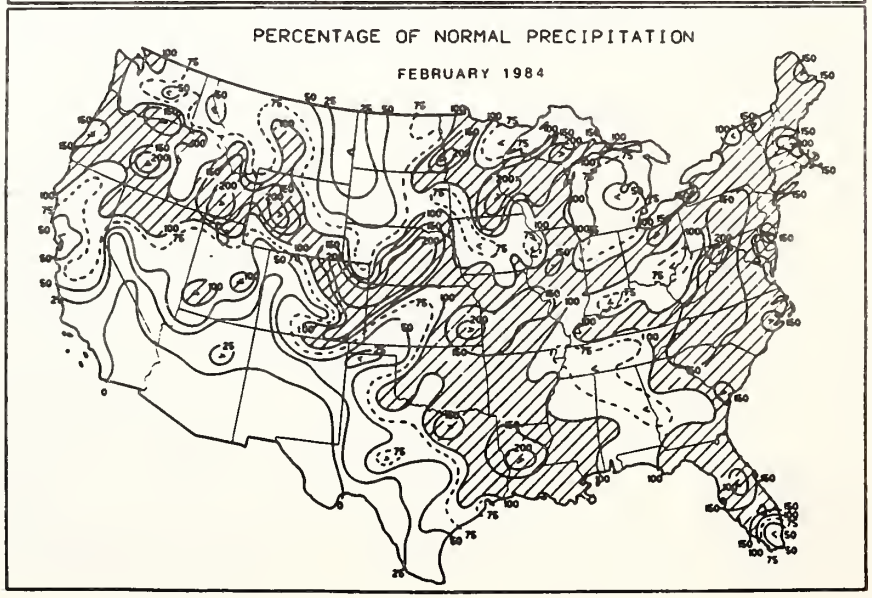
PERCENTAGE OF NORMAL PRECIPITATION
FEBRUARY 1984

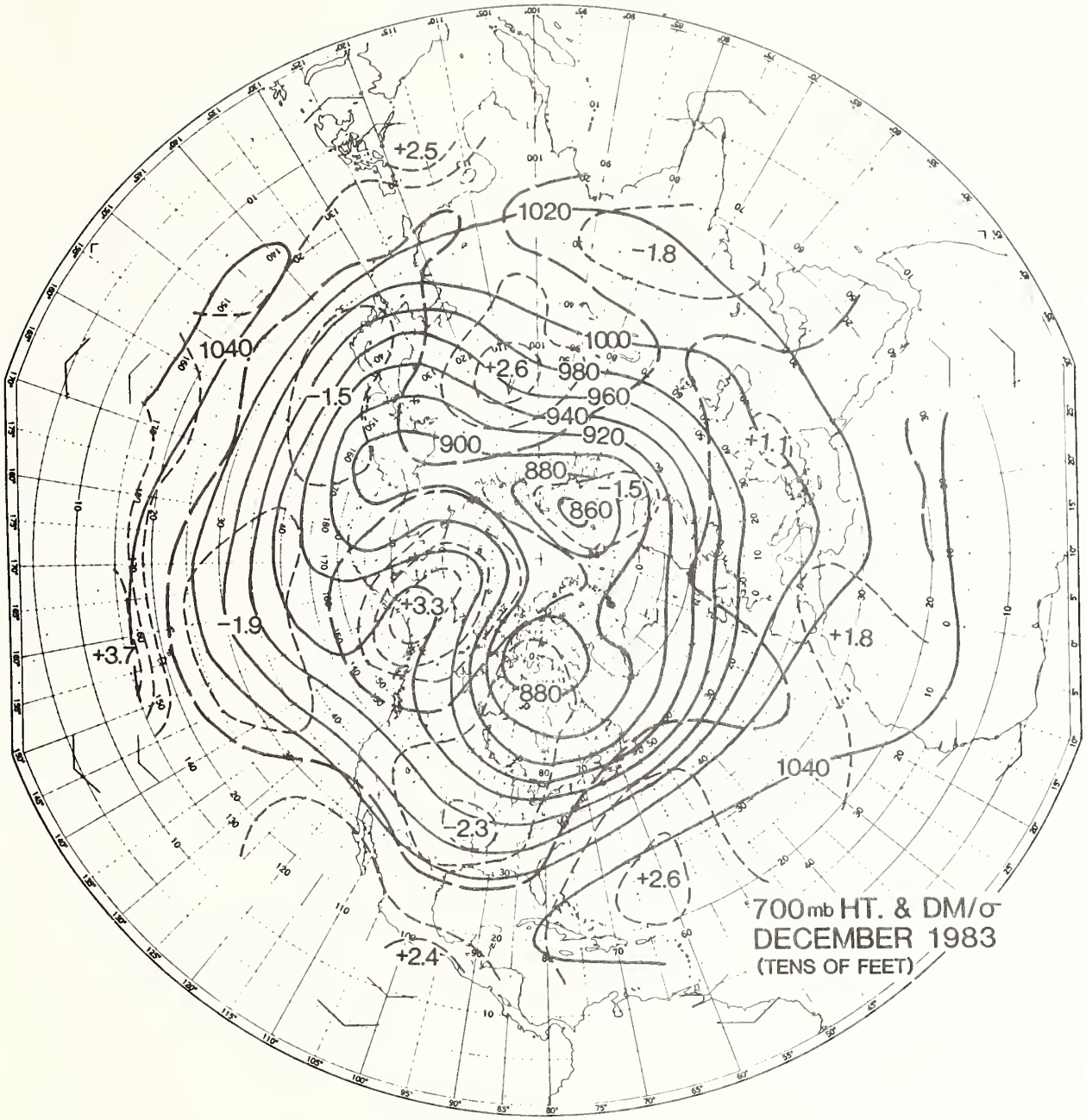
+2.5
1020
-1.8
1040
1000
+2.6
980
960
-1.5
940
920
900
+1.1
880
-1.5
860
+3.3
-1.9
+3.7
+1.8
880
1040
-2.3
+2.6
+2.4
700 mb HT. & DM/σ
DECEMBER 1983
(TENS OF FEET)

5

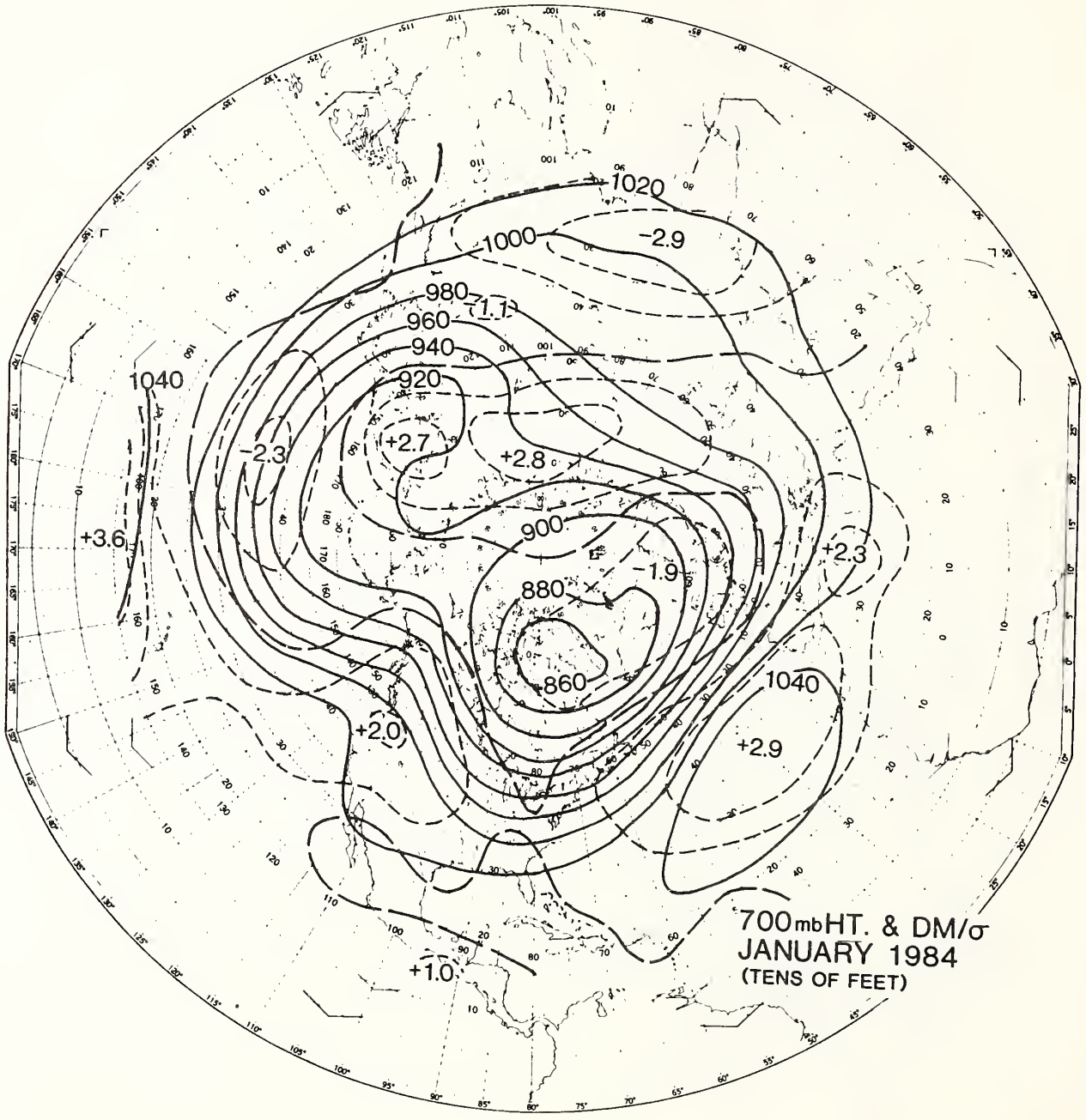
1020
1000
-2.9
980
-1.1
960
940
920
1040
-2.3
+2.7
+2.8
+3.6
900
-1.9
+2.3
880
860
1040
+2.0
+2.9
+1.0
700mbHT. & DM/σ
JANUARY 1984
(TENS OF FEET)

6

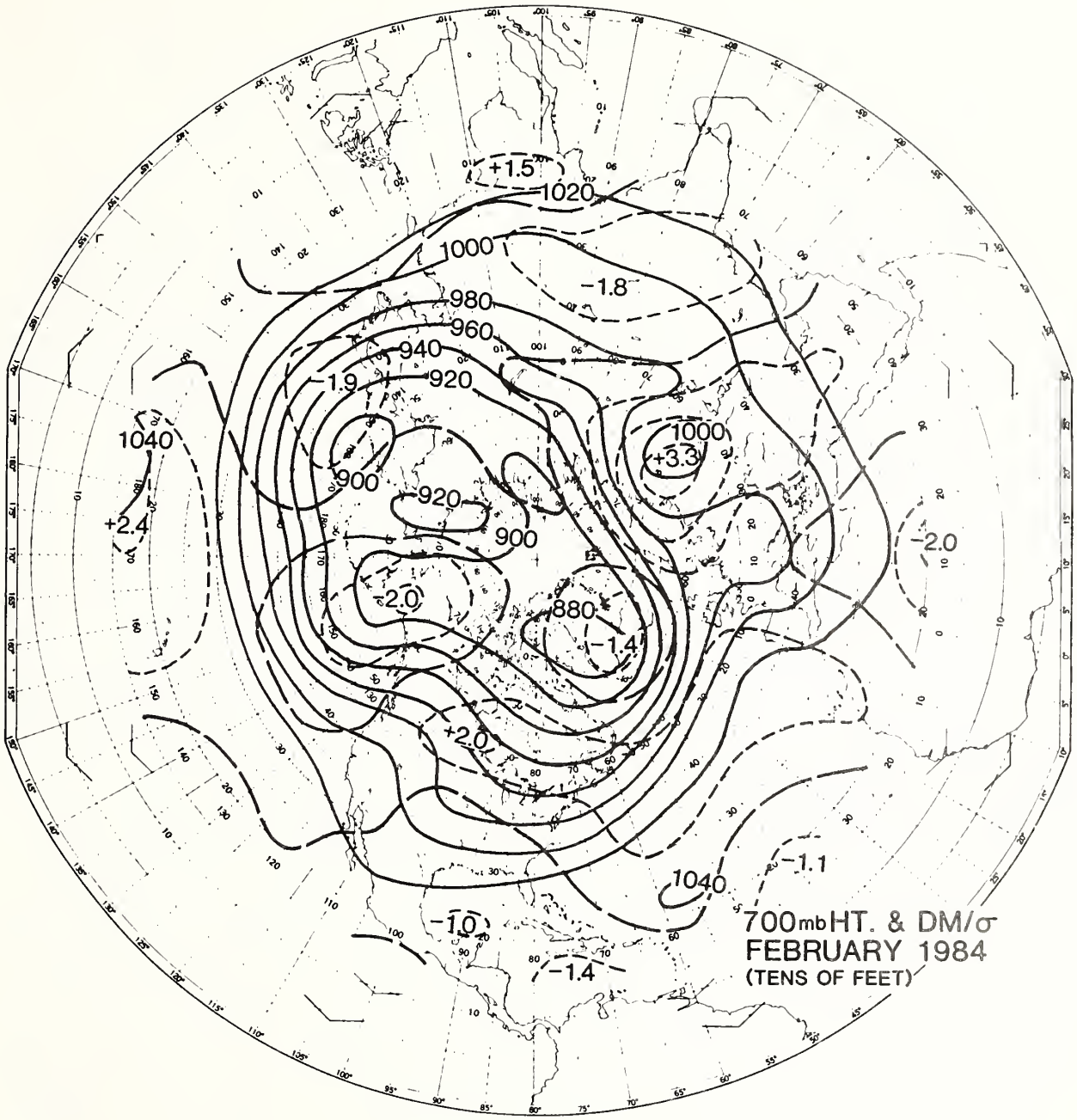
+1.5
1020
1000
-1.8
980
960
940
1.9
920
1040
1000
+3.3
900
920
900
+2.4
-2.0
2.0
880
-1.4
+2.0
1040
-1.1
-1.0
-1.4
700mb HT. & DM/σ
FEBRUARY 1984
(TENS OF FEET)

7

UPPER AIR TEMPS, NORMS AND DEW POINTS AT 40°N, 85°W

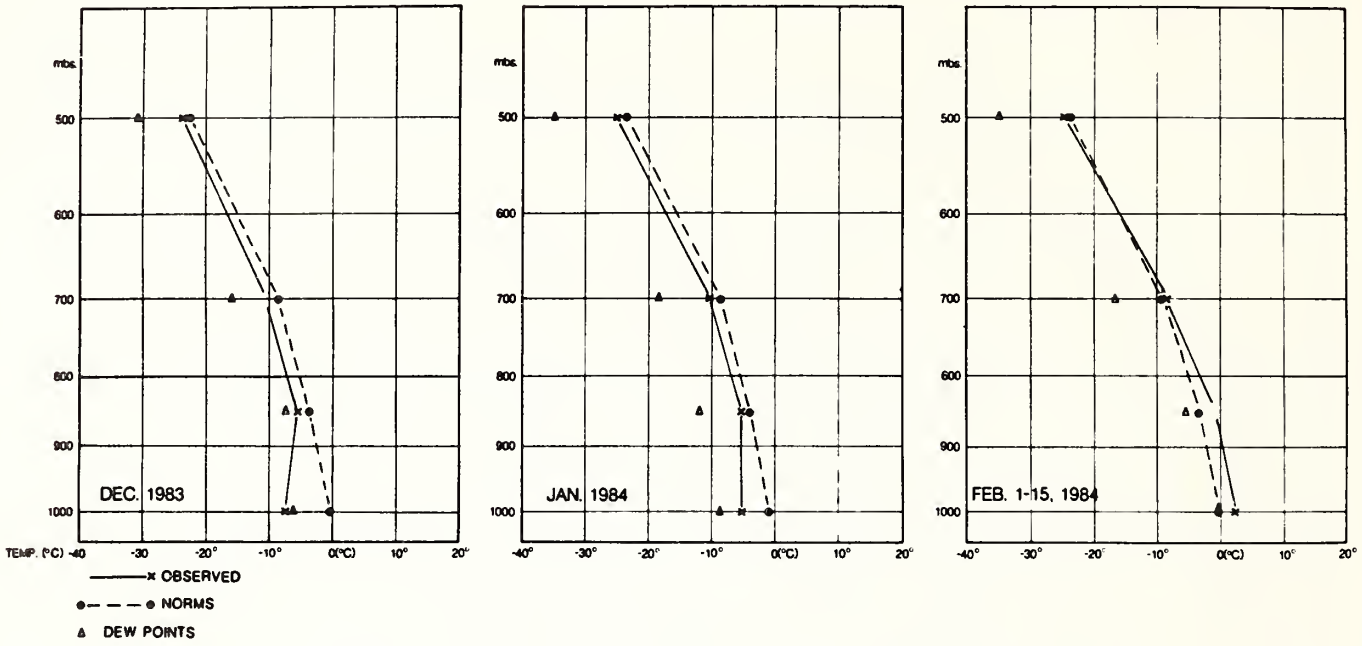

8

UPPER AIR TEMPS, NORMS AND DEW POINTS AT 35°N, 85°W

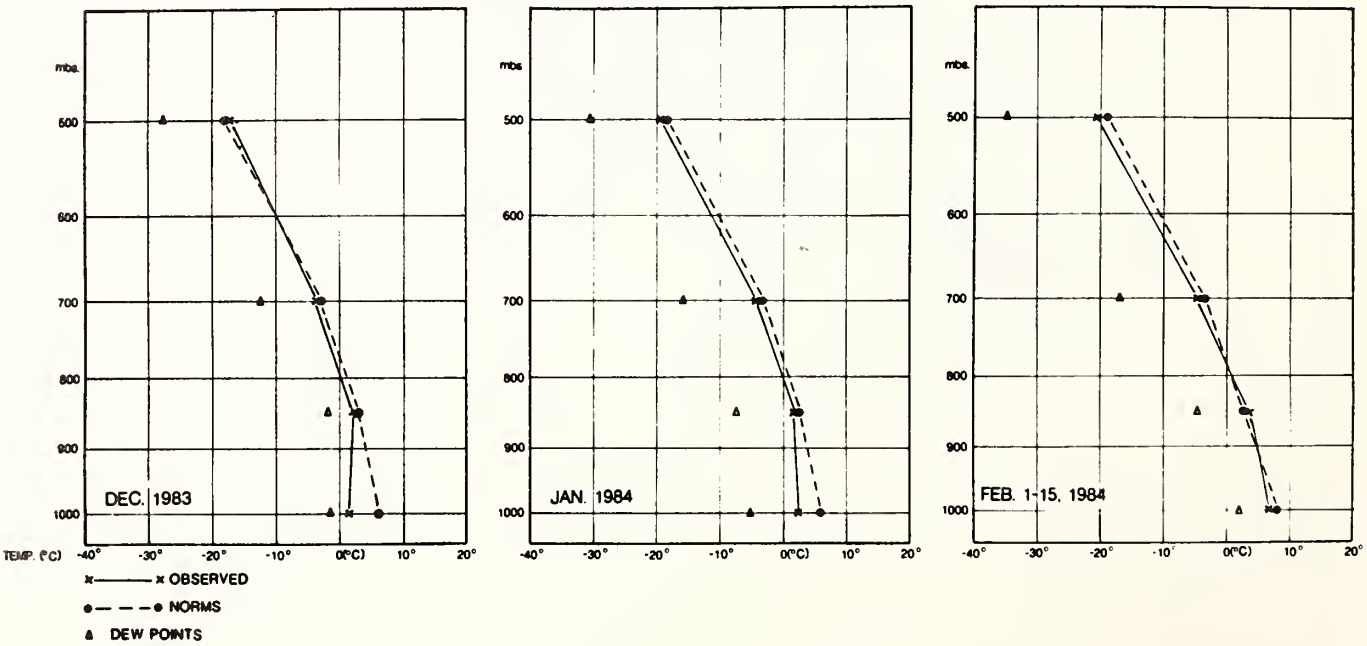

9

MONTHLY TEMPERATURE ANOMALIES (°C)

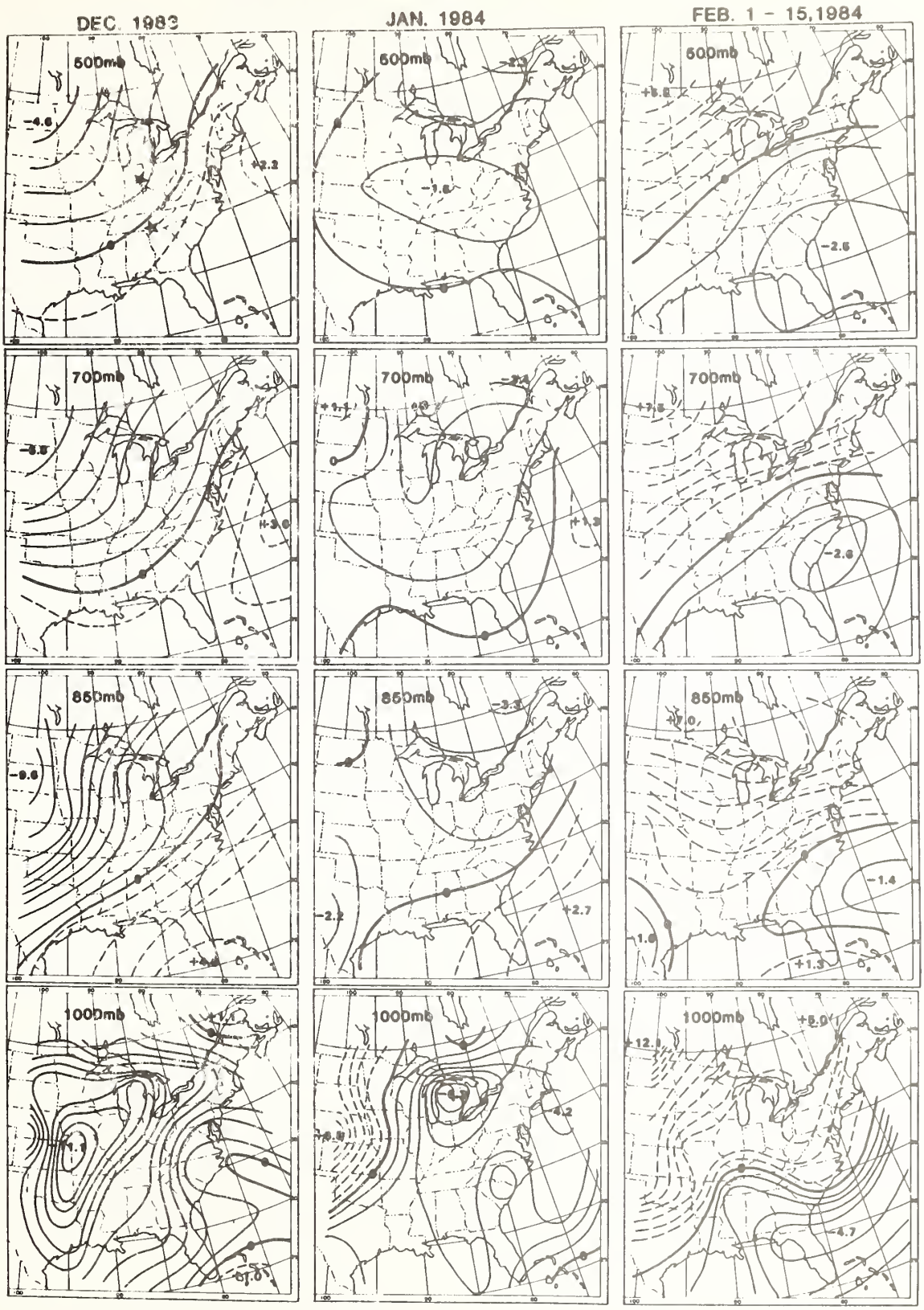

10

BLOCKING AS AN EXPLANATION OF THE SEVERE COLD OF WINTER 1983-84

by

R. S. Quiroz
Climate Analysis Center
NMC, NWS, NOAA
Washington, D. C. 20233

Introduction The forecasting of seasonal and monthly mean temperature is often made difficult by cold-to-warm or warm-to-cold transitions within the season or month. A case in point is the winter of 83-84, which over the greater part of North America was severely cold in December (coldest December over the U. S. in at least 5 decades), very cold in January, and abnormally warm in February. For details, see Quiroz (1984, MWR). Fig. 1 gives weekly resolution for surface temperature departure from normal (TDN) averaged over 3 U. S. latitudes, along with blocking information to be described below. Note the exceptional cold centered on the second half of December and middle half of January, followed by February "warmth".

Blocking observed, winter 1983-84 Using flow-oriented criteria for defining blocking (Quiroz, 1983, IAMAP Meeting, Hamburg), we have shown a nearly four-fold increase in the number of "blocking days" over the east Pacific and Western North America from winter 82-83 to winter 83-84 (Fig. 15 of Quiroz, 1984). Major winter blocking episodes (6 days or more with index of strength of associated meridional flow, N, greater than 20, Fig. 1 top) were on December 15-30 centered near 155°W, January 8-21, near 145°W; and in the Atlantic-European area on February 4-26, near 5°E. Fig. 2 shows the blocking patterns at 500 mb (filtered zonal wave 0-5 maps) on Dec. 23, Jan. 16, and Feb. 15. Note corresponding shifts in the main region of relatively flat quasi-zonal flow from northern Eurasia, to the North Atlantic, to the west Pacific.

Comparison of U. S. temperature and blocking Note in Fig. 1 the near coincidence of blocks over western North America and periods of severely cold temperature over the U. S., with blocking appearing to lead by a few days. The December block was the strongest observed in the hemisphere during 7/83-6/84, having the greatest measure of meridional flow (N=24), with intense cold air advection southward over the continent, and having the largest 5-day mean 500-mb height anomaly (500 gpm).

In contrast to early winter, February was nearly totally lacking in "blocking days" over North America. The extraordinary warmth was associated with a simultaneous eastward progression of positive height anomaly in mid-latitudes both over North America and the east Atlantic in the first half of the month (Fig. 3), with a SW component of flow added over N. A. by mid-month. In the European area, the eastward shifting height anomaly combined with a retrogressing wave 1 feature in high latitudes to form blocking in that region.

The simplest possible measure of blocking over western N. A. is the height in the Alaska-Yukon area. Fig. 4 compares 500 mb heights at 65°N, 140°N and weekly surface TDN over the U. S. (40°N), showing quite good

agreement. This is consistent, although on a sub-monthly time-scale, with Klein's (1983, MWR) finding that monthly mean 700-mb heights over Alaska are highly useful for specifying surface temperature in the U. S. in winter.

The influence of snowcover is of interest (see e.g., Wagner, 1973, MWR), but it is believed that this factor would have been quite small and limited to small regions, in comparison with cold-air advection during the blocks.

Remarks on the time and space distribution of blocking Why blocking is favored in one winter or one geographical region is a matter of great practical and theoretical interest. Fig. 5 shows blocks observed in the hemisphere during the extended period 11/83-6/84 and indicates interesting transitions during Nov.- April from primary dominance of blocking near Greenwich in November, shifting to western N. A. in Dec.-Jan., thence via Eurasia back to the Atlantic-European sector in Feb.-Mar., with nearly equal activity in Europe and N. Amer. thereafter.

Elsewhere (Quiroz, 1983, Hamburg) we have shown that travelling planetary waves, usually k1, may have an important influence on the development and evolving structure of blocks. Fig. 6 shows the trajectory of the ridge of k1 (travelling) from mid-Nov. to Jan. 30. The major block this winter (Dec. 15-30) was explainable nearly entirely in terms of interaction between k1 (t) and quasi-stationary k2 in the Alaskan area. If we add to Fig. 5 the phase data for k1 (t), we find a strong indication that the regional distribution of blocks, in time, was largely influenced by the phase changes of k1. We are now studying this behavior during the past three years, with the hope that systematic monitoring of planetary wave developments may ultimately help in the prediction of blocking activity.

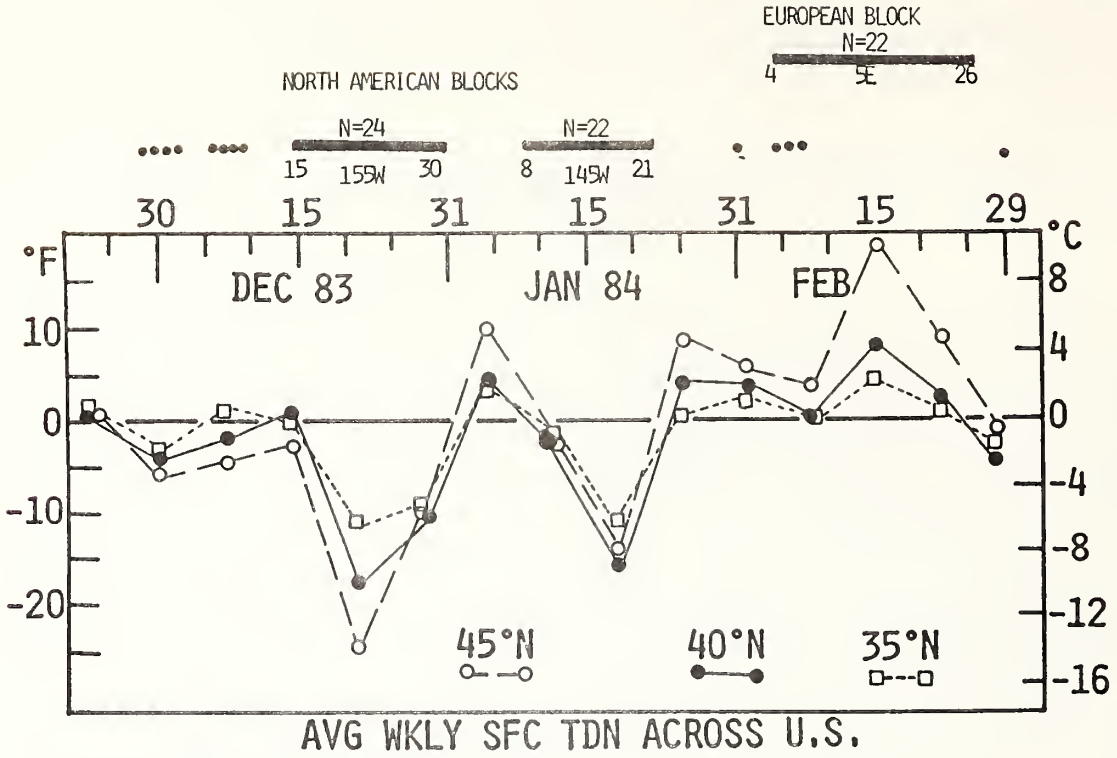

•• other "blocking days"

FIG. 1. SURFACE TEMPERATURE DEPARTURE FROM NORMAL ACROSS U.S. AT SPECIFIED LATITUDES. MAJOR BLOCKING EPISODES ARE SHOWN ABOVE WITH BEGINNING AND ENDING DATES, CENTRAL LONGITUDE, AND MERIDIONAL FLOW INDEX (N).

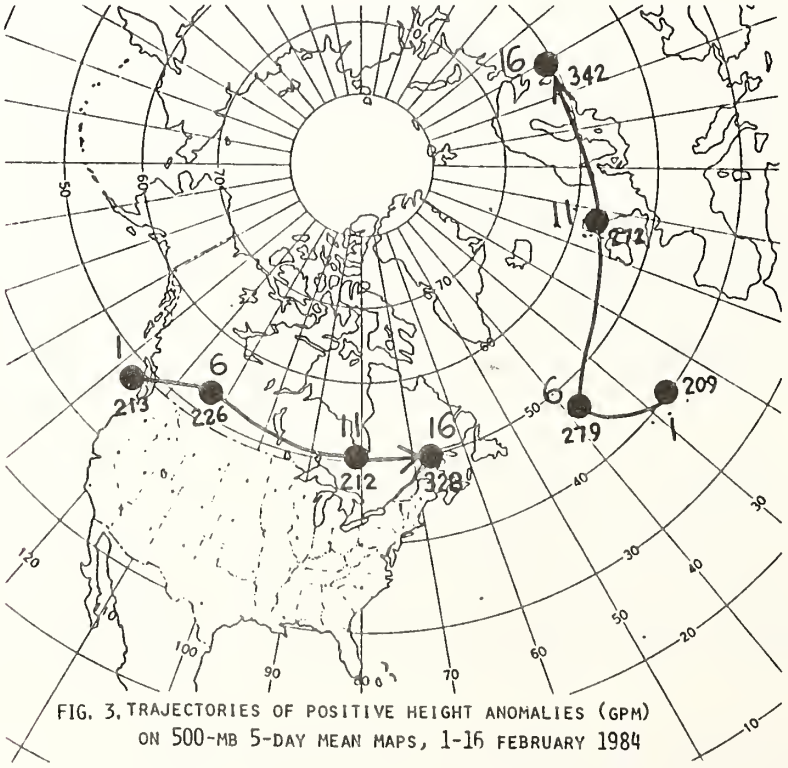

FIG. 3. TRAJECTORIES OF POSITIVE HEIGHT ANOMALIES (GPM) ON 500-MB 5-DAY MEAN MAPS, 1-16 FEBRUARY 1984

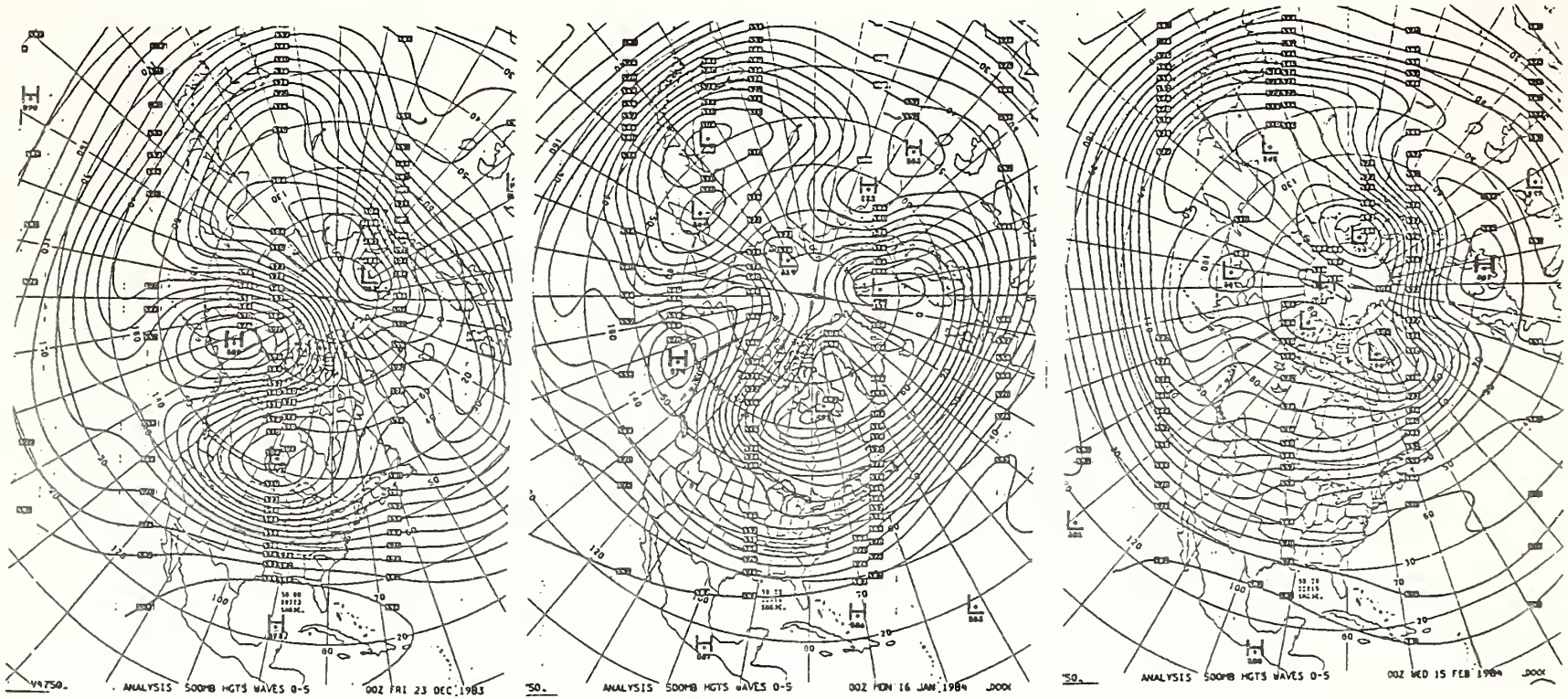
ANALYSIS 500MB HGTS WAVES 0-5
00Z FRI 23 DEC 1983
ANALYSIS 500MB HGTS WAVES 0-5
00Z MON 16 JAN 1984
ANALYSIS 500MB HGTS WAVES 0-5
00Z WED 15 FEB 1984

Fig. 2. Filtered 500-mb maps (zonal waves 0-5) showing flow patterns near height of development of major winter blocks over western North America (left and center) and Europe (right).

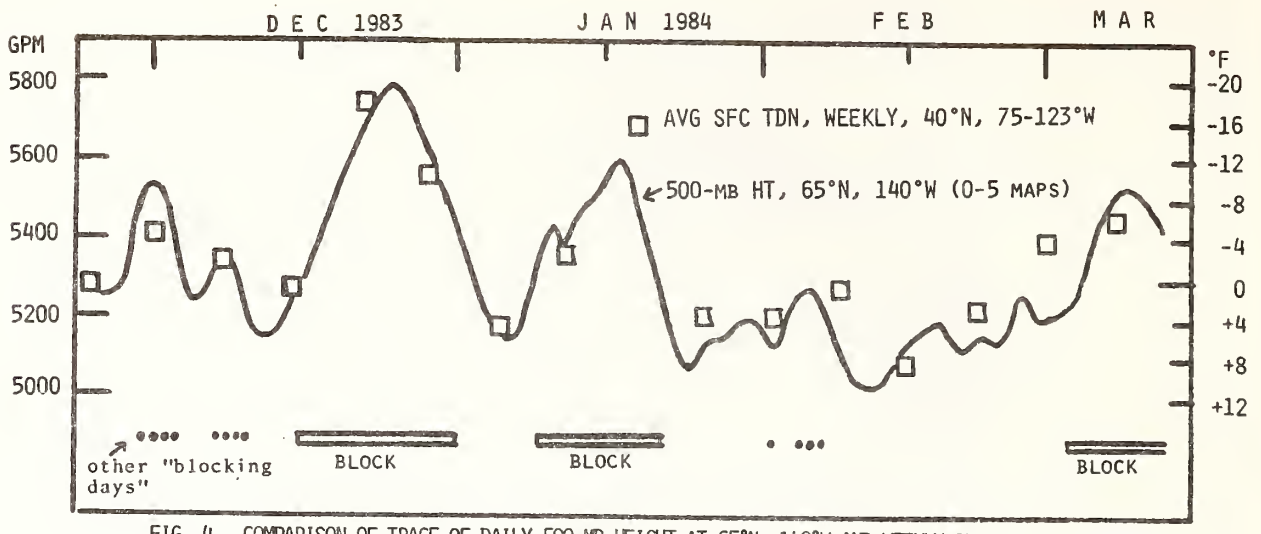

FIG. 4. COMPARISON OF TRACE OF DAILY 500-MB HEIGHT AT 65°N, 140°W AND WEEKLY SURFACE TDN OVER U.S. AT 40°N, WITH NORTH AMERICAN BLOCKS INDICATED AT BOTTOM.

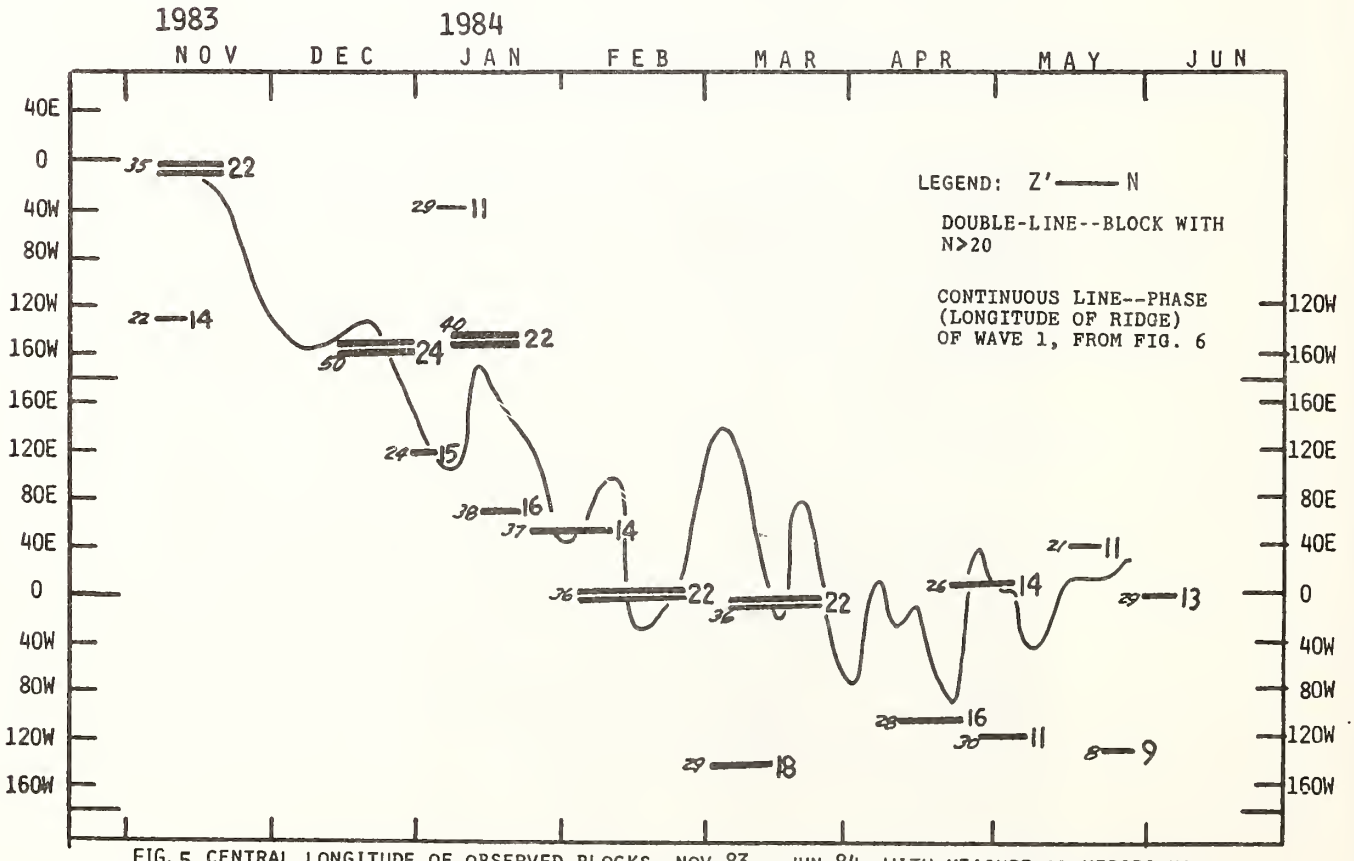

FIG. 5. CENTRAL LONGITUDE OF OBSERVED BLOCKS, NOV 83 - JUN 84, WITH MEASURE OF MERIDIONAL FLOW (N) (FROM DAILY WAVE 0-5 500-MB MAPS) AND ASSOCIATED HEIGHT ANOMALY (Z'), IN DECAMETERS (FROM 5-DAY MEAN 500-MB MAPS)

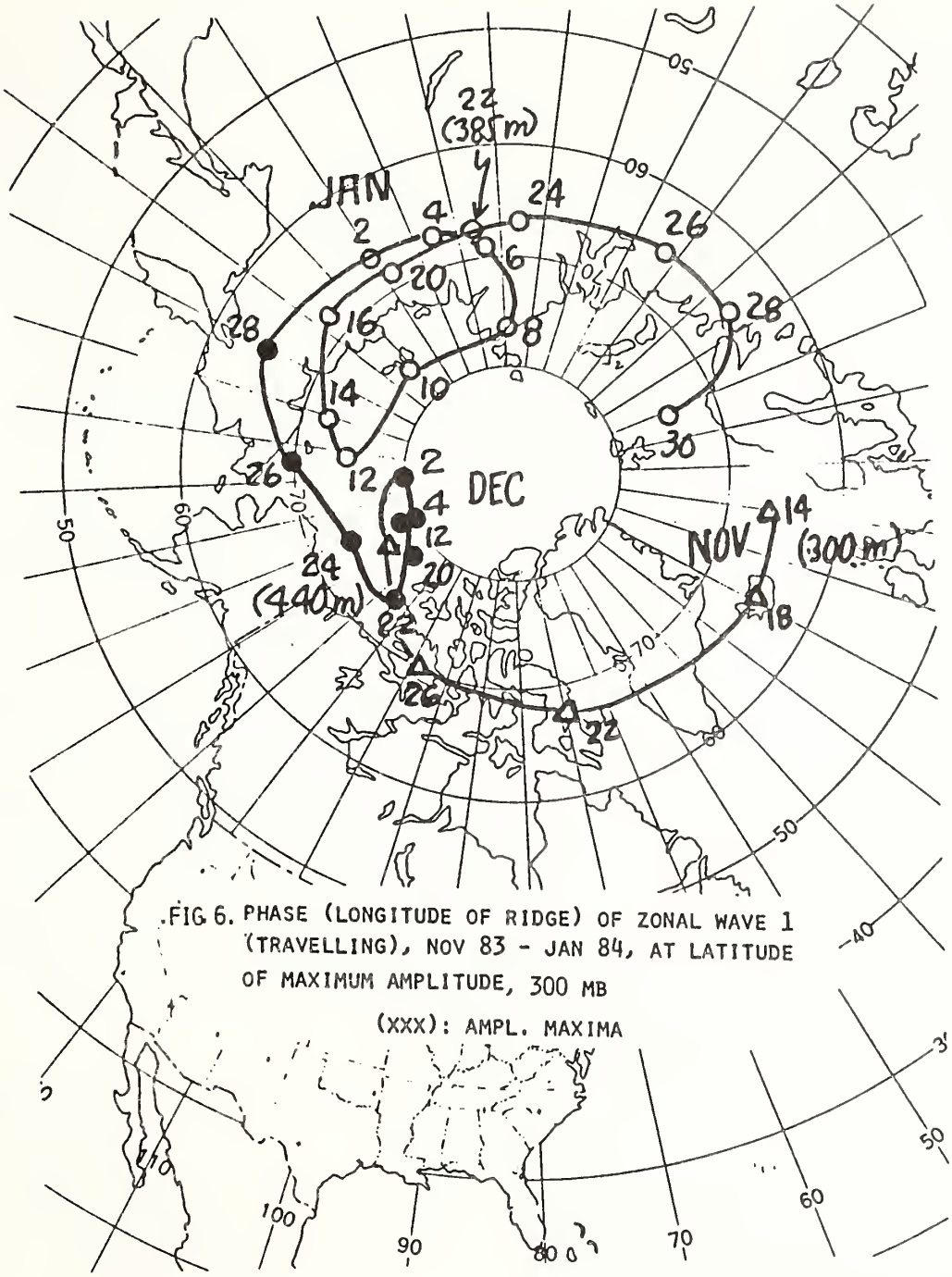

FIG 6. PHASE (LONGITUDE OF RIDGE) OF ZONAL WAVE 1 (TRAVELLING), NOV 83 - JAN 84, AT LATITUDE OF MAXIMUM AMPLITUDE, 300 MB

(XXX): AMPL. MAXIMA

Circulation and Weather for MAM and JJA 1984

A. James Wagner and Chester F. Ropelewski
Climate Analysis Center
NMC, NWS, NOAA, Washington, D.C. 20233

Most of the equatorial Pacific indices revealed that the atmosphere was in the cool/positive phase of the ENSO phenomenon (Table 1). The Pacific trade-wind indices were all strongly positive, with magnitudes of over 2σ in the area west of the dateline from March through June. There was a tendency for the area of maximum anomaly to move eastward and weaken with time. The 200 mb zonal wind index east of the dateline was near or above normal, with a tendency to increase with time. The outgoing long wave radiation (OLR) index near the dateline declined slowly from strongly to moderately positive values, indicating a general supression of convective activity in that area. The Indian summer monsoon was characterized by an excess of rainfall in the northern provinces and a tendency for a deficiency in some parts of southern India.

Values of the SOI itself and the sea surface temperature anomalies (SSTA) in key areas of the eastern Pacific oscillated around zero with no discernible trends.

The JJA (June, July, August) SST and SSTA fields are shown in Figure 1. Note the well-defined minimum of SST along the equator in the eastern Pacific, which is the normal, non-El Niño pattern, and contrasts strongly with the pattern of warmth still in evidence during summer 1983. The large area of negative SSTA in the central north Pacific has been a persistent feature of the past several seasons, although its intensity has diminished from that of a year ago. Most of the SSTA's were positive in the Southern Hemisphere, most notably over the South Atlantic where values of more than $+2^{\circ}C$ off the west coast of Africa suggest an Atlantic parallel to the South American-Pacific El Niño.

The low-level (850 mb) wind speeds and their anomalies changed markedly from MAM (March, April, May) 1983, when the ENSO event was near its peak, to the same season of 1984 (Fig. 2). The most notable difference is over the equatorial Pacific, where anomalous westerlies of over 5m sec^{-1} east of the dateline in 1983 were followed by anomalous easterlies of the same magnitude near and just west of the dateline in 1984. Other reversals which had significant weather implications occurred off the California coast and over the equatorial Atlantic and northwestern Brazil.

Upper troposphere winds also underwent marked changes from 1983 to 1984. Anomalous easterly components of 10 to 15 m sec^{-1} over the equatorial eastern Pacific in 1983 were replaced by westerlies that were about 5 m sec^{-1} stronger than normal (Fig. 3). The N.H. subtropical westerlies were at least 10 m sec^{-1} stronger than normal over a large area from the dateline across the southwestern U.S. and northern Mexico to the Atlantic east of Florida during the ENSO event, but ridging over the eastern Pacific pushed the westerlies further north in 1984, resulting in a much drier season over the southwestern U.S. in an area of anomalous anticyclonic northerly flow. Over the equatorial Atlantic, abnormally strong westerlies in 1983 were replaced by easterly anomalous flow in 1984.

The Northern Hemisphere 700 mb circulation was characterized by strong anomalies in MAM (Fig. 4). Heights in the United States and Europe were more than 30 m less than normal, and those South of the Aleutians approached -90 m. Even though the mid-latitude westerlies were unusually fast over the Pacific between the stronger than normal subtropical ridge and deep Aleutian Low, they did not reach the record values of 1983.

Northern Hemisphere temperature anomalies during spring 1984 can be looked at in two different ways; the magnitude of the anomaly and its significance measured as a percentile of the normal (Gaussian) distribution. The map of the temperature anomaly itself (Fig. 5) emphasizes departures from normal in higher variability areas such as high latitude continents, where substantial positive anomalies were associated with the strong ridges over eastern Siberia, northwestern Canada, and northwestern Russia. A pocket of cold air prevailed in the vicinity of Greenland and the Davis Strait in connection with a stronger than normal trough.

The areas of negative temperature anomaly over the United States and western Europe were around 1-2^{o}C, but their true significance is brought out only by the percentile map (Fig. 6). These areas of colder than normal weather were both within the 10% coldest springs based on data from 1951-80, and were of similar statistical significance to the previously mentioned positive anomalies at high latitudes. Several climate divisions in the northeastern and midwestern part of the United States reported the coldest spring in the past 54 years. Other areas of modest (+1^{o}C) anomalous warmth in the tropics averaged within the 10% warmest springs, most notably the Sahel area of west Africa, where drought continued.

Because of the high spatial and temporal variation of precipitation, it is best shown as percentiles of a skewed distribution. Thus the precipitation percentiles in Fig. 7 are with respect to a gamma distribution rather than a normal distribution. Precipitation totals for MAM were above the 70th percentile over the northwestern and eastern U.S. and across southern Europe, within and east of the strong mean troughs mentioned previously. Some locations in the middle Atlantic states and New England had the wettest spring in the past 54 years.

Anomalies of the N. H. summer mean 700mb circulation were generally weaker than spring's, with significantly enhanced ridges only over the eastern Atlantic and northern Russia. Except for a fairly strong trough off the west coast, anomalies in the vicinity of the United States were very weak (Fig. 8).

The largest temperature anomalies in JJA occurred in connection with the Russian ridge, where below normal averages were observed in an area where anomalous northerly flow brought cold air southward from the ice-covered Arctic Ocean (Fig. 9). A large area of negative temperature anomaly also occurred over eastern Europe and western Russia, in the area of enhanced northerly flow east of the strong ridge near the British Isles. Above normal temperatures were also observed over much of Canada, as well as over Japan, which had a cooler than normal spring.

The N. H. summer temperature percentile map (Fig. 10) snows that all the above mentioned anomalies were in the extreme 10% wings of the distribution, with the one over eastern Europe and the eastern Mediterranean being the most extensive. A small area of significant warmth was also located over the

British Isles, close to the strong ridge. Strong positive temperature anomalies also continued over much of the Sahel. After an early June heat wave in the East, temperature anomalies for the entire summer over the United States were relatively weak, as implied by the height anomaly pattern. Over the country, as a whole, temperatures averaged near normal.

The precipitation percentile map for the N. H. summer shows the dry conditions over the Sahel and portions of central Asia (Fig. 11). Areas on the wet side included western Russia, northeastern Asia and much of northern Canada and Greenland. The entire western third of the United States was wetter than usual, and extensive areas of the Rockies and Plateau were in the 90th percentile. Actual amounts totaled up to 300 cm, a considerable rainfall for a normally semiarid area. No extensive areas of drought were observed over the United States, but portions of the Great Plains and central Mississippi Valley did become dry in August following an abnormally wet early summer.

Date 1984	Tahiti-Darwin SOI	PACIFIC TRADEWIND INDICES 5N-5S 135E-180	5N-5S 175W-140W	5N-5S 135W-120W	OUTGOING LONGWAVE RADIATION INDEX 5N-5S 160E-160W	PACIFIC 200 MB ZONAL WIND INDEX 5N-5S 165W-110W	PACIFIC SST Niño 1+2 0-10S 90W-80W		Niño 3 5N-5S 150W-90W		Niño 4 5N-5S 160E-150W		SLP ANOMALIES Tahiti	Darwin
AUG	0.1	0.1	0.6	1.4	0.8	1.6	-0.5	20.4	-0.5	24.2	0.0	28.2	-0.4	-0.4
JUL	0.0	1.4	0.8	1.2	1.2	0.7	0.4	21.9	-0.5	24.8	-0.3	28.0	0.4	0.4
JUN	-1.2	2.0	1.9	1.4	1.2	0.9	-0.1	22.6	-0.6	25.5	-0.3	28.1	-0.4	0.9
MAY	-0.0	2.1	1.7	1.1	1.4	1.4	-0.3	23.5	0.0	26.6	-0.4	28.0	0.1	0.2
APR	0.4	2.4	0.9	0.2	1.8	0.8	0.8	25.9	-0.2	27.0	-0.4	27.8	0.9	0.7
MAR	-0.8	2.2	0.9	0.5	1.8	0.1	0.1	25.9	0.0	26.7	-0.4	27.5	-0.7	0.6

TABLE 1 - Atmospheric and SST index values for the most recent 6 months. Atmospheric indices are standardized by the standard deviation of the appropriate monthly mean except for the Tahiti and Darwin SLP anomalies which are in mb. SST indices are in ^{o}C. Note that positive (negative) values of the 200 mb Zonal Wind index imply westerly (easterly) anomalies; positive (negative) values of the Trade Wind Indices imply easterly (westerly) anomalies.

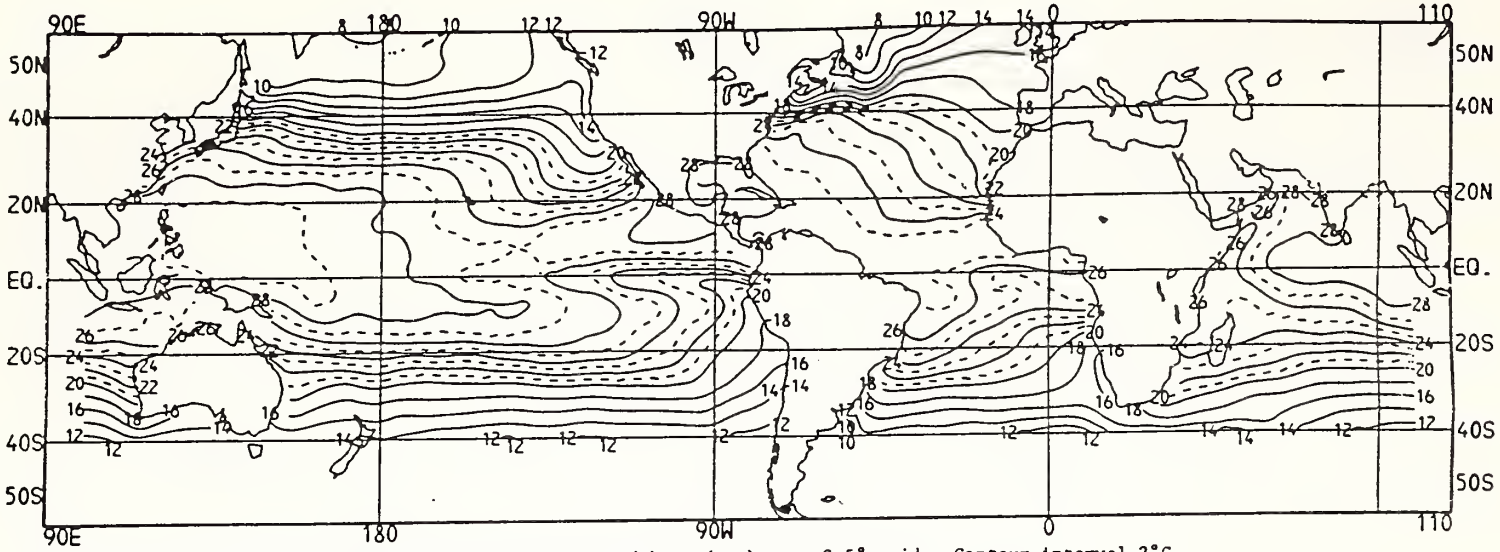

FIGURE 1a - SEA SURFACE TEMPERATURE, JJA 1984 (ship and buoy data) on a 2.5° grid. Contour interval 2°C. Temperatures >20°C are contoured every degree with odd contours dashed.

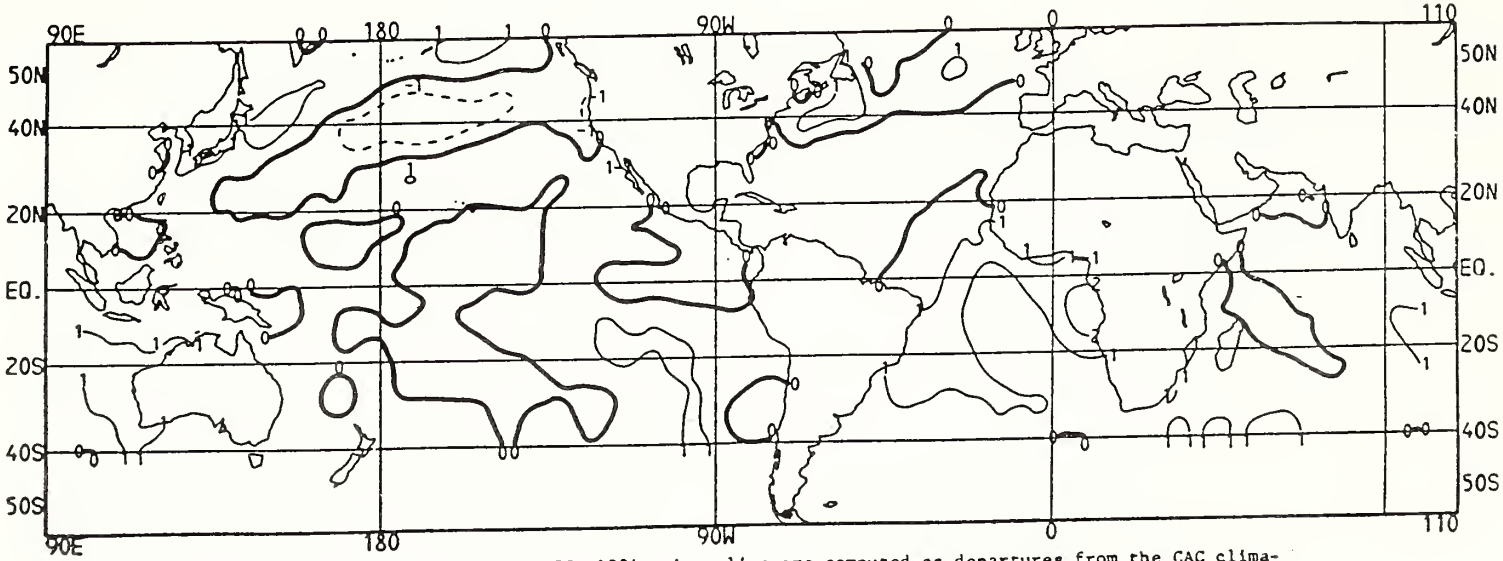

FIGURE 1b - SEA SURFACE TEMPERATURE ANOMALIES, JJA 1984. Anomalies are computed as departures from the CAC climatology (Reynolds, NOAA Tech Report NWS 31, 1982). Contour interval 1°C with negative anomalies dashed.

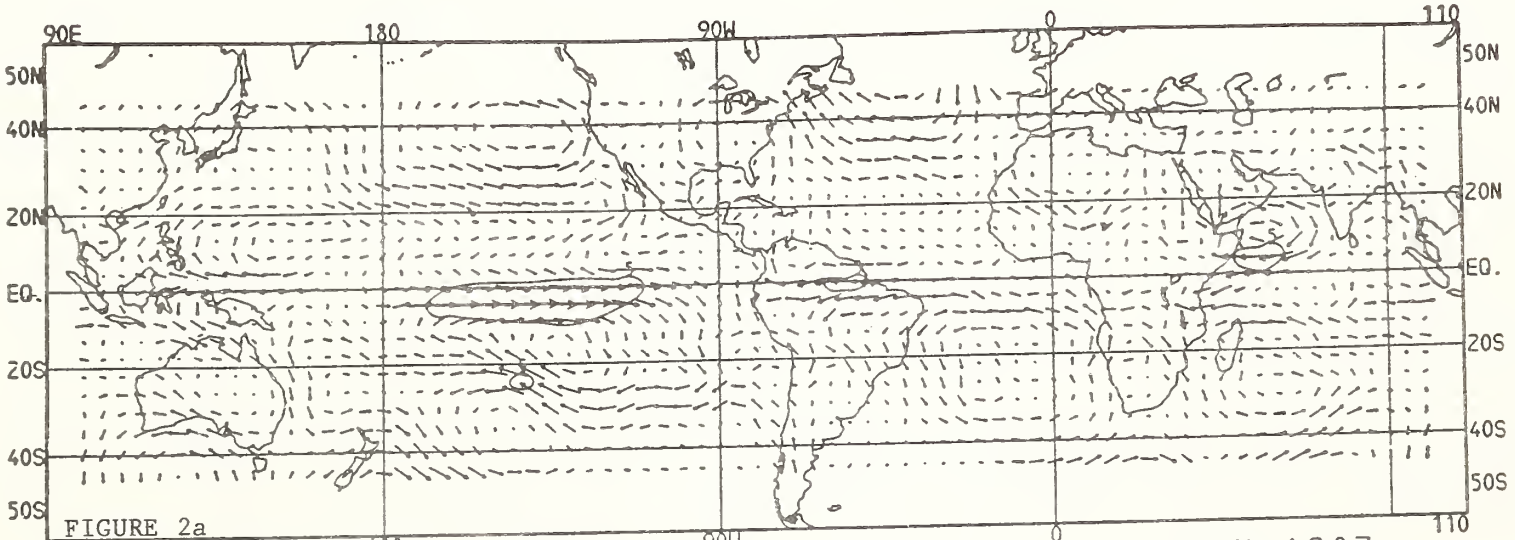

FIGURE 2a

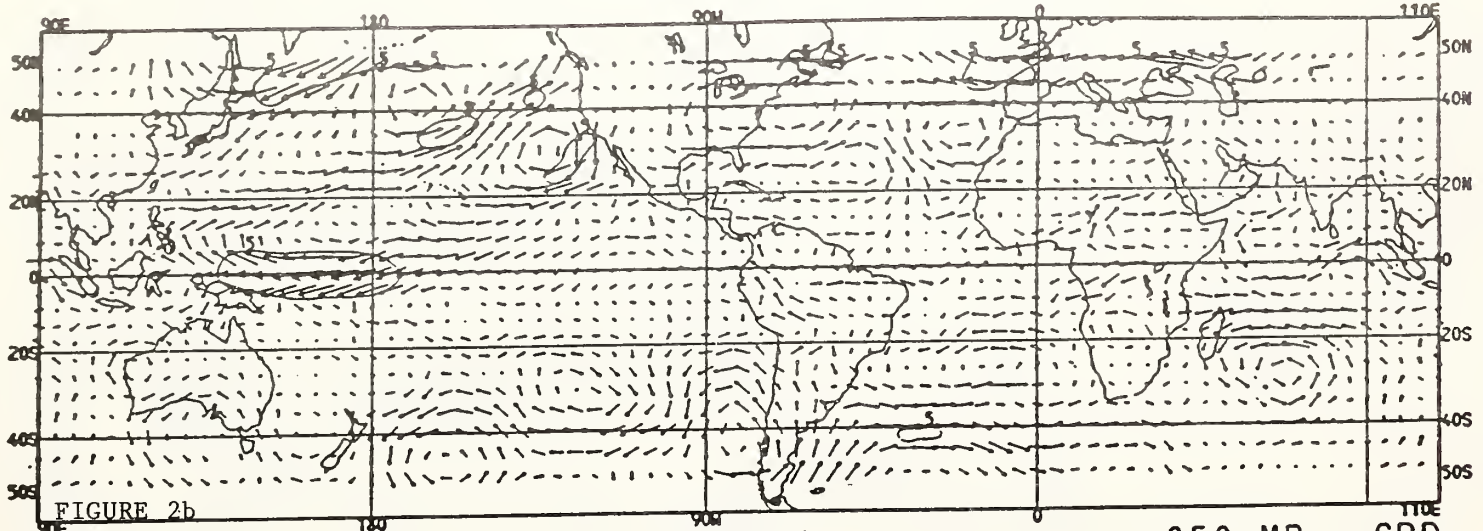

FIGURE 2b

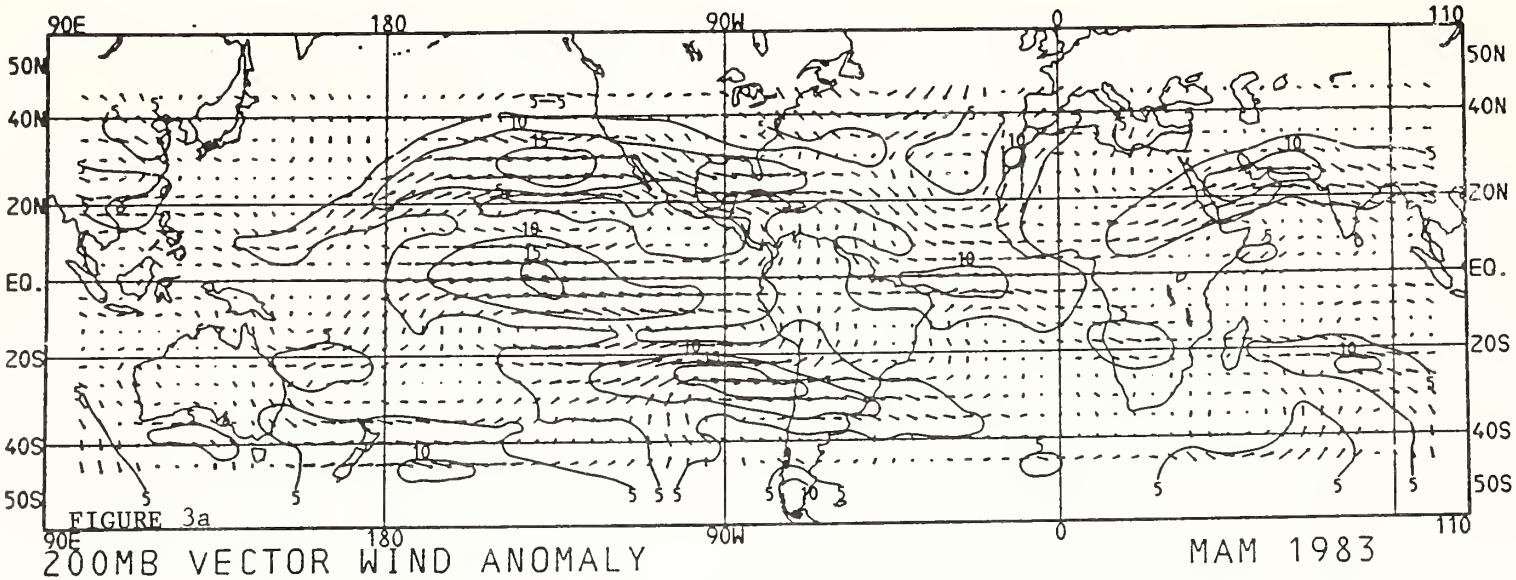

FIGURE 3a

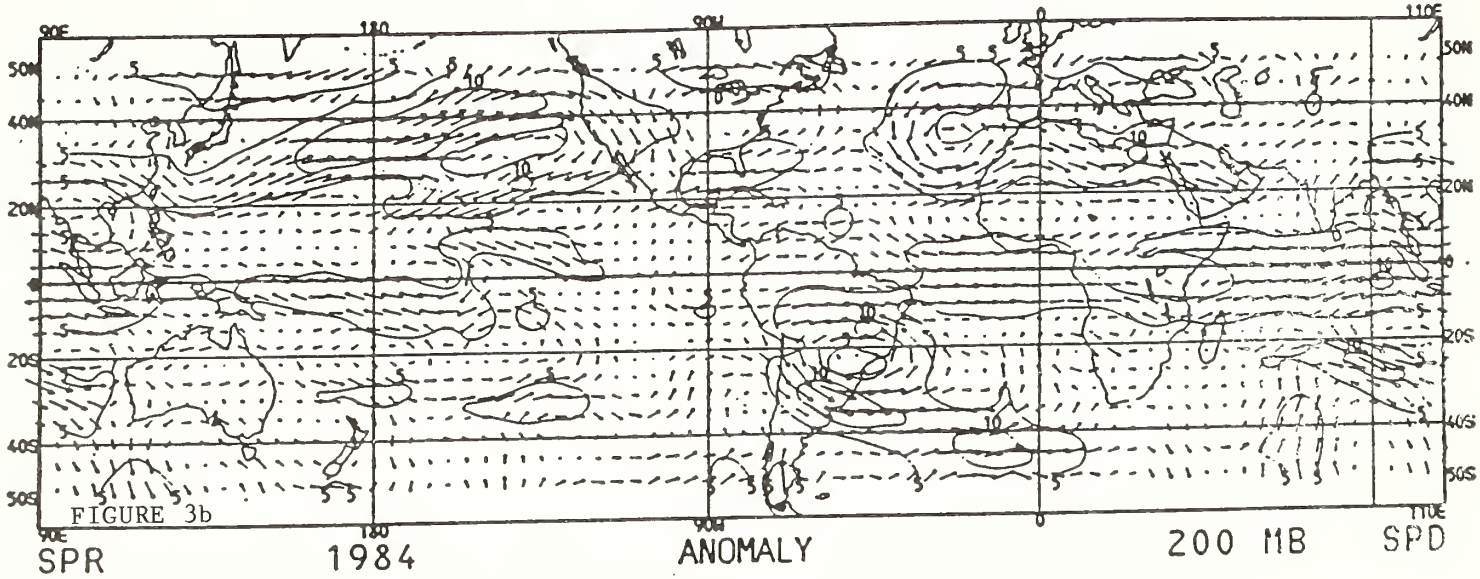

FIGURE 3b

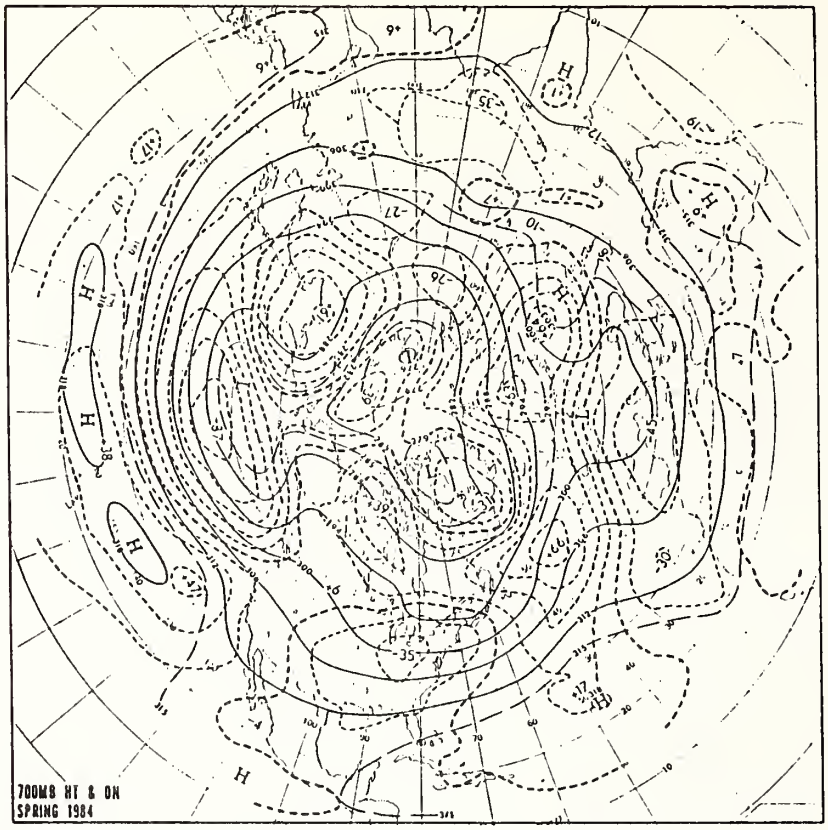

FIGURE 4 - Northern Hemisphere 700 mb height (solid) at intervals of 6 dam and height anomaly (dashed) at intervals of 15 m for spring 1984.

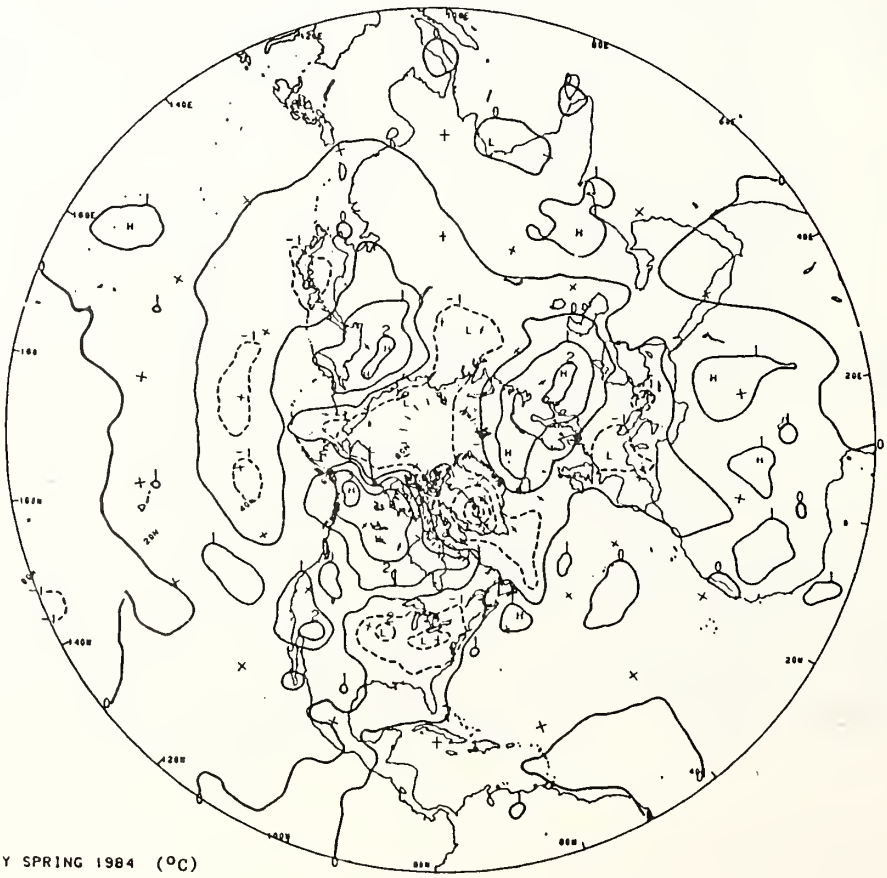

FIGURE 5 - TEMPERATURE ANOMALY SPRING 1984 (°C)

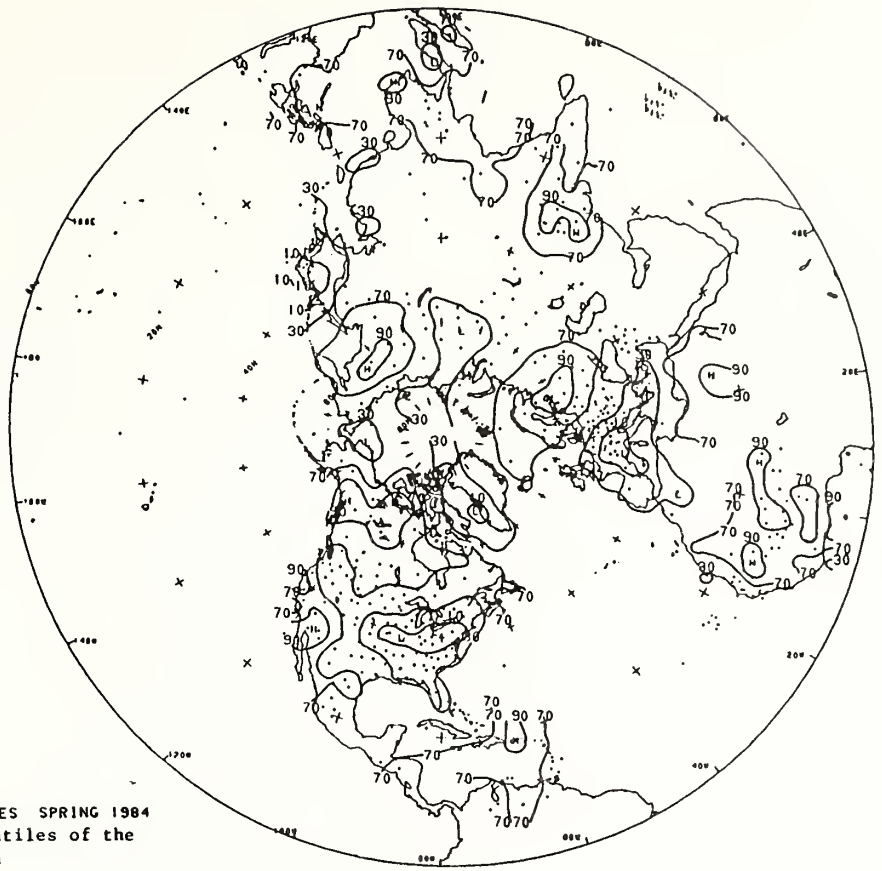

FIGURE 6 - TEMPERATURE PERCENTILES SPRING 1984
expressed as percentiles of the normal distribution

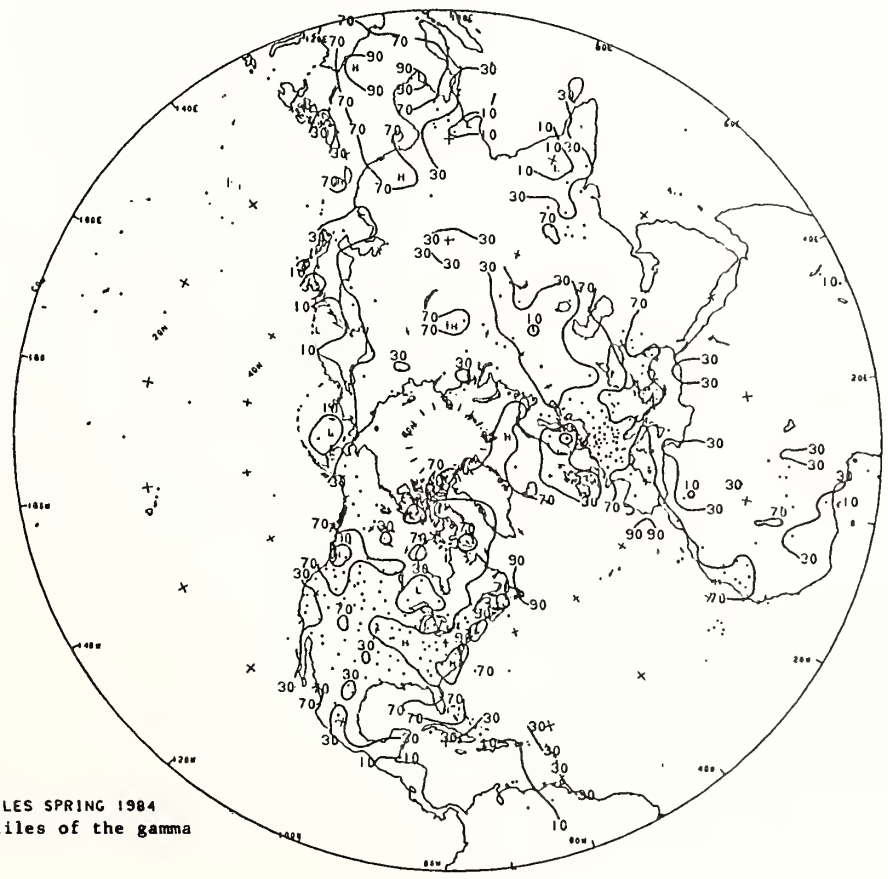

FIGURE 7 - PRECIPITATION PERCENTILES SPRING 1984
expressed as percentiles of the gamma distribution

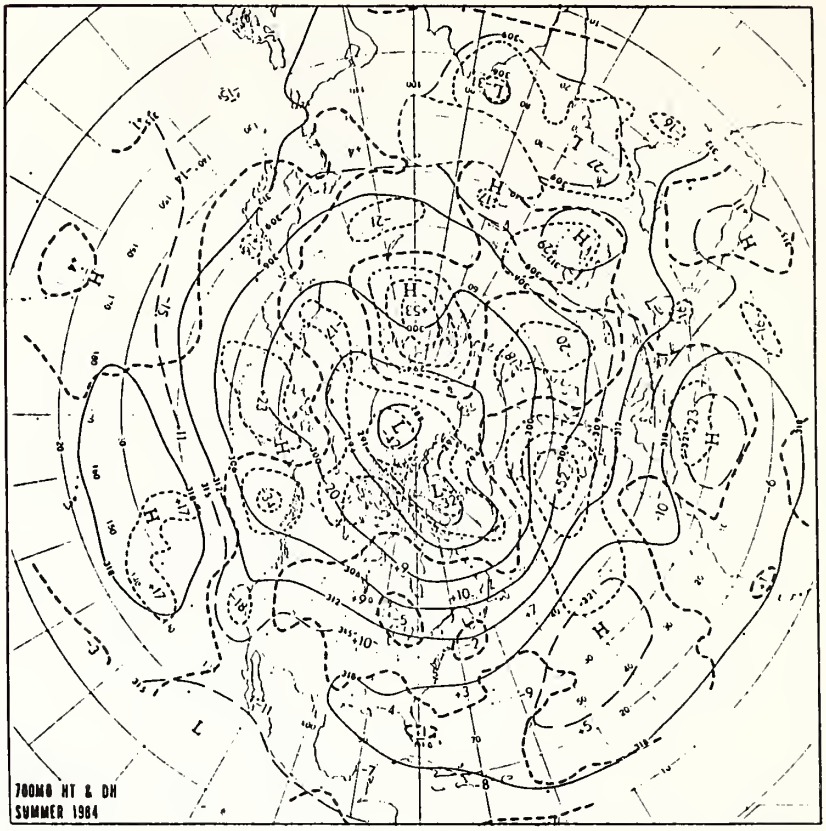

FIGURE 8 - Northern Hemisphere 700 mb height (solid) of intervals of 6 dam and height anomaly (dashed) of intervals of 15 m for summer 1984.

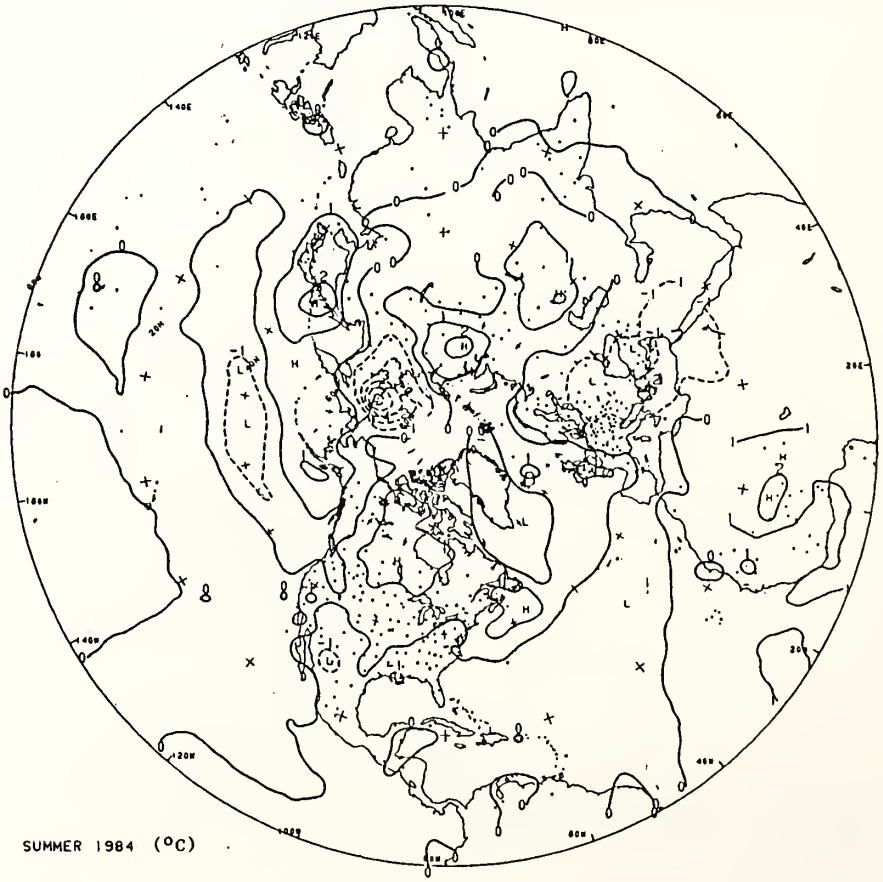

FIGURE 9 - TEMPERATURE ANOMALIES SUMMER 1984 (°C)

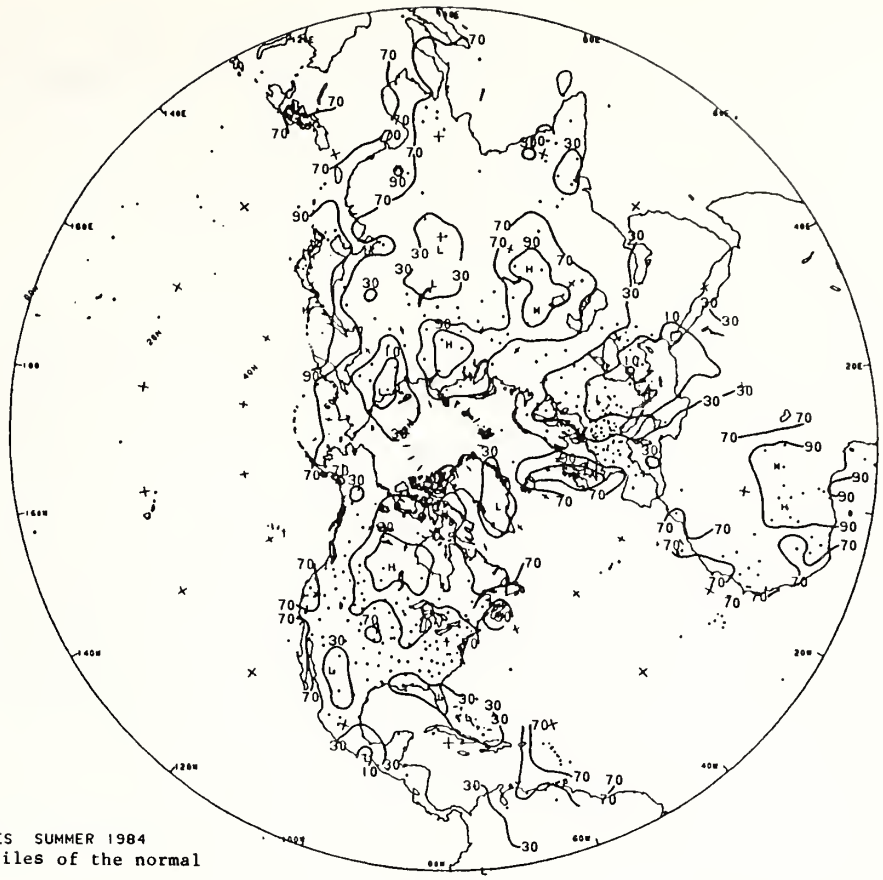

FIGURE 10 - TEMPERATURE PERCENTILES SUMMER 1984
expressed as percentiles of the normal distribution

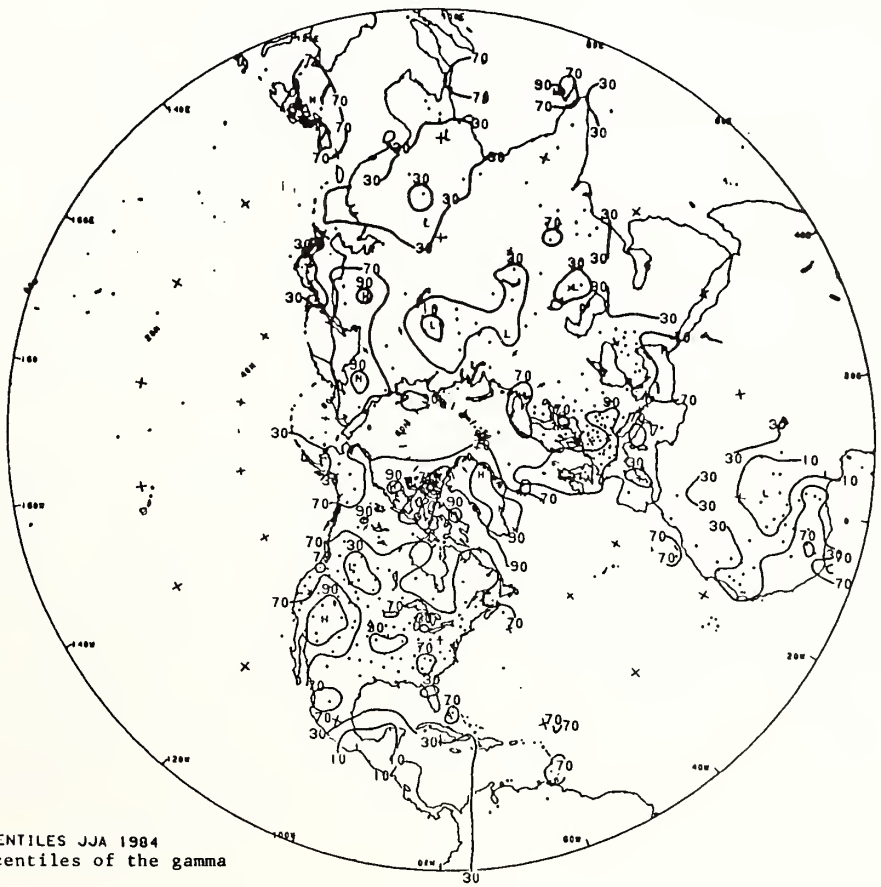

FIGURE 11 - PRECIPITATION PERCENTILES JJA 1984
expressed as percentiles of the gamma distribution

ON THE RELATIONSHIP BETWEEN NORTH ATLANTIC SEASONAL SST ANOMALIES WITH UNITED STATES SURFACE TEMPERATURE ANOMALIES

Daniel R. Cayan
Scripps Institution of Oceanography
La Jolla, California 92093

A North Atlantic sea surface temperature (SST) data set (Figure 1) was used to form regional average anomalies from areas exhibiting relatively strong temporal persistence. The two SST areas considered (Figure 2) were both located in the western North Atlantic, "Region 1" offshore of the northeastern United States, and "Region 2" in the subtropic area of the Caribbean and to its east. These regions are defined in the four month lag autocorrelation field over the North Atlantic in Figure 3; for comparison the four month lag autocorrelation for the North Pacific is shown in Figure 4. (Note that in the North Pacific the amplitude and spatial extent of the maximum autocorrelation coefficients are similar to those in the North Atlantic, but clustered in around the eastern boundary rather than the western.) Time series of the SST in the two regions are graphed in Figure 5; the variance of Region 1, reflecting its midlatitude, western boundary location is quite high, while the variance of Region 2 is rather small, being a subtropical area. Both regions exhibit a fairly decided low frequency character, although Region 2 appears more homogeneous throughout the 1949-1981 record length.

The time series of seasonal average SST from these two regions, along with those of station temperature for a grid covering the coterminous United States, were filtered by removing their linear trend, and then cross correlated to estimate the degree of linear relationship between SST and surface air temperature (SAT) within this dependent sample. Contemporaneously, the strongest correlations of these North Atlantic SST indices with United States SAT appear in winter and summer (Figures 6 and 7). In general, these show a tendency for the Southeast to be out of phase with the Northwest, a well-known spatial pattern. Not surprisingly, the correlations with Region 1 SST exhibit their highest values in the Northeast, while those with the subtropical SST (Region 2) are mostly strongest in the southern United States. Maximum correlations exceed 0.6, shading on these figures is at the 0.3 and 0.5 levels.

Some significant correlations also emerge at seasonal lags. For example, Figures 8 and 9 show the four one-season lag correlation fields of SST leading United States SAT for Regions 1 and 2. These have a similar pattern to the contemporaneous correlations (spring-to-summer resembling summer contemporaneous, and fall-to-winter resembling winter contemporaneous), with relatively strong values. Spring and Fall SAT are not well related to the prior season's SST of either region. Looking further, even at two seasons lag, there is evidence of apparent SST leading SAT, especially in the Region 2 relationships. The patterns of note, summer-to-winter and winter-to-summer, are shown in Figure 10. Notice here the strongest correlations are stationed in the West, rather than the Southeast, as in the previous cases.

In summary, some potentially useful relationships between North Atlantic regional SST and United States SAT at seasonal time scales are present in the 33-year sample considered here. One possible link of the North Atlantic SST behavior to the large scale atmosphere/ocean system may run through the large scale structure of ENSO, as suggested by G. Rasmusson at this workshop. It appears that North Atlantic Region 2 may be quite strongly coupled with the tropical Pacific, as indicated by seasonal lag correlations shown in Table I. Here we see that tropical Pacific SST in region "3" (5°N to 5°S, 170°W to 120°W, courtesy of T. Barnett/T. Tubbs) is rather strongly related to Region 2 SST but not Region 1 (not shown). These correlations are strong on a contemporaneous basis, and are skewed at seasonal time lags suggesting that the Pacific leads the North Atlantic, but not vice-versa. Interestingly, the tropical Pacific region "5" along coastal South America is also significantly related, but the correlations are lower and have a somewhat more complicated lag structure, perhaps indicating a longer lag, as shown in Table I. Finally, some rather strong correlations also emerge with North Pacific SST off the California coast in region "6", which shows a slight tendency to lead SST in North Atlantic Region 2. These rather simple indicators apparently reflect a large scale signal that runs through the ocean-atmosphere system. It remains to determine if these relationships hold up in an independent data set and to establish possible mechanisms of the atmosphere-ocean system that create them.

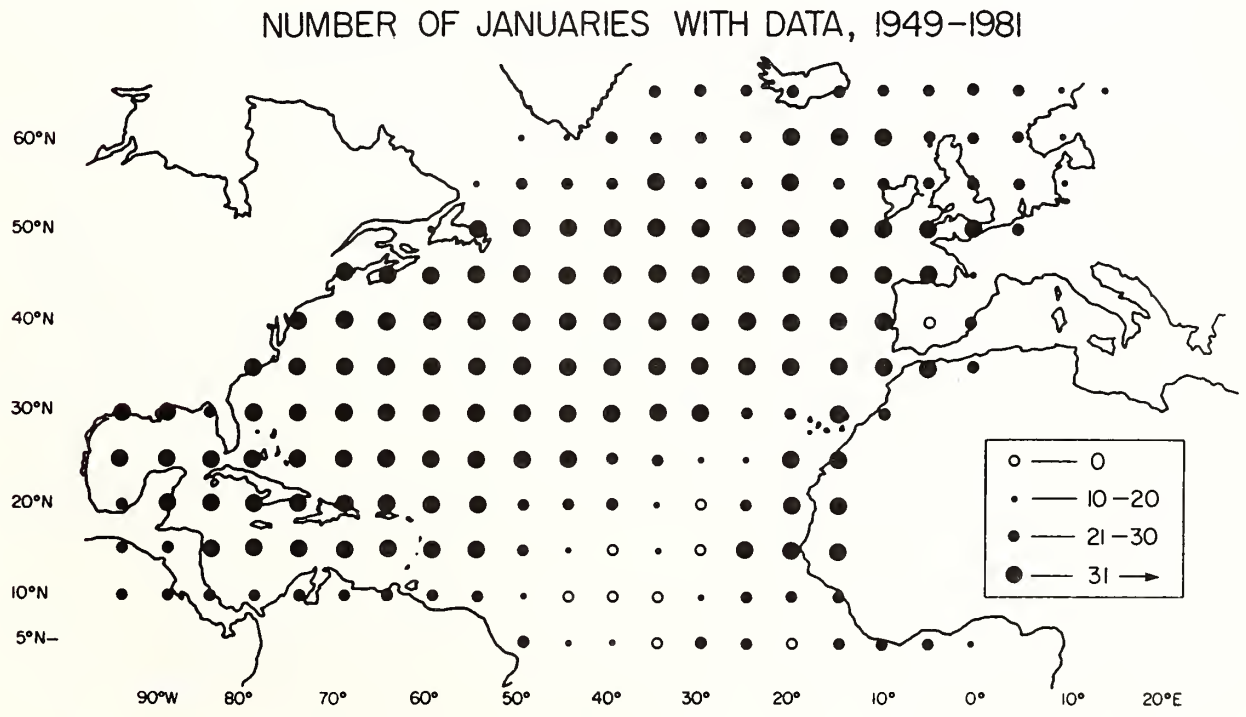

FIGURE 1

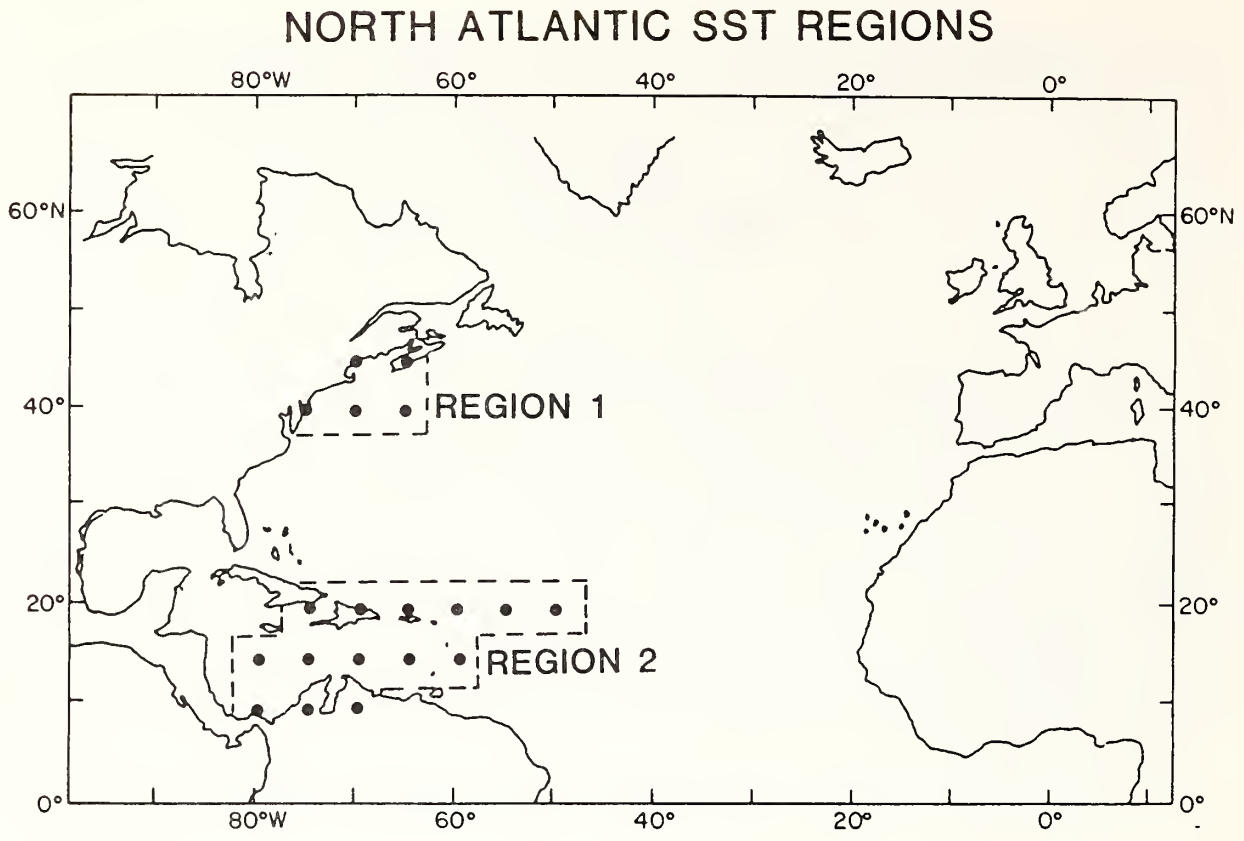

FIGURE 2.

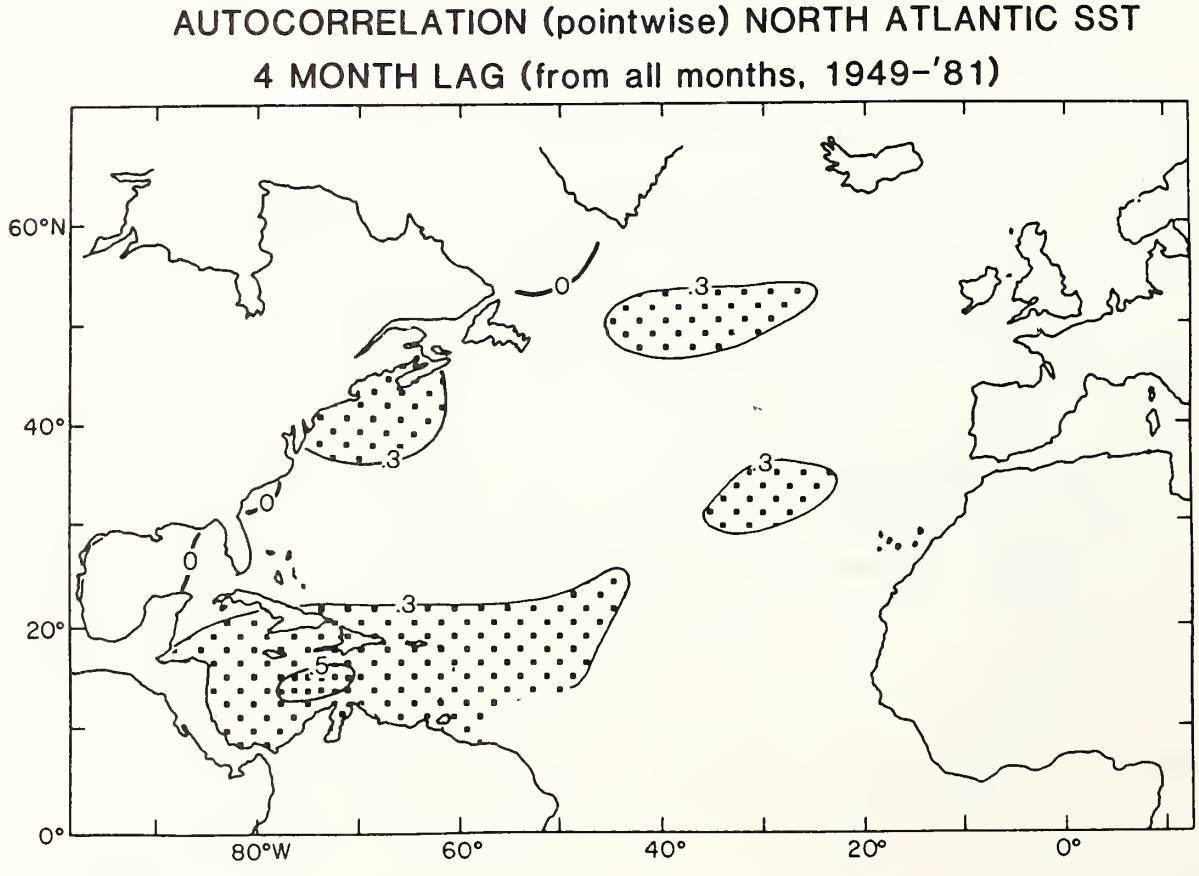

FIGURE 3.

AUTOCORRELATION (pointwise) NORTH PACIFIC SST
4 MONTH LAG (from all months, 1947-'82)

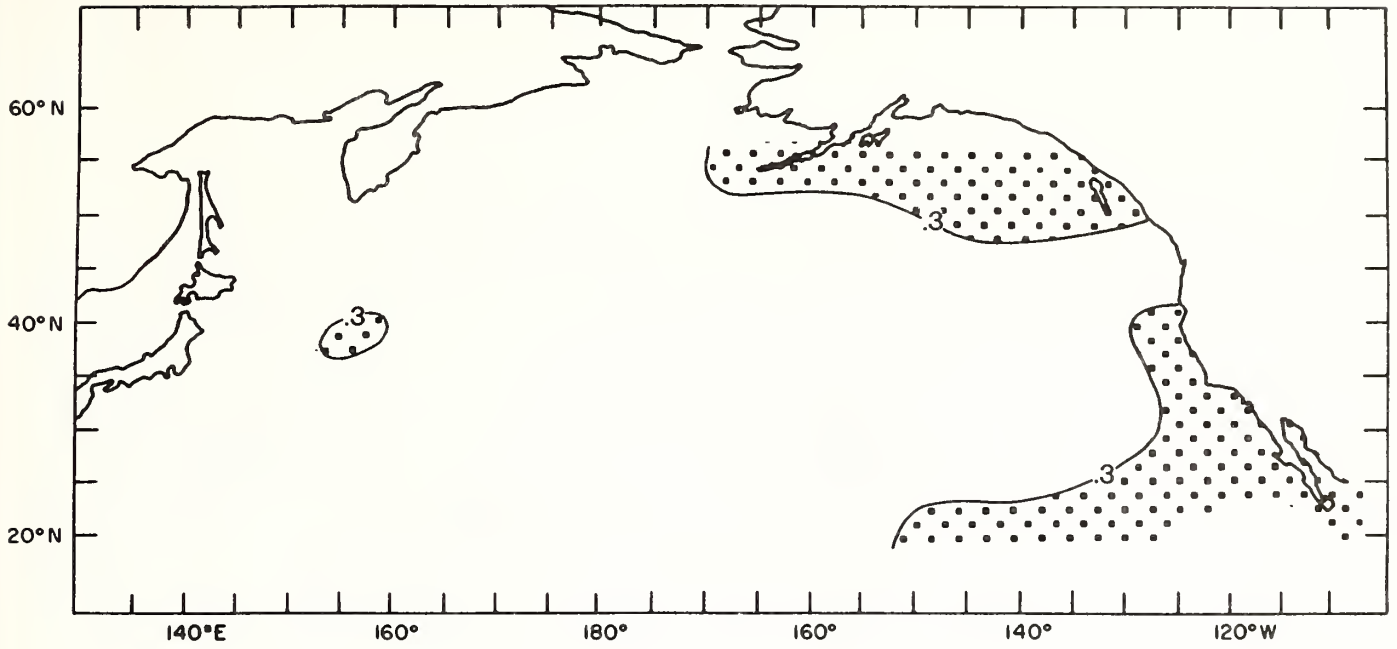

FIGURE 4.

NORTH ATLANTIC AREA AVERAGE SST ANOMALIES
(seasonal, 1949 - 1981)

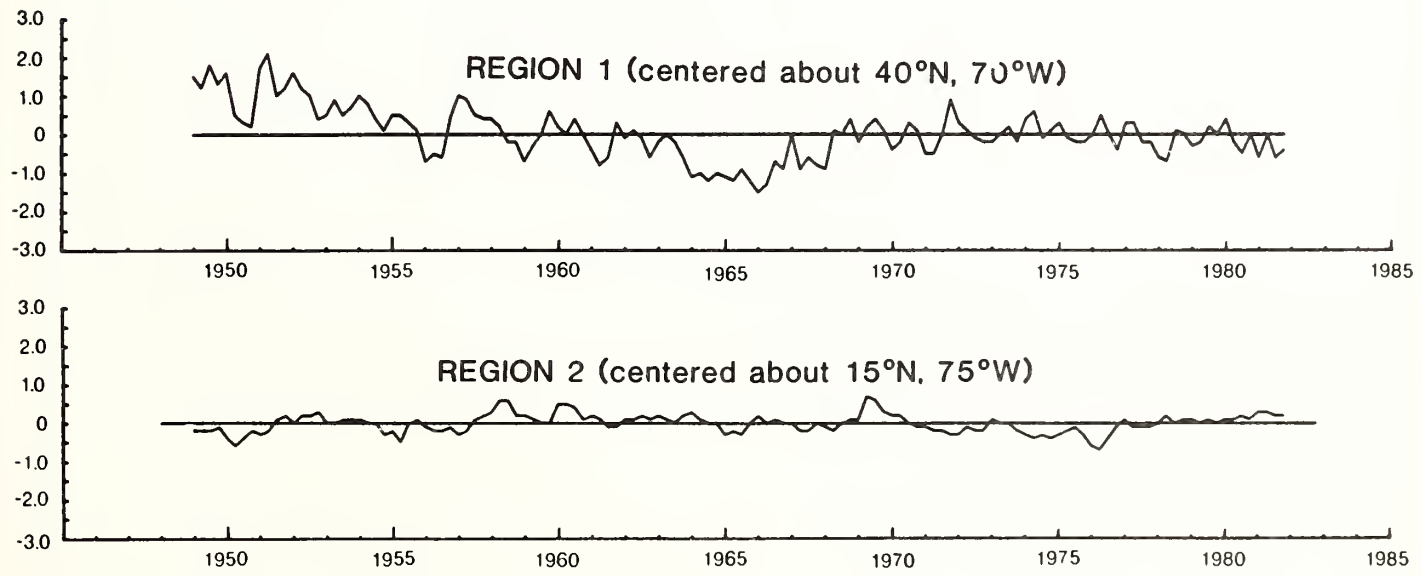

FIGURE 5.

CONTEMPORANEOUS SEASONAL CORRELATIONS

NORTH ATLANTIC SST (reg. 1) vs US TEMP (109 stn's)

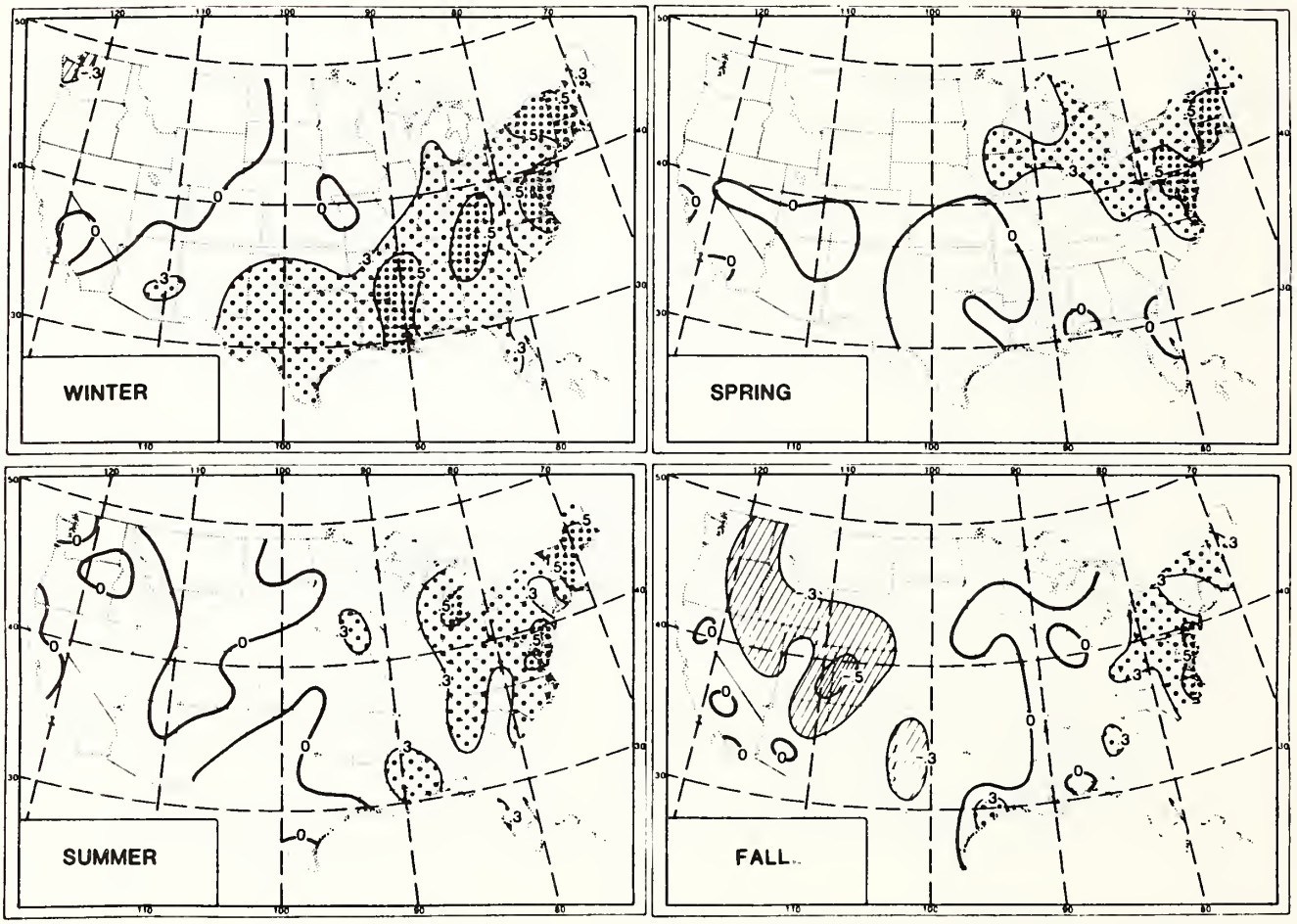

FIGURE 6.

CONTEMPORANEOUS SEASONAL CORRELATIONS

NORTH ATLANTIC SST (reg. 2) vs US TEMP (109 sta's)

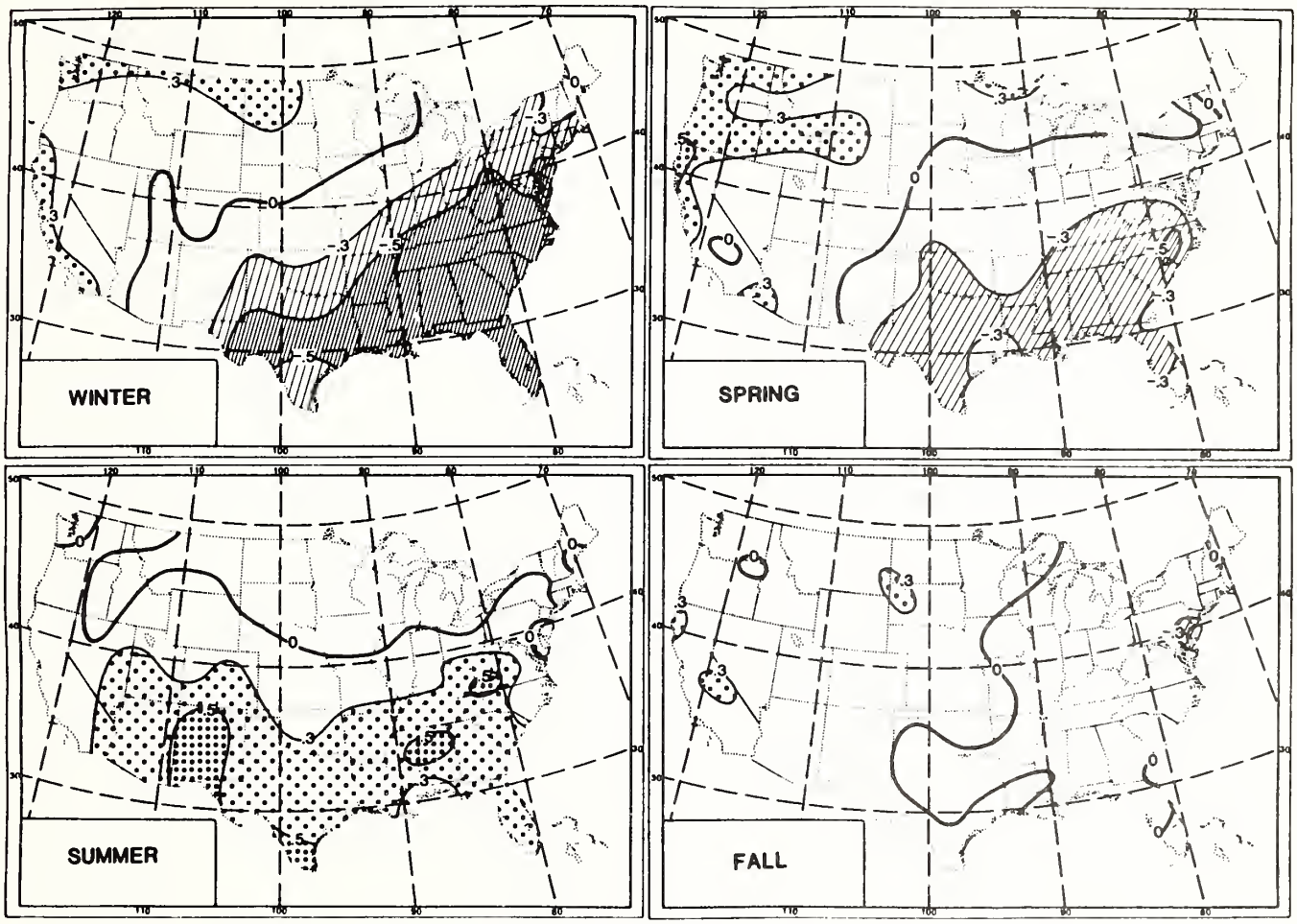

FIGURE 7.

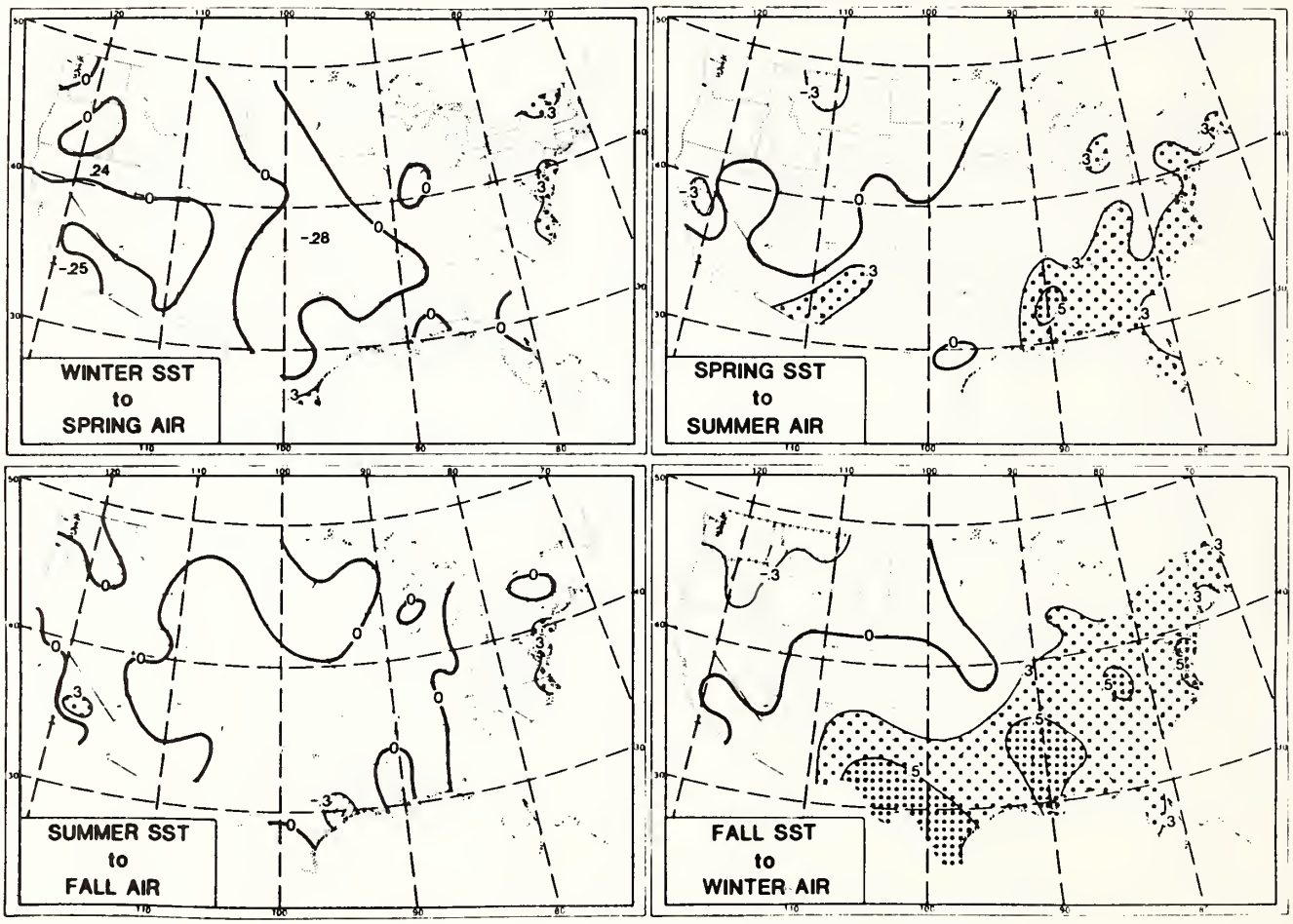
ONE SEASON LAG CORRELATIONS
NORTH ATLANTIC SST (reg. 1) LEADS US TEMP (109 stn's)
WINTER SST
to
SPRING AIR
SPRING SST
to
SUMMER AIR
SUMMER SST
to
FALL AIR
FALL SST
to
WINTER AIR

FIGURE 8.

ONE SEASON LAG CORRELATIONS

NORTH ATLANTIC SST (reg. 2) LEADS US TEMP (109 stn's)

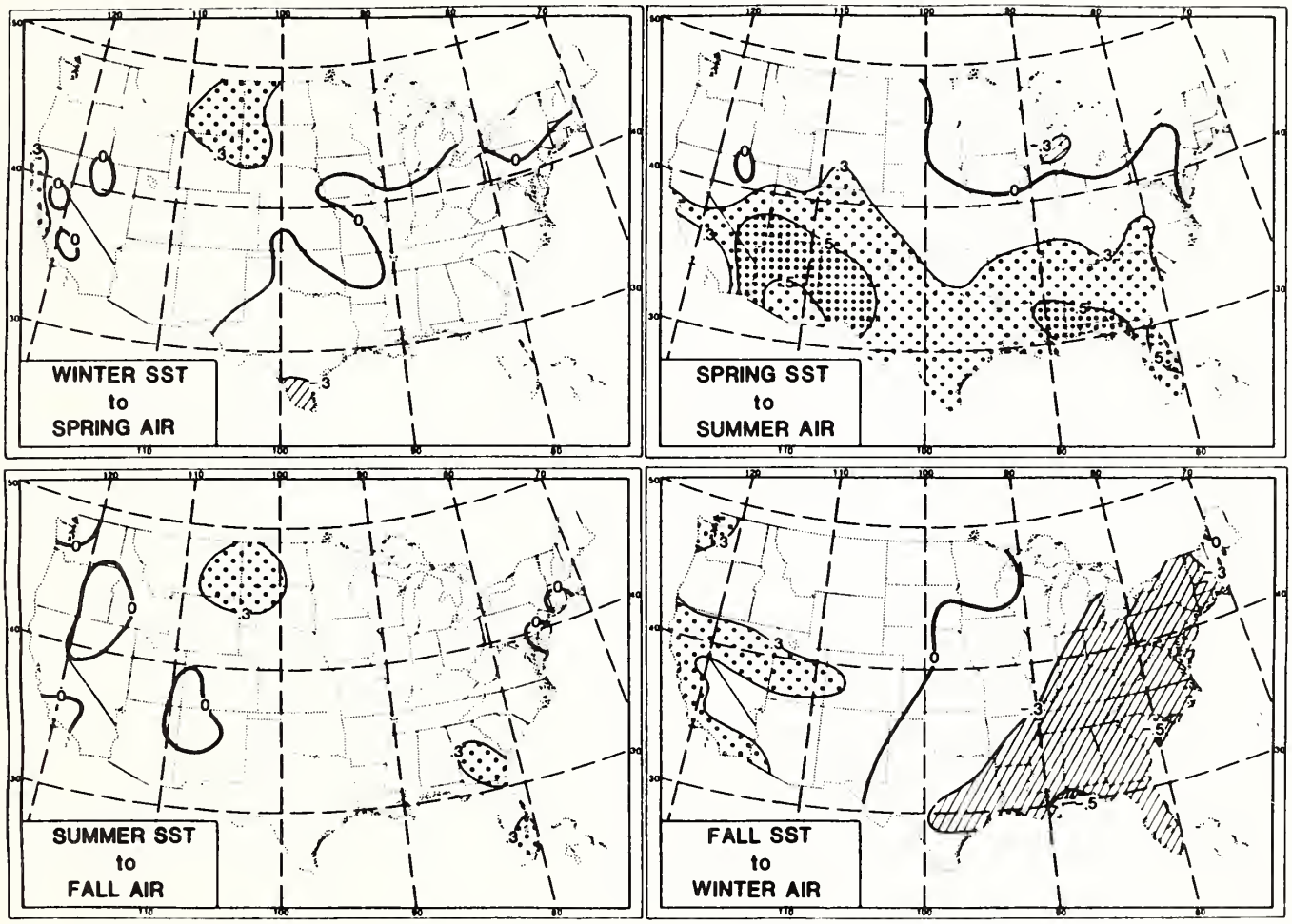

FIGURE 9.

TWO SEASON LAG CORRELATIONS

NORTH ATLANTIC SST (reg. 2) LEADS US TEMP (109 stn's)

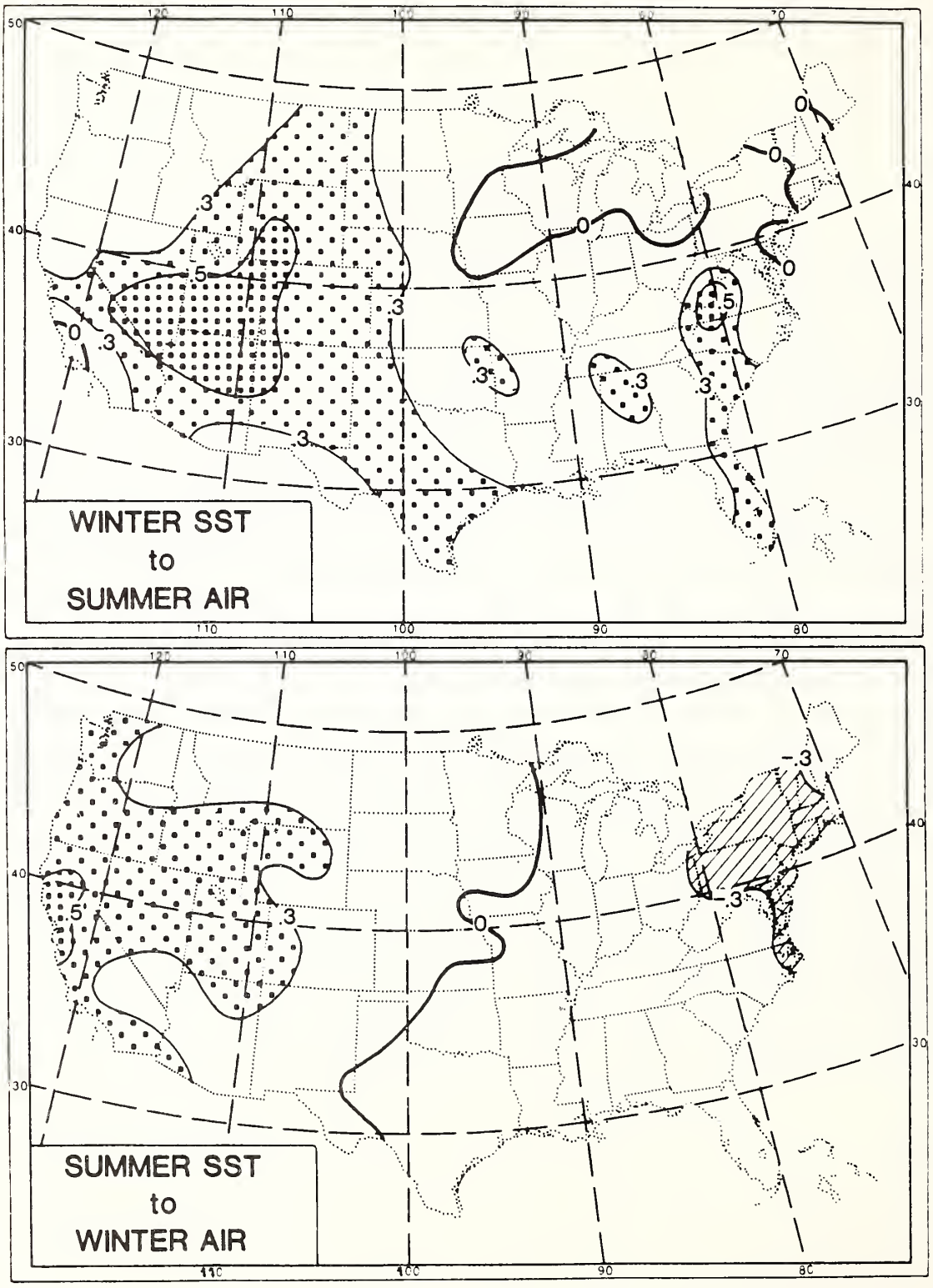

FIGURE 10

TABLE I

CROSS CORRELATIONS OF NORTH ATLANTIC REGION SST WITH

NORTH PACIFIC REGIONAL SST

Winter North Atlantic Region 2

Seasonal Lag*	-4	-3	-2	-1	0	1	2	3	4
Pacific Region 3	.24	.60	.66	.62	.64	.35	-.07	-.25	-.15
Pacific Region 5	.17	.42	.37	.53	.42	-.29	-.52	-.32	-.36
Pacific Region 6	.42	.66	.54	.56	.62	.57	.47	.04	.16

Spring North Atlantic Region 2

Seasonal Lag	-4	-3	-2	-1	0	1	2	3	4
Pacific Region 3	.41	.51	.56	.68	.58	.14	-.04	.12	-.02
Pacific Region 5	.34	.35	.55	.46	.05	-.22	.00	-.08	-.18
Pacific Region 6	.57	.57	.43	.48	.56	.52	.05	.16	.19

*Lags defined such that Pacific SST lags North Atlantic Region 2 by the number of seasons specified.

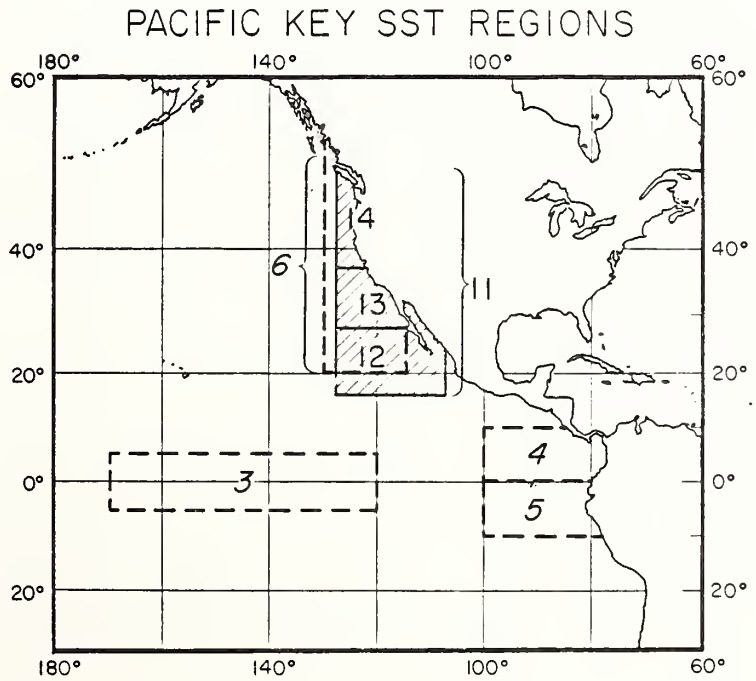

WORLDWIDE MARINE TEMPERATURE VARIATIONS ON THE SEASON TO CENTURY TIME SCALE

C.K. Folland, D.E. Parker and M. Newman

British Meteorological Office
Bracknell, Berkshire, United Kingdom

1. INTRODUCTION

Recently, the first two authors published an analysis of global and N. Hemisphere sea surface temperature (SST) and night marine air temperature (MATN) variations during 1856-1981 (1)., following the publication of preliminary results (2). The work is partly motivated by the desire to find out, in the context of a long-term research programme on long-range forecasting for UK, whether a deterministic explanation can be sought for any of several substantial long-lasting circulation fluctuations in the N. Atlantic region over the last century. These have sometimes led to large fluctuations in mean temperature or rainfall within the UK that have been coherent over decades.

Figs 1A and 1B illustrate two (of several) examples. In Fig 1A the vertical bars on the January and October 20-year running mean Central England Temperature (CET) graphs represent typical temperature ranges for the central 20% (middle "quint") of the frequency distribution of monthly CET for the months concerned, defined over a typical 30 year period (actually 1951-80). Monthly forecasts of temperature anomaly are currently made in terms of one of the five quints in each of 10 districts covering the UK similar to Central England in area. It is clear that persistent temperature fluctuations have occurred which are large compared with the

size of a typical central quint (October is specially notable). In some cases those fluctuations have been related to atmospheric circulation changes (eg Fig 1B).

A further example is that since about 1965 summer (June - August) rainfall has declined to such an extent (due to anomalously persistent anticyclones) that two major summer drought emergencies have occurred (1976 and 1984) when dry summers followed dry springs; of the 11 driest summers since 1766, four appear to have occurred between 1976 and 1984 including the driest (1976) and second driest (1983).

2. INSTRUMENTAL CORRECTIONS

A crucial aspect of the analysis reported in (1) concerned the determination of a set of corrections for changes in instrumental practices. MATN and (in World War 2) day marine air temperatures were used to help solve the difficult problem of identifying changes in the biases in SST measurements. The paper also describes how the MATN data were themselves corrected for estimated changes in the mean height of screens above the sea as ships increased in size. Detailed accounts of the corrections, quality control of the ship reports etc appear in references 3-6. Recently we have completed detailed comparisons between post-war "bucket" and "non-bucket" observations (the latter are mostly derived from engine intake data) between 1975 and 1981, a period for which we believe the individual ship report indicators for these data types are reasonably reliable. Note that "buckets" are now mostly insulated (eg as used by the UK Voluntary Observing Fleet) and will have biases that differ from those of "uninsulated" buckets which were prevalent before about 1942. Fig 2 shows zonally averaged differences between bucket and non-bucket observations (based on about 1.5 million bucket and 3 million non-bucket

data). The differences are physically reasonable; bucket temperatures are slightly cooler than engine intake temperatures overall (mean difference -0.08°C) but with a tendency for bucket temperatures to be relatively least cold (or absolutely warmer) in local summer and coolest in local winter. The magnitude of the overall difference provides a justification for neglecting the difference between the two observation types since World War 2 as we did in (1) though Fig 2 indicates refinements to this assumption are possible.

3. RESULTS

Figs 3-6 provide selected analyses of SST and MATN anomaly data which will be fully reported in forthcoming papers. Instrumental corrections as described in (1) have been applied to the data. Figs 3(a) - (e) give season by season SST and MATN time series (based on 5° x 5° areas) for 4 large ocean areas between Jan/Mar 1856 and April/June 1984 (only to 1981 for MATN). Quality controlled telecommunicated data have been used to update SST after 1981. The ocean areas are (a) Globe (b) N. Hemisphere (c) S. Hemisphere (d) Tropical E. Pacific (170°E - American Coast, 20°N - 20°S) (e) Tropical W. Pacific (120°E - 170°E, 20°N - 20°S). The October to December season close to the peak of each El Nino warm phase that we have identified (8) is indicated by arrows in the same graphs. Figs 4(a) - (b) show detrended maximum entropy spectra for series (b) (c) (d) and (e) such that an area under any curve, plotted in the frequency domain, gives the corresponding detrended variance (which is little different from the original variance). The SST time series and spectra show that small, seasonally varying corrections (typically $\pm$0.1°C) are needed before about 1940 in addition to the mean correction of +0.3°C hitherto applied. A scheme which includes an attempt to physically model seasonally varying SST

corrections is under development. Other outstanding features of the spectra (excluding long term variations) include considerable variance in the 15-21 year range, depending on geographical region chosen, and a 9.5 month peak in the Tropical West Pacific SST series, absent in the corresponding MATN series, but present in the SST for this area with comparable power in the shorter periods 1946-80 and 1961-80 when no significant annual peaks occur. No other SST series of ocean basin size (of a total of 20 that we have analysed) shows a prominent peak near 9 months, though we have observed appreciable peaks near 9 months in several smaller ocean regions. Figure 5a shows a graph of seasonal values of Northern Hemisphere SST and MATN, centrally plotted after application of a 41-term triangular filter which is almost opaque to periodicities shorter than 5 years and transparent to periodicities longer than 20 years. Figure 5b shows a graph similar to Fig 5a except that from 1891 onwards the values of MATN have been augmented by a Russian Northern Hemisphere land air temperature data set as described and corrected by Robock (9), rearranged so as to produce 5° x 5° area seasonal anomalies from a 1951-60 average. Note that the air temperature curves in fig 5a and 5b are basically similar but fig 5b reflects the fact that Northern Hemisphere land air temperature warmed more quickly between the early years of the twentieth century and 1940. In addition Robock's land air data shows a slightly smaller trough to peak range than the MATN or indeed the land data of Jones et al (10): we hope to combine Jones et al's data with our MATN data in due course.

Figs 6(a) - (b) shows the first two global SST eigenvectors, derived from the correlation matrix, based on seasonal anomalies for 10° x 10° areas for 1901-80. EOF1 (11% of variance) shows the long term trend and EOF 2 (6% of variance) illustrates El Nino-related SST variations (similar

to but rather stronger than that of Hsiung and Newell for 1949-79 (11)). Fig 7(a) shows the similarity between time series of EOF 1 and the Global SST series (Fig 3a) (correlation = -0.93) and Fig 7(b) likewise compares time series of coefficients of EOF 2 with the tropical E. Pacific series (Fig 3d) (correlation = 0.61). Lag correlations are being computed.

Finally Fig 8 shows a result which we feel demands special attention. The diagram, which shows zonally and decadally averaged SST anomaly, relative to 1951-60, indicates that since about the decade 1956-65 the southern hemisphere has warmed and the northern hemisphere cooled, though warming may have restarted in the northern hemisphere in recent years (Fig 3b). The net effect is that the zonally and decadally averaged SST difference between about 40°S and 40°N has increased by about 0.7°C since 1951-60; in the Atlantic sector, a similar or larger change has been mainly concentrated in tropical latitudes. These observations indicate the possibility of significant long-term changes in the seasonally varying positions of the rising and descending branches of the Hadley circulation. Rind and Rossow (12), using the GISS AGCM, indicate that the zonally-averaged positions of the rising arms of the Hadley cells could be particularly sensitive to the latitude of the absolute maximum SST. Many well known observational and modelling studies of the atmospheric response to El Nino SST variations indicate this result on a regional space scale, while other studies suggest that a critical SST of about 27°C to 28°C is required for deep convection to be sustained over the oceans. It is suggested that on decadal time scales noticeable global and regional effects of changes of SST gradient of the kind shown in Fig 8 on the Hadley cell circulation should be sought.

REFERENCES

1. C.K. Folland, D.E. Parker and F. E. Kates (1984) "Worldwide marine temperature fluctuations 1856-1981". Nature, 310, pp 670-3.

2. Folland, C.K. and Kates F.E. (1984) (ed. A Berger et al) Milankovitch and Climate Part II pp 721-727.

3. J. H. Minhinick and C.K. Folland (1984) The Meteorological Office Historical Sea Surface Temperature Data Set (MOHSST). Met. Office Synoptic Climatology Branch Memo 137.

4. D. E. Parker (1984) The Meteorological Office Historical Marine Air Temperature Data Set (MOHMAT). Met. Office Synoptic Climatology Branch Memo 138.

5. D. E. Parker and C.K. Folland (1984) Adjustment of night-time marine air temperatures to compensate for changes of observing elevation. Met Office Synoptic Climatology Branch Memo 141.

6. D. E. Parker (1984) An analysis of marine temperatures during the Second World War. Met. Office Synoptic Climatology Branch Memo 142.

7. D. E. Parker and C. K. Folland (1984) The effects of changes of averaging method and reference period on decadal anomalies of marine temperature. Met Office Synoptic Climatology Branch Memo 143.

8. M R Newman (1984) Observational Aspects of the El Nino and the Atmospheric Response. Met. Office Synoptic Climatology Branch Memo 148.

9. A Robock (1982) The Russian Surface temperature dataset JAM 21, pp 1781-1785.

10. P D Jones, T M L Wigley and P M Kelly (1982) Variations in surface air temperatures: Part 1, Northern Hemisphere 1881-1980. Mon. Weath. Rev., 110, pp 59-70.

11. J Hsiung & R E Newell (1983) The principal non-seasonal modes of variation of global sea surface temperatures. J. Phys. Ocean., 13, pp 1957-1967.

12. D Rind & W B Rossow (1984) The effects of physical processes on the Hadley Circulation. JAS 41, pp 479-507.

Central England Temperature 1659–1983
20-year running means

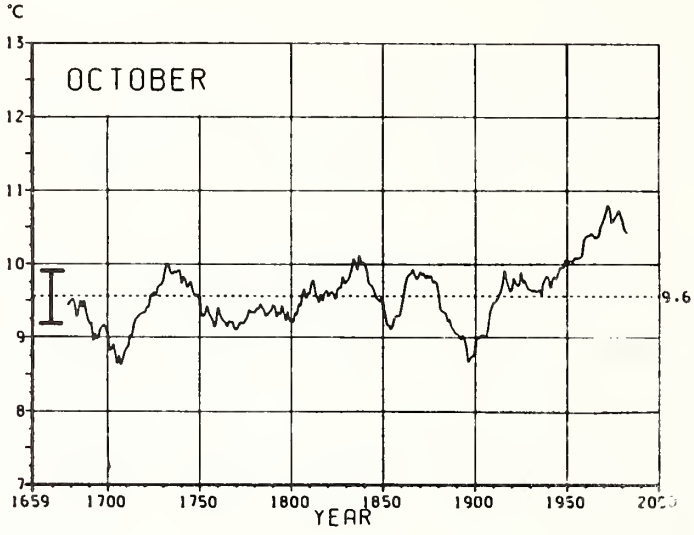

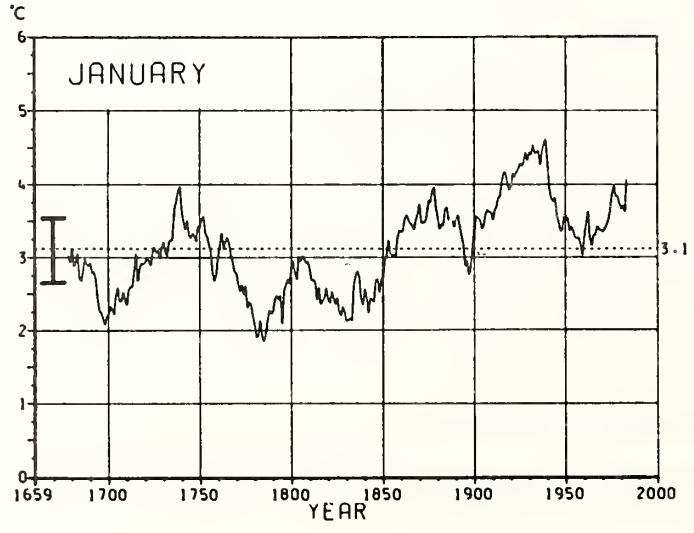

Figure 1a

JANUARY 1901-30 MEAN SURFACE PRESSURE ANOMALY (1951-70 BASE PERIOD)

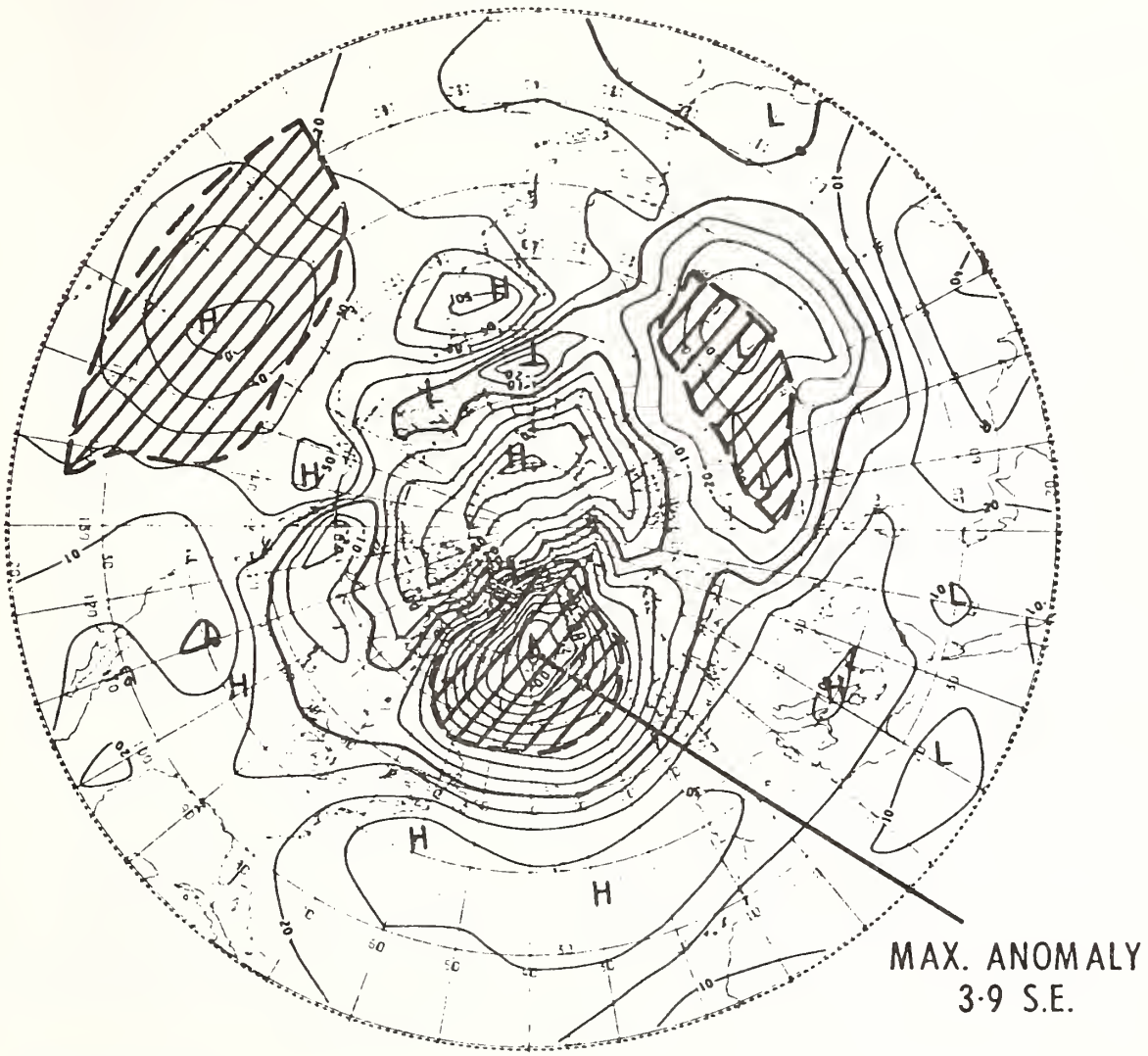

anomaly mb x 10

Areas of 5% significant difference using "t" test (approx assessment)

NB Other areas of large anomaly not shaded as data too doubtful

FIGURE 1b

FIGURE 2. ZONAL AVERAGE BUCKET MINUS NON-BUCKET SST 1975-1981
5° SQUARE VALUES COMPUTED USING ≥8 INDIVIDUAL MONTHS WITH BOTH INSTRUMENTAL TYPES
ZONAL AVERAGE PLOTTED IF ≥50% OF RELEVANT SQUARES HAVE COMPUTED VALUE
(BRACKETED POINTS = 40%-50%)

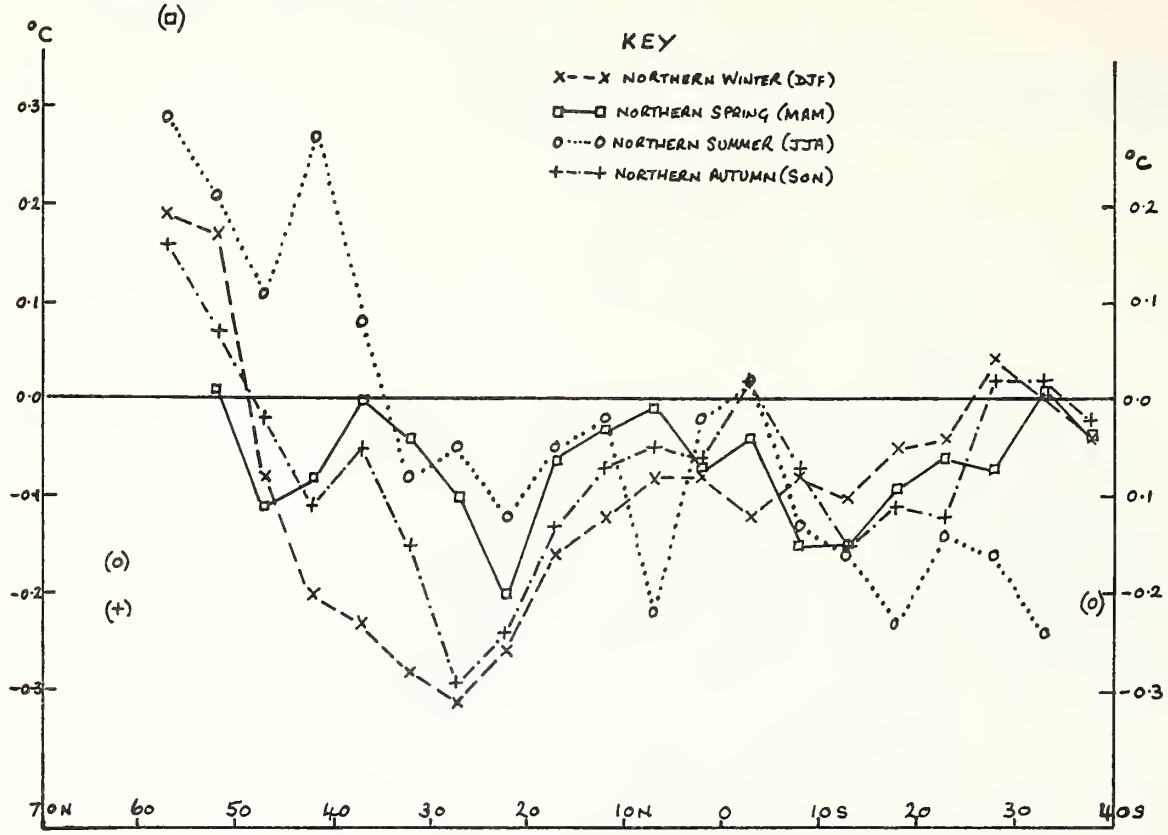

SEASONAL SST AND MATN ANOMALIES FROM 1856 WITH RESPECT TO 1951-60 MEANS AVERAGED OVER THE GLOBE. SOLID LINE IS MATN ANOMALY - DASHED LINE IS SST ANOMALY

Arrows mark Oct-Dec of El Nino years (8)

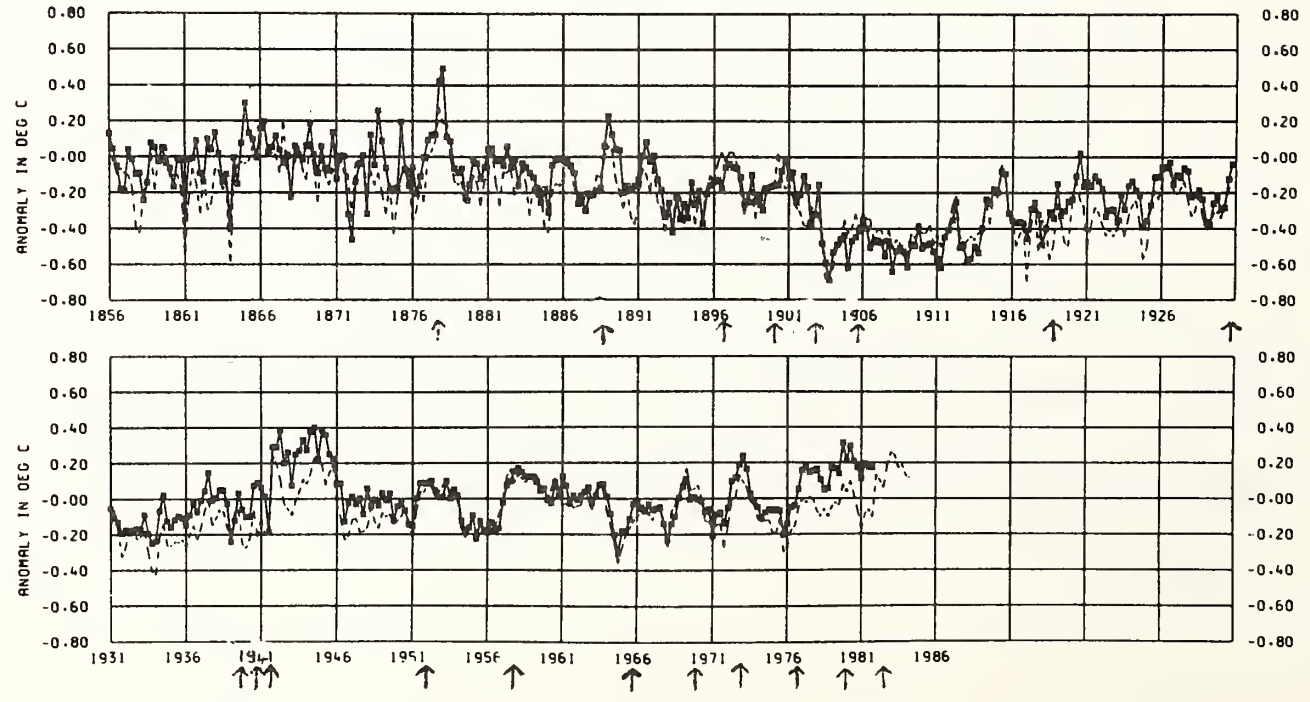

FIGURE 3a

SEASONAL SST AND MATN ANOMALIES FROM 1856 WITH RESPECT TO 1951-60 MEANS AVERAGED OVER THE NORTHERN HEMISPHERE: SOLID LINE IS MATN ANOMALY - DASHED LINE IS SST ANOMALY

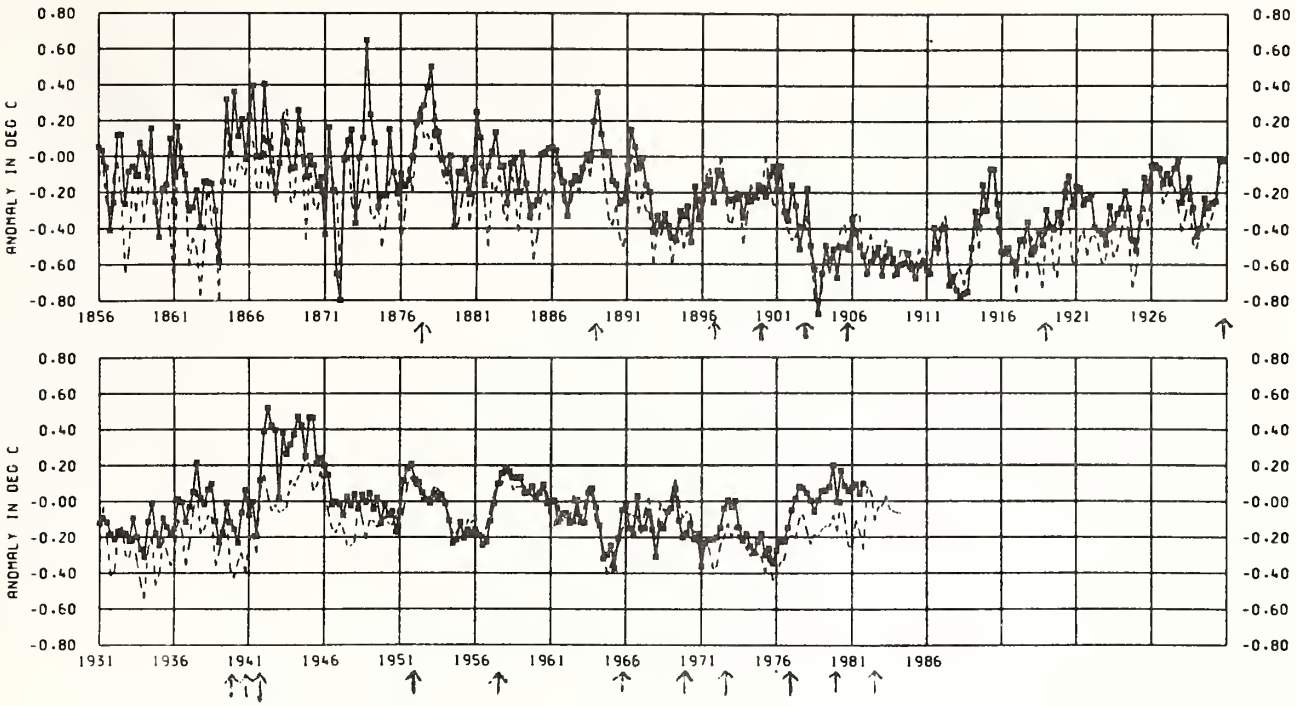

FIGURE 3b Arrows mark Oct-Dec of El Nino years (8)

SEASONAL SST AND MATN ANOMALIES FROM 1856 WITH RESPECT TO 1951-60 MEANS AVERAGED OVER THE SOUTHERN HEMISPHERE: SOLID LINE IS MATN ANOMALY - DASHED LINE IS SST ANOMALY

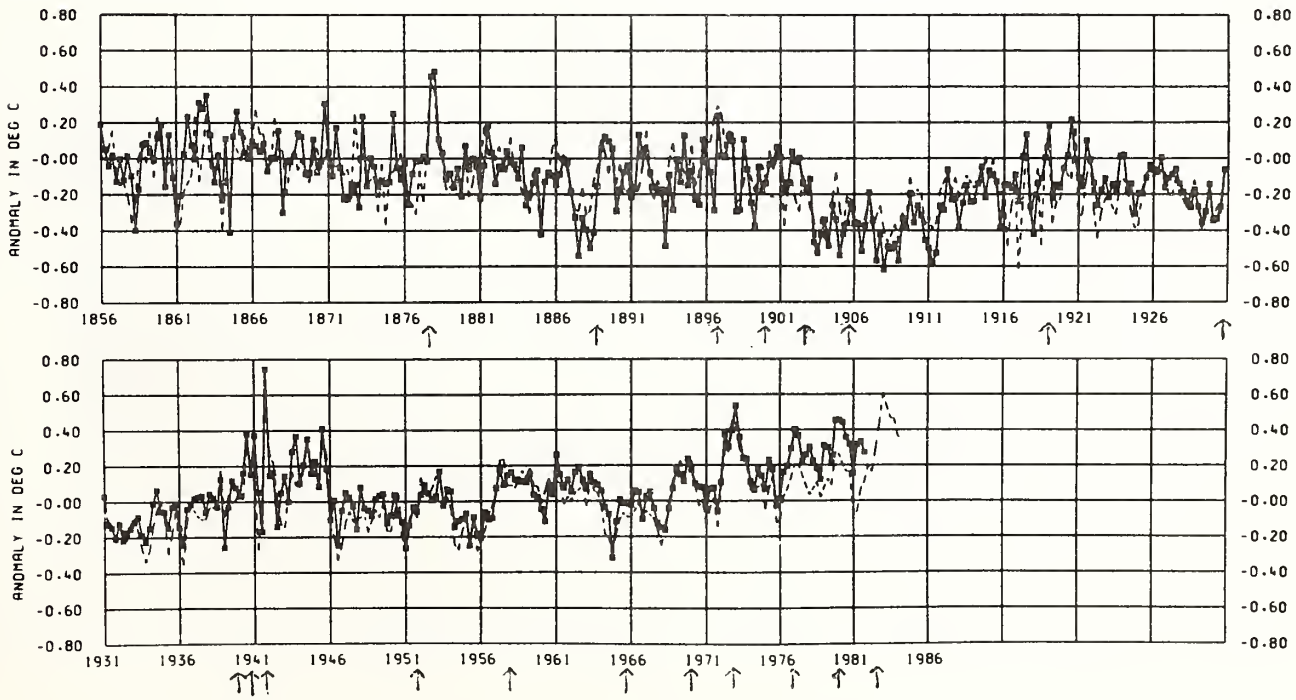

FIGURE 3c Arrows mark Oct-Dec of El Nino years (8)

SEASONAL SST AND MATN ANOMALIES FROM 1856 WITH RESPECT TO 1951-60 MEANS AVERAGED OVER THE EAST TROPICAL PACIFIC: SOLID LINE IS MATN ANOMALY - DASHED LINE IS SST ANOMALY

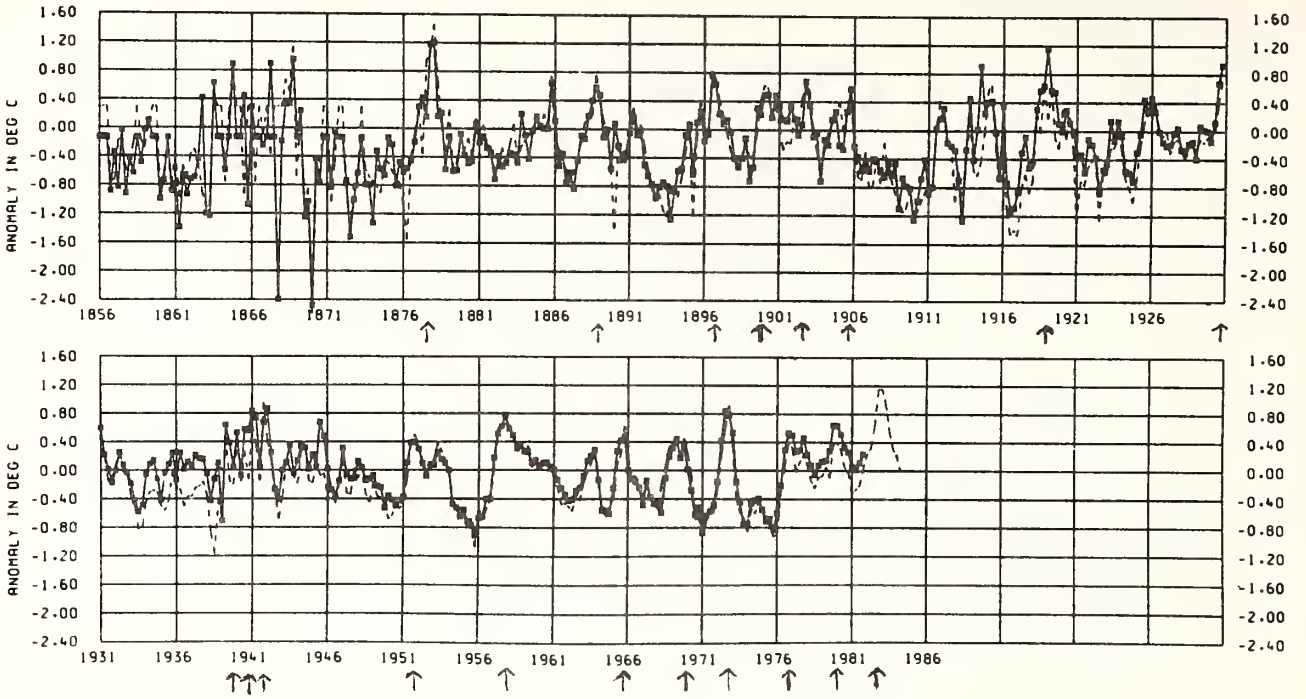

FIGURE 3d Arrows mark Oct-Dec of El Nino years (8)

SEASONAL SST AND MATN ANOMALIES FROM 1856 WITH RESPECT TO 1951-60 MEANS AVERAGED OVER THE WEST TROPICAL PACIFIC: SOLID LINE IS MATN ANOMALY - DASHED LINE IS SST ANOMALY

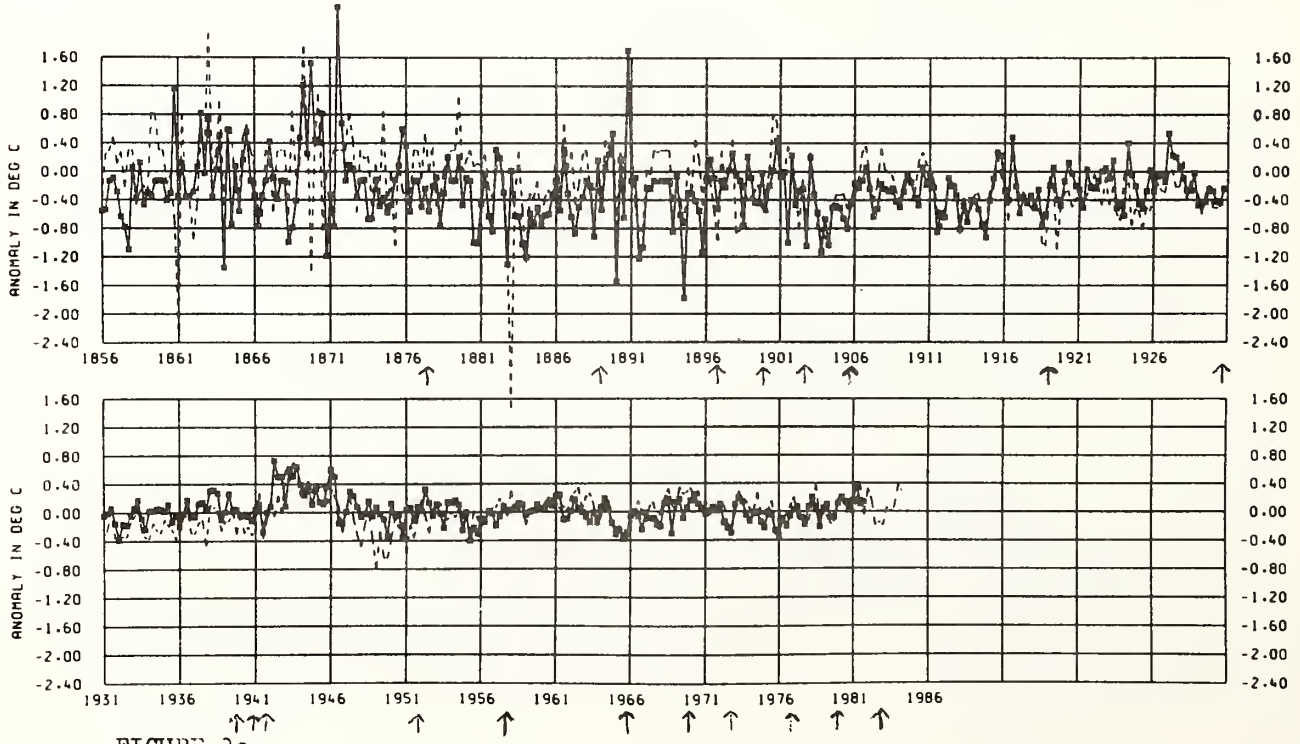

FIGURE 3e Arrows mark Oct-Dec of El Nino years (8)

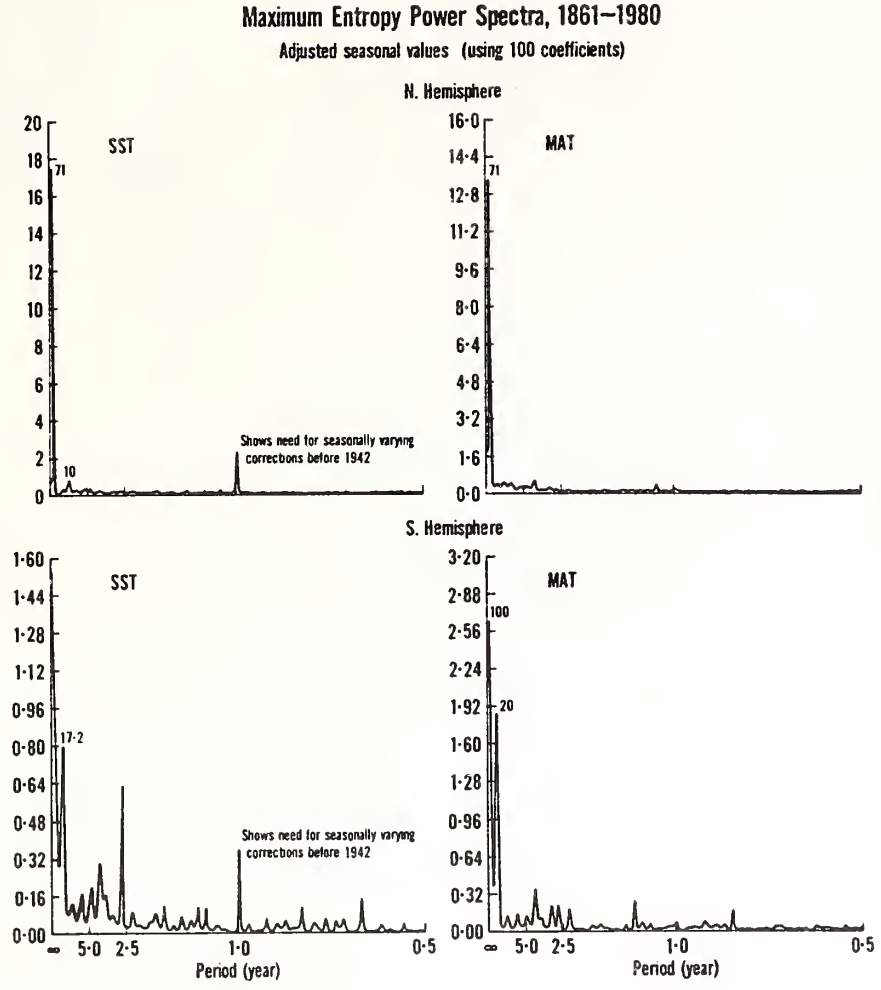

FIGURE 4a

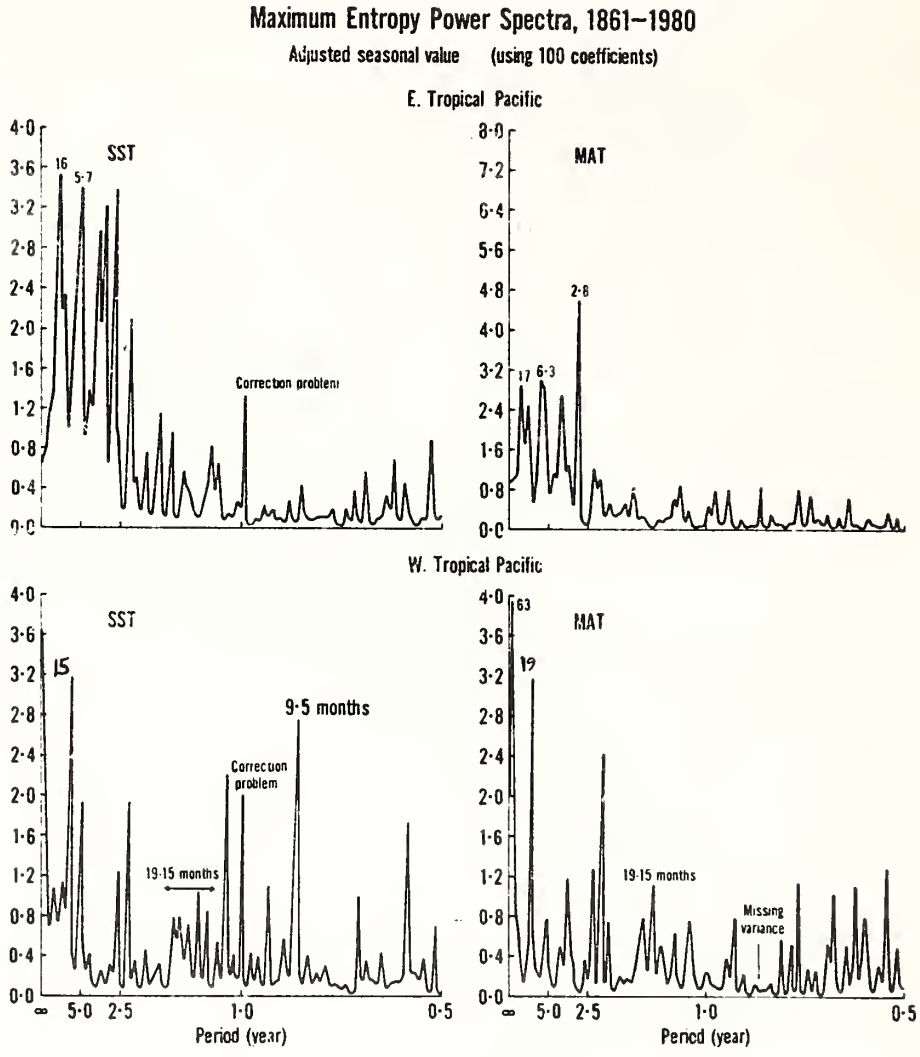

FIGURE 4b

FILTERED SERIES OF SEASONAL NORTHERN HEMISPHERE SST AND MATN ANOMALIES W.R.T. 1951-60.

HEAVY LINE IS MATN AND LIGHT LINE IS SST.

Values are plotted at the centre date of the moving 41-term triangular filter (see text).

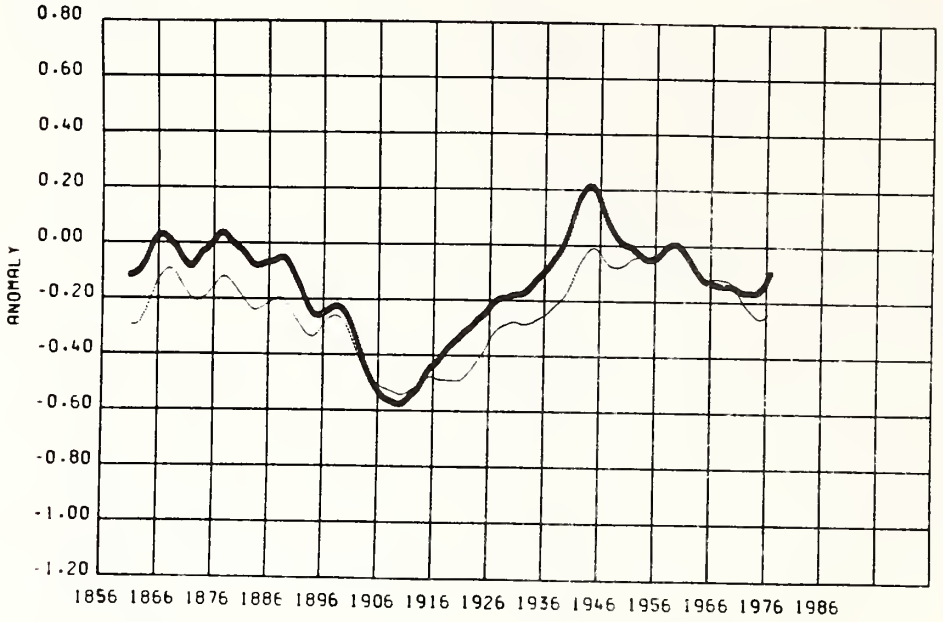

FIGURE 5a

FILTERED SERIES OF SEASONAL NORTHERN HEMISPHERE SST AND COMBINED MATN/LAND AIR TEMPERATURE ANOMALIES W.R.T. 1951-60.

HEAVY LINE IS AIR TEMPERATURE AND LIGHT LINE IS SST.

Values are plotted at the centre date of the moving 41-term triangular filter (see text).

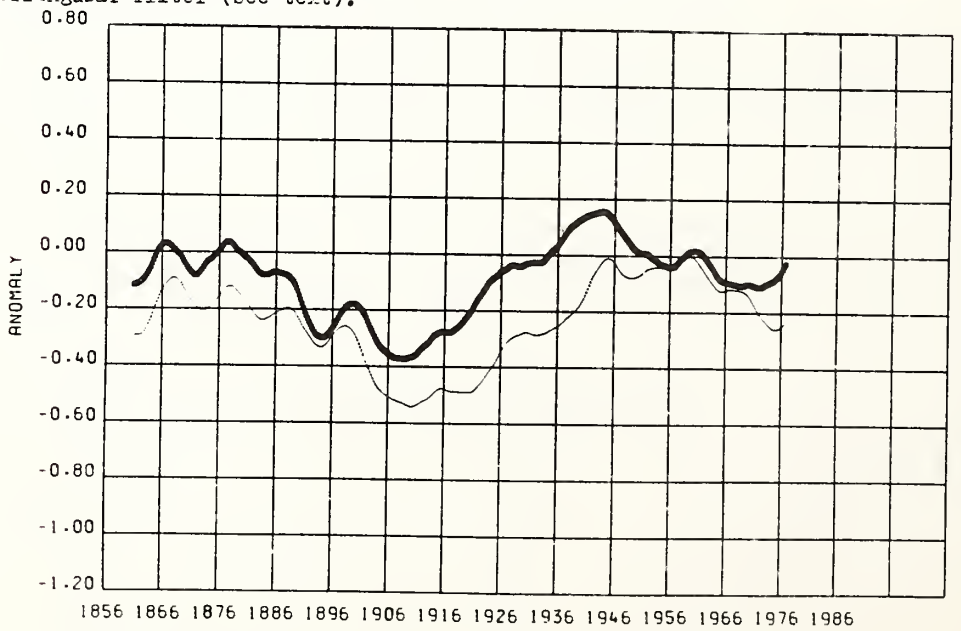

FIGURE 5b

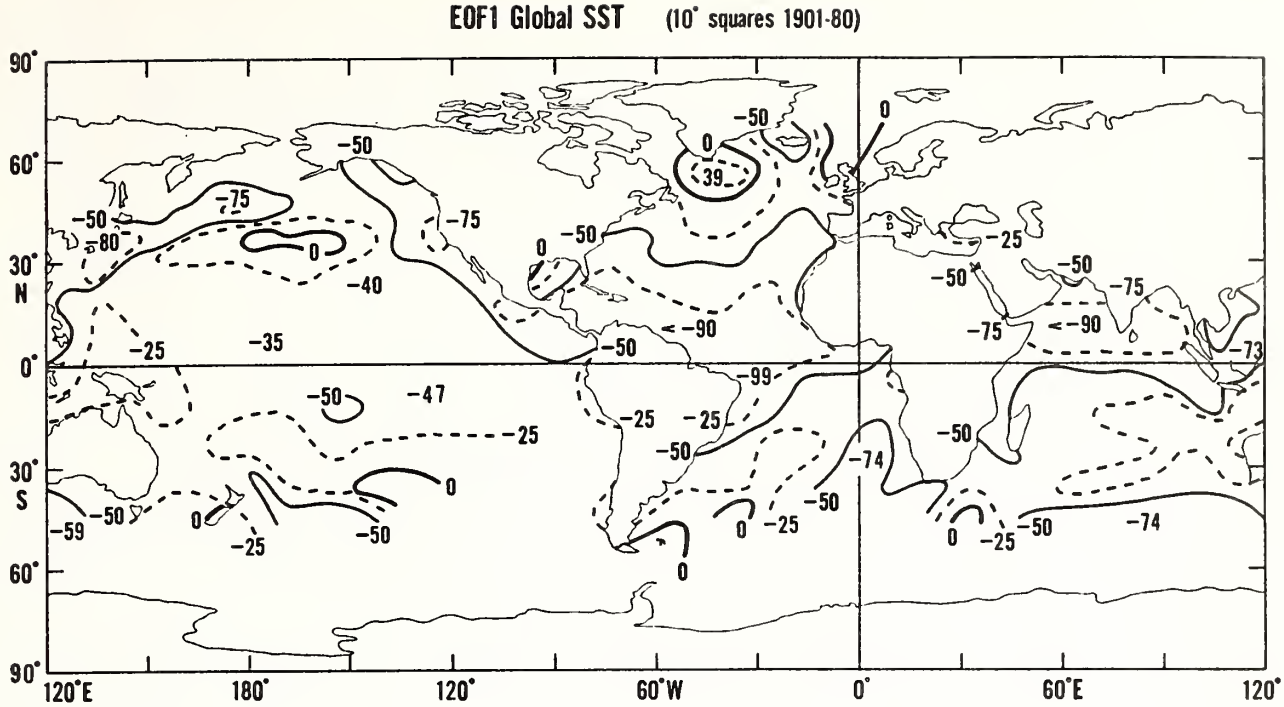

FIGURE 6a

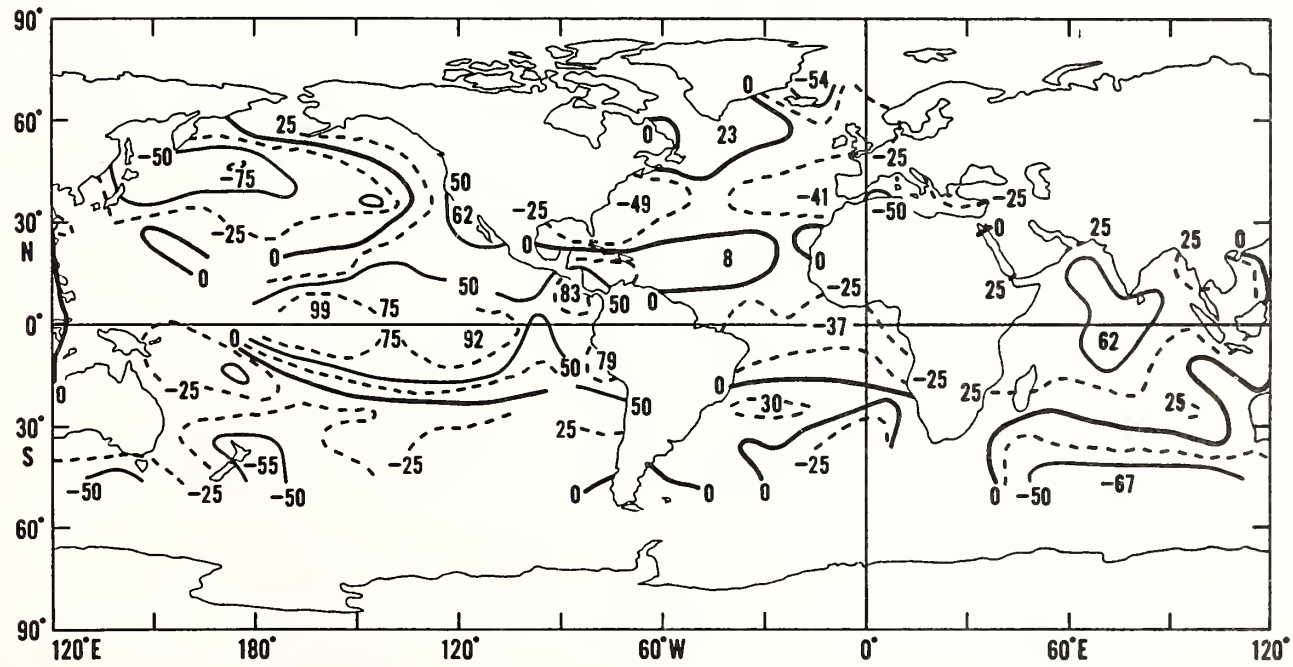

FIGURE 6b

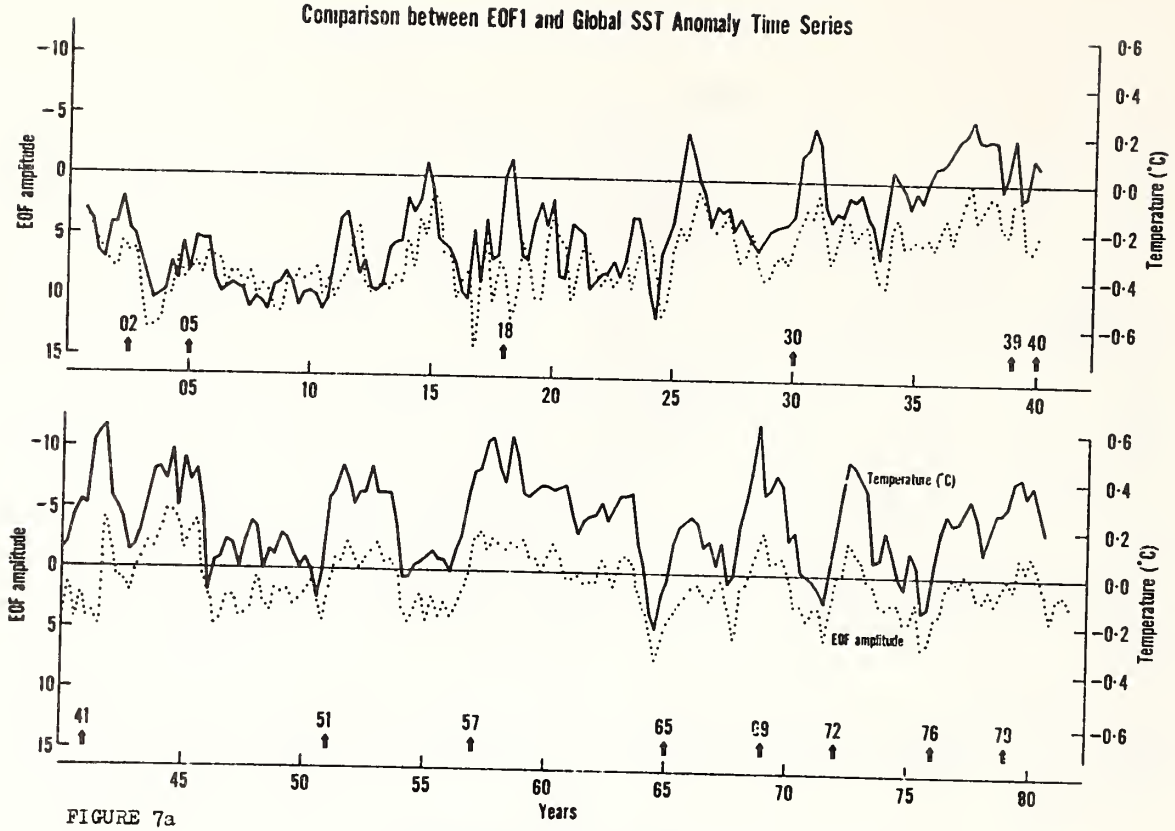

FIGURE 7a

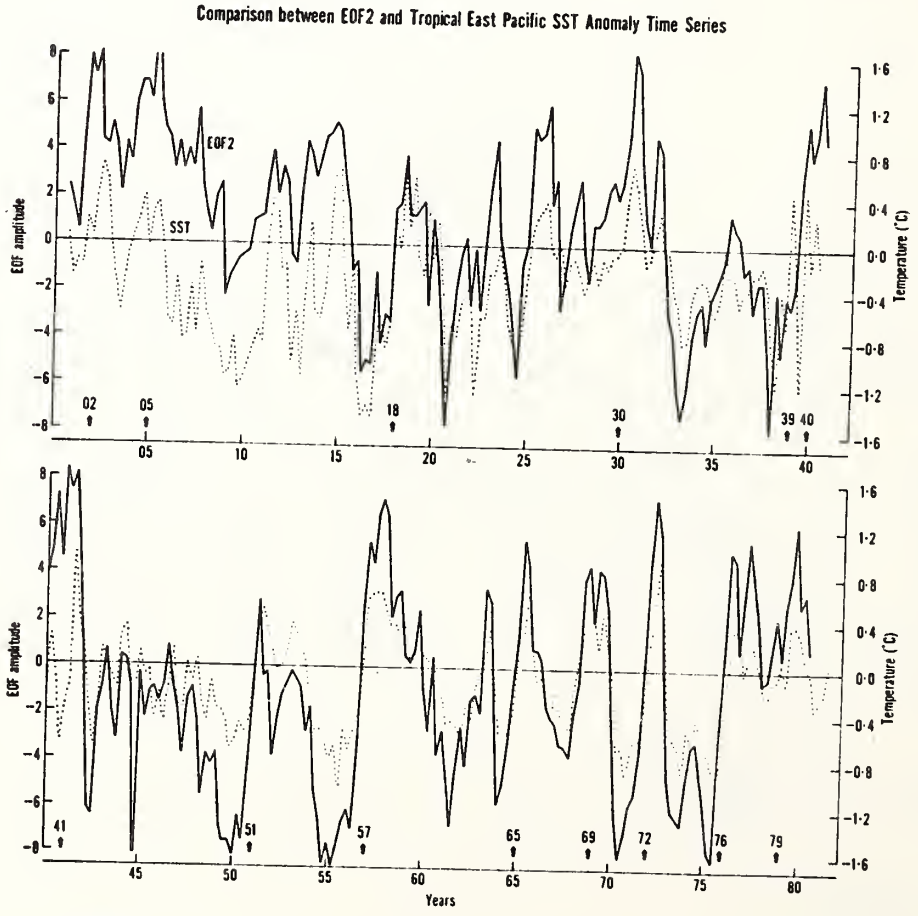

FIGURE 7b

Zonally-averaged SST anomalies

(relative to 1951-60)

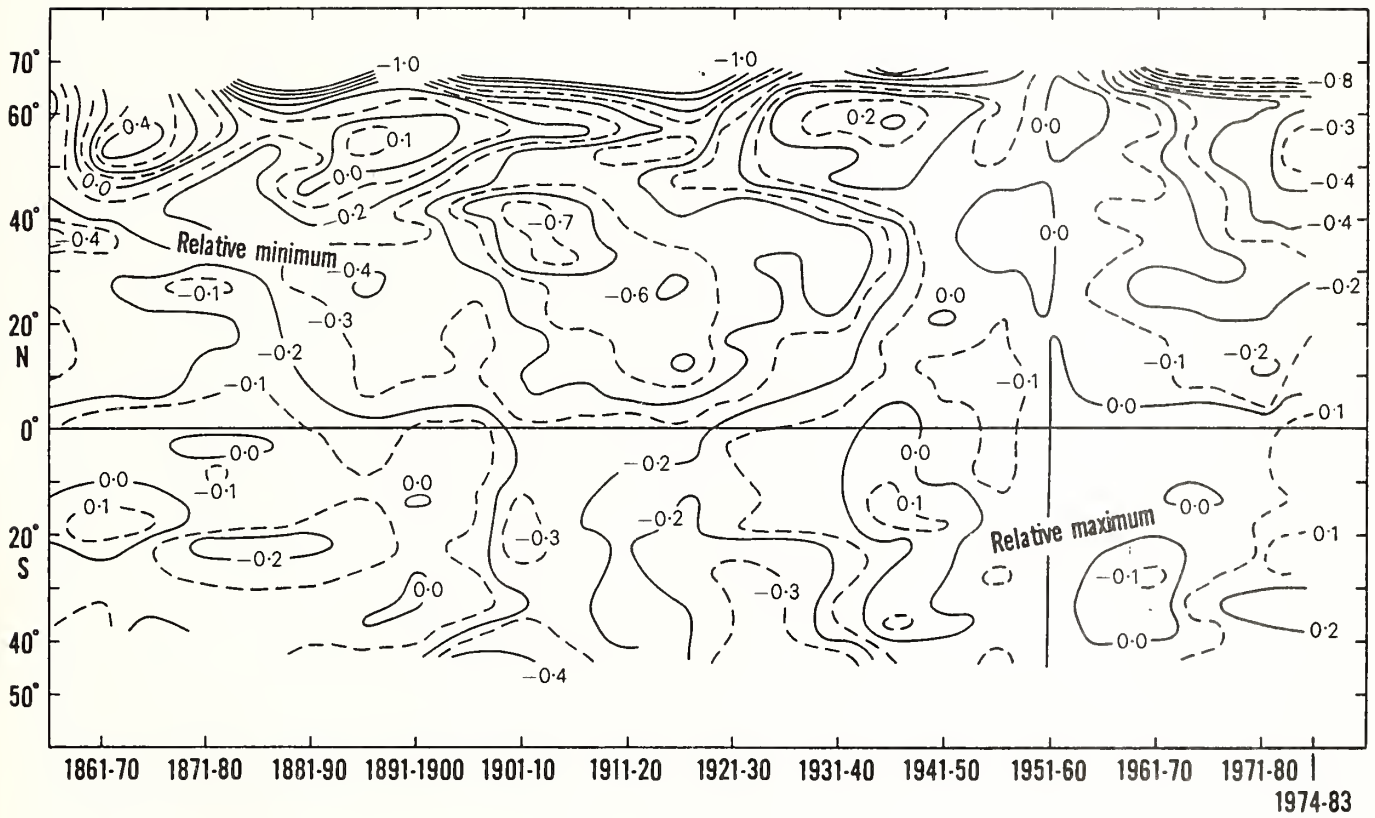

FIGURE 8

Recent Unusual Mean Winter Temperature Across the Contiguous United States

Thomas R. Karl
National Climatic Data Center
Asheville, North Carolina 28801-2696

Robert E. Livezey
Edward S. Epstein
Climate Analysis Center
Camp Springs, Maryland 20746

A long time series (1895-1984) of mean areally-averaged winter temperatures in the contiguous United States depicts an unprecedented spell of abnormal winters beginning with the winter of 1975-76. The data set used to obtain areally-weighted average winter temperatures consisted of monthly averages of temperature for each of 344 state climatic divisions in the contiguous United States and, prior to 1931, monthly averages of statewide average of temperature derived by a simple average of the data from all stations within a state. The data set was then corrected for spatial density of stations prior to 1931, systematic time of observation bias, and urban warming. Each of these corrections were empirically derived by previously published correction factors or by comparison to a fixed network in the case of station density prior to 1931. A plot of the time series with time of observation and urban warming corrections versus the series without these corrections is depicted in Fig. 1.

The recent spell of large departures from normal of the mean winter temperature is evident beginning in 1975-76 (Fig. 1). The normalized departures (Z) from the long-term mean for these winters are listed in Table 1. The objective is to estimate the return period of a series of eight winters having six abnormal winters as defined by the least abnormal (lowest /Z/) of the six winters: 1975-76, 1976-77, 1977-78, 1978-79, 1980-81, and 1982-83. We used Monte Carlo simulations to estimate the return period of such a series of unusual winters because the proper use of the Binomial Probability Model is not straightforward and can lead to unrealistically high return periods. A first-order autoregressive process was used to generate 200 sets of 10,000 pseudo-random numbers (X) with a mean of zero and a standard deviation of one. Any given X at time t is defined by

$$X_t = rX_{t-1} + Z_t,$$

and Z_t is an independent normal random deviate with mean zero and standard deviation of $\sqrt{(1-r^2)}$. This discrete autoregressive process has the property of a lag one autocorrelation coefficient equal to r. The persistence observed in the mean winter temperature time series is simulated in the Monte Carlo experiments by setting r = 0.11.

Table 2 depicts the methodology used in this Monte Carlo study in order to calculate the return period of a given event. The large time step taken after a single event is found (the row in Table 2 corresponding to the label "3Y 5N") ensures that each event is counted independently of other events. Each set of 10,000 "years" provides a count of the number of independent events meeting the prescribed criteria. The return period is estimated after 200 sets of time series are generated. Table 3 contains the results of a number of Monte Carlo simulations. The confidence intervals in Table 3 represent the uncertainty of our knowledge of the "true" return periods because we chose to limit our Monte Carlo calculations to 200 runs of 10,000 years (2×10^6 years in all).

The recent variability is either a moderately rare event in a reasonably stationary climate or it represents climate change. Which is the correct view is beyond the scope of this paper. Whatever the case, in one sense at least (a national average temperature), the climate of the past several winters has been very unusual, and is unprecedented in the past 89 winters. Some research has already addressed some of the potential causes for the recent spell of unusual winters by addressing specific unusual winters, but it is hoped that the work reported here can generate additional interest in this recent period of unusual mean winter temperatures. How the nation coped with this unusual variability could also be the subject for climate impact studies.

List of Figures:

Fig. 1 Time series of mean winter temperatures (1895 is the winter of 1895-96) depicted by solid dots. Horizontal dashed line is the long-term mean, solid line is ± 1.179 or ± 1.253 standard deviations from the mean in (a) and (b), respectively.

List of Tables:

Table 1 Normalized mean winter temperatures with and without corrections for observation times and urban affects.

Table 2 Searching scheme used in the Monte Carlo study. Example is for at least six of eight values of $X_t > Z$ (Y implies yes, N implies no, and NE implies number of events). Horizontal lines indicate the set under consideration.

Table 3 Return period estimates based on Monte Carlo simulations using various limits to define unusual winters within the period 1975-76 through 1983-84.

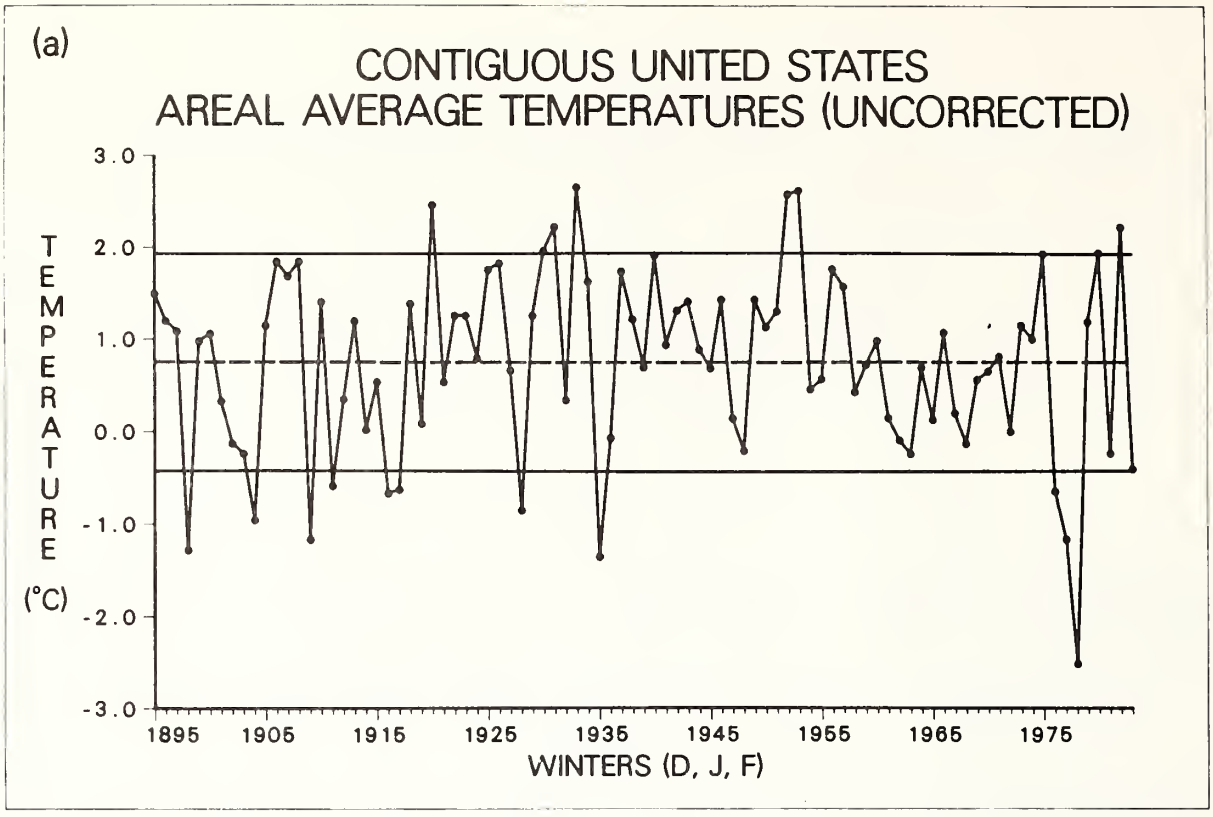

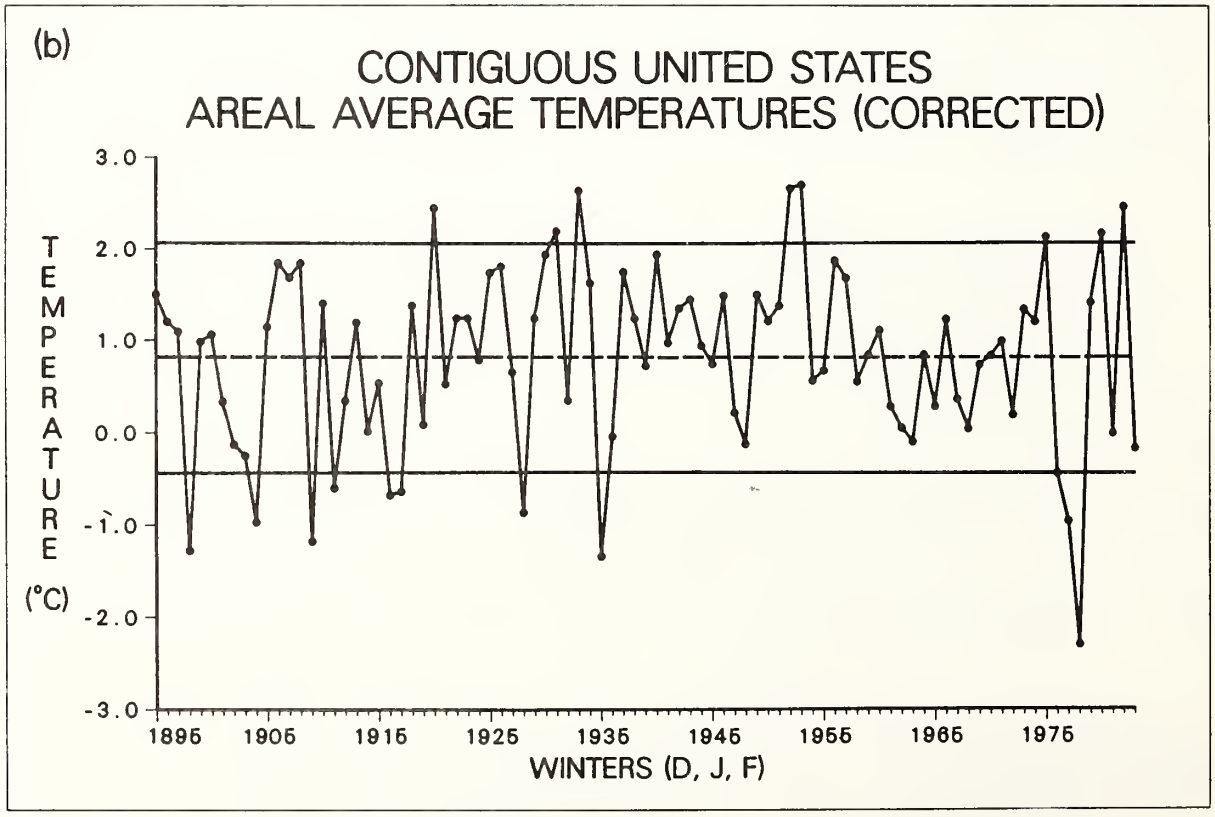

Fig. 1 Time series of mean winter temperatures (1895 is the winter of 1895-96) depicted by solid dots. Horizontal dashed line is the long-term mean, solid line is ± 1.179 or ± 1.253 standard deviations from the mean in (a) and (b), respectively.

Table 1. Normalized mean winter temperatures with and without corrections for observation times and urban affects.

WINTER	NORMALIZED DEPARTURES (Z) Z - SCORES	
	NO CORRECTION	CORRECTION
1975-76	1.179	1.326
1976-77	-1.389	-1.253
1977-78	-1.907	-1.775
1978-79	-3.251	-3.120
1979-80	0.442	0.604
1980-81	1.189	1.366
1981-82	-0.981	-0.821
1982-83	1.467	1.657
1983-84	-1.150	-0.982

Table 2. Searching scheme used in the Monte Carlo study. Example is for at least six of eight values of $X_t > Z$ (Y implies yes, N implies no, and NE implies number of events). Horizontal lines indicate the set under consideration.

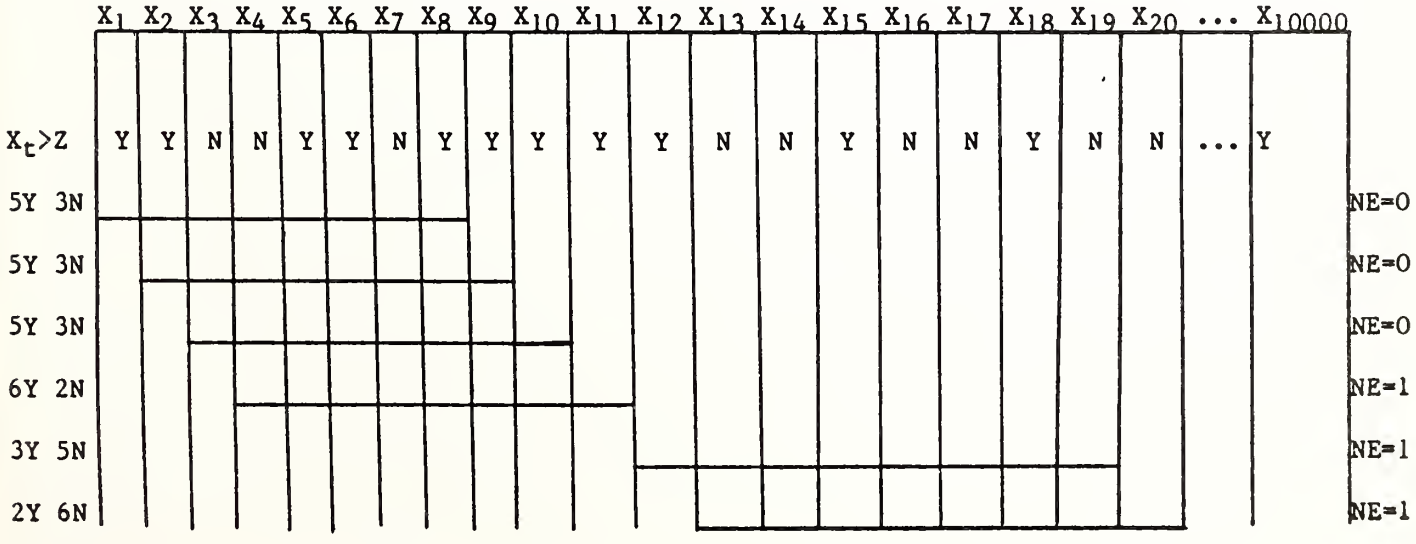
X1 X2 X3 X4 X5 X6 X7 X8 X9 X10 X11 X12 X13 X14 X15 X16 X17 X18 X19 X20 ... X10000
Xt>Z Y Y N N Y Y N Y Y Y Y Y N N Y N N Y N N ... Y
5Y 3N NE=0
5Y 3N NE=0
5Y 3N NE=0
6Y 2N NE=1
3Y 5N NE=1
2Y 6N NE=1

Table 3. Return period estimates based on Monte Carlo simulations using various limits to define unusual winters within the period 1975-76 through 1983-84.

SIMULATION	CATEGORY	MINIMUM NUMBER OF WINTERS	r	CORRECTION FOR OBSERVATION TIMES AND URBAN AFFECTS?	RETURN PERIOD OF EVENT (YRS)	5 AND 95% CONFIDENCE LIMITS (YRS)
1	$/Z/\geq 1.253$	6 of 8	0.11	YES	1164	1094-1243
2	$/Z/\geq 1.179$	6 of 8	0.11	NO	625	595-657
3	$/Z/\geq 1.179$	6 of 8	0.00	NO	681	651-714
4	$Z\leq -1.253$	3 of 3	0.11	YES	550	524-578
5	$Z\leq -1.389$	3 of 3	0.11	NO	1010	949-1080
6	$/Z/\geq 0.821$	8 of 9	0.11	YES	467	449-486
7	$/Z/\geq 0.981$	8 of 9	0.11	NO	2096	1924-2303
8	$/Z/\geq .982$	7 of 9	0.11	YES	341	330-352

Towards understanding the geographical distribution and seasonality in persistence of monthly mean surface air temperature over the U.S.A.

H. M. Van den Dool and W. H. Klein
Department of Meteorology
University of Maryland
College Park, MD 20740

Using the traditional linear correlation (ρ) between anomalies in monthly mean air temperature (MMAT) occurring in adjacent months, we will describe the distribution of ρ over the U.S.A. and its variation with season. $\rho(i,s,\tau,n,m)$ is a function of the starting month (i), the station (s), the lag (τ), and the period over which calculations were performed (starting year n, ending year m). In this report τ will be 1 month exclusively. The data set used is the 80 year (1900-1979) record for 61 stations over the U.S.A. as described by Walsh and Mostek (1980).

One of our major concerns is the reliability and reproducibility of ρ. In order to increase the sample size (and decrease the sampling error) we will average ρ over seasons and the whole year in the following symbolic way:

WINTER = (N/D + D/J + J/F + F/M)/4

SPRING = (F/M + M/A + A/M + M/J)/4

SUMMER = (M/J + J/J + J/A + A/S)/4

FALL = (A/S + S/O + O/N + N/D)/4

YEAR = (D/J + ... N/D)/12

(In spite of averaging over seasons and the year, we are studying month-to-month persistence!!)

Another concern is the influence of trends (due to urbanization, changes in exposure, etc.). In order to remove these artifacts, a running 30 year mean was subtracted from the series. This procedure usually decreases the autocorrelation. All results discussed below are for detrended data.

Fig. 1 shows the distribution of yearly mean ρ over the U.S. for 1900-1979. The number of pairs of data involved (per station) is 80 x 12 = 960. Assuming a normal distribution and an expected value $\langle\rho\rangle = 0$, the sampling error of the quantity shown in Fig. 1 should be about 0.03. At all stations the auto-correlation in the yearly pooled data mode is clearly larger than zero. In the interior of the country MMAT anomalies are short-lived ($\rho \sim 0.1$). However, at the West-, East- and Gulf coasts, the South West desert and the Great Lakes area, ρ is appreciably higher (up to 0.47 in San Diego).

Splitting the 1900-1979 period into 1900-1939 and 1940-1979 we can check how stable Fig. 1 is. Since the difference between the two periods (Fig. 2) rarely exceeds 0.13 (= $2\sqrt{2}$ • sampling error for 40 years of data (0.046)), we accept the null hypothesis that the month-to-month autocorrelations during the first and the second 40 year periods were essentially the same.

Comparing Fig. 1 with a similar map for monthly mean 700 mb heights (Fig. 1 in Van den Dool and Livezey (1984)), we conclude that in the interior of the U.S. and over the Gulf coast persistence in circulation anomalies would suffice as a first order explanation for persistence in MMAT anomalies. This conclusion also is based on the fact that on a yearly basis the local (overhead) height specifies the MMAT better than any remote height. In all other areas ρ in Fig. 1 seems to be much larger than can be expected from persistence of the atmospheric circulation alone. We speculate that in those areas (West coast, East coast, Great Lakes, South West desert) local interaction with the lower boundary reddens the spectrum of MMAT anomalies.

Figures 3 through 6 show month-to-month persistence of MMAT-anomalies in a seasonally pooled data mode, for the period 1900-1979. The sample size is 80 x 4 = 320, leading to about 0.06 sampling error at every station in any of these maps. Perhaps the most striking feature is that Fig. 3 to 6 are relatively similar, or, that seasonality is not large. The most notable exception is the appearance of an interior maxmimum (axis Texas to Wisconsin) in the summer season. Closer inspection reveals that the interior minimum is most widespread in fall and spring. This is what one would expect if MMAT anomalies were completely determined by simultaneous circulation anomalies since circulation anomalies are least persistent in spring and fall (Namias, 1952; Van den Dool and Livezey, 1984).

References

Walsh and Mostek, 1980: Mon. Wea. Rev., 108, 615-630.
Namias, 1952: Bull. Amer. Meteor. Soc., 33, 279-285.
Van den Dool and Livezey, 1984: Mon. Wea. Rev., 112, 610-615.

Acknowledgement

The data for the 61 U.S. stations were provided by Dr. J. E. Walsh. Figures were drafted by Hal Bloom and Chuck Mulchi. The research was supported by the Climate Dynamics Program, Division of Atmospheric Sciences, National Science Foundation, under Grant ATM-8314431 and by the Climate Analysis Center, NOAA, under Grant NA 83AA-D-00048.

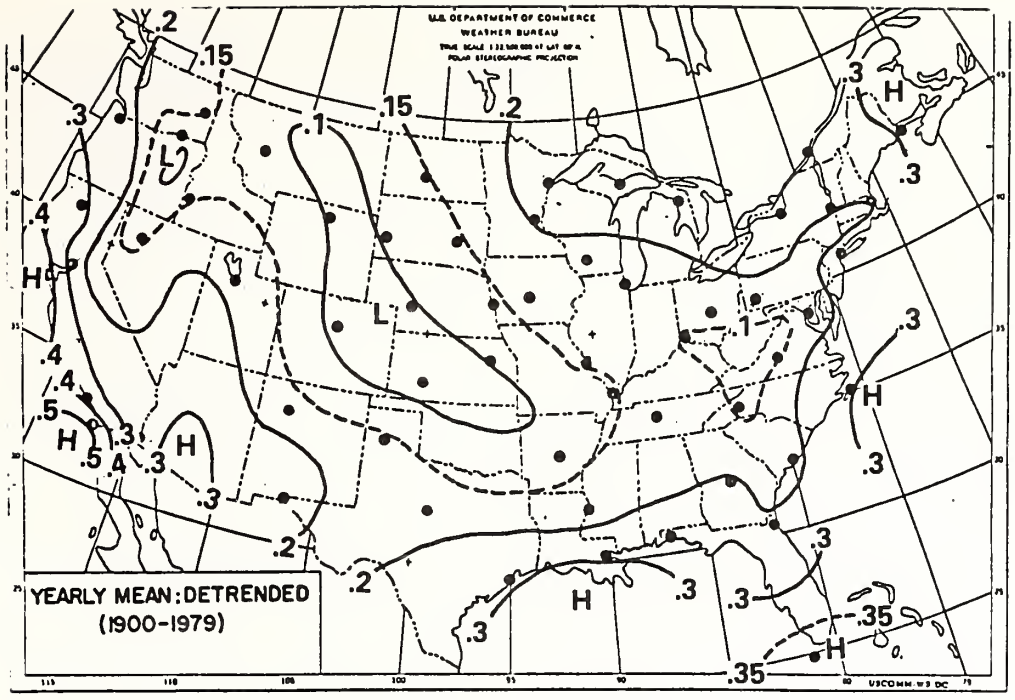

Fig. 1 The month-to-month correlation ot monthly mean surface air temperature anomalies over the U.S.A., for the period 1900-1979, on a yearly basis. The analysis is based on data at 61 stations located by the dots.

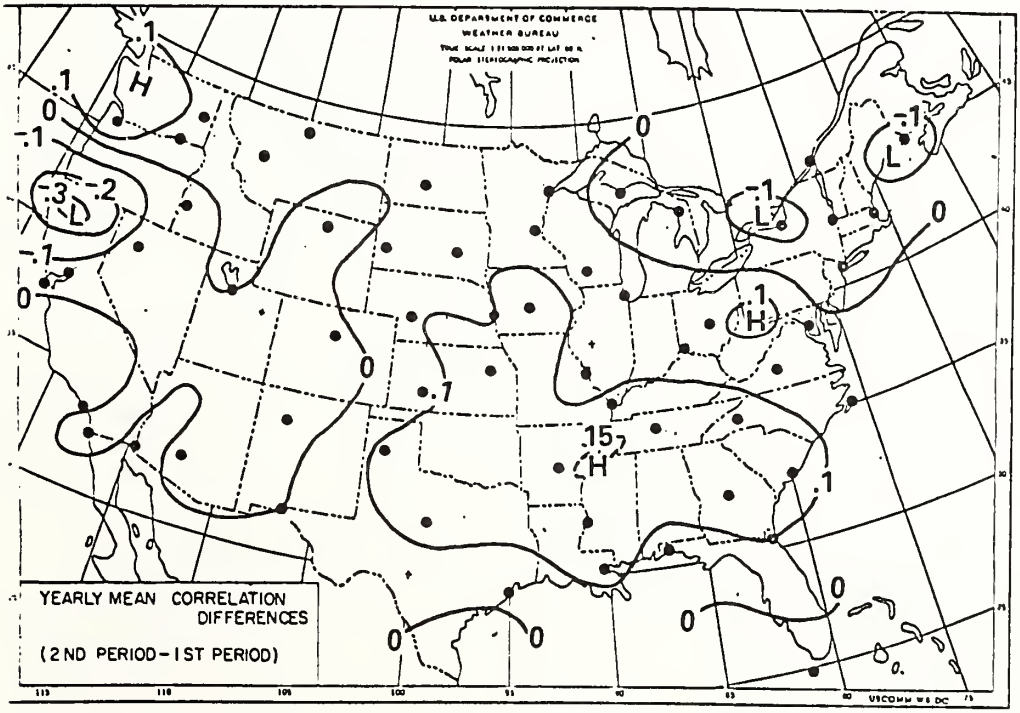

Fig. 2 The difference in month-to-month correlation, on a yearly basis, between 1900-1939 and 1940-1979.

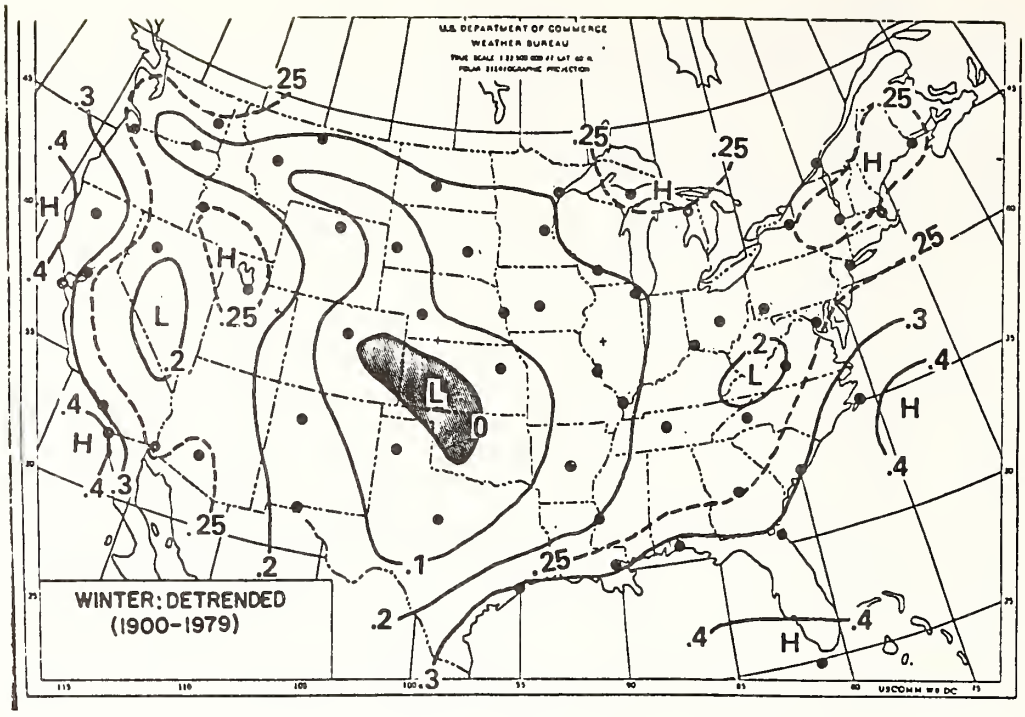

Fig. 3 As Fig. 1 but now for winter.

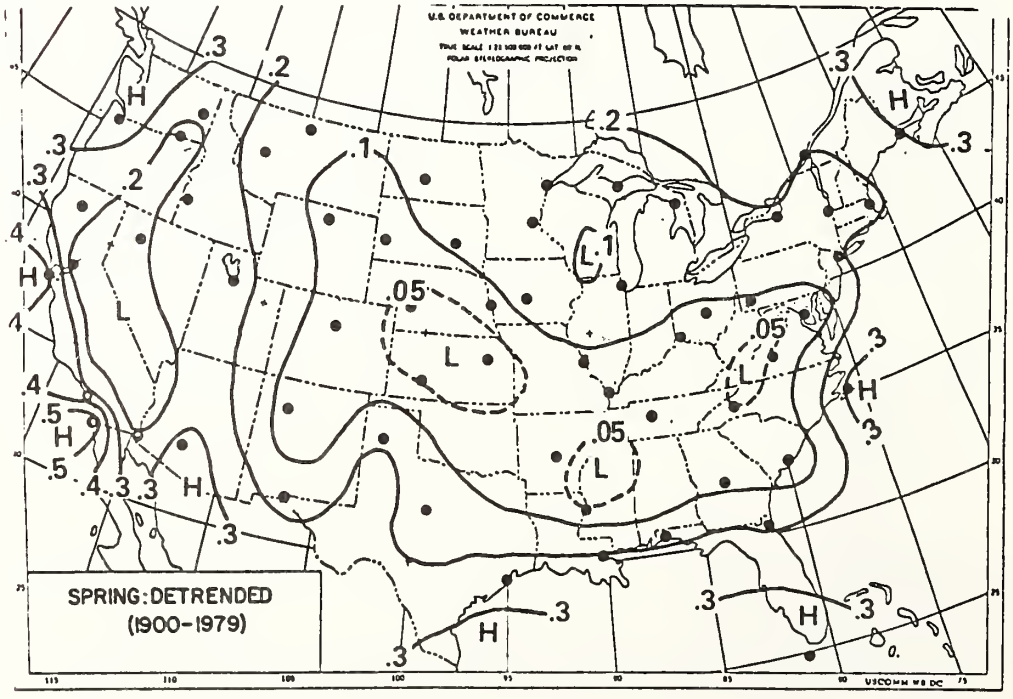

Fig. 4 As Fig. 1 but now for spring.

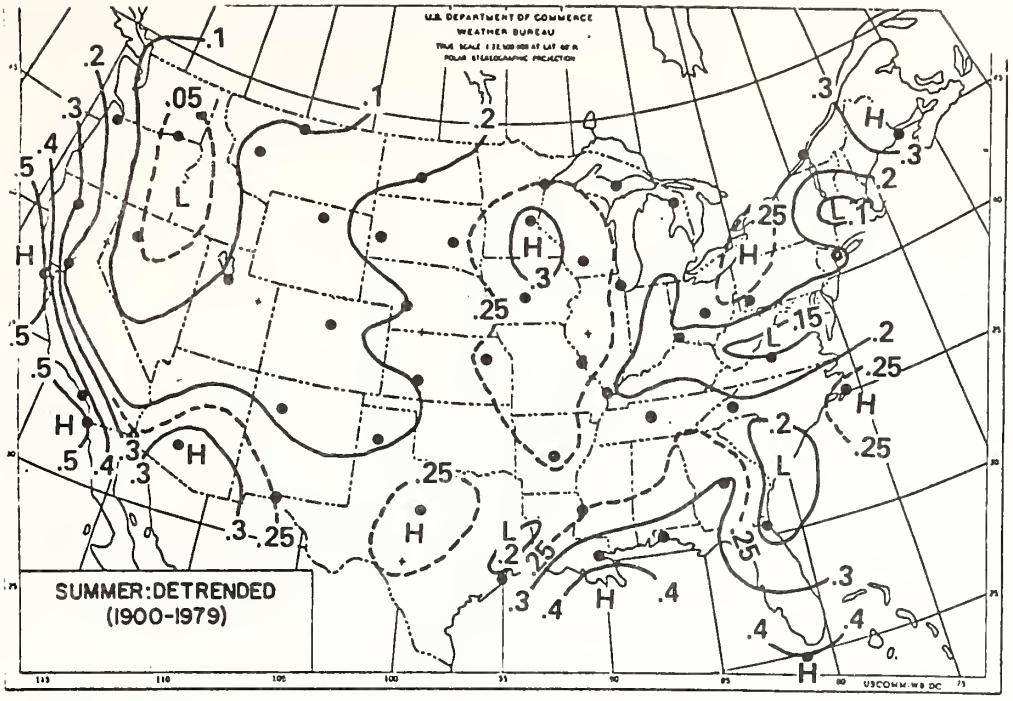

Fig. 5 As Fig. 1 but now for summer

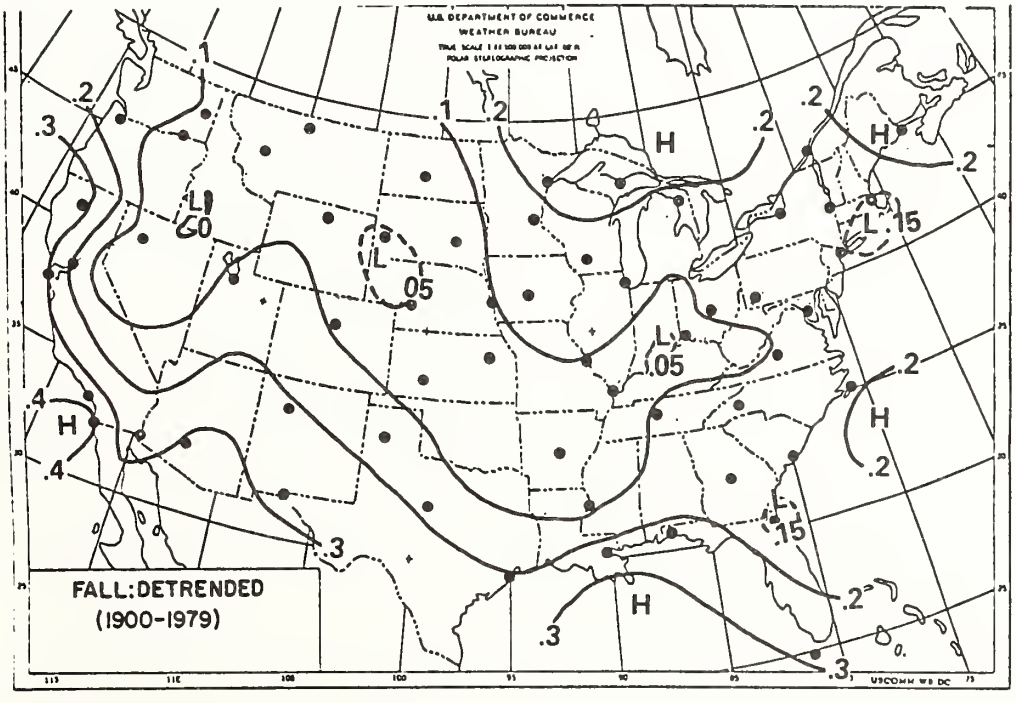

Fig. 6 As Fig. 1 but now for fall.

Temperature and Precipitation Trends in North America

G. Kukla and J. Gavin
Lamont-Doherty Geological Observatory
Palisades, New York 10964

T. R. Karl
NOAA/National Climatic Data Center
Asheville, North Carolina 28801

Trends in monthly mean maximum, minimum and average temperature as well as precipitation were calculated over the 1941-80 interval for 122 to 130 U.S. and Canadian stations. Correlation coefficients were used to measure the association between each element and time (in 40 equal time steps) and were tested for local significance using a Monte Carlo technique. Field significance tests were then used to determine whether the percentage of stations in the network with $\geq$ 90% local significance level is greater than expected due to chance. Stations were selected to minimize as much as possible the potential influence of urbanization. The criteria used in the station selection as well as the details of the procedure are described elsewhere (Karl, et. al., 1984).

Figures 1 and 2 show examples of the geographic distribution of the temperature trends in January and July. In general, the east cooled during most of the year whereas little change or warming trends are observed in the west. Table 1 shows the results of field significance tests for temperature and precipitation. Practically no stations were found to have locally significant trends in precipitation, so the field significance tests were based on the proportion of all stations with positive and negative trends.

The most interesting feature is the significant decrease in the diurnal temperature range which occurs in every month. Tests were then made to determine whether the decrease of the range was associated with an increase in precipitation. The results shown in Table 2, based on 1000 Monte Carlo simulations, do indicate such a relationship, particularly in summer and early fall (Table 2, fig. 3). An increase in the range appears to be associated with a decrease in precipitation mainly during spring and summer.

We conclude that increased atmospheric humidity and cloudiness which would be expected to accompany increases of precipitation may have led, in part, to the observed decrease of the diurnal temperature range.

This work is supported by the Dept. of Energy, Carbon Dioxide Research Division under Grant DE-AC02-83ER60162.

References

Karl, T.R., G. Kukla and J. Gavin (1984) Decreasing diurnal temperature range in the United States and Canada from 1941-80, J. of Climatology and Applied Meteorology 23, (November issue).

FIELD SIGNIFICANCE FOR TEMPERATURE AND PRECIPITATION

	INCREASING					DECREASING				
MONTH	MAX	MIN	AVG	RNG	PCP	MAX	MIN	AVG	RNG	PCP
JAN						99	99	99	99	
FEB				90		90	95	95	95	
MAR									95	
APR									95	
MAY				90					95	
JUN	99	95	95	99		95	95	90	99	90
JUL		95				90			99	
AUG		95				95	90		99	
SEP		95			90	95			99	
OCT						95	90	95	95	
NOV									95	
DEC					90				90	

TABLE 1: Field significance (90%,95% or 99% levels) of the trends in the monthly mean maximum (MAX), minimum (MIN), average (AVG), diurnal range (RNG) and total precipitation (PCP).

PROBABILITIES

MONTH	DECREASED RNG INCREASED PCP	INCREASED RNG DECREASED PCP
JAN	.97	.06
FEB	.30	.45
MAR	.86	.61
APR	.95	.89
MAY	.78	.93
JUN	.78	.99
JUL	.99	.28
AUG	.95	.93
SEP	.98	.33
OCT	.97	.38
NOV	.82	.89
DEC	.91	.44

TABLE 2: Probability that the percent of stations with decreasing (increasing) range (RNG)and increasing (decreasing) precipitation (PCP) is not due to chance alone. Values of $\geq .90$ are underlined.

FIGURE CAPTIONS

Figure 1: Areas of locally significant (90% level) positive (+) and negative (-) trends of mean monthly maximum and minimum surface air temperatures delimited by thin contours. January for the 1941-80 interval. Heavy line for zero trend. Stations with significant (90% level) increase in the diurnal temperature range shown by solid circles, decrease by solid triangles. Remaining stations shown by asterisks.

Figure 2: Same as above, for July.

Figure 3: Stations with the decrease of the diurnal temperature range significant at the 90% level shown by solid circles, the remainder by solid triangles. Those stations with statistically significant increase of the range shown by open circles and the remainder by open triangles. Sites with increasing precipitation encircled.

Figure 1

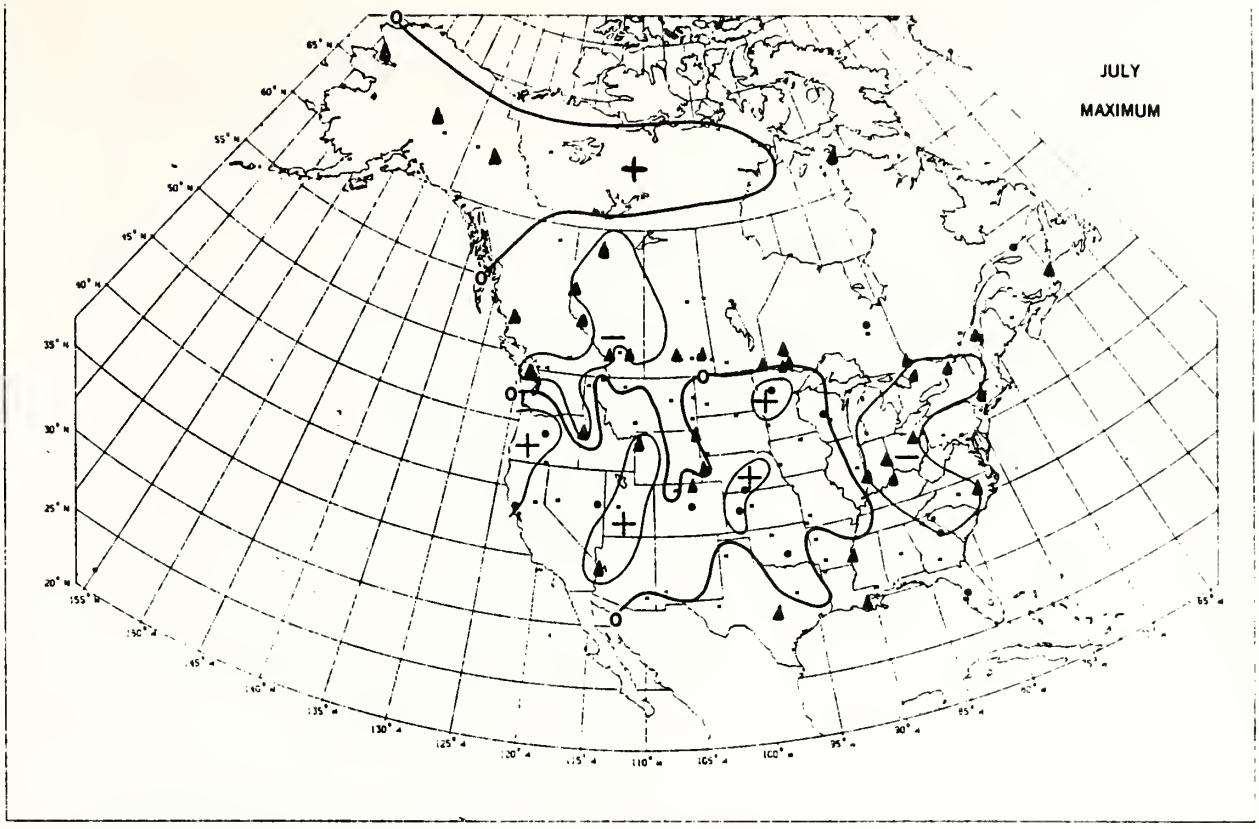

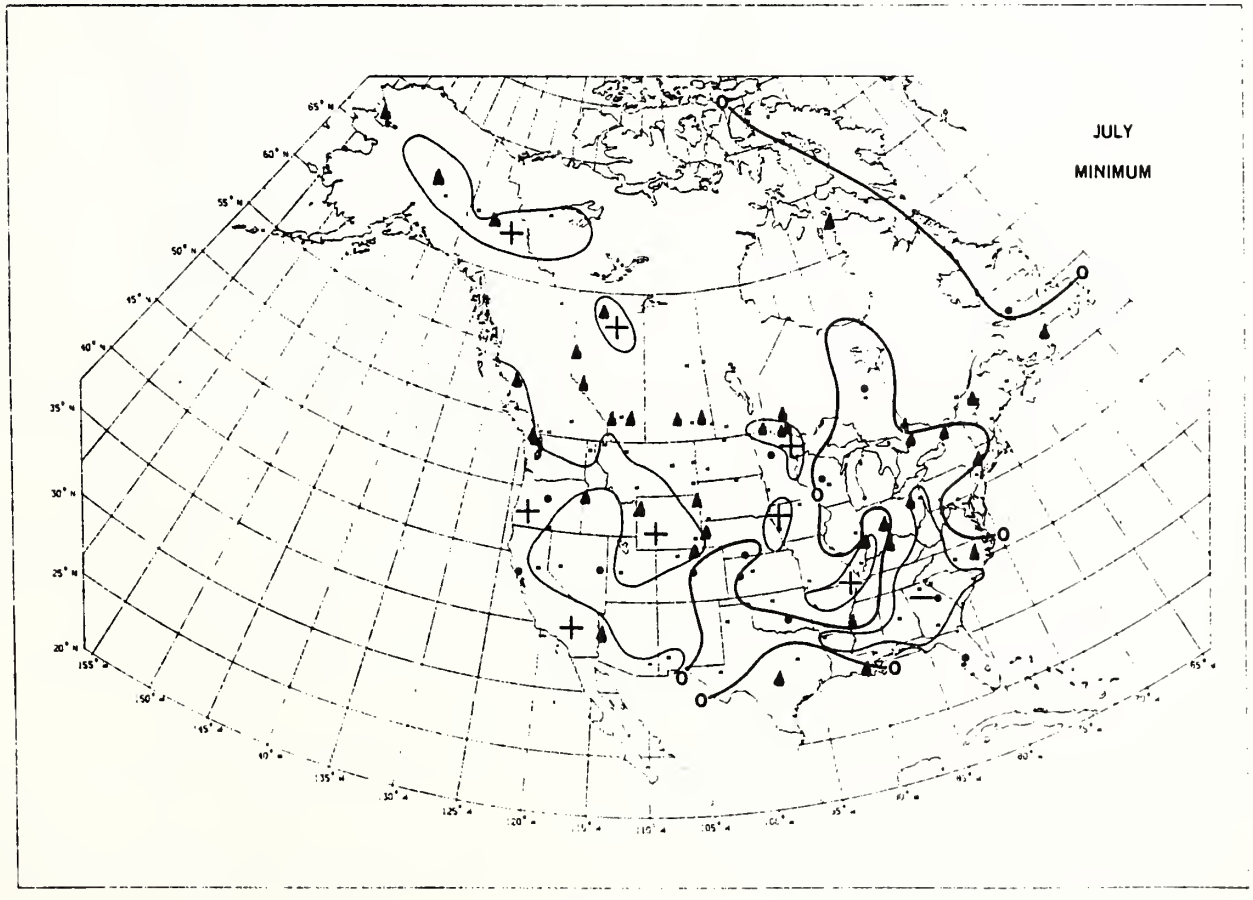

Figure 2

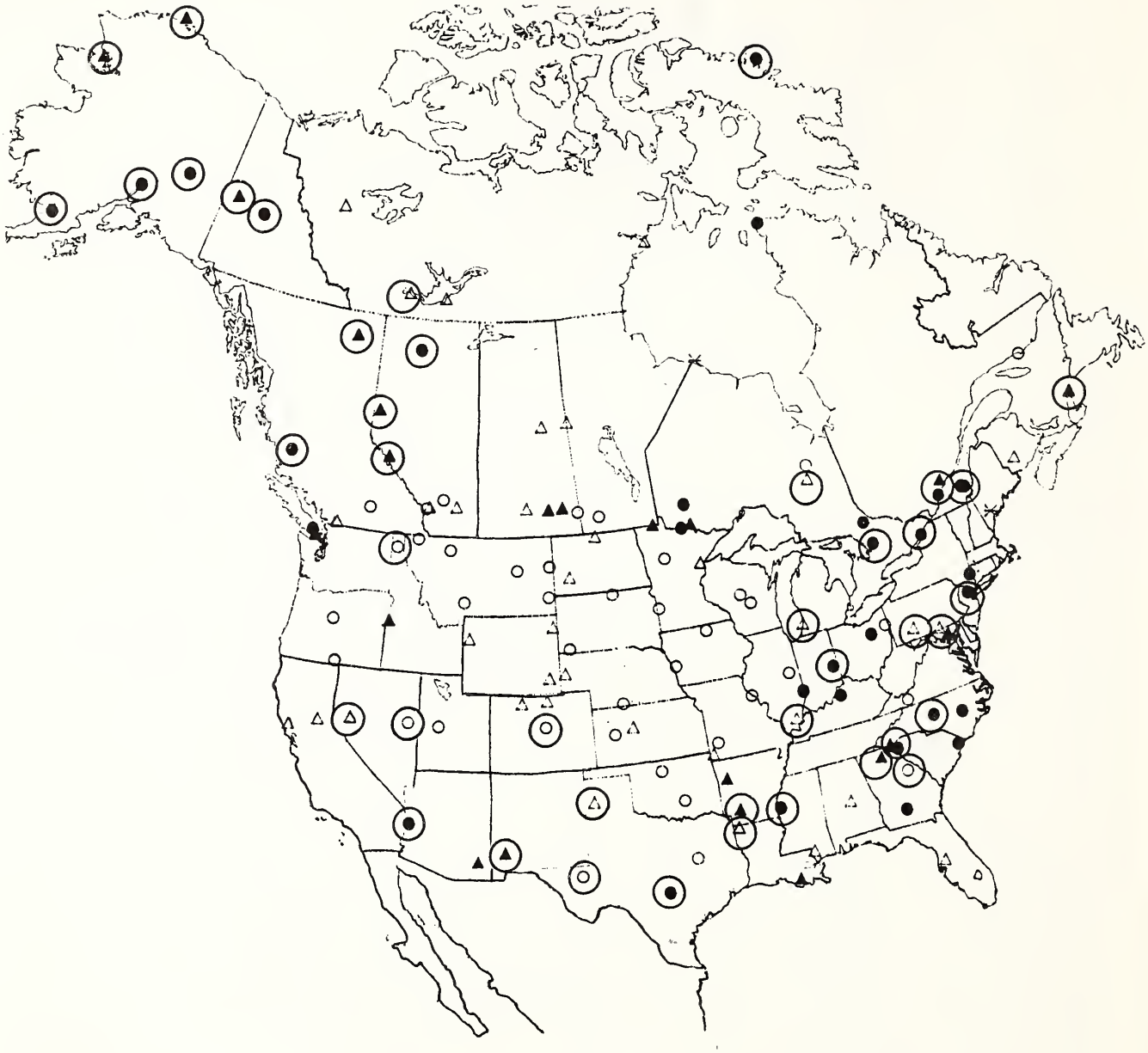

Figure 3.

Recent Long-Term Climatic Change over the Eastern Tropical and Subtropical Pacific and its Ramifications

William H. Quinn and Victor T. Neal
College of Oceanography
Oregon State University
Corvallis, Oregon 97331

This report includes further information concerning the climatic change that has affected much of the tropical and subtropical Pacific over recent years (Quinn and Neal, 1983, 1984). It provides an additional approach for monitoring and assessing the ENSO events, based on changes noted at sites located in the southeast trade band. It also includes a discussion of related changes noted at tropical North Pacific sites.

Figure 1 shows the location of sites referred to here. The next three figures re-introduce evidence pertaining to the long-term climatic change. Figure 2 shows four of the Southern Oscillation index (SOI) anomaly plots we have been using. These indices represent to a great extent the atmospheric forces acting on that part of the Pacific Ocean affected by the southeast trades and their westward extension in the equatorial easterlies. Note the significant reduction in these indices since mid-1976. Figure 3 shows atmospheric thickness trends at three tropical Pacific sites (Majuro I., Johnston I., and Antofagasta, Chile) in relation to the Easter-Darwin SOI. The thickness changes tend to represent oceanic effects on the overlying atmosphere. Here we note a significant increase in the thicknesses after mid-late 1976. Since the thicknesses are for the 200-850 mb layer, it indicates that a large part of the tropical Pacific troposphere is involved in the climatic change. Figure 4 shows the Rapa-Darwin, Totegegie-Darwin, and Tahiti-Darwin integrated index anomaly plots which were overlaid in Figure 3 of the recent Quinn and Zopf (1984) article. These plots show the cumulative rise in index anomalies from a low point in early 1970 to a peak in early 1976 and the subsequent cumulative fall to a low point in early 1983. It was during the period of cumulative fall (from the second quarter of 1976 to the first quarter of 1983) that we noted the large-scale climatic changes over much of the tropical and subtropical Pacific which appeared to bring about ecological changes in several of the west coast fisheries of the Americas (Quinn and Neal, 1983, 1984).

Figure 5 shows the Hao-Darwin integrated index anomaly plot along with a similar plot for the Hao component from early 1969 through mid-1984. As expected, the Hao-Darwin integrated anomaly trend is similar to the trends for the other indices in Figure 4. The contents of Figure 5 indicate that both cores of the SO have been strongly involved in both the long-term climatic change between 1970 and early 1983 and the interannual changes related to the 1972-73, 1976-77 and 1982-83 El Niños.

Failure to recognize the latent strength and dire consequences of the 1982-83 ENSO event, even while it was underway (during the first three quarters of 1982), caused all of us to re-study available evidence and to re-evaluate our climatic monitoring systems. The pre-event anti-El Niño phase of the SO still appears to be the best place to start when considering the

probability of occurrence and assessing the developmental potential for an impending event.

Earlier findings (Quinn, 1980) indicated that southeast Pacific subtropical ridge components of the SOI's usually showed trend changes associated with the SO several months earlier than did the equatorial low component at Darwin. This, coupled with the fact that the southeast trades play a large part in the pre-event anti-El Niño buildup of the warm water head in the western tropical Pacific, directed our search for precursor evidence to this southeast Pacific generation region. Climatological data for Atuona, Hao, Totegegie and Tahiti were of particular interest; and, the most obvious diagnostic significance appeared to lie in the 200-850 mb thickness anomaly trends. Although thickness changes may lag several months behind the SST changes that cause them (Quinn et al., 1981), this southeast trade region is expected to experience some of the earliest developmental conditions. And, since we may remain in the anti-El Niño buildup phase for many months (Quinn et al., 1978), thickness trends during this phase should have precursor value. Figure 6 shows monthly thickness anomaly plots for Atuona, Hao and Tahiti prior to, during and following the 1982-83 ENSO event. These three sounding sites showed their anti-El Niño low anomalies in January 1982: Atuona (-72.2 gpm), Hao (-72.2 gpm) and Tahiti (-35.8 gpm). These anti-El Niño troughs occurred about the same time as a prominent anti-El Niño trough in the Peruvian coastal SST's and a related but less prominent SOI peak (Figure 7). We had about 15 years of data for Atuona over a record with several breaks; nevertheless, it is interesting that the three lowest monthly average 200-850 mb thickness values occurred in January 1972 (10,856 gpm), January 1976 (10,846 gpm) and January 1982 (10,850 gpm), prior to the onset of the three most recent El Niños.

As expressed in Quinn and Zopf (1984), the unusual strength of the 1982-83 ENSO event was attributed to the combined long-term cumulative effect and strong short-term ENSO effect which resulted in the exceptionally low SOI's of early 1983. The presence of the two peaks (June 1982 and early 1983) in the thickness plots (Figure 6) is interesting since two peaks were also noted in the sea level records for southern Ecuador and northern and central Peru and in the Peruvian coastal SST records. Although the thickness peaks precede the sea level and SST peaks off southern Ecuador and Peru, it may be that the changes in winds resulting in the relaxational release of the internal equatorial Kelvin wave (Wyrtki, 1975) and the changes in strength of the equatorial counter currents (all of which in turn affect coastal Ecuador and Peru), also resulted in the SST changes that caused the thickness changes in the overlying atmosphere noted here. Thickness changes tend to represent cumulative effects of the underlying ocean surface on the overlying atmosphere and, therefore, may provide an estimate of the magnitude of an ENSO event.

The foregoing findings led to further interest in how the climatic change and 1982-83 ENSO were reflected in sounding data north of the equator. Figure 8 shows the average annual 200-850 mb thickness values for 1964-83 at Wake, Truk, Majuro and Tarawa Islands (all of which are west of the 180° meridian). In each case, above average thickness values persist after 1976. Figure 9 shows average annual 200-850 mb thickness values for 1964-83 at Lihue and Hilo in the Hawaiian Is. and Johnston Island (all of which are east of the 180° meridian). Here again, above average values persist after 1976. And, although the 1983 values show a rising trend, data for the first half of 1984 indicate there will be a large decrease in the average thickness for 1984.

Figure 10 shows a 3-month running mean plot of thickness anomalies for Johnston I., based on the 1964-76 averages. Figure 11 shows a similar plot for Hilo. Similar data for Lihue show essentially the same trends as those for Hilo. These three northeast trade wind sites clearly show the climatic shift that occurred during late 1976; and, of course, the extreme thickness peak coincides timewise with the strong North Pacific subtropical jet stream and the extreme weather activity reported in southern California in early 1983.

Monthly thickness anomaly plots for Lihue and Hilo show trends quite similar to those for the three sites south of the equator (Figure 6); and although the anti-El Niño trough occurs two months earlier south of the Equator, the two peaks show up near the same time on both sides of the equator. These findings indicate the importance of taking into account activity over the North Pacific with regard to the ENSO events, as pointed out by Namias (1973).

Acknowledgments

We thank the Director of the Civil Aviation Service and Chief of the Meteorological Service of French Polynesia; the Director of the Australian Bureau of Meteorology; the National Climatic Data Center, NESDIS, NOAA; the Climatic Analysis Center and National Meteorological Center, NWS, NOAA for their support of this study. We thank Dave Zopf, College of Oceanography, Oregon State University, for stimulating comments and data processing support. We greatly appreciate the SST analyses and weather information provided by Forrest Miller of the Inter-American Tropical Tuna Commission, La Jolla, California. Support for this research through National Science Foundation Grant No. ATM-8306 135 under the Climate Dynamics program of the Division of Atmospheric Sciences and a grant from The Tinker Foundation Incorporated is gratefully acknowledged.

References

Namias, J., 1973. Response of the equatorial counter-current to the subtropical atmosphere. Science 181:1245-1247.

Quinn, W. H., 1980. The false El Niño and recent related climatic changes in the southeast Pacific. In: Proceedings of the Fourth Climate Diagnostics Workshop, p. 233-244, J. S. Winston, editor, NOAA Climate Analysis Center, National Weather Service, Washington, D.C.

Quinn, W. H. and V. T. Neal, 1983. Long-term variations in the Southern Oscillation, El Niño and Chilean subtropical rainfall. Fish. Bull., U.S. 81:363-374.

Quinn, W. H. and V. T. Neal, 1984. Recent climatic change and the 1982-83 El Niño. In: Proceedings of the Eighth Climate Diagnostics Workshop, p. 148-154, J. L. Rasmussen, editor, NOAA Climate Analysis Center, National Weather Service, Washington, D.C.

Quinn, W. H. and D. O. Zopf, 1984. The unusual intensity of the 1982-83 ENSO event. Tropical Ocean-Atmosphere Newsletter, No. 26, 17-20.

Quinn, W. H., D. O. Zopf, K. S. Short and R. T. W. Kuo Yang, 1978. Historical trends and statistics of the Southern Oscillation, El Niño, and Indonesian droughts. Fish. Bull., U.S. 76:663-678.

Quinn, W. H., S. K. Esbensen and D. B. Enfield, 1981. Interannual climatic anomalies: Do they propagate? In: Proceedings of the Fifth Climate Diagnostics Workshop, p. 123-137, J. S. Winston, editor, NOAA Climate Analysis Center, National Weather Service, Washington, D.C.

Wyrtki, K., 1975. El Niño--the dynamic response of the equatorial Pacific Ocean to atmospheric forcing. J. Phys. Oceanogr. 5:572-584.

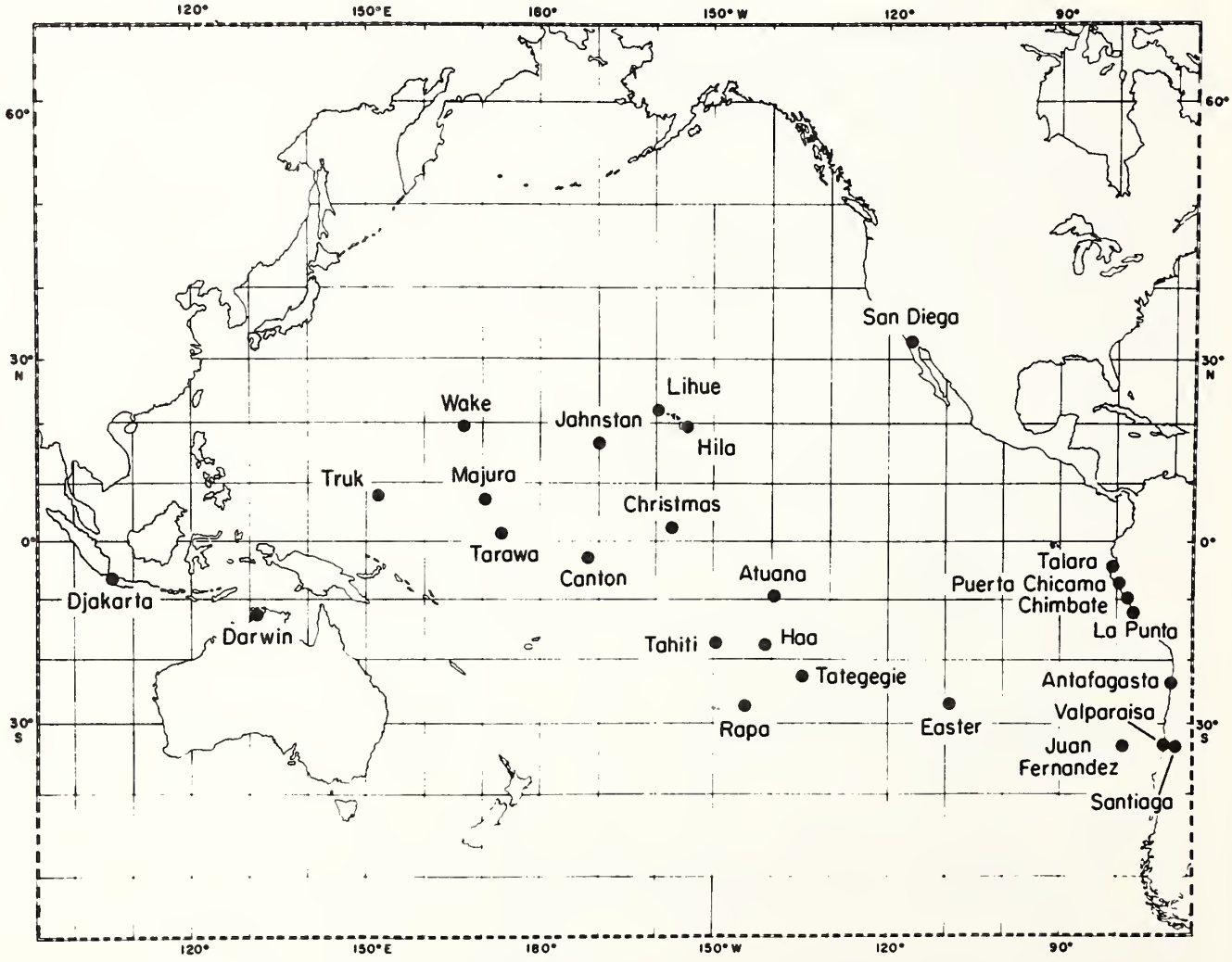

Fig. 1. Locator chart for referenced sites.

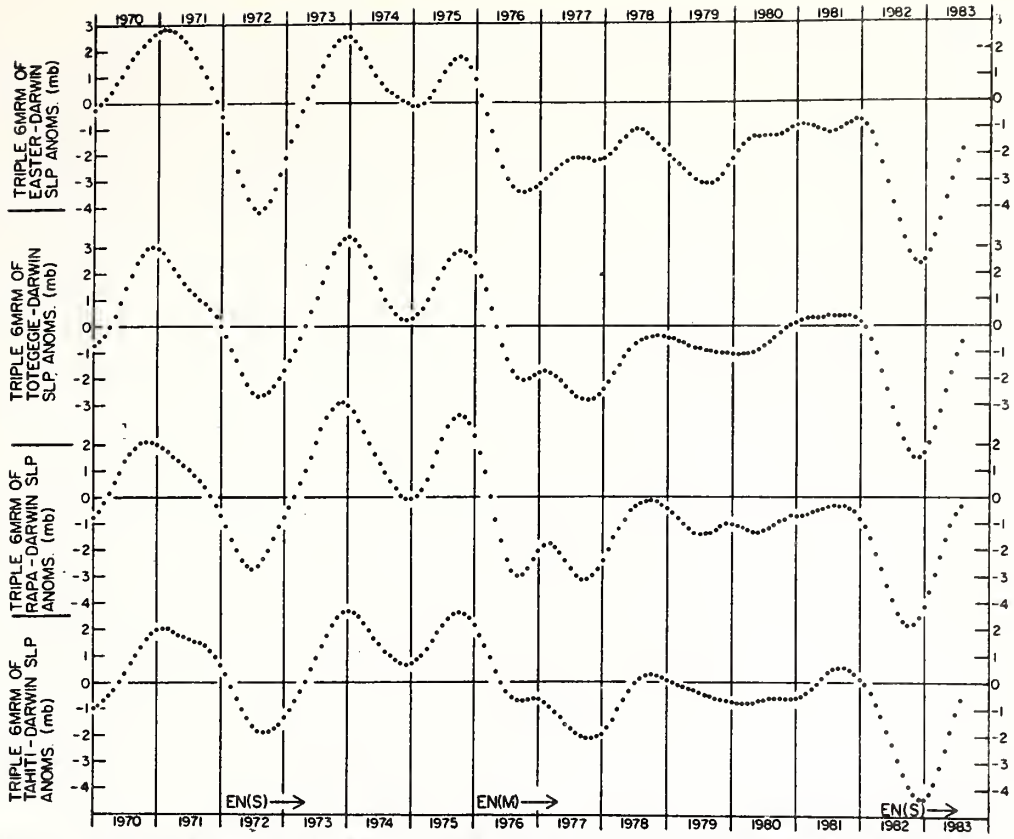

Fig. 2. Triple 6-month running mean plots of anomalies of difference in sea level pressure (mb) between: Easter I. and Darwin, Totegegie and Darwin, Rapa and Darwin, Tahiti and Darwin. El Niño events are noted in strong (S) and moderate (M) intensity.

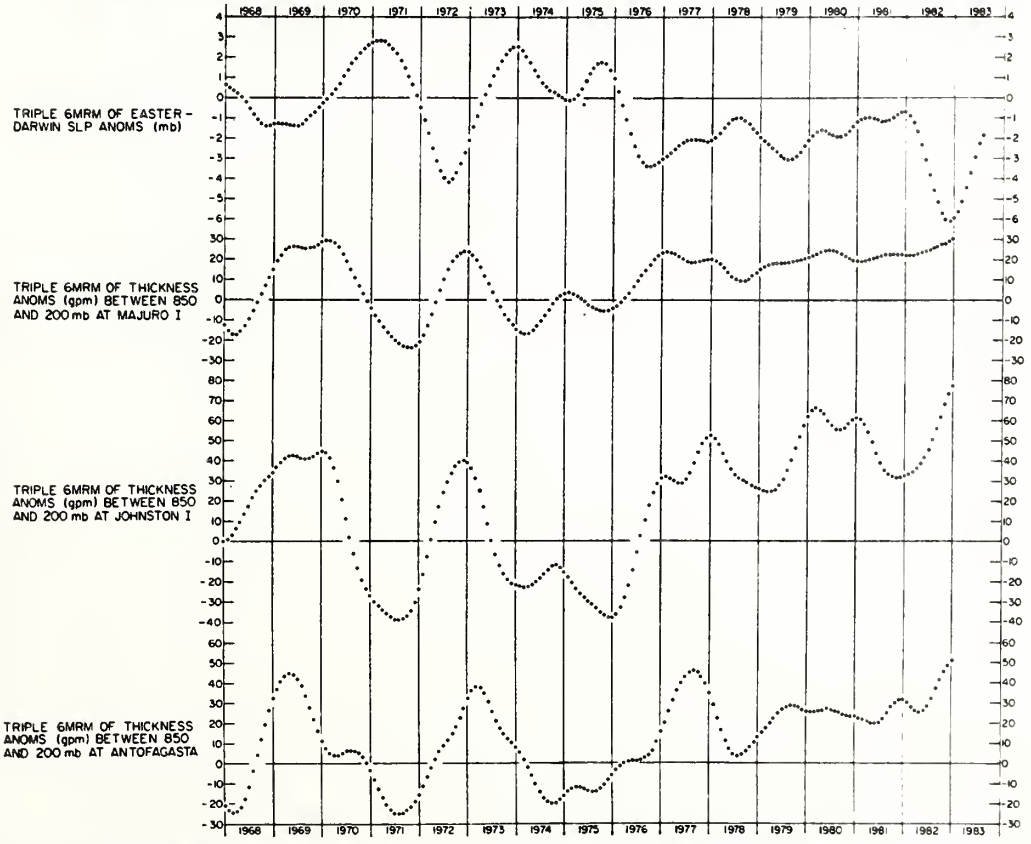

Fig. 3. Triple 6-month running mean plots of 200-850 mb thicknese anomalies (gpm) for Majuro I., Johnston I. and Antofagasta, Chile in relation to a similar plot of anomalies of difference in sea level pressure (mb) between Easter I and Darwin.

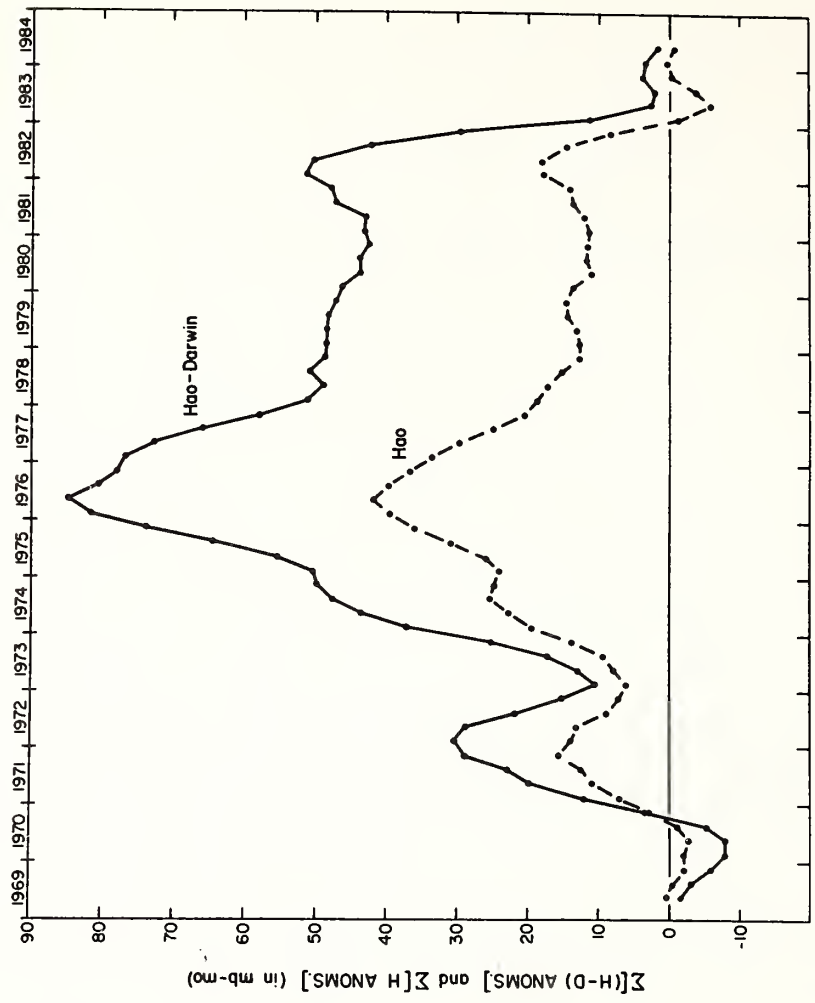

Fig. 5. Plot of integrated index anomalies (in mb-months) for the Hao-Darwin SOI along with a similar plot for just the Hao component. Quarterly average values are entered (i.e., January-March average plotted at February, April-June average plotted at May, etc.)

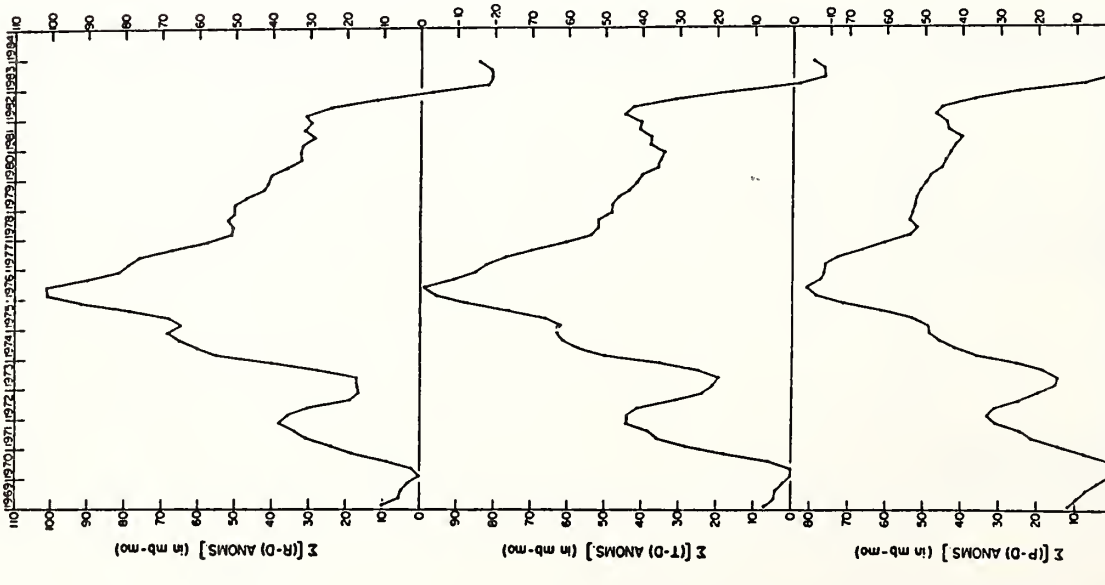

Fig. 4. Plots of integrated index anomalies (in mb-months) for Rapa-Darwin, Totegegie-Darwin, and Tahiti-Darwin SOI's (from Quinn and Zopf, 1984).

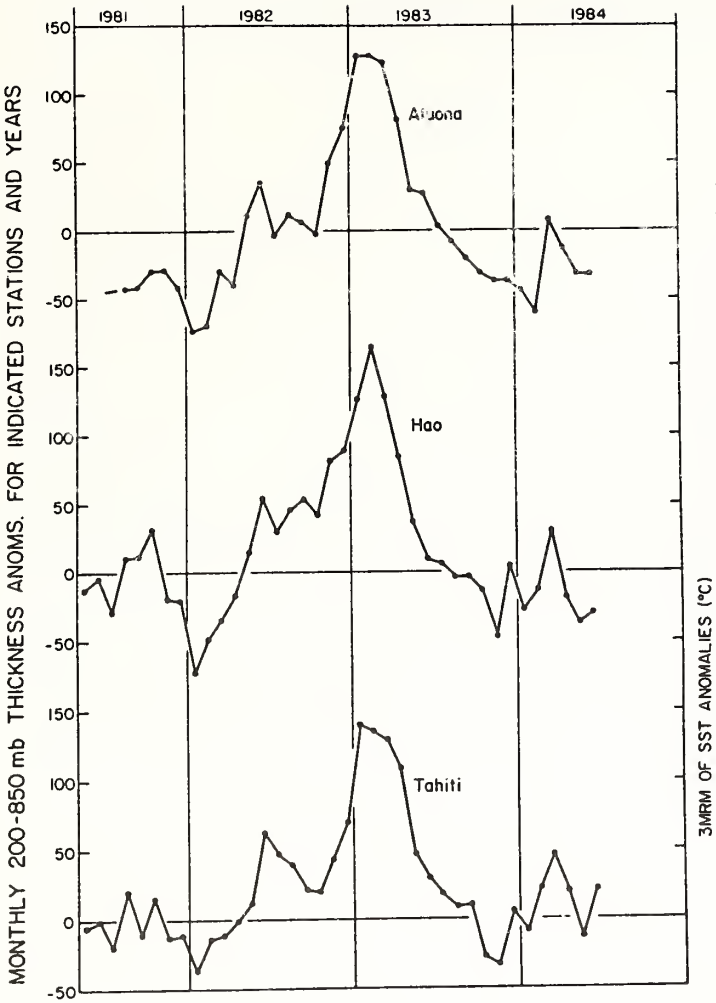

Fig. 6. Plot of monthly 200-850 mb thickness anomalies (gpm) for Atuona, Hao, and Tahiti prior to, during and following the 1982-83 ENSO event.

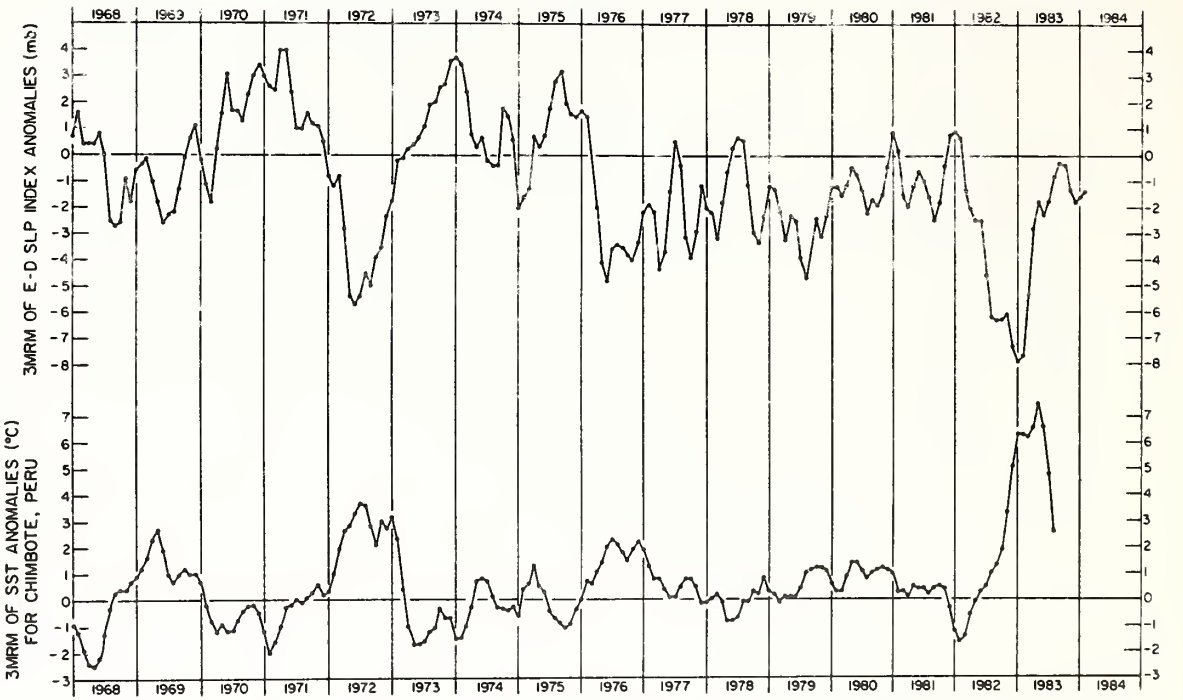

Fig. 7. Three month running mean plots of: anomalies of difference in sea level pressure (mb) between Easter I. and Darwin and sea surface temperature anomalies (°C) for Chimbote, Peru.

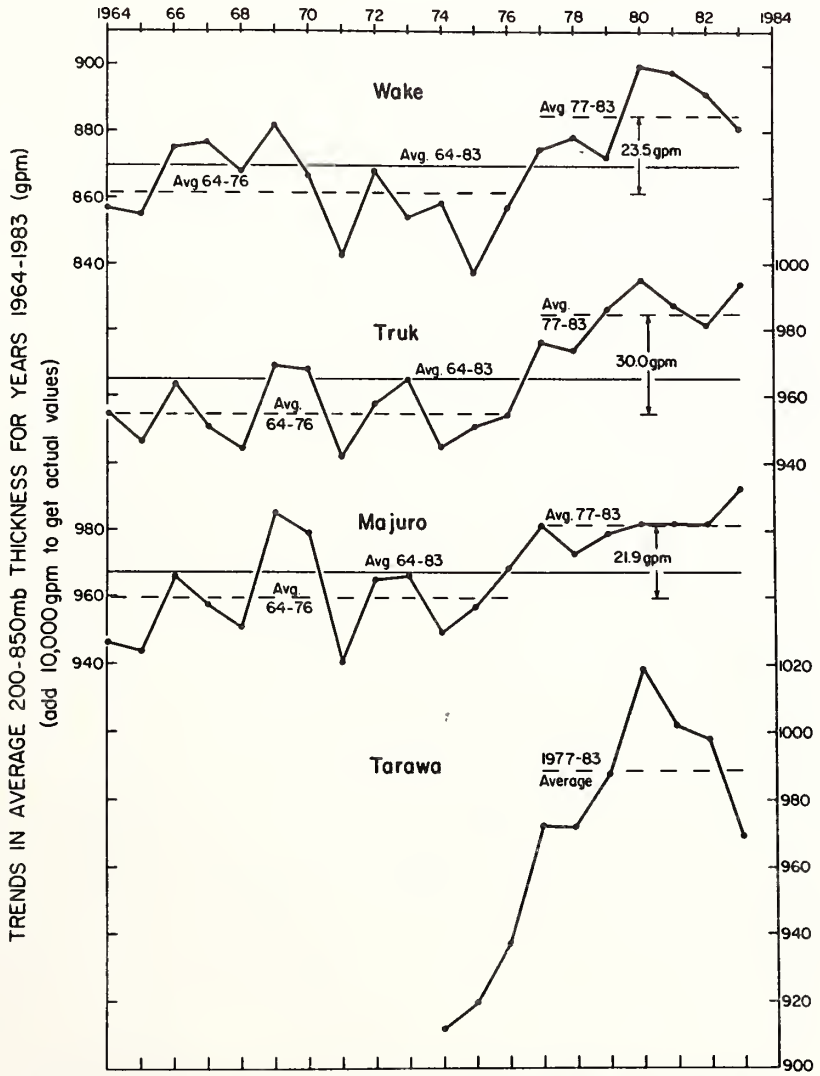

Fig. 8. Annual average plots of 200-850 mb thickness (gpm) for the years 1964-83 for Wake, Truk, Majuro and Tarawa Islands. Average annual values for 1964-83, 1964-76 and 1977-83, and the difference between the latter two averages are indicated.

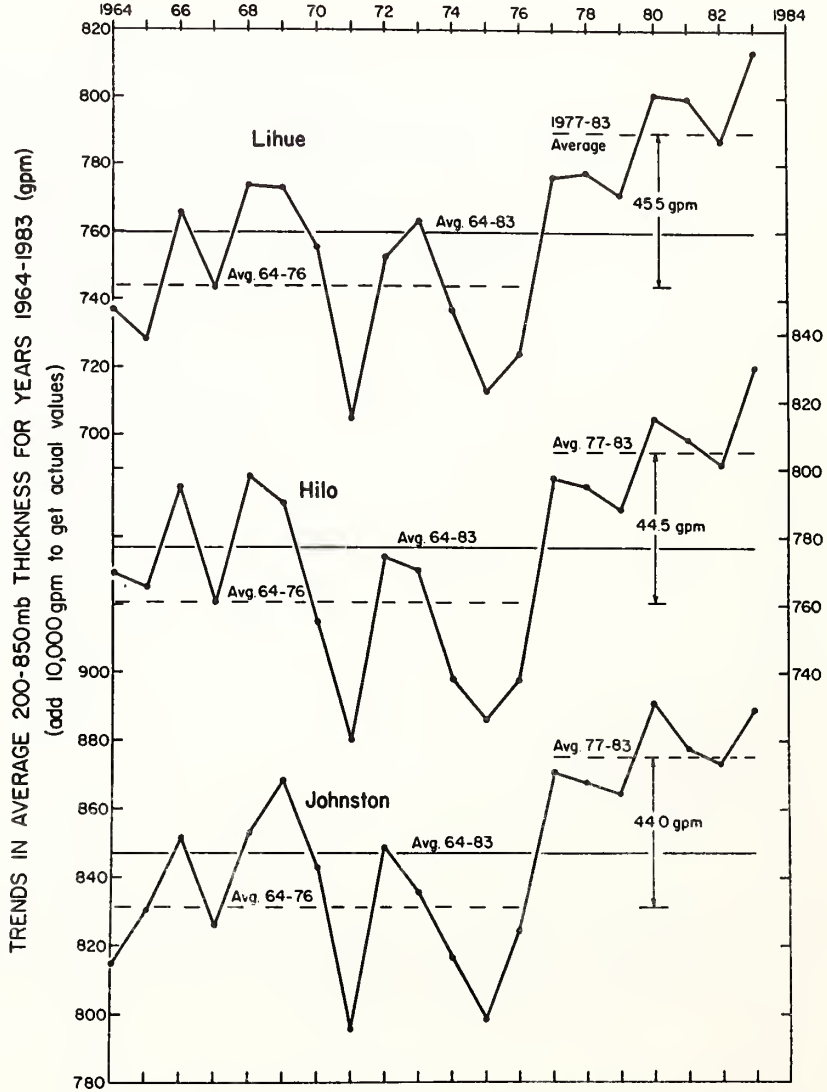

Fig. 9. Annual average plots of 200-850 mb thickness (gpm) for the years 1964-83 for Lihue and Hilo, Hawaii, and for Johnston I. Average annual values for 1964-83, 1964-76 and 1977-83, and the difference between the latter two averages are indicated.

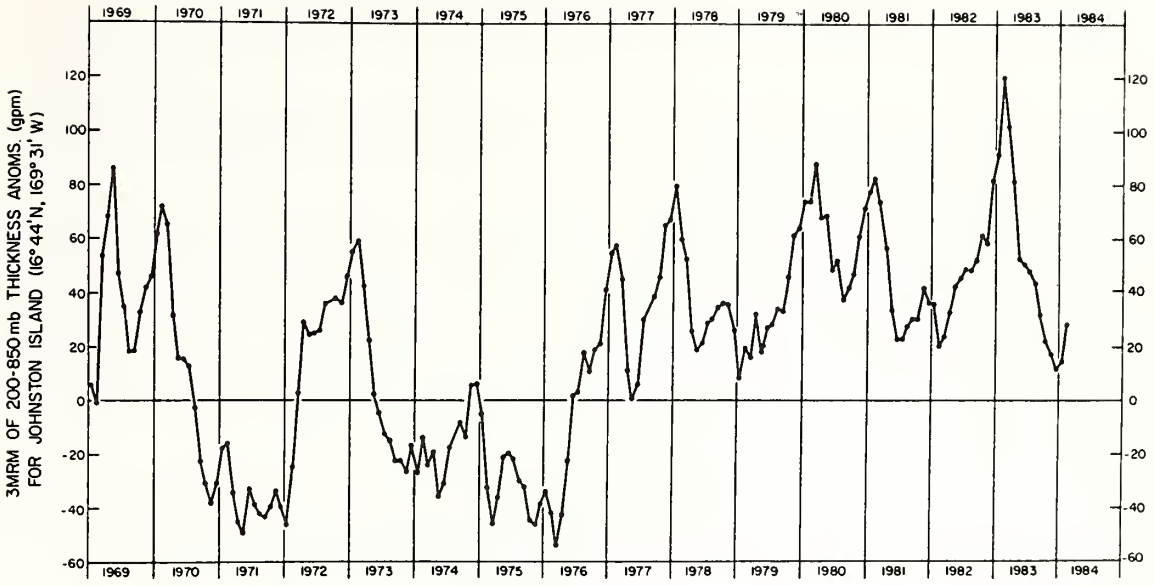

Fig. 10. Three month running mean plot of 200-850 mb thickness anomalies (gpm) for Johnston I.

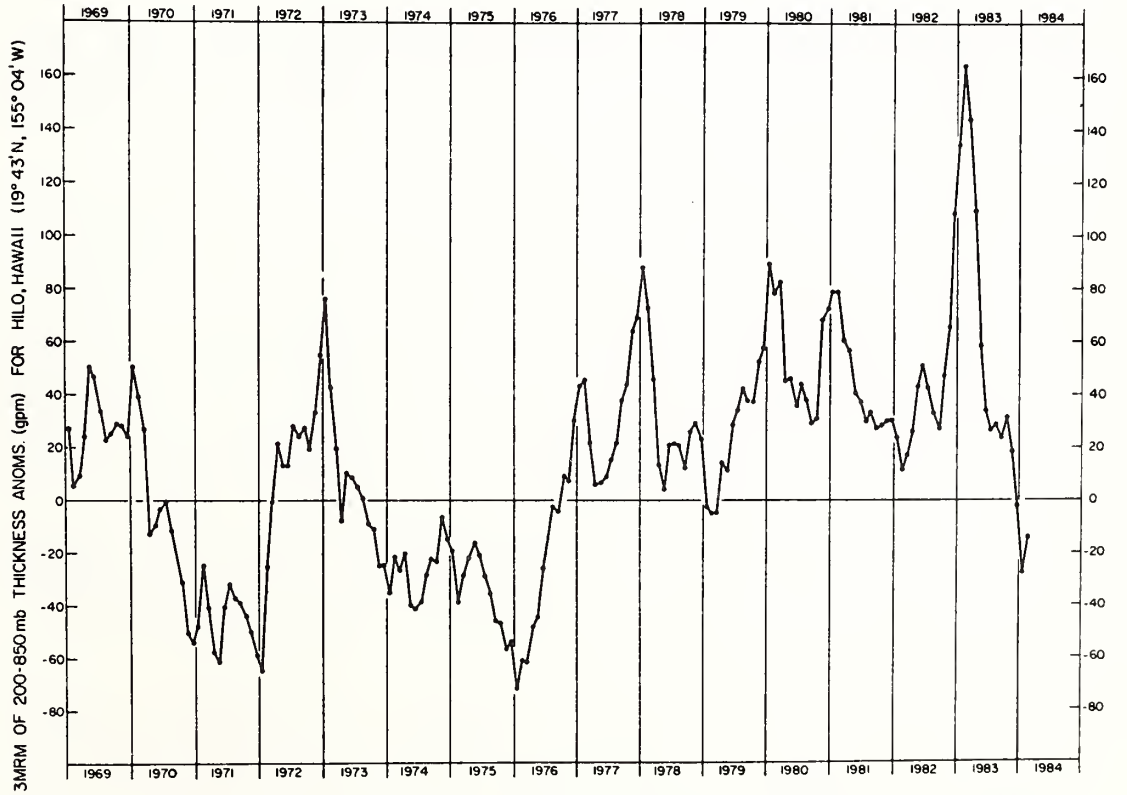

Fig. 11. Three month running mean plot of 200-850 mb thickness anomalies (gpm) for Hilo, Hawaii.

GLOBAL RELATIONSHIPS WITH THE SOUTHERN OSCILLATION

P. B. Wright, T. P. Mitchell and J. M. Wallace
JISAO, University of Washington, Seattle

We are preparing an atlas comprising maps of correlation and regression coefficients between various surface meteorological fields over the global oceans and an index of the Southern Oscillation (SO).

The fields are: sea-surface temperature (SST), sea-level pressure (SLP), sea minus air temperature (S-A), cloudiness and wind components. The data are monthly anomalies in 4° latitude by 10° longitude areas for the period 1950-79, generated from the 'COADS' set supplied by J. O. Fletcher. The SO index is the SLP anomaly at Darwin averaged over the twelve months beginning in April of one year and ending in March of the next; this is reversed in sign to the traditional SO index.

Global maps of correlation and regression coefficients are calculated for six seasons defined relative to the twelve months of the SO index (Fig. 1). This choice provides a description of the time evolution of seasonal anomalies relative to fluctuations of the SO. Thus the maps for DJF1, for example, indicate precursors to SO anomalies, those for SON simultaneous relationships, and those for MAM2 post-lag relationships.

The maps reveal many interesting features, some very familiar, others less so. Sample maps for the Indian and Pacific sectors are shown (Figs. 2-5). We here mention a few of the features, with emphasis on the less familiar. The anomalies mentioned tend to be associated with high Darwin pressure, and anomalies of opposite sign with low Darwin pressure.

1. SON is the season with the strongest correlation patterns. The SST field (Fig. 2) shows a highly correlated negative anomaly over Indonesia with an extension southeastwards, and a positive anomaly over the north Indian Ocean. In the SLP field (Fig. 3) negative anomalies, though strongest near Tahiti, appear to extend across the Equator. The equatorial wind field (Fig. 4) exhibits easterly anomalies in the Indian Ocean, westerly anomalies north of New Guinea, and convergence over the east Pacific. There is a large region of below normal cloudiness centered over Indonesia, and the extreme east equatorial Pacific also has below normal cloudiness.

2. The sequence of SLP maps for the six seasons shows the strongest positive correlations near 80°E in MAM1, 120°E in SON, and 150°E in DJF2. T. P. Barnett has also found evidence of an eastward phase progression of tropical SLP anomalies related to the SO.

3. In the precursor season DJF1 a number of features exhibit significant correlations with the Darwin index. One region of interest is in the southeast Pacific, where all the fields have correlations of magnitude 0.5 or greater. A year of high Darwin pressure

tends to be preceded in this region by relatively warm sea (Fig. 5), low pressure, low cloudiness and weakened southeasterly winds.

One strength of this atlas is that it presents relationships between the SO and several different fields. The ability to superpose the anomaly fields for different variables may help us to elucidate the dominant physical processes operating in different regions in different seasons. For example, one might compare the SST anomalies in the Indonesia region and in the central south Pacific in SON (Fig. 2). Over Indonesia the negative SST anomalies are accompanied by below normal cloudiness and above normal S-A, whereas over the central south Pacific the negative SST anomalies are accompanied by southerly wind anomalies and below normal S-A. These differences suggest that different processes might be dominant in maintaining the negative SST anomalies in the two regions.

FIGURE CAPTIONS:

Fig. 1 Averaging periods used in the study.

Fig. 2 Correlation coefficients x 10 between SST in 4° latitude by 10° longitude areas in SON and the Darwin index. Plus and minus signs denote correlations of the relevant sign between +0.24 and -0.24.

Fig. 3 As Fig. 2, but for SLP in SON.

Fig. 4 Vector resultants of regression coefficients of zonal and meridional wind components in SON on the Darwin index.

Fig. 5 As Fig. 2, but for SST in DJF1.

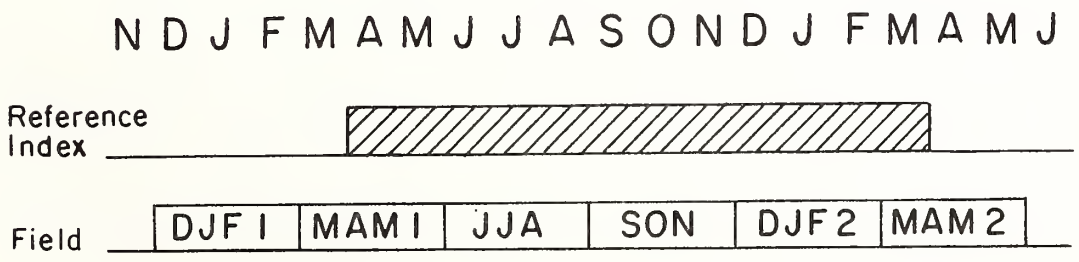

Fig. 1. Averaging periods used in study.

Fig. 2 SST , SØN CØRRELATIØN WITH DARWIN YEAR

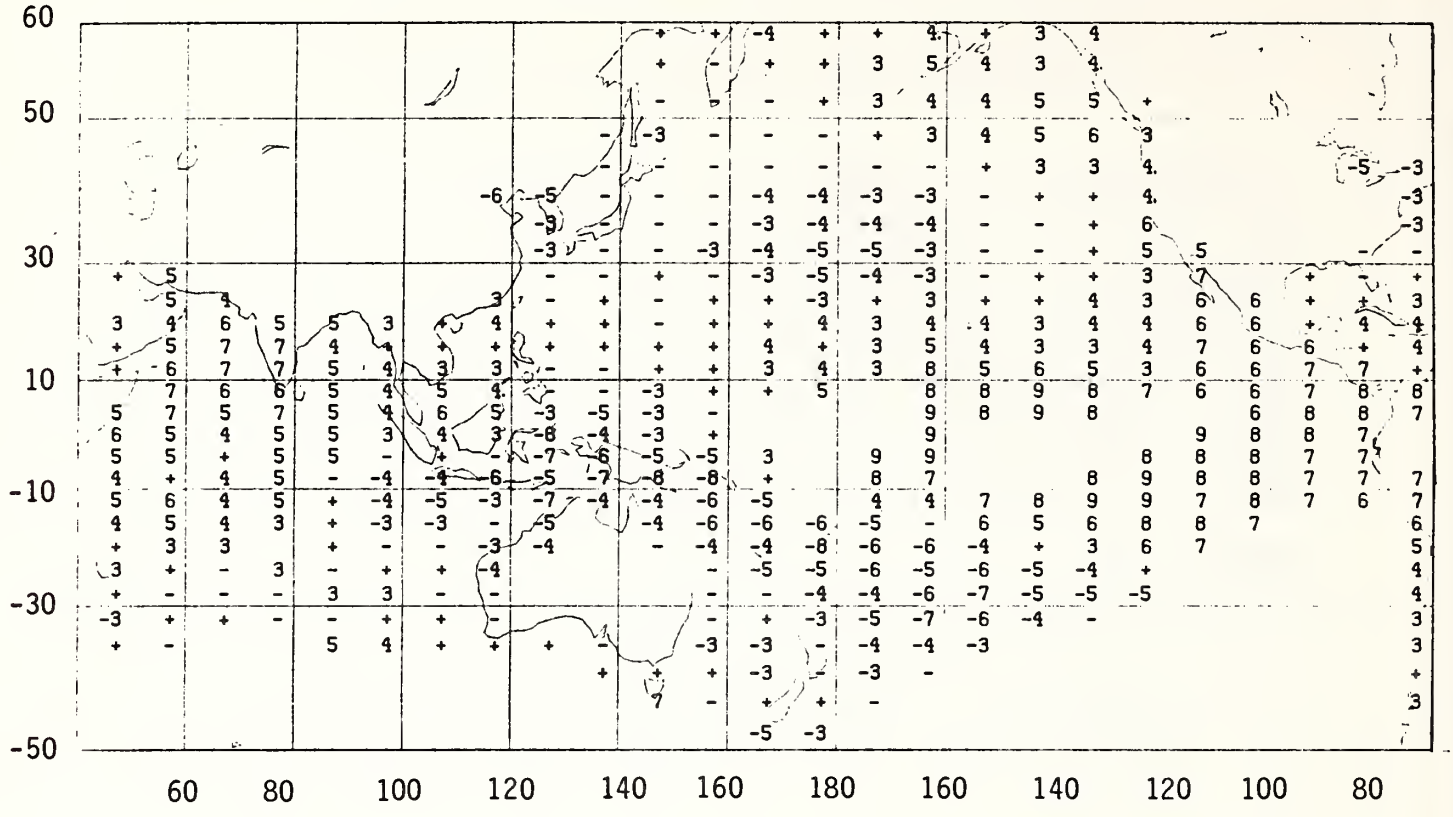

Fig. 3 PRESSURE SØN CØRRELATIØN WITH DARWIN YEAR

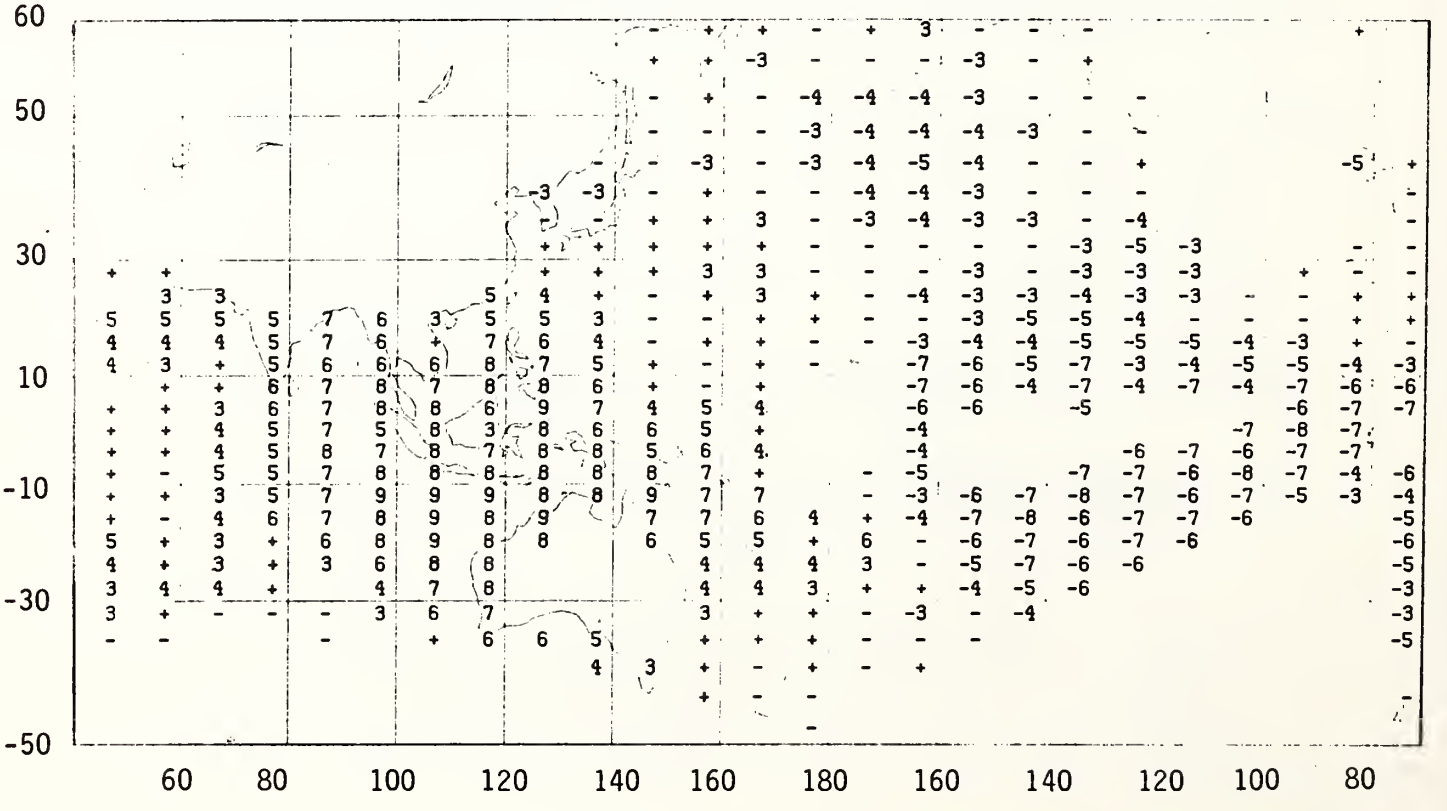

Fig. 4

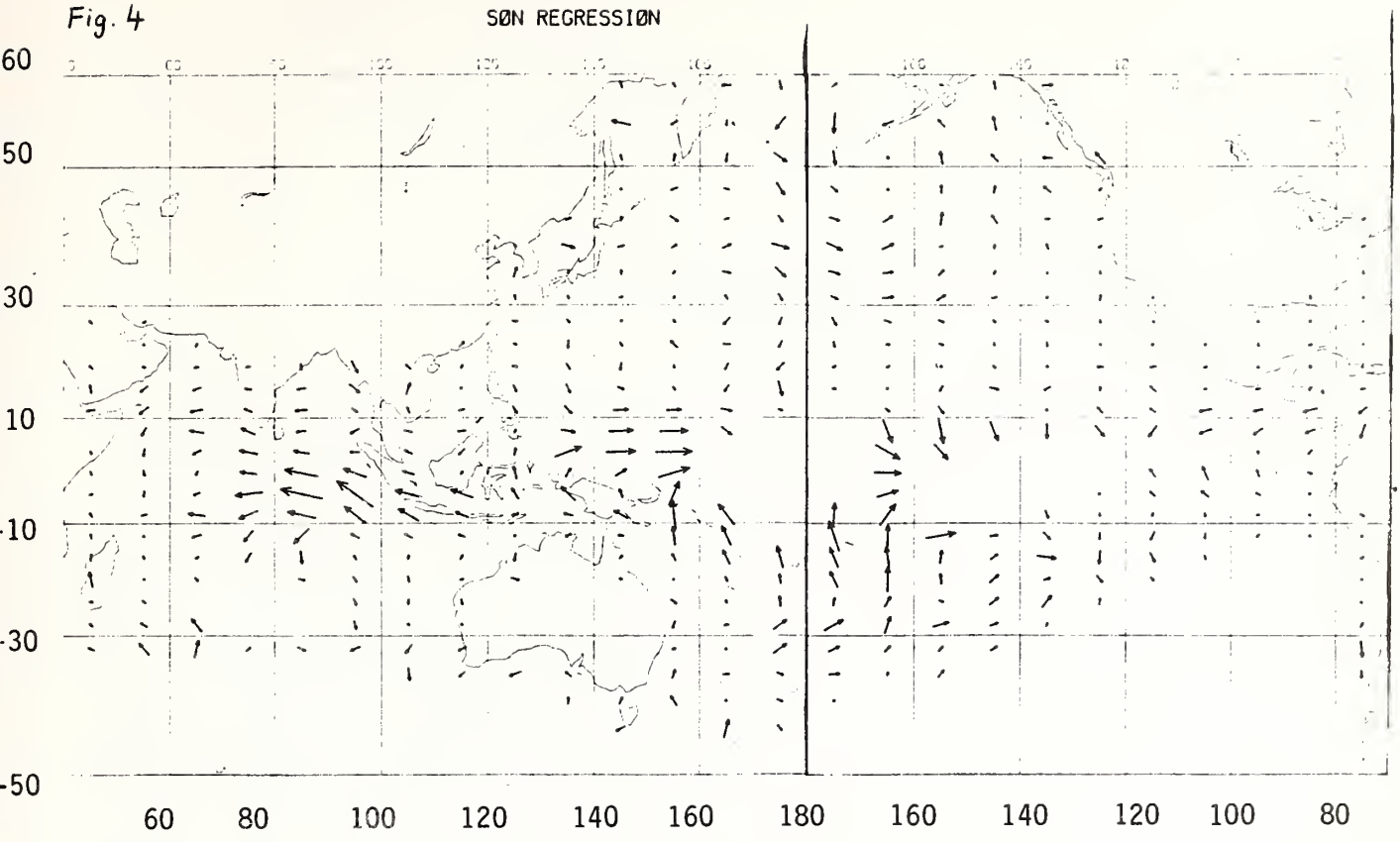

Fig. 5 SST , DJF1 CØRRELATIØN WITH DARWIN YEAR

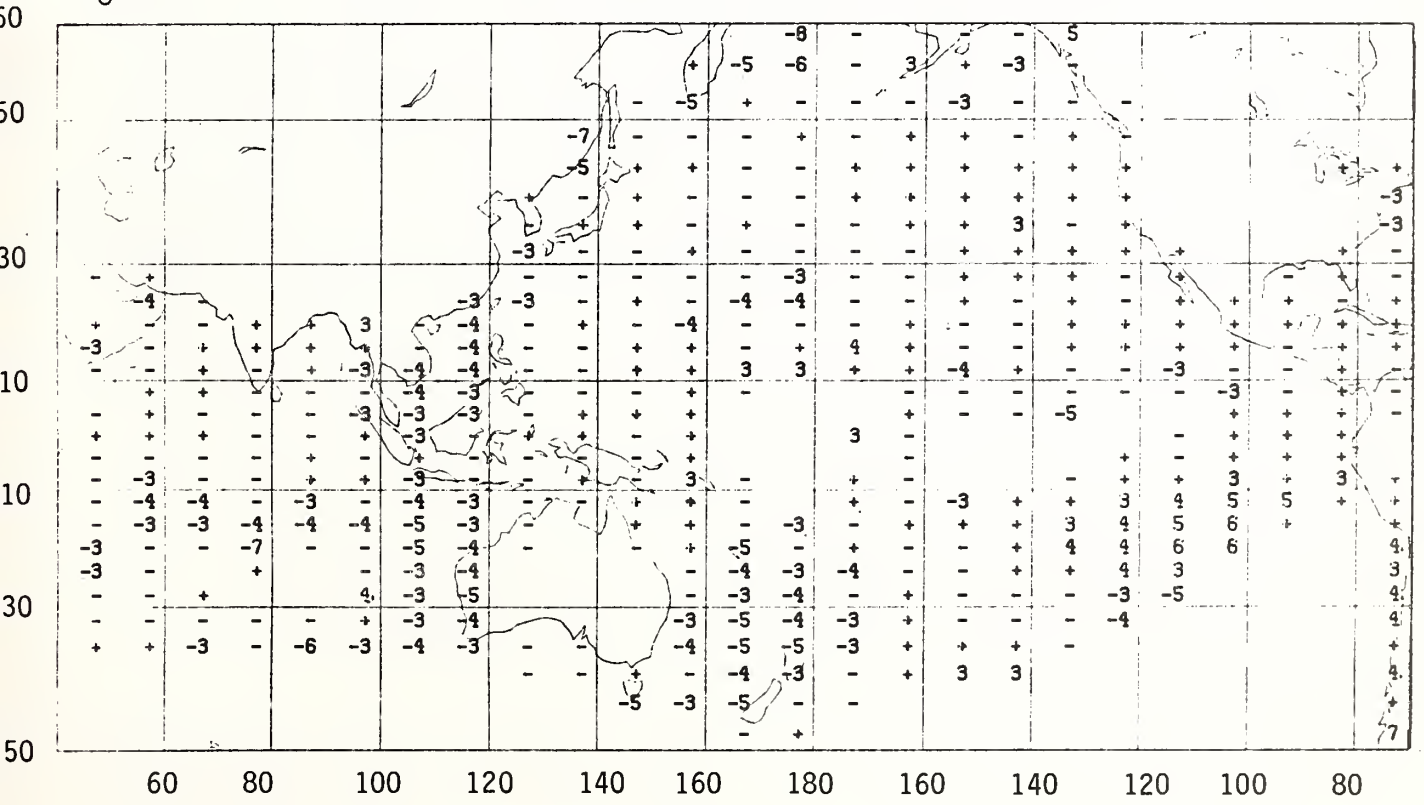

Time Series Modeling of the Southern Oscillation

Pao-Shin Chu
Department of Atmospheric Sciences
Oregon State University
Corvallis, Oregon 97331

Richard W. Katz
Environmental and Societal Impacts Group
National Center for Atmospheric Research
Boulder, Colorado 80307

An index consisting of the difference of normalized sea-level pressure departure between Tahiti and Darwin during 1935-83 is used to monitor the Southern Oscillation (SO) fluctuations. Using a time-domain approach, autoregressive-moving average (ARMA) processes are applied to model the Southern Oscillation Index (SOI) on a monthly and seasonal basis. An objective model selection procedure is used to help identify the appropriate time series model.

It is shown that a low-order ARMA process, namely ARMA(1,1), adequately fits the monthly SOI. According to this process, the SOI for the current month can be expressed as a function of the state of the previous month SOI and a current month's random error plus a previous month's error. The complexity of the noise terms may account for some abrupt changes which occur occasionally in the monthly data. Strong midlatitude forcing as induced by the cold surge during winter season appears to be one of many possible mechanisms which would perturb the large-scale mass circulation in the SO regime on a short time basis.

For the seasonal data, an AR(3) process is found to be the most adequate time series model. For this process, the current value of the SOI can be represented in terms of its immediate three past values and a noise term. The rather long carry-over effect (three seasons) is suggestive of a pronounced signal reflected in the seasonal data. Previous studies (Horel and Wallace, 1981; Rasmusson and Carpenter, 1982; etc.) indicate that the life time of an anomalous warm sea surface temperature in the equatorial Pacific associated with the SO may last for one year. This slow change in thermal forcing together with large thermal inertia in the tropical oceans offer an explanation for this long memory over at least three seasons.

Satellite Observations of a Large-Amplitude 40-50 Day Oscillation in Upper Tropospheric Temperature over the Equatorial Pacific Ocean during the 1982-83 ENSO Event

Edward I. Tollerud[1]
CIRES
University of Colorado
Boulder, CO 80309

Using observations from radiosonde stations, Madden and Julian (1972) were able to describe oscillations with periods near 40-50 days in the wind, pressure, and temperature fields at several locations in the global tropics, particularly over the Pacific Ocean. They also noted some striking similarities between the structure of these oscillations and the atmospheric anomalies associated with ENSO events. More recently, Ka-Ming Lau (1984) has suggested that fluctuations in the amplitude of the oscillation may in fact trigger ENSO events.

This paper describes an oscillation with a period near 50 days that was observed in the atmospheric temperature fields over the equatorial Pacific Ocean in 1982-83. As the results will show, there is an apparent relationship between the amplitude of the oscillation and the on-going ENSO event.

The data used in this study are temperature retrievals from NOAA polar-orbiting satellites. The basic averaging unit applied to the retrievals was 5 days in duration and 5° of latitude and longitude in horizontal dimension. While providing sufficient time resolution to describe oscillations of the period of interest, this choice of averaging period and area also results in an adequate sample of retrievals in each averaging area. Fields of these averages were used to construct time series and sections like those presented here.

The presence of a 40-50 day temperature oscillation in the 200-300 mb layer is suggested qualitatively by the time series of Fig. 1. The relatively short period of record limits the credibility of quantitative spectral analysis. When standard spectral techniques were applied, however, a marginally significant peak appeared near 50 days in the spectra of the time series of Fig. 1 and in the spectra of other time series constructed using different averaging areas. In the first half of the period the amplitude is largest (3-4°K), decreasing somewhat in the second half. ENSO-related anomalies were also largest in the mid and eastern Pacific during the first half of the period and decreased to near normal by the period's end.

Two features are especially noticeable in the time-longitude section in Fig. 2. The first is the nearly simultaneous warming associated with the oscillation over virtually the entire central and eastern Pacific (it should be noted that an eastward propagating mode previously identified in

---

[1]Present affiliation: National Research Council Resident Research Associate, NOAA/ERL/WRP, Boulder, Colorado 80303

oscillations of this kind would be obscured by the averaging applied to this data). Secondly, a finer structure is suggested by increased amplitudes at certain longitudes, especially between 120°W and 160°W in early 1983. These increased amplitudes occur in regions where ENSO-related anomalies are also large (cf. the monthly averages of OLR anomalies presented by Gill and Rasmusson, 1983).

During the second half of the period the warmings are largest near the equator (Fig. 3). During the height of the ENSO event, on the other hand, they extend at least as far as 20°N and 20°S, with largest values south of the equator.

The observations presented describe a 40-50 day oscillation in atmospheric temperature over the tropical Pacific, an oscillation whose amplitude appears to be modulated by the presence of large ENSO-related anomalies. Just what the relationship between these oscillations and ENSO circulations is must wait upon further analysis. Of particular interest would be an extension of this case study to include higher-latitude observations (to examine the latitudinal extent of the major warming episodes) and observations during the early part of the ENSO event. Comparison should also be made with observations during a non-ENSO year.

REFERENCES

Gill, A.E. and E.M. Rasmusson, 1983: The 1982-83 climate anomaly in the equatorial Pacific. Nature, 306, 229-234.

Lau, K.-M., 1984: Bimodal climate state, atmosphere-ocean interaction and El Nino/southern oscillation. Proc. 15th Conf. on Hurricanes and Tropical Meteorology, 64-67 (Miami, Florida, January, 1984).

Madden, R.A. and P.R. Julian, 1982: Description of global-scale circulation cells in the tropics with a 40-50 day period. J. Atmos. Sci., 29, 1109-1123.

FIGURE CAPTIONS

Fig. 1 Temperature of the 200-300 mb layer averaged over consecutive 5-day periods within the zonal strip between 0°-5°S and 90°W-180°.

Fig. 2 Selected contours of the temperature of the 200-300 mb layer. The section was constructed using temperatures along a longitudinal strip between 0°-5°S.

Fig. 3 Selected contours of the temperature of the 200-300 mb layer. The section was constructed using temperatures along a meridional strip between 155°W-160°W.

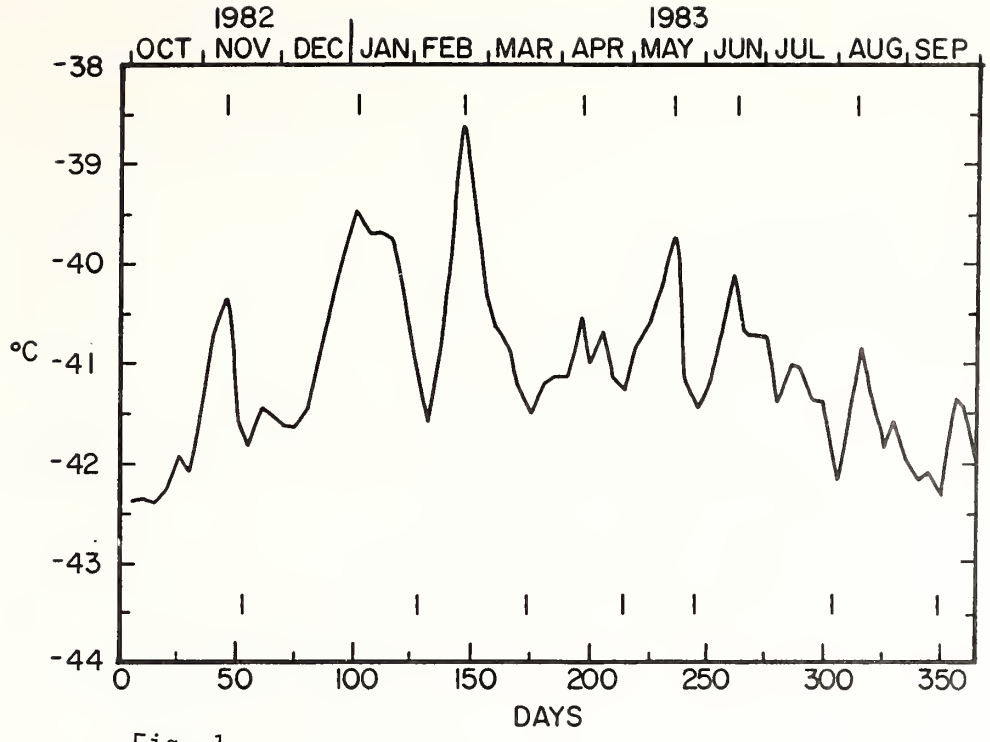
1982
1983
OCT
NOV
DEC
JAN
FEB
MAR
APR
MAY
JUN
JUL
AUG
SEP
-38
-39
-40
-41
-42
-43
-44
°C
0
50
100
150
200
250
300
350
DAYS

Fig. 1

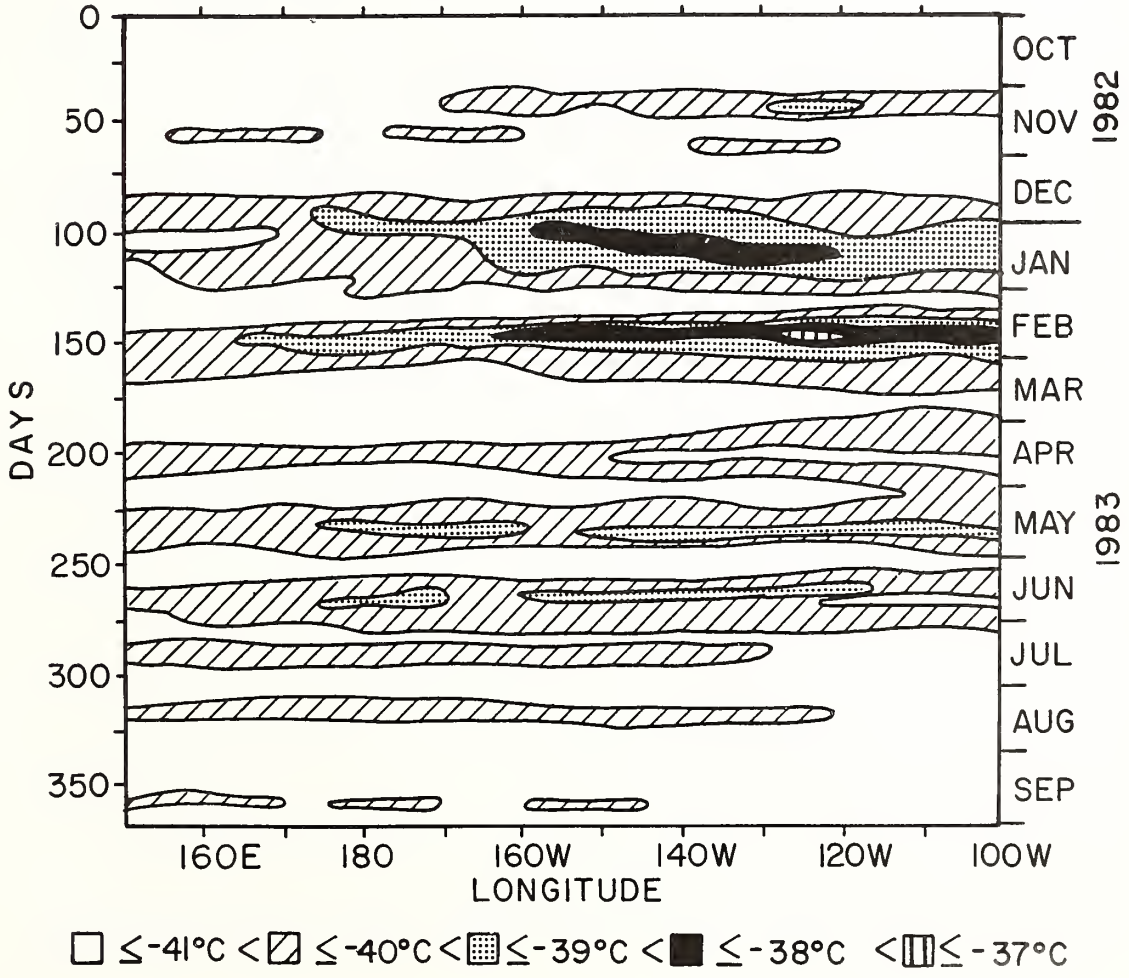
0
50
100
150
200
250
300
350
DAYS
OCT
NOV
DEC
JAN
FEB
MAR
APR
MAY
JUN
JUL
AUG
SEP
1982
1983
160E
180
160W
140W
120W
100W
LONGITUDE
≤-41°C
≤-40°C
≤-39°C
≤-38°C
≤-37°C

Fig. 2

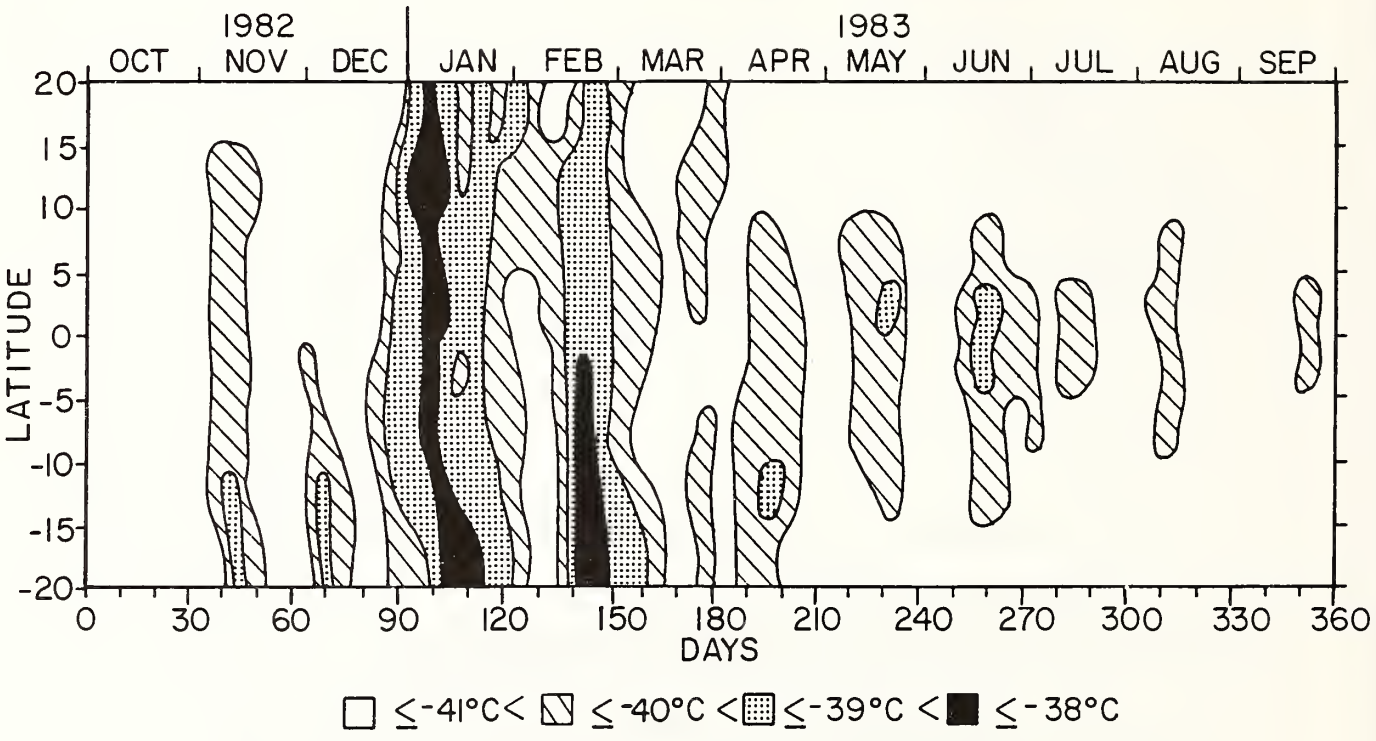
1982
1983
OCT
NOV
DEC
JAN
FEB
MAR
APR
MAY
JUN
JUL
AUG
SEP
20
15
10
5
0
-5
-10
-15
-20
LATITUDE
0
30
60
90
120
150
180
210
240
270
300
330
360
DAYS
≤-41°C< ≤-40°C <≤-39°C < ≤-38°C

Fig. 3

Subseasonal and Interannual Variations of Tropical Convection and the El Nino/Southern Oscillation

K.M. Lau
Laboratory for Atmospheres
NASA Goddard Space Flight Center
Greenbelt, MD 20771

and
P.H. Chan
Applied Research Corporation
Landover, MD 20785

It was found that during the northern winter, fluctuation in tropical convection is dominated by eastward propagating cloud clusters from the Indian Ocean. Most of these clusters reach as far as the central Pacific. Longitude-time sections of outgoing longwave radiation (OLR) anomaly along the equator show that there are about 3 to 4 such episodes each winter. Also, simultaneous OLR anomalies over the equatorial central Pacific (ECP) and the maritime continent (MC) are negatively correlated and their variations are dominated by a 40-60 day period, suggesting the presence of a standing wave phenomenon.

Such combination of propagating and standing phenomena can be captured by the extended empirical orthogonal function (EEOF) analysis. The EEOF method combines the temporal as well as the spatial correlation information to produce eigenmodes which have space-time dependence. In our case we use a 5 day and a 10 day lag in addition to the simultaneous spatial correlation. Each of the resulting EEOF gives us a sequence of three maps, one at day 0 and the other at day 5 and day 10. Fig.1 gives the series of the time coefficient over the seven winters. It is obvious that the two modes have variations of 40-60 day period. Fig.2 shows the first two EEOF, each consisting of a sequence of three maps. Since the second mode preceeds the first by about 15 days (fig.1) we can concatenate the two modes into a single series of 6 maps, each separated by 5 days.

The major features are: 1) The first two EEOF depict an east-west dipole which originates from the Indian Ocean and propagates into the central Pacific. The signal diminishes over the eastern Pacific. 2) There is some magnification of its amplitude when the dipole is situated over the MC and ECP. 3) The propagating speed is about 4m/s and when the dipole is over the MC and ECP it slows down to 1-2m/s, with the center over ECP remains quasi-stationary.

It is suggested that the 40-60 day oscillations, interacting with the seasonal cycle may trigger a major El Nino event. Fig.3 shows the longitude-time section of 5-day running mean OLR anomaly for the period of July 82 to June 83 over the equator between 60E and 60W. It is apparent that the El Nino is preceeded by a series of eastward instusion of energetic convective activity described above. During the El Nino period the convective activity over the ECP continues to undergo strong 40-60 day oscillations. Convective cloud clusters originating from the Indian Ocean still tend to propagate eastward but are suppressed over the region of enhanced subsidence represented by positive OLR anomaly over the MC.

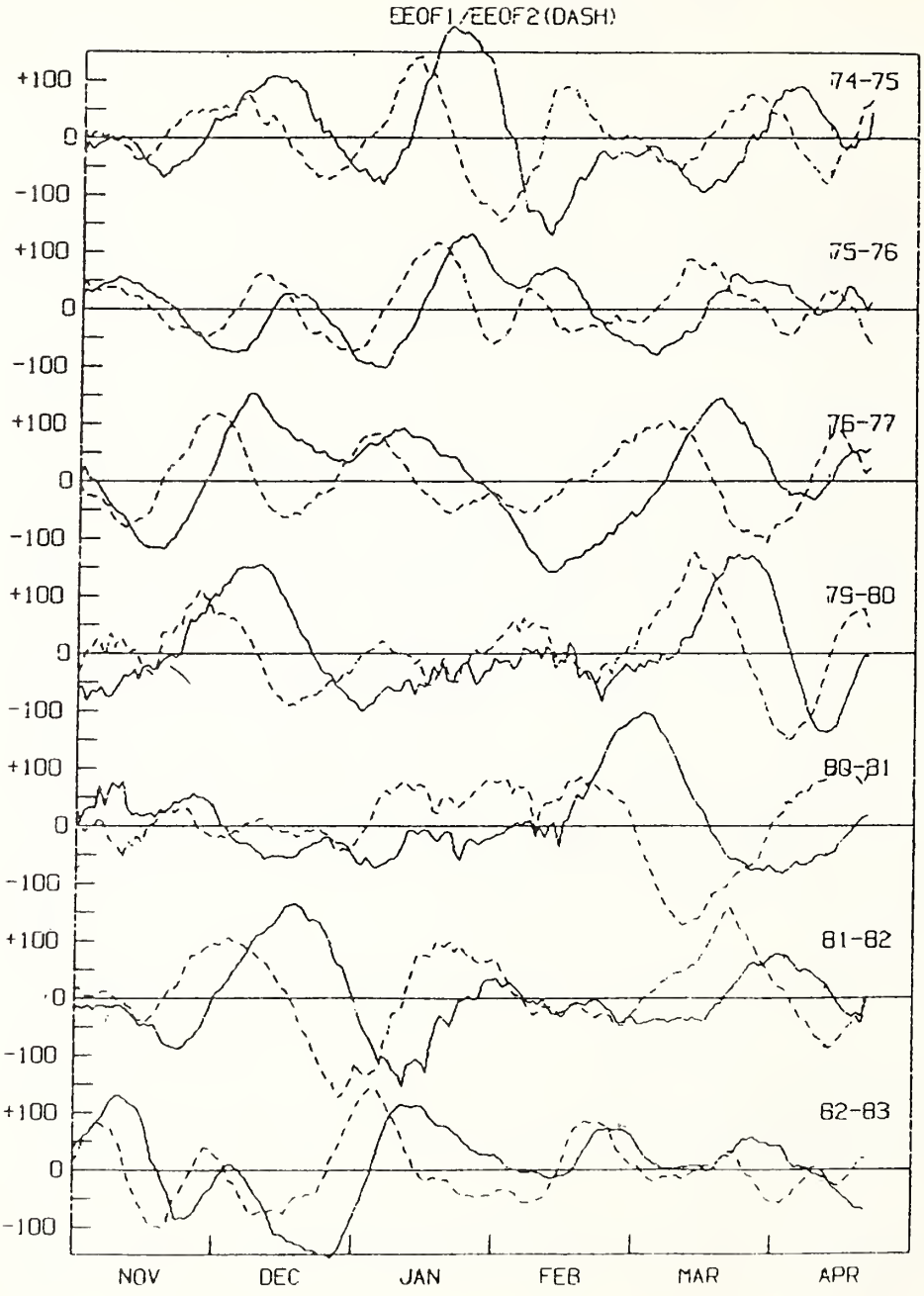

Fig. 1: Series of time coefficients of EEOF 1 and 2 for the 7 winters.

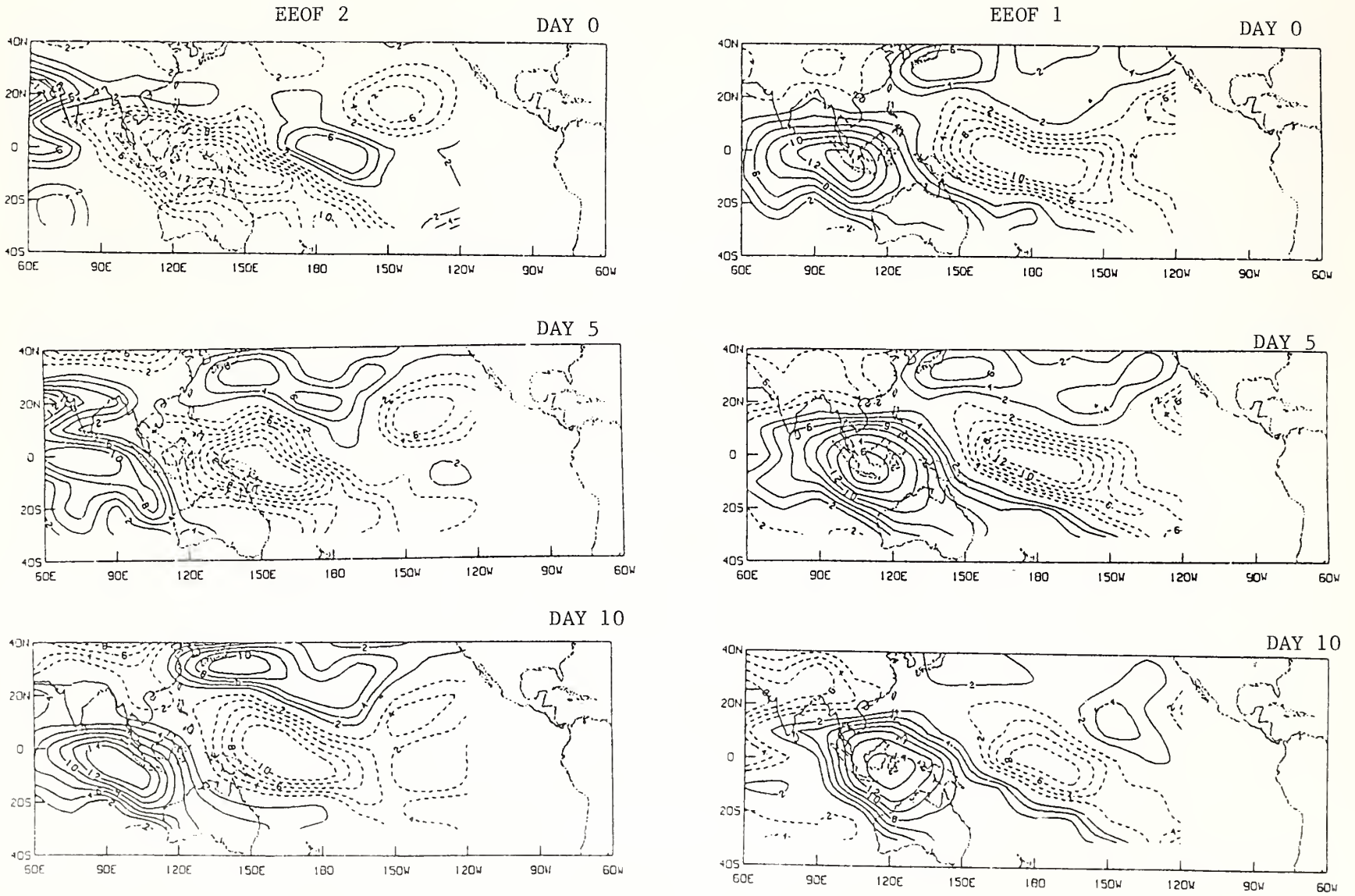

Fig. 2: EEOF 1 and 2.

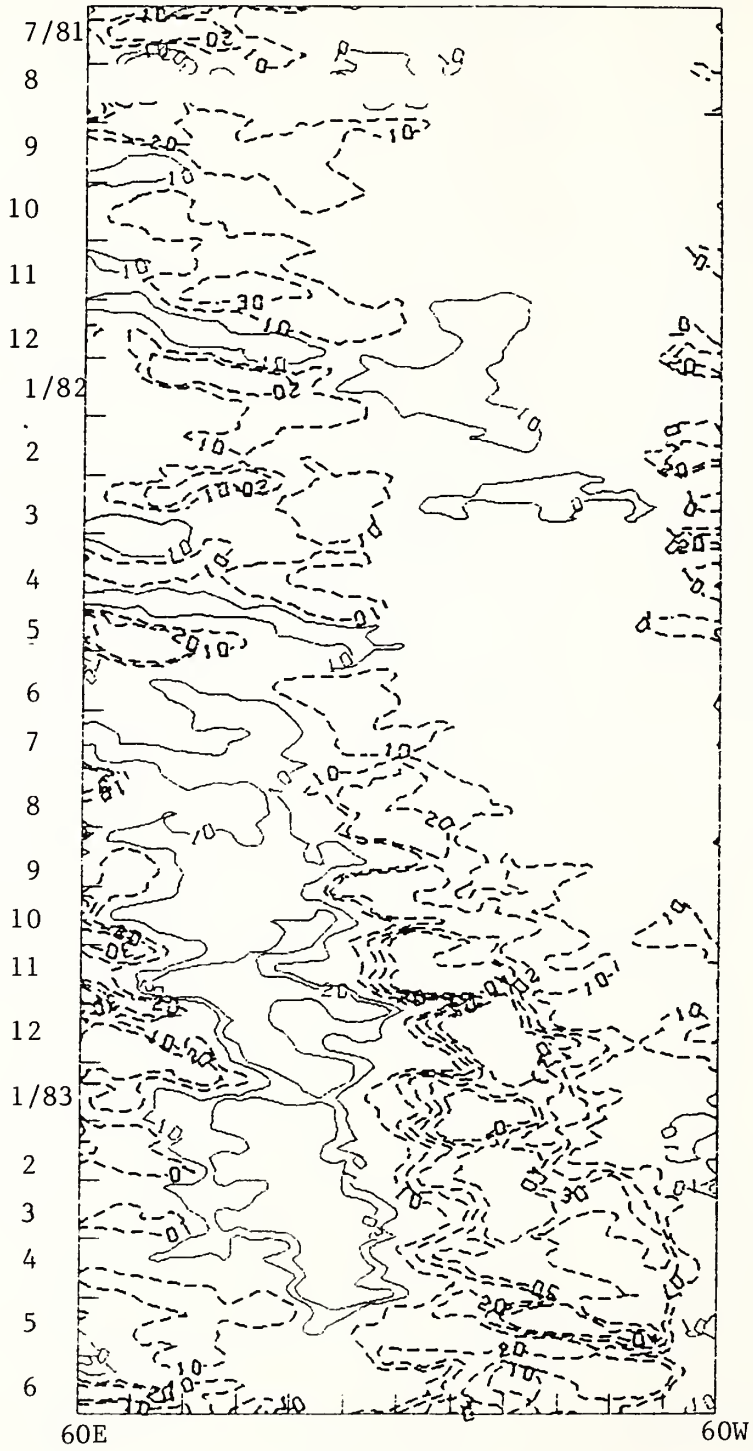

Fig. 3: Longitude-time section of OLR anomaly. Unit in watts/m^2.

The Annual Variation in the Vertical Structure of the 40-50-Day Tropical Oscillation

Roland A. Madden

National Center for Atmospheric Research
P. O. Box 3000, Boulder, CO 80307

1. Introduction

Spectra based on relatively long time series (5-10 or more years) of station pressure and upper air data from tropical regions reveal relatively broad spectral peaks whose maxima typically fall in the 40-50 day period range. In particular, the lower tropospheric zonal wind is very coherent and out-of-phase with the upper tropospheric zonal wind. To date, these results have been based on time series which span all seasons. Our aim here is to learn something of the annual variation of this vertical structure.

2. Data

Time series of wind data were taken from rawinsonde records available at NCAR. A summary of the rawin data is presented in Table 1. All data started on 1 July. The shortest record was 1980 days at Recife, Brazil, and the longest was 10400 days at Truk Island. Data from the first available sounding for each day were selected. As a result a time series does not necessarily come from the same time each day. Values for days which had no data available were estimated by linear interpolations in time. Some stations had a considerable amount of missing data, particularly at 150 mb; however, inspection of the time series at these stations indicated that there were no continuous gaps as long as 40 days. The annual variation was removed from the data by first computing averages over all years for each day of the year. These ensemble averages were Fourier analyzed and the first, second, and third harmonics of the annual variation were then subtracted from each individual year of data.

3. Local cross spectrum analysis

In order to isolate the annual variation of the vertical structure of the 40-50 day oscillation we have used a technique we will call "local" cross spectrum analysis. It is similar to cross spectrum analysis in that we estimate variability and covariability in given frequency intervals, but it is different in that the estimates are not averaged over an entire time series or segment of the time series. In that sense it is "local" in time. The method is described in the following.

Figure 1 shows the coherence squared between the 850 mb and 150 mb zonal winds based on 19, 512-day segments from Truk Island and a conventional cross-spectrum analysis. Segments were chosen consecutively with no regard to season. The high coherence peaking at 50-day periods is

associated with phase angles of 180° or half a cycle. That is, 850 and 150 mb zonal winds are out-of-phase. Superposed on the coherence is the response of a filter which is unity at 49-day periods. This filter was used to compute the "local" spectral values in the 40-80 day range.

Filtering was accomplished by first Fourier transforming 540-day segments. Each segment began on 1 July of a given year. That is

$$u_p(t) = \bar{u}_p + \sum_{\omega=1/N}^{.5} a_p(\omega)\cos\omega t + b_p(\omega)\sin\omega t \qquad (1)$$

where N is the length of the series, in this case 540, $\bar{u}_p$ is the average over N values, p is the pressure level (either 850 or 150). Filtered data are simply (1) multiplied by the filter response of Fig. 1 after the mean has been subtracted, or

$$\mathcal{U}_p(t) = \sum_{\omega=1/N}^{.5} [a_p(\omega)\cos\omega t + b_p(\omega)\sin\omega t] \cdot G(\omega) \qquad (2)$$

The local spectrum of the u wind at p can be estimated by

$$S_p(t) = \langle \mathcal{U}_p(t)^2 \rangle \qquad (3)$$

where the bracket, < >, represents an ensemble average over all years for the "t"th day of the year.[1] Similarly the local cospectrum is

$$Co(t) = \langle \mathcal{U}_{850}(t) \cdot \mathcal{U}_{150}(t) \rangle \qquad (4)$$

In order to estimate the local quadrature spectrum we use a Hilbert transform to shift the 150-mb wind.

$$\hat{\mathcal{U}}_{150}(t) = \sum_{\omega=1/N}^{.5} [b_p(\omega)\cos\omega t - a_p(\omega)\sin\omega t] \cdot G(\omega) \qquad (5)$$

The local quadrature spectrum is thus

$$Qu(t) = \langle \mathcal{U}_{850}(t)\, \hat{\mathcal{U}}_{150}(t) \rangle \qquad (6)$$

The local coherence squared is

$$Coh^2(t) = \left(Co(t)^2 + Qu(t)^2\right)/\left(S_{850}(t)\, S_{150}(t)\right) \qquad (7)$$

and the local phase is

$$\phi(t) = \mathrm{Atan}\left(Qu(t)/Co(t)\right) \qquad (8)$$

[1] A 49-day running average was used in addition to the ensemble averaging to produce smoother values of $S_p(t)$, $Co(t)$, and $Qu(t)$.

4. Results

Figure 2 contains local coherence squared and phase angles for the 19 stations studied. The results from each station are plotted from October (left) through September (right). It is interesting to note the contrast between Koror, Truk, and Majuro in the Northern Hemisphere and stations from Canton westward to Nairobi in the Southern Hemisphere. High coherence and the out-of-phase relationship between low and high troposphere are most evident in the summer hemisphere. We speculate that this results from the seasonally migrating ITCZ which acts, through convection, as a link between low and high troposphere.

Table 1

	Station	Latitude (deg min)	Longitude (deg min)	Number of days in series	Year series starts	Number Interpolated 850	150
ADE	Aden	12 50N	45 02E	5166	1952	43	58
ASC	Ascension	7 58S	14 24W	3955	1959	19	18
BAL	Balboa	8 58N	79 33W	4320	1952	21	95
BAN	Bangkok	13 44N	100 30E	2709	1958	435	583
CAN	Canton	2 46S	171 43W	4810	1954	45	101
COC	Cocos	12 11S	96 50E	7120	1957	409	999
DAK	Dakar	14 44N	17 30W	2861	1955	171	233[1]
DAR	Darwin	12 00S	130 52E	7880	1955	10	216
GAN	Gan	00 41S	73 09E	2340	1964	267	337
HON	Honiara	9 25S	159 58E	6540	1959	38	299
KOR	Koror	7 20N	134 29E	9280	1954	304	648
LAE	Lae	6 44S	147 00E	5990	1957	25	964
LIM	Lima	12 01S	77 08W	7670	1958	860	1849
MAJ	Majuro	7 05N	171 23E	7090	1961	28	120
NAI	Nairobi	1 18S	36 45E	3805	1957	303[2]	701
PIA	Piarco	10 35N	61 21W	2556	1972	141	167
REC	Recife	8 07S	34 55W	1980	1959	257	299
SIN	Singapore	1 22N	103 55E	4990	1959	161	662
TRU	Truk	7 27N	151 50E	10400	1952	236	550

[1] 200 mb used at Dakar
[2] 700 mb used at Nairobi

Figure captions

Figure 1 Coherence squared between 850 and 150-mb u winds at Truk (dash-dot line). The scale is indicated on the right. Filter response, $G(\omega)$, designed to isolate variability on the 40-50 day range (solid line). The scale is indicated on the left.

Figure 2 Local coherence squared and phase determined from each of the 19 stations listed in Table 1. Scales are indicated on the far left panels. Tick marks approximately set off months beginning with October on the left and extending through September.

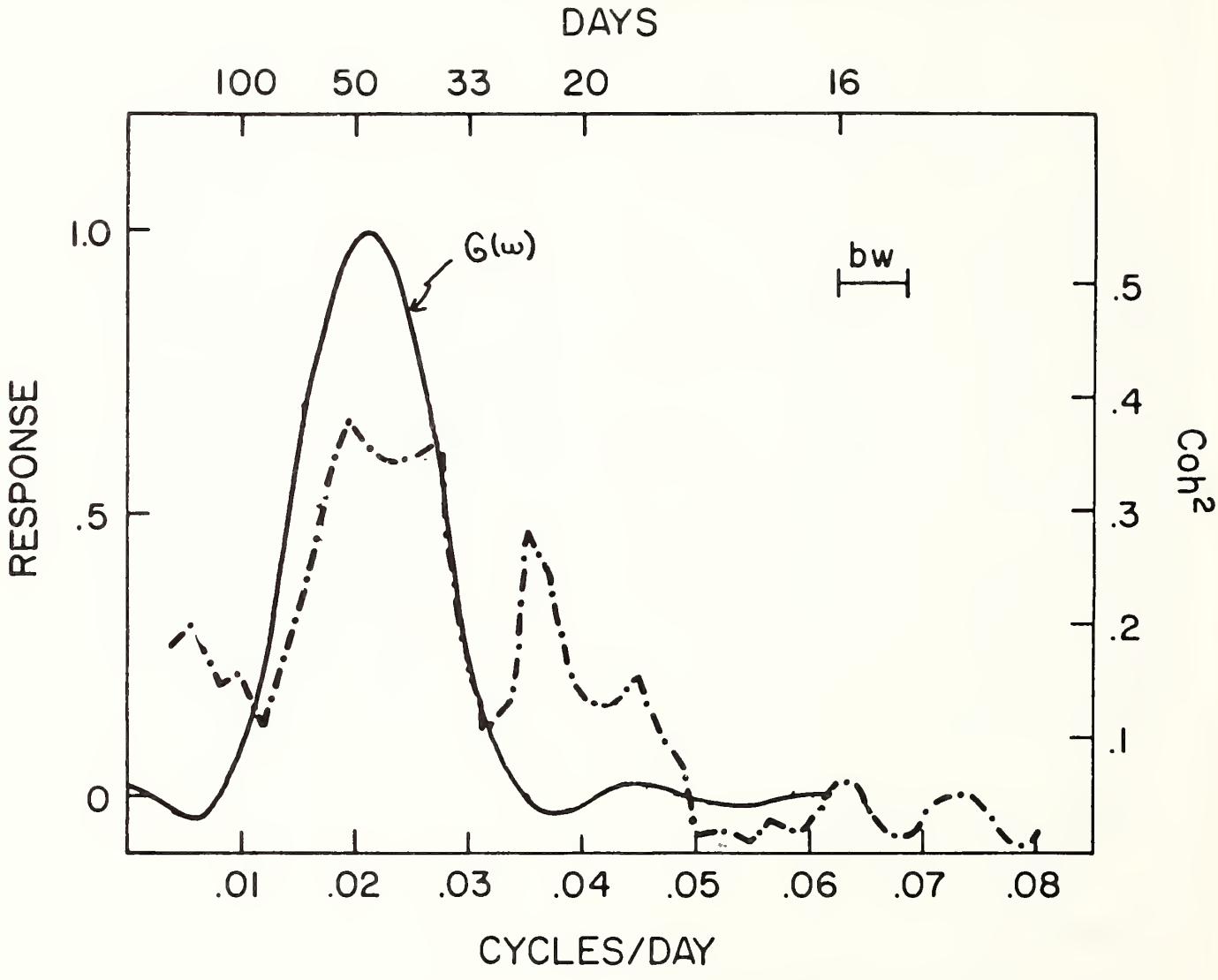
DAYS
100
50
33
20
16
1.0
.5
0
RESPONSE
G(ω)
bw
.5
.4
.3
.2
.1
Coh²
.01
.02
.03
.04
.05
.06
.07
.08
CYCLES/DAY

1

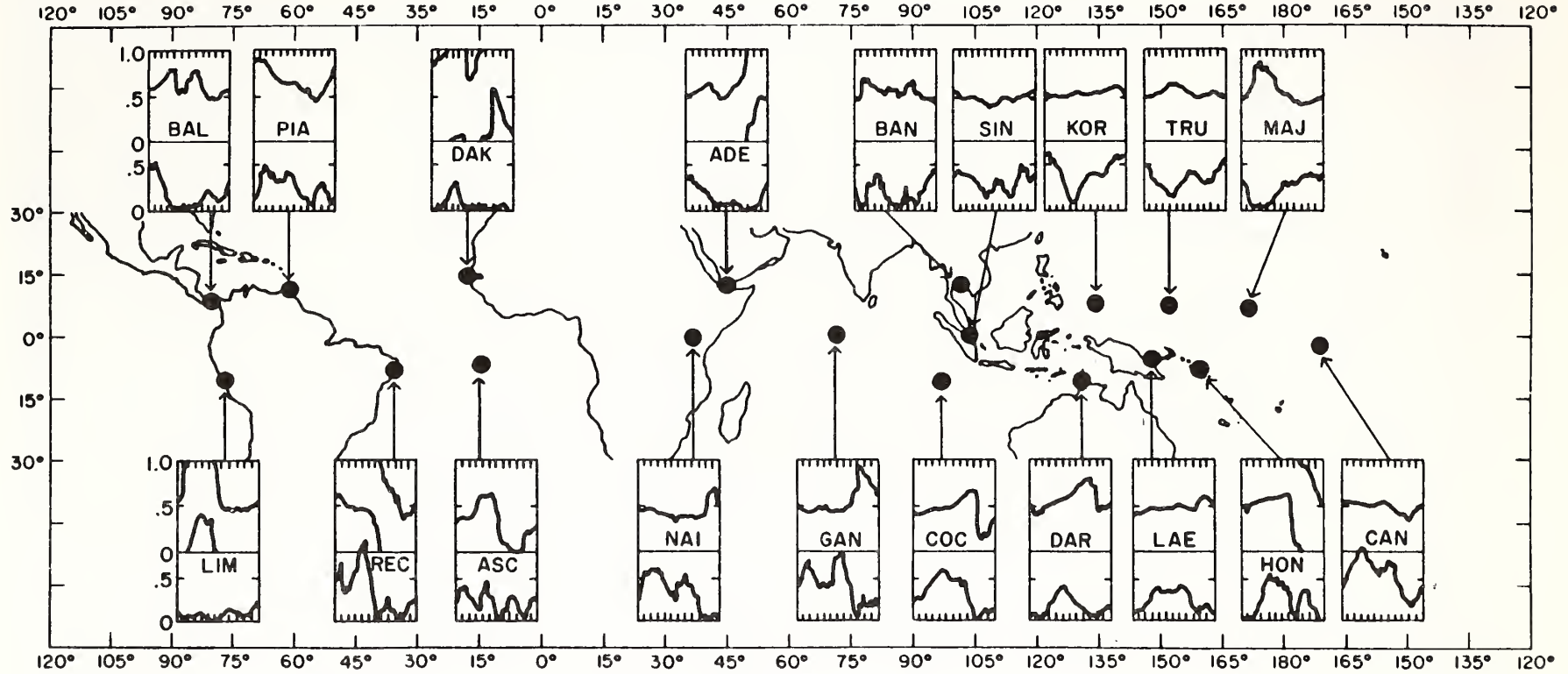
120° 105° 90° 75° 60° 45° 35° 15° 0° 15° 30° 45° 60° 75° 90° 105° 120° 135° 150° 165° 180° 165° 150° 135° 120°
1.0
.5
0
.5
0
BAL
PIA
DAK
ADE
BAN
SIN
KOR
TRU
MAJ
30°
15°
0°
15°
30°
1.0
.5
0
.5
0
LIM
REC
ASC
NAI
GAN
COC
DAR
LAE
HON
CAN
120° 105° 90° 75° 60° 45° 30° 15° 0° 15° 30° 45° 60° 75° 90° 105° 120° 135° 150° 165° 180° 165° 150° 135° 120°

2

Life cycle of a 28-72 day atmospheric oscillation during northern winter

Klaus M. Weickmann
and
John E. Kutzbach

Center for Climatic Research
University of Wisconsin-Madison
1225 W. Dayton Street
Madison, Wisconsin 53706

Since Madden and Julian's (1971, 1972) discovery of a 40-50 day oscillation in the tropical atmosphere, observational work has fallen into two categories:

1) case studies of individual seasons concentrating particularly on the FGGE (1979) year (e.g., Krishnamurti and Subrahmanyam, 1982; Murakami et al., 1983; Quah, 1984; Lorenc, 1984; Weickmann, 1982; Weickmann and Kutzbach, 1983) and

2) ensemble averaged studies of many seasons concentrating on the last 10 years (e.g., Yasunari, 1980, 1981; Sikka and Gadgil, 1980; Lau and Chan, 1983a, 1983b; Anderson and Rosen, 1983; Weickmann, 1983; Weickmann, Lussky and Kutzbach, 1985; Knutson, 1984).

This study falls into the latter category; we investigate the spatial and temporal characteristics of 28-72 day fluctuations in NMC-analyzed 250mb wind and satellite-derived outgoing longwave radiation (OLR). The ensemble-averaged statistics to be described are calculated using 9 different (1974-1984) NOV-APR and MAY-OCT periods. This data base gives approximately 36 realizations of 28-72 day oscillations for each "season."

An overview of the seasonal differences in the spatial structure and the propagation characteristics of 28-72 day oscillations in 250mb wind and OLR are described first. This is followed by description of the life cycle of 28-72 day oscillations during northern winter; the life cycle highlights a systematic relationship between the evolution of OLR and the 250mb circulation.

The OLR and 250mb wind data sets have been described and used previously in Weickmann (1983), and Weickmann and Kutzbach (1981, 1982, 1983). Details concerning analysis techniques can be found in Weickmann, Lussky and Kutzbach (1985, hereafter WLK) and Knutson (1984).

The mean NOV-APR and MAY-OCT patterns of OLR (Fig. 1) display areas of maximum monsoonal cloudiness (tropical OLR less than 230 w/m^2) centered 5-10° south of the equator during northern winter and 5-10° north of the equator during northern summer. The distribution of ensemble averaged 28-72 day OLR variance during each season (Fig. 2), also shows a north/south shift indicating that the maximum activity associated with 28-72 day oscillations tracks the seasonal evolution of monsoonal cloudiness. The schematic arrows on Fig. 2 portray the direction of OLR propagation in regions most prominently affected by 28-72 day oscillations during northern winter and northern summer. In both seasons, eastward propagation occurs over the Indian Ocean and western equatorial Pacific. In addition, during northern summer,

northward propagation along 80°E and 120°E is well-defined. The plus and minus signs on Fig. 2 denote the major centers of action associated with 28-72 day oscillations; the dotted or solid signs signify tendency for a dipole relationship between two centers of action (e.g., in Fig. 2b when it is cloudy near 10°N, 130°E, it tends to be clear near EQ, 80°E and near 15°N, 100°W).

The 28-72 day fluctuations of OLR are embedded in the 250mb base state winds shown in Fig. 3a (3b) for northern winter (northern summer). A major difference between the seasons is the degree of zonal asymmetry in the windfield particularly when comparing the tropics and southern hemisphere during northern summer with the tropics and northern hemisphere during northern winter. During northern winter, large wavenumber 1 and 2 contributions are made to the northern hemisphere basic state by the east Asian and North American jets and to the tropical base state by the equatorial westerlies over the eastern Pacific and Atlantic Oceans. By comparison, during northern summer, the base state in the southern hemisphere extratropics appears more zonally symmetric, while in the tropics easterlies prevail at all longitudes, also suggesting a larger wavenumber 0 component.

These differences in basic states may partially account for the different propagation characteristics displayed by 250mb 28-72 day zonal wind fluctuations during northern summer and northern winter (Fig. 4). In general, continuous eastward propagation of 250mb u-component anomalies predominates during northern summer (dashed lines in Fig. 4b denote regions of most prominent propagation) whereas more discontinuous eastward development of 250mb zonal wind anomalies predominates during northern winter (solid lines in Fig. 4a denote wind anomalies at a certain phase of a northern winter 28-72 day oscillation). In both seasons, the observed tropical/subtropical wind anomalies can be interpreted in terms of modeling results (e.g., Gill, 1980; Webster, 1972 and Anderson, 1984) which show downwind twin cyclones (and equatorial westerlies) and upstream twin anticyclones (and equatorial easterlies) as the stationary response to diabatic forcing in the tropics. However, the observed eastward propagation of 28-72 day oscillations has not been successfully modeled. The mechanisms leading to the higher latitude anomalies in Fig. 4a are also unclear but certainly involve an interaction between the subtropical/tropical anomalies and the higher latitude flow.

Having described some general characteristics of the 28-72 day OLR and 250mb zonal wind fluctuations during northern summer and northern winter, we now present a brief but more detailed description of the 28-72 day life cycle during northern winter. Fig. 5 shows the results of an ensemble cross-spectral analysis of OLR based on 9 northern winter seasons. A five point spatial average centered at EQ, 100°E was used as a basepoint time series. For purposes of this report, only the numbered, encircled regions are important; the details of the analysis are covered in WLK.

The numbered regions depict schematically the global evolution of 28-72 day OLR anomalies starting (arbitrarily) near EQ, 100°E (region 1) and moving consecutively from there to regions 2, 3, 4, and back to 1. The elapsed time between each number represents approximately 1/4 cycle or 7-18 days. The 4 - 1 - 2 - 3 sequence depicts the eastward propagation of OLR anomalies over the Indian Ocean and the western Pacific. The 2 - 3 - 4 sequence depicts a "jump" of OLR anomalies to the tropical Atlantic and South America which occurs after OLR anomalies develop near 160°W.

Figure 6 shows composite 250mb streamfunction anomalies which accompany the evolution of the OLR anomalies in Fig. 5. The composites were based on

mid-latitude circulation indices designed to emphasize the circulation features shown schematically in Fig. 4. The stippled (clear) regions which are enclosed by solid lines represent the negative (positive) OLR anomalies which accompany the composite streamfunction anomalies while the heavy solid lines with arrows represent schematic streamlines. The life cycle of 28-72 day atmospheric fluctuations can be described as follows:

I. With cloudiness (negative OLR anomaly) near EQ, 100°E (Fig. 6a), the dominant tropical/subtropical circulation anomalies consist of twin anticyclones (and equatorial easterlies) stretching from South America eastward to Indonesia and twin cyclones (and equatorial westerlies) stretching from Indonesia to near 140°W. The easterly anomalies north of the northern hemisphere subtropical cyclone are on the order of 10-15 m/s and imply a contracted east Asia jet. Simultaneously, an anomalous trough near western Canada supports a stronger mid-latitude westerly flow into the U.S. west coast.

II. As cloudiness shifts eastward to EQ, 140°E, twin anticylcones are still evident from near EQ, 0°E to Indonesia (Fig. 6b); however, the long fetch of equatorial easterlies has been interrupted (near EQ, 80°E) and the whole anticyclonic pattern appears in transition. The subtropical cyclones which were over the Pacific Ocean have nearly dissipated while a similiar subtropical cyclone pattern has developed over the Atlantic Ocean. This Atlantic anomaly pattern now suggests a contracted North America jet. In fact, at the intermediate time between Figs. 6a and 6b, (not shown), twin subtropical cyclones dominate from near the Asian coast to the Atlantic Ocean while twin subtropical anticyclones cover the remainder of the tropical belt. The mid-latitude zonal wind anomalies associated with these wavenumber-1-dominated subtropical cyclones and anticyclones suggest an eccentric 250mb circumpolar vortex over the northern hemisphere - contracted in regions of subtropical cyclones (and suppressed equatorial cloudiness) and expanded in regions of subtropical anticyclones (and enhanced equatorial cloudiness).

III. With cloudiness near 10°S, 160°W and clearing near 100°E (manifested as a northeastward shift by the South Pacific Convergence Zone), a complete reversal of circulation anomalies is observed (Fig. 6c). Twin subtropical cyclones (and equatorial westerlies) now extend from South America eastward to Indonesia while twin subtropical anticyclones (and equatorial easterlies) extend from Indonesia to 140°W. The mid-latitude westerly anomalies associated with the northern hemisphere anticyclone over the subtropical Pacific Ocean support a strong and extended EAJ with anomalous ridging downstream near 120°W. The details of this transition in the global circulation are relatively complex (i.e., eastward and northward propagation of existing anomaly patterns as well as development of new anomaly patterns are involved) and will be the subject of a future study.

IV. When cloudiness develops near 10°S, 160°W, negative OLR anomalies also start to develop east of South America and over Pakistan (Fig. 6c). Seven to ten days later these two regions of negative OLR anomaly have shifted to eastern South America and equatorial Africa (Fig. 6d). These OLR developments are accompanied by transition and breakdown of the twin subtropical cyclones (and equatorial westerly anomalies) over the Atlantic Ocean-Indian Ocean sector and

establishment of twin subtropical anticyclones over the Atlantic Ocean sector. The subtropical anticyclones which were previously located over the Pacific Ocean have again nearly dissipated. The intermediate time between Figs. 6c and 6d is again characterized by a strong wavenumber 1 pattern (not shown) with subtropical anticyclones from near the Asian coast to the Atlantic Ocean and twin subtropical cyclones over the remainder of the tropical belt. The mid-latitudes wind anomalies associated with these subtropical circulation features again suppport an eccentric 250mb circumpolar vortex although in this phase of 28-72 day oscillations the vortex is expanded toward the Pacific Ocean-North American-Atlantic Ocean sector.

I. To complete the 'life cycle,' the cloudiness over equatorial Africa consolidates over the western Indian Ocean, propagates to 100°E and we return to Fig. 6a.

In summary, some aspects of the global evolution of 28-72 day oscillations have been presented. Many questions remain regarding the details of the winter life cycle and characterization of 28-72 day life cycles during other seasons. The role of mid-latitude eddies and their interaction with the subtropical anticyclones and cyclones requires investigation. The dynamical mechanisms responsible for the slowly evolving circulation and OLR anomaly patterns are also not understood. These will be areas of future study.

Figures

Figure 1. Nine-year mean OLR during a) November - April and b) May - October. Contour interval is 10 Watts/m^2 and contour labels have been divided by 10.

Figure 2. Nine-year mean OLR variance in the 28-72 day period range during a) November - April and b) May - October. Contour interval is see text.

Figure 3. Ten-year mean 250mb winds (isotachs and arrows) during a) November - April and b) May - October. Isotach contour interval is 10m/s and contour labels have been divided by 10.

Figure 4. Ten-year mean 250mb u-component variance in the 28-72 day period range during a) November - April and b) May - October. Contour interval is a) $10(m/s)^2$ by 10 and b) $8(m/s)^2$. The contour labels on 4a have been divided by 10.

Figure 5. OLR cross-spectral results valid for November-April for basepoint centered at EQ, 100°E. The individual phase arrows portray coherence-squared and phase information in the 28-72 day band. The length of the phase arrow is proportional to the statistical significance associated with the coherence-squared. Every latitude point and every other longitude point having a significance level of at least 80% is plotted; these are the smallest arrows. Gridpoints having significance levels of greater than 99% are marked with a dot on the shaft of the phase arrow. The arrow direction denotes phase relative to the basepoint time series. An arrow pointing north (south) signifies an in-phase (out-of-phase) relationship between the gridpoint and the basepoint. Clockwise rotation (CCW) of the arrow means that the gridpoint lags (leads) the basepoint. A sequence of phase arrows which rotate clockwise when viewed from west to east (south to north) define the regions of eastward (northward) propagation. See text.

Figure 6. Aspects of the life cycle of the 28-72 day atmospheric oscillation during northern winter. Time runs from a to b to c to d to a. The individual panels represent composites of anomalous streamfunction for: a) negative PAC index, b) negative ATL index, c) positive PAC index and d) positive ATL index. The contour interval is 2.0×10^7 m^2/sec; intermediate contours in the vicinity of Africa are dashed. Solid lines on a-d enclose regions of anomalous enhanced (stippled) or suppressed (clear) cloudiness. The heavy solid lines with arrows are schematic streamlines while the H's and L's represent anticyclonic and cyclonic circulation centers respectively. The dots represent points which passed a two-sided t-test at the 95% level (Chervin and Schneider, 1976).

References

Anderson, J.R. and R.D. Rosen, 1983: The latitude height structure of 40-50 day variations in atmospheric angular momentum. J. Atmos. Sci., 40, 1584-1591.

Anderson, J.R., 1984: personal communication.

Chervin, R.M., and S.H. Schneider, 1976: On determining the statistical significance of climate experiments with general circulation models. J. Atmos. Sci., 33, 405-412.

Knutson, Thomas R., 1984: Global scale intraseasonal Oscillations of outgoing longwave radiation and 250mb zonal wind during Northern Hemisphere summer. Master's Thesis, Department of Meteorology, University of Wisconsin-Madison, 129 pp.

Krishnamurti, T.N. and D. Subrahmanyam, 1982: The 30-50 day mode at 850mb during MONEX. J. Atmos. Sci., 39, 2088-2095.

Lau, K.M. and P.H. Chan, 1983a: Short-term climate variability and atmospheric teleconnections from satellite-observed outgoing longwave radiation. Part I: Simultaneous relationships. J. Atmos. Sci., 40, 2735-2750.

Lorenc, A.C., 1984: The evolution of planetary-scale 200mb divergent flow during the FGGE year. Quart. J. Royal Meteor. Soc., 110, 427-441.

Madden, R.A. and P.R. Julian, 1971: Detection of a 40-50 day oscillation in the zonal wind in the tropical Pacific. J. Atmos. Sci., 28, 702-708.

Madden, R.A. and P.R. Julian, 1972: Description of global scale circulation cells in the tropics with a 40-50 day period. J. Atmos. Sci., 29, 1109-1123.

Murakami, T., T. Nakazawa, and J. He, 1983: 40-50 day oscillations during the 1979 northern hemisphere summer. Dept. of Meteor., Univ. Hawaii, (UHMET 83-02), 133 pp.

Quah, L.-C., 1984: On the 30-50 day oscillation during the 1978-79 northern winter. J. Meteor. Soc. Japan, 62, 261-272.

Sikka, D.R. and S. Gadgil, 1980: On the maximum cloud zone and the ITCZ over Indian longitudes during the South West monsoon. Mon. Wea. Rev., 108, 1840-1853.

Yasunari, T., 1980: A quasi-stationary appearance of 30 to 40 day period in the cloudiness fluctuations during the summer monsoon over India. J. Meteor. Soc. Japan, 58, 225-229.

Yasunari, T., 1981: Structure of an Indian summer monsoon system with a period around 40 days. J. Meteor. Soc. Japan, 59, 336-354.

Weickmann, K. M., 1982: Intraseasonal fluctuations in near global-scale modes of circulation and outgoing longwave radiation during northern hemisphere winter. Ph.D. thesis, Department of Meteorology, University of Wisconsin-Madison, 107 pp.

Weickmann, K.M., 1983: Intraseasonal circulation and outgoing longwave radiation modes during northern hemisphere winter. Mon. Wea. Rev., 111, 1838-1858.

Weickmann, K. M. and J. E. Kutzbach, 1981: Low frequency circulation modes as revealed by eigenvector analysis of the 250 mb and 850 mb wind fields, Proceedings of the Fifth Climate Diagnostics Workshop (J.S. Winston, ed.), Univ. of Washington, Seattle, Oct. 22-24, 1980, 384-391.

Weickmann, Klaus M. and J.E. Kutzbach, 1982: The major circulation shift of February 1981 as revealed by real-time monitoring of windfield eigenvectors. Proc. Sixth Annual Climate Diagnostics Workshop (J.S. Winston, ed.), Lamont-Doherty Geological Observatory, Columbia University, Oct. 14-16, 1981, pp. 87-94.

Weickmann, Klaus M. and J.E. Kutzbach, (1983). Global circulation and radiation modes during 1982 compared to previous seven years. Proc. Seventh Annual Climate Diagnostics Workshop, NCAR, Boulder, CO., Oct. 18-22, 1982, pp. 13-23.

Weickmann, K.M., G.R. Lussky, and J.E. Kutzbach, 1985: A global-scale analysis of intraseasonal fluctuations of outgoing longwave radiation and 250mb streamfunction during northern winter. (accepted Mon. Wea. Rev.)

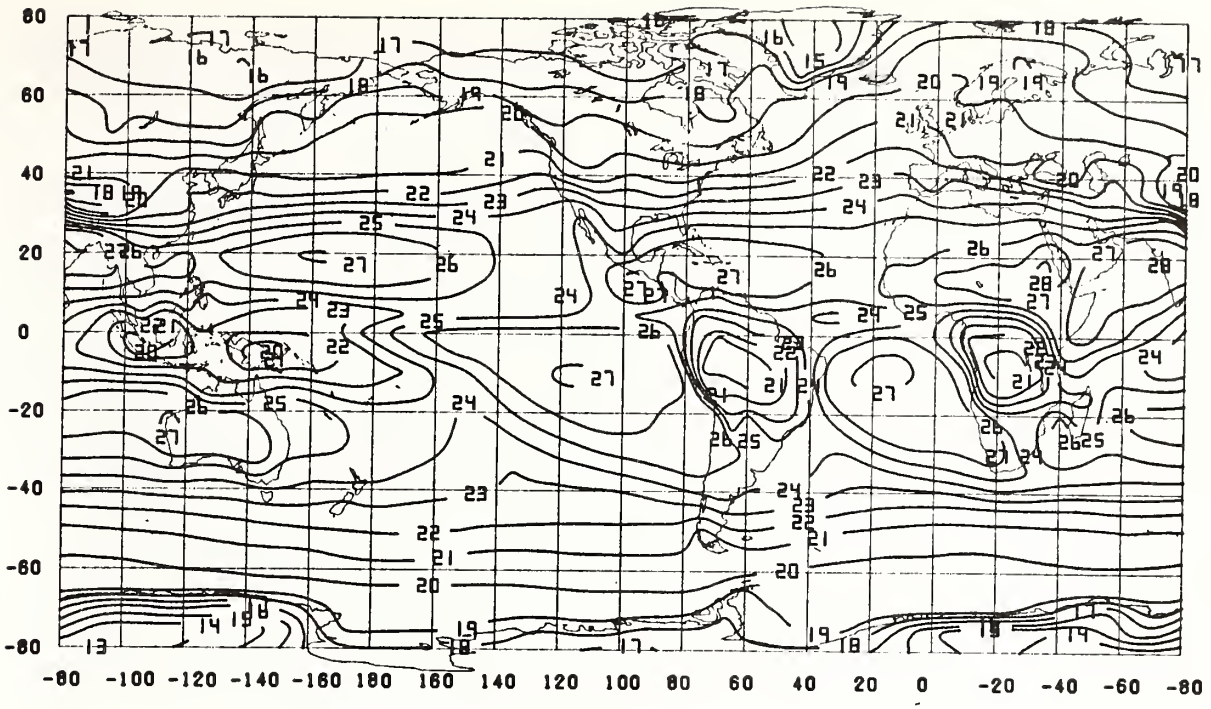
80
60
40
20
0
-20
-40
-60
-80
-80 -100 -120 -140 -160 180 160 140 120 100 80 60 40 20 0 -20 -40 -60 -80

a

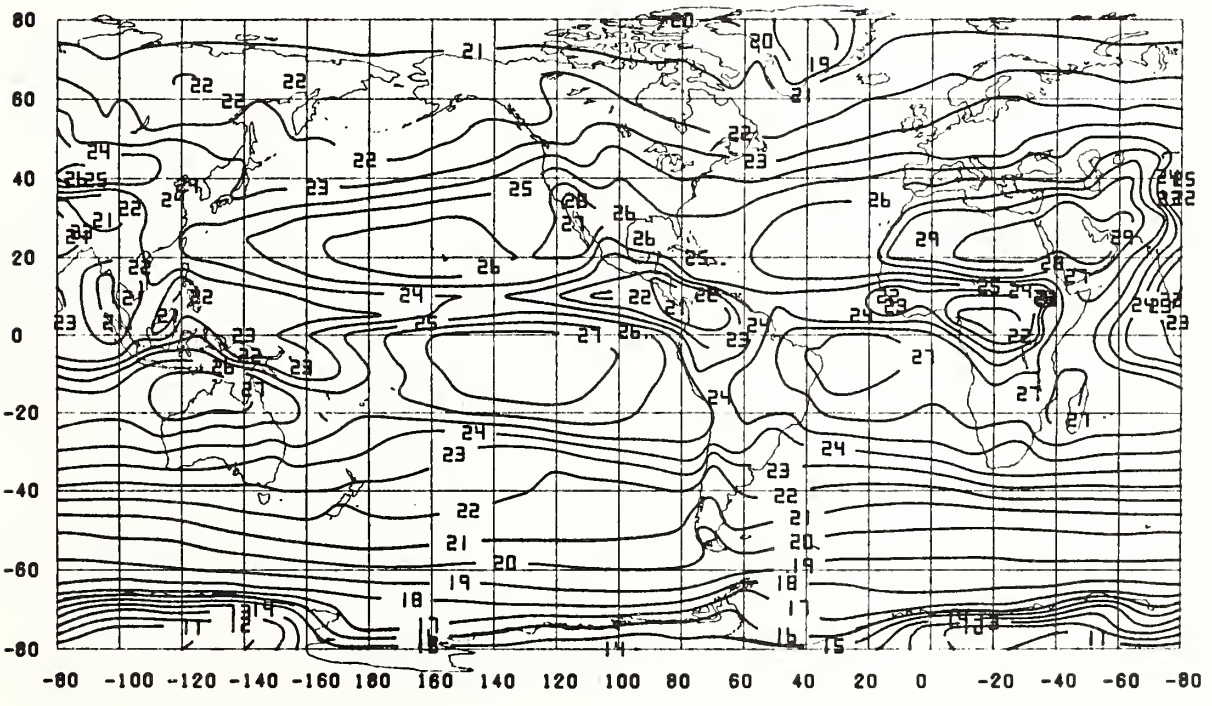
80
60
40
20
0
-20
-40
-60
-80
-80 -100 -120 -140 -160 180 160 140 120 100 80 60 40 20 0 -20 -40 -60 -80

b

1

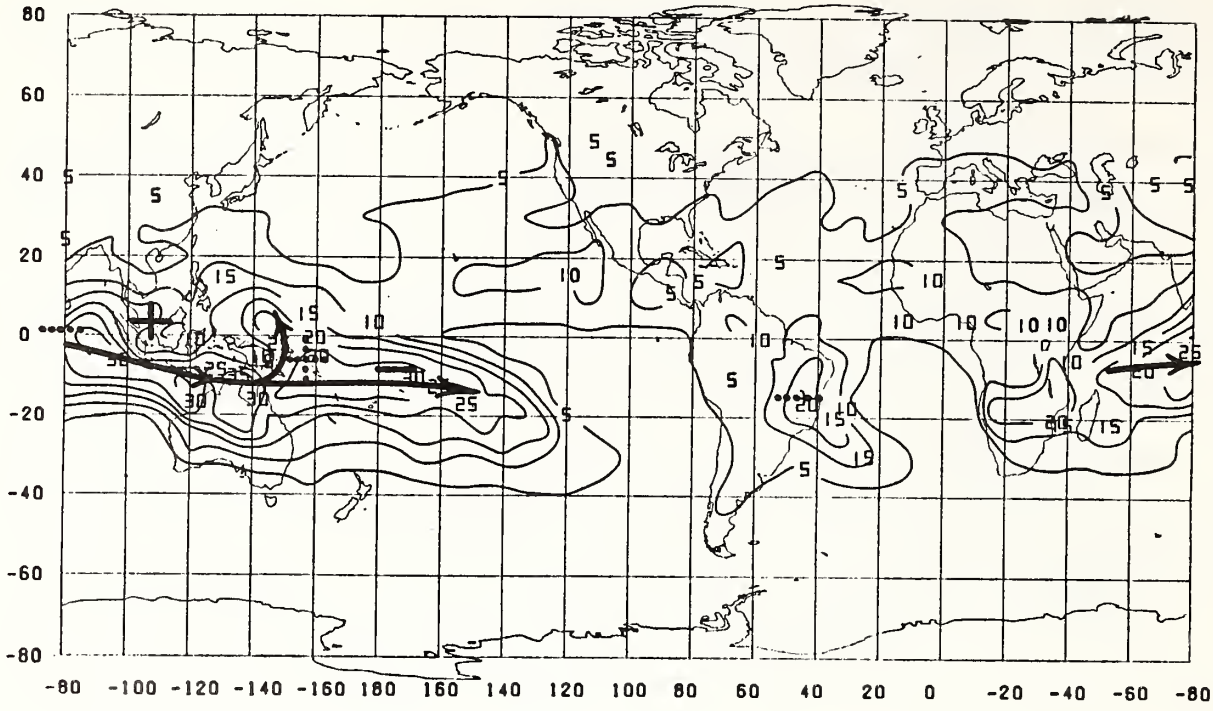
80
60
40
20
0
-20
-40
-60
-80
-80 -100 -120 -140 -160 180 160 140 120 100 80 60 40 20 0 -20 -40 -60 -80

a

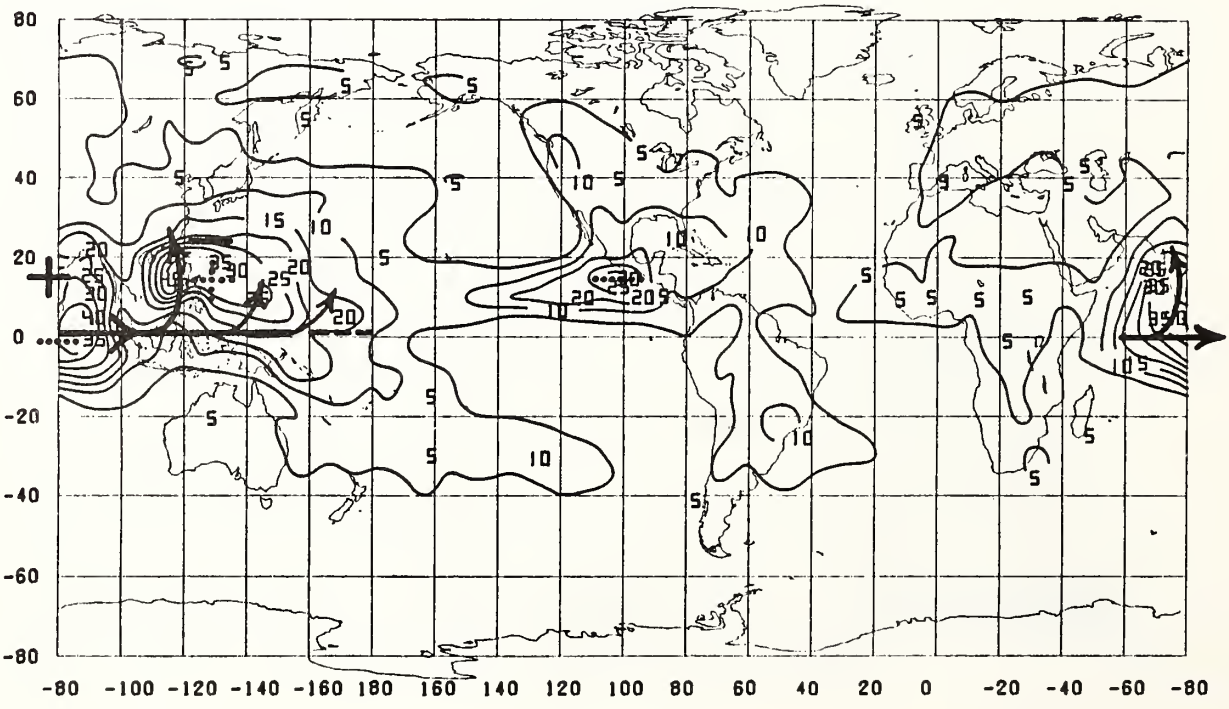
80
60
40
20
0
-20
-40
-60
-80
-80 -100 -120 -140 -160 180 160 140 120 100 80 60 40 20 0 -20 -40 -60 -80

b

2

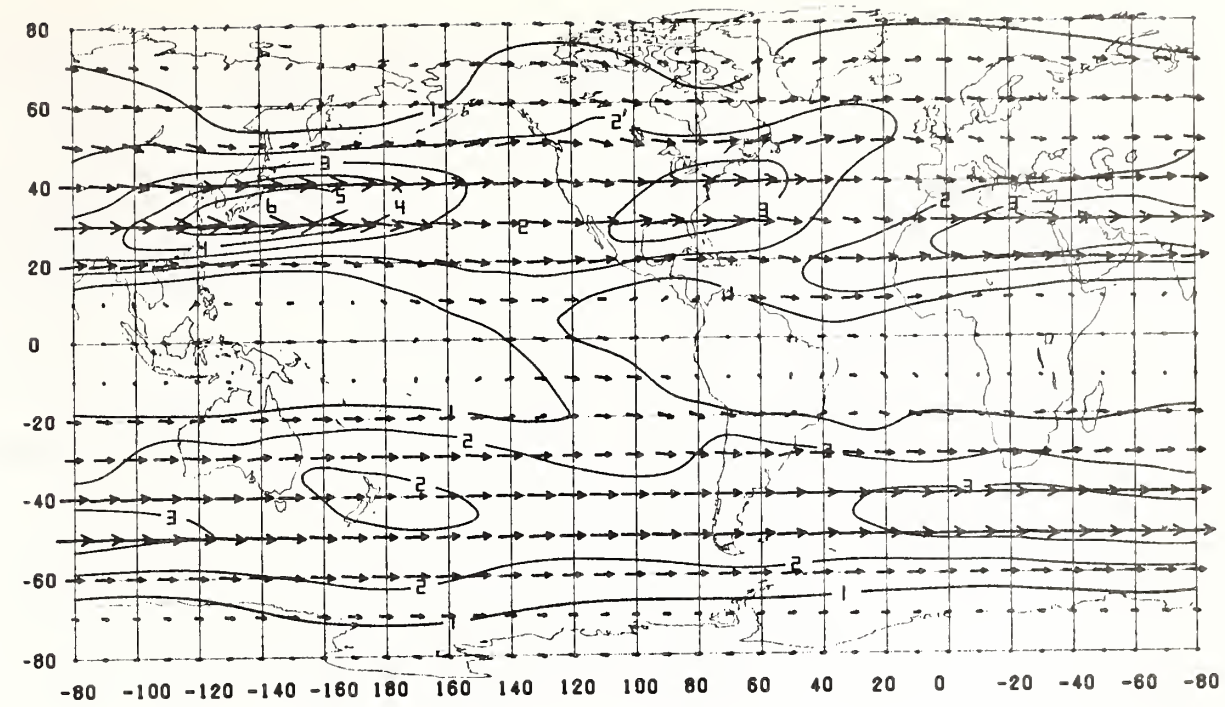
80
60
40
20
0
-20
-40
-60
-80
-80 -100 -120 -140 -160 180 160 140 120 100 80 60 40 20 0 -20 -40 -60 -80

a

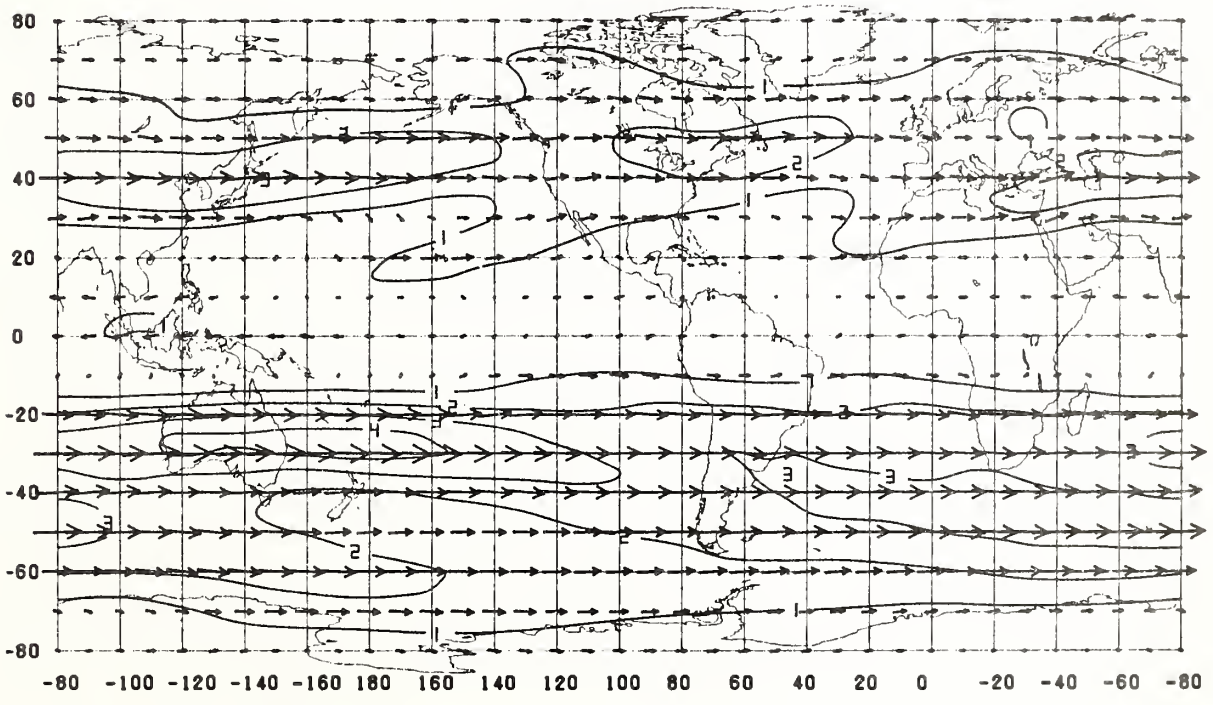
80
60
40
20
0
-20
-40
-60
-80
-80 -100 -120 -140 -160 180 160 140 120 100 80 60 40 20 0 -20 -40 -60 -80

b

3

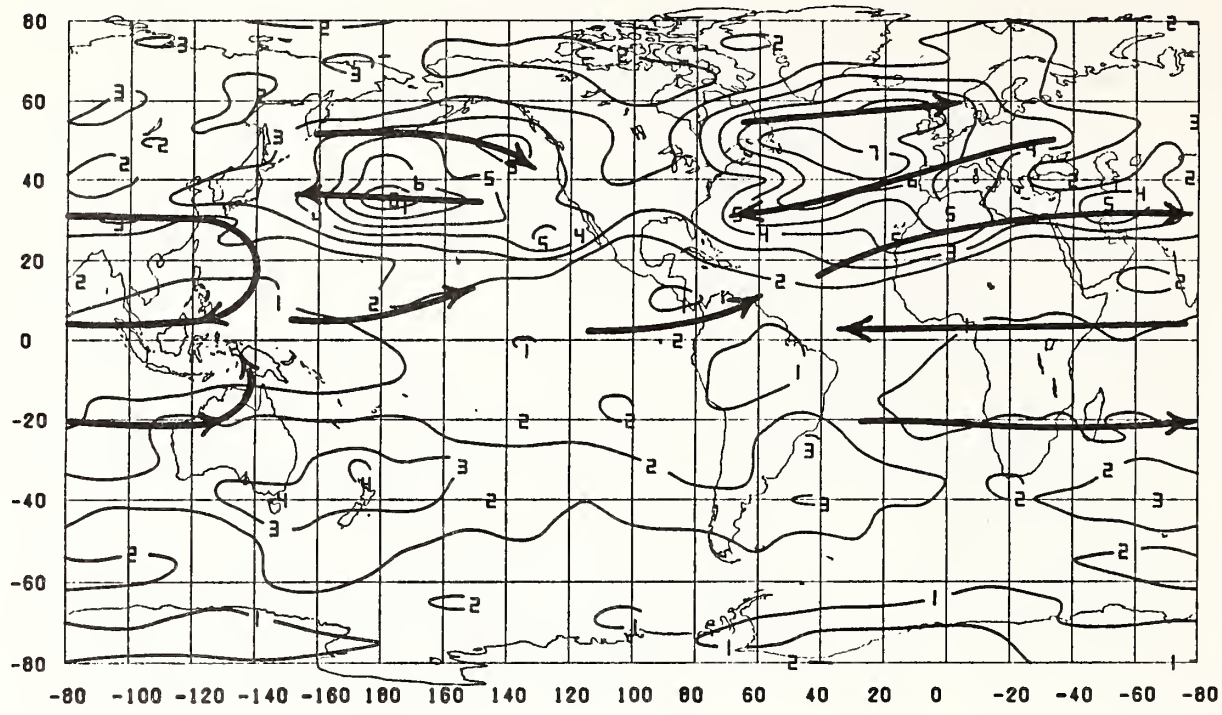
80
60
40
20
0
-20
-40
-60
-80
-80 -100 -120 -140 -160 180 160 140 120 100 80 60 40 20 0 -20 -40 -60 -80

a

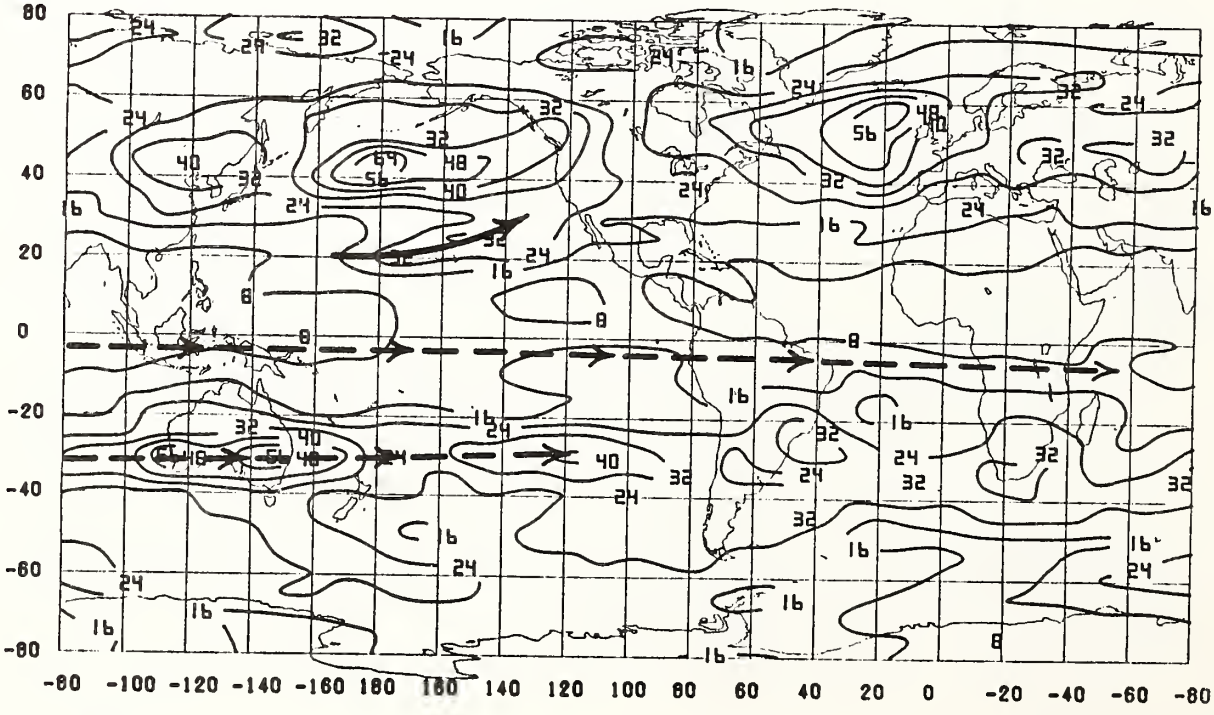
80
60
40
20
0
-20
-40
-60
-80
-80 -100 -120 -140 -160 180 160 140 120 100 80 60 40 20 0 -20 -40 -60 -80

b

4

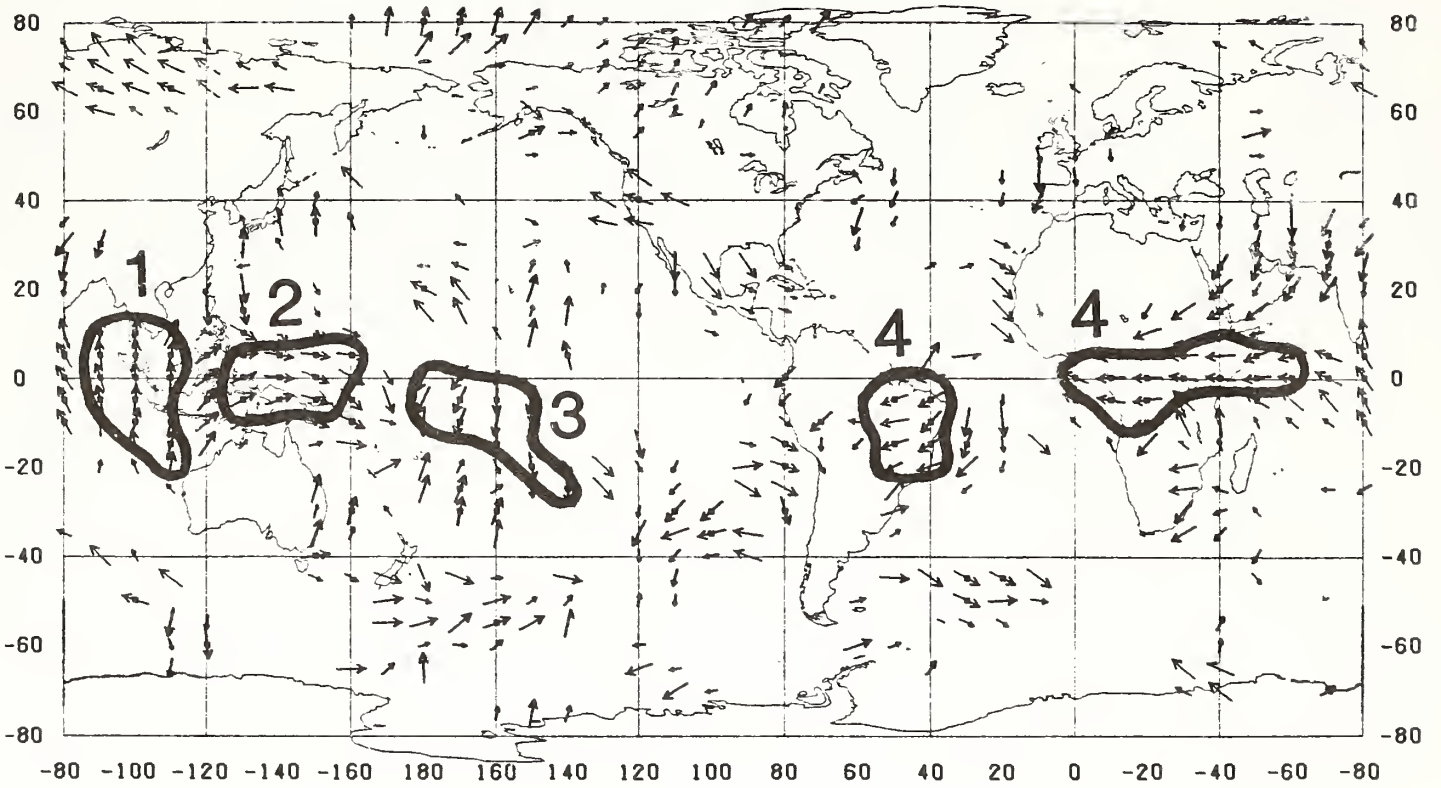
80
60
40
20
0
-20
-40
-60
-80
-80 -100 -120 -140 -160 180 160 140 120 100 80 60 40 20 0 -20 -40 -60 -80
1
2
3
4
4

5

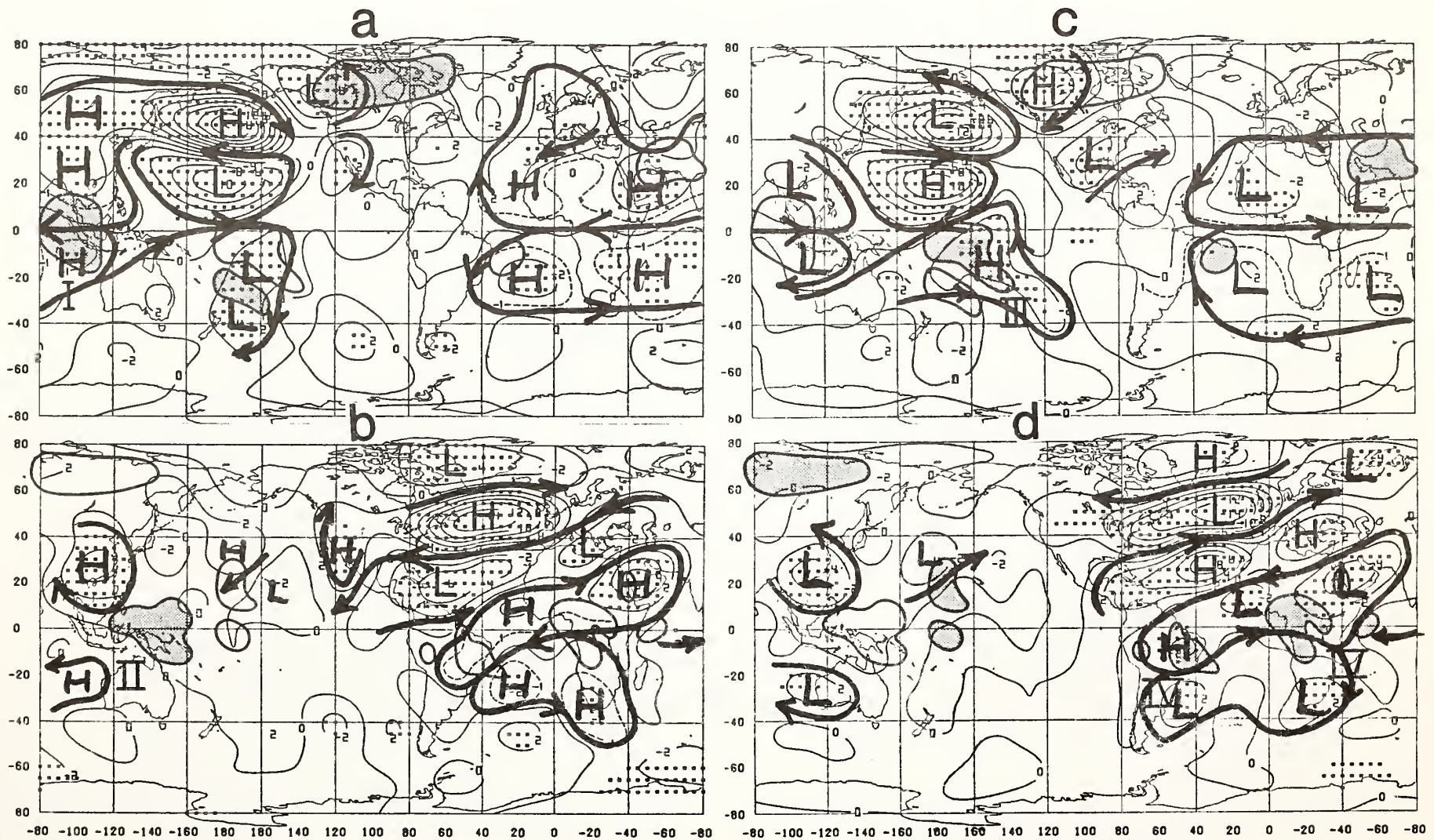
a
c
b
d
I
II
III
IV
80
60
40
20
0
-20
-40
-60
-80
-80 -100 -120 -140 -160 180 160 140 120 100 80 60 40 20 0 -20 -40 -60 -80

The Distribution of Rainfall along the Coast of Northern Peru during 1982-83

J. D. Horel and A. Cornejo-Garrido
Climate Research Group
Scripps Institution of Oceanography
La Jolla, CA 92093

Torrential rainfall and severe flooding along the normally arid coast of northern Peru caused considerable hardship to the inhabitants of that region during 1983. Although past episodes of intense convection in this region have been linked to the El Nino phenomenon, the mechanisms responsible for the changes in the regional atmospheric circulation have yet to be adequately explained. We have obtained rainfall and surface wind observations from a network of roughly 50 stations in northern Peru, in addition to gridded data sets available in the United States. We present here preliminary results on the conditions along the west coast of South America during the 1982-83 El Nino epsiode.

Convection near the coast of northern Peru was most intense during April 1983. Fig. 1a shows the distribution of outgoing infrared radiation (IR) over the eastern Pacific and South America during April 1983. A region of low IR (frequent convection) extends along the coasts of Ecuador and northern Peru. Convection was greatest during the night near the coast while offshore, convection was more frequent during the day (Fig. 1b).

The distribution of rainfall between $3^{o}S$ and $6^{o}S$ during April 1983 is shown in Fig. 2. The largest rainfall totals were found in the coastal plain with several stations recording totals in excess of 900 mm. Fig. 3 shows the distribution of rainfall as a function of longitude. The rainfall totals at stations at the higher elevations were near normal during 1983. From January to February 1983, the largest rainfall amounts were observed in the foothills of the Andes while after February 1983, the greatest rainfall totals were found closer to the coast.

Sea surface temperatures (SSTs) along the west coast of South America were unusually high during 1983. Fig. 4 shows the time evolution of surface equivalent potential temperature (θ_e) and rainfall during 1982-83 at selected coastal stations. The evolution of θ_e along the coast is nearly identical to that of SST (not shown). However, the presence of a warm, moist boundary layer is a necessary but not sufficient condition for convection to take place near the coast of South America; the strong static stability of the surface layer in this region must also be overcome. For example at Lobos de Afuera, large rainfall amounts were observed only during April 1983, even though the boundary layer had been unusually warm for several months prior to April.

Our preliminary analyses of the distribution of daily rainfall, IR, and surface wind suggest that the mechanisms responsible for the convective activity before mid-March 1983 differed from those for the period after mid-March. During the earlier period, distinct episodes of convection were evident and many of these could be related to outbreaks of convection in the Amazon Basin which were advected across the Andes Mountains by the prevailing easterly winds. For example, the nighttime IR maps for February 1-3, 1983 in Fig. 5 show the northwestward progression of a region of intense convection from the Amazon basin to the west coast. The prevailing upper level wind circulation on February 2 is shown in Fig. 6; note that the 200 mb wind flow is southeasterly across the Andes Mountains. In contrast, convection occurred nearly continuously along the coast from mid-March to early June 1983. The convection was strongly modulated by the diurnal cycle (Fig. 1b) and on many occasions the convection appeared to form along the coast and then move offshore.

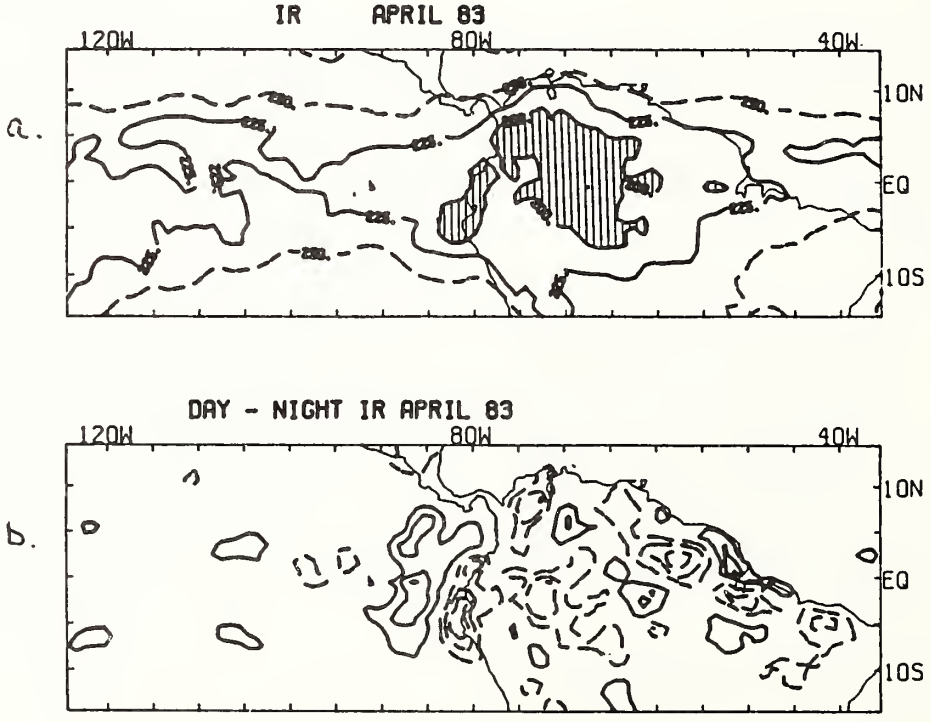

Fig. 1. Outgoing infrared radiation (IR) during April 1983. a.) average of the day (1430 LST) and night (230 LST) values. The contour interval is 25 watts/m•m; solid (dashed) contours represent values less than or equal to (greater than) 225 watts/m•m. Regions with IR values less than 200 watts/m•m are shaded. b.) average difference between the day and night values. The contour interval is 12.5 watts/m•m: solid (dashed) contours indicate maximum convection during the day (night). The Earth Radiation Budget data was interpolated from the NMC polar stereographic grid to a 1 x 1 latitude-longitude grid.

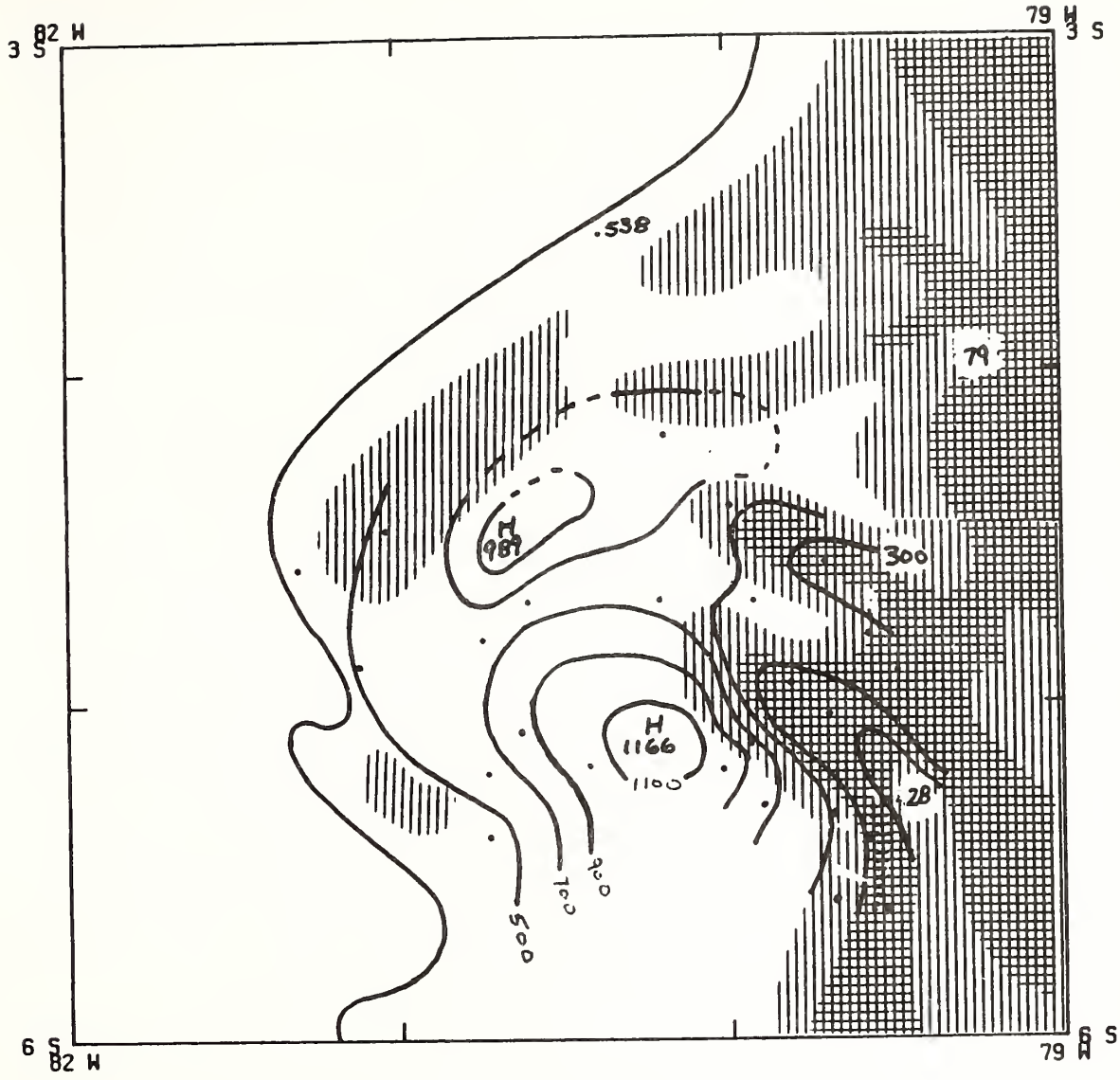

Fig. 2. Monthly total rainfall (in millimeters) at stations in northern Peru for April 1983. The contour interval is 200 mm. Station locations are indicated by dots. Topography is indicated by shading: vertical lines denote heights in excess of 300 m while hatching indicates heights in excess of 2000 m.

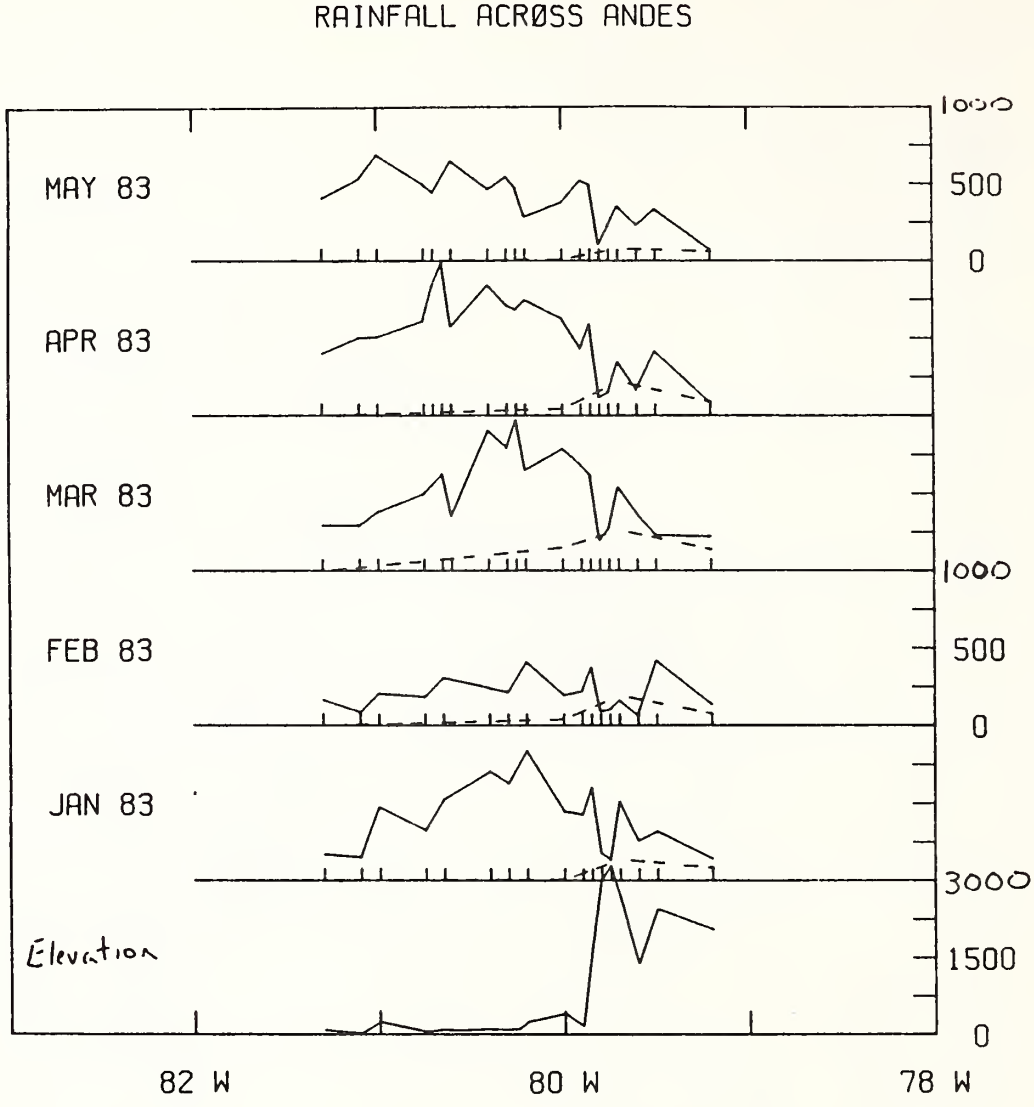

Fig. 3. Monthly total rainfall (solid line; in millimeters) at stations between 4° and 5°S from January to May 1983 as a function of longitude. The median rainfall is indicated by the dashed line. The longitudes of the stations are denoted by small tic marks. The elevations (in meters) of the stations are shown on the lowest curve.

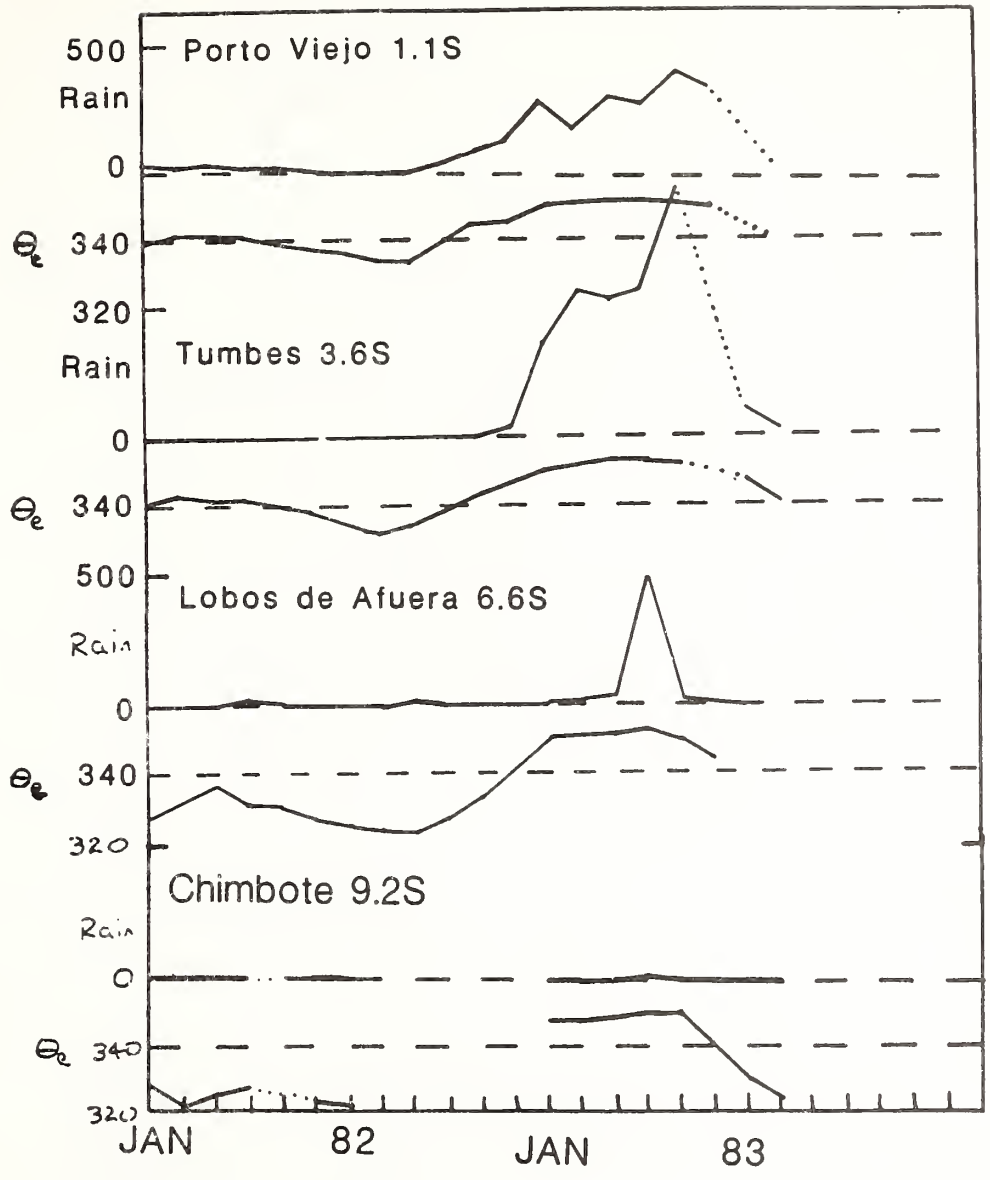

Fig. 4. Monthly total rainfall (in millimters) and surface equivalent potential temperature, θ_e, (in °C) at selected stations along the coast. Dashed lines indicate linear interpolation across a missing value.

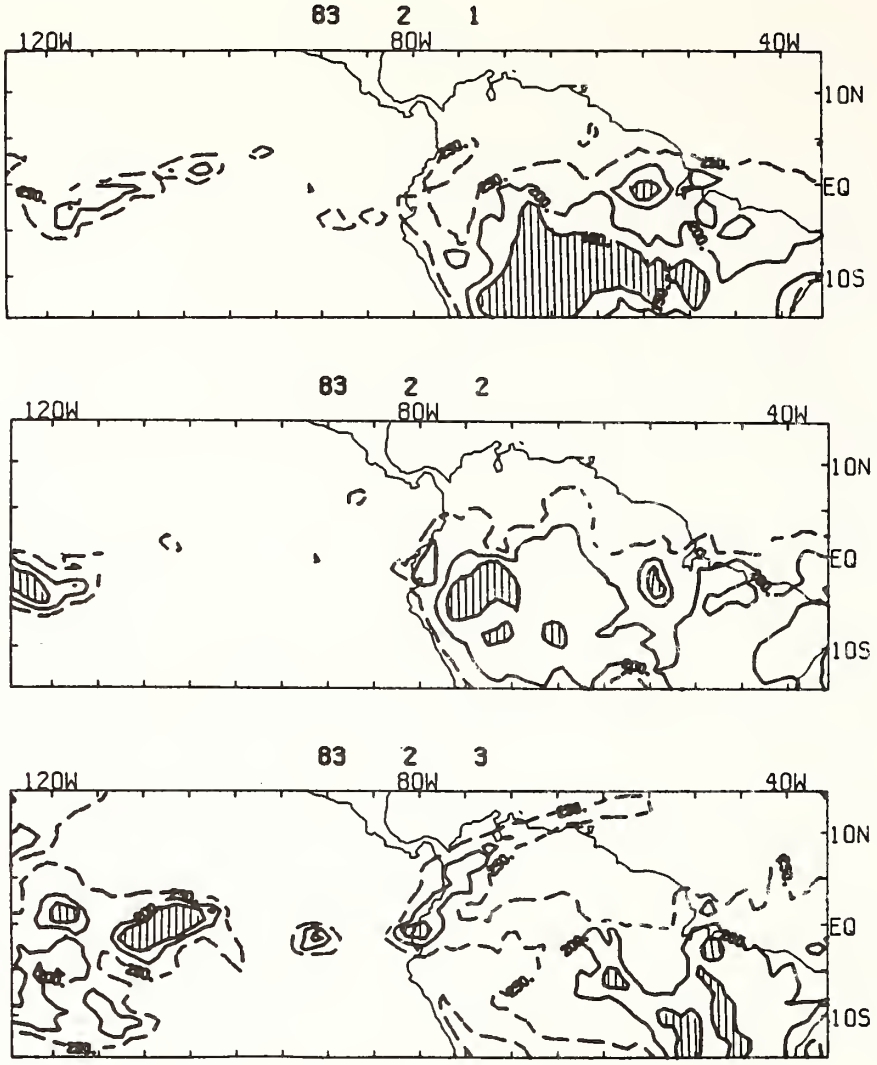

Fig. 5. IR at night (230 LST) for February 1-3, 1983. The contour interval is 50 watts/m*m; solid (dashed) contours indicate values less than or equal to (greater than) 200 watts/m*m. Regions with values less than 150 watts/m*m are shaded.

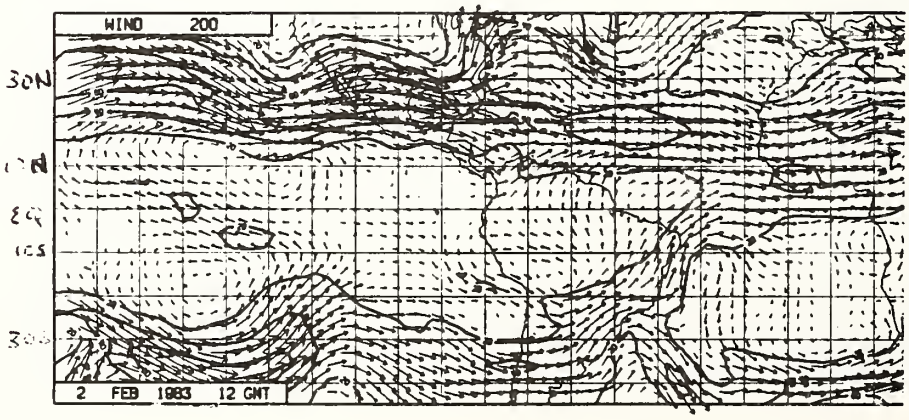

Fig. 6. 200 mb vector winds for 1200 GMT, February 2, 1983. From the European Center for Medium-range Weather Forecasting analysis.

Peru Coastal Winds During 1982-1983

D.B. Enfield and P.A. Newberger
College of Oceanography
Oregon State University
Corvallis, OR 97331

As part of the NOAA EPOCS (Equatorial Pacific Ocean Climate Studies) program we have been compiling and processing meteorological data from synoptic weather stations along the Peru coast since early 1982. Taken over a multi-year period, this kind of data can provide valuable information -- e.g., on coastal wind variability -- at a variety of time scales ranging from diurnal to interannual. This paper concerns synoptic data on winds from seven coastal stations from northern and central Peru, from 1 January 1981 to the last quarter of 1983 (Figure 1). To isolate synoptic and longer time scale variability from the diurnal signal, the basic data were smoothed with a low-low pass (LLP) filter having a half-amplitude at 40 hours and decimated to six-hourly values. A second set of time series was formed by further smoothing the LLP data with a very low pass (VLP) filter having half-amplitude at 30 days. The LLP variability is shown in the following figures as vector sticks, while both the LLP and VLP time series are shown in plots of the alongshore wind component.

Comparison of the 1982-1983 data with the 1981 data and with the results of previous studies (Enfield, 1981a,b,c) reveals that 1982 was normal and 1983 was anomalous (Figures 2 and 3). In 1981-1982 the LLP winds remained steady in the upwelling favorable sense, with monthly computed directional stabilities of 90% or more (Figure 4). Though significant inter-daily variability normally occurs, it only results in reversals (northerlies) at Callao, where monthly mean winds are rather low throughout much of the year. The general characteristics of the low frequency (VLP) variability were also normal in 1982 (Figure 3). For example, the Talara winds were strong, ranging from 5 to 9 m/sec and having their annual minimum in February-March (see Enfield, 1981a,b). The southernmost stations (Chimbote and Callao) have their annual minimum winds during the austral winter months, essentially out of phase with the offshore trades and with the northernmost stations (Enfield, 1981b). Notice that there is little indication of anomalous activity in the winds during the last quarter of 1982, even though El Niño conditions had already begun within the adjacent ocean environment.

In 1983, the anomalous conditions associated with the El Niño were most obvious at Talara and Paita, where unusual northerly events began in late January and continued into June (Figures 5 and 6) and the directional steadiness decreased significantly (Figure 4). The most abnormal month was April, with a near-zero mean at Talara and relatively weak winds at all stations north of Chimbote. Careful examination reveals that individual events are coherent over these five northern stations. The six-month period was also characterized by anomalous rainfall north of Chimbote, with the greatest amounts being registered at the northernmost stations (Horel and Cornejo-Garrido, 1984). At Callao the winds became unusually strong and stable in the upwelling favorable sense, in agreement with Enfield (1981a), and northerly events did not occur there.

How far south did the anomalous synoptic events penetrate in 1983? From Figures 2 and 3 it appears that Chimbote and Callao were not affected, but from the more detailed plot in Figure 5 it is clear that the Lobos wind was frequently weak in March and April, the most anomalous period. The 25-day period expanded in Figure 6 for January and February is particularly interesting because two oceanographic cruises were conducted then. The times that the research vessels Humboldt and Wecoma were near the coastal stations are shaded in Figure 6 and the geographic distributions of wind vectors for the two cruises are shown in Figures 7 and 8. In both cases the winds off Talara and Paita were clearly weak and variable. Also, in both cases the ships arrived near Lobos several days later, by which time the winds at that station had returned to normal. Prior to that, they had undergone a brief weakening at the same times the ships were off Talara and Paita. It appears that the winds south of Lobos and Chiclayo were not anomalously weak in 1983, while the strongest anomalies occurred in the region of the Sechura Desert (Talara, Paita and Piura), in agreement with Horel and Cornejo-Garrido (1984).

This is the first opportunity we've had to analyze the winds from Lobos Island, a station that has only been operating for a few years. Unlike the other stations, Lobos undergoes periods of several weeks at a time in which the mean wind is significantly stronger and synoptic scale variability is more energetic. During these periods maximum daily winds of gale force are frequently reported, called "rafagas" by the Peruvians. The Lobos data is also interesting because, although isolated northerly events did reach that far south in 1983, the mean (VLP) winds were generally stronger in that year than

in 1982 (Figure 3). This is consistent with the impressions of Peruvian and U.S. oceanographers, who encountered generally windier conditions along most of the Peru coast during this El Niño episode, and with the results of Enfield (1981a,c), who has studied monthly data over a 20 year period that included four other ENSO episodes.

We wish to acknowledge our counterpart institution in Peru, the Direccion de Hidrografia y Navegacion de la Marina (DHNM), which has cooperated with us throughout the EPOCS program and has provided the data for Paita, Lobos and Callao. We also thank the Corporacion Peruana de Aviacion Civil (CORPAC), which provided the data for all other stations.

References

Enfield, D.B. (1981a): Thermally driven wind variability in the atmospheric boundary layer above Lima, Peru. J. Geophys. Res.. 86, 2005-2016.

Enfield, D.B. (1981b): Annual and nonseasonal variability of monthly low-level wind fields over the southeastern tropical Pacific. Mon. Wea. Rev., 109, 2177-2190.

Enfield, D.B. (1981c): El Niño: Pacific eastern boundary response to interannual forcing. In: Resource Management and Environmental Uncertainty: Lessons from Coastal Upwelling Fisheries, M.H. Glantz and J.D. Thompson, Eds., Wiley and Sons, Interscience, New York, 213-2544.

Horel, J.D. and A. Cornejo-Garrido (1984): Evolution of meteorological conditions along the northwest coast of South America during 1982-83. Tropical Ocean-Atmosphere Newsletter, No. 23, 16-17.

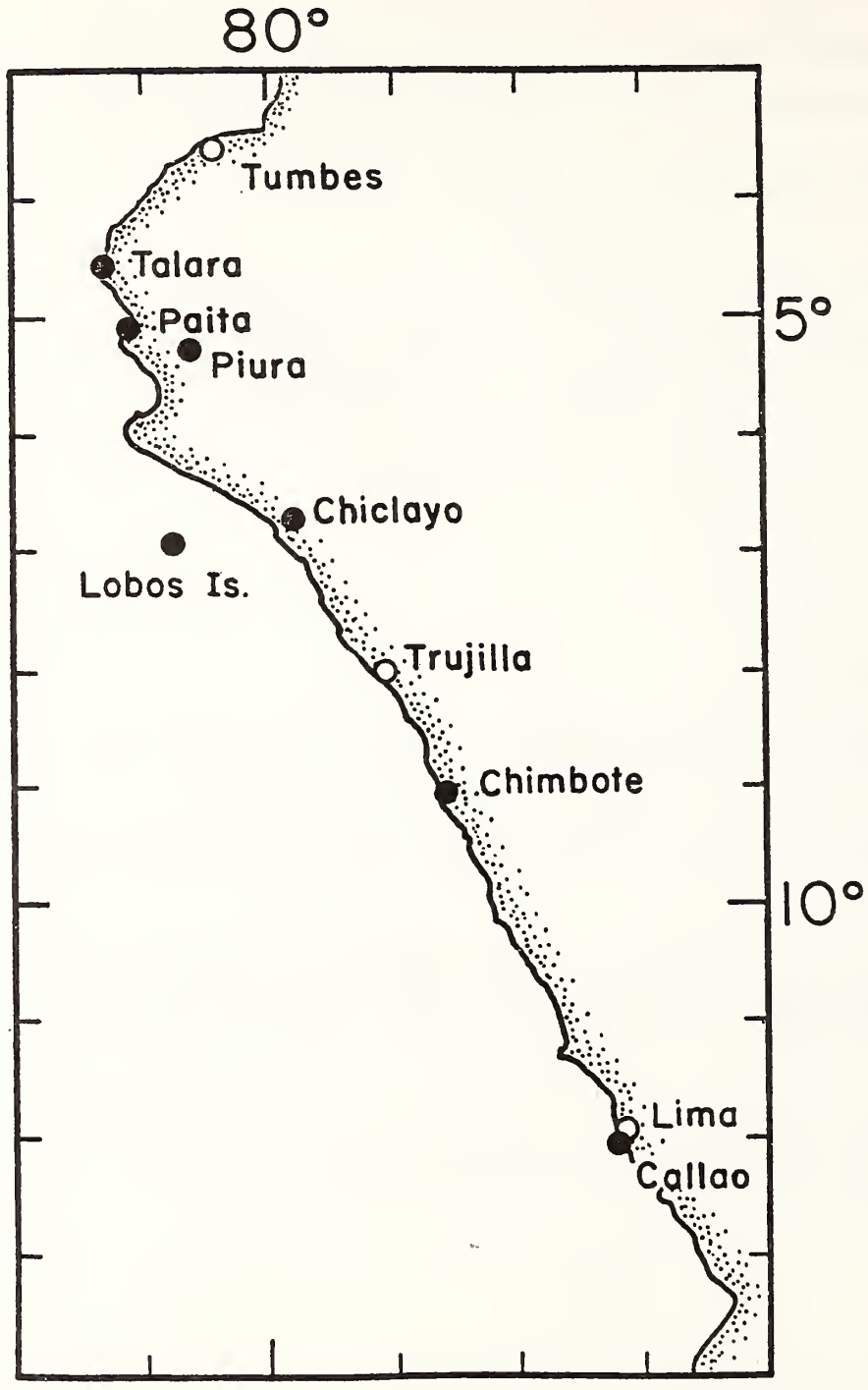

Figure 1. Location map showing the geographical distribution of stations. Solid circles indicate stations for which we have processed meteorological data for 1981-83 and open circles indicate other meteorological stations for which we will process data by a later date (open circles).

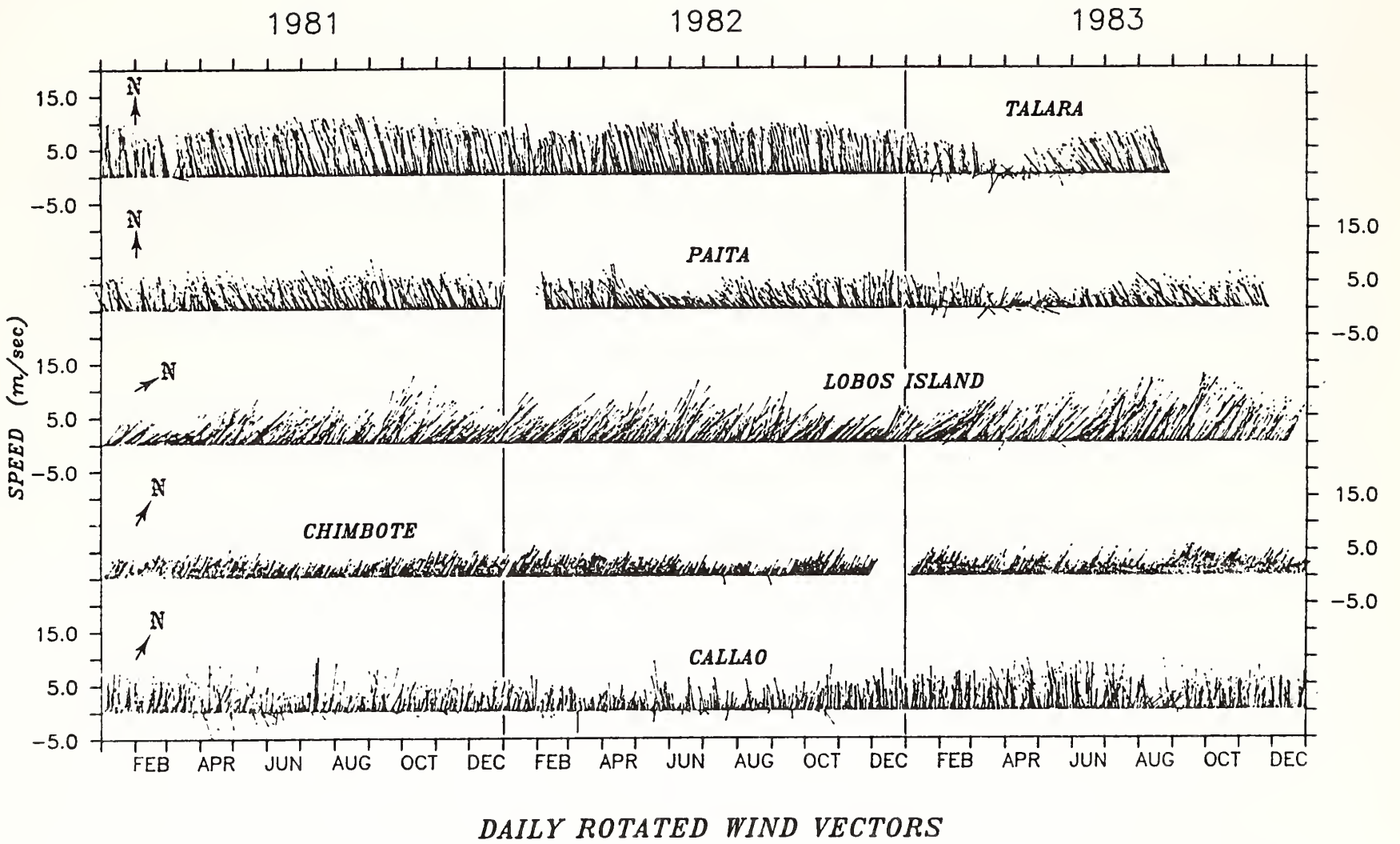

Figure 2. Daily vector sticks of filtered (LLP) wind data from five coastal stations in northern and central Peru. In each case, the alongshore direction is oriented upward and the ordinate provides a scale against which vector length may be related to speed.

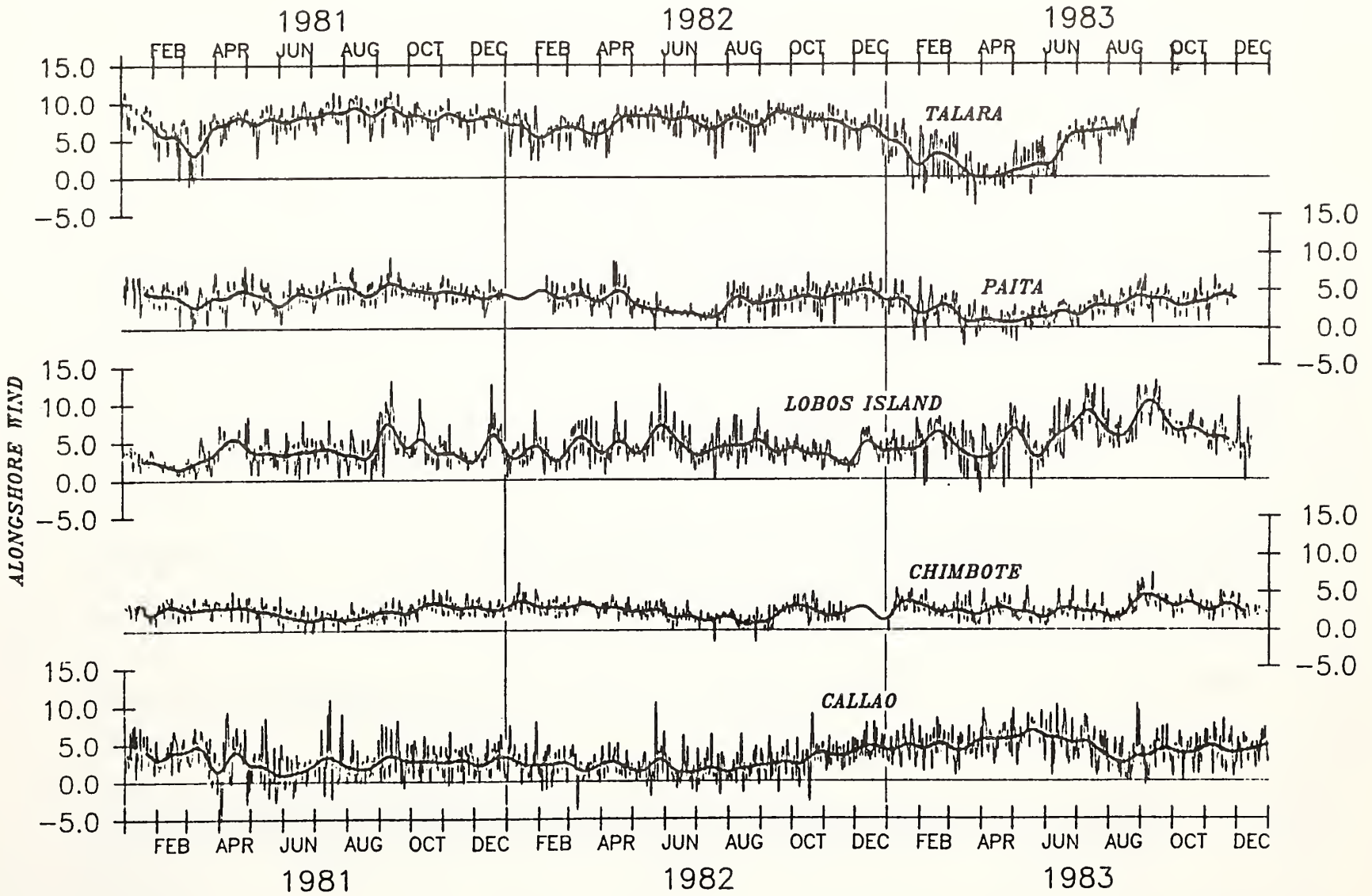

Figure 3. Time series of the filtered (LLP and VLP) alongshore wind component at five coastal stations in northern and central Peru. Characteristics of the LLP and VLP filters are described in the text.

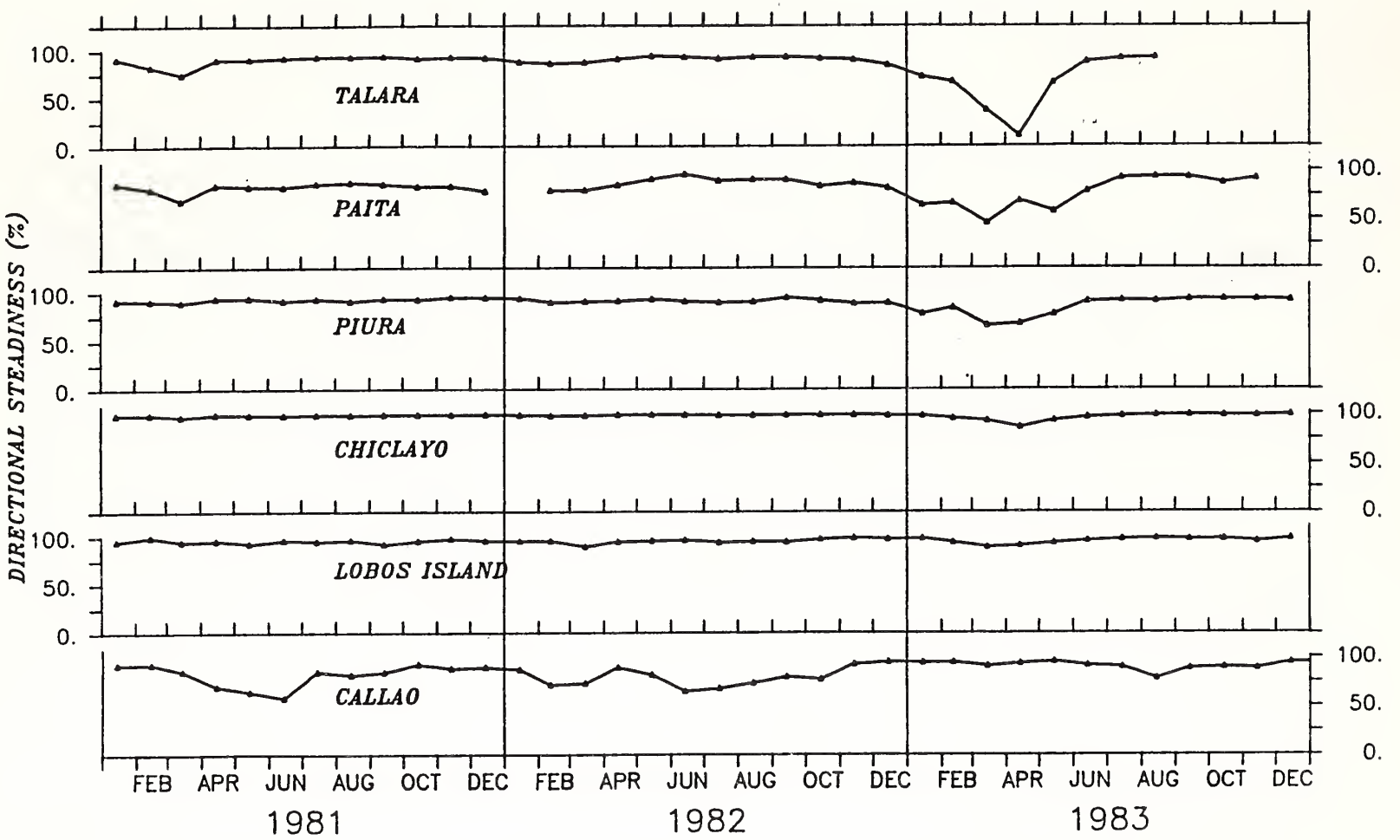

Figure 4. Monthly values of the directional steadiness, computed as the ratio of the vector averaged speed to the scalar averaged speed and expressed in percent.

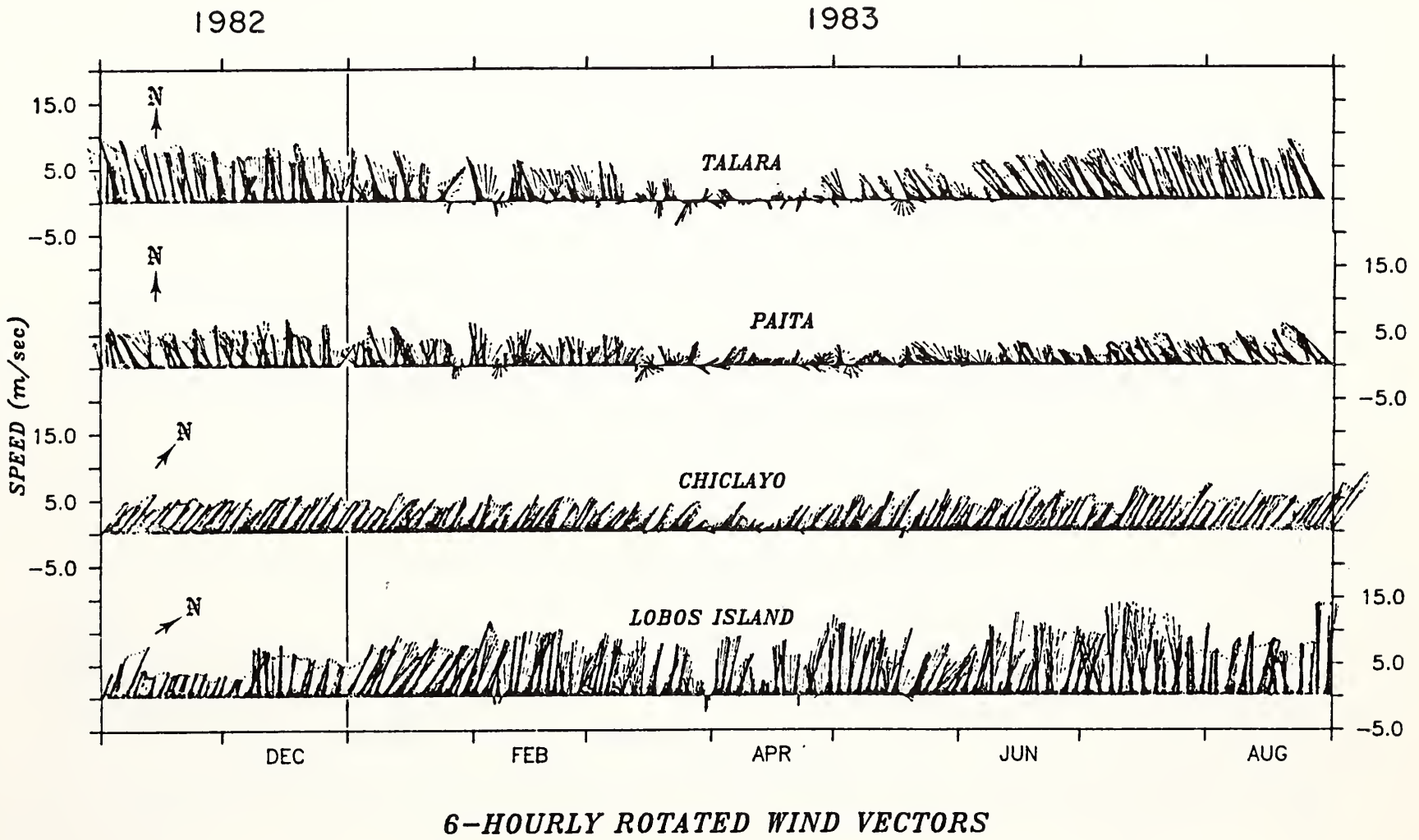

Figure 5. Six-hourly vector sticks of filtered (LLP) wind data from four stations, with the alongshore direction oriented upward as in Figure 2.

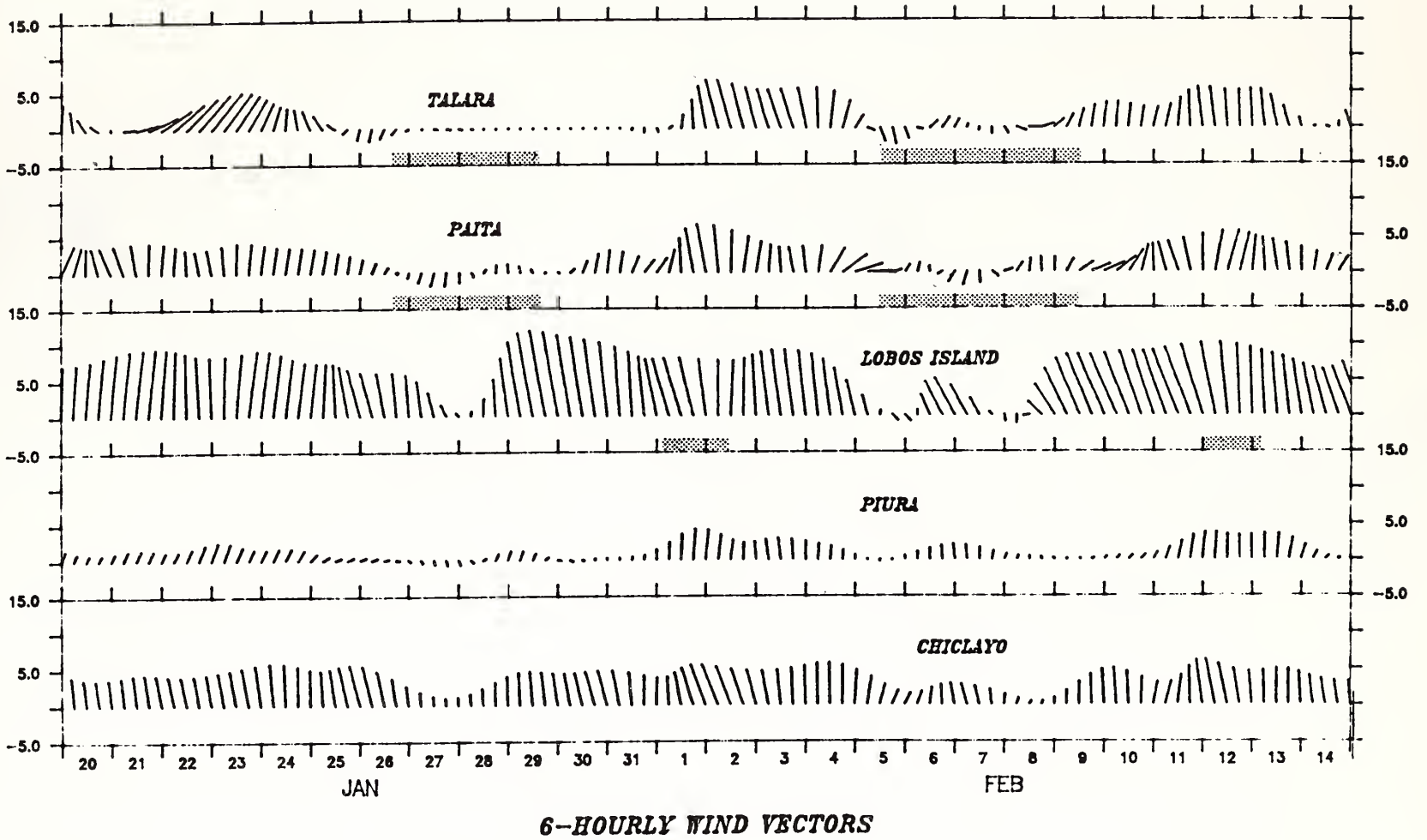

Figure 6. As in Figure 5, but expanded for a 25-day period in January-February 1983. Shaded along the time axes for Talara, Paita and Lobos are the periods during which the R/V Humboldt and R/V Wecoma operated near these stations.

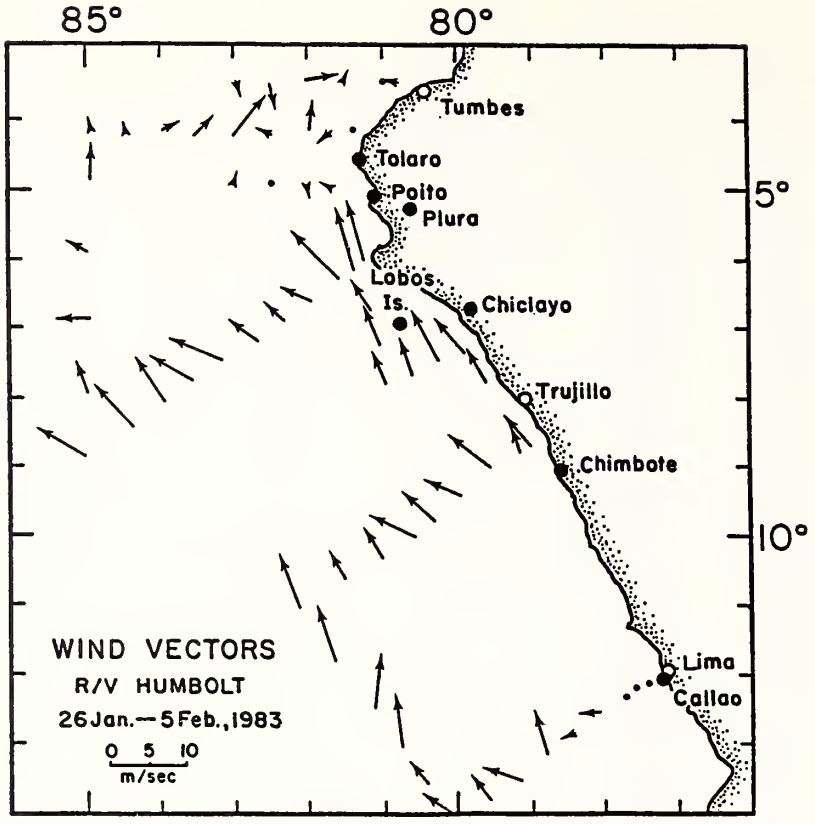

Figure 7. Vector plots of surface wind observations during the cruise of the R/V Humboldt.

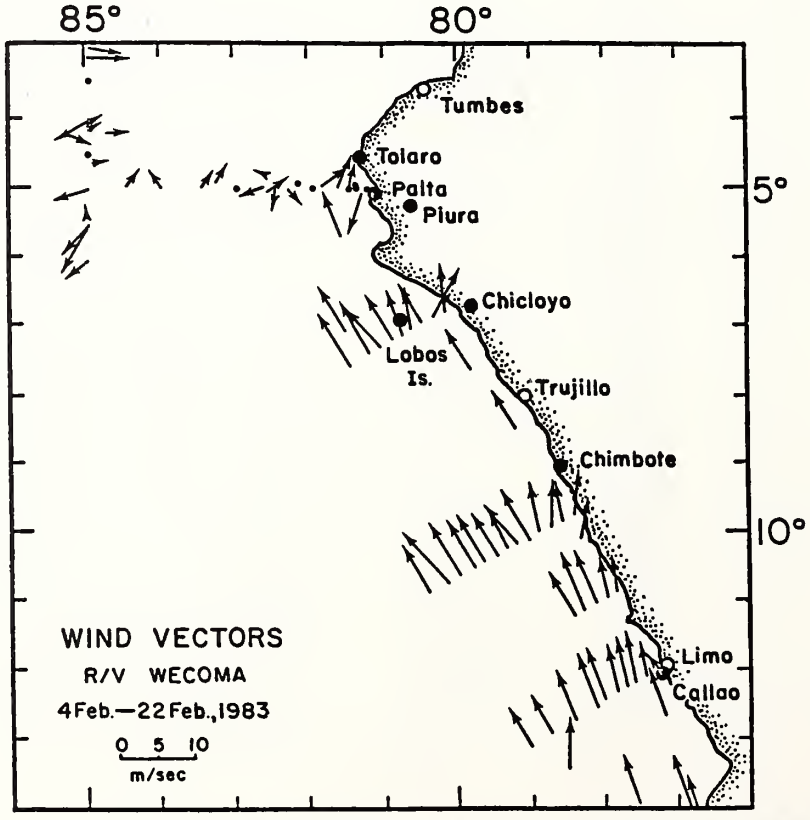

Figure 8. Vector plots of surface wind observations during the cruise of the R/V Wecoma.

Climatic Events of the West Coast of Southern Africa

Sharon Nicholson and Dara Entekhabi
Clark University
Geography Department
Worcester MA 01610

The cold Benguela current off the west coast of Southern Africa flows adjacent to an extensive strip of coastal desert much like the Peruvian-Atacama desert of South America. In the latter region the el Nino phenomenon and the associated augmentation of rainfall is well known. Along the Southern African coast, an el-Nino like recurrent appearance of warm-water was described early in the century by German colonalists in Swakopmund and Walvisbai. Suggestions have been made that the warm water is here also coupled with increased coastal rainfall and possibly with the Southern Oscillation as well. The research described here tests that idea by using time series analysis and multi-year composites to examine the relationship between rainfall, SSTs and the Southern Oscillation. The data base consists of monthly SST data for 1948 to 1972 for the Marsden squares shown in Fig. 1 and derived from the TDF-11 data set, monthly rainfall data for the coastal stations indicated and for 84 regions covering the entire continent. The length of the rainfall records varies considerably, but most coastal stations have data for at least the period 1948 to 1972 and the regional series generally commence around 1901 and extend to 1973.

The fluctuations of sea-surface temperatures during the analysis period are similar in all three coastal sectors; the coincidence of warm-water years in all three sectors is particularly striking. A combined series for the three sectors (Fig. 2) also suggests a tendency for warm-water years to coincide with low index years of the Southern Oscillation (Tahiti - Darwin, normalized). One noteable exception is 1953, a Pacific el-Nino episode and low index year; it was one of the coldest years in the southeast Atlantic. Although the latter half of 1965 was exceptionally cold, extreme warming in 1964/65 paralleled the abrupt change from high to low SOI. Two more recent ENSO events, 1976 and 1982, were also warm-water years along the Benguela coast.

The distribution of rainfall as a function of month and latitude is compared for warm-water and cold-water years. In all cases, rainfall is enhanced in warm-water years (Fig. 3) in all months of the wet season, but especially so in March and April, the months of highest SSTs. Similarly, rainfall is consistently reduced in cold-water years (Fig. 4). Here, the exception proves the rule; 1965 was originally classified as a cold-water year because of the extreme anomalies at the end of the year. The period of warming early in 1965 was one of markedly enhanced rainfall, but the latter half of the years was virtually rainless. The differences between warm-water and cold-water years are more striking when rainfall along the coast is plotted for the two composites (Fig. 5); in some cases, several hundred mm/mo in warm-water years, compared with 20 to 50 mm/mo in cold-water years, with the greatest differences occurring in March. It is interesting to note that the persistence of rainfall anomalies in those months (as measured by month-to-month correlation coefficients) is remarkably high, as it is also between the Dec/Jan/Feb/Mar season and the Apr/May season (Figs. 6 and 7). This suggests the influence of slowly-varying boundary forcing, such as SSTs.

Spectral analysis is used to determine the relationship between SSTs along the Benguela coast, coastal rainfall and the Southern Oscillation. The spectrum of the SOI (Fig. 8), derived using the Blackman-Tukey method, shows that the maximum variability is concentrated at 5 to 6 years, but peaks are also evident at about 3.6 and 2.3 years; spectral peaks in these periods are common in rainfall series throughout the African continent. The SST series for the sector 10-20° S also peaks at 5 to 6 years and some semblance of that peak is also evident in the other two areas, but closer to the equator the maximum spectral energy is concentrated between about 2.3 and 3.6 years. The 9-month peak which is evident in the northern-most SST sector was shown by Fowland to occur throughout much of the Atlantic. The coherence square between the SOI and the SSTs is high for the two southern-most sectors in the range of 2 to 6 years, suggesting a close relationship between these two parameters (Fig. 9).

Peaks at 5 to 6 years are common in the regional rainfall series in the northern part of the analysis region (Fig. 10). In the more southern regions (Fig. 11), where the 5 to 6 year peak in SSTs is considerably weaker, the regional rainfall spectra are dominated by higher frequency peaks on the order of 2 to 4 years. The co-spectra of rainfall and SSTs have not yet been derived, but the co-spectra of rainfall and the SOI and the coherence square (derived in a preliminary analysis) suggest a strong relationship between the two in the northern areas of the analysis sector.

In conclusion, the results of this study suggest that a clear association exists between sea-surface temperatures and rainfall along the Benguela coast of southern Africa. Strong similarities exist between the spectra of SSTs, the Southern Oscillation Index and rainfall (at least in the northern sectors), with peaks at about 5 to 6 years being common. A preliminary look at coherence estimates suggests that a strong association between the SOI and SSTs in the analysis sector and between the SOI and rainfall in the coastal regions. The details of the linkages and the causal relationships remain to be established.

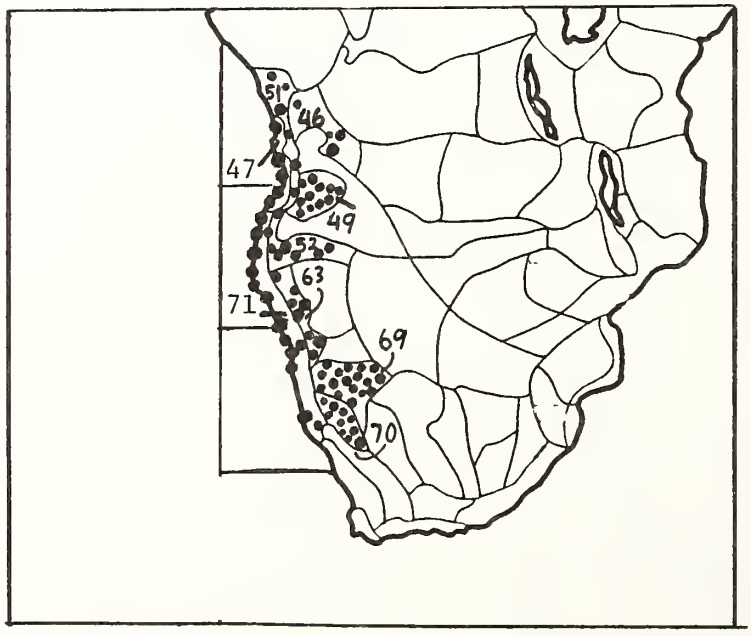

Fig. 1. Location of SST Analysis Sectors, Rainfall Stations, and Rainfall Regions in Southern-Hemisphere Africa (numbered regions are shown in Figs. 10 and 11).

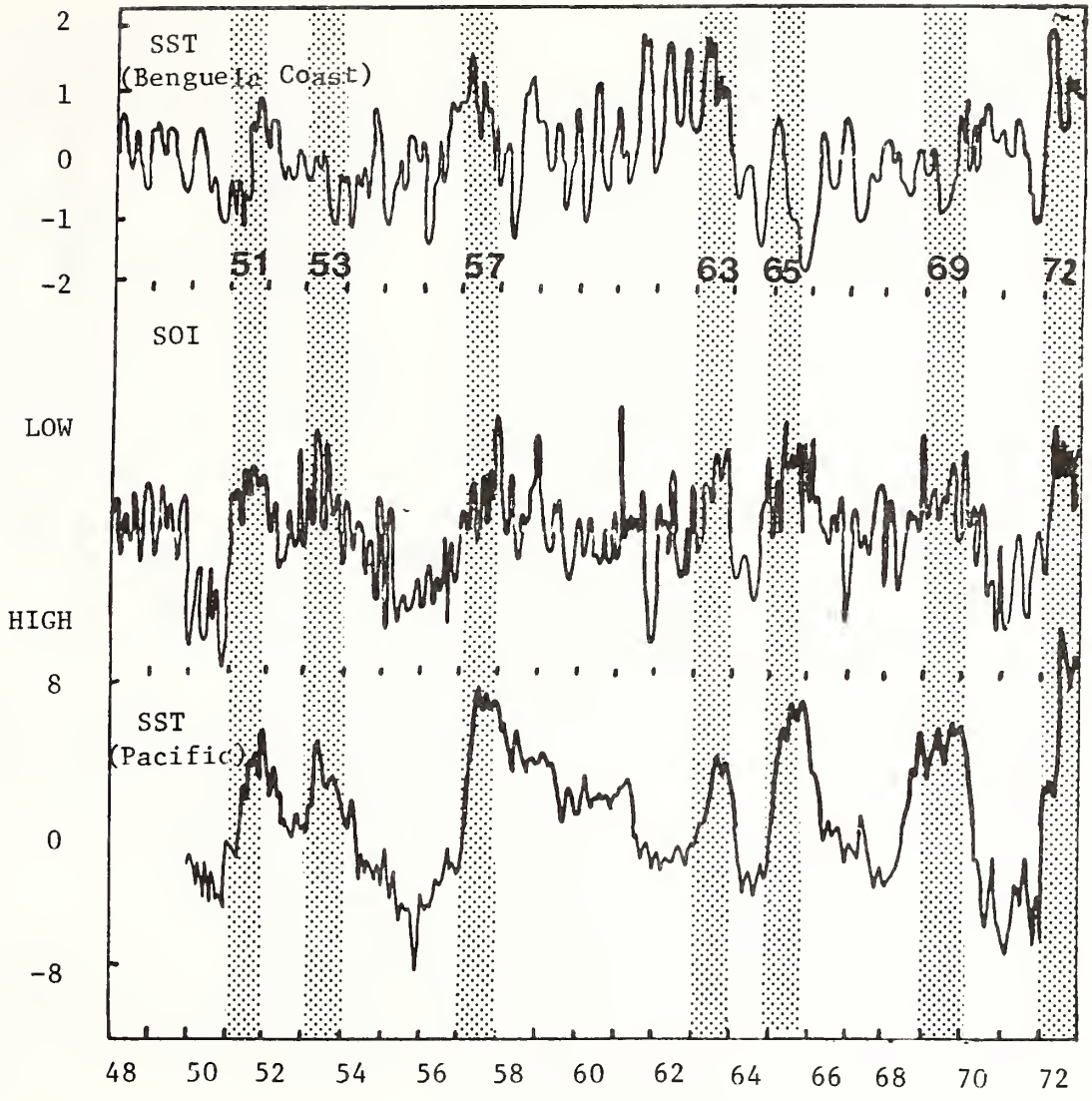

Fig. 2. The Southern Oscillation Index (Tahiti-Darwin Surface Pressure) Compared to Sea-Surface Temperatures in the Pacific and in the Atlantic along the Benguela Coast. Temperature Departures in ^{o}C; Shading Indicates Years of Pacific El Nino Events. Atlantic Temperatures, 0^{o} S to 30^{o} S, 3-Month Averages.

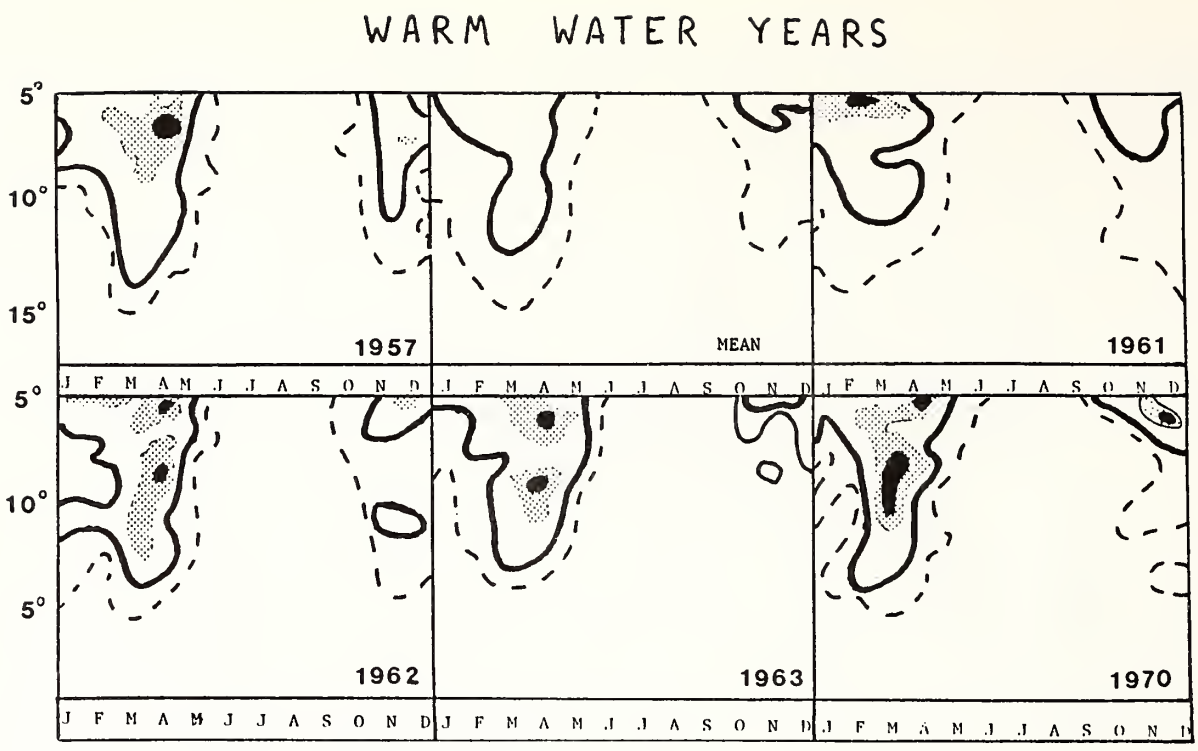

Fig. 3. Rainfall (mm/mo) along the Benguela Coast as a Function of Latitude and Month during Warm Water Years along the Coast

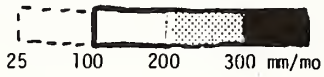

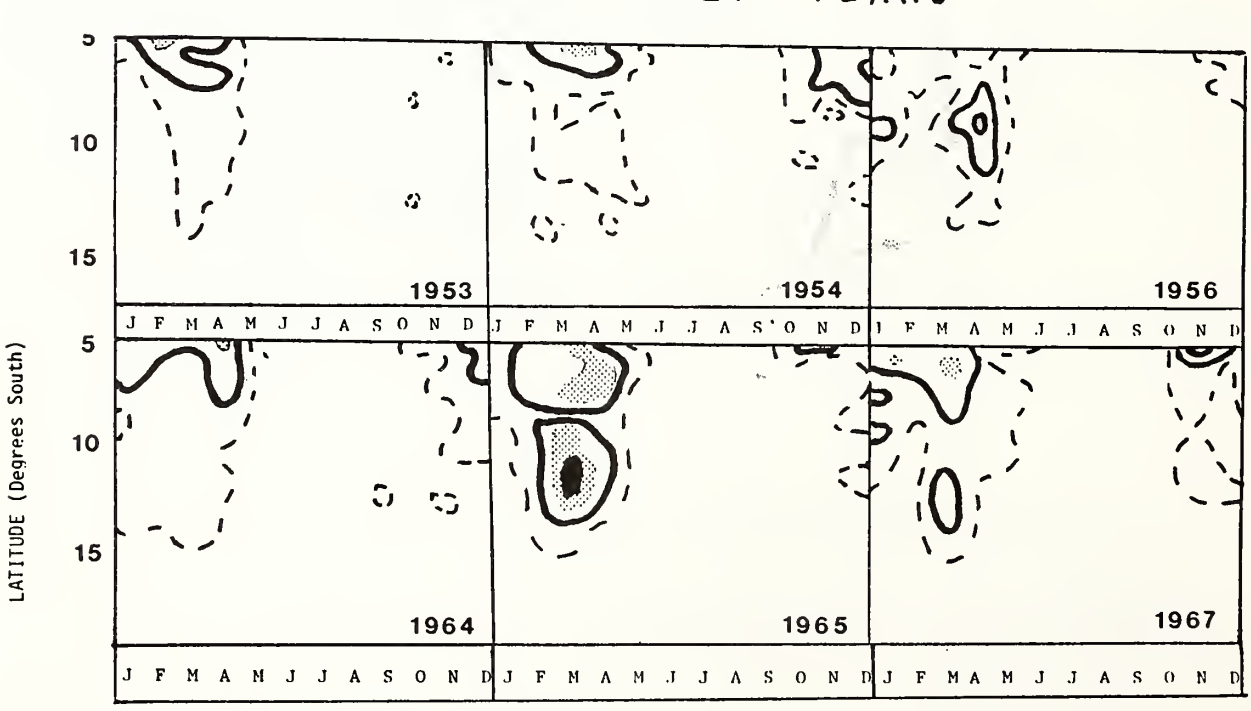

Ftg. 4. Rainfall (mm/mo) along the Benguela Coast as a Function of Latitude and Month during Cold Water Years along the Coast

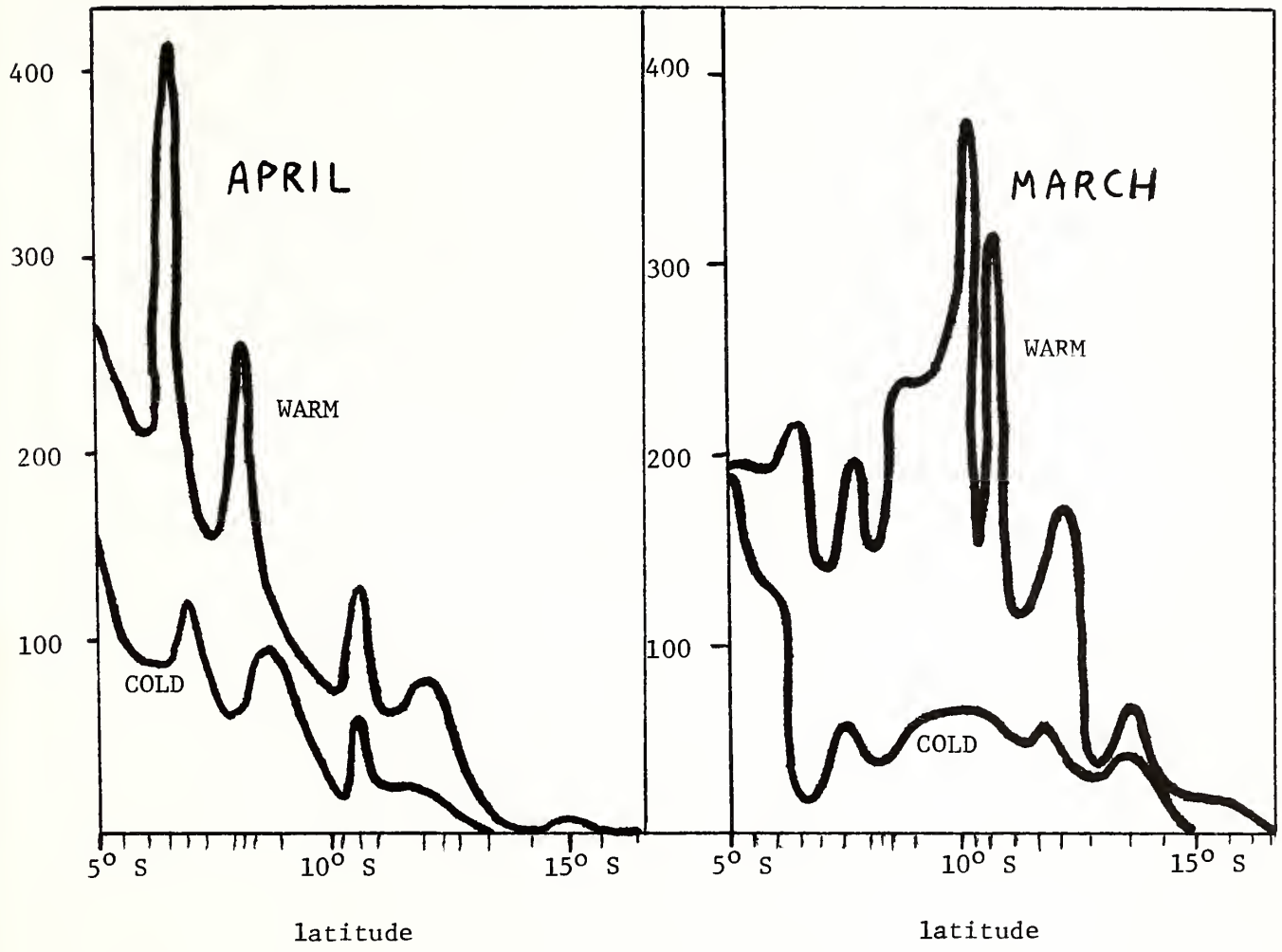

Fig. 5. Monthly Rainfall along the Southwestern Coast of Africa during Warm Water and Cold-Water Composites (five years each).

MARCH WITH APRIL

APRIL WITH MAY

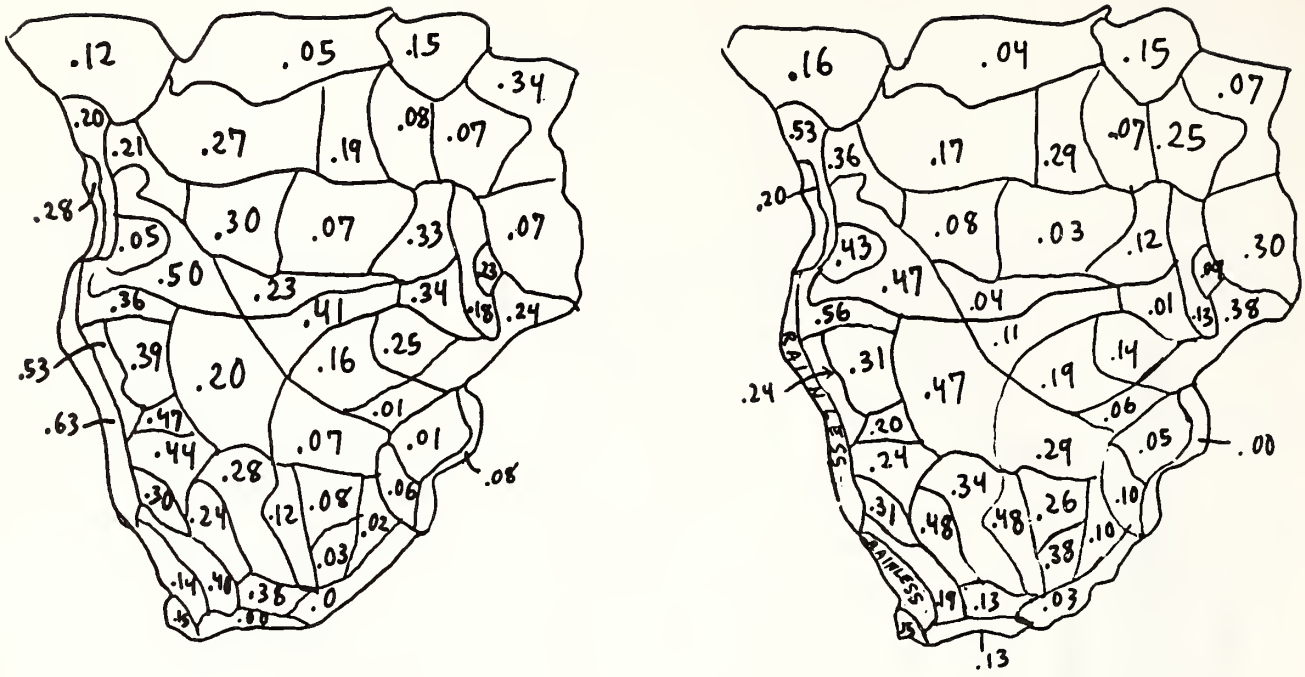

Fig. 6. The Correlation between Regional Rainfall Departures in March and April and in April and May (expressed as a linear correlation coefficient, approximately 70 correlation pairs).

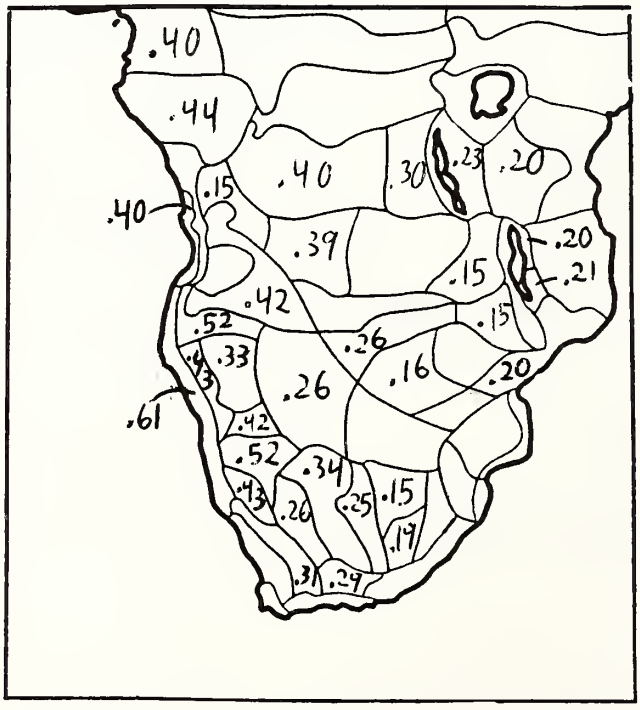

Fig. 7. Correlation between Seasonal Rainfall Departures (regionally-averaged): December-to-March with April-May (correlations $\geq .15$ are indicated, approximately 70 correlation pairs).

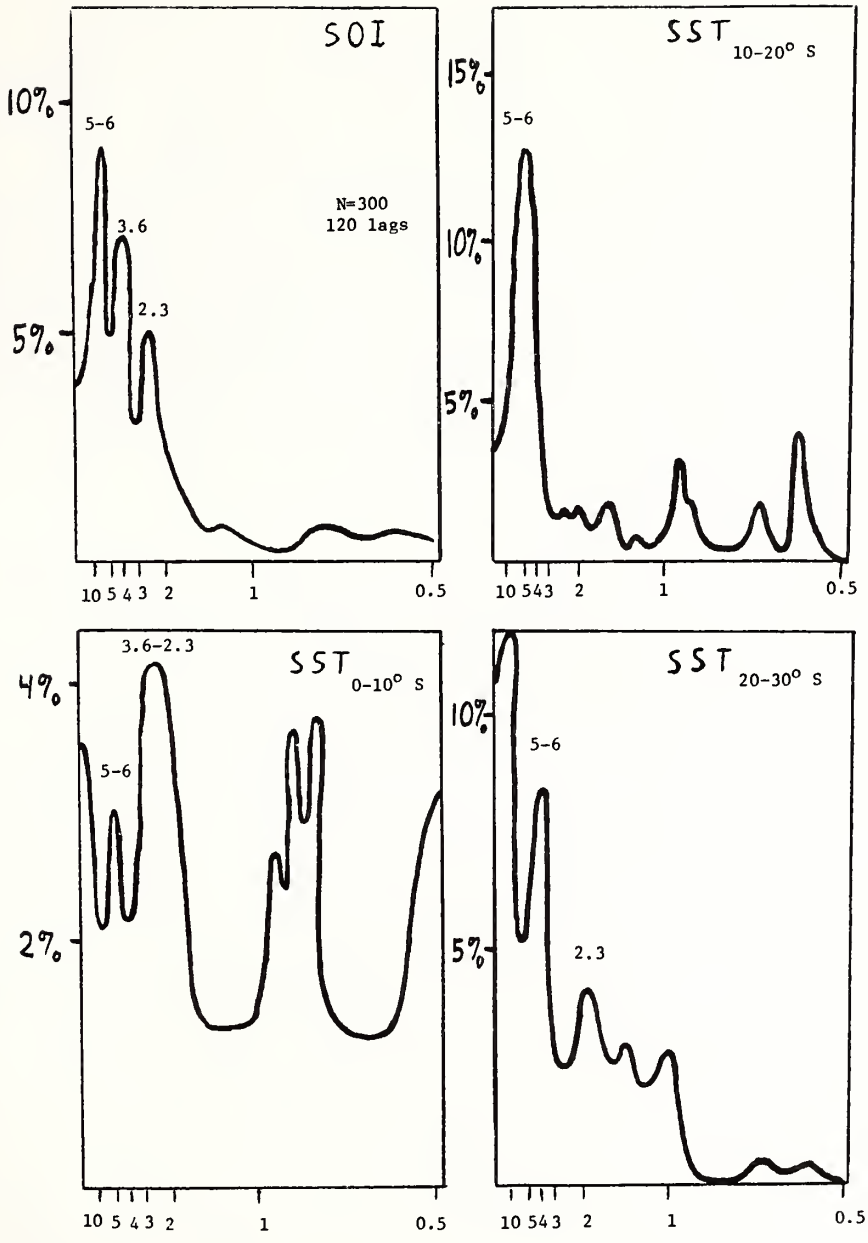

PERIOD (YEARS)

Fig. 8. Spectra of Southern Oscillation (Tahiti-Darwin) and Sea-Surface Temperature along the Benguela Coast, 10° S to 20° S.

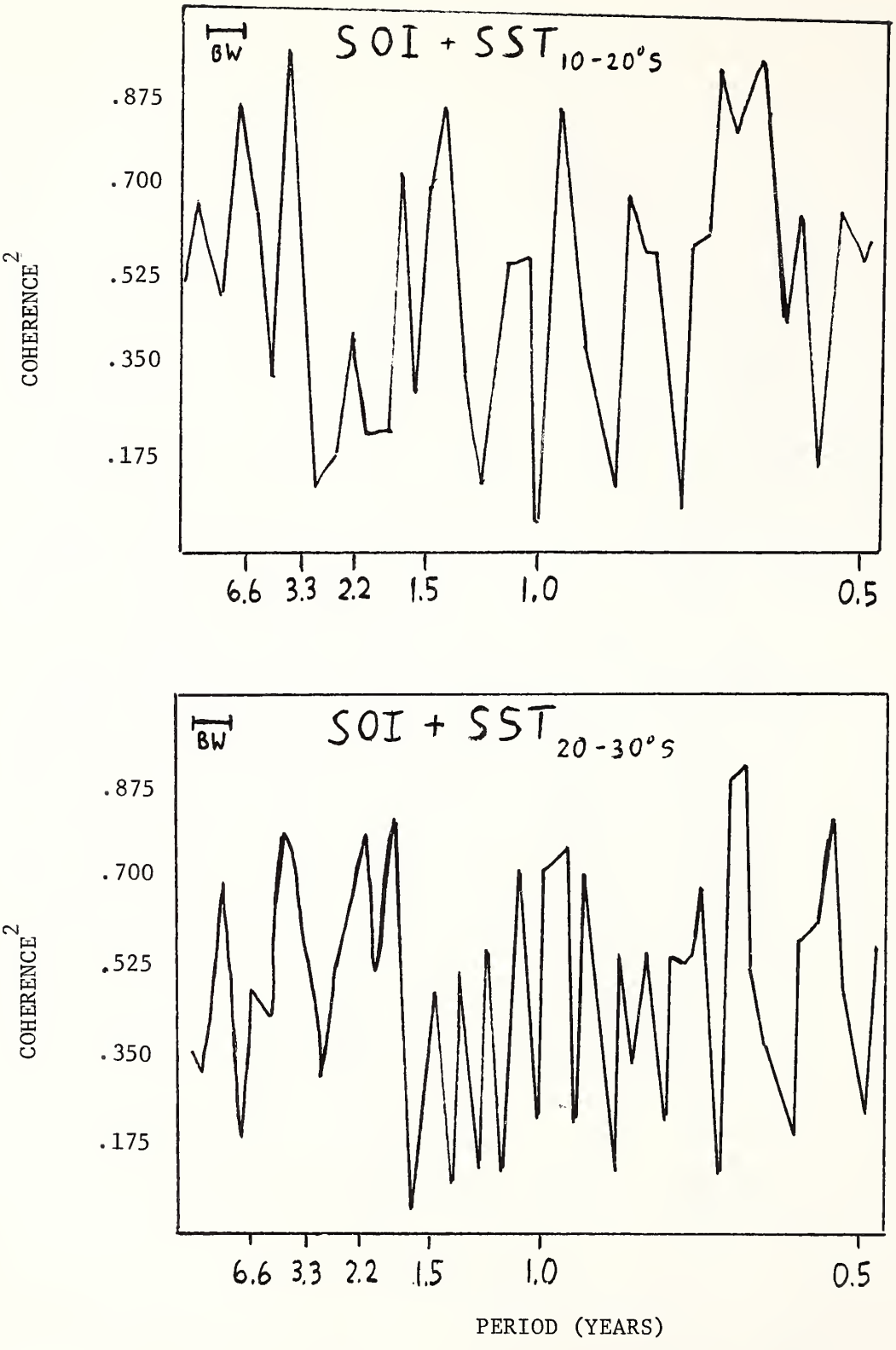

Fig. 9. The Spectral Coherence between the SOI and SSTs in Two Southeastern Atlantic Sectors (spectra in Fig. 8).

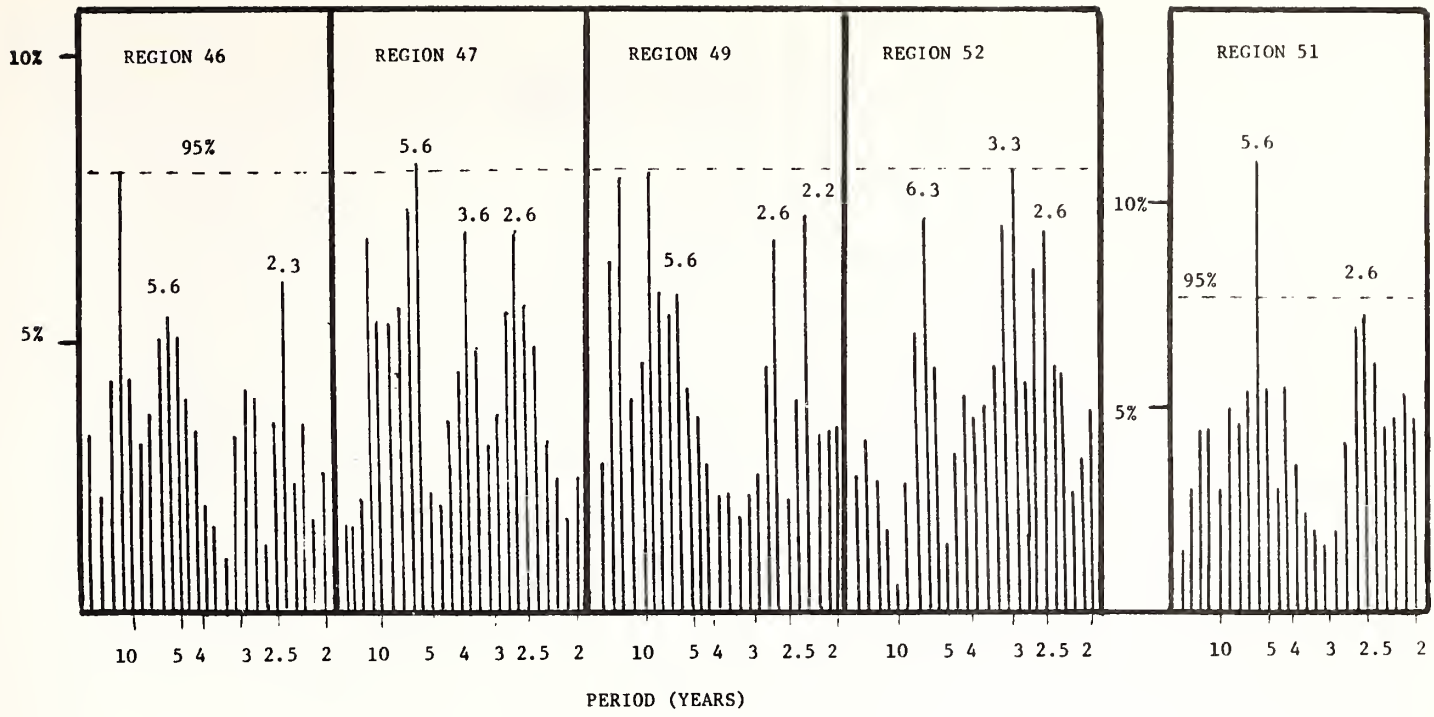

Fig. 10. Normalized Power Spectra of Rainfall Variability 1901 to 1973 for Various Coastal Regions of Southwestern Africa (for region location, see Fig. 1).

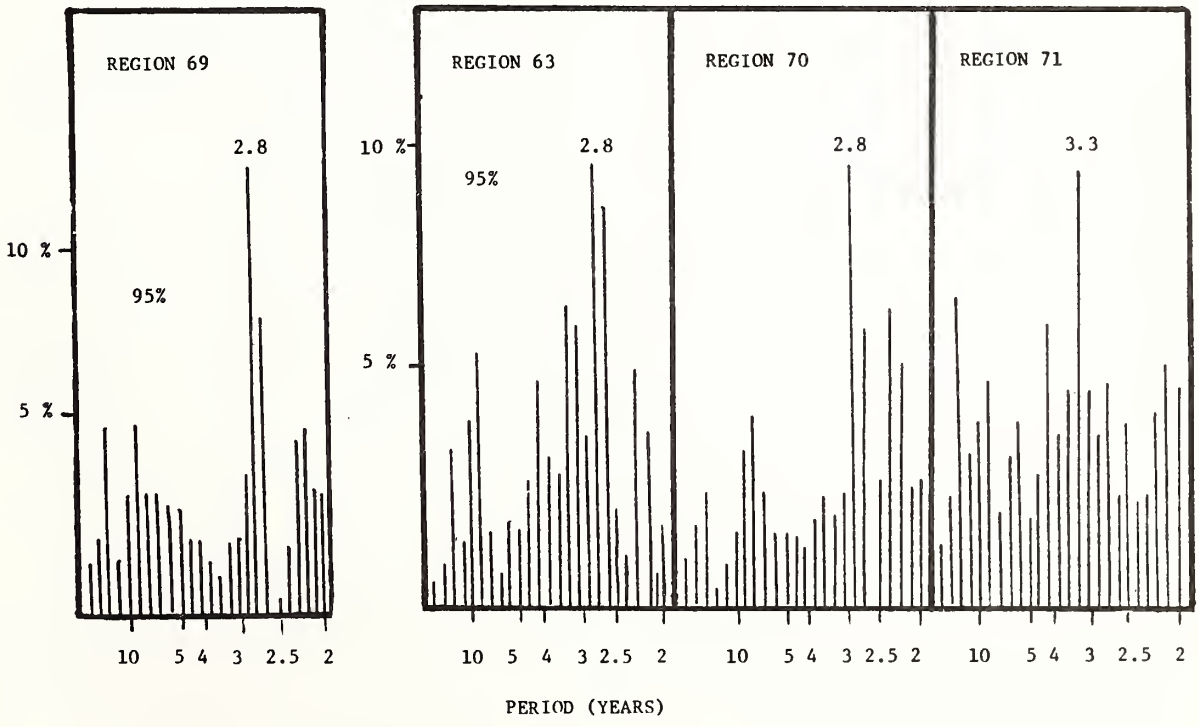

Fig. 11. Normalized Power Spectra of Rainfall Variability 1901 to 1973 for Various Coastal Regions of Southwestern Africa (for region location, see Fig. 1).

Several Aspects of Interannual Variability in the California Current System

C.N.K. MOOERS
L.C. BREAKER

Naval Postgraduate School
Monterey, California 93943

Sea-surface temperature (SST) time series of daily observations acquired along the Central California coast are examined for interannual variability. A 13-year record off Pt. Sur clearly reveals three warming episodes that coincide with Equatorial ENSO events, the 1972-73, 1976-77, and the 1982-83 events (Fig. 1). Also a warming was observed in 1979; this episode coincides with a relatively weak ENSO event observed mainly in the Western and the Northeastern Pacific, Donguy (1981); Tabata (1981). These mid-latitude responses have been referred to as "California El Ninos", McGowan (1984).

Trend analysis of the Pt. Sur time series revealed a significant increase in SST over the past 13 years (~1.2C/decade). Both the most recent El Nino episode and a large-scale warming that started in 1976, Quinn and Neal (1983) appear to have contributed to the long-term increase.

The raw SST data off Pt. Sur suggested that mid-latitude warming occurs mainly during fall and winter; two-way layouts of the monthly means and standard deviations tended to confirm this observation, Breaker et al. (1984). The first mode of a time domain EOF analysis indicated most of the variability did in fact occur between September and March and that it was associated in each case with an El Nino warming episode (ibid., Fig. 2).

The most recent warming episode off Central California was unusual both for the magnitude of the anomaly and for its duration. The anomaly reached 5C during September and October 1983, and it persisted for approximately 20 months (Fig. 3), almost twice as long as the previous episodes in the

sequence. A conservative estimate for the total time that such episodes influenced the Central California coast since 1971, relative to the overall record length is ca. 30%!

Several factors undoubtedly contributed to the 1982-83 warming off Central California. Anomalously strong onshore transport occurred during the winter of 1982-83, Bakun (1983), a factor which most likely contributed to the accumulation of warm water off Central California during the following spring and summer. Satellite IR imagery and the redistribution of subtropical fish 500 km north of their usual habitat, however, suggested the importance of alongshore transport during the most recent episode off Central California as well. Local winds which are usually favorable for upwelling during spring and summer were weaker than usual due to the westward displacement of the subtropical high-pressure cell. Usually, winds less favorable for upwelling lead to higher SSTs; during 1983, however, the ocean warm mixed layer was much thicker than normal and as a result, even stronger-than-normal winds favorable for upwelling might not have been sufficient to upwell water with significantly lower temperatures. Finally, the warmer SSTs off Central California significantly reduced the coastal fog and stratus that are usually associated with cold upwelled water along the coast. Reduced cloud cover in turn caused an increase in solar insolation, another factor contributing to higher SSTs.

Spectral analysis of SSTs at three locations along Central California (Pt. Sur, Pacific Grove, and the Farallons) and alongshore wind stress at one location (Pt. Sur) revealed an approximate 46-day periodicity (Fig. 4). Cross-spectrum analysis between alongshore wind stress and SST off Pt. Sur indicates that the wind leads temperature by about nine days. A delay of this

magnitude between the local alongshore wind and SST is consistent with local forcing. It is possible that this periodicity is related to the 40-to-50 day oscillation in the tropical troposphere, Madden and Julian (1971). We intend to conduct a cross-spectral analysis between zonal winds from Canton Island with alongshore wind stress and SST off Pt. Sur to explore this possibility.

REFERENCES

Bakun, A. (1983) NOAA/NMFS/Pacific Environmental Group.

Breaker, L.C., P.A.W. Lewis, and E.J. Orav (1984) Interannual variability in sea-surface temperature at one location along the Central California coast. Naval Postgraduate School Tech. Rpt. NPS55-84-012, Monterey, 15pp.

Donguy, J.R., C. Henin, A. Morliere, and J.P. Robert (1982) Appearances in the Western Pacific of phenomena induced by El Nino in 1979-80. Tropical Ocean-Atmosphere Newsletter, 10, 1-2.

Madden, R.A. and P.R. Julian (1971) Detection of a 40-50 day oscillation in the zonal wind in the tropical Pacific. Jour. of Atmos. Sci., 28, 702-708.

McGowan, J.A. (1984) The California El Nino, 1983. Oceanus, 27, 48-51.

Quinn, W.H. and V.T. Neal (1983) Long-term variations in the southern oscillation, El Nino and Chilean subtropical rainfall. Fish. Bull., 81, 363-374.

Tabata, S. (1981) Oceanic time-series measurements from Station P and along line P in the NE Pacific Ocean. Papers presented at meeting on Time Series of Ocean Measurements, Ed. by D.J. Ellett. World Climate Research Programme, Tokyo, 171-192.

SEA-SURFACE TEMPERATURE AT GRANITE CANYON
3/1/71 TO 3/1/84

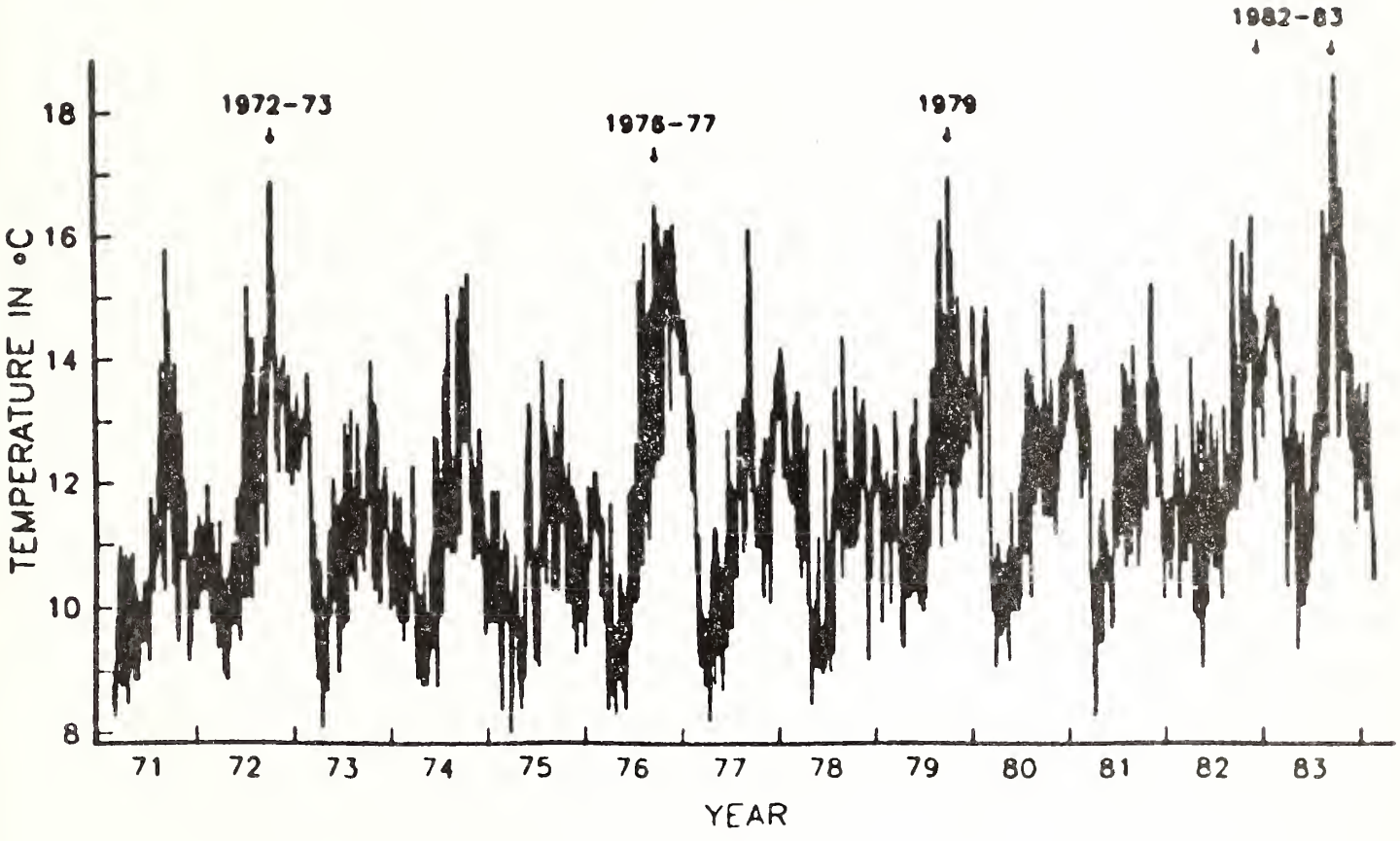

FIGURE 1

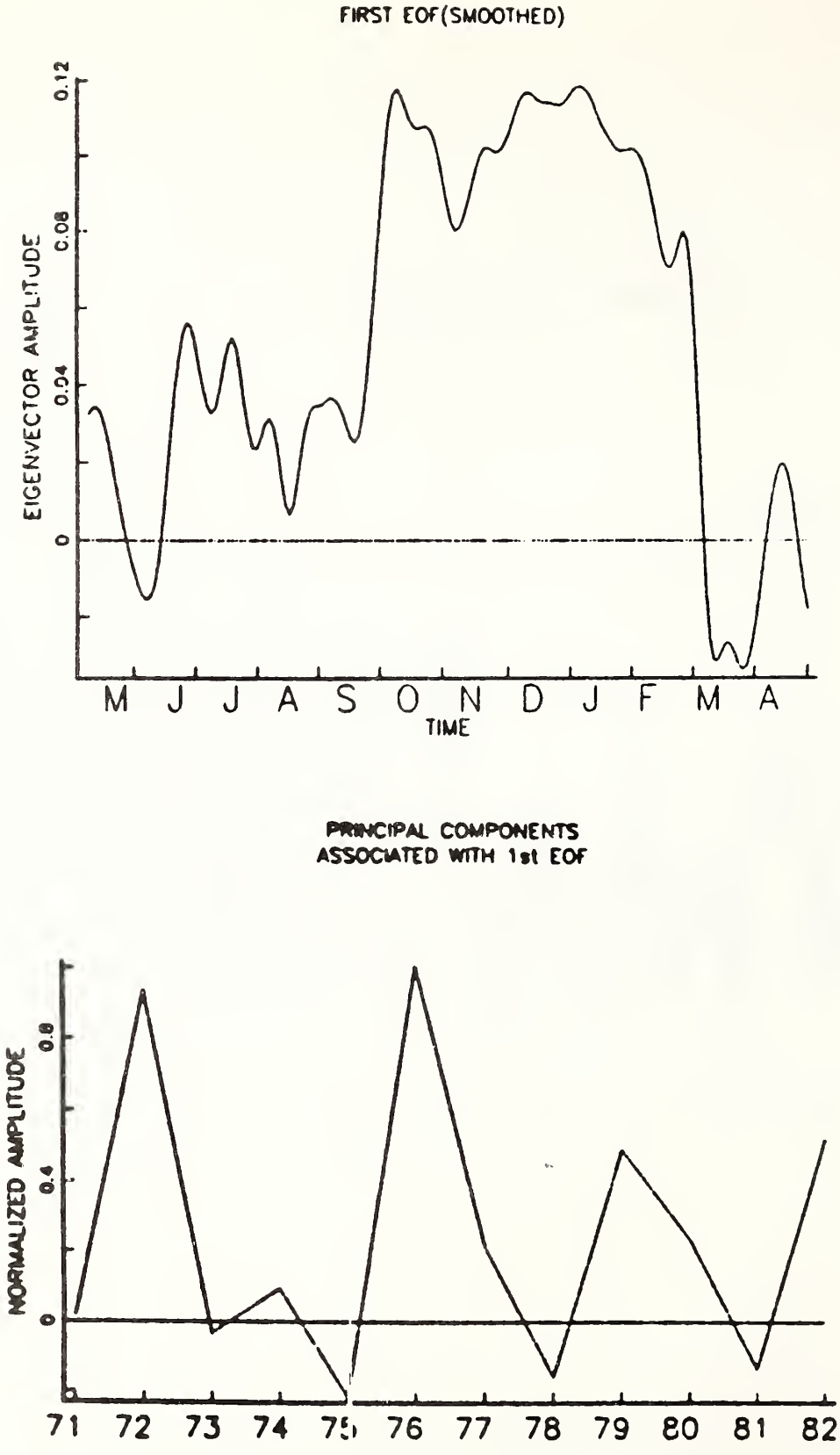
FIRST EOF(SMOOTHED)
EIGENVECTOR AMPLITUDE
0.12
0.08
0.04
0
M J J A S O N D J F M A
TIME
PRINCIPAL COMPONENTS
ASSOCIATED WITH 1st EOF
NORMALIZED AMPLITUDE
0.8
0.4
0
71 72 73 74 75 76 77 78 79 80 81 82

FIGURE 2

TWO-YEAR COMPARISON OF SEA-SURFACE TEMPERATURES
AT GRANITE CANYON

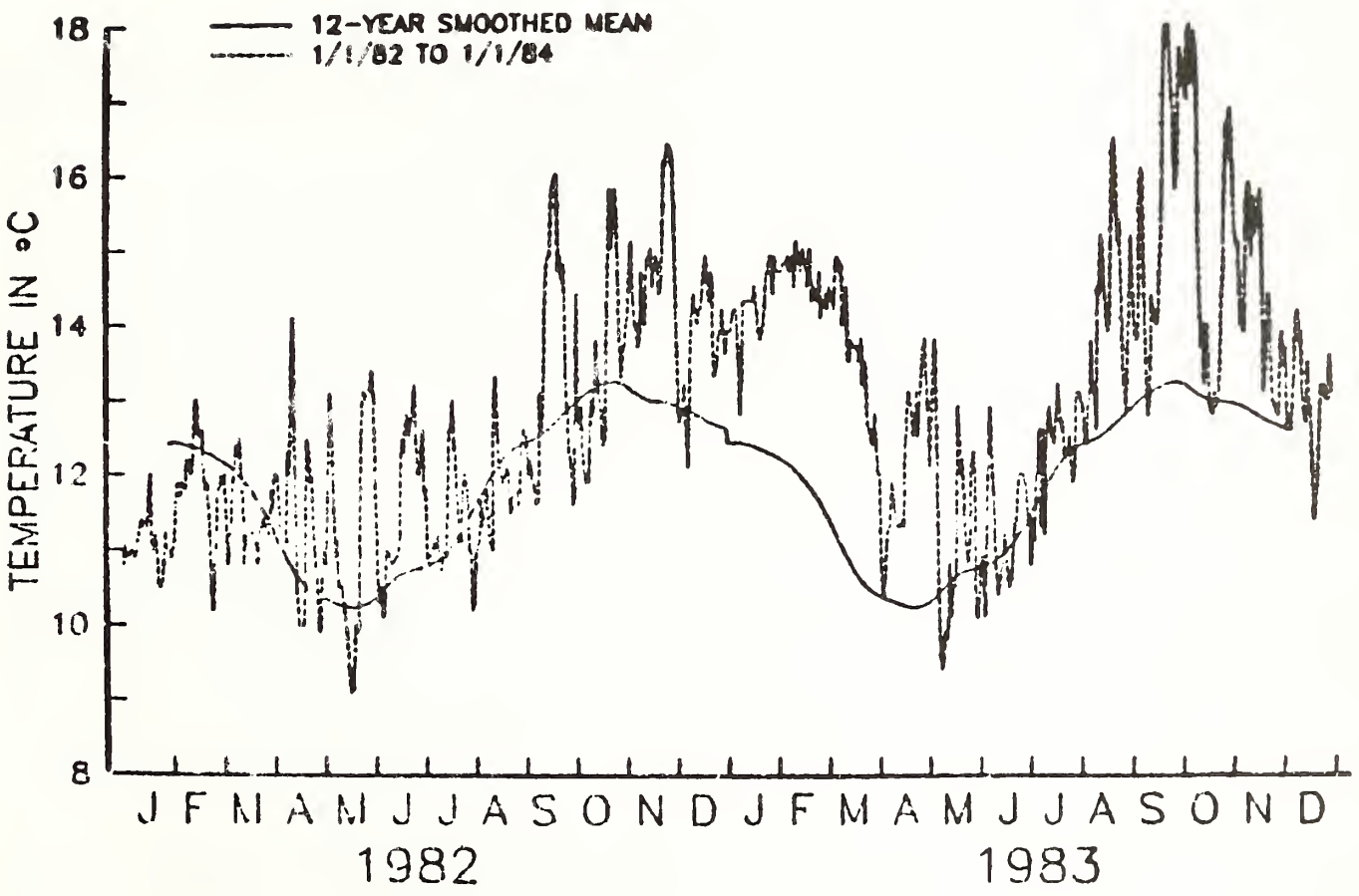

FIGURE 3

PERIODOGRAMS

LINEAR TREND,ANNUAL CYCLE AND 1st HARMONIC REMOVED IN EACH CASE

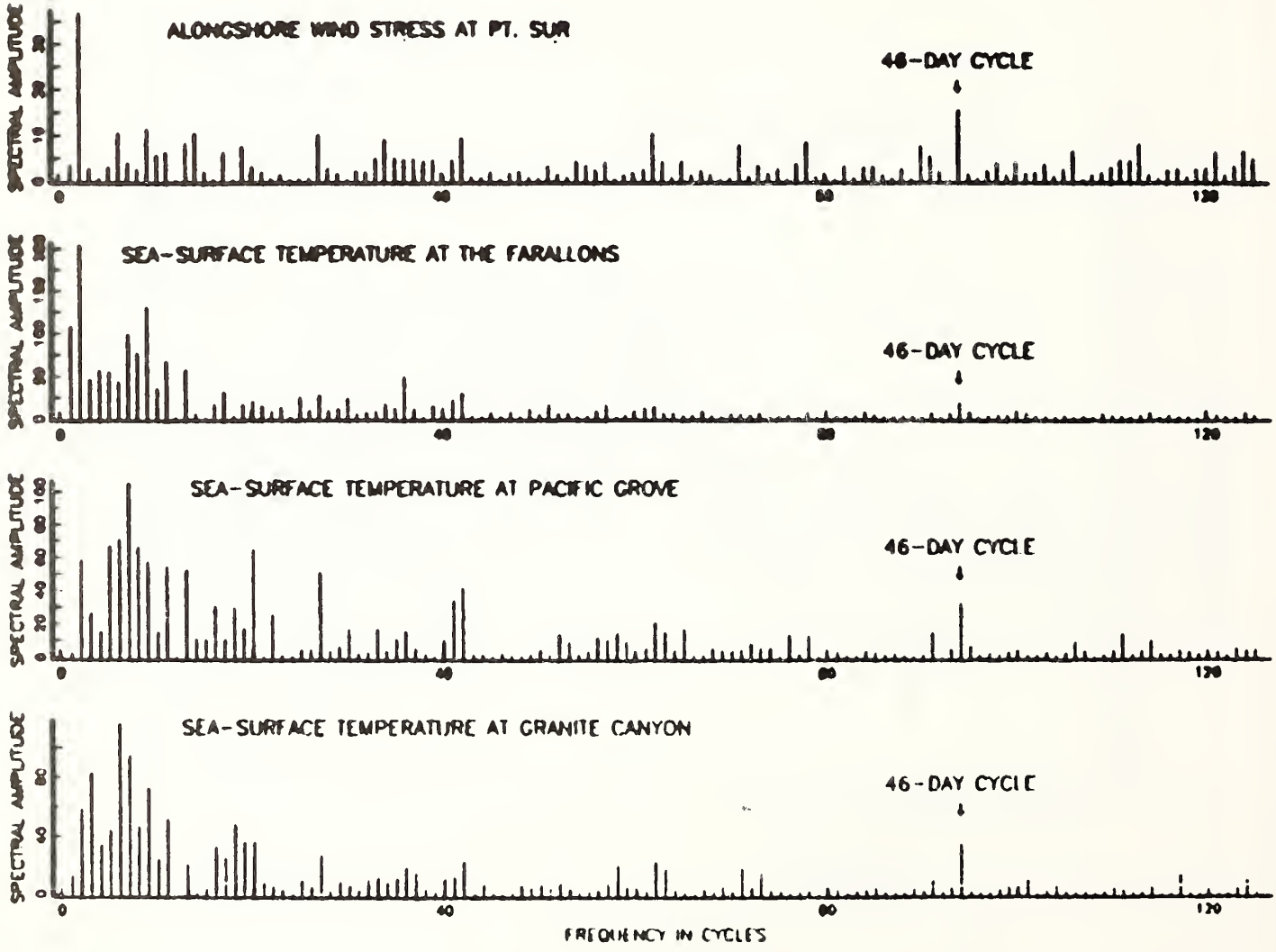

FIGURE 4

Warm and Cold Episodes in the California Current:

A Case for Large-Scale Mid-Latitude Atmospheric Forcing

James J. Simpson

Marine Life Research Group, A-030

Scripps Institution of Oceanography

La Jolla, CA 92093

This paper examines time series of oceanographic variables which indicate the occurrence of warm (El Niño-like) and cold (anti-El Niño-like) periods in the California Current. Large-scale distributions of atmospheric data are then used to show that the most intense mid-latitude warm periods generally are contemporaneous with periods of pronounced tropical ENSO activity and that the most intense mid-latitude cold periods are contemporaneous with periods of non-ENSO activity. Strong mid-latitiude warm periods, however, can occur without contemporaneous tropical ENSO activity. Likewise, mid-latitude cold periods also can develop contemporaneously with tropical ENSO activity. In all cases, however, mid-latitude warm periods are associated with an expansion and intensification of the Aleutian Low, while the corresponding cold periods are associated with an expansion and intensification of the North Pacific High. Oceanographic data support the conclusion that mid-latitude warm (cold) periods in the California Current are related to observed anomalous atmospheric circulation through enhanced onshore (offshore) large-scale wind-driven oceanic transport.

Shown in Fig. 1 are six-month running mean time series of temperature, salinity, density, and sea level anomaly from the Scripps pier. These anomalies are the monthly means minus the long-term monthly mean. Sea level was corrected for secular rise and inverse barometer. Periods of positive temperature anomaly are associated with negative density and positive sea level anomalies. Often these same periods are associated with negative salinity anomaly (i.e. 1925-26, 1940-41, 1976-77, 1982-83). Positive salinity anomaly at the Scripps pier, however, sometimes occurs during warm periods (i.e. 1957-58).

Triple six-month running means of Tarawa rainfall anomaly and of the Rapa-Darwin pressure anomaly are shown in Fig. 2. Positive rainfall and negative pressure anomalies are good indicators of tropical ENSO activity (Quinn *et al.*, 1978). These data, other longer-term time series of rainfall and pressure anomalies (see Quinn *et al.*, 1978), and the data in Fig. 1 were used to identify periods of tropical ENSO activity contemporaneous with the mid-latitude warm periods shown in Table 1. The strength of the ENSO activity listed in Table 1 is based upon the classification procedure developed by Quinn *et al.* (1978).

Shown in Fig. 3 are the six-month running means of the 77-year mean monthly sea level anomalies, defined as the 77-year monthly mean minus the 77-year annual mean. The calculation of these anomalies incorporated the effects of both secular rise and the inverse barometer.

Also shown in Fig. 3 are six-month running mean monthly sea level anomalies one standard deviation (σ) above (representing warm periods) and below (representing cold periods) the 77-year means. All three curves have the same basic shape. Thus, warm and cold periods in the California Current follow the same seasonal cycle. In warm periods, however, there is a continuing increase in sea level during late summer and fall not seen in the 77-year mean anomaly. During cold periods (Fig. 3) coastal sea level is very low in late spring and summer, and it drops off earlier (Sept.-Oct.) and more rapidly than during warm periods. The individual years marked in Fig. 3 correspond to record monthly high or low values of sea level in the 77-year record. They provide independent confirmation of the validity of the procedure (see Table 1) used to classify warm and cold periods in the California Current.

Large-scale wintertime (D, J, F) mid-latitude 700-mb height pressure anomalies and the observed contemporaneous SST anomaly (J) for 1957-58, 1969-70, 1972-73, 1976-77 and 1982-83 are shown in Fig. 4. The 1930-31 warm period (Fig. 4) is represented by an SLP anomaly because the 700-mb height anomaly was not recorded during 1930-31. Moderate to strong contemporaneous ENSO activity occurred in the tropics during these same periods (see Table 1). In each case the mid-latitude atmosphere was dominated by an expansion and intensification of the Aleutian Low. Likewise, these periods are characterized by positive coastal SST anomalies with cross-shelf length scales of order 1,000 km and negative open-ocean SST anomalies with even larger length scales.

The physical processes associated with the mid-latitude warm periods (Fig. 4) can be examined by considering in detail the statistical relations between the 700-mb height anomaly and the contemporaneous SST anomaly for the 1982-83 event. Shown in Fig. 5a is the winter 1983 mean anomaly of the 700-mb height over the North Pacific. This anomaly is the difference between the 26-year seasonal climatological mean and the seasonal mean divided by the standard deviation of the seasonal mean (Namias, 1979). Shown in Fig. 5b is an observed contemporaneous winter (e.g. February, 1983) SST anomaly. It is representative of winter 1982-83 (compare January, 1983 [Fig. 4] with February, 1983 [Fig. 5b]). Shown in Fig. 5d is the winter 1982-83 SST anomaly specified from the contemporaneous winter 700-mb height anomaly (Fig. 5a) using the method of Namias and Born (1972). Data were provided by J. Namias. There is excellent qualitative agreement between the scales of the statistically specified SST anomaly (Fig. 5d) and those of the observed SST anomaly (Fig. 5b). These data also show that an anomalous wind field can simultaneously produce the positive coastal and negative central Pacific SST anomalies observed during 1982-83.

To examine the spatial relationships involved in the above specifications, some primary 700-mb height predictors (tails of arrows) and their predicands (heads of arrows) for the winter SST anomalies (Fig. 5d), as derived from the 1948-81 winter data and from contemporaneous winter data by the method of Namias and Born (1972) are shown in Fig. 5c. Numbers in Fig. 5c associated with the predicands represent percentage of the variance in the SST field for the dependent sample data accounted for by the primary predictor. These values clearly show that the predictor-predicand relationships of Fig. 5c are statistically significant. A negative sign (Fig. 5c) indicates that positive coastal SST anomaly is associated with an atmospheric low over the central Pacific, whereas a positive sign (Fig. 5c) means it is associated with an atmospheric high (i.e. ridge) over North America. Such a large-scale atmospheric pressure system was observed during the 1982-83 event (Fig. 5a). These predictor-predicand relationships also suggest that the winter 1982-83 SST anomaly field was remotely forced by large-scale anomalous winds over the Arctic and central Pacific. Further, the statistically specified SST anomaly (Fig. 5d) is in agreement with independently calculated (Haney *et al.*, 1983) and statistically specified (Davis, 1976) anomalous wind-SST relationships for the mid-latitude North Pacific.

The large-scale atmospheric pressure pattern (Fig. 5a) should be geostrophically balanced by a mean wind field coming from the south-southwest. Such winds also are consistent with the observed enhanced onshore transport in the California Current (Fig. 6) and with upwelling indices for the period (see Simpson, 1985). The negative salinity and positive temperature anomalies of Fig. 6 unambiguously establish onshore transport of Pacific Subarctic water from the west-northwest direction; a result consistent only with large-scale atmospheric forcing as a driving mechanism for warming periods in the California Current. Similar patterns of negative subsurface salinity anomaly and positive subsurface temperature anomaly (not shown) also were observed during the other major and moderate mid-latitude warming events for which data is available (i.e. 1940-41, 1957-58, 1976-77).

Large-scale wintertime (D, J, F) mid-latitude 700-mb height pressure anomalies and the observed contemporaneous SST anomalies (J) for 1949-50, 1950-51, 1970-71, 1971-72, and 1974-75 are shown in Fig. 7. The 1932-33 cold period (Fig. 7) is represented by an SLP anomaly because the 700-mb height anomaly was not recorded during 1932-33. No ENSO activity occurred in the tropics during these same periods (see Fig. 1 and Table 1). In each of these cases the mid-latitude atmosphere is dominated by an expansion and intensification of the North Pacific High over the open ocean and the development of a pronounced low (trough) over North America. Likewise, these periods are characterized by negative coastal SST anomalies with cross-shelf length scales of order 1,000 km and positive open-ocean SST anomalies with even larger length scales.

Cross-shelf vertical sections of temperature and salinity anomaly along CalCOFI line 90 for a cold period (January, 1975) in the California Current are shown in Fig. 8. The TS characteristics of this anomalous water mass uniquely identify the source of the water as upwelled subsurface inshore water (see Reid, 1960). Pronounced upwelling (i.e. Fig. 8) is unusual during winter in the California Current; generally upwelling is most pronounced in late spring and summer (Hickey, 1979). The anomalous, wintertime atmospheric pressure patterns associated with cold periods in the California Current (Fig. 7), however, should be geostrophically balanced by an enhanced mean equatorward wind field. Such winds are consistent with the contemporaneous offshore transport (Fig. 8) observed during cold periods in the California Current.

Shown in Fig. 9a are wintertime (D, J, F) 700-mb height anomalies and contemporaneous SST anomalies (J) for the warm period 1960-61 and fall (S, O, N) anomalies for the warm period (1967-68) in the California Current. The 1967-68 warm period developed earlier than usual and it persisted through winter 1968. These warm periods occurred without contemporaneous tropical ENSO activity. Similar data for a cold period (1969) in the California Current with contemporaneous tropical ENSO activity (see Fig. 1, Table 1) are shown in Fig. 9b. Again, cold periods in the California Current are associated with an expanded North Pacific High and warm periods are associated with an expanded Aleutian Low. These data show that mid-latitude warm and cold periods can develop independently of tropical ENSO activity. These data, coupled with that in Figs. 1, 4, 7 and Table 1, however, show that the most intense mid-latitude warm periods develop during periods of contemporaneous tropical ENSO activity and that the most intense mid-latitude cold periods develop during periods of contemporaneous non-ENSO activity in the tropics.

In summary, warm periods in the California Current are associated with an expanded Aleutian Low, high coastal sea level, and an anomalous high rate of increase in sea level. This anomalous high rate of increase in sea level is compensated for by a corresponding rapid and large rate of depression of the inshore thermocline (Reid and Mantyla, 1976). Hence, the subsurface thermal anomalies characteristic of warm periods in the California Current (i.e. Fig. 6) are produced dynamically, rather than thermodynamically, through the combination of enhanced onshore transport of Pacific Subarctic water (Simpson, 1984b, 1985) and the related

downward tilt of the inshore thermocline. The positive coastal SST anomalies, however, are partially thermodynamically produced through enhanced near surface absorption of solar radiation (see Simpson, 1985). By contrast, the normal seasonal low inshore oceanic baroclinic pressure is even lower during cold periods in the California Current and the tilt of the inshore thermocline is upward. Necessarily, the pressure differential between the inshore low and the offshore high oceanic baroclinic pressure field is enhanced, the southeastward transport of the California Current is increased, the inshore California Countercurrent occurs later in the year, and its northwestward transport is diminished relative to mean flow conditions in the California Current. Cold coastal anomalies are a dynamical consequence of these changes in ocean circulation induced by an expanded North Pacific High. All the results show that warm and cold periods in the California Current are part of a large-scale (i.e. basin-wide) mid-latitude air-sea interaction.

References

Davis, R. E., 1976: Predictability of sea surface temperature and sea level pressure anomalies over the North Pacific Ocean. *J. Phys. Oceanogr.*, **6**, 249-266.

Fisheries Information, 1960-1980. National Oceanic and Atmospheric Administration, U. S. Department of Commerce, Washington, D. C.

Haney, R. L., B. H. Houtman, and W. H. Little, 1983: The relationship between wind and sea surface temperature anomalies in the mid-latitude North Pacific Ocean. *Atmosphere-Ocean*, **21**, 168-186.

Hickey, B. M., 1979: The California Current System — Hypotheses and Facts. *Prog. Oceanogr.*, **8**, 191-279.

Namias, J., 1979: Northern hemisphere seasonal 700 mb height and anomaly charts, 1947-1978, and associated North Pacific sea surface temperature anomalies. CalCOFI Atlas No. 27, University of California, San Diego, 275 pp.

Namias, J., and R. M. Born, 1972: Empirical techniques applied to large-scale and long-period air-sea interactions, a preliminary report. SIO Ref. Ser. 72-1, Scripps Institution of Oceanography, University of California, San Diego, 47 pp.

Quinn, W. H., D. O. Zoff, K. S. Short, and R. T. W. Kuo Yang, 1978: Historical trends and statistics of the Southern Oscillation, El Niño and Indonesian Droughts. *Fish. Bull.*, **76**, 663-678.

Reid, J. L., Jr., 1960: Oceanography of the Eastern North Pacific in the Last 10 Years. *Calif. Coop. Oceanic Fish. Invest. Rep.*, **7**, 77-90.

Reid, J. L., and A. W. Mantyla, 1976: The effect of the geostrophic flow upon coastal sea elevations in the northern North Pacific Ocean. *J. Geophys. Res.*, **81**, 3100-3110.

Simpson, J. J., 1984a: A simple model of the 1982-83 Californian "El Niño." *Geophys. Res. Lett.*, **11**, 237-240.

Simpson, J. J., 1984b: El Niño-induced onshore transport in the California Current during 1982-83. *Geophys. Res. Lett.*, **11**, 233-236.

Simpson, J. J., 1985: The Aleutian low teleconnection between tropical ENSO and mid-latitude North Pacific El Niño-like events. Submitted to *J. Geophys. Res.*.

Table 1: Comparison of tropical ENSO and mid-latitude events

YEAR	*TROPICS*		*MID-LATITUDE*	
	Type	*Strength*	*Type*	*Strength*
1930-31	ENSO	strong	warm	strong
1940-41	ENSO	strong	warm	strong
1957-58	ENSO	strong	warm	strong
1969-70	ENSO	weak/moderate	warm	weak/moderate
1972-73	ENSO	strong	warm	moderate/strong
1976-77	ENSO	moderate	warm	moderate
1982-83	ENSO	very strong	warm	very strong
1932-33	non-ENSO	strong	cold	strong
1948-49	non-ENSO	strong	cold	strong
1949-50	non-ENSO	strong	cold	strong
1970-71	non-ENSO	moderate	cold	moderate
1971-72	non-ENSO	moderate	cold	moderate
1974-75	non-ENSO	very strong	cold	very strong
1960-61	non-ENSO	moderate	warm	moderate
1967-68	non-ENSO	moderate	warm	moderate
1968-69	ENSO	moderate	cold	moderate

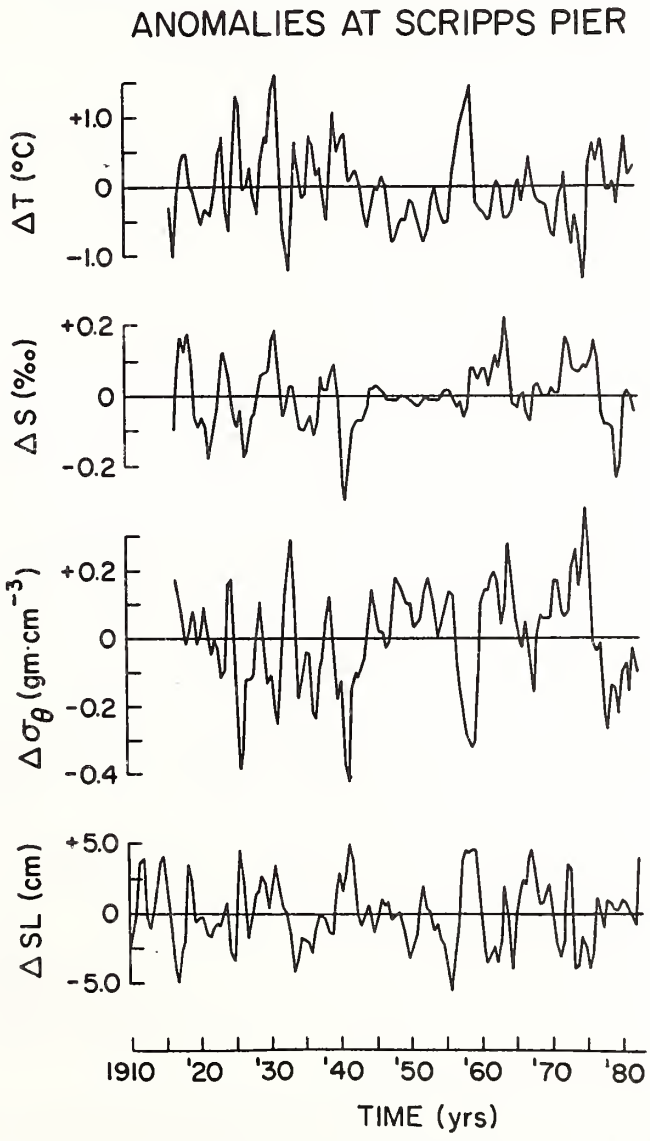

Fig. 1. Six-month running mean time series of temperature, salinity, density and sea level anomaly at the Scripps pier. Prior to 1925, the sea level data is from the San Diego tide gauge.

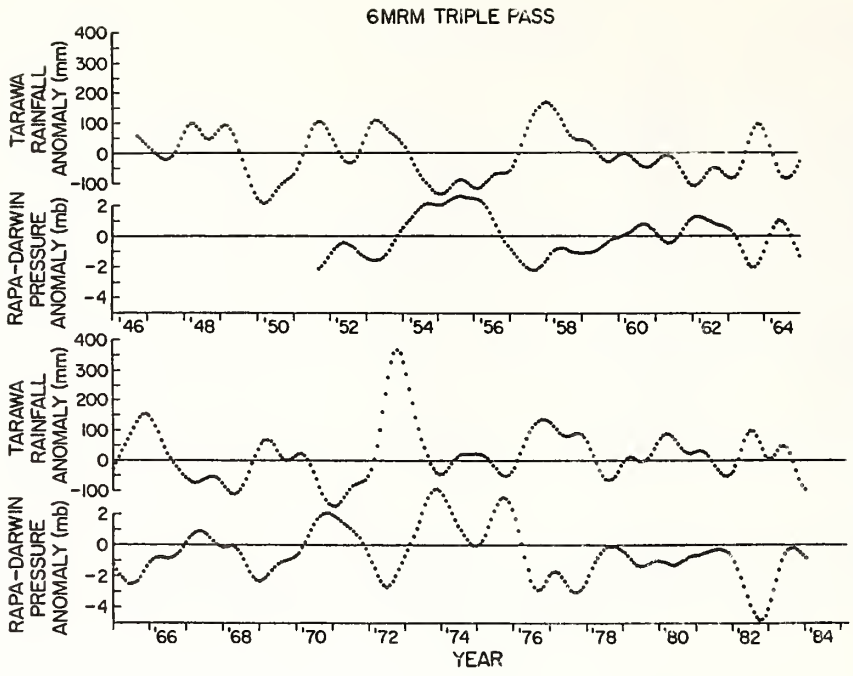

Fig. 2. Triple six-month running means of Tarawa rainfall anomaly and Rapa-Darwin pressure anomaly (courtesy of Dr. William Quinn).

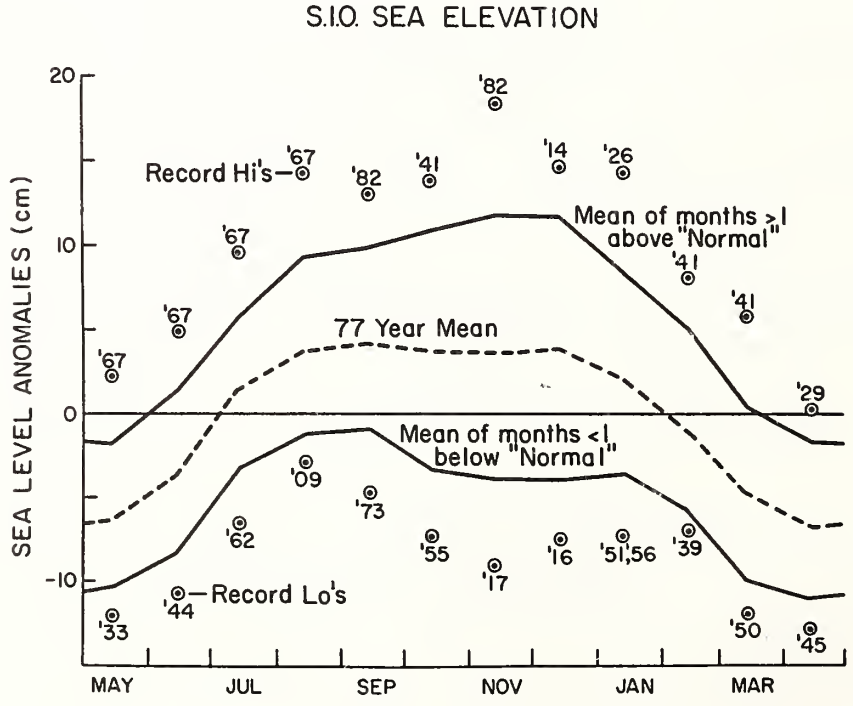

Fig. 3. Six-month running mean time series of long-term mean monthly sea level minus annual mean. Time series one standard deviation above (warm periods) and below (cold periods) the 77-year mean anomaly also are shown (from Simpson, 1984a).

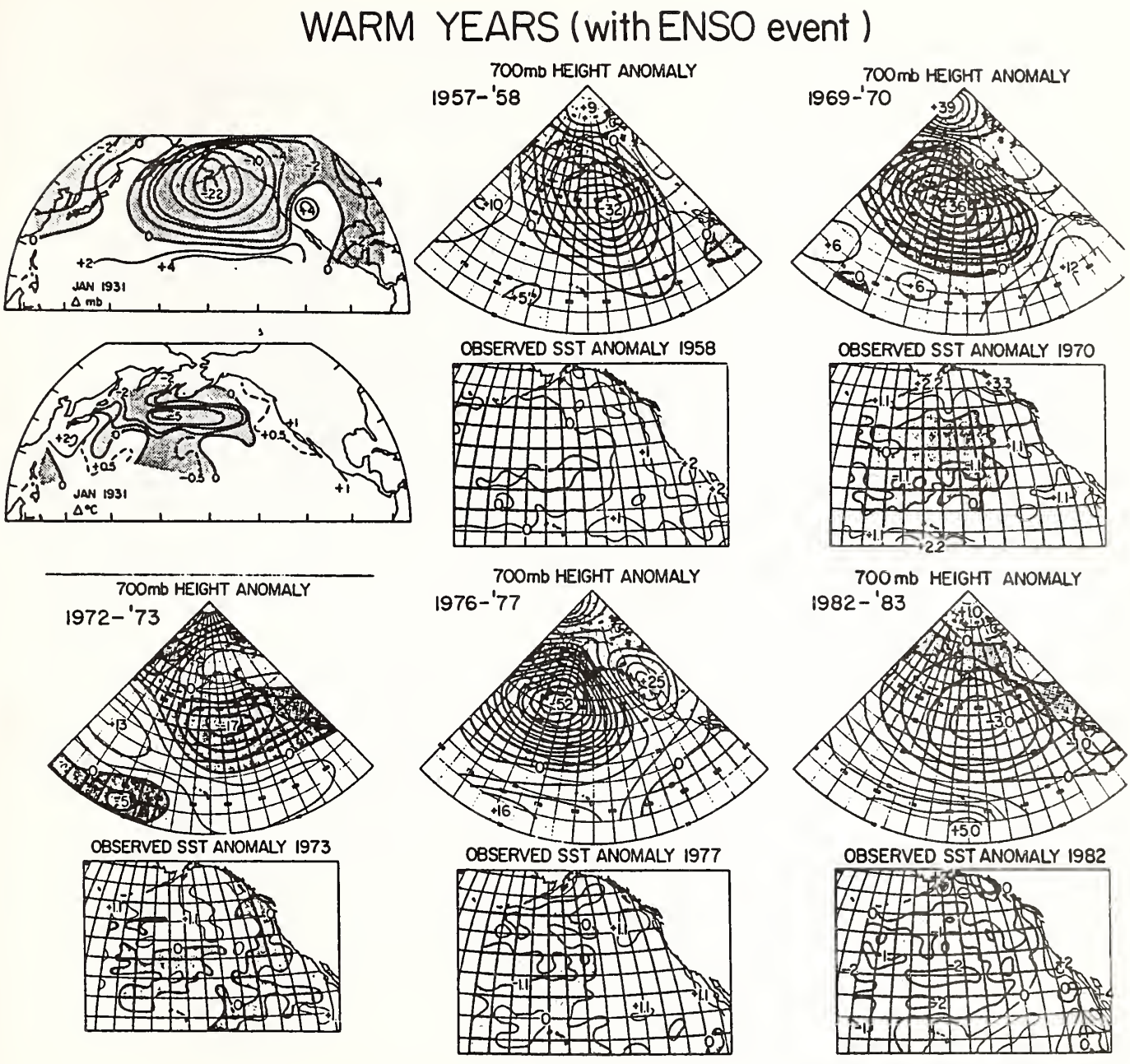

Fig. 4. Large-scale wintertime (D, J, F) mid-latitude 700-mb height pressure anomalies and the observed contemporaneous SST (J) anomaly for the years shown. An SLP anomaly is used for 1930-31. Data are from Reid (1960), Namias (1979) and *Fisheries Information*.

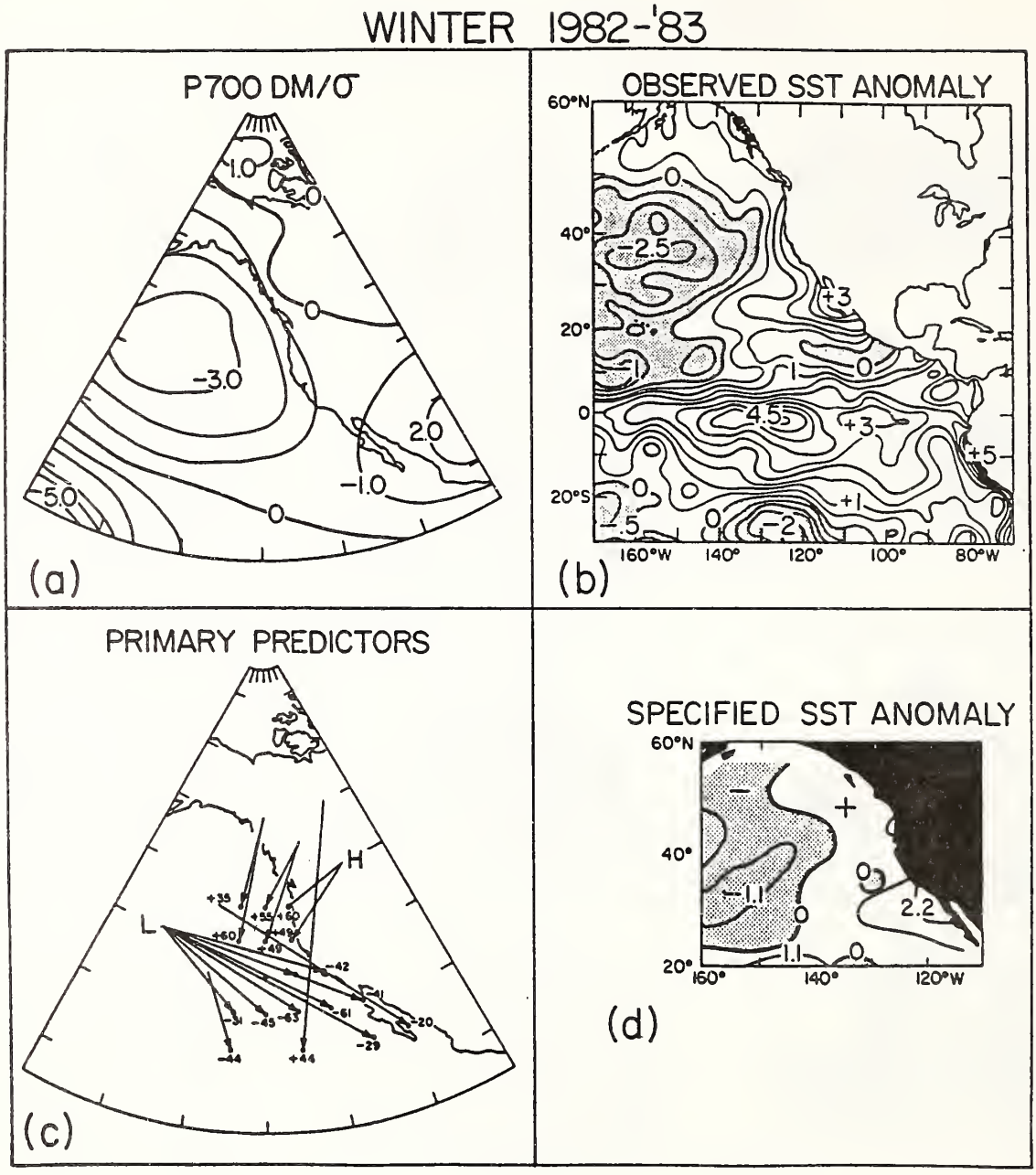

Fig. 5 (a) Winter 1982-83 700-mb height anomaly expressed as standard deviations about long-term mean, (b) observed winter SST anomaly, (c) primary predictors (tails of arrows) and predicands (heads of arrows) for (d) contemporaneously specified winter SST anomaly using the method of Namias and Born (1972).

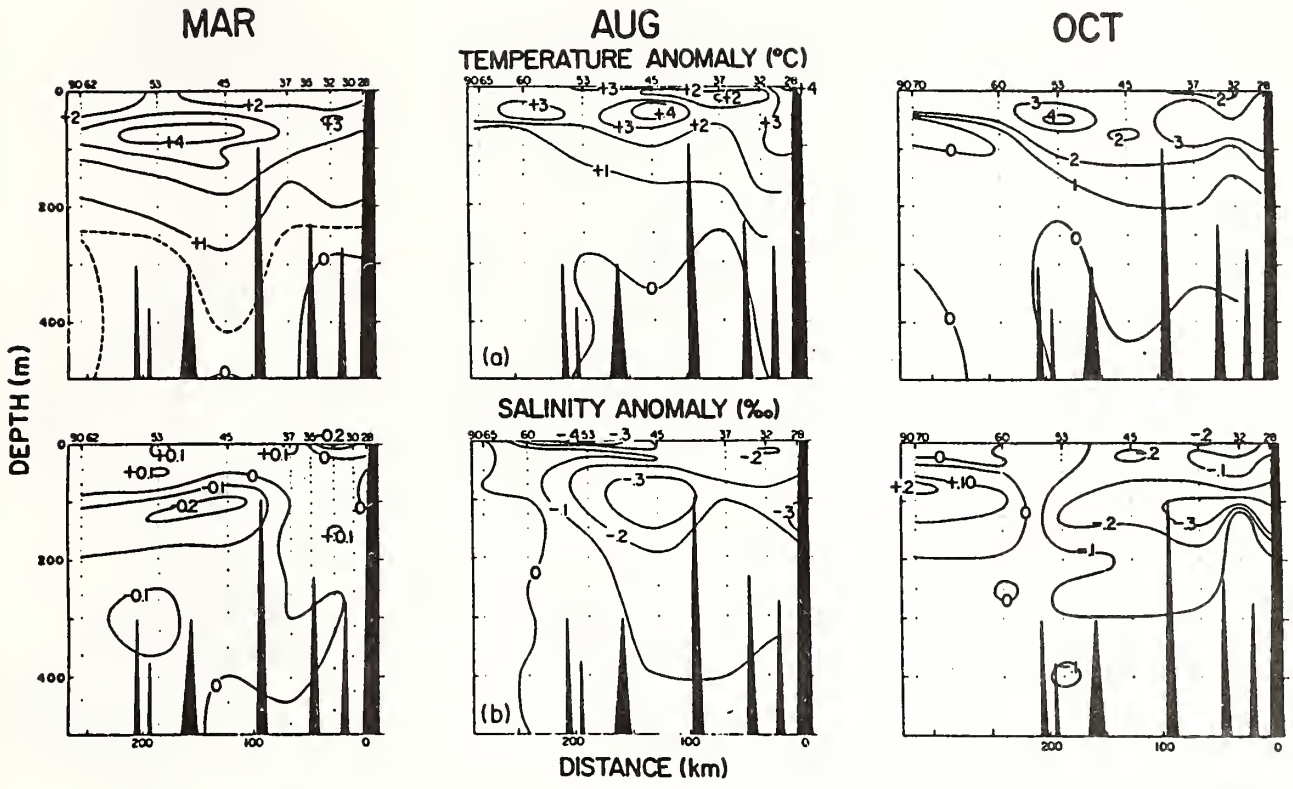

Fig. 6. Series of cross-shelf sections of (a) temperature, and (b) salinity anomaly along CalCOFI line 90, 1983. The negative salinity anomalies unambiguously establish onshore transport of Pacific Subarctic water from the west-northwest. Method of preparation of these sections is given by Simpson, 1984b, 1985.

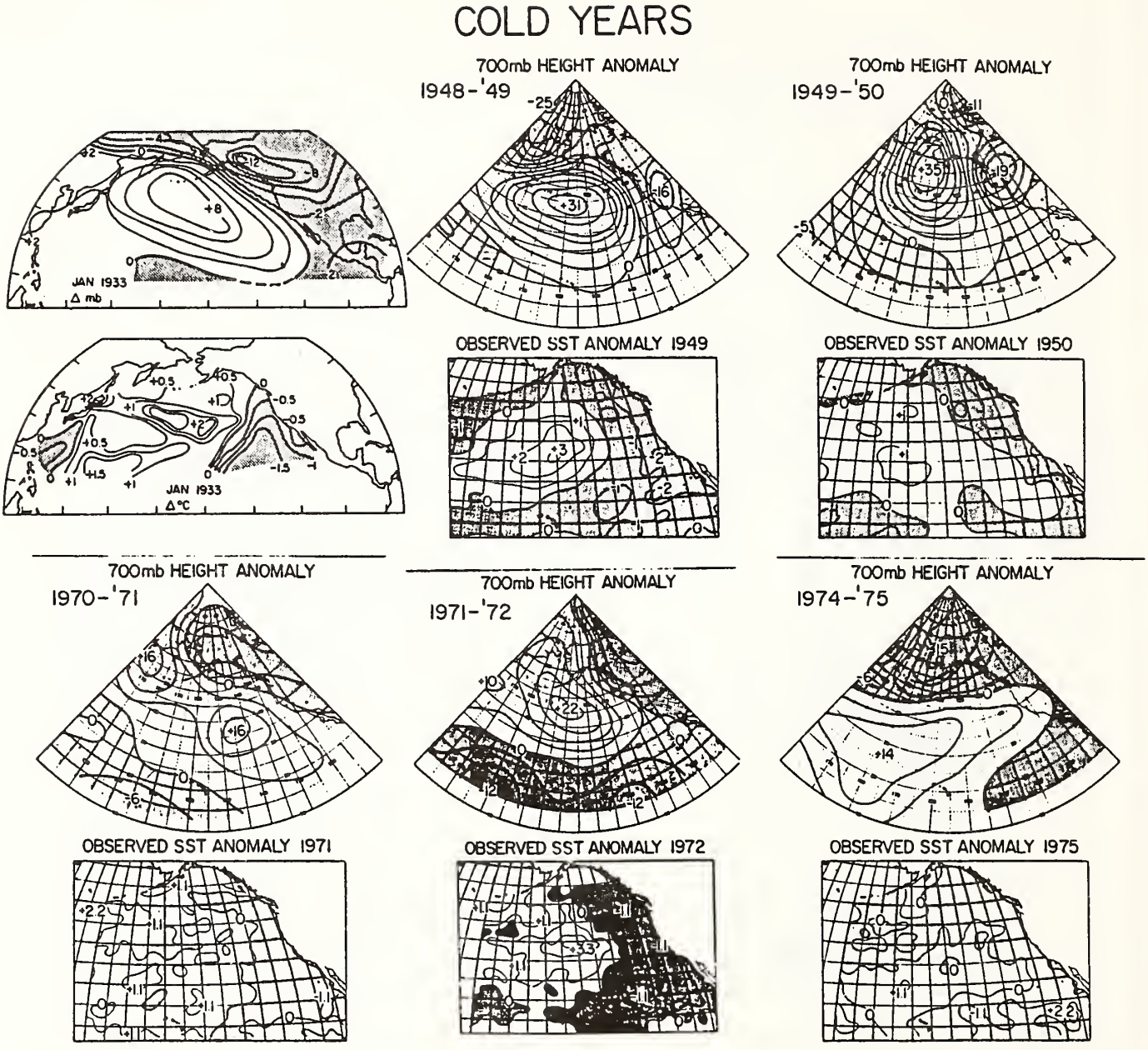

Fig. 7. Large-scale wintertime (D, J, F) mid-latitude 700-mb height pressure anomalies and the observed contemporaneous SST (J) anomaly for the cold periods shown. An SLP anomaly is used for 1932-33. Data are from Reid (1960), Namias (1979) and *Fisheries Information*.

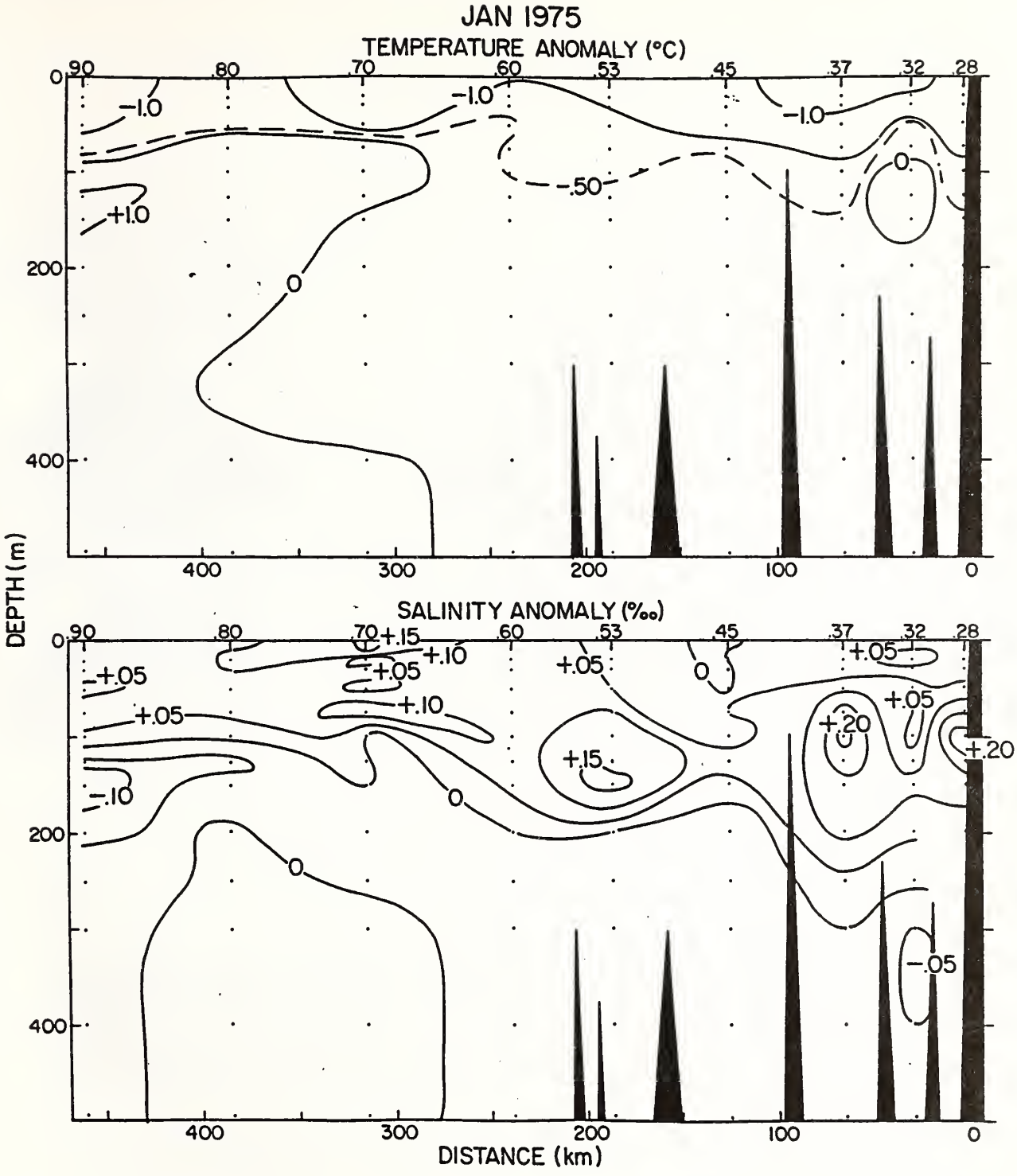

Fig. 8. Cross-shelf sections of (a) temperature, and (b) salinity anomaly along CalCOFI line 90 for a cold period (1975) in the California Current. The negative temperature and positive salinity anomalies resulted from enhanced offshore transport associated with the intensified North Pacific High (see Fig. 7).

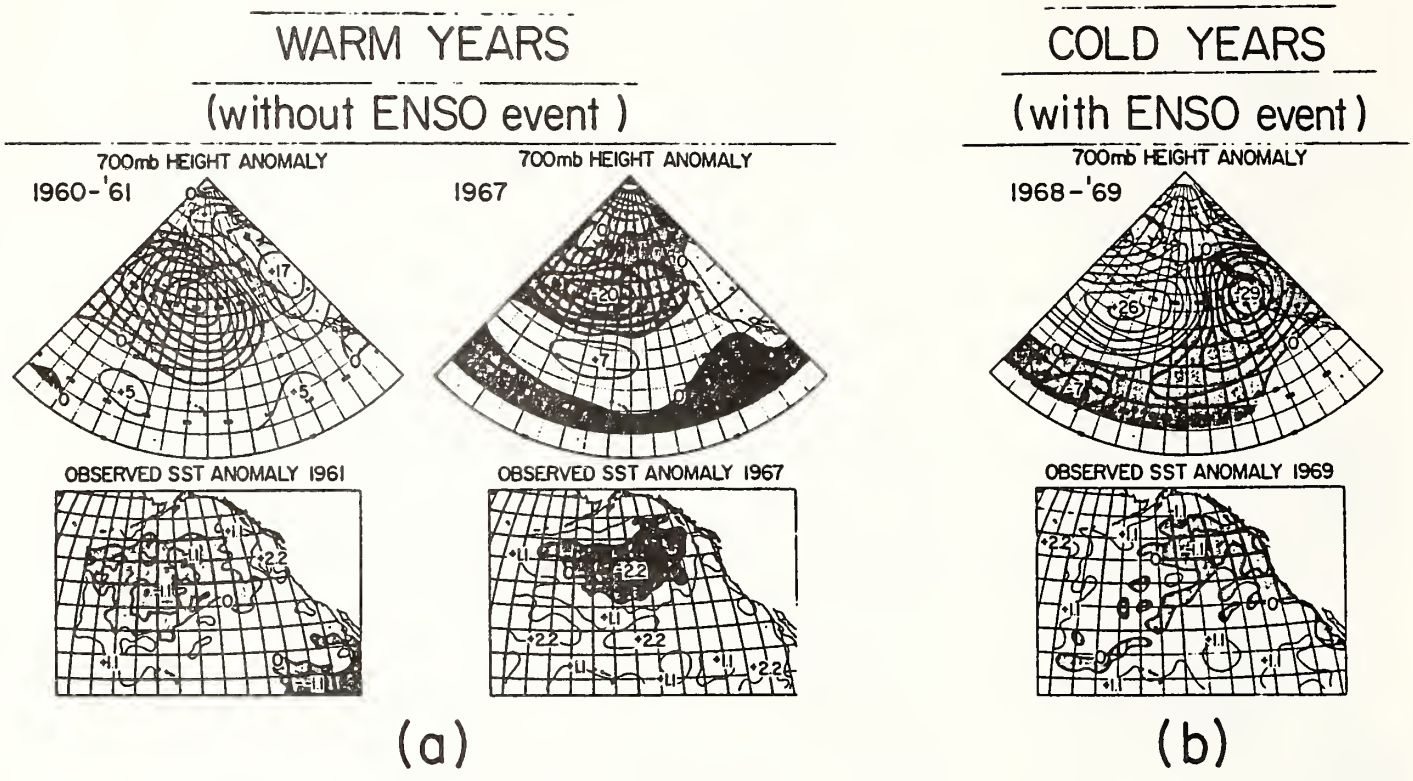

Fig. 9 (a) Large-scale wintertime (D, J, F) mid-latitude 700-mb height anomalies and observed contemporaneous SST anomalies (J) for the 1960-61 warm period and fall (S, O, N) anomalies for the 1967-68 warm period in the California Current. The 1967 SST anomaly is for October. These warm periods occurred without contemporaneous tropical ENSO activity. (b) A wintertime (D, J, F) cold period (1968-69) in the California Current associated with contemporaneous ENSO activity.

RELATIONSHIPS BETWEEN PACIFIC NORTHWEST COAST CLIMATE AND ENSO EVENTS

Brent Yarnal
Cooperative Institute for Research in Environmental Sciences
University of Colorado/NOAA
Boulder, Colorado 80309

The extremes in climate experienced during the 1982-83 ENSO have generated considerable interest in the effect such episodes have on regional climatic variation. Surprisingly, not much is known about the relationships between ENSO events and the climate of the Pacific Northwest. Here, associations between ENSO events and the winter climate of eight coastal climatological divisions (Figure 1) will be investigated, with special emphasis given to the Washington coast and southeastern Alaska in the later parts of the paper.

In each division, winter conditions are warm to very warm in about two-thirds of the eleven ENSO events analyzed, thus producing a significantly above normal temperature mean when all ENSO years are averaged (Figure 2). On the other hand, winter precipitation during ENSO events is extremely variable along the west coast (Figure 3). Because the precipitation departures are approximately balanced between the above and below normal categories, mean precipitation for all ENSO winters tends to fall in the normal range. A significant exception is the northern California coast, which on average experiences wet conditions during ENSO winters.

Winter temperature is positively correlated along the coast during all ENSO episodes (Table I). However, precipitation correlations between divisions are not so simple during ENSO years (Table II). For example, southeastern Alaska is virtually uncorrelated with all divisions from the northern British Columbia coast south to Oregon and negatively correlated with the California coastal divisions.

To determine the atmospheric circulation associated with above and below normal temperature and precipitation departures during ENSO winters, normalized 700mb anomalies are composited. The months (DJF) used are those with normalized departures greater than 0.50 or less than -0.50 at each division. For illustrative purposes, southeastern Alaska and the Washington coast are compared and contrasted here because of the lack of correlation of their precipitation data (Table II).

Figures 4, 5 and 6 show the 700mb anomalies experienced when ENSO winter mean monthly temperatures are above normal in southeastern Alaska, along the Washington coast and in both locations at the same time, respectively. In each case, a clear Pacific/North American (PNA) pattern is evident. Temperatures are above normal in southeastern Alaska in these months because of the strong southwesterly cyclonic flow of subtropical marine air generated between the negative anomaly center in the northeastern Pacific and the positive anomaly over northwestern North America. Above normal temperatures along the Washington coast result from either the same southwesterly cyclonic flow or the south-southwesterly anticyclonic flow that results if the anomalous ridge moves slightly to the west and sets up over Washington. Above normal temperatures at any division during ENSO winters are always associated with the 700mb patterns described above.

Figures 7 and 8 illustrate the 700mb anomalies that occur during ENSO winters and are related to below normal precipitation in southeastern Alaska and above normal precipitation along the Washington coast, respectively.

Figure 9 is the 700mb anomaly pattern associated with precipitation that is simultaneously below normal in southeastern Alaska and above normal on the Washington coast. In each case, southeastern Alaska is experiencing anomalous southeasterly cyclonic flow off the continent while the Washington coast is receiving southwesterly cyclonic flow off the Pacific. In all three patterns, the Aleutian low and the ridge over the North American Cordillera, both integral components of the PNA pattern, have shifted well to the southeast of their usual PNA positions. Other 700mb composites (not shown) display more PNA-like patterns and are associated with different precipitation regimes along the Anglo-American coast. Subtle shifts in the position of the trough and ridge system of the PNA can result in radical extremes in precipitation at any of the coastal divisions.

In summary, ENSO winters are usually associated with above normal temperatures along the west coast of Anglo-America. The PNA pattern that often sets up during an ENSO winter results in the advection of subtropical marine air all along the coast. Precipitation patterns are extremely variable and are much more sensitive than temperature to the shifts in the positions of the positive and negative anomaly centers of the PNA.

Table I. Correlations of normalized temperature departures during ENSO winters (DJF).

	SE ALASKA	NORTH BC	VAN ISLAND	WASH-INGTON	OREGON	NORTH CAL	CENTRAL CAL	SOUTH CAL
SE ALASKA	1.00							
NORTH BC	0.89*	1.00						
VAN ISLAND	0.78*	0.74*	1.00					
WASHINGTON	0.71#	0.58	0.94*	1.00				
OREGON	0.58	0.65	0.90*	0.91	1.00			
NORTH CAL	0.58	0.56	0.81*	0.89*	0.91*	1.00		
CENTRAL CAL	0.58	0.57	0.77*	0.84*	0.90*	0.95*	1.00	
SOUTH CAL	0.68#	0.59	0.83*	0.84*	0.88*	0.82*	0.87*	1.00

*Significant at $\alpha = 0.01$ and 9 degrees of freedom.

#Significant at $\alpha = 0.05$ and 9 degrees of freedom.

Table II. Correlations of normalized precipitation departures during ENSO winters (DJF).

	SE ALASKA	NORTH BC	VAN ISLAND	WASH-INGTON	OREGON	NORTH CAL	CENTRAL CAL	SOUTH CAL
SE ALASKA	1.00							
NORTH BC	0.09	1.00						
VAN ISLAND	-0.17	0.48	1.00					
WASHINGTON	0.05	0.23	0.65#	1.00				
OREGON	-0.14	0.03	0.32	0.81*	1.00			
NORTH CAL	-0.57	-0.34	0.21	0.40	0.71#	1.00		
CENTRAL CAL	-0.70#	-0.33	0.24	0.13	0.33	0.87*	1.00	
SOUTH CAL	-0.64#	-0.20	0.44	0.01	0.01	0.55	0.78*	1.00

*Significant at $\alpha = 0.01$ and 9 degrees of freedom.

#Significant at $\alpha = 0.05$ and 9 degrees of freedom.

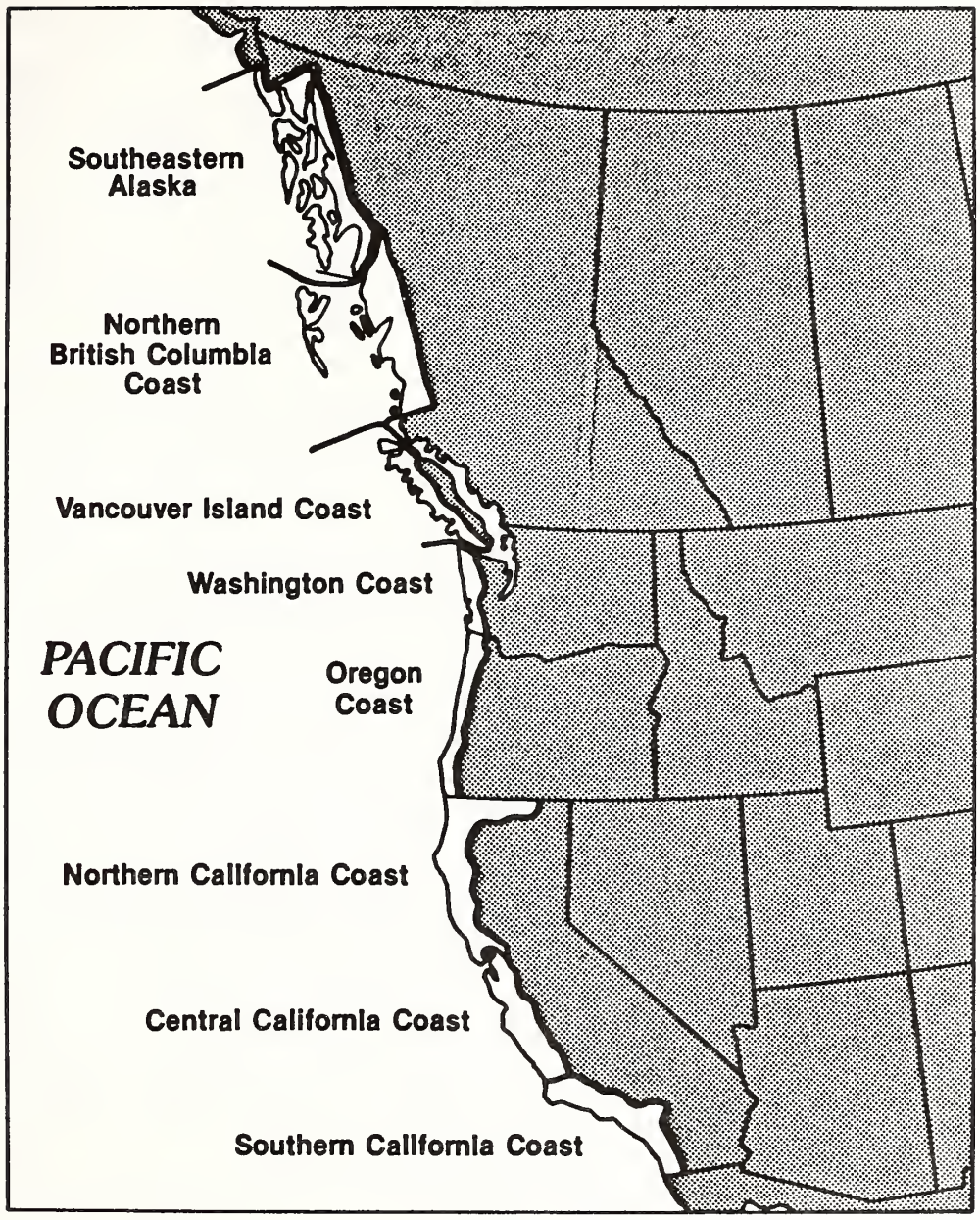

1. The climatological divisions of the Anglo-American coast.

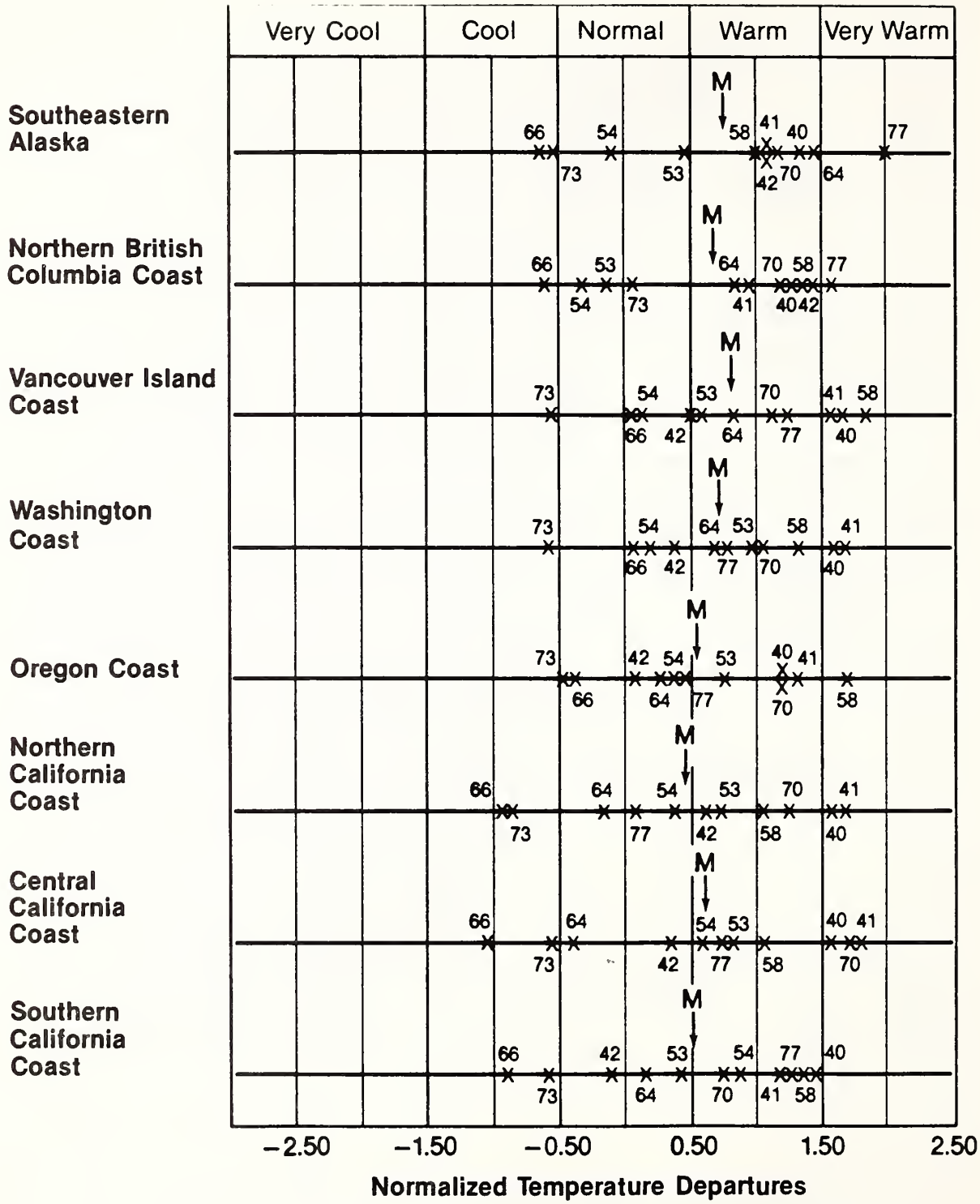

2. Normalized temperature departures of the coastal divisions during ENSO winters (DJF).

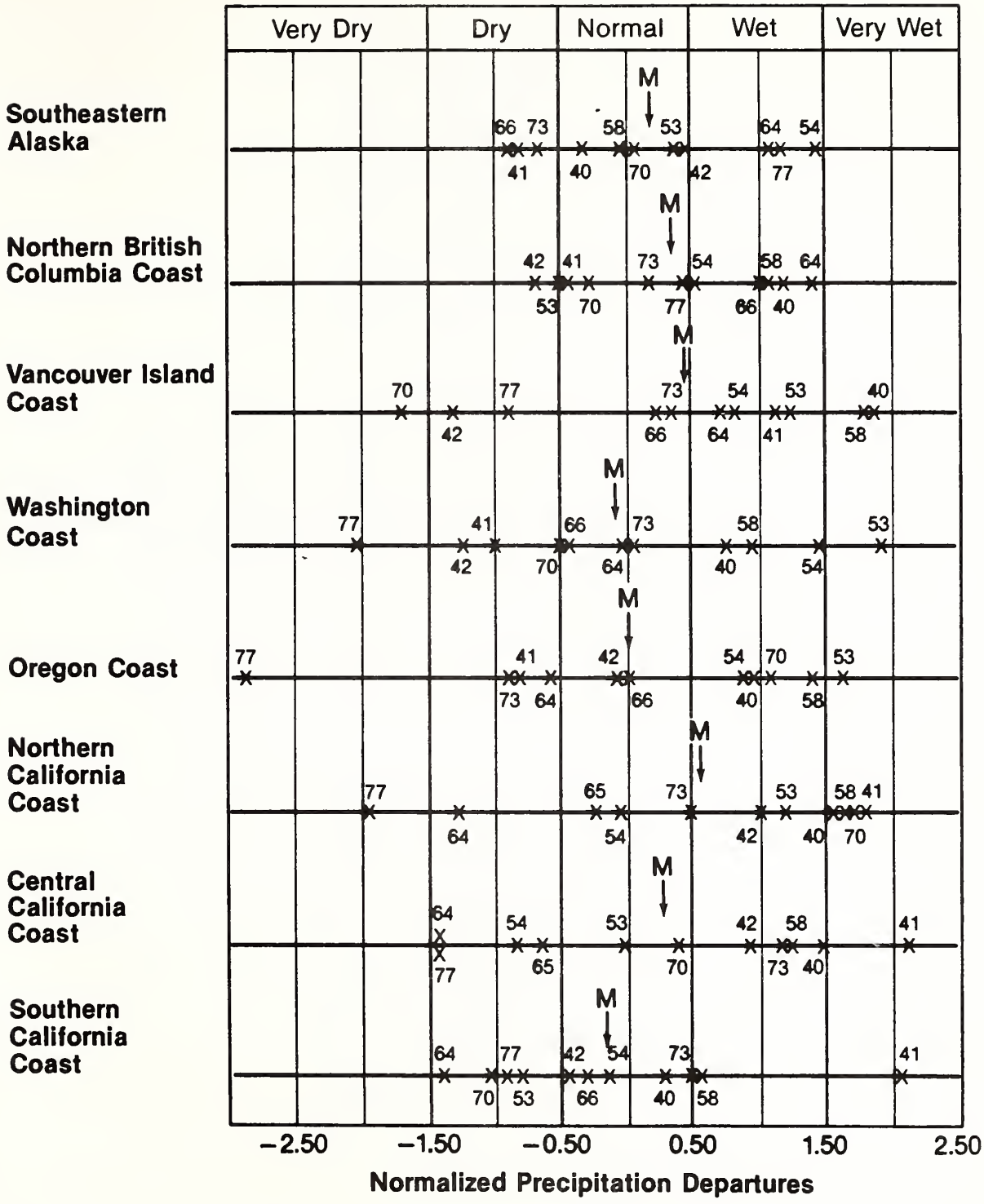

3. Normalized precipitation departures of the coastal divisions during ENSO winters (DJF).

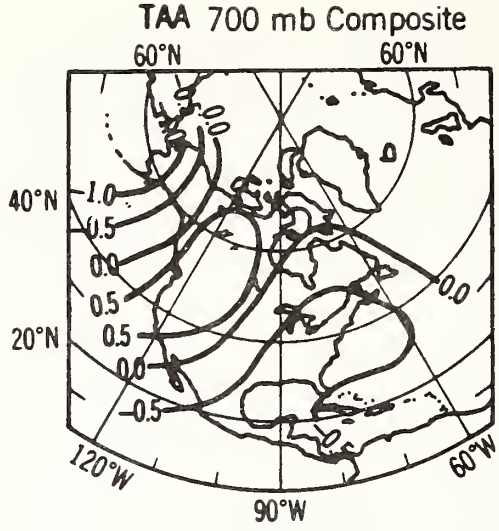

4. Normalized 700mb anomalies for those ENSO winter months when temperature in southeastern Alaska was above normal. The months used were Dec 52, Feb 53, Dec 53, Jan 58, Dec 63, Jan 64, Feb 64, Dec 69, Feb 70, Dec 76, Jan 77 and Feb 77.

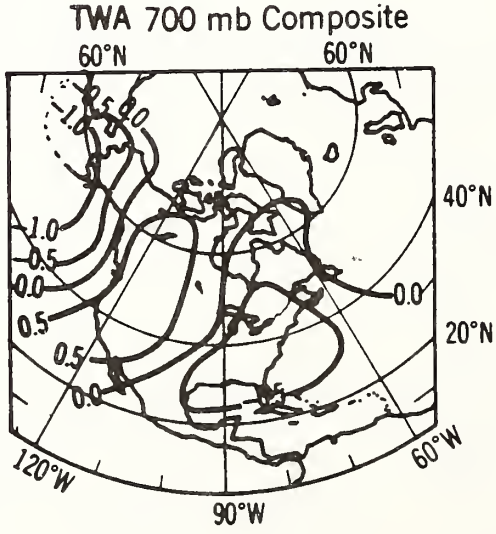

5. Normalized 700mb anomalies for those ENSO winter months when temperature along the Washington coast was above normal. The months used were Jan 53, Dec 53, Jan 58, Feb 58, Dec 63, Jan 64, Dec 69, Feb 70, Dec 76 and Feb 77.

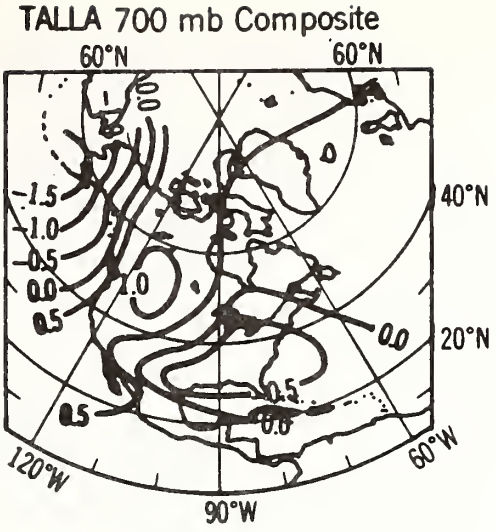

6. Normalized 700mb anomalies for those ENSO winter months when temperature both in southeastern Alaska and along the Washington coast was above normal. The months used were Dec 53, Jan 58, Dec 63, Jan 64, Dec 69, Feb 70, Dec 76 and Feb 77.

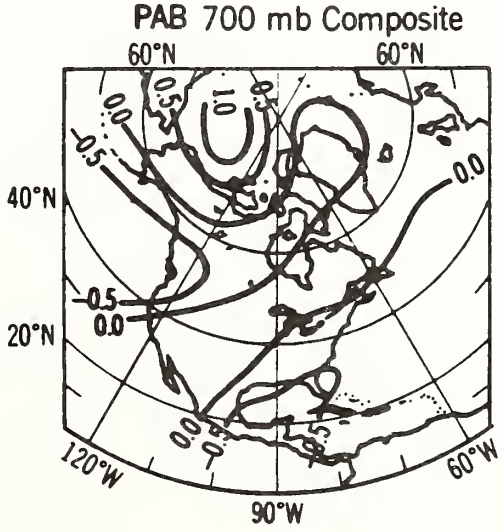

7. Normalized 700mb anomalies for those ENSO winter months when precipitation in southeastern Alaska was below normal. The months used were Jan 53, Jan 54, Feb 58, Jan 66, Jan 70 and Dec 72.

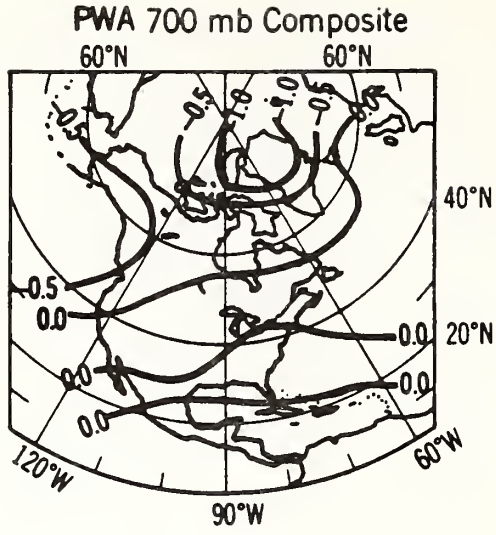

8. Normalized 700mb anomalies for those ENSO winter months when precipitation along the Washington coast was above normal. The months used were Dec 52, Jan 53, Dec 53, Jan 54, Feb 54, Jan 58, Feb 58, Jan 64 and Dec 72.

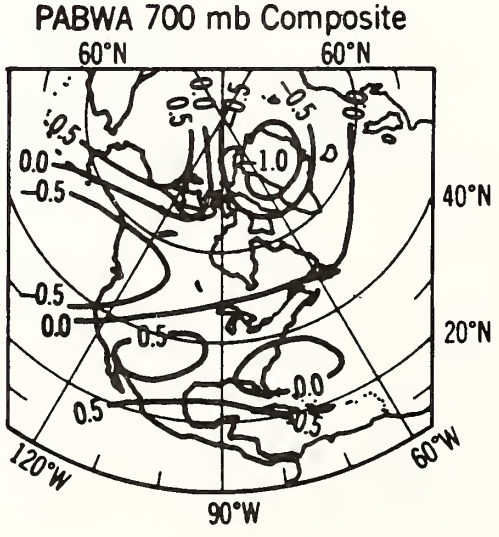

9. Normalized 700mb anomalies for those ENSO winter months when precipitation was below normal in southeastern Alaska, but above normal along the Washington coast. The months used were Jan 53, Jan 54, Feb 58 and Dec 72.

EVIDENCE OF AN 18 YEAR CYCLE IN PACIFIC NORTHWEST PRECIPITATION DATA

Philip A. Peck and Vernon C. Bissell
National Weather Service
Portland, Oregon 97218

This was a preliminary report on the basis of evidence that a cyclical pattern of about 18 years recurrence is seen in precipitation at selected stations in Western Oregon and Western Washington. The coincidence of these climate fluctuations with total solar eclipse events having periodicities of the same interval suggests that the causation may be lunar-gravitational. Drought cycles based on tree-ring analysis by Mitchell, Stockton and Meko were then compared with Pacific Northwest precipitation changes and compared with total solar eclipse periodicities. Total solar eclipse over the northern hemisphere were considered to provide the best lunar-rainfall relationship.

Nine stations in Western Washington and Northwest Oregon shown in Table 1 were used in this study. Four of these station's records were extended by using data from adjacent stations and normalizing the data. All stations have a marked winter rainfall climate.

Fig. 1 is a summation of annual precipitation for a group of three Pacific Northwest sites. Fig. 2 shows the group data after being processed by a smoothing filter. Fig. 3 resulted from applying a band pass filter with a peak frequency response of about 18 years to the group precipitation data. This was to remove high frequency noise as well as longer-term effects which may be superimposed on the signal. Other groupings were also tested using both individual stations and groupings of several stations. The analysis detected a strong response of an approximate 18 year signal in the data.

The notion that extraterrestrial forces could influence terrestrial weather has been investigated for centuries. However, consistent correlation between specific phenomena have been scarce. Therefore, the most unexpected results of this study was the discovery that fluctuations of annual precipitation in the Pacific Northwest coincided closely with the 18.03 solar total eclipse saros cycles and their corresponding 54 year repetition. Table 2 shows that the correlation is consistently good with small errors spanning thirteen events. Dates of maximum and minimum precipitation regimes were determined from the band-pass filtered data.

Results of the band-pass filter analysis were plotted on a dial harmonic graph (Figure 4) where r_i is the magnitude of the filtered peak (or valley) above (or below) zero, and theta is the phase (timing) of the event with respect to the interval between corresponding saros eclipses. The points of each group, maxima and minima precipitation events, did not plot randomly about the origin, but clustered on opposite sides of the origin indicating the filtered time series

has a periodicity and that it followed the period of the saros cycle. The results (Table 3) of F-tests on highs and lows of band-pass filtered data show the 18 year cycle is significant at the .75 level for all groupings. Two-thirds pass at the .90 and .95 level. The degrees of freedom used in the F-test were adjusted downward to account for "overlapping" of filtered data.

Mitchell, Stockton and Meko presented evidence of a 22 year drought cycle over western United States west of the Mississippi River and related it to the 22 year Hale Sunspot cycle. Table 4 compares these western United States drought peaks with the saros cycle and the Pacific Northwest maximum precipitation peaks. There is an in-step and close negative correlation between the two climate events and a close positive correlation with the saros cycle dates. Table 5 extends the comparison of the western United States drought peaks with the saros cycle and the Hale Sunspot cycle. It's apparent from the table that neither the Hale Sunspot cycle nor the total eclipse cycle can demonstrate complete statistical association with this drought evidence. However, there is evidence that the strong drought signal centered on 1781 was predominantly a West Coast event (after Fritts 1965) and that this extreme drought event coincides with and supports the Pacific Northwest precipitation cycle.

This report gives evidence for a high level of confidence that a cycle of about 18 years recurrence is present in precipitation data at selected stations in the Pacific Northwest. These climate oscillations coincide closely with total solar eclipse events which have periodicities of the same interval. Climate data from tree-ring analysis over western United States also seem to be highly correlated to total solar eclipse periodicities and highly correlated, albeit in a negative sense, to Pacific Northwest climate regimes.

It is important to note that the successful test of the hypothesis that annual precipitation in the Pacific Northwest corresponds with the 18 year saros cycle does not prove a causation involved with lunar-gravitational effects. However, the results should certainly provide an impetus for research into gravitational forcing as a possible causative mechanism for periodic phenomena in the atmosphere.

FIGURE 1

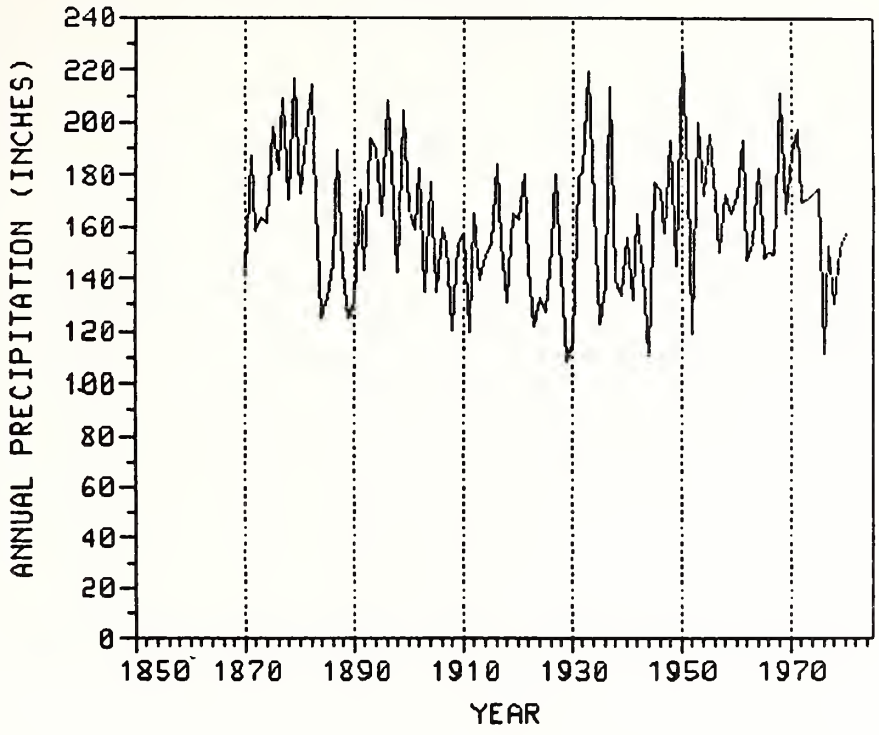

FIGURE 2

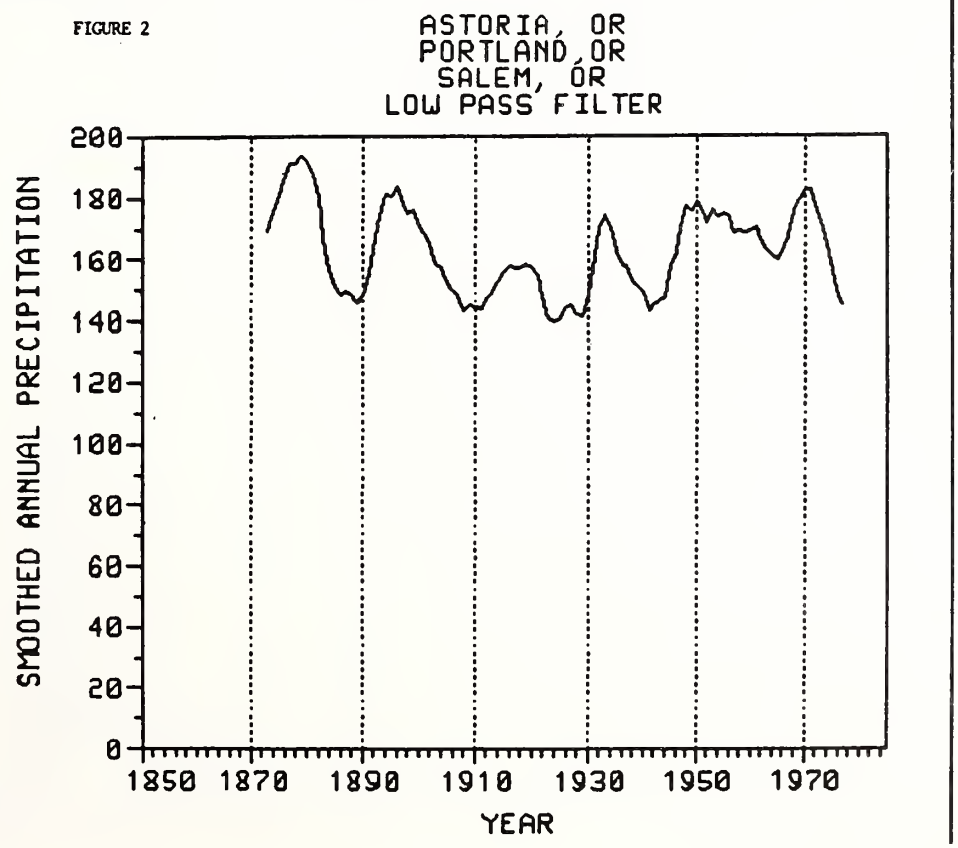

FIGURE 3

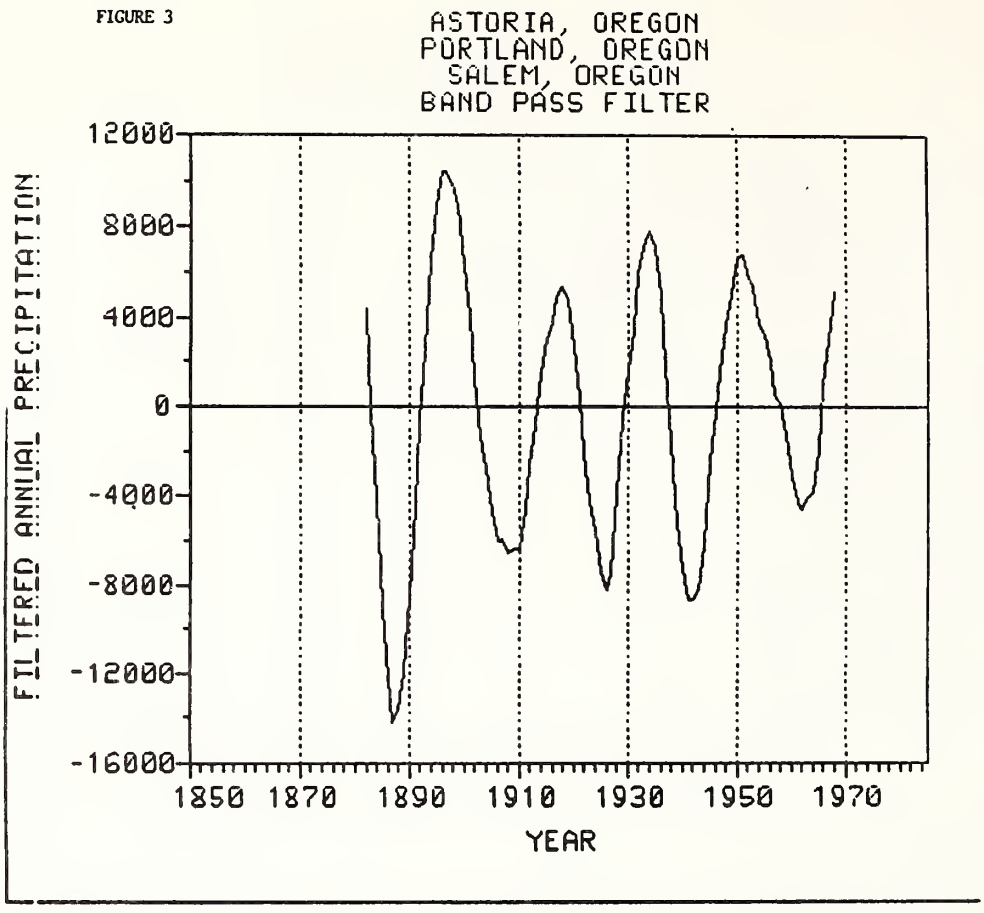

TABLE 2. Correlation between Pacific Northwest Precipitation Cycles and Total Solar Eclipse Cycles

Epoches of Pacific Northwest Maximum and (Minimum) Precipitation Cycles	Total Eclipse Cycle Average Date	ΔT			
1865.0	1862.3	-2.7 yrs			
(1871.0)	1869.8	-1.2			
1878.0	1880.4	2.4			
(1887.3)	1888.4	1.1			
1897.4	1898.5	1.1			
(1908.6)	1907.5	-1.1			
1918.3	1916.5	-1.8			
(1926.4)	1925.5	-0.9			
1934.5	1934.5	-0-			
(1942.0)	1943.6	1.6			
1950.6	1952.5	1.9	Discrepancy	=	1.48 yrs
(1962.5)	1961.5	-1.0	Mean algebraic error	=	0.15 yrs
1969.0	1971.5	2.5	RMS	=	1.65 yrs

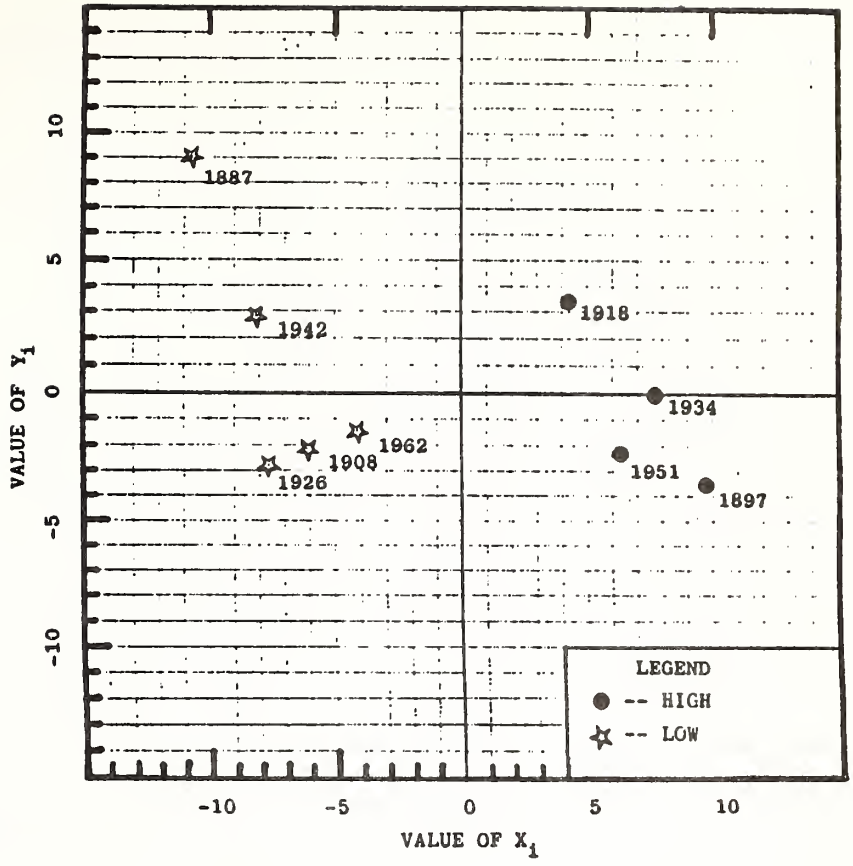

FIGURE 4

"DIAL HARMONIC" PLOT FOR BAND PASS FILTER OUTPUT USING PORTLAND (OR), ASTORIA OR), AND SALEM (OR)

TABLE 3

SUMMARY OF F-TESTS ON PEAKS AND LOWS OF BAND-PASS FILTERED ANNUAL PRECIPITATION DATA

GROUP	N	F Value	H_o REJECTED AT CONFIDENCE LEVEL OF (using adjusted confidence levels)* 0.75	0.90	0.95	.975	0.99
1. PORTLAND							
Highs	5	9.66	Yes	Yes	Yes	Yes	No
Lows	5	9.11	Yes	Yes	Yes	No	No
2. ASTORIA							
Highs	5	14.55	Yes	Yes	Yes	Yes	No
Lows	6	5.22	Yes	Yes	Yes	No	No
3. SALEM							
Highs	4	3.42	Yes	No	No	No	No
Lows	5	9.53	Yes	Yes	Yes	Yes	No
4. PORTLAND, CASCADE LOCKS							
Highs	4	3.64	Yes	No	No	No	No
Lows	4	4.99	Yes	No	No	No	No
5. SEATTLE, OLYMPIA							
Highs	4	5.26	Yes	Yes	Yes	No	No
Lows	4	4.79	Yes	No	No	No	No
6. PORTLAND, ASTORIA, SALEM, SEATTLE, OLYMPIA, CASCADE LKS							
Highs	4	9.83	Yes	Yes	Yes	No	No
Lows	4	4.79	Yes	No	No	No	No
7. ABERDEEN, NEWPORT							
Highs	3	25.93	Yes	Yes	Yes	No	No
Lows	4	15.32	Yes	Yes	Yes	Yes	No
8. ASTORIA, PORTLAND, SALEM							
Highs	4	13.01	Yes	Yes	Yes	Yes	No
Lows	5	9.01	Yes	Yes	Yes	No	No
TOTAL			16/16	11/16	11/16	5/16	0/16

*Uncorrelated would be tested using F(2,2N-2), but above tabulation shows test results using F(2,k(2N-2)) with k=5/9.

TABLE 4. Correlation between Pacific Northwest Wet Regimes and Western United States Drought Periods.

Average Lead Time = 1.4 yrs

Total Eclipse Cycle (Average Date)	Pacific NW Wet Cycles	Lead Time	Western U.S. Dry Cycles
1851.8			
1862.3	1865.0	-3.0	1862.0
1869.8			
1880.4	1878.0	+4.0	1882.0
1888.4			
1898.5	1897.4	+3.1	1900.5
1907.5			
1916.5	1918.3	-1.3	1917.0
1925.5			
1934.5	1934.5	+0.5	1935.0
1943.6			
1952.5	1950.6	+4.9	1955.5

TABLE 5. Comparison on Saros (Total Eclipse) cycle and Hale Sunspot Cycle with Western United States Drought Cycle since AD 1700.

Saros Cycle	ΔT	Western U. S. Drought Cycle	ΔT	Hale Sunspot Cycle
1715.9	(-2.1)	1711.5 (1718)	0.0	1711.5
1733.9	-2.6	1736.5	-3.3	1733.2
1751.9	-5.1	1757.0	-1.5	1755.5
1770.6) out of 1788.6) phase		1781.0	-5.7	1775.3
1807.2	+5.7	1801.5	-3.1	1798.4
1825.2	+2.2	1823.0	+0.2	1823.2
1843.3	-1.7	1845.0	-2.6	1843.4
1862.3	+0.3	1862.0	+5.2	1867.2
1880.4	-1.6	1882.0	+7.4	1889.4
1898.5	-2.0	1900.5		Skip
1916.5	-0.5	1917.0	-3.8	1913.2
1934.5	-0.5	1935.0	-1.6	1933.4
1952.5	-3.0	1955.5	-1.4	1954.1

Time-Averaging the Flux-Profile Relationship

Larry Mahrt[1], Claude Berthou[2 3], Pascal Marquet[2 4], and Jean-Claude André[2]

[1] Department of Atmospheric Sciences, Oregon State University, Corvallis (USA)
[2] Centre National de Recherches Météorologiques (DMN/EERM), Toulouse (France)
[3] Present address: Service Météorologique Inter-Régional Nord, Le Bourget (France)
[4] Present address: Service Météorologique Inter-Regional Ouest, Rennes (France)

December 1984

1. Introduction

Surface fluxes are generally related to mean flow variables by use of the bulk aerodynamic relationship and associated surface exchange coefficient. However, use of long time steps, as well as implied averaging over grid volumes can greatly alter the formal relationship between the flux and the mean flow.

The bulk aerodynamic relationship for the surface turbulent flux can be written as:

$$\left(\overline{w'\phi'}\right)_{sfc} = C_\phi \, \overline{V} \left(\overline{\phi}_{sfc} - \overline{\phi}\right) \qquad (1)$$

$$\overline{\phi} \equiv \phi + \phi' \qquad (2)$$

where ϕ is the transported quantity such as momentum, heat or moisture, C_ϕ is the surface exchange coefficient, $\overline{V}$ is the wind speed and the overbar represents time averaging. Theoretically, the specification of the exchange coefficients are based on time averaging over periods which are larger than the dominant turbulent time scales but not so large so as to include time variations due to mesoscale phenomena or diurnal variations. Then use of existing values or relationships for C_ϕ is valid only if there is no motion or variation on time scales between turbulent time scales and the model time step. Otherwise ϕ' includes variations on time scales larger than turbulent time scales and the available relationships for C_ϕ no longer apply.

The bulk aerodynamic relationship for surface heat flux, evaluated by averaging over arbitrary time steps, can be written in the format

$$\langle w'\theta' \rangle_{sfc} = C_\theta \, \langle V \rangle \left(\langle \theta_{sfc} \rangle - \langle \theta \rangle\right) \qquad (3)$$

This relationship is not equivalent to (1) unless the time step becomes identical to an average appropriate to calculation of turbulent fluxes symbolized by the overbar in (1). Otherwise the usual formulation for the exchange coefficient based on turbulence theory does not formally apply to (3).

As an example, the exchange coefficient C_θ defined by (3) is evaluated from Wangara data for the case where <> represents the diurnal average. The resulting exchange coefficient is found to be generally negative, representing average upward heat flux which is counter to the average stable temperature gradient.

To account for this transfer, we define a countergradient temperature correction in analogy to the countergradient correction applied to vertical heat

transfer in the convective boundary layer. Then the modified bulk aerodynamic relationship can be written as

$$\langle w'\theta' \rangle_{sfc} = C_\theta \langle V \rangle \, (\langle \theta_{sfc} \rangle - \langle \theta \rangle + \Delta\theta_{cg}) \qquad (4)$$

This modification allows the new exchange coefficient C_θ to assume only positive values. In particular, we now compute C_θ as a function of Richardson number using the formulation of Louis (1981)[1] and solve (4) for $\Delta\theta_{cg}$.

It is important to note that $\Delta\theta_{cg}$ in (4) represents a correction for the fact that the turbulent flux in (5-6) is related to the vertical temperature difference computed on a time scale much longer than the turbulent motions responsible for the heat flux; the actual turbulent transport would not be counter to the gradient if computed on the appropriate turbulent time scales.

Relationship (4) was evaluated using Wangara temperature data at 1m and 4m and winds at 4m. For the 33 Wangara days with complete data, the correction term $\Delta\theta_{cg}$ averages .87K and significantly exceeds the term associated with the averaged gradient $\langle\theta_{sfc}\rangle - \langle\theta\rangle$ which averaged only -.27K. This indicates that the averaged heat flux on this time scale is dominantly countergradient. However, the bulk aerodynamic relationship still seems useful since the correction is closely related to the Richardson number Ri as computed from 4m winds and temperature and 1m temperature. In general, weak winds lead to both large Richardson number and large diurnal temperature variation. The latter corresponds to situations requiring substantial correction to the heat flux formulation. It would be much preferable to formulate $\Delta\theta_{cg}$ in terms of a temperature scale representing the diurnal variation of stability. However, in modelling situations, only the averaged vertical temperature difference is available which is not adequately related to the diurnal variation of stability to use as a temperature scale without increasing scatter.

Much of the variation of $\Delta\theta_{cg}$ can be explained by a linear relationship to the Richardson number of the form

$$\Delta\theta_{cg}(K) = 0.188(K) + 10.52(K)\ Ri \ . \qquad (7)$$

This relationship has been calibrated for diurnal averages. It is not known how much this relationship would vary with other meteorological situations and with choice of levels for computing gradients and the Richardson number.

If we use the 33-day average of the variables in order to simulate a model based on monthly averages, the mean actual temperature difference is +.27K (stable); however, again the actual mean heat flux is upward so that the countergradient correction factor is greater than the average actual temperature difference. Here the mean correction value is .62K.

The countergradient correction addresses the most flagrant averaging errors in the simplest possible manner and should at least correct for the sign error in the surface heat flux. However, the countergradient correction is not expected to be useful for momentum.

Louis, J.-F., 1981: Future developments at ECMWF. In Proc. Workshop on Planetary Boundary-Layer Parameterization, European Center for Medium Range Weather Forecasts, Reading, 249-260.

ATMOSPHERIC GENERAL CIRCULATION MODEL SIMULATIONS OF THE MODERN ANTARCTIC CLIMATE

Michael E. Schlesinger

Department of Atmospheric Sciences
and
Climatic Research Institute
Oregon State University
Corvallis, Oregon 97331

In this paper the modern summer and winter climates in and around Antarctica simulated by six contemporary global atmospheric general circulation models (AGCMs) are compared with the corresponding observed climates. The models are listed in Table 1 along with their characteristics and simulations. The simulated and observed climates are presented in terms of their surface air temperatures, sea-level pressures, precipitation rates, and cyclogenesis and cyclone tracks. Results for selected model simulations are presented in Figs. 1-3. A more complete presentation and intercomparison of the simulated and observed climates is given by Schlesinger (1984). A discussion of this intercomparison is given below.

Surface Air Temperature

The surface air temperatures simulated by the models over Antarctica are 10°C warmer than the observed temperatures in summer, and 15°C warmer in winter. These errors may be a consequence of the models' prescribed topographies which have been smoothed in accord with their horizontal resolution and are, therefore, of lower elevation than in reality. Alternatively, the surface air temperature observations of Taljaard *et al.* (1969) may be colder than reality. In fact, the most recently published global atmospheric circulation statistics (Oort, 1983) show observed temperatures over Antarctica which are 20°C warmer than the Taljaard *et al.* (1969) observations for summer, and 30°C warmer in winter. Clearly, if these most recently published observations are correct the models are 10° to 15°C colder than reality rather than vice versa!

The surface air temperatures simulated by the models over the Antarctic sea ice are generally warmer than the observed temperatures in summer, and both warmer and colder in winter. These errors are not due to the models' prescribed topographies, and there appears to be less difference between the Taljaard *et al.* (1969) and Oort (1983) observations around the Antarctic coast. It may be that too much solar radiation is absorbed by the sea ice as a result of its prescribed surface albedo being too small, or that too much longwave radiation is incident on the sea ice as a result of an overestimate in the simulated cloudiness and/or a cloud emissivity which is too large. In any event, the most recent (satellite) observations of the extent of sea ice (Zwally *et al.* 1983) show that the Antarctic sea ice prescribed for some of the AGCMs, at least those based on the data of Alexander and Mobley (1976), is more extensive than in reality. (However, this would likely cause those models to underestimate the surface air temperature over the sea ice.)

The surface air temperature simulated by the models over the southern hemisphere oceans is in reasonable agreement with the observed surface air temperatures. This of course is not surprising since the underlying sea surface temperatures are prescribed and, therefore, strongly constrain the surface air temperatures. In fact, the surface air temperature errors which are displayed by the models over the oceans may, to a large extent, reflect the differences among the observed sea surface temperature data sets shown in Table 1. Consequently, to validate the AGCMs over the ocean it is necessary to compare their simulated surface fluxes of heat (and moisture and momentum), in addition to their surface air temperatures, with the observations insofar as possible.

Sea-Level Pressure

The sea-level pressures simulated by the models are in reasonable agreement with the observed sea-level pressures in the southern hemisphere subtropics in both summer and winter. The models are less successful in simulating the subpolar trough (SPT) around Antarctica, generally placing it equatorward of its observed position with an intensity that is too weak. The OSU model simulates the summer SPT with some fidelity, while the NCAR model simulates the winter SPT reasonably well. Only the UCLA model reproduces both the summer and winter SPT with some accuracy. Since this model has the highest horizontal resolution of all the grid point models (Table 1), its comparatively superior performance suggests that horizontal resolution may be an important factor in simulating the SPT reasonably well. This conjecture is given some support by the weak SPT simulated by the grid point model with the lowest horizontal resolution, namely, the GISS model. In any event the models' relatively poor simulation of the SPT is tantamount to the simulated surface geostrophic westerly winds being generally much weaker than the observed geostrophic westerly winds. This surface wind error is likely to cause serious errors in the simulated sea surface temperatures and oceanic circulation around Antarctica when the AGCMs are coupled with dynamical models of the ocean.

The sea-level pressures simulated over Antarctica by all the models are higher than the observed sea-level pressures by 20 to 50 mb in winter. It is likely that these errors are due in part to the methods used to reduce the surface pressure to sea level over the great elevation of most of Antarctica. However, the facts that the simulated surface air temperatures are warmer than the observed temperatures and the prescribed surface elevation less than in reality suggest that the sea-level pressures should be underestimated by the models. Also, not all the models overestimate the Antarctic sea-level pressure in summer; the GISS and OSU models give a reasonably accurate representation, and the UCLA model considerably underestimates the observed sea-level pressure. This suggests that at least part of the winter sea-level pressure errors represents an actual error in the distribution of mass over Antarctica. This conjecture is given some support by the models' underestimate of the SPT, an error which occurs over the ocean and, therefore, clearly is not due to any reduction to sea level error.

Precipitation

The Jaeger (1976) precipitation observations show a precipitation maximum greater than 5 mm day^{-1} at 60°S around much of Antarctica in summer (January), and a precipitation minimum less than 0.5 mm day^{-1} at 60°S also around much of Antarctica in winter (July). None of the models simulates the observed summer maximum, and only two of the models display precipitation rate features which bear some resemblance to a minimum, albeit weaker and more equatorward than the observed. However, the absence of these summer and winter precipitation extrema in the model simulations may not be errors because the Möller (1951) seasonal precipitation observations (December-January-February and June-July-August) show neither the summer maximum nor the winter minimum.

On the other hand, both the Jaeger (1976) and Möller (1951) observations show a precipitation maximum in excess of 5 mm day^{-1} located off the west coast of South America near 50°S in summer and 45°S in winter. Most of the models are not successful in simulating this precipitation maximum. The GFDL model simulates a summer maximum but with half the observed intensity and no winter maximum, the NCAR model simulates the winter maximum with about the observed intensity but no summer maximum, and the GISS, GLAS and OSU models neither maximum. Only the UCLA model reproduces the precipitation maximum in both summer and winter.

The precipitation simulated by the models is generally larger than the observed precipitation over East Antarctica, and less than the observed over the Palmer Pensinsula and the coast of Ellsworth Land. However, the latter may not be a simulation error because the Möller (1951) precipitation observations are about half the Jaeger (1976) precipitation observations in this region. Although a precise comparison between the simulated and observed precipitation rates over the Antarctic interior cannot be made for all the models because of the lack of sufficiently small contour levels, the models generally appear to overestimate the observed rate by a factor of about two.

Cyclogenesis and Cyclone Tracks

The results from the predecessors of two of the models considered here show an absence of cyclogonesis over the east coast of South America and southeast of Africa. As suggested by Mechoso *et al.* (1979), this may be a consequence of the models' smoothed representations of the Andes Mountains and the African Highlands. On the other hand, the results of Mechoso (1981) suggest that if the elevation of Antarctica were raised, more cyclones would form off the coast of Antarctica in apparent further disagreement with the observations.

Recommendations

Based on the discussion above, the following recommendations for further research are made:

- Critically appraise the observations and quantify their standard errors
- Determine why most models underestimate the intensity of the Antarctic subpolar trough, and why most improvements in this feature result in the generation of an "Arctic subpolar trough"
- Determine whether the errors in the simulated surface air temperatures, precipitation rates and cyclogenesis are the result of the prescribed orography being too low in elevation and too smooth
- Determine whether sea-level pressure errors over Antarctica are due to an erroneous method of reduction to sea level or represent an error in the distribution of mass.
- Compare the models' simulated variables in the free atmosphere such as temperature, winds, moisture and clouds with observations
- Compare the components of the surface energy budget (solar radiation, upward and downward longwave radiation, sensible and latent heat fluxes) simulated by the models with observations
- Extend the comparisons shown here and recommended above to as many AGCMs as possible.

Acknowledgements

I would like to thank Douglas G. Hahn, Jim Hansen, Jagadish Shukla, Eric J. Pitcher and Carlos R. Mechoso for making available to me the results from the GFDL, GISS, GLAS, NCAR and UCLA models, respectively. I express my gratitude to R.L. Mobley for preparing the graphics for the OSU model, L. Riley for typing the manuscript, M.B. Schlesinger and M.L. Schlesinger for their help with the figures, and J. Stark for drafting the figures. Support for this study was provided by the Polar Research Board of the National Academy of Sciences, and the National Science Foundation under grant ATM-8205992.

REFERENCES

Alexander, R.C., and R.L. Mobley, 1976: Monthly average sea-surface temperatures and ice pack limits on a 1° global grid. *Mon. Wea. Rev., 104*, 143-148.

Bakayev, V.G., ed, 1966: *Atlas Antarktiki Moscow*, Glavnoe Upravlenie Geodezii i Kargografii MG SSSR, 225 pp.

British Meteorological Office, 1977: Monthly Ice Charts, Meteorological Office, London Road, Bracknell, Berkshire.

Defant, A., 1961: *Physical Oceanography, Vol. I.* Pergamon, New York, 729 pp.

Hahn, D.G., 1983: Personal communication.

Hansen, J., G. Russell, D. Rind, P. Stone, A. Lacis, S. Lebedeff, R. Ruedy and L. Travis, 1983: Efficient three-dimensional global models for climate studies: Models I and II. *Mon. Wea. Rev., 111* 609-662.

Jaeger, L., 1976: Monatskarten des Niederschlags für die ganze Erde. *Ber. Deutsch. Wetterdienstes* Nr. 139, Offenbach, 38 pp.

Jenne, R.L. 1975: Data sets for meteorological research. NCAR Technical Note NCAR-TN/IA-111, National Center for Atmospheric Research, Boulder, CO, 194 pp.

Manabe, S., and D.G. Hahn, 1981: Simulation of atmospheric variability. *Mon Wea. Rev., 109,* 2260-2286.

Mechoso, C.R., 1981: Topographic influences on the general circulation of the Southern Hemisphere: A numerical experiment. *Mon. Wea. Rev., 109,* 2131-2139.

Mechoso, C.R., M.J. Suarez and A. Arakawa, 1979: July simulation by the UCLA general circulation model. In *Fourth Conference on Numerical Weather Prediction,* Amer. Meteor. Soc., 282-289.

Mechoso, C.R., M.J. Suarez, K. Yamazaki, J.A. Spahr and A. Arakawa, 1982: A study of the sensitivity of numerical forecasts to an upper boundary in the lower stratosphere. *Mon. Wea. Rev., 110,* 1984-1993.

Möller, F., 1951: Vierteljahrskarten des Niederschlags fur die ganze Erde. *Petermann's Geog. Mitt., 95,* 1-7.

Oort, A.H., 1983: Global Atmospheric Circulation Statistics, 1958-1973. NOAA Professional Paper No. 14, U.S. Government Printing Office, Washington, D.C., 180 pp.

Pitcher, E.J., R.C. Malone, V. Ramanathan, M.L. Blackmon, K. Puri and W. Bourke, 1983: January and July simulations with a spectral general circulation model. *J. Atmos. Sci., 40,* 580-604.

Robinson, M., and R. Bauer, 1981: *Oceanographic Monthly Summary, 1*, No. 2, NOAA National Weather Service, W322, Washington, D.C., pp. 2-3.

Schlesinger, M.E., and W.L. Gates, 1981: Preliminary analysis of the mean annual cycle and interanual variability simulated by the OSU two-level atmospheric general circulation model. Report No. 23, Climatic Research Institute, Oregon State University, Corvallis, OR, 47 pp.

Schutz, C., and W.L. Gates, 1971: Global climatic data for surface, 800 mb, 400 mb: January. R-915-ARPA, The Rand Corporation, Santa Monica, CA, 173 pp.

Schutz, C., and W.L. Gates, 1972: Global climatic data for surface, 800 mb, 400 mb: July. R-1029-ARPA, The Rand Corporation, Santa Monica, CA, 180 pp.

Taljaard, J.J., H. van Loon, H.L. Crutcher and R.L. Jenne, 1969: *Climate of the Upper Air: Southern Hemisphere. Vol. 1. Temperatures, Dew Points and Heights at Selected Pressure Levels*. NAVAIR Publ. 50-1C-55, Naval Weather Service Command, Washington, D.C.

U.S. Naval Oceanographic Office (U.S. Navy Hydrographic Office), 1944. World Atlas of Sea Surface Temperatures, 2nd ed., H.O. Publ. No. 225, Washington, D.C.

U.S. Naval Oceanographic Office, 1957. Oceanographic Atlas of the Polar Seas, Part I. Antarctic. H.O. Publ. No. 705, Washington, D.C.

U.S. Naval Oceanographic Office, 1958. Oceanographic Atlas of the Polar Seas, Part II. Arctic. H.O. Publ. No. 705, Washington, D.C.

U.S. Naval Oceanographic Office, 1967a. Monthly charts of mean, minimum, and maximum sea surface temperature of the Indian Ocean. SP-99, Washington, D.C.

U.S. Naval Oceanographic Office, 1967b. Oceanographic Atlas of the North Atlantic Ocean, Section II: Physical Properties. Publ. No. 700, Washington, D.C.

U.S. Naval Oceanographic Office, 1969. Monthly charts of mean, minimum, and maximum sea surface temperature of the North Pacific Ocean. SP-123, Washington, D.C.

Wigle, W.F., and B.R. Mendenhall, 1974: Climatology of upper thermal structure of the seas. Technical Report M-196, Meteorology International Incorporated, Monterey, CA, 79 pp.

Zwally, H.J., J.C. Comiso, C.L. Parkinson, W.J. Campbell, F.D. Carsey and P. Gloersen, 1983: Antarctic sea ice, 1973-1976: Satellite passive microwave observations. NASA SP-459, National Aeronautics and Space Administration, Washington, D.C., 206 pp.

TABLE 1. GENERAL CIRCULATION MODELS, CHARACTERISTICS AND SIMULATIONS

MODEL	CHARACTERISTICS			SIMULATIONS
	Number of Vertical Layers & Top Pressure	Horizontal Representation & Resolution	Prescribed SST Sea Ice	Identity of Summer/ Winter Months and Number Averaged
GFDL[a] (Manabe & Hahn, 1981; Mechoso, 1981; Hahn 1983)	9 0 mb	Spectral, 15 waves in both latitude & longitude	U.S. Naval Oceanographic office (1944, 1957, 1958, 1967a,b, 1969)	Jan/Jul 15
GISS[b] (Hansen *et al.*, 1983)	9 10 mb	Grid Point, 8° latitude & 10° longitude	Robinson & Bauer (1981)	Jan/Jul[g] 5
GLAS[c] (Shukla *et al.*, 1981)	9 10 mb	Grid Point, 4° latitude & 5° longitude	SST: Same as GFDL Sea Ice: British Met. Office (1977)	Feb/Jul 1
NCAR[d] (Pitcher *et al.*, 1983)	9 0 mb	Spectral, 15 waves in both latitude & longitude	Alexander & Mobley (1976)	Jan/Jul Perpetual[h]
OSU[e] (Schlesinger & Gates, 1981)	2 200 mb	Grid Point, 4° latitude & 5° longitude	Alexander & Mobley (1976)	Jan/Jul 10
UCLA[f] (Mechoso 1979, 1982)	15 1 mb	Grid Point, 2.4° latitude & 3.0° longitude	SST: Wigle & Mendenhall (1974); Antarctic sea ice: Bakayev (1966); Arctic sea ice: Defant (1961)	Jan/Jul 1

[a]Geophysical Fluid Dynamics Laboratory/NOAA, Princeton University, NJ.

[b]NASA Goddard Space Flight Center Institute for Space Studies, New York, NY.

[c]NASA Goddard Space Flight Center Laboratory for Atmospheric Sciences Modeling and Simulation Facility, Greenbelt, MD.

[d]National Center for Atmospheric Research, Boulder, CO.

[e]Oregon State University Climatic Research Institute, Corvallis, OR.

[f]University of California, Los Angeles Department of Atmospheric Sciences.

[g]For precipitation the seasonal averages for December-January-February and June-July-August are shown.

[h]Each simulation was for 200 days with fixed (perpetual) insolation, SST and sea ice.

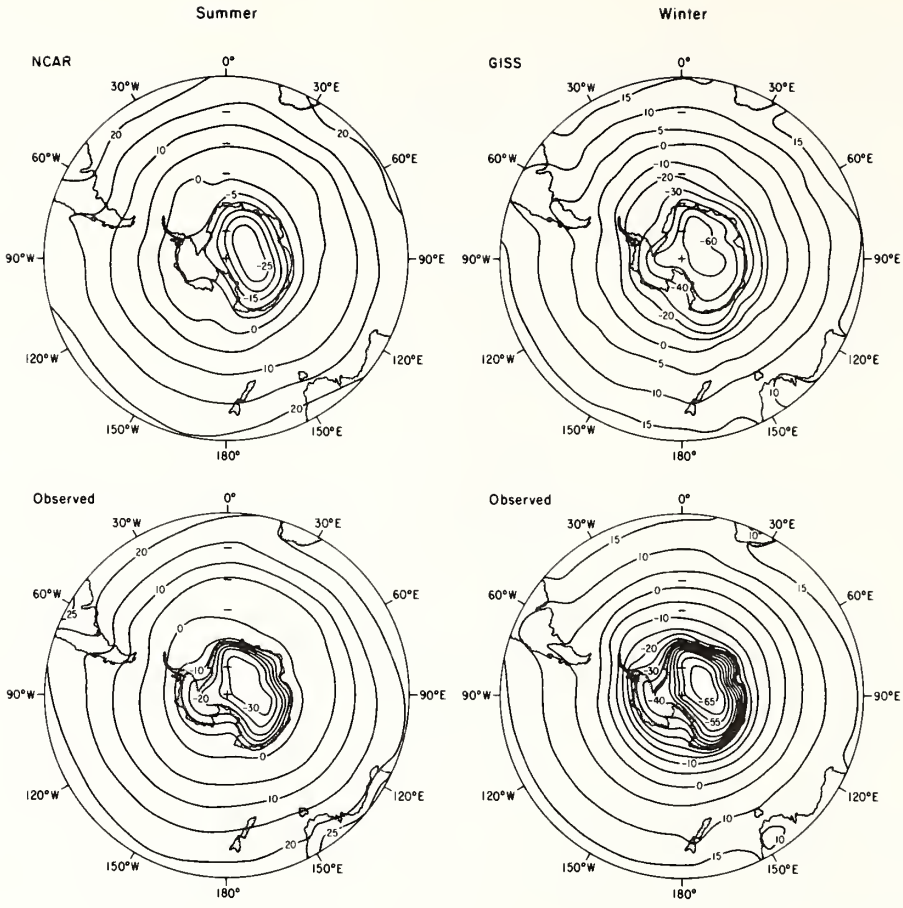

Fig. 1. The simulated and observed southern hemisphere surface air temperatures (°C) for summer and winter. The mean January temperature simulated by the NCAR model is shown for summer, and the mean July temperature simulated by the GISS model is shown for winter. The observed January and July temperatures are based on Taljaard *et al.* (1969) as available from the NCAR archive (Jenne 1975).

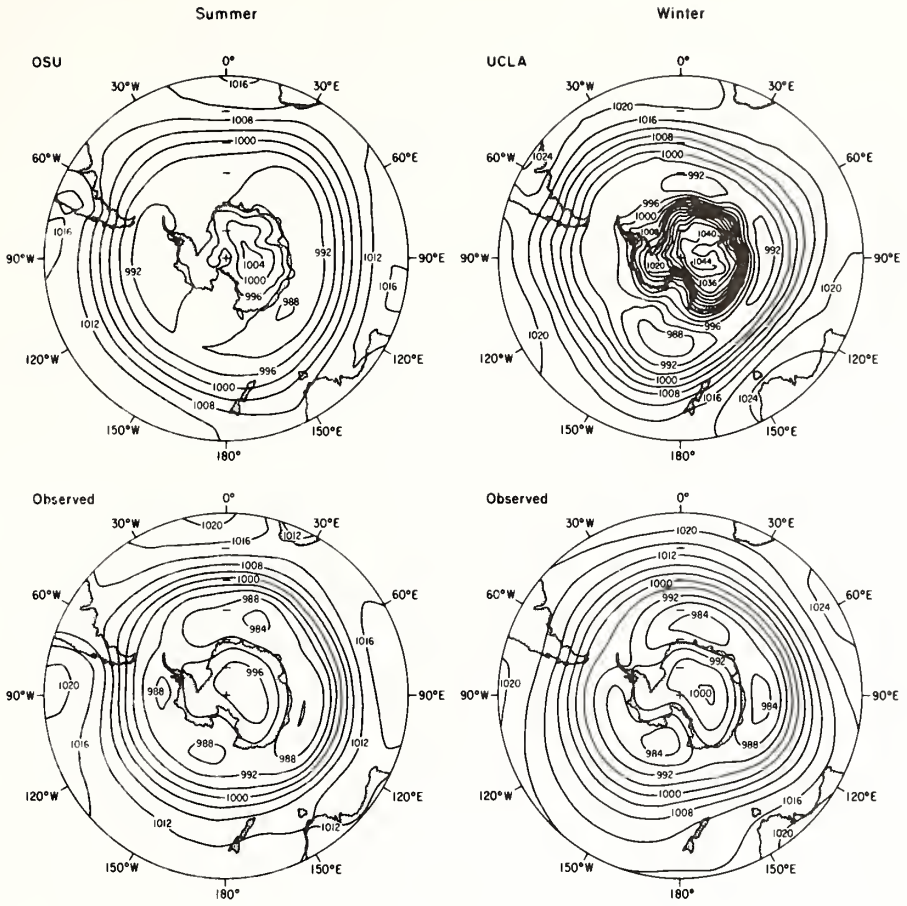

Fig. 2. The simulated and observed southern hemisphere sea-level pressure (mb) for summer and winter. The mean January sea-level pressure simulated by the OSU model is shown for summer, and the mean July sea-level pressure simulated by the UCLA model is shown for winter. The observed January and July sea-level pressures are based on Taljaard *et al.* (1969), as tabulated by Schutz and Gates (1971, 1972).

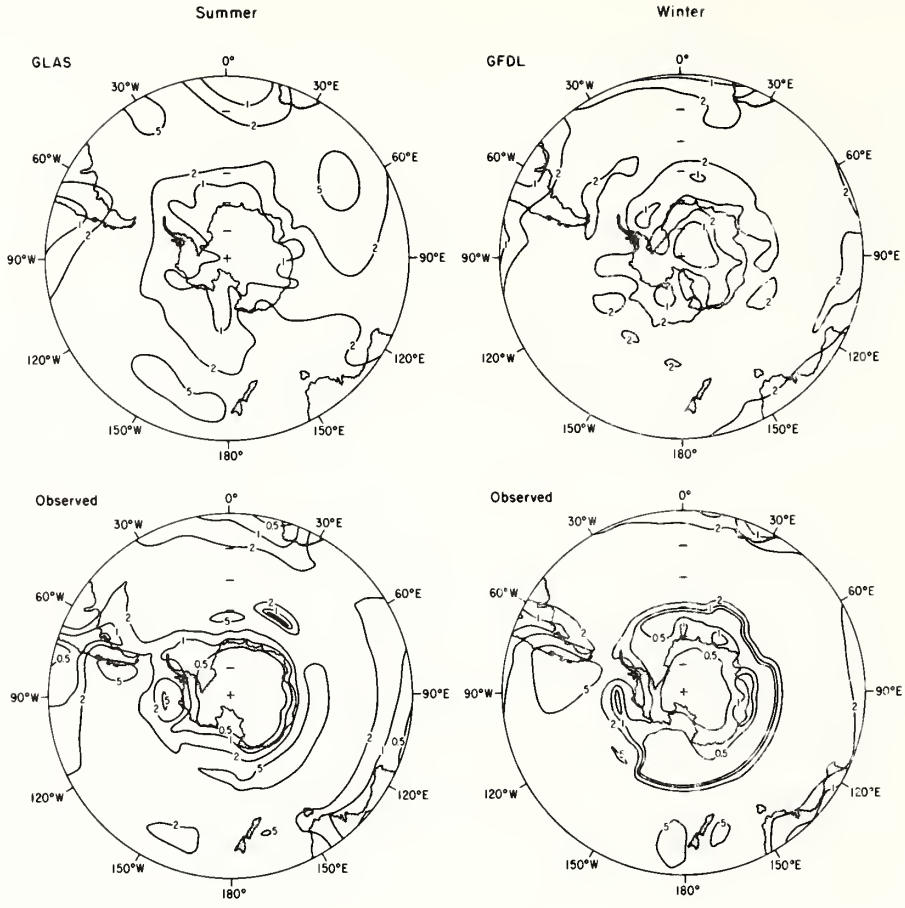

Fig. 3. The simulated and observed southern hemisphere precipitation rate for summer and winter. The mean February precipitation rate simulated by the GLAS model is shown for summer, and the mean July precipitation rate simulated by the GFDL model is shown for winter. The observed January and July precipitation rates are based on Jaeger (1976).

Atmospheric Response to an Equatorial Pacific Sea Surface Temperature Anomaly: The Effects of Orography

M.L. Blackmon and G.T. Bates
National Center for Atmospheric Research
Boulder, CO 80307

J.E. Geisler
Department of Meteorology
University of Utah
Salt Lake City, UT 84112

We first describe the design of our general circulation model experiments, all of which have been done using the Community Climate Model (CCM) at NCAR. All of these experiments are perpetual January, and they start at day 200, this being the time taken to spin up the model to some natural climatic state which we take as the initial condition in all the experiments. A typical experiment runs for 1200 days after that. We take this record and divide it into eight 90-day segments, each separated by a 60-day segment which we cut out of the record. This leaves us with 8 independent 90-day realizations of winter climate, each of which is then averaged over the 90-day span. We refer to the average of those eight samples as an "ensemble average." We have two basic categories of such ensemble-average winter climates. One is the control ensemble; the other is the anomaly ensemble, in which the SST pattern is that used for the control experiment plus some SST anomaly in the equatorial Pacific.

Fig. 1a shows the SST anomaly that was used for the study we report on here. It has the shape of the Rasmusson and Carpenter composite anomaly, with the amplitude scaled up by a factor of two to provide something typical of an individual (rather than a composite) warm equatorial Pacific event. Maps of the anomalous atmospheric response to this SST anomaly are derived by subtracting ensemble-average control-run fields from ensemble-average anomaly-run fields. Fig. 1b shows the 200 mb height anomaly. We focus on two features of this anomalous response: the tropical anticyclone pair and the chain of alternating highs and lows that has come to be called the PNA pattern.

Not shown here is a positive anomaly of precipitation, amounting to about 226 cm per month, located between the centers of the tropical anticyclone pair pattern. It is generally agreed that upward vertical motion balancing the associated latent heat release is what spins up the tropical anticyclone pair. There are, however, two schools of thought regarding the dynamics involved in the maintenance of the PNA pattern. One says that the PNA pattern is a standing Rossby wave forced by anomalous latent heat release -- that is, that the pattern is maintained against dissipation by a flux of energy from the tropics into middle latitudes. The other school says that the PNA pattern is a preferred mode of the atmosphere that draws energy from the basic-state (time-average) flow of the midlatitude upper

troposphere, primarily through a term $(v'^2 - u'^2)\partial\bar{u}/\partial x$, this eddy-mean flow interaction being essentially a form of barotropic instability in a zonally asymmetric mean flow. In this picture the tropical heating anomaly serves to excite the mode, which then feeds off the midlatitude flow field, growing to some considerably larger amplitude and maintaining itself.

The real truth may be somewhere in between. The purpose of this paper is to present results of a recent experiment indicating that the eddy-mean flow interaction seems to be an important mechanism in the CCM. To do this, we change the basic state $\bar{u}$ field in such a way that $\partial\bar{u}/\partial x$ is decreased in the region of the PNA pattern where this energy generation term

$$(v'^2 - u'^2)\frac{\partial \bar{u}}{\partial x}$$

is largest and show that in this new $\bar{u}$ field the amplitude of the PNA pattern is much reduced.

In Fig. 2a we show contours of $\partial\bar{u}/\partial x$ in the standard basic state. In Fig. 2b we show again the PNA pattern from Fig. 1b. Note the superposition of an elongated height anomaly ($u'^2 > v'^2$) and the region of negative $\partial\bar{u}/\partial x$ in the midlatitude Pacific.

In order to change the basic state flow pattern, we remove all orography from the model and repeat the SST anomaly experiment just described. In Fig. 3a we show $\partial\bar{u}/\partial x$ for this no-orography basic state. In Fig. 3b we show the 200 mb height anomaly that is due to the presence of the SST anomaly in Fig. 1a. We return to this slide in a moment, but first compare the result with the 200 mb height anomaly in the standard basic state experiment (Fig. 4). The essential point is that the amplitude of the tropical anticyclone pair is larger in the new experiment. So also is the rainfall anomaly (30 cm per month versus 226), although that is not shown here. The PNA pattern, on the other hand, is reduced in amplitude by something like a factor of two in the new experiment. Also of interest is the appearance of a PNA-type pattern in the Southern Hemisphere.

Comparing Figs. 2a and 3a, we see that the energy generation parameter $\partial\bar{u}/\partial x$ in the no-orography experiment is reduced by some 30% in the midlatitude Pacific region. Also, for reasons not clear, the height field anomaly in the region (Fig. 3b) is much more circular than before (Fig. 2b), giving $u'^2 \approx v'^2$ in the region. Both factors conspire to reduce the rate of energy extraction from the basic state $\bar{u}$ field.

That is our result, but I would like to go on to describe another matter of interest, and that is a comparison of the $\bar{u}$ field in the cases with and without orography. The respective fields are shown in Figs. 5a and 5b. There is not as large a difference between these two fields as we expected to find. In particular the $\bar{u}$ jet on the coast of Asia is not greatly altered by the removal of orography. We can say quite conclusively from these two experiments that this jet is maintained by land-sea thermal contrast rather than by orographic forcing. We note also that the lateral extent and intensity of the region of easterlies extending westward from Indonesia to India is also not a consequence of orography. The North American jet is somewhat diffused by the removal of orography but remains an identifiable feature.

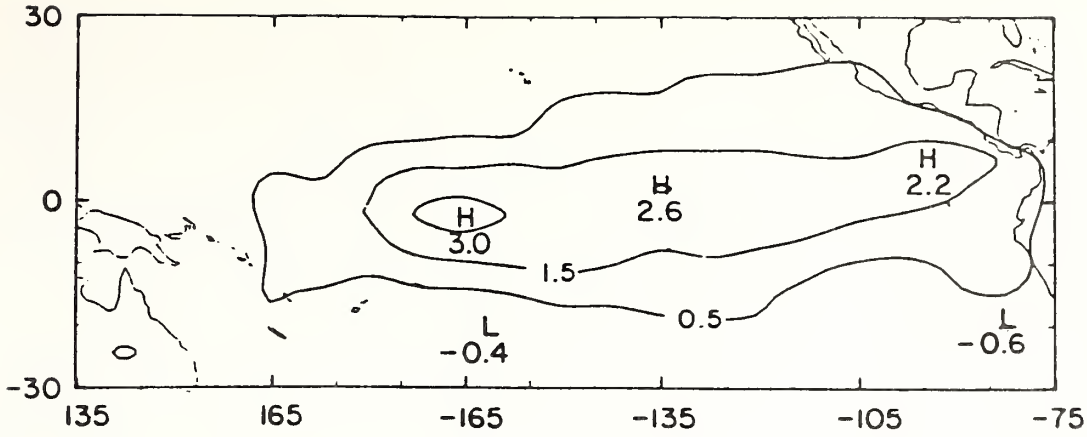

Fig. 1a Equatorial Pacific sea surface temperature anomaly (K) used in this model study.

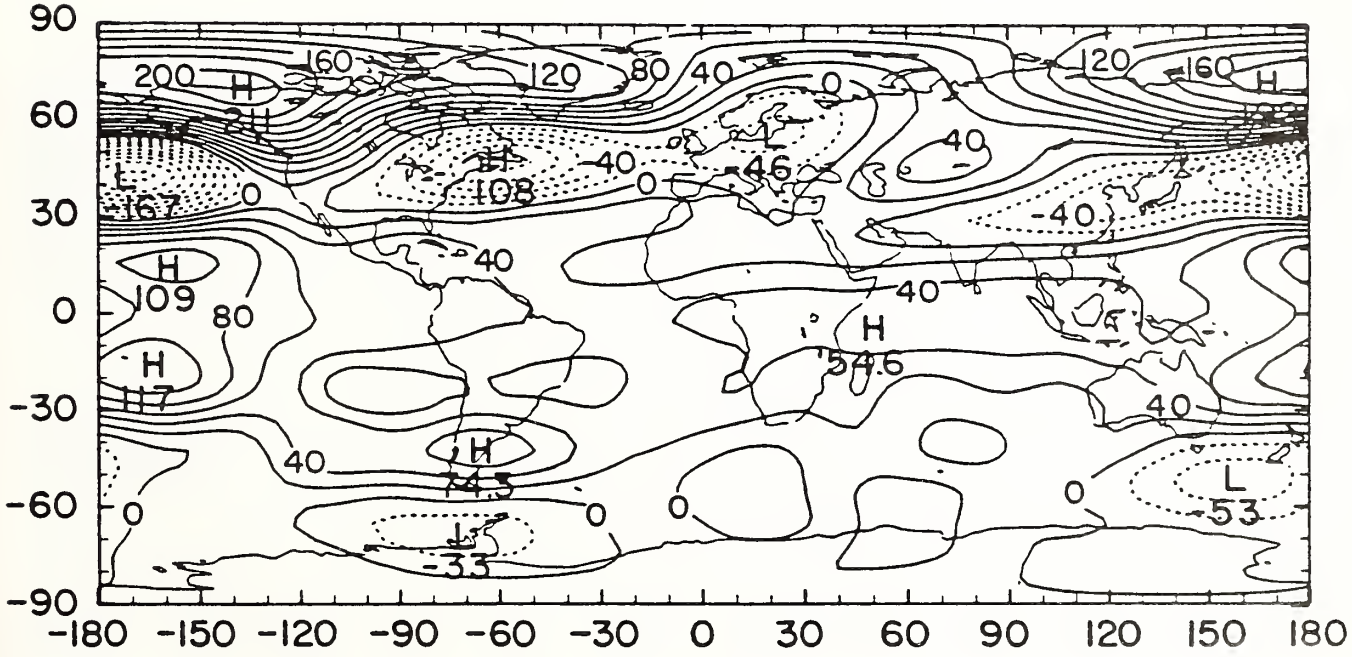

Fig. 1b Anomaly run minus control run 200 mb height (m);

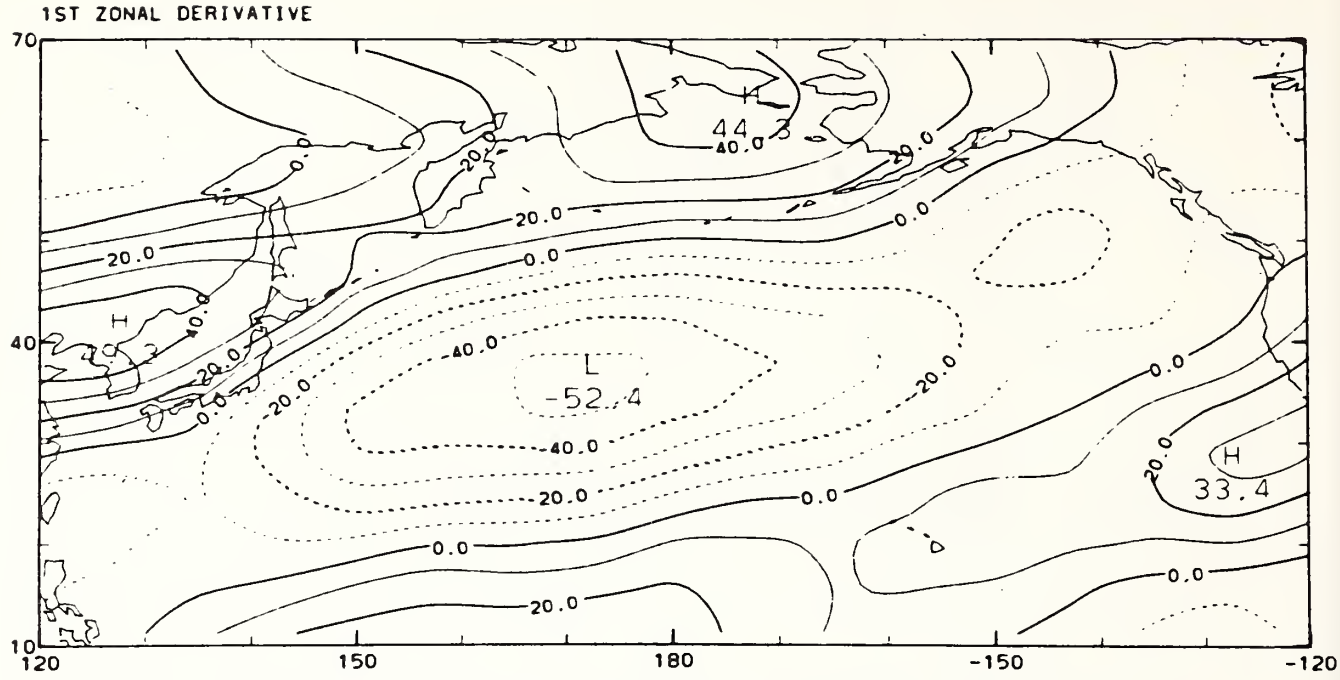

Fig. 2a Zonal gradient of time-mean 200 mb zonal flow ($\partial\bar{u}/\partial x$) over the North Pacific in the control run; orography present in model.

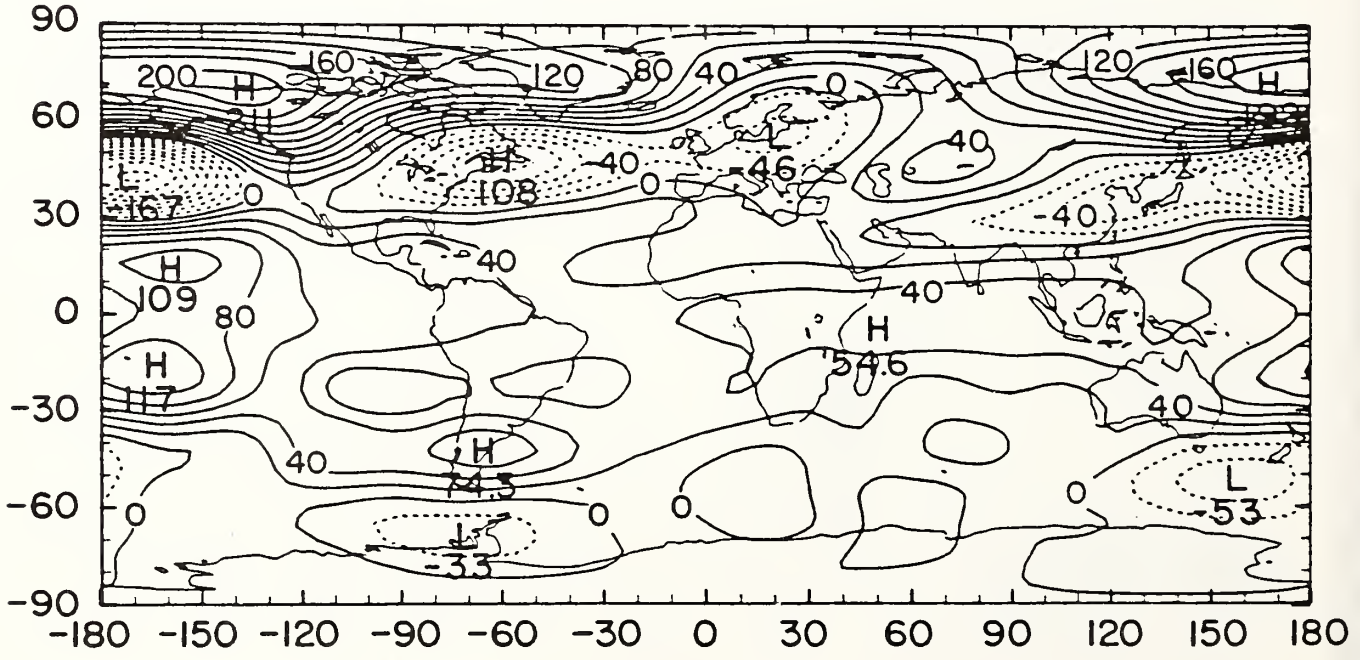

Fig. 2b Anomaly run minus control run 200 mb height (m); orography present in model.

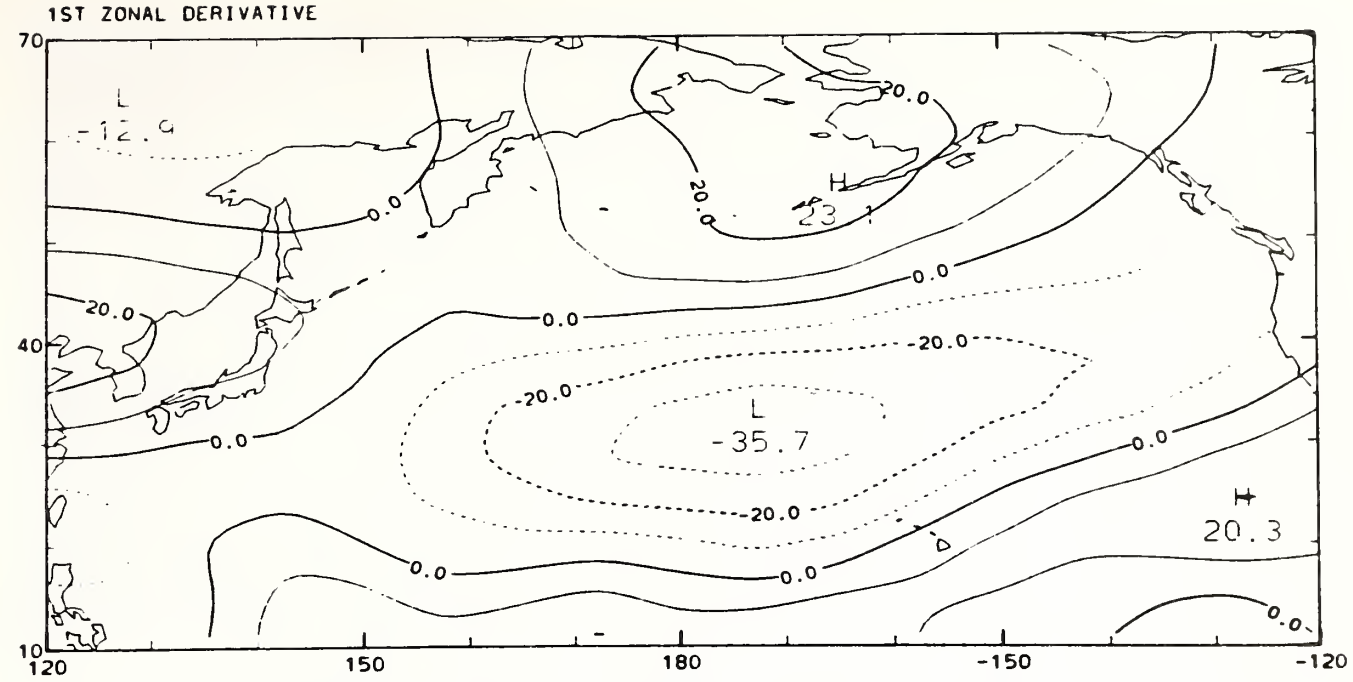

Fig. 3a Zonal gradient of time-mean 200 mb zonal flow ($\partial\bar{u}/\partial x$) over the North Pacific in the control run; no orography present in model.

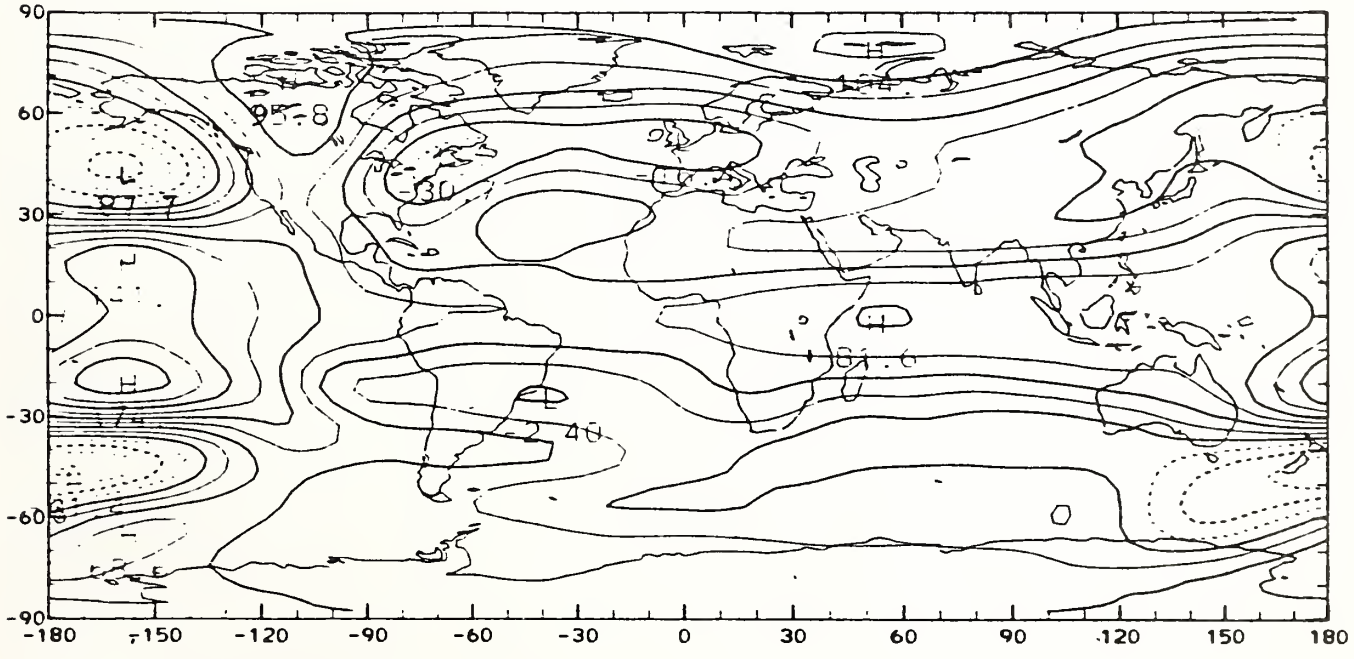

Fig. 3b Anomaly run minus control run 200 mb height (m); no orography present in model.

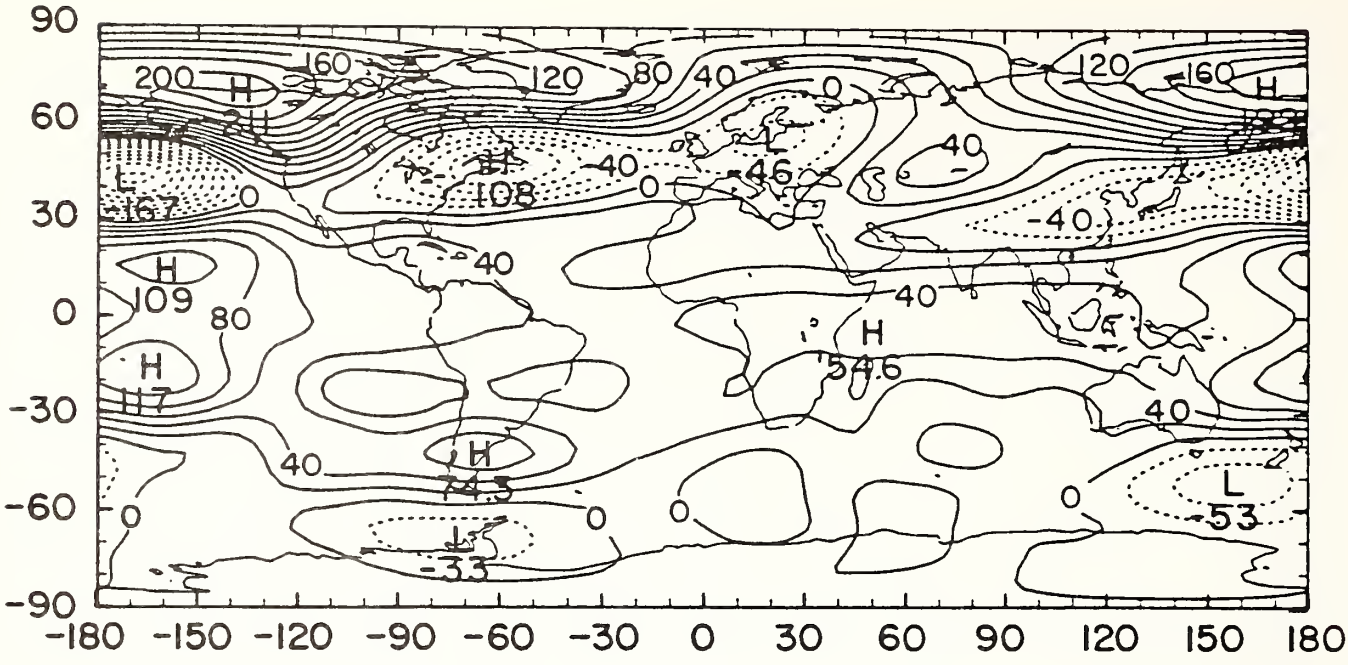

Fig. 4a Anomaly run minus control run 200 mb height (m); orography present in model.

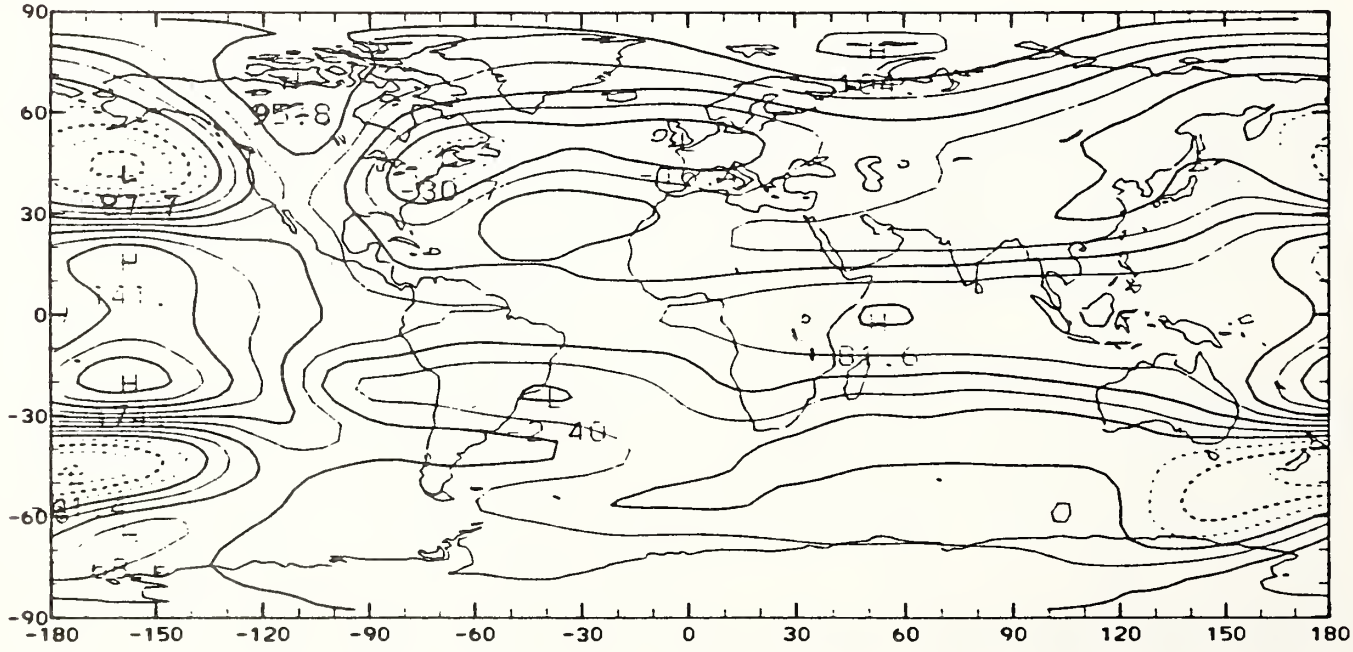

Fig. 4b Anomaly run minus control run 200 mb height (m); no orography present in model.

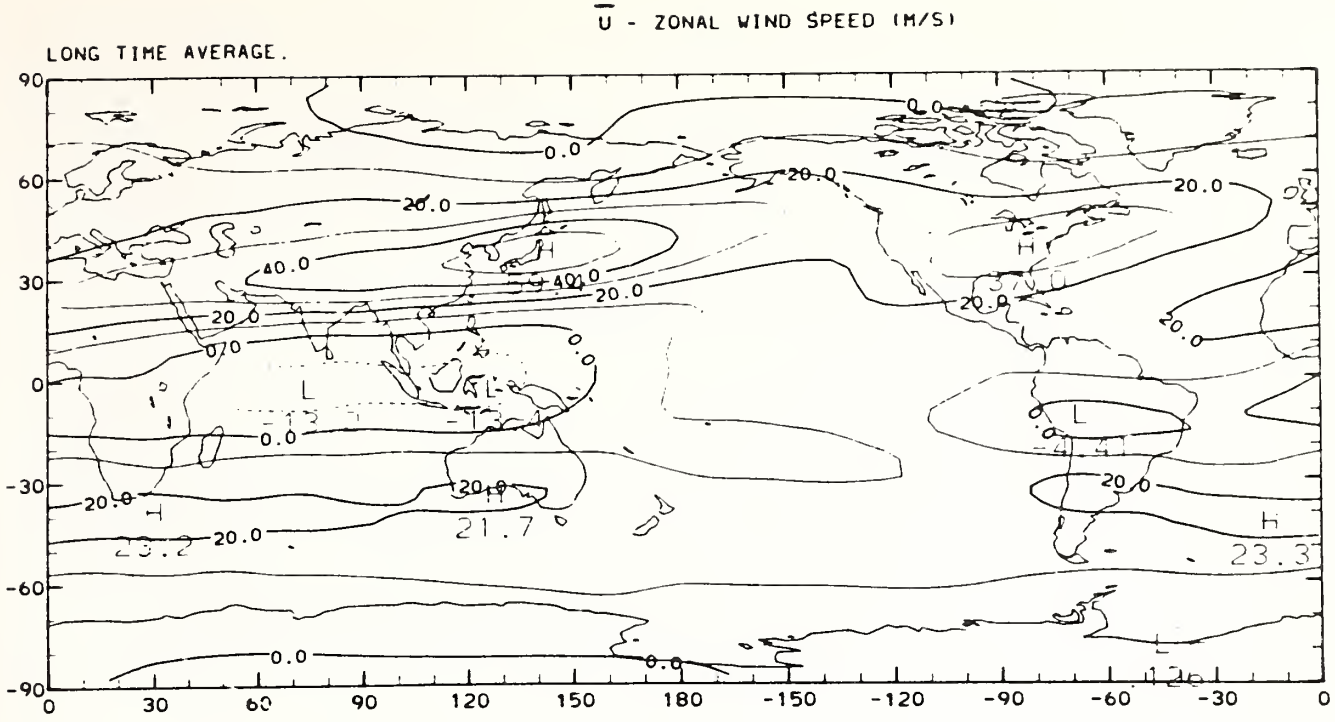

Fig. 5a Time-mean 200 mb zonal flow ($\bar{u}$) in control run; orography present in model.

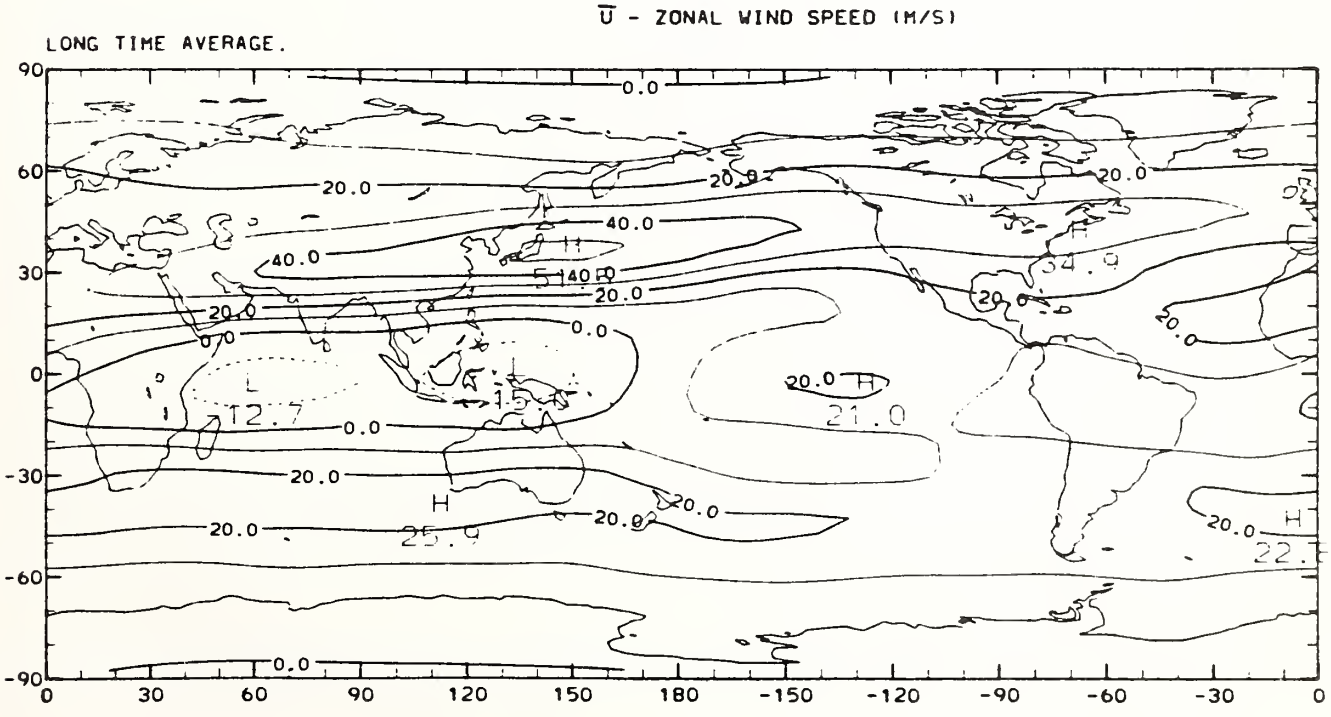

Fig. 5b Time-mean 200 mb zonal flow ($\bar{u}$) in control run; no orography present in model.

HORIZONTAL FLUXES IN REAL AND MODEL ATMOSPHERES

G.J. Boer
Canadian Climate Centre
Downsview, Ontario

1. INTRODUCTION

Large-scale vertically integrated fluxes of moisture and energy, together with the associated distribution of sources and sinks, are basic climatological parameters of the atmosphere. Global distributions of these quantities have only recently become available from the FGGE III-b data set.

The comparison of these quantities obtained from observations with those from general circulation models, such as the Canadian Climate Centre GCM (Boer et al., 1985a, b), serves as a useful check on both the model and the data and provides insight into the budgets and balances of these quantities.

2. VERTICALLY INTEGRATED BUDGETS

The equation for an atmospheric quantity X is written in flux form as

$$\frac{\partial X}{\partial t} + \nabla \cdot X \underset{\sim}{V} + \frac{\partial}{\partial p} X \omega = S$$

Vertical integration and time averaging gives, to good approximation,

$$\nabla \cdot \underset{\sim}{F} = S$$

where

$$\underset{\sim}{F} = \int_o^{p_o} \bar{\beta}\, \overline{X \underset{\sim}{V}}\, dp/g, \quad S = \int_o^{p_o} \bar{\beta}\, \bar{S}\, dp/g,$$

p_o is a constant $> p_s$ and β is the unit function such that $\beta = 1$, $p < p_s$: $\beta = 0$, $p > p_s$.

The flux vector $\underset{\sim}{F}$ is decomposed into its mean and transient parts

$$\underset{\sim}{F} = \underset{\sim}{F}_M + \underset{\sim}{F}_T = \int_o^{p_o} \bar{\beta}\, \bar{X}\, \bar{\underset{\sim}{V}}\, dp/g + \int_o^{p_o} \bar{\beta}\, \overline{X' \underset{\sim}{V}'}\, dp/g$$

and into rotational and divergent components

$$\underset{\sim}{F} = \underset{\sim}{F}_R + \underset{\sim}{F}_D = \underset{\sim}{k} \times \nabla\psi + \nabla\chi$$

The divergent component of the flux vector is associated with the distribution of sources and sinks in the atmosphere since $\nabla \cdot \underset{\sim}{F}_R = 0$ while $\nabla \cdot \underset{\sim}{F}_D = S$. The flux vector $\underset{\sim}{F}$ may be decomposed into four terms, $\underset{\sim}{F} = \underset{\sim}{F}_{MR} + \underset{\sim}{F}_{TR} + \underset{\sim}{F}_{MD} + \underset{\sim}{F}_{TD}$.

In general $\underset{\sim}{F}_{MR} > > \underset{\sim}{F}_{TR}$ and the rotational component of the flux vector is dominated by the mean flow component. Moreover

$$\underset{\sim}{F}_{MR} \sim \int_o^{p_o} \bar{\beta}\, \bar{X}\, \underset{\sim}{\bar{V}}_R \, dp/g$$

approximately so that the rotational component of the flux vector is associated with the rotational component of the wind velocity. Similarly, $\underset{\sim}{F}_{MD} > \underset{\sim}{F}_{TD}$ over much of the atmosphere, especially in the tropics, although the two components are of the same order at higher latitudes and the transient component dominates in some areas. While the rotational component of the mean flux vector is closely related to the rotational component of the mean flow, it is less the case that the divergent component of the mean flux is given in terms of the divergent component of the flow. Thus while

$$\underset{\sim}{F}_{MD} \sim \int_o^{p_o} \bar{\beta}\, \bar{X}\, \underset{\sim}{\bar{V}}_D \, dp/g$$

is approximately the case for some parameters it is a reasonable approximation for others only in the tropical region.

3. BUDGETS OF ATMOSPHERIC QUANTITIES

The budgets of moisture and total energy are

$$\nabla \cdot \underset{\sim}{Q} = E - P \qquad \underset{\sim}{Q} = \int_o^{p_o} \bar{\beta}\, \overline{q\, \underset{\sim}{V}} \, dp/g$$

$$\nabla \cdot \underset{\sim}{E} = H = R_N + H_S + LP \qquad \underset{\sim}{E} = \int_o^{p_o} \bar{\beta} \, \overline{(C_p T + \phi + K)\underset{\sim}{V}} \, dp/g$$

where E - P is evaporation minus precipitation, $H = R_N + H_S + LP$ is radiation, sensible heat flux from the surface and latent heat source/sink terms.

4. RESULTS

The moisture and energy fluxes in the atmosphere (FGGE-IIIb) and in the Canadian Climate Centre general circulation model climatology (P5Z) are displayed in the accompanying figure. These diagrams represent large scale transports for the globe. The divergent components are of particular interest as they are related to the distribution of sources and sinks. The broad patterns of transport of moisture from source to sink regions is portrayed as is that for energy. Note that the sink region of moisture in the tropics is a source region for energy (from latent heat release) and that energy is exported to the cold interior regions of winter continents where it is lost to space.

The model results reproduce those of the atmosphere with reasonable fidelity. These fields represent basic transport process in the atmosphere and more systematic and rigorous intercomparison should provide new insight into both atmospheric and model behaviour.

References

Boer, G.J., N.A. McFarlane, R. Laprise, J.D. Henderson and J.-P. Blanchet, 1985: The CCC Spectral Atmospheric General Circulation Model, accepted for publication ATMOSPHERE-OCEAN.

Boer, G.J., N.A. McFarlane and R. Laprise, 1985: The Climatology of the CCC GCM as Obtained from a Five Year Simulation, accepted for publication ATMOSPHERE-OCEAN.

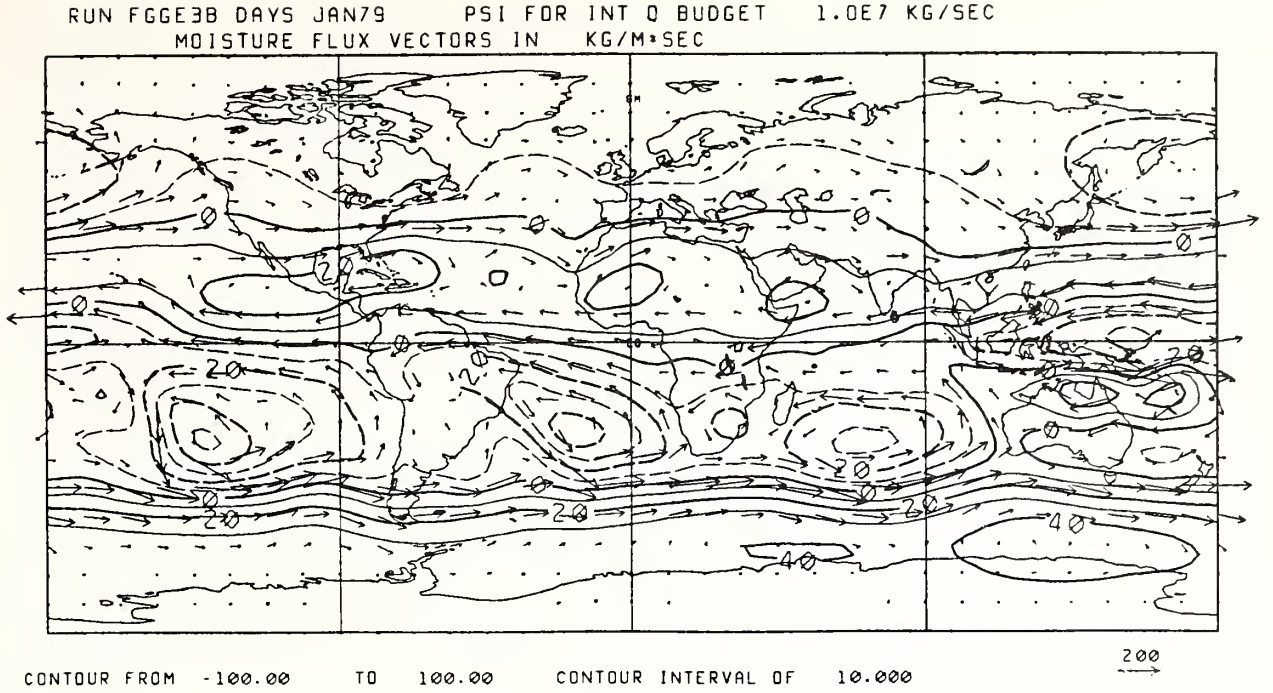
RUN FGGE3B DAYS JAN79 PSI FOR INT Q BUDGET 1.0E7 KG/SEC
MOISTURE FLUX VECTORS IN KG/M*SEC
200
CONTOUR FROM -100.00 TO 100.00 CONTOUR INTERVAL OF 10.000

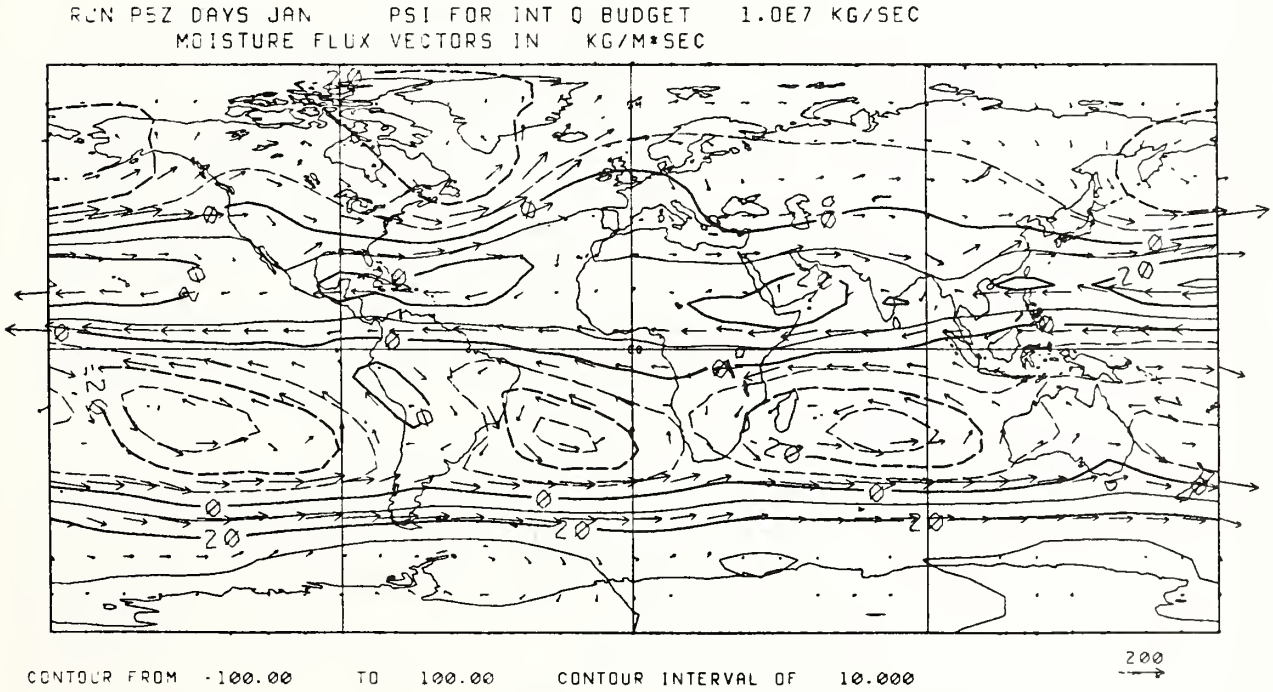
RUN PEZ DAYS JAN PSI FOR INT Q BUDGET 1.0E7 KG/SEC
MOISTURE FLUX VECTORS IN KG/M*SEC
200
CONTOUR FROM -100.00 TO 100.00 CONTOUR INTERVAL OF 10.000

1

Rotational components of the moisture flux vector and associated streamfunction from FGGE data and the GCM.

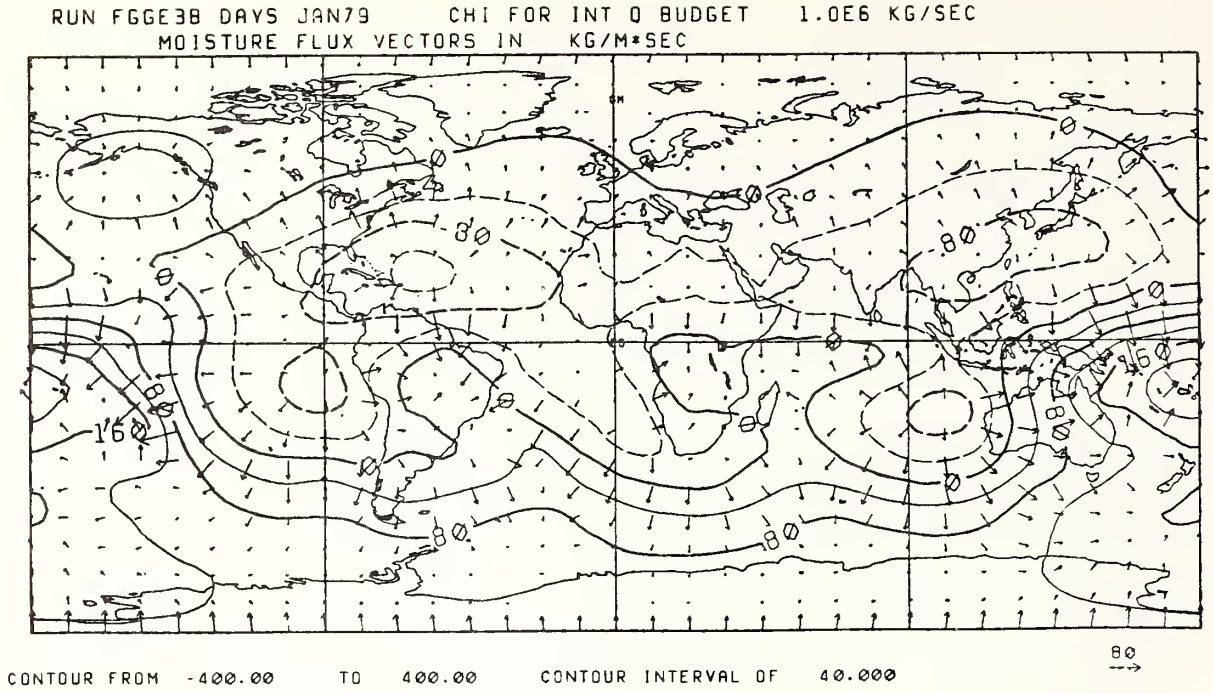
RUN FGGE3B DAYS JAN79 CHI FOR INT Q BUDGET 1.0E6 KG/SEC
MOISTURE FLUX VECTORS IN KG/M*SEC
80
CONTOUR FROM -400.00 TO 400.00 CONTOUR INTERVAL OF 40.000

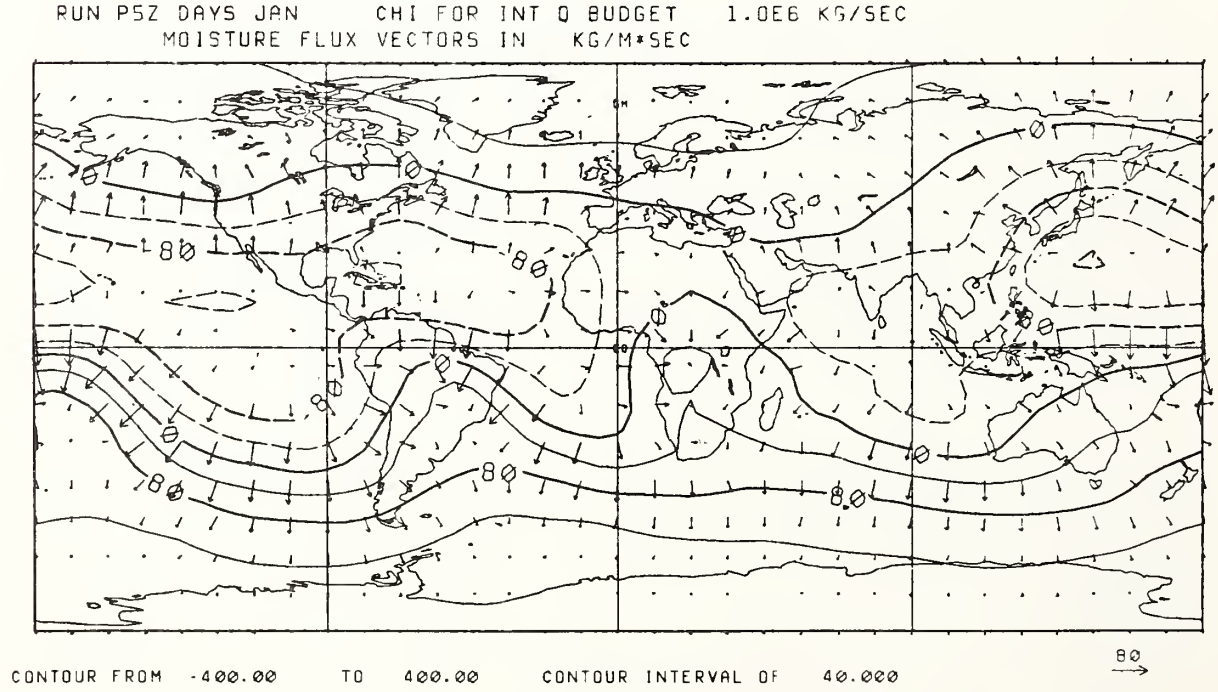
RUN P5Z DAYS JAN CHI FOR INT Q BUDGET 1.0E6 KG/SEC
MOISTURE FLUX VECTORS IN KG/M*SEC
80
CONTOUR FROM -400.00 TO 400.00 CONTOUR INTERVAL OF 40.000

2

Divergent components of the moisture flux vector and associated potential function from FGGE data and the GCM.

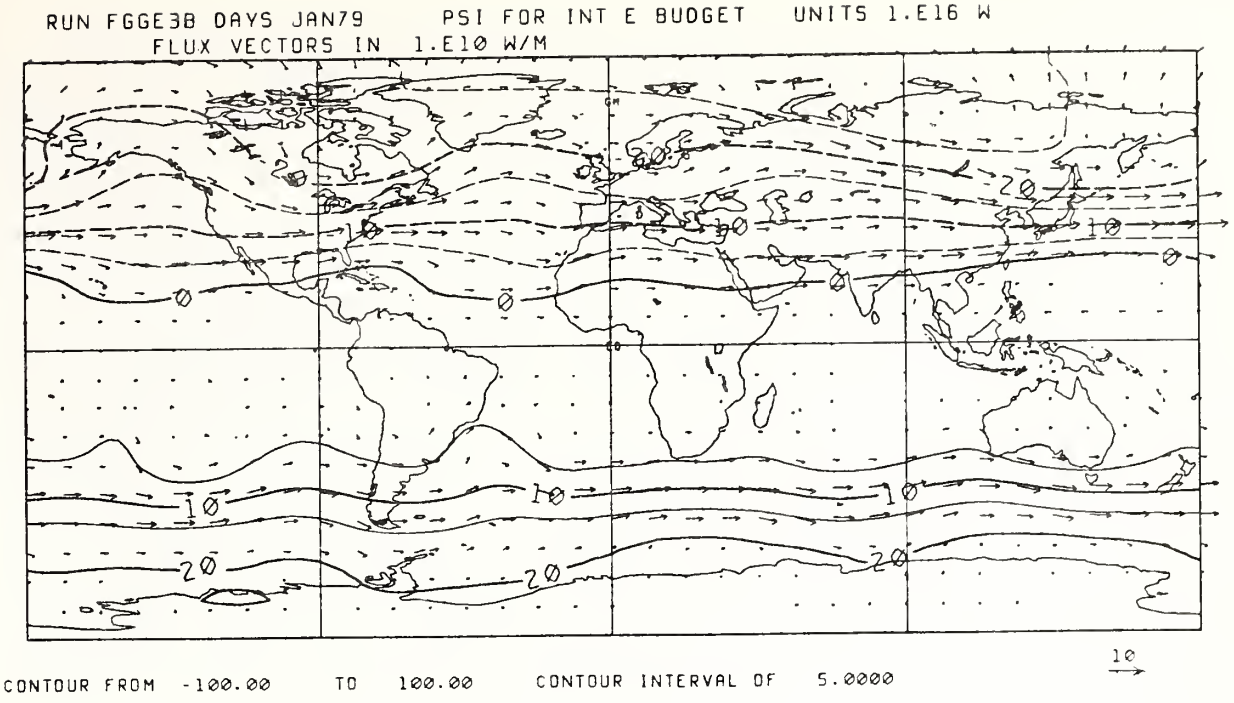
RUN FGGE3B DAYS JAN79 PSI FOR INT E BUDGET UNITS 1.E16 W
FLUX VECTORS IN 1.E10 W/M
10
CONTOUR FROM -100.00 TO 100.00 CONTOUR INTERVAL OF 5.0000

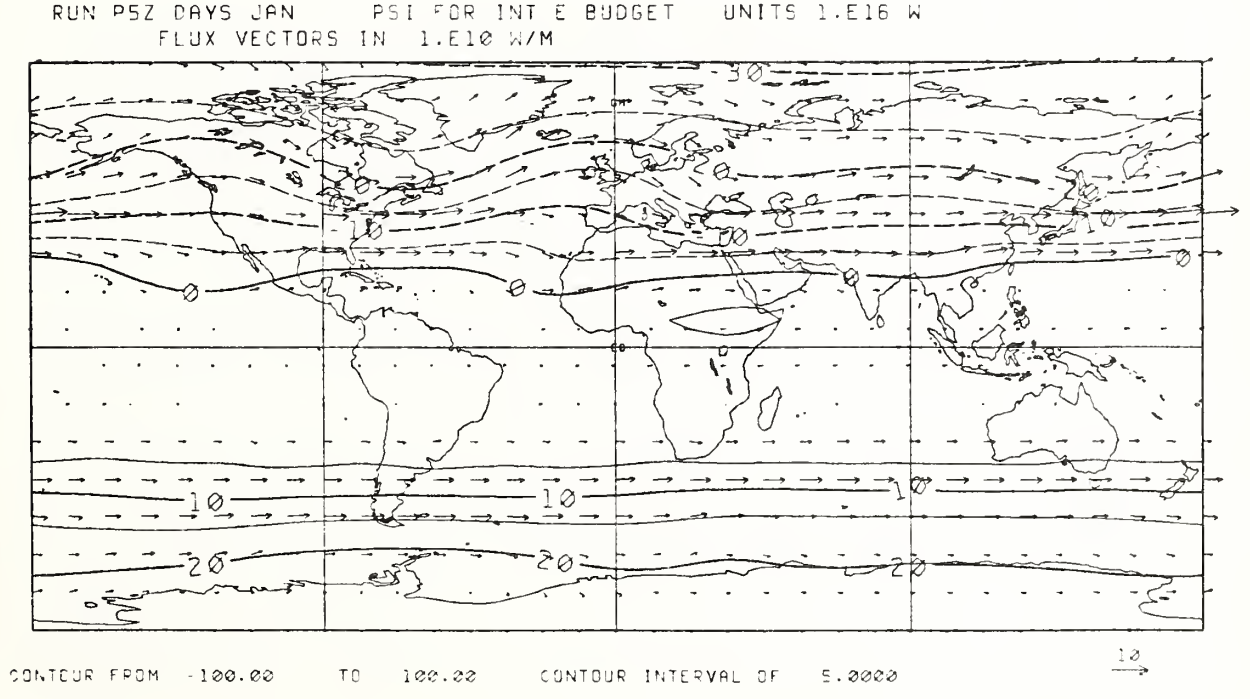
RUN P5Z DAYS JAN PSI FOR INT E BUDGET UNITS 1.E16 W
FLUX VECTORS IN 1.E10 W/M
10
CONTOUR FROM -100.00 TO 100.00 CONTOUR INTERVAL OF 5.0000

3

Rotational components of the energy flux vector and associated streamfunction from FGGE data and the GCM.

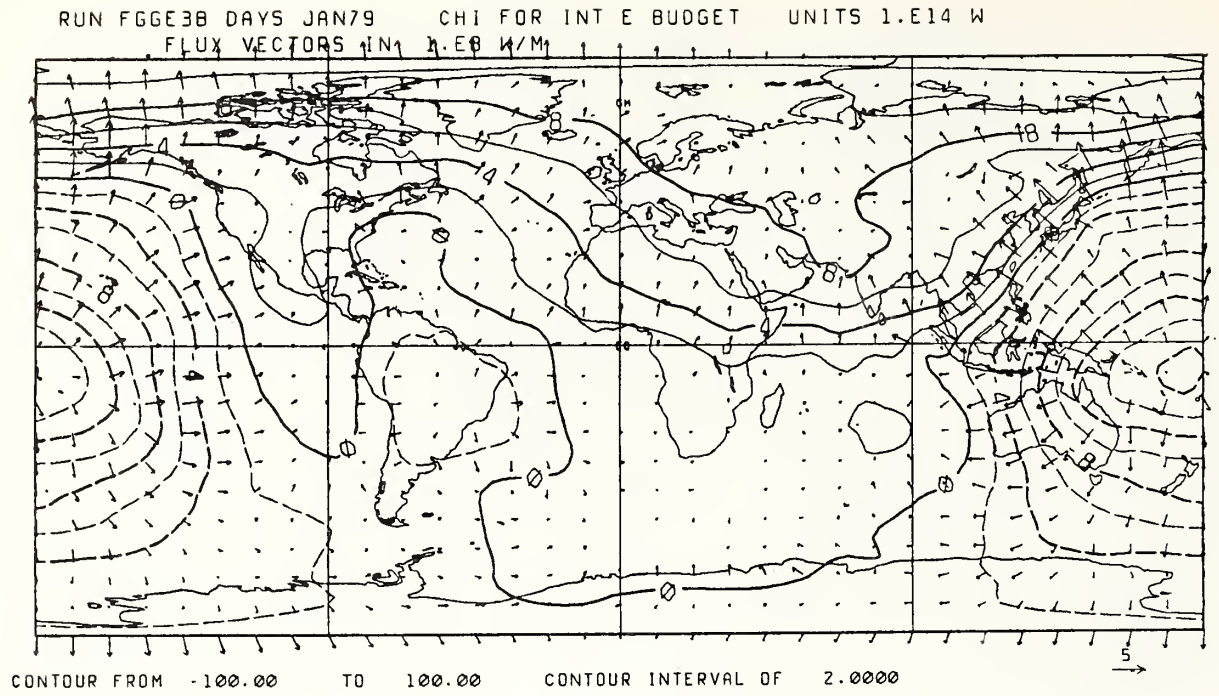
RUN FGGE38 DAYS JAN79 CHI FOR INT E BUDGET UNITS 1.E14 W
FLUX VECTORS IN 1.E8 W/M
CONTOUR FROM -100.00 TO 100.00 CONTOUR INTERVAL OF 2.0000

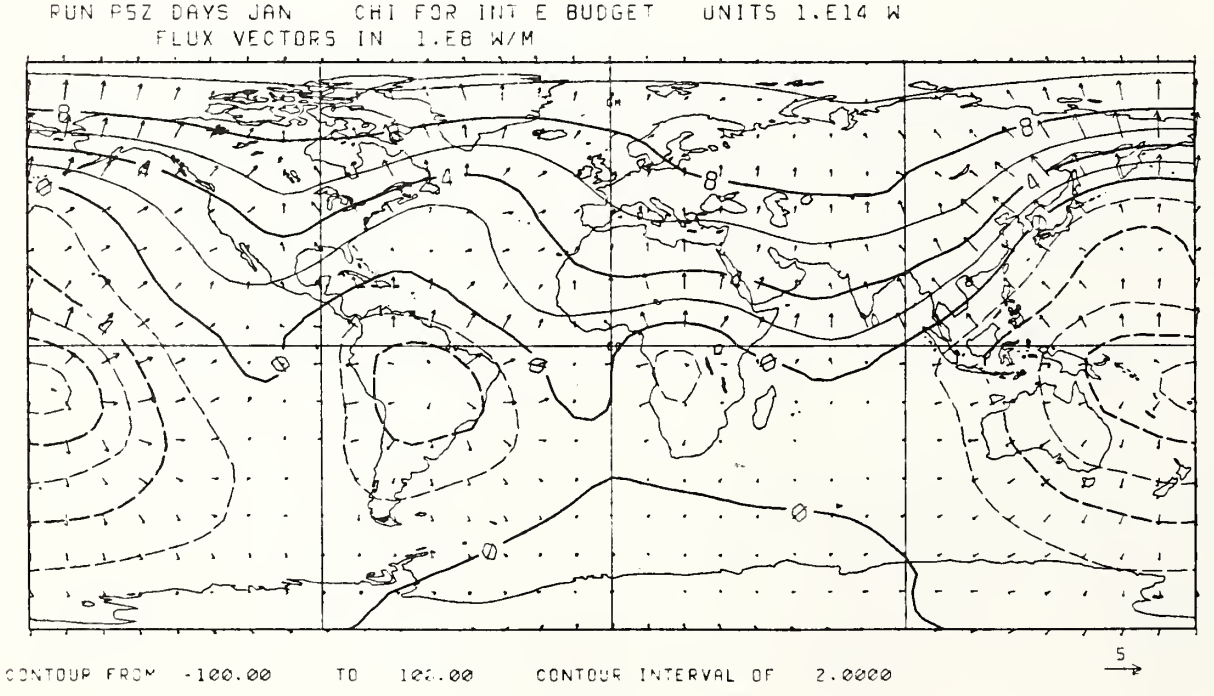
RUN P5Z DAYS JAN CHI FOR INT E BUDGET UNITS 1.E14 W
FLUX VECTORS IN 1.E8 W/M
CONTOUR FROM -100.00 TO 100.00 CONTOUR INTERVAL OF 2.0000

4

Divergent components of the energy flux vector and associated potential function from FGGE data and the GCM.

THE IMPACT OF HEAT SOURCES IN THE TROPICS ON THE ATMOSPHERIC CIRCULATION

R. Mureau KNMI, The Netherlands
J.D. Opsteegh KNMI, The Netherlands
J.S. Winston University of Maryland

Observational and GCM studies have produced evidence of the importance of heat sources in the tropics for the global atmospheric circulation. Linear steady state models have been considered a useful tool to demonstrate the process of energy propagation out of the tropics, and have in a qualitative way contributed to the understanding of GCM's and also of the real atmosphere. Little is known, however, to what extent linear models can produce quantitatively realistic circulation patterns in response to observed forcing. We have investigated this by attempting to simulate with a linear 15 layer steady state model the observed anomalies for a large number of seasons. We have used seasonal mean outgoing longwave radiation (OLR) anomalies in the tropics as a proxy for the anomalous seasonal mean diabatic heating (cf. Arkin, Ph.D.Thesis, 1984), for all seasons during the years 1974-1983. Other forcing terms have been ignored. Simulated anomalous streamfunctions at 300 mb and 700 mb are objectively verified, by computing pattern correlation coefficients (pcc). Since we have neglected other forcing terms we can only expect significant pcc's in those seasons when the anomalous tropical diabatic heating is strong. The pcc for each season is given in fig. 1. Comparing the upper panel with the lower panel, which displays an index of the strength of the heating, we can see that this is the case in the fall of 1982 and the winter of 1982/83. The pcc for these 2 seasons is large. For the other seasons there is in fact no reason to believe that the tropical diabatic heating is strong enough to explain the observed variance. Incidental large pcc's may be a matter of pure chance for these cases. The anomalous streamfunctions for the winter 1982/83 as displayed in fig. 2a, b, c, d compare very well with observations, especially in the Central Tropical Pacific.

The response appears to be sensitive to the vertical resolution of the model. We demonstrate this by choosing 2 different vertical profiles for the diabatic heating (fig. 3). In the Mature Cloud Cluster (MCC) profile (Hartmann et al., JAS, 1984) all latent heat is released in the layers between 100 mb and 600 mb. This profile was also used in fig. 1. In the second profile heat is released over a larger depth. The model was run for both heating profiles in the winter seasons. The correlations show that the results using the MCC profile are better at the 700 mb level for almost all individual winter seasons (fig. 4).

The vertical resolution is also important for the description of the vertical structure of the basic state. In 2-layer models the basic state of the upper part of the atmosphere is poorly represented. The presence of westerlies in the upper tropical atmosphere is however very important for extra tropical propagation of energy. If we keep, in the 15-layer model, the basic state wind constant above the 300 mb level, thus removing a small band of westerlies in the tropics at the 233 mb level, we suppress transport of energy into mid-latitudes drastically (fig. 5, compare with fig. 2).

We conclude that for cases with strong tropical heat sources linear models have the capability of producing a response which is positively correlated with the observations. In some cases a high vertical resolution is essential in obtaining significant teleconnection patterns.

Figure captions

Fig.1 Time series of pattern correlation coefficients between observed anomalous streamfunctions and modeled anomalous streamfunctions (upper panel) and time series of strength of anomalous diabatic heating (lower panel). The correlations have been calculated for two levels (300mb: solid line, and 700mb: dashed line) for the region between 50 S and 50 N (Tropics and lower mid-latitudes).

Fig.2 Anomalous modeled and observed streamfunctions for the winter 1982/83.

Fig.3 Vertical profiles for diabatic heating. The Mature Cloud Cluster profile is indicated by the dashed curve.

Fig.4 Time series of pattern correlation coefficient for the 2 different vertical heating profiles (winter cases). As in fig.1 .

Fig.5 Anomalous modeled streamfunction for winter 1982/83 with adapted basic state (see text).

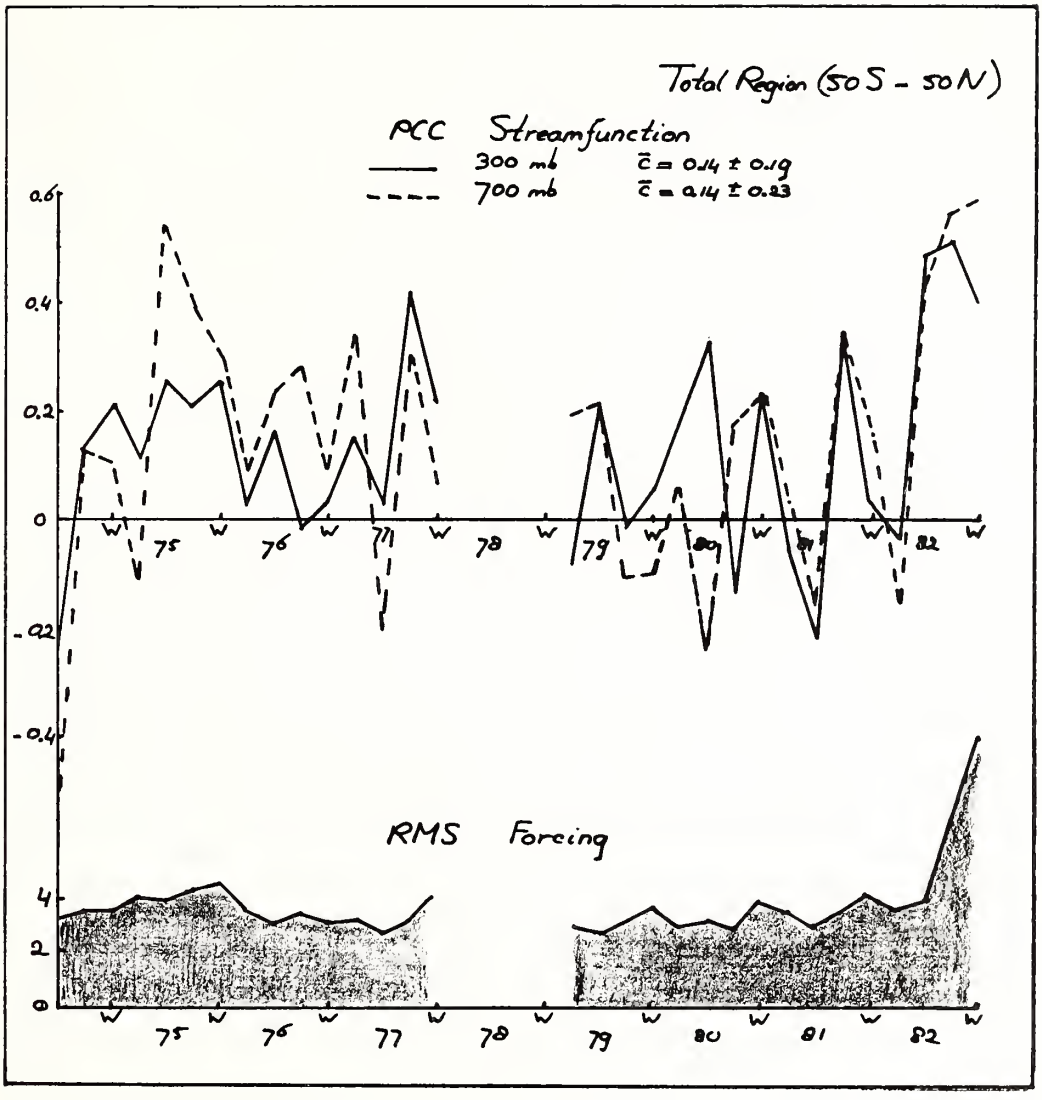
Total Region (50S - 50N)
PCC Streamfunction
300 mb $\bar{c}$ = 0.14 ± 0.19
700 mb $\bar{c}$ = 0.14 ± 0.23
0.6
0.4
0.2
0
-0.2
-0.4
75
76
77
78
79
80
81
82
RMS Forcing
4
2
0

1

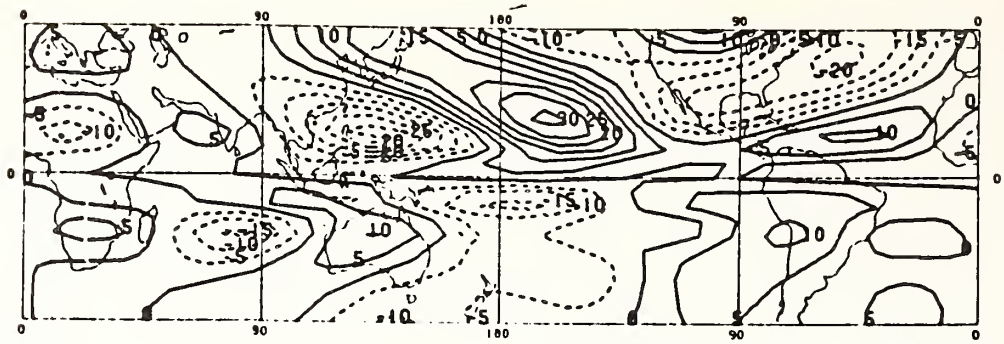

Model PSI 300mb Winter 1983

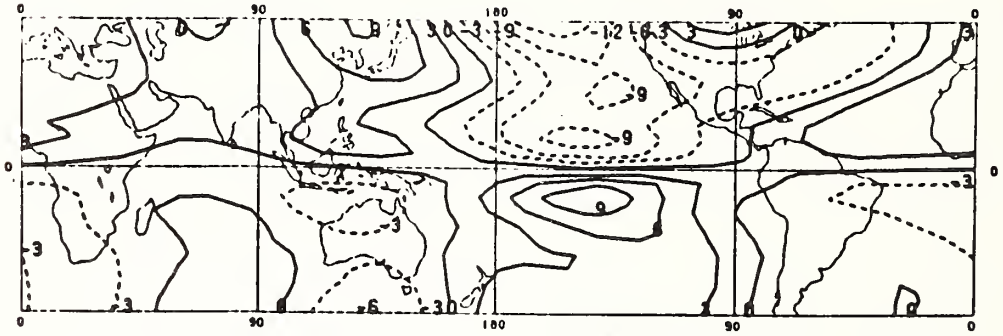

Model PSI 700mb Winter 1983

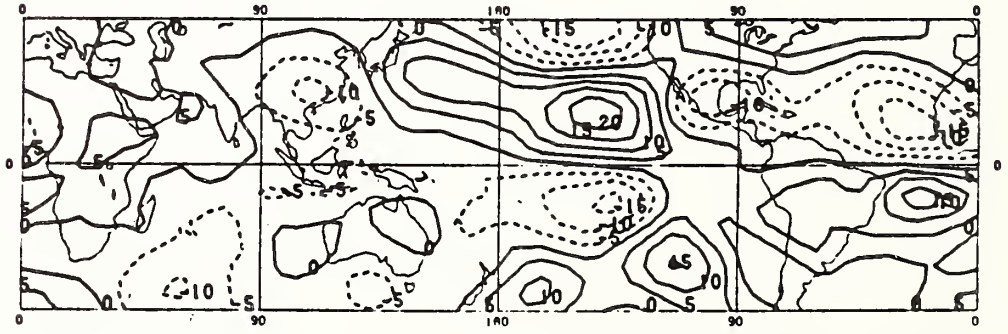

Obs. PSI 300mb Winter 1983

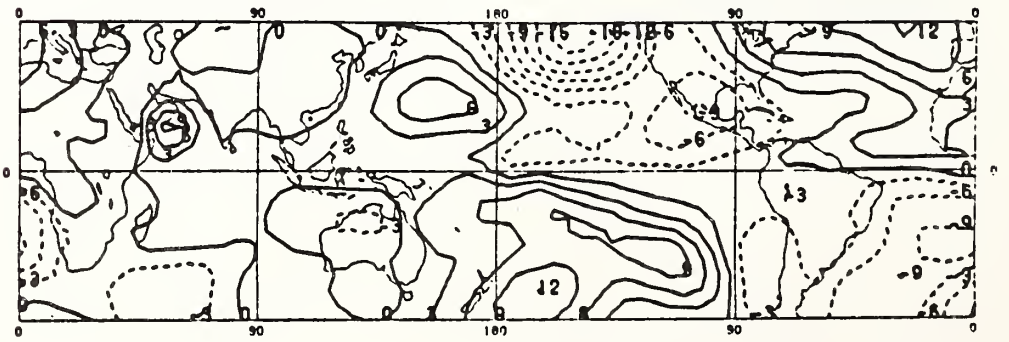

Obs. PSI 700mb Winter 1983

2

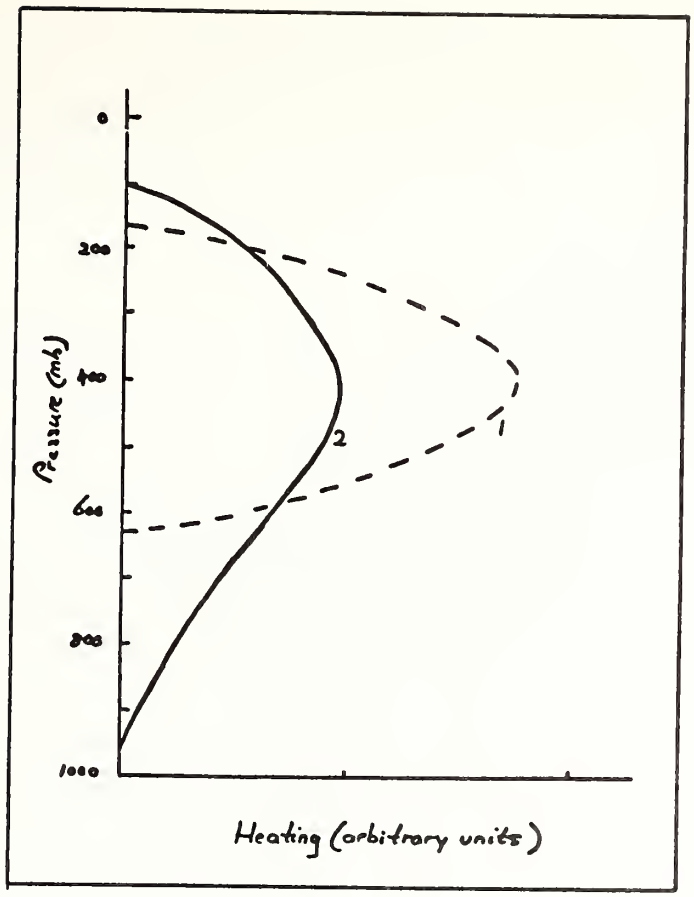
0
200
400
600
800
1000
Pressure (mb)
2
1
Heating (orbitrary units)

3

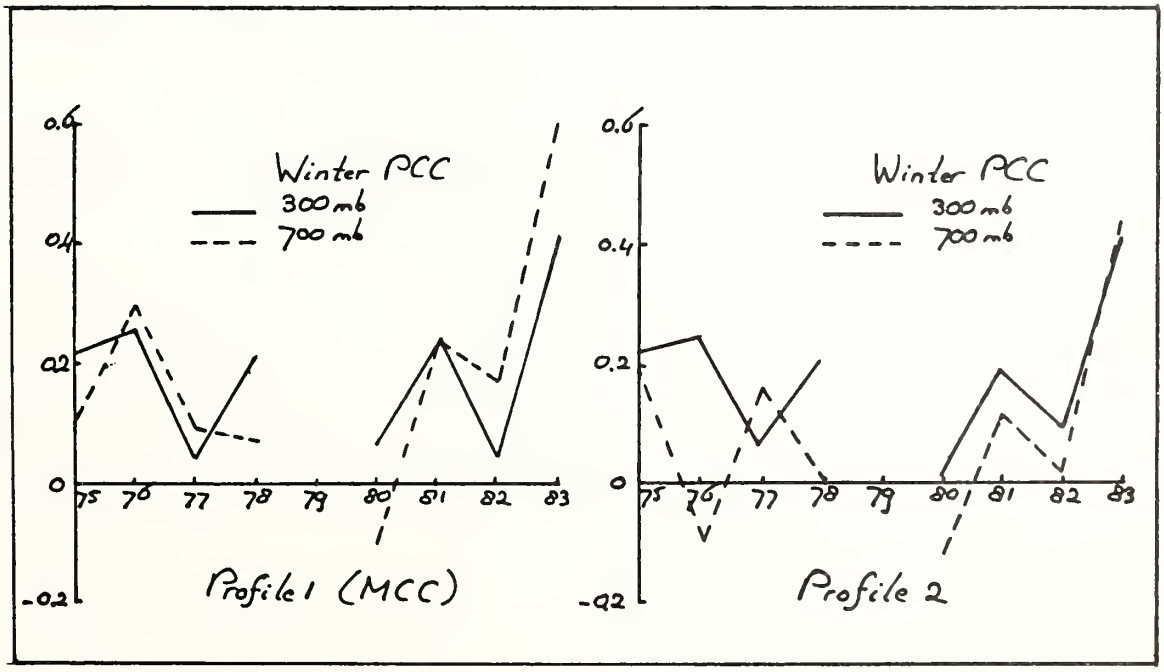
0.6
0.4
0.2
0
-0.2
Winter PCC
300 mb
700 mb
75 76 77 78 79 80 81 82 83
Profile 1 (MCC)
0.6
0.4
0.2
0
-0.2
Winter PCC
300 mb
700 mb
75 76 77 78 79 80 81 82 83
Profile 2

4

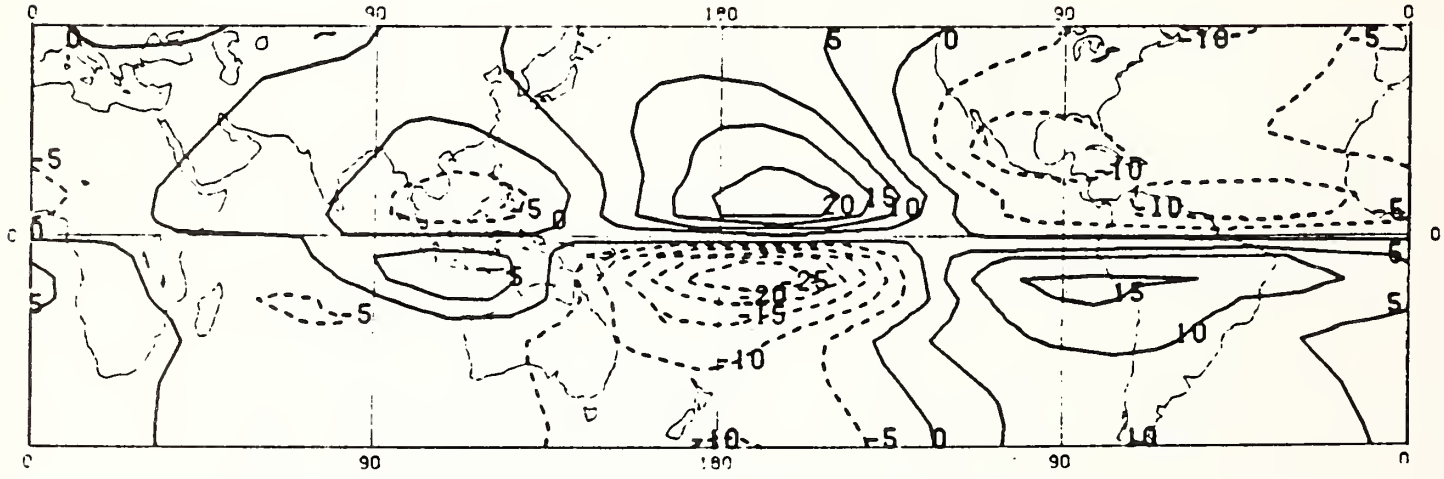

Model PSI 300mb Winter 1983

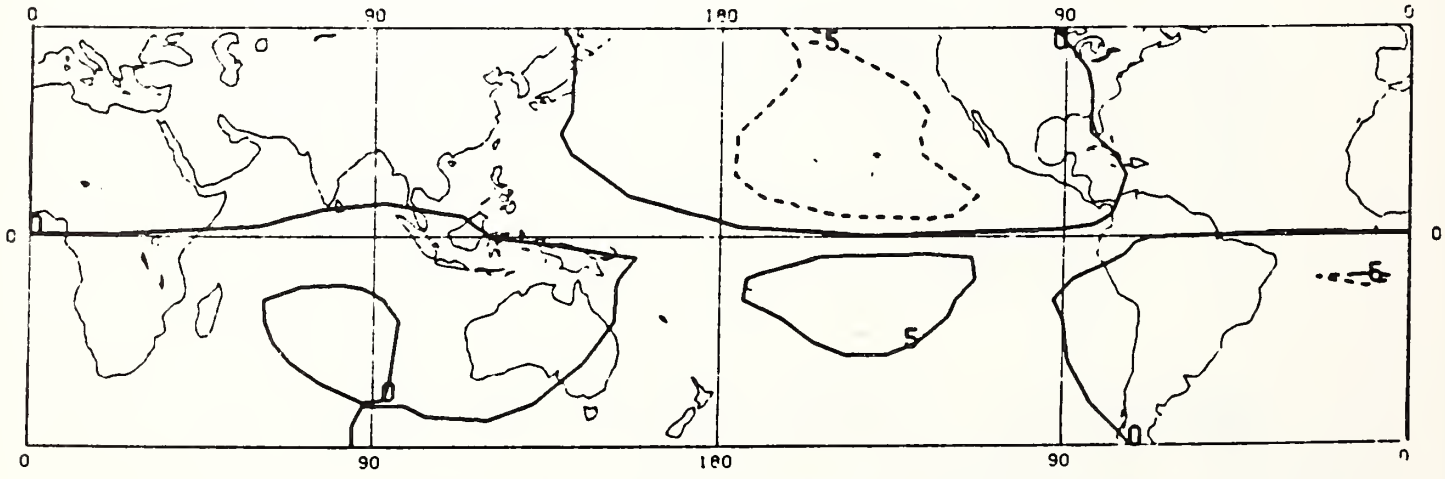

Model PSI 700mb Winter 1983

5

THE EFFECT OF ANOMALOUS SNOW COVER ON THE GENERAL CIRCULATION OF THE ATMOSPHERE USING A SIMPLE CLIMATE MODEL

by

Alan Robock and James W. Tauss
Department of Meteorology
University of Maryland
College Park, Maryland 20742

The effect of anomalous snow cover has long been studied as having a pronounced influence on the temperature of the overlying atmosphere (Landsberg, et al., 1941; Namias, 1960; Wagner, 1974; Dewey, 1977; Yeh, et al., 1982; Foster, et al., 1983). However, little if any literature has described the incorporation of such a forcing into a climate model to investigate the anomalous atmospheric response. It is the purpose of this paper to study the effects of such anomalous forcings when imposed on a given basic state using a simple, linear, steady-state climate model. Some preliminary results are discussed.

The model is described by Opsteegh and Mureau (1983). The equations are linearized with respect to a fixed, zonally averaged basic state. The equations for the time-mean anomalous response to a time-mean forcing are then calculated. There are 15 levels in the vertical and the model equations are formulated in sigma coordinates. It is semi-spectral with gridpoints in the meridional direction and wave components in the zonal direction.

Digitized NOAA satellite-derived snow cover data (Dewey and Heim, 1981) for 1967-1982 are used to create a January snow climatology map for the Northern Hemisphere. Because of some early data discrepancies over the Himalayas, the snow climatology for that region only covers the years 1976-1982. Subsequently, anomalous forcing fields are created for January 1976-1982. To create 3-dimensional forcing fields, vertical profiles of diabatic heating are parameterized in terms of the anomalous heating.

The first model runs contain 'idealized' snow anomalies to examine the anomalous response of the atmosphere. This 'idealized' anomaly is created by removing climatologically present snow cover where it was found at least 50% but not more than 100% of the time during the month (negative snow

anomaly) or adding snow cover to those areas exhibiting between 0% and 50% climatologically present snow cover (positive snow anomaly). A reasonable vertical profile of diabatic heat for a mid-latitude surface forcing such as this is selected to be ±1.0° C/day for the negative (heat source) or positive (heat sink) anomaly at the lowest model level (967 mb).

The forcing field resulting from the idealized snow anomaly case is imposed upon the January climatological basic state. The anomalous response is shown in figs. 1 and 2 for a North American positive January snow anomaly. In another run the model was forced with a European as well as a North American positive snow anomaly (not shown). For both cases, the response is zonal in character. Strong surface high pressure (fig. 1) is seen just downstream of the forcing with weaker low pressure upstream. At 300 mb (fig. 2), a strong trough is seen just downstream of the forcing with weaker high pressure upstream.

These results are similar in pattern to results by Egger (1977) who used sea surface temperature (SST) fields as an anomalous surface forcing. Egger's model contained only two levels in the vertical. Since very similar patterns are obtained with both models, the increase in vertical resolution seemed to offer little additional information about the response.

The next series of experiments takes the actual observed snow anomalies for the month of January (both positive and negative) and adds the two anomalous fields to create a 'total' forcing field. Because the model is linear, the addition of the anomalous fields in this fashion is a valid assumption. For these model runs, a vertical profile of ±2.0/ ±1.0/ ±0.5°C/day was also tested. When observed January snow anomaly fields are used as a forcing, the model response is closer to observation using this ±2.0/ ±1.0/ ±0.5° C/day vertical profile.

In fig. 3 (for 1977), the observed positive height anomaly at 700 mb over Alaska and Northern Europe agrees with the model. The broad negative height anomaly observed over Siberia and the North Central Pacific also appears in the model response. However, other features are erroneous such as the model response of positive height anomaly over Northeast China, the model's southern displacement of the westerlies over Southern Europe and the lack of the observed trough over the Eastern United States.

In fig. 4 (for 1978), the positive height anomaly in Western Canada, the broad negative height anomaly pattern stretching from Siberia through the Central North Pacific and the positive height anomaly in Northern Europe compares well with the model results. Again, however, the positive height anomaly over Northeast China is an erroneous model response and the the high and low height anomaly centers are reversed over the Eastern United States and North Atlantic.

Summary and Conclusions

Some factors associated with snow cover but not parameterized in this model include no change in albedo with latitude, no consideration of latent and sensible heat fluxes and no consideration of the effects of transients. Furthermore, enhanced baroclinicity and the associated vorticity forcing or dissipation to accompany the imposed diabatic heating are not included.

Because the model is linear, one expects the strongest forcing to produce the strongest responses. The mean monthly snow cover for January 1977 and 1978 ranked 1st and 4th highest respectively across the Northern Hemisphere (Wiesnet and Matson, 1979). Still there are many regions where poor correlations between model response and observation are seen.This leads one to tentatively conclude that the many factors not parameterized in this model may mask the effect of anomalous snow cover to the point where only random correlations can be recognized or that the effect of a strong, shallow, surface forcing in the middle and high latitudes has a much smaller effect on the general circulation than previously proposed.

Many more experiments must be done to determine if agreement between model output and observations is due to chance or due to a real snow effect. The effects of anomalous outgoing longwave radiation (OLR) will also be included, and it will be determined if snow cover forcing can help improve the results obtained only with OLR.

References

Dewey, Kenneth, 1977: Daily maximum and minimum temperature forecasts and the influence of snow cover. Mon. Weather Rev., 105, 1594-1596.

Dewey, Kenneth and Richard Heim Jr., 1981: Satellite observations of variations in northern hemispheric snow cover. NOAA Tech Rep., NESS 87.

Egger, J., 1977: On the linear theory of the atmospheric response to sea surface temperature anomalies. J. Atmos. Sci., 34, 603-614.

Foster, James, Manfred Owe and Albert Rango, 1982: Snow cover and temperature relationships in North America and Eurasia. J. Clim. and App. Met., 22, 460-469.

Landsberg, Helmut, G.P. Cressman and H.K. Saylor, 1941: The influence of a snow cover on air temperature. Proceedings - Central Snow Conference, Vol 1, 45-48.

Namias, Jerome, 1960: Influences of abnormal surface heat sources and sinks on atmospheric behavior. Proceedings of the International Symposium on Numerical Weather Prediction in Tokyo.

Oort, A. H., 1983: Global atmospheric circulation statistics 1958-1973. NOAA Professional Paper 14.

Opsteegh, J.D. and Robert Mureau, 1984: Description of a 15-layer steady-state atmospheric model. Unpublished Manuscript.

Wagner, James, 1974: The influence of average snow depth on monthly mean temperature anomaly. Mon. Weather Rev., 101, 624-626.

Wiesnet, Donald and Michael Matson, 1979: The satellite-derived northern hemispheric snow cover record for the winter of 1977-78. Mon. Weather Rev., 107, 928-933.

Yeh, T.C., R.T. Wetherald and S. Manabe, 1983: A model study of the short-term climatic and hydrologic effects of sudden snow cover removal. Mon. Weather Rev., 111, 1013-1024.

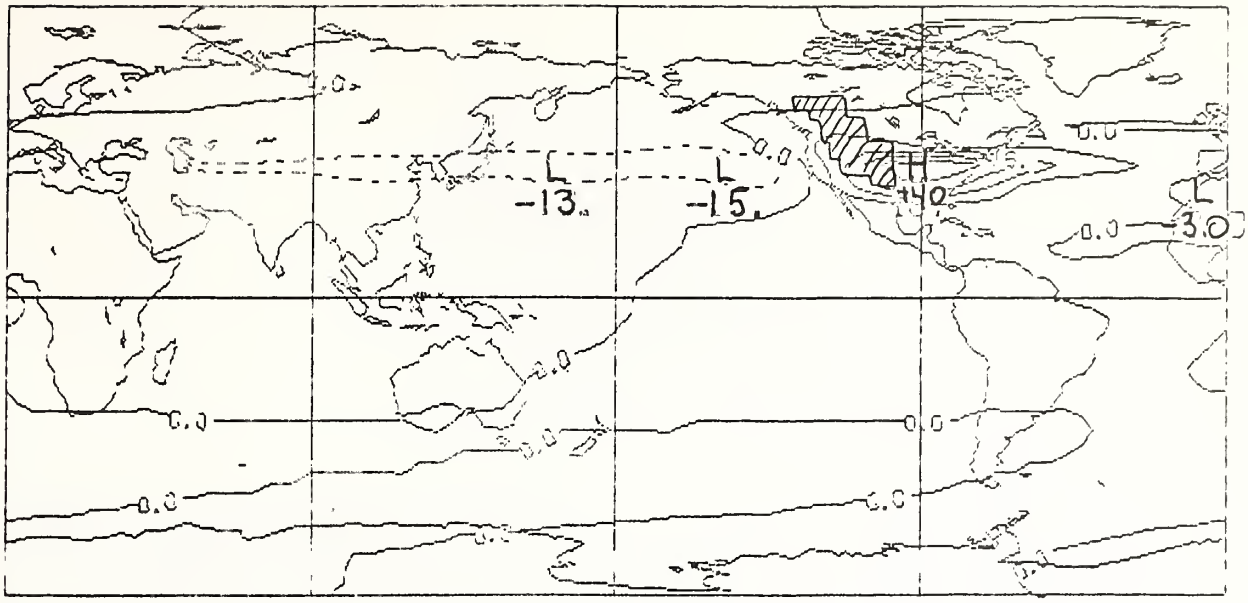

Fig. 1. Surface pressure (units of 0.1 mb) North American positive 'idealized' snow anomaly for January. 'Idealized' snow cover area is shaded.

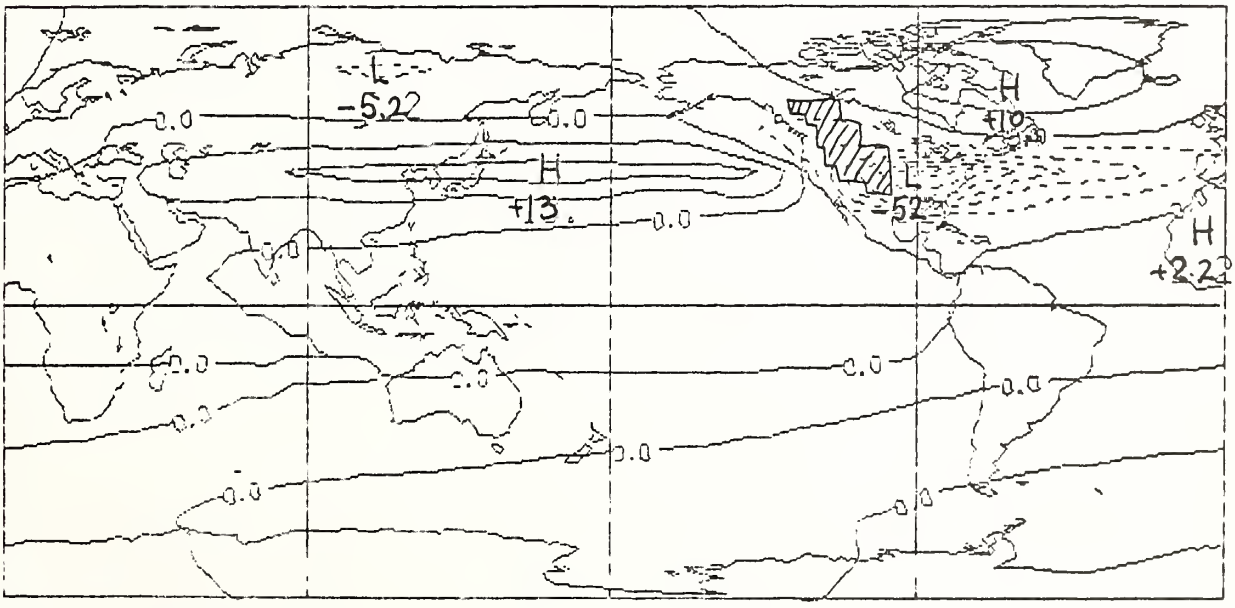

Fig. 2. Same as Fig. 1 except 300 mb Geopotential (units of m.).

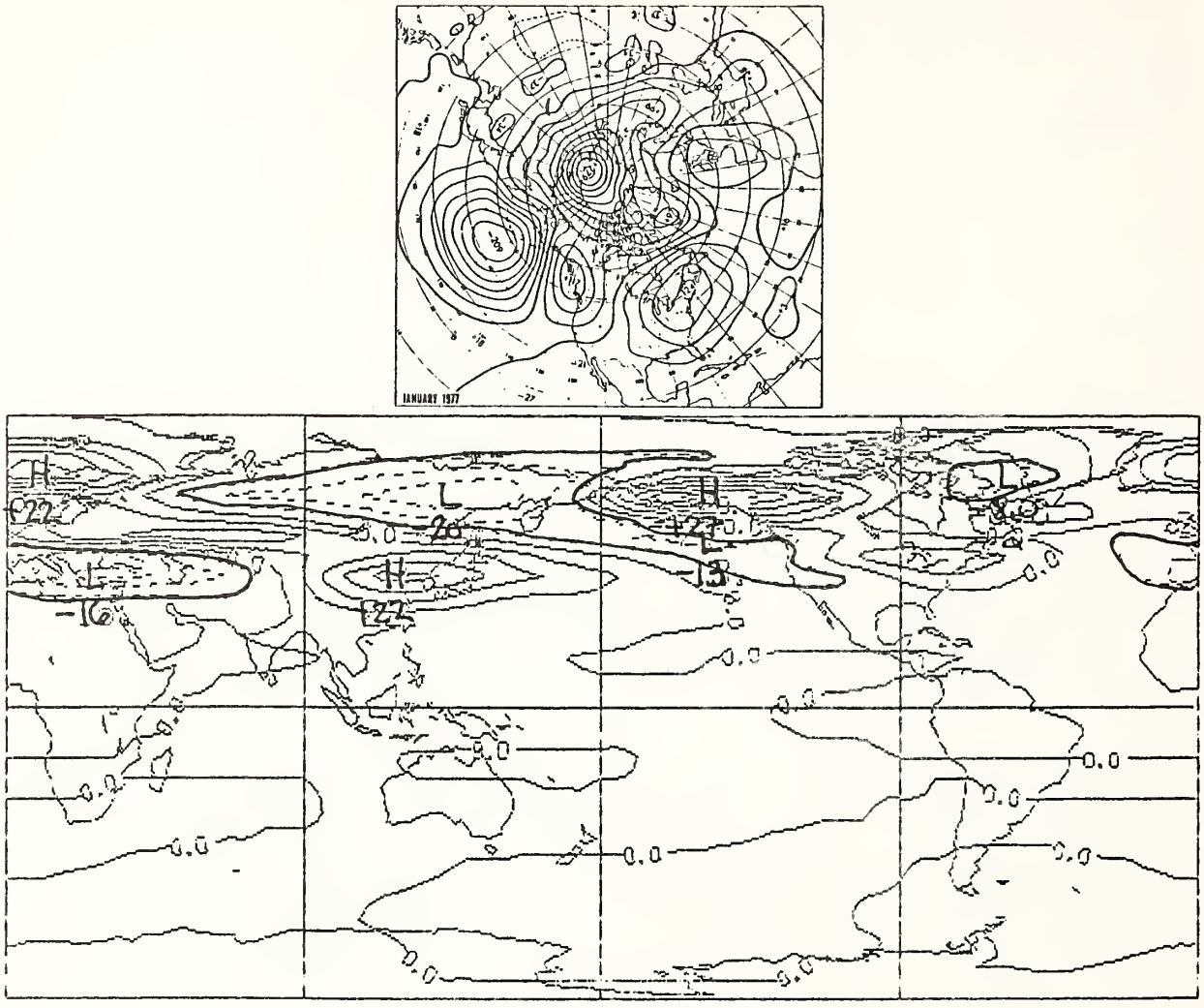

Fig. 3. Departure from normal of mean 700 mb height (m) for January 1977, observed (top) and model (bottom)

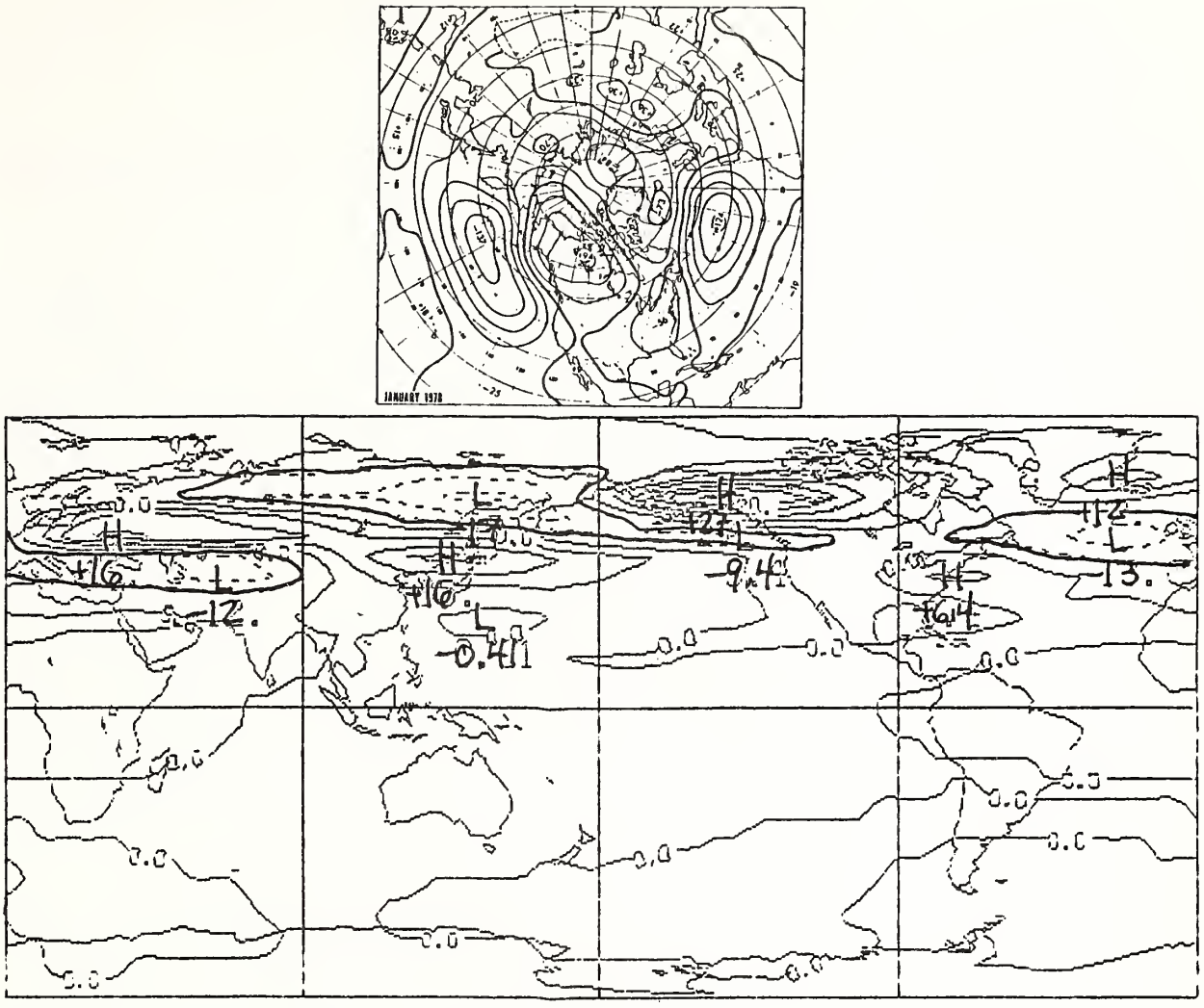

Fig. 4. Same as Fig. 3. except for January 1978.

Interannual climate variability in a low vertical resolution spectral atmospheric model

Hal B. Gordon
Australian Numerical Meteorology Research Centre
PO Box 5089AA, Melbourne, Australia

A 2-level spectral atmospheric model has been integrated for a total of 10 model years. This run is now being analysed and some preliminary results are presented here concentrating on the interannual variability (IV) generated.

The formulation of the spectral model in flux form has been described in Gordon (81), and details of performance at rhomboidal wavenumber R15 are given in Gordon (83). In the 10 year run, R21 was used, and the model physics is based upon that given in Gates et al. (71) for the RAND 2-level model. Ground hydrology is accounted for with snow cover prediction allowing for a variable surface albedo, and simple thermodynamic ice models are used at the poles allowing for self generated ice cover.

The ice model is buffered from the annually fixed sea surface temperatures (interpolated from monthly data sets) by means of a mixed layer ocean (MLO) grid point. The operation of the growth and decay of ice cover is straightforward: if an MLO point reaches freezing, ice is formed, and the next adjacent (equatorward) sea point assumes an MLO role. The reverse happens for melting conditions. In this way the need for a full ocean model is avoided. The combined model can thus be thought of as modeling all the major components of the earth-atmosphere system, except for the fixed (per year) ocean temperatures. Any IV generated will then be due to these components only, and the (expected) deficit in IV will be mainly due to the use of constant ocean temperatures per year.

In the analysis so far, the IV of the dynamical fields have been investigated by comparing seasonal means of IV for (Dec, Jan, Feb) and (Jun, July, Aug) for the 10 years against the observational data of Oort (83). In view of the large number of global maps required for a full evaluation, and the amount of detail involved, only one map is given here. This is for temperature at 700 mb for DJF - see Fig. 1. This shows appreciable IV compared to the observations, especially in the mid to high latitudes. There are systematic differences, part of which will be due to the low resolution of the model, and part due to the use of a particular observational data set. As a general statement, in most of the dynamical fields investigated (temperature, winds, geopotential heights etc.) the model underestimates the IV by roughly 50%, with the tropics faring the worst. This is not surprising in view of the importance of the SST's in the tropics on the atmospheric flow, and the use of fixed SST values from year to year is thus expected to diminish the IV generated by the model in the tropics.

In the case of the model performance in regard to the ice cover generated, given in Figs 2,3 are the instantaneous ice cover (and snow) for years 4-6 on April 16 and October 16 respectively. The ice is seen to have reasonable changes of extent between seasons, together with appreciable IV of distribution (note that grid boxes are 5.63° EW by 3.21°NS approx).

In order to give a basic idea of the amount of IV generated by the model, the separate hemispheric mean temperatures at 700 mb and 300 mb are plotted for January and July, along with observations from Oort (83) for the NH, and from Karoly (private communication) for the SH. These are shown in Figs 4, 5. It is clear from these that the model underestimates the IV by about 50%.

Similar diagrams are given for the mean evaporation (less sublimation) and the rainfall: Figs. 6, 7. Both the evaporation and rainfall show appreciable IV. By comparing these two, it is seen that the evaporation has very similar hemispheric means, whereas the rainfall has rather different magnitude hemispheric means, which may be viewed as an indication of the cross equatorial transport of moisture achieved by the model.

In conclusion, the model is found to underestimate the IV by about a half in general terms, with the tropics showing the greatest deficiency in IV. It is clear that the addition of interactive ocean model will be necessary to achieve adequate IV, especially in the tropics.

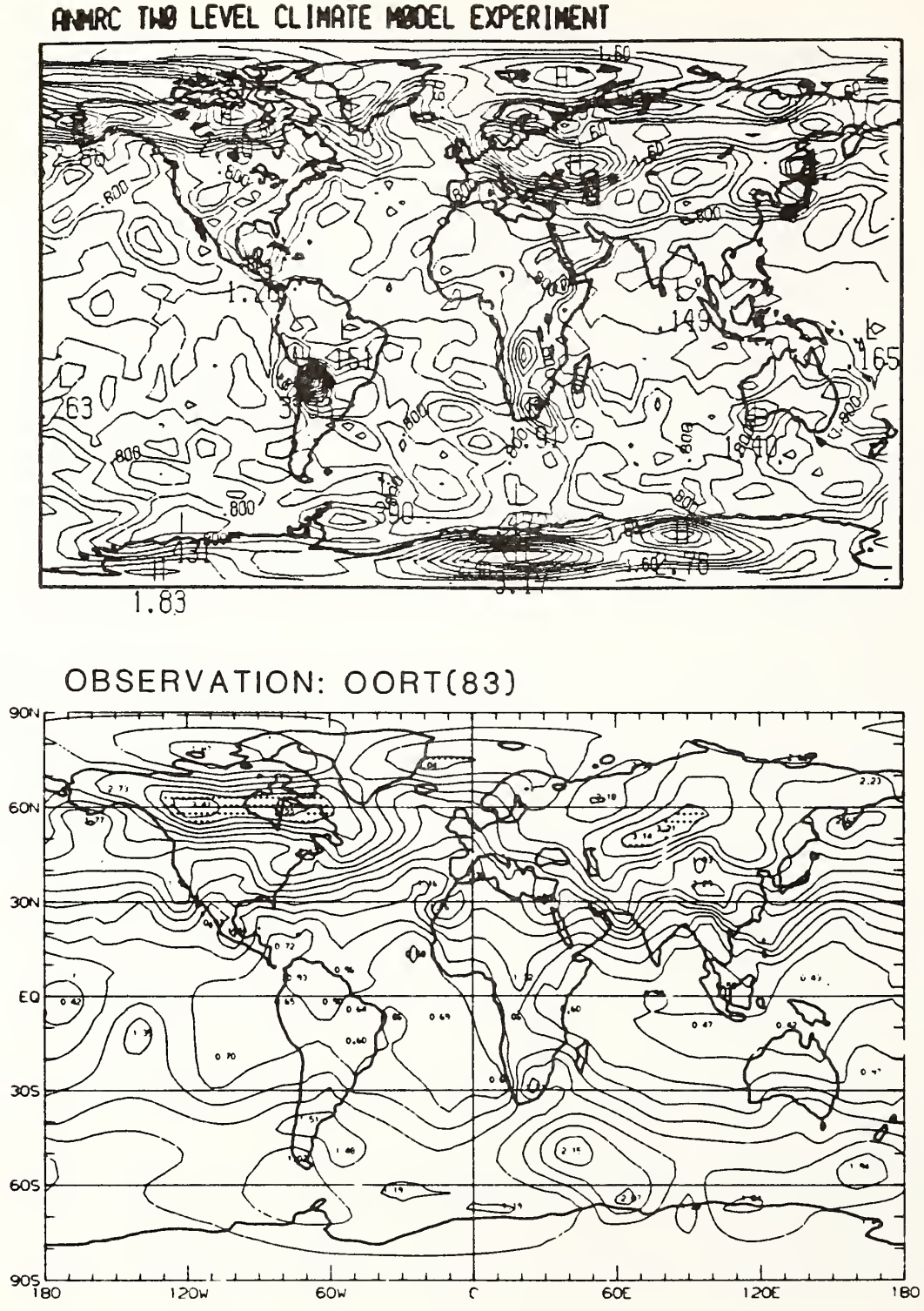

Fig. 1 : (Dec,Jan,Feb) 700 mb Temperature Interannual Variability

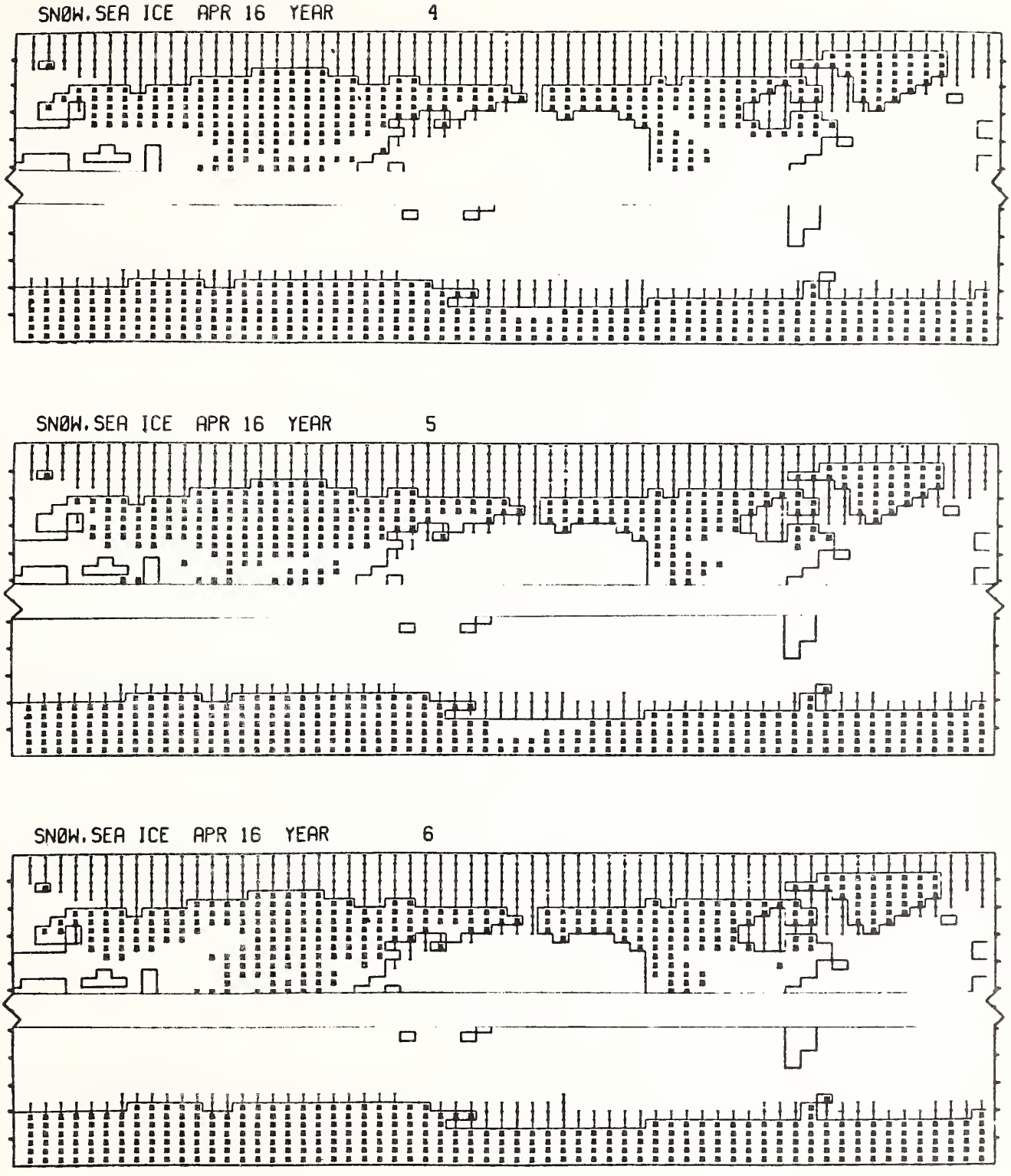
SNØW.SEA ICE APR 16 YEAR 4
SNØW.SEA ICE APR 16 YEAR 5
SNØW.SEA ICE APR 16 YEAR 6

Fig. 2

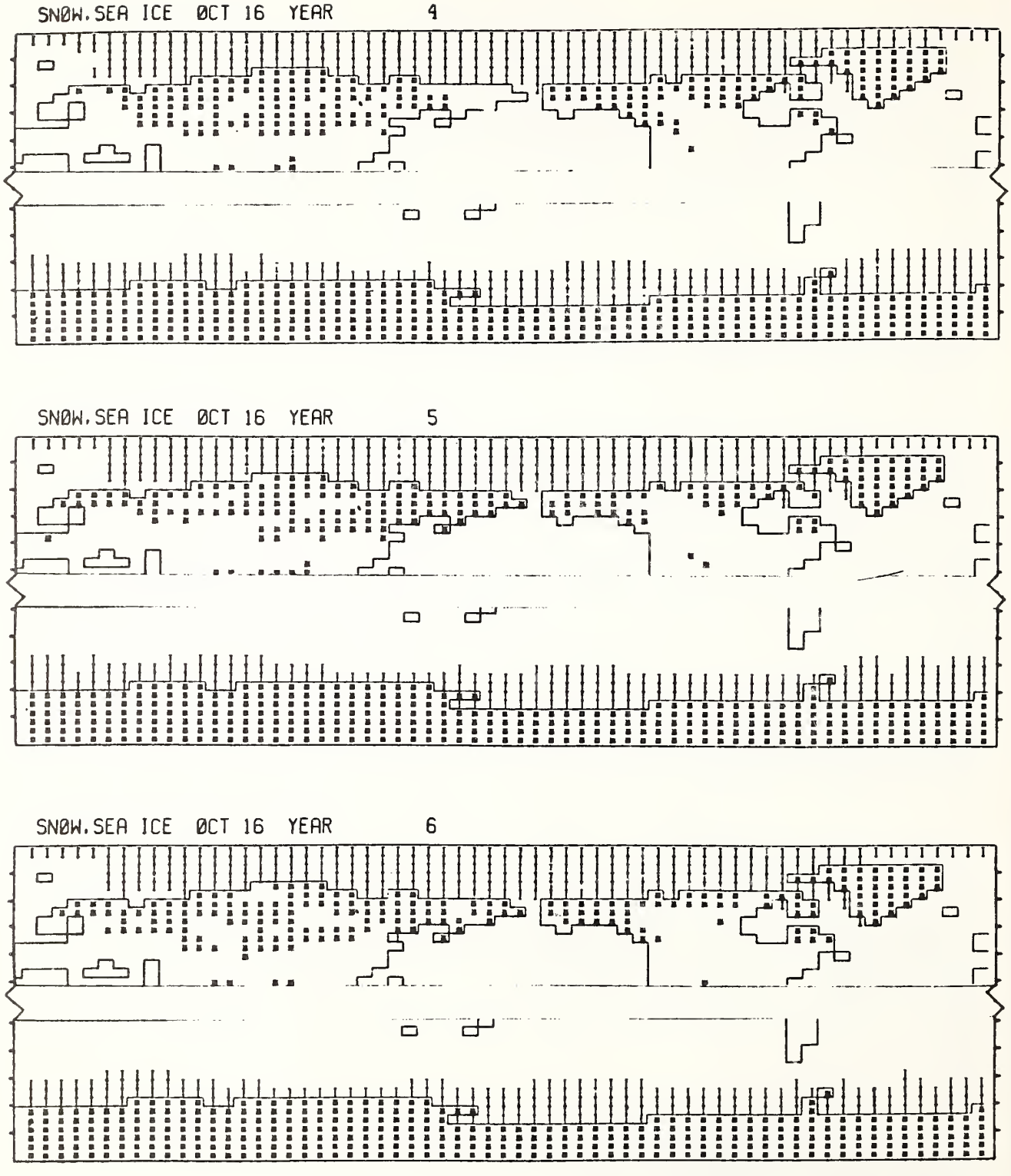
SNØW.SEA ICE ØCT 16 YEAR 4
SNØW.SEA ICE ØCT 16 YEAR 5
SNØW.SEA ICE ØCT 16 YEAR 6

Fig. 3

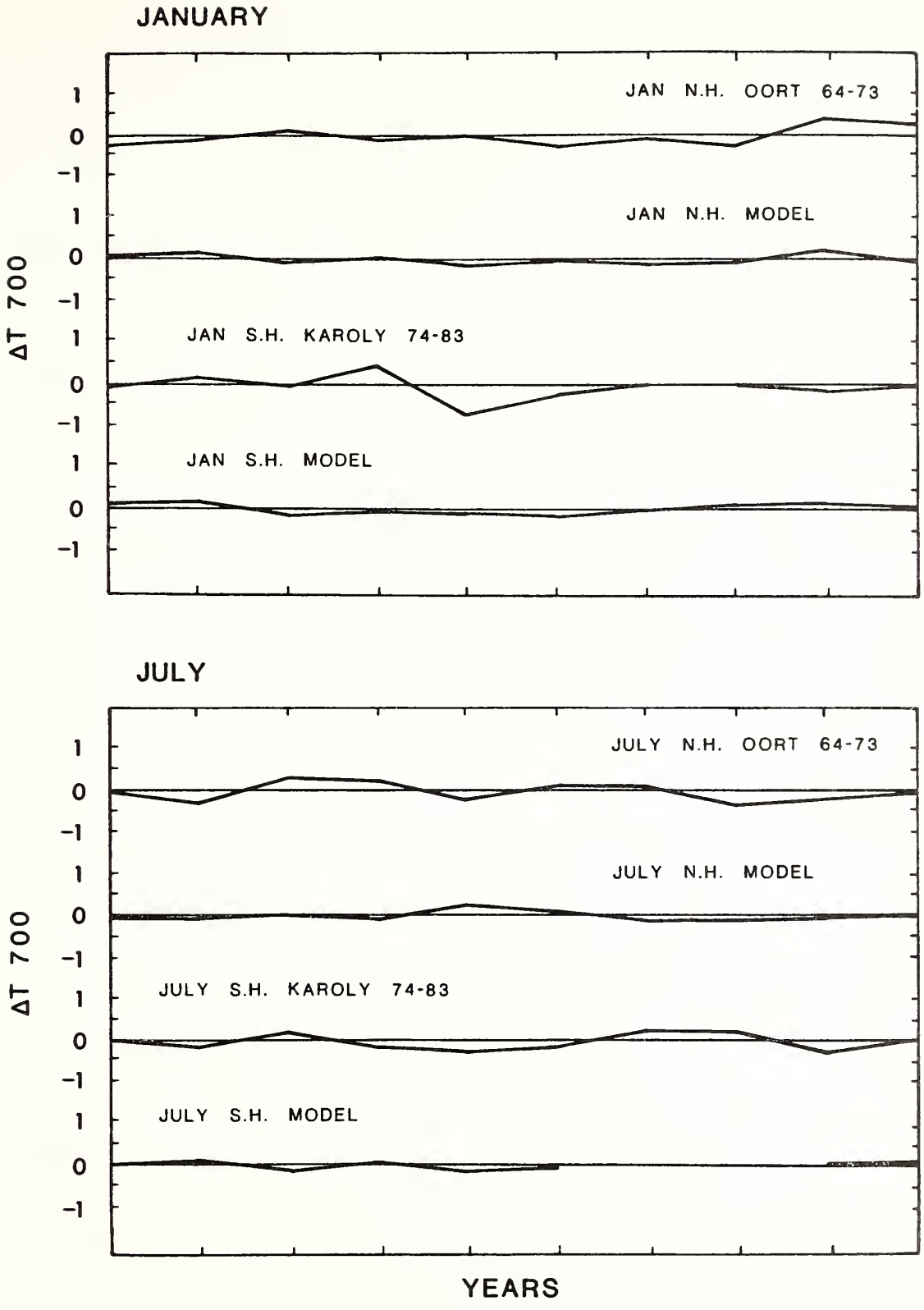

Fig 4 Hemispheric temperature variations at 700mb about a 10 year mean.

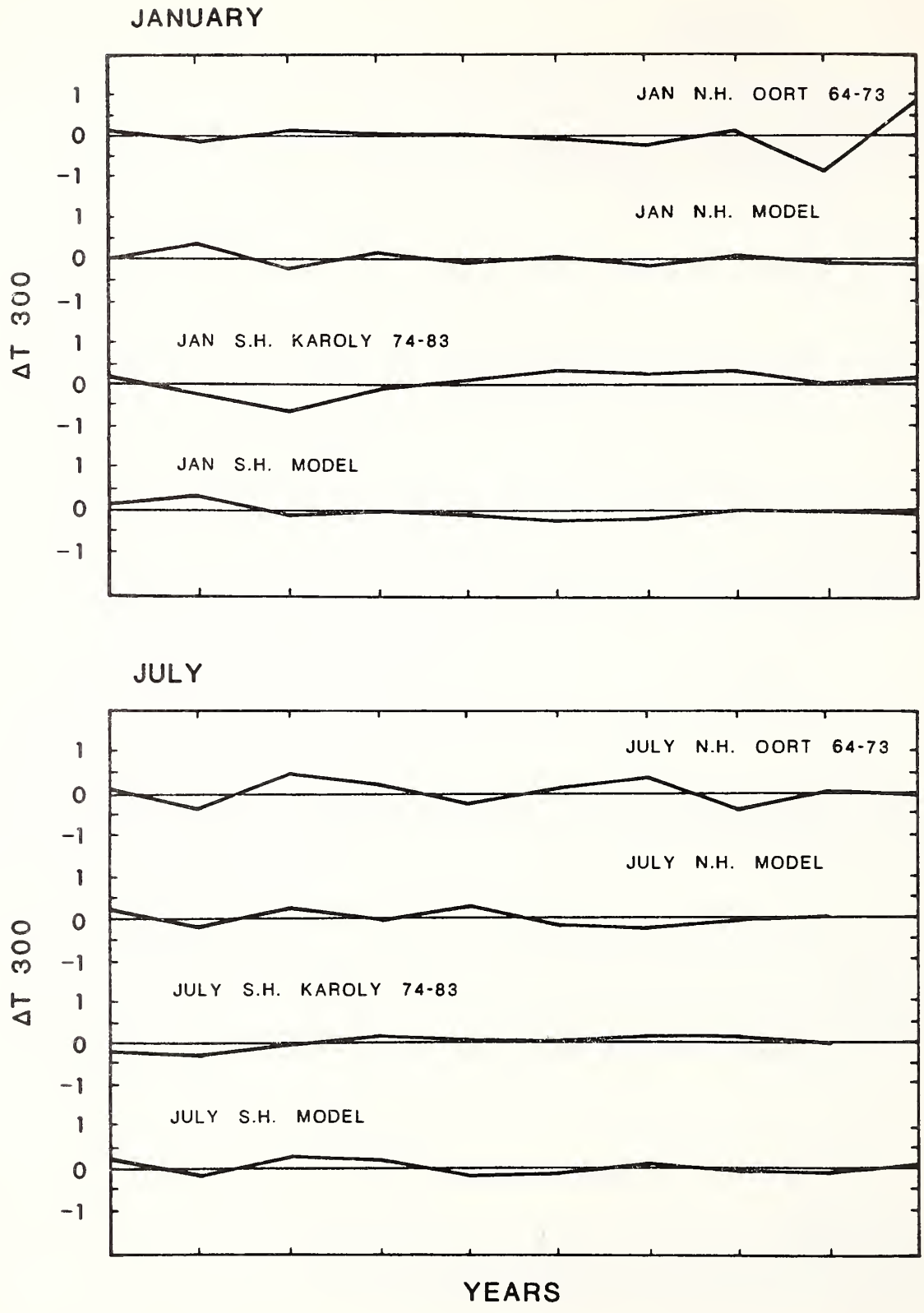

Fig 5 Hemispheric temperature variations at 300mb about a 10 year mean.

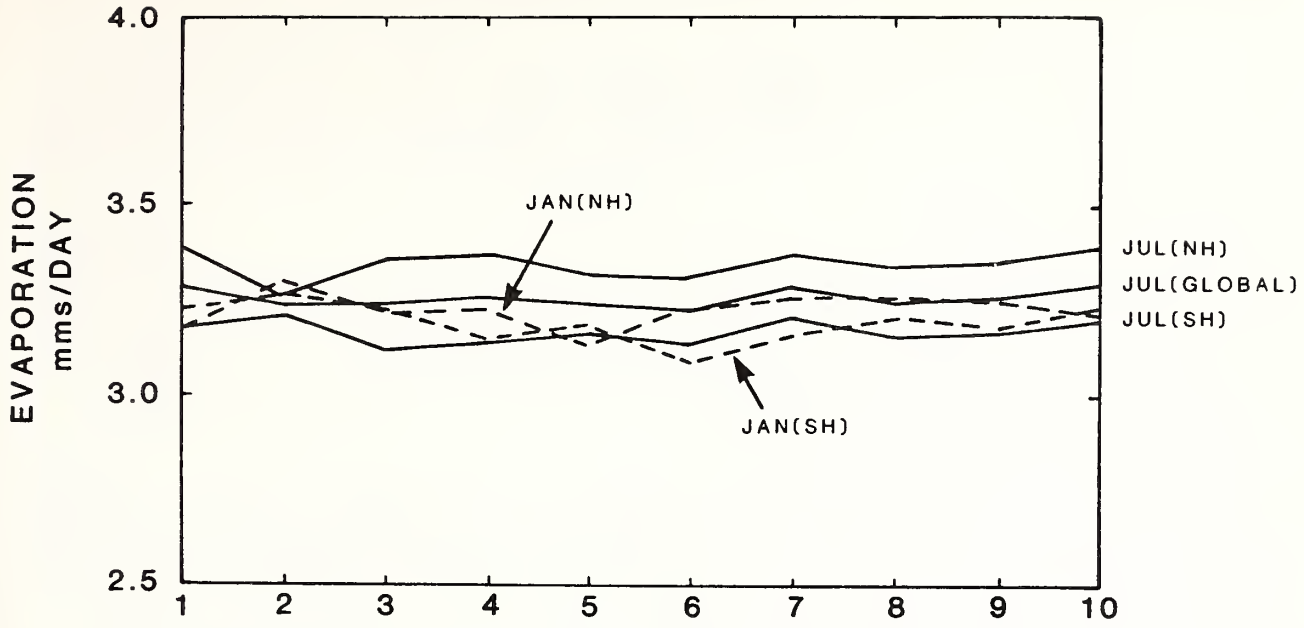

Fig 6 Model hemispheric mean evaporation (less sublimation) for January and July.

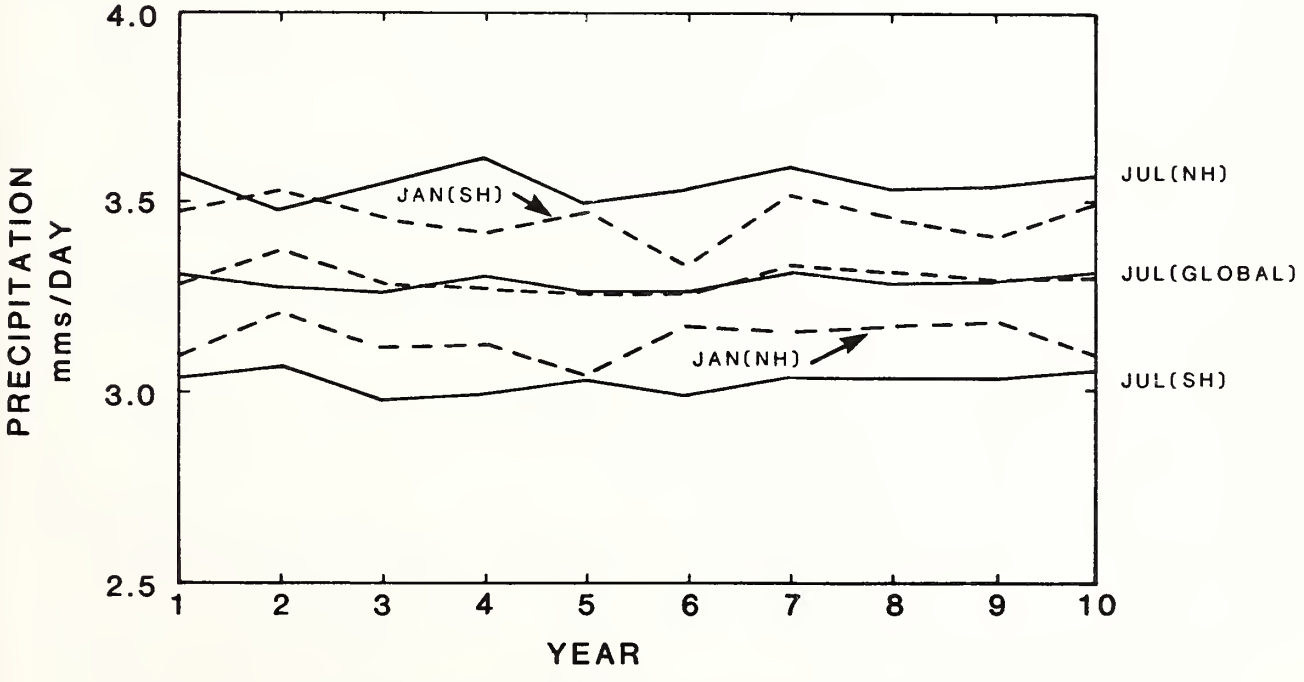

Fig 7 Model hemispheric mean Precipitation for January and July.

Variability simulations with a steady, linearized primitive equations model

James L. Kinter III
NASA Goddard Space Flight Center
Greenbelt, MD 20771

and

Sumant Nigam
Department of Earth, Atmospheric and Planetary Sciences
Massachusetts Institute of Technology
Cambridge, MA 02139

Solutions of the steady, primitive equations on a sphere, linearized about a zonally symmetric basic state are to be computed for the purpose of simulating monthly mean variability in the troposphere. The basic states are observed, winter monthly mean, zonal means of zonal and meridional velocities, temperatures and surface pressures computed from the 15 year NMC time series. A least squares fit to a series of Legendre polynomials is used to compute the basic states between 20 N and the equator, and the hemispheres are assumed symmetric. The model is spectral in the zonal direction, and centered differences are employed in the meridional and vertical directions. Since the model is steady and linear, the solution is obtained by inversion of a block, pente-diagonal matrix.

The model simulates the climatology of the GFDL nine level, spectral general circulation model quite closely, particularly in middle latitudes above the boundary layer (Nigam, 1984). This experiment is an extension of that simulation to examine variability of the steady, linear solution.

In creating a verification data set for this experiment, we noticed that there are some differences between monthly mean variability and seasonal mean variability in the winter troposphere. In particular, the seasonal mean variability more clearly reflects the wave train in the north Pacific and North

American regions (see figures 1 and 2). Also, the center of large monthly mean variability in the central north Atlantic (figure 1) is considerably weaker on the seasonal mean map. We intend to examine these features of tropospheric variability in future experiments.

Reference

Nigam, S., 1984: "On the structure and forcing of tropospheric stationary waves." Ph.D. Thesis, Princeton University, 203 pp.

Figures

Figure 1: Root mean square 300 mb height monthly mean departures from December, January and February climatologies (15 year means) averaged over the three months.

Figure 2: Root mean square 300 mb height seasonal mean departures from winter climatology.

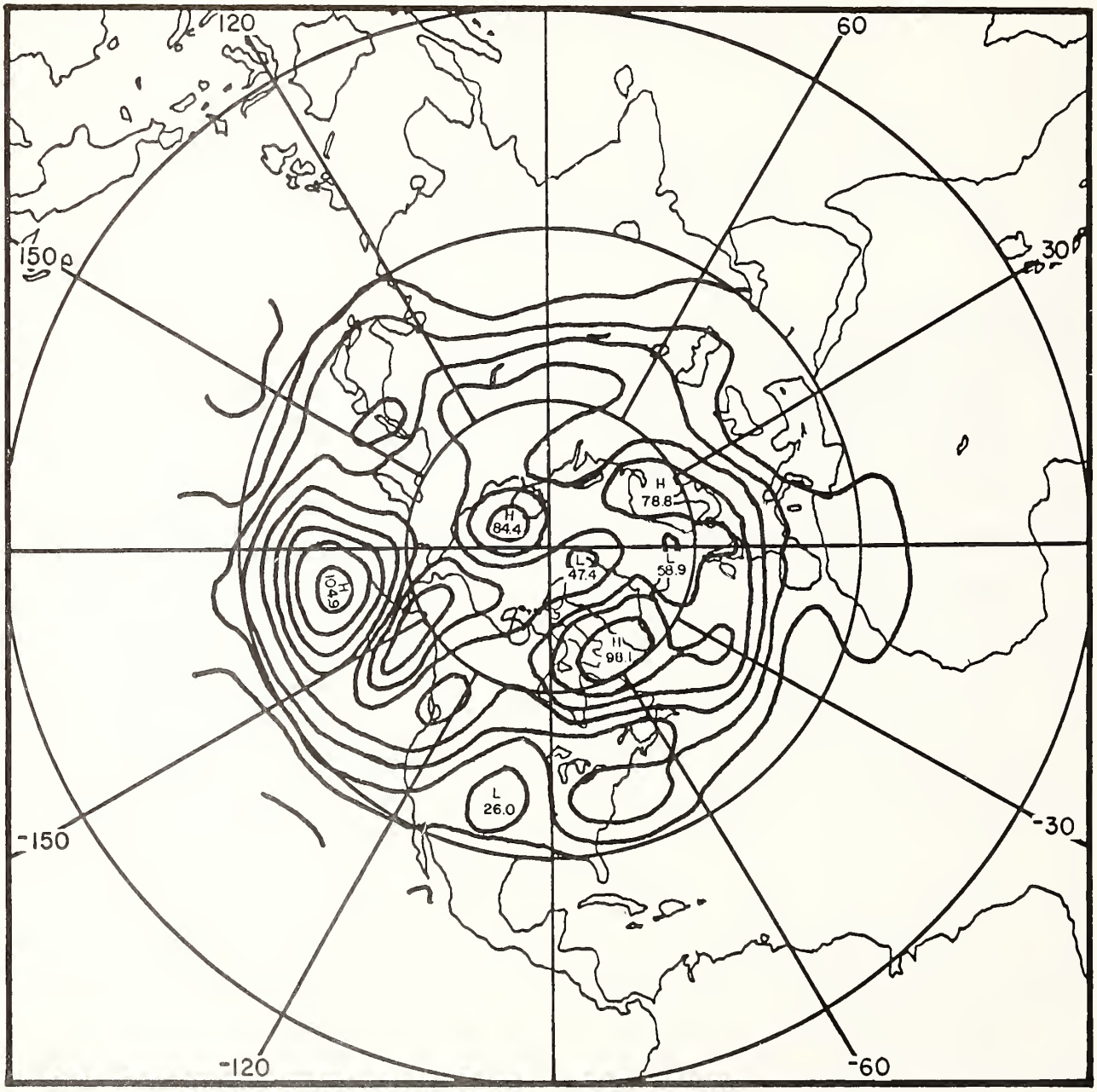

FIGURE 1

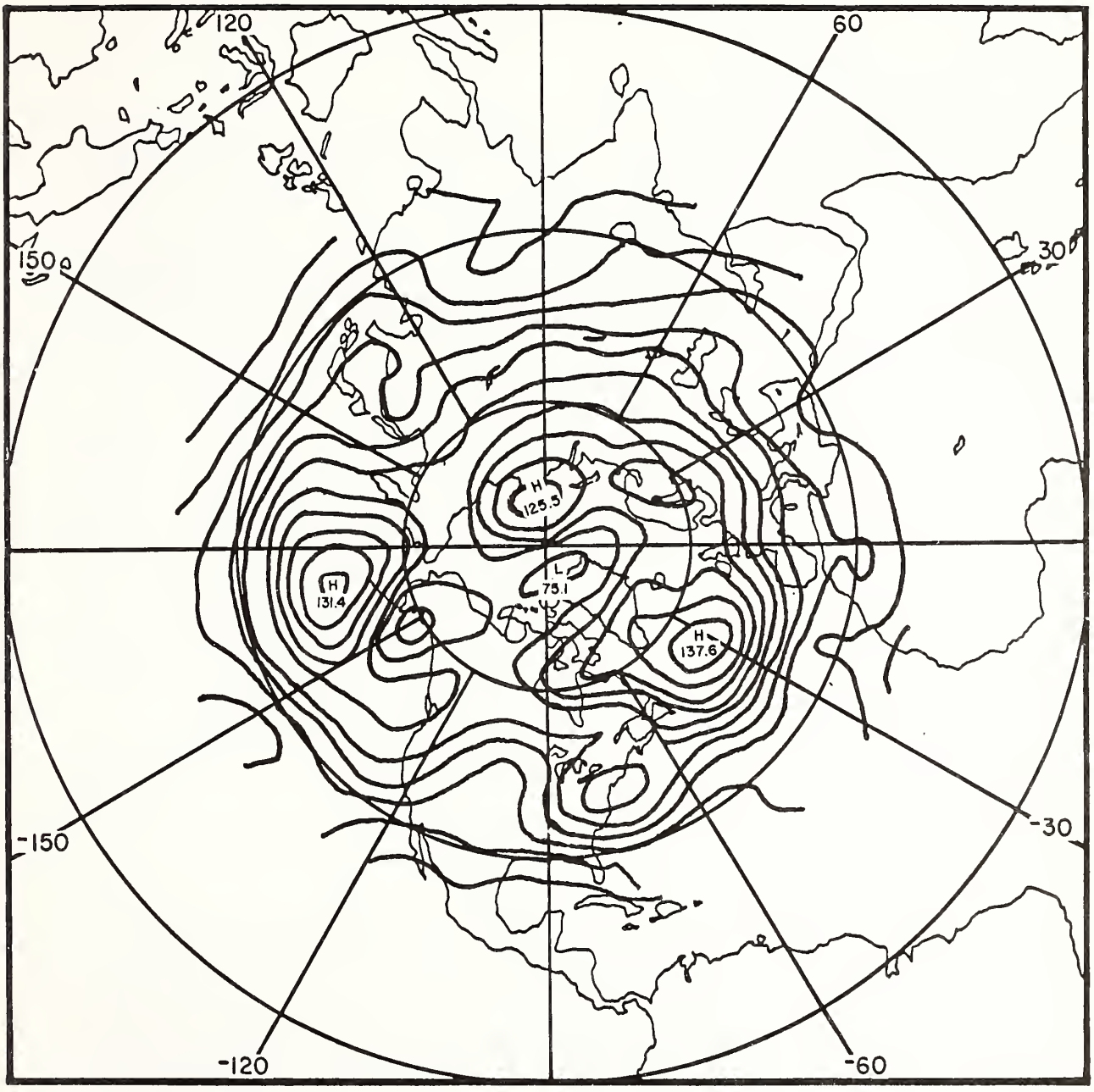

FIGURE 2

Understanding El Niño Events using a Simple Dynamical Atmosphere Model

Bryan C. Weare
Department of Land, Air and Water Resources
University of California
Davis, CA 95616

This paper outlines a simple model which illustrates possible feedback mechanisms linking oceanic surface conditions with tropical atmospheric heating and surface circulation. The results of the model suggest the importance of feedback mechanisms in the initiation and development of El Niño episodes.

The basic model is patterned after the reduced gravity model on an equatorial β-plane introduced by Gill in 1980. The equations giving solutions for the perturbations of the winds (u', v') pressure (p'), vertical velocity (w') and potential temperature (θ') are

$$\varepsilon u' + \bar{U}\frac{\partial u'}{\partial x} + \frac{1}{\rho_s}\frac{\partial p'}{\partial x} - \beta y v' = 0 \qquad (1)$$

$$\varepsilon v' + \bar{U}\frac{\partial v'}{\partial x} + \frac{1}{\rho_s}\frac{\partial p'}{\partial y} + \beta y u' = 0 \qquad (2)$$

$$\varepsilon \theta' + \bar{U}\frac{\partial \theta'}{\partial x} + w'\frac{\partial \theta_s}{\partial z} = Q' \qquad (3)$$

$$\frac{\partial u'}{\partial x} + \frac{\partial v'}{\partial y} + \frac{1}{\rho_s}\frac{\partial}{\partial z}(\rho_s w') = 0 \qquad (4)$$

$$\frac{\partial p'}{\partial z} = g\,\rho_s\,\theta'/\theta_s \qquad (5)$$

where the usual meteorological conventions are largely followed and ε is a dissipation constant of about 0.02, $\bar{U}$ is a mean zonal wind of -5 m/s, ρ_s and θ_s are reference vertical profiles of density and potential temperature, and Q' is a heating rate stimulating the forced solution. This Q' is usually prescribed to represent the intensity and distribution of anomalous rainfall and hence latent heating of the atmosphere.

Unlike most previous uses of this model the forcing function Q will not be fixed but will be a function of the model circulation together with fixed oceanic conditions. The form of Q has been derived from considering the vertically integrated equation describing the conservation of moisture, which in a steady state may be approximately written as $Q = LP = L(E - \nabla \cdot Q_w)$. L is the latent heat of evaporation, P the precipitation, E the evaporation from the

surface and $\nabla \cdot Q_w$ the divergence of the vertically integrated flux of moisture. The evaporation is estimated by a "bulk" formula using model derived wind speeds and observed surface layer humidity and sea surface temperature. The moisture divergence is estimated from surface layer moisture convergence based upon model winds and observed surface layer humidities.

When these substitutions are made and the result linearize about a mean Q, then the perturbation heating may be expressed as

$$Q' = L[-\lambda(\underbrace{\bar{U}\frac{\partial q'}{\partial x}}_{A} + \underbrace{\bar{q}\,\nabla\cdot\underline{\vec{v}}' + \underline{\vec{v}}'\cdot\nabla\bar{q}}_{B}) + \mu\,\underbrace{C_E(\bar{U}\,\Delta q + \underline{\vec{v}}'\,\overline{\Delta q})}_{C}] \qquad (6)$$

where λ is an equivalent depth relating the surface layer divergence to the vertically integrated value, μ is the fraction of evaporated moisture which condenses in the middle troposphere, C_E is an exchange coefficient and Δq is the observed air-sea humidity difference. The overbars denote time averages and the underlines the model (Eqn. 1-5) dependent terms.

A number of experiments have been performed with the model comprising Eqn. 1-6 using $\bar{q}$ shown in Fig. 1a and assuming $\overline{\Delta q} = 0.25\bar{q}$. Humidity perturbation q' were imposed at 2.5°N (see Fig. 1b) and 22.5°S where it was assumed $\Delta q' = 0.25q'$. The resultant heating and wind fields using only term A in Eqn. 6 are considered the response without circulation feedback, since term A is a function of only the fixed $\bar{U}$ and the observed q'. These Q' for the q' at 2.5°N and 22.5°S are shown in Fig. 2a,b, respectively.

Fig. 3-8 indicate the response of the model to term B, convergence and advection of the mean humidity, and term C, surface evaporation, for initial q perturbation at 2.5°N and 22.5°S. The basic conclusions are:

1) The convergence and advection of mean moisture tend to narrow the scale of the relative heating and wind perturbation, especially for initial q perturbations near the equator.

2) The evaporation feedback tends to broaden the scale of the heating and wind perturbations (toward that of $\bar{q}$).

3) Both sets of feedback mechanisms tend to shift the heating and wind departures equatorward for the initial perturbation near 22.5°S.

4) Both sets of feedbacks tend to shift the resultant heating and wind perturbations to the west for the 22.5°S perturbation.

The latter two conclusions suggest a mechanism whereby subtropical perturbations in q and SST may lead to relatively strong equatorial wind changes. The El Niño composites of Rassmusson and Carpenter and Weare both suggest SST departures in the central and eastern Pacific near 25°S in the autumn season before El Niño (see Fig. 9a). This pattern (together with the observed q') were used to force the model (Eqn. 1-6) and the resultant heating and wind fields are shown in Fig. 9b and 10a, respectively. Fig. 10b shows the observed wind field anomalies for the composite El Niño. While the match is only fair the model result does seem to predict the relatively large equatorial wind anomalies in the western Pacific and the weak anomalies in the eastern ocean.

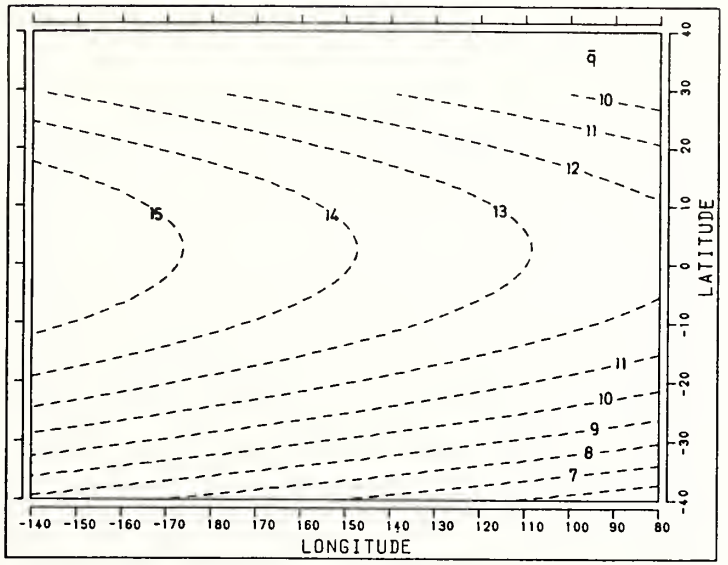

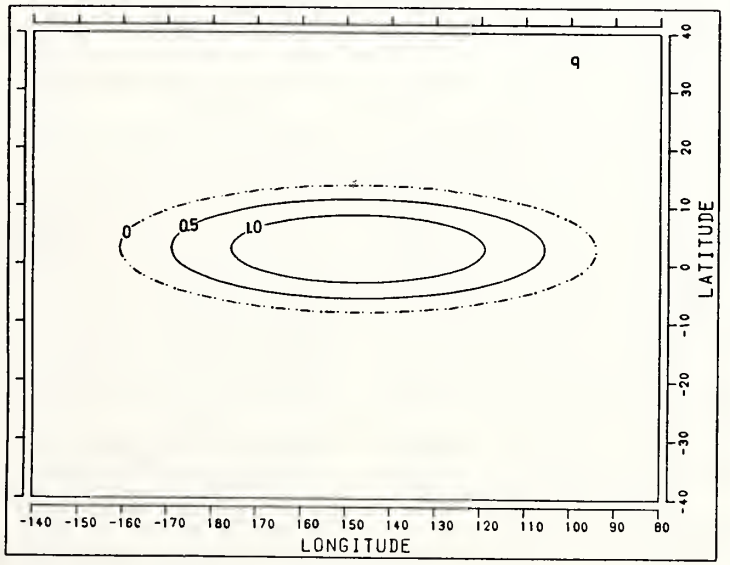

Fig. 1 a) Mean surface humidity $\bar{q}$ used in the sensitivity experiments of the model Eqn. 1-6; $\overline{\Delta q} = 0.25\bar{q}$.
b) Perturbation specific humidity q' centered at 2.5°N used as the fixed forcing of Eqn. 6; $\Delta q' = 0.25q'$. The perturbation specific humidity centered at 22.5°S has the same shape as that illustrated in b).

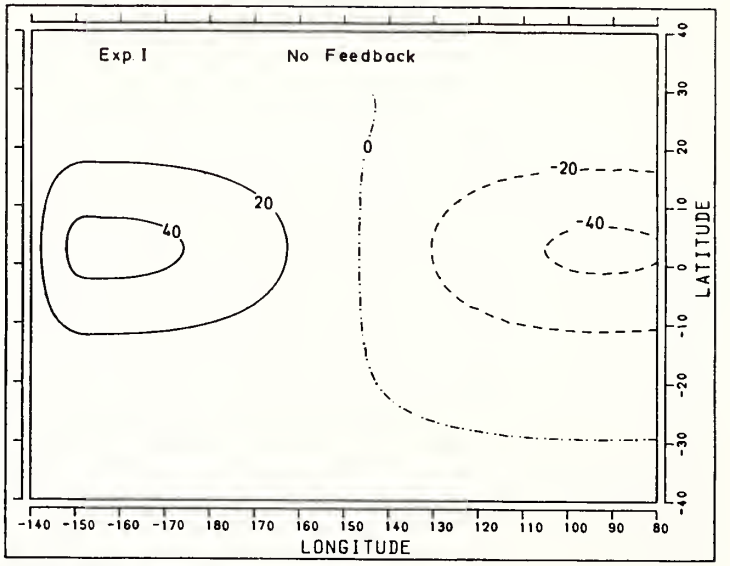

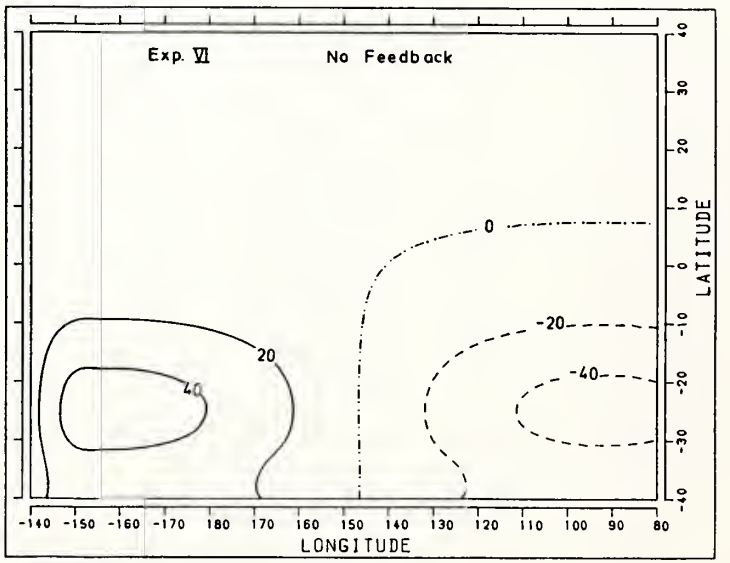

Fig. 2 The "fixed" heating of the model Eqn. 1-6 derived from only term A of Eqn. 6 for the q' centered at a) 2.5°N and b) 22.5°S. These are referred to as the forcing without model wind feedbacks.

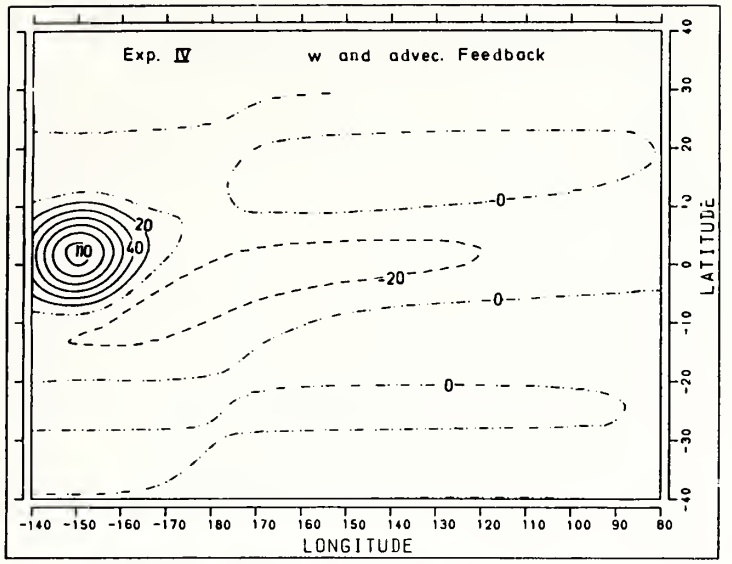

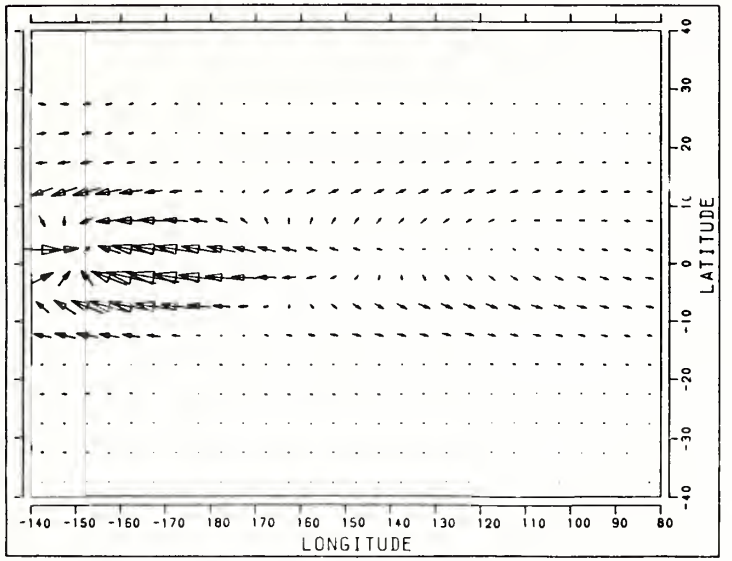

Fig. 3 The heating and wind fields for the model, including terms A and B in Eqn. 6 for q' near 2.5°N. The convergence and advection have shifted the relative heating westward and reduced its geographical scale relative to that of the "fixed" heating in Fig. 2a.

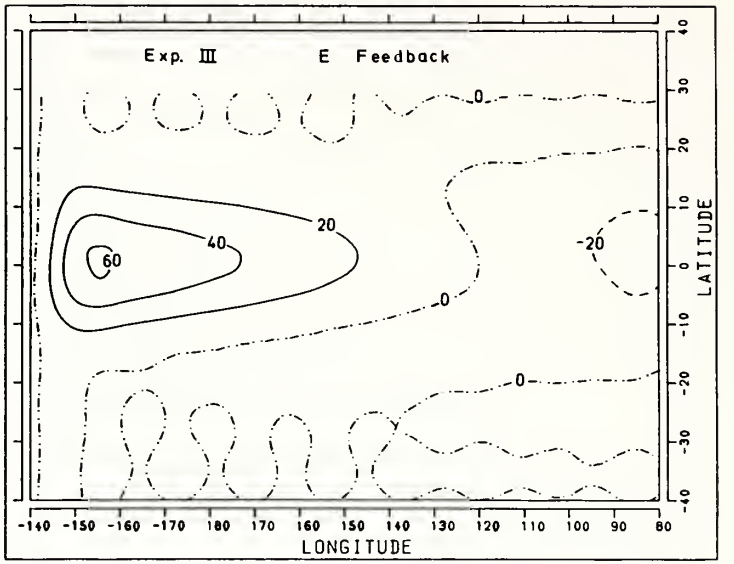

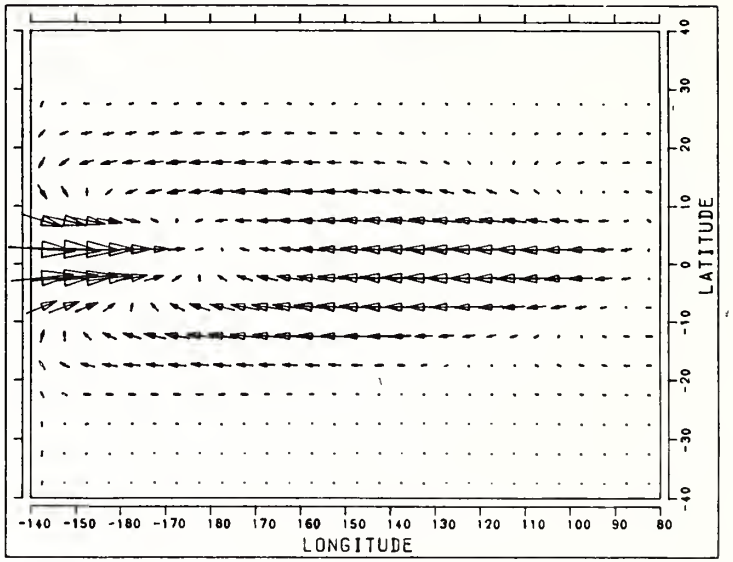

Fig. 4 The heating and wind fields as in Fig. 3 for terms A and C in Eqn. 6. The evaporation terms have tended to maintain or increase the scale of the fixed heating shown in Fig. 2.

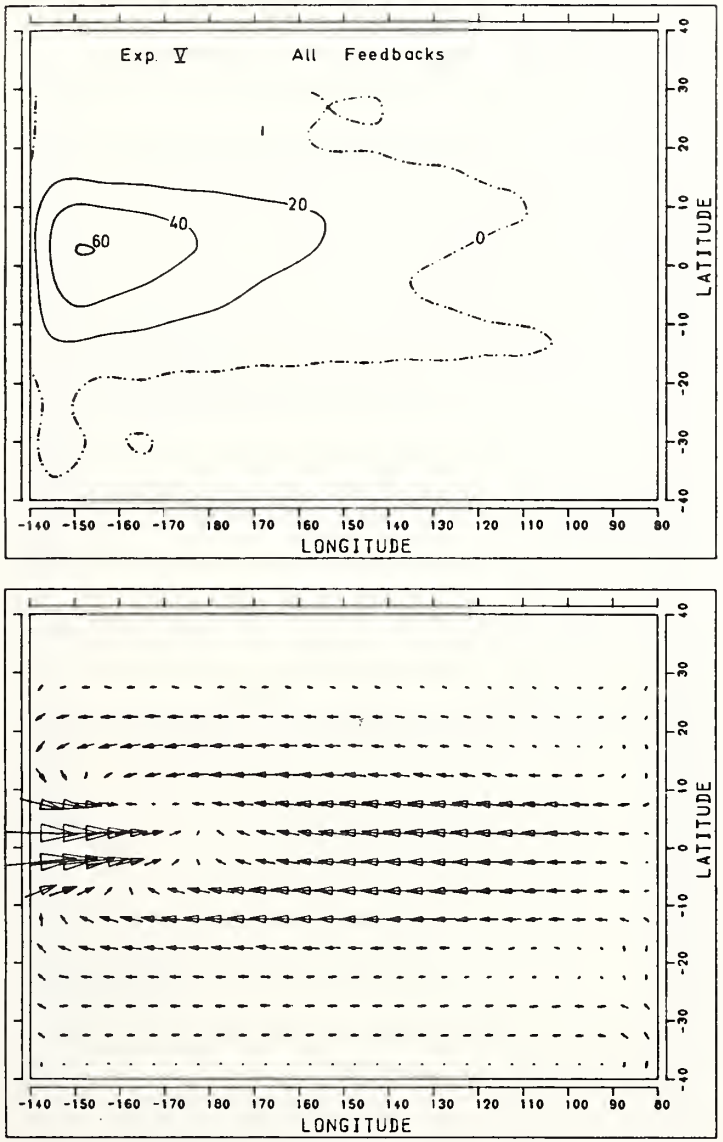

Fig. 5 The heating and wind fields as in Fig. 3 for all terms in Eqn. 6. The results are more similar to those in Fig. 2 or 4 than Fig. 3 suggesting that the evaporative terms tend to dominate. Observed El Niño wind and heating departures (diagnosed from satellite derived outgoing long-wave radiation) tend to show scales similar to these.

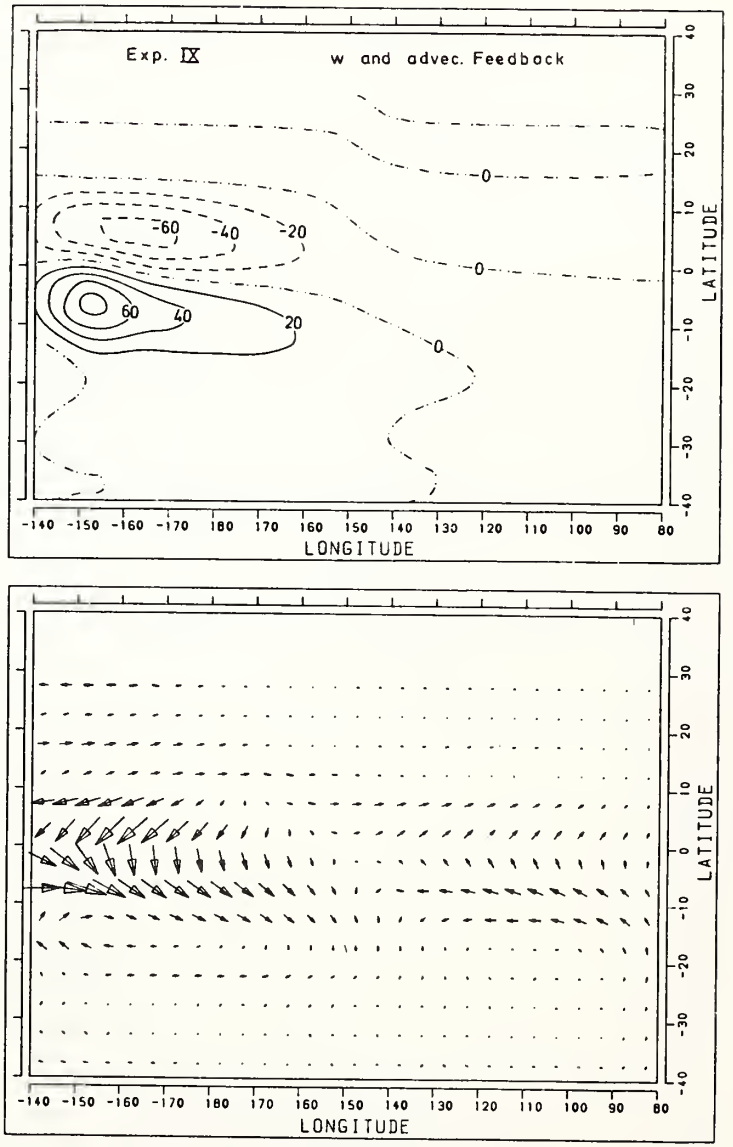

Fig. 6 The heating and wind field for the model including terms A and B in Eqn. 6 for q' near 22.5°S. The convergence and advection have shifted the relative heating zone far equatorward and westward and have induced a relative cooling zone to the north of the equator compared to the "fixed" heating illustrated in Fig. 2b.

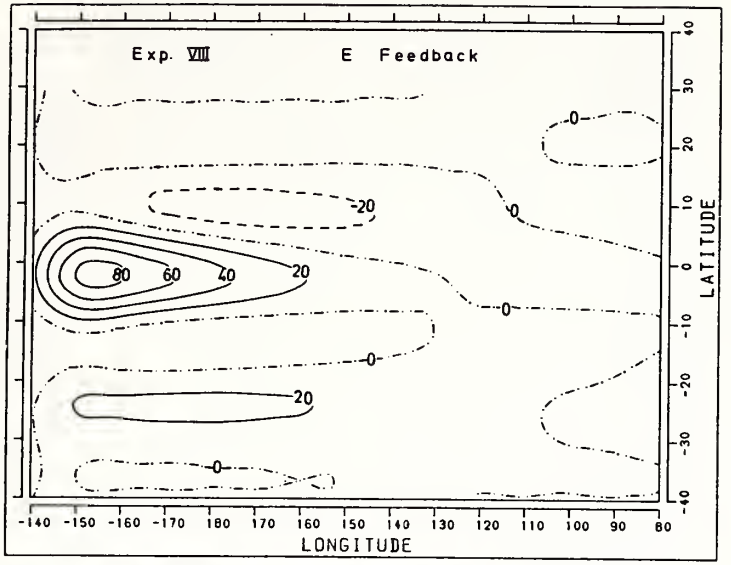

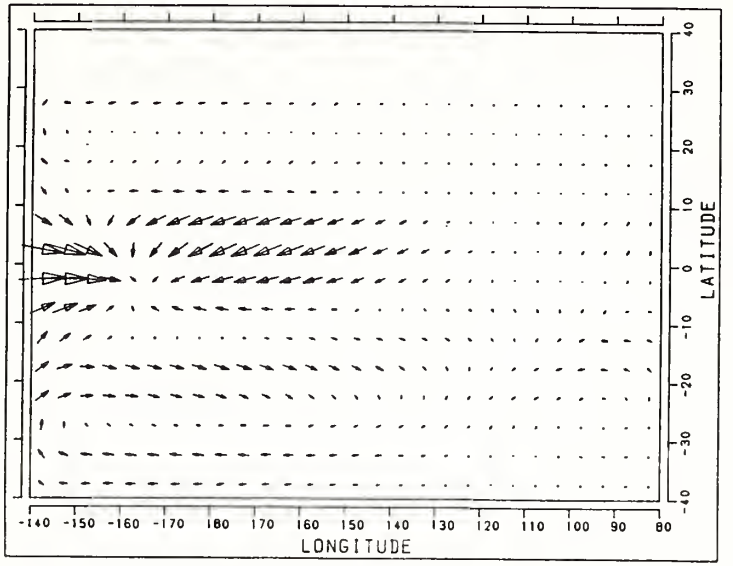

Fig. 7 The heating and wind fields as in Fig. 6 for terms A and C in Eqn. 6. The evaporation feedback has tended to shift the main heating zone far equatorward compared to that shown in Fig. 2b.

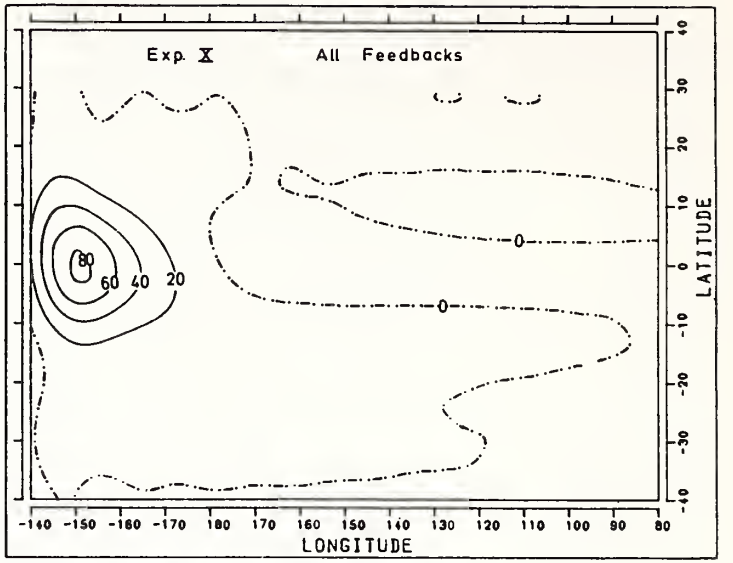

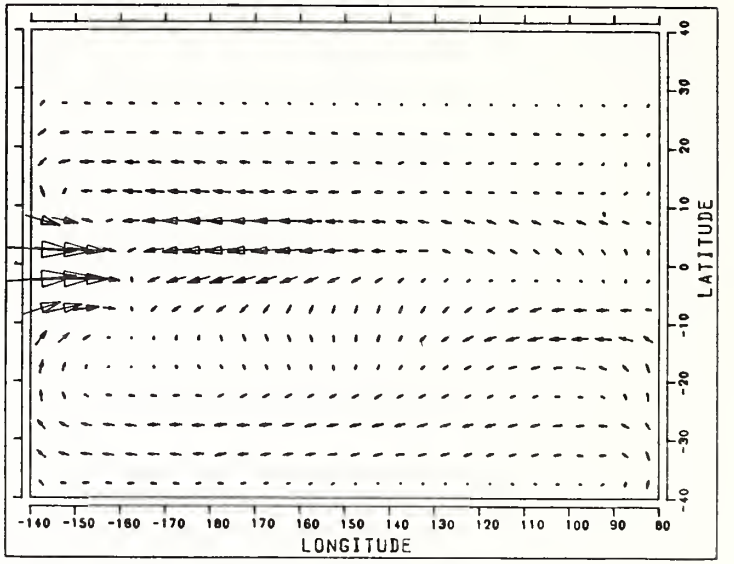

Fig. 8 The heating and wind field as in Fig. 6 for all terms in Eqn. 6. The heating zone is now concentrated in the western equatorial region despite the fact that the initial perturbation is near 22.5°S. This result is remarkably similar to that for a equatorial perturbation shown in Fig. 5.

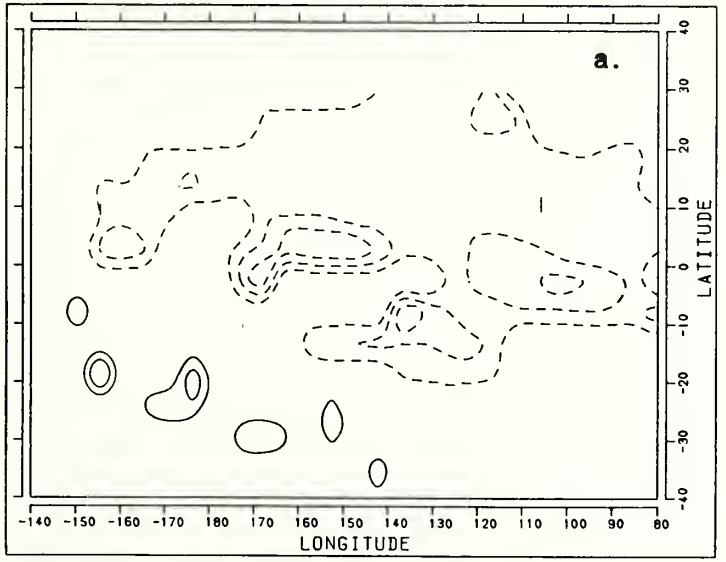

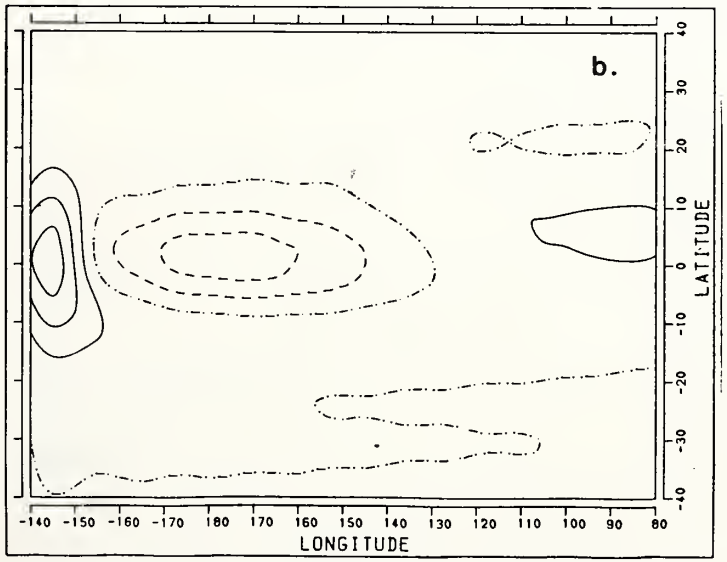

Fig. 9 a) Observed SST anomaly for the autumn before the composite El Niño of 1957, 65, 72 and 76. Note the warm anomalies between 20° and 30°S in the general region of the dateline.
b) The model heating, using the above SST departure and also the observed q departures in Eqn. 6 including all terms. Note the equatorward and westward shift of the heating zone relative to the region of the positive SST departures.

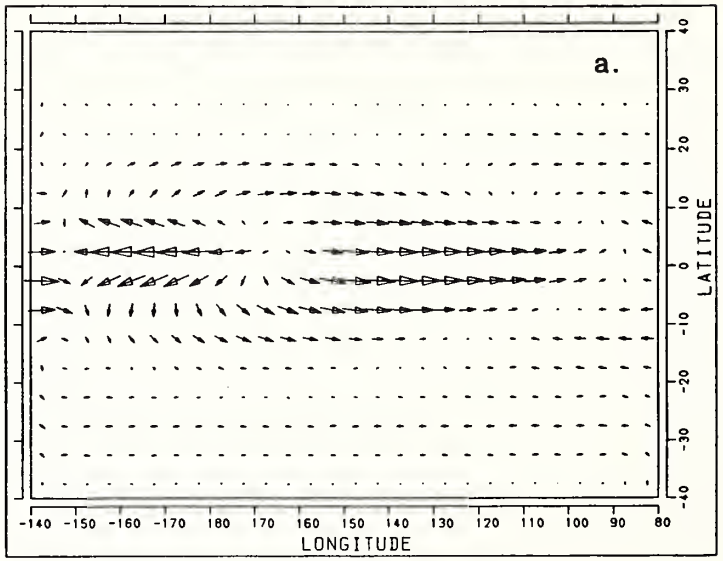

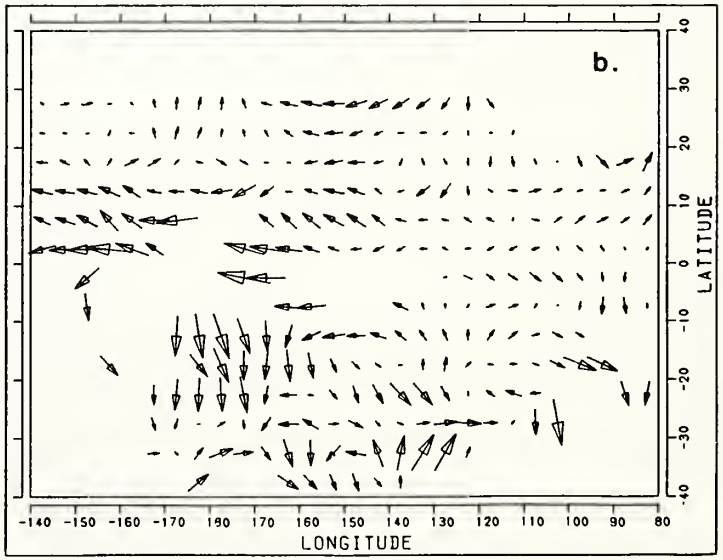

Fig. 10 a) Model derived surface wind field for the pre El Niño autumn whose SST departures and heating perturbation are illustrated in Fig. 9.
b) Observed departures of surface wind for the pre El Niño season. Areas in b) with no arrows are either over continents (far northeast and southwest) or with insufficient observations. Note the anomalous easterlies in the western equatorial region in both a) and b).

Anomaly General Circulation Models

A. Navarra
GFDP, Princeton University
Princeton, New Jersey 08542

K. Miyakoda
GFDL/NOAA, Princeton University
Princeton, New Jersey 08542

1. Introduction

This work represents the extension of our previous paper on the barotropic anomaly model (Navarra and Miyakoda, 1983); the paper describes more references on the basic concept and history of the anomaly model. After obtaining an encouraging result from the barotropic model, we decided to proceed to construct a baroclinic anomaly model, based on an existing GCM. Both a time-dependent, non linear version, and a steady, linear version of the anomaly model have been prepared, but we will discuss here only the application of the steady, linear model. Since the full GCM and the anomaly GCM are closely related, the anomaly model may facilitate the investigation of dynamical characteristics of the solution of full GCM, if an appropriate set of basic state and forcing is specified.

Linear models have been considered by a number of investigators in the past, among others, Hoskins and Grose (1977), Hoskins and Karoly (1981), Nigam (1983), but our approach is different from the works mentioned above. They treated deviated circulation fields from the zonal mean basic state, whereas our model treats deviations from climatology, and therefore, the basic state is of non-zonal symmetry. Including the zonal variations of basic state is not merely a mathematical extension, but new dynamical processes such as the effect of the standing wave pattern on the forced waves in the mid-latitudes can be handled.

From a mathematical point of view, the restriction of the zonally symmetric critical line will be relaxed. In an asymmetric linear model there is no critical line, because meridional advection usually compensates when $\bar{u} = 0$, and so the equations are regular everywhere. This point may have some implications for the propagating waves from heat sources south of the equator.

2. The anomaly model

The procedure to obtain the anomaly model from a GCM has already been described and therefore we will sketch only the essential parts.

We use the primitive equation for vorticity and divergence in the spectral model formulation. In the vertical, sigma coordinates are used, while for the horizontal direction an expansion in terms of spherical harmonics $Y_{nm} = P_{n,m}(\phi)\exp(im\lambda)$ of all physical fields is employed. We now divide variables, temperature T, for example, into two parts, i.e. $T = T_c + T'$, where $(\ )_c$ is the climatological basic state and $(\ )'$ is the deviation from it. The same is done with the heating Q. The climatology is defined to be the result of an ensemble average operation and therefore it may depend on x, y, σ, and also on the time t. We obtain a set of equations for the anomalies, by substituting the split variables in the primitive equations. We first get the equations for the climate part by ensemble averaging. Subtraction of the climate equations from the total equations will yield a set of equations for the anomalies.

They are the equations for the time-dependent, non linear version of the anomaly model.

In the following, a linear, steady model will be described by time-averaging the equation for the anomalies and neglecting non-linear terms and Reynold terms (second-order correlation in the ensemble mean). Symbolically, the linear equation may be written as

$$\frac{d\zeta'|_n^m}{dt} = L^{\zeta}(\zeta',D',T',P')|_n^m - K_m\zeta'|_n^m \qquad (2.1)$$

$$\frac{dD'|_n^m}{dt} = L^{D}(\zeta',D',T',P')|_n^m - K_m D'|_n^m \qquad (2.2)$$

$$\frac{dT'|_n^m}{dt} = L^{T}(\zeta',D',T',P')|_n^m + Q'/C_p|_n^m - K_H T'|_n^m \qquad (2.3)$$

$$\frac{dP'|_n^m}{dt} = L^{P}(\zeta',D',T',P')|_n^m \qquad (2.4)$$

where ζ' is the vorticity, D' the divergence, T' is the temperature, $P' = \ln(1 + (p_s)'/(p_s)_c)$, P_s is the surface pressure, Q' is the heat source. The L's are linear operators depending on the basic state and K_m, K_H are friction coefficients. Boundary friction and Newtonionan cooling are included in the L's. The time derivatives are of course zero.

This system of equations, however, poses a problem because of a large number of unknowns involved. The basic model we use is a spectral transform model, with rhomboidal truncation 15 (R15) and 9 vertical levels. For this resolution there are about 13000 unknowns. Mathematically, the problem is that of solving a very large system of linear equations. Many methods have been developed to treat this kind of problem but relatively few are general enough to be applied to the linearized primitive equation. Navarra (1985) has shown that one of these methods, based on the projection on the Krylov space, can be applied successfully to this system. The Krylov method is the approach taken in this paper to solve the equation $Ax = F$, where the variable x represents the unknowns as ζ_n^m, D_n^m; F represents the external forcing as Q'; and the matrix A consists of the basic climatological variables as v_c, ζ_c, D_c, T_c, and $(p_s)_c$. The orographic effect is implicitly included in $(p_s)_c$.

3. The January 1983 Case

We have applied the linear anomaly model to the January 1983 case. This month includes an exceptionally large sea surface temperature anomaly in the eastern Pacific, associated with the El Niño event. Presumably, the SST anomaly caused an extraordinarily strong atmospheric heating.

It is our interest to study the atmospheric response to this heating. The linear anomaly model is used in this framework to analize how much the tropical forcing contributes to the formation of the January 1983, monthly mean, anomaly pattern over the globe.

A number of studies have been done on the propagation of linear wave packets from the tropics (Hoskins and Karoly, 1981; Schneider, 1984). A uniqueness of the present work is the treatment of baroclinic linear waves in the basic three-dimensional climatological fields.

In order to specify the basic state and the anomalous heating, 8 different January forecasts were performed with the full R15 model, with a simple formulation of physics, in which moisture was also included. The initial conditions used were January 1, 1977, 1978, 1979, 1980, 1981, 1982, 1983 and January 16, 1979. The data vorticity, divergence, temperature and surface pressure were stored at 24 hours intervals. Also the heating generated from the large scale condensation process, convective adjustment, radiation and surface heat fluxes were added every 24 hours and stored as $Q(x,y,t)$.

The sea surface temperature is specified at the lower boundary. To generate the anomaly forcing for January 1983, a forecast was made with the observed SST distribution from Reynolds (CAC). In a second test the distribution of SST was slightly modified so as to be more similar to the pattern of outgoing long wave radiation. In the third test, the heating distribution was further modified to be a simple pattern.

The distribution of anomaly outgoing long wave radiation for the winter 1982-1983 shows a characteristic structure consistent with above normal heating east of the dateline, slightly south of the equator, and below normal heating in the West Pacific. The heating in Figure 1 illustrates the third case to represent this basic pattern. The amplitude of the heating function is given by a cosine square in both longitude and latitude. It is symmetric with respect to the equator, with a maximum at 210°, and a minimum of the same amplitude at 150°. The vertical profile is given by a sine, centered around 500 mb. It is purely internal heating, since $Q' = 0$ a the top and the bottom levels and it has the same sign trough the whole atmosphere.

The anomaly pattern obtained by solving system (2.10)- (2.4), with the heating in Figure 1, is shown in Figure 2. The basic state used here is the model 8-cases climatology and a rhomboidal R7 truncation is used.

Figure 3 shows the observed streamfunction anomaly at 200 mb for January 1983, averaged over the last twenty days of the month. The convention used here is that the flow is clockwise around positive centers and counterclockwise around negative centers. The most prominent feature is the anticyclonic pair in the central Pacific, which can be considered as part of the quadrupole system extending over North America. The system also includes a strong jet over the central Pacific, that corresponds to a south shift of the Asian jet.

Comparing Figures 2 and 3, it is interesting to note that there is a similarity despite the simple linear model. The anticyclonic pair over the Pacific, however, does not have the correct shape and the centers are shifted too much west, but the pair over North America is well positioned and the inclination of the axis of the dipole is also similar. The Pacific jet, however, is entirely missing as also is the low in the North Pacific. Over the Indonesia region the centers of the anomalies are displaced too much west, but there is a hint of the equatorial jet, even if it is not broad enough.

4. Conclusion

An anomaly model based on a spectral general circulation model (GCM) is formulated and applied to the simulation of January 1983 case. The steady anomaly model is solved by a matrix method, using the Krylov technique to handle large linear systems. A comparison with observation reveals that the patterns and the phases of the solution bear some resemblance to the observed in the Pacific-North American sector, but the intensity and location of the Pacific Jet

is poorly represented. Nonetheless, the steady linear model seems to have potential as a tool for a quick look guidance on the distribution and overall characteristics of the anomaly pattern.

References

Hoskins, B. J., and D. J. Karoly, 1981: The steady linear response of a spherical atmosphere to orographic and thermal forcing. J. Atmos. Sci., 38, 1179.

Navarra, A., and K. Miyakoda, 1983: Anomaly model using a barotropic vorticity equation. Proc. of the 6th Conf. on Numerical Weather Prediction, Omaha, Nebraska, Amer. Met. Soc., 419-421.

Navarra, A., 1985: A geophysical application of the Krylov method. (In preparation)

Nigam, S., 1983: On the structure and forcing of tropospheric waves. Ph.D. Thesis, Princeton University, Princeton, N. J., 203pp.

Schneider, E., 1984: Stationary Rossby wave propagation through easterly layers. J. Atmos. Sci., 41, 2069.

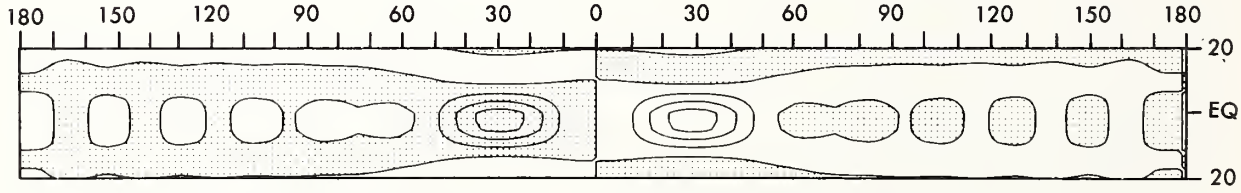

Fig. 1. -- Longitude-latitude map of the heating distribution at 500 mb. Dateline is at the center. Negative areas are stippled, and the contour interval is .7 deg/day.

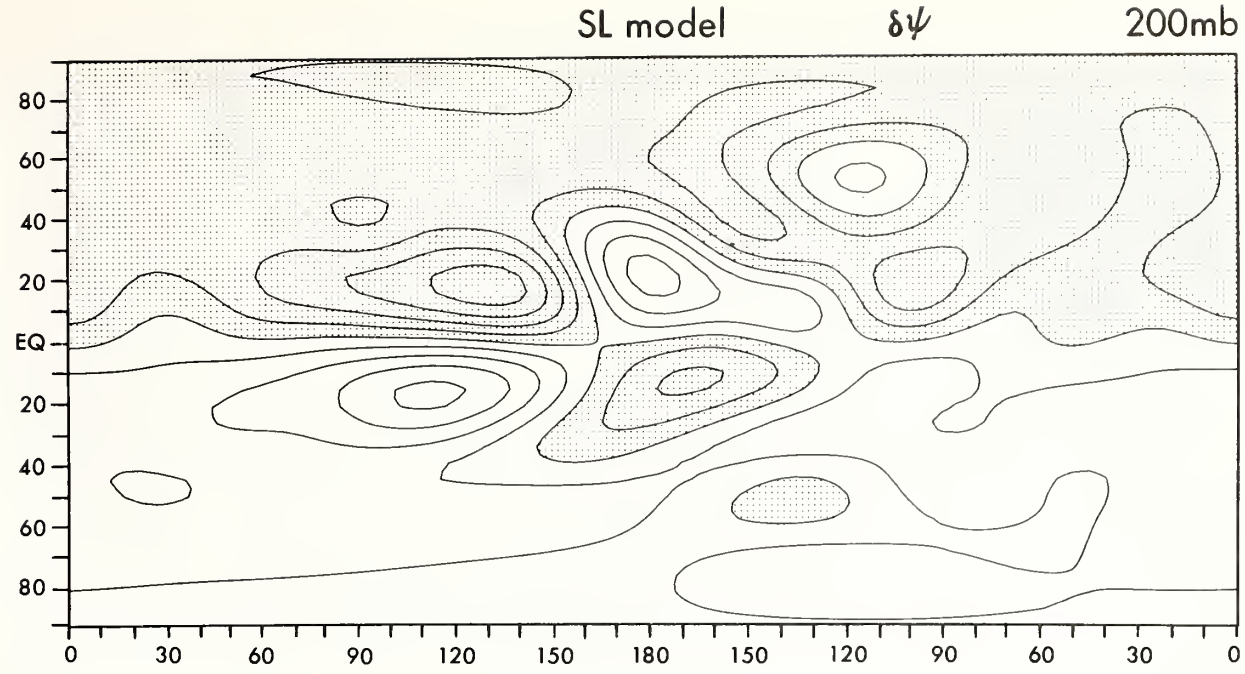

Fig. 2. -- Longitude-latitude map of the anomaly streamfunction diagnosed by the steady linear baroclinic model, using the heating prescribed in Figure 1. Negative values are stippled, and the contour used is 1. x 10^6.

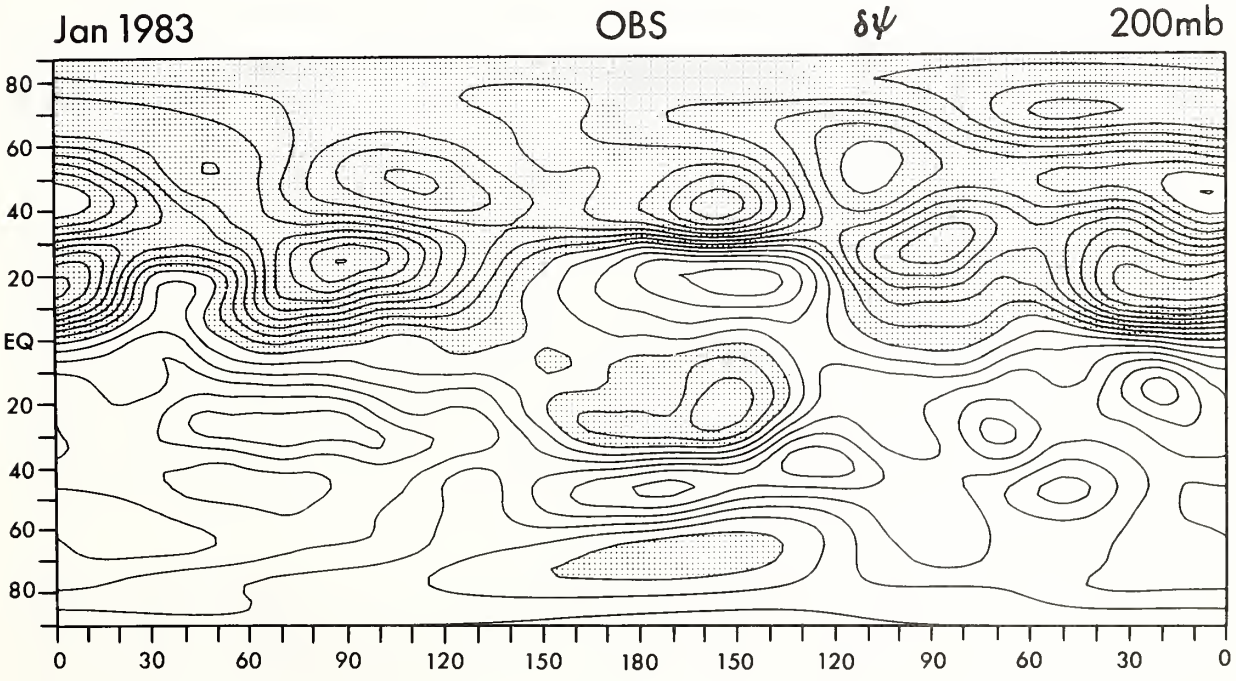

Fig. 3. -- Longitude-latitude map (dateline in the center) of the observed distribution of anomaly streamfunction at 200 mb averaged over January 10-30, 1983. Negative values are stippled and the contour used is 5. x 10^6.

TRANSITION FROM THE SOUTHERN TO NORTHERN HEMISPHERE SUMMER MONSOON

Takio Murakami
Department of Meteorology
University of Hawaii
Honolulu, Hawaii 96822

To facilitate the discussion, we separate any meteorological variable into two important components: The first component is symmetric about the equator and shows relatively small seasonality. The second component is asymmetric about the equator with convective zones showing a distinct seasonal pattern between the Southern and Northern Hemisphere summer. For example, OLR (outgoing longwave radiation) can be partitioned into two components as follows:

$$OLR^{+} = 1/2(OLR_N + OLR_S),$$
$$OLR^{-} = 1/2(OLR_N - OLR_S),$$

where OLR^{+} and OLR^{-} represents the symmetric and asymmetric components, respectively; $OLR_N(OLR_S)$ denotes OLR in the Northern (Southern) Hemisphere. OLR^{+} is small, irrespective of season, over equatorial Africa (20°-40°E), the maritime continent (100°-160°E), and equatorial South America (110°-70°W). These are three of the most convectively active regions near the equator. Response to OLR^{+} is generally confined to the equatorial latitudes and is often called the "Walker Circulation".

OLR^{-} is positive and substantial over the maritime continent (Sumatra, Borneo, New Guinea) during the Southern Hemisphere summer monsoon. The response is of Rossby type with cross-equatorial low-level northerlies and upper-level southerlies (Hadley circulation). During the Northern Hemisphere summer monsoon, OLR^{-} becomes negative over the equatorial Indian Ocean where cross-equatorial low-level southerlies are capped by cross-equatorial upper-level northerlies.

The asymmetric component OLR^{-}, measured at 10° of latitude away from the equator, changes from positive to negative during the transition from the Southern to Northern Hemisphere summer monsoon. Near equatorial North Africa and the maritime continent, OLR^{-} becomes zero around 15 April, while over Central America, near zero OLR^{-} occurs at the end of March (Fig. 1). In association with the occurrence of near zero OLR^{-}, 850 mb U^{-} at 10° of

latitude away from the equator changes from negative (easterly) to positive (westerly) near the three equatorial convective regions. This corresponds to the withdrawal of the Southern Hemisphere monsoonal westerlies and the first establishment of the Northern Hemisphere monsoonal westerlies at 850 mb. The monsoon onset (near zero $\overline{OLR}$) over Indochina and the Malaysian Peninsula occurs as a part of the global-scale phenomenon. Over central India, the monsoon begins about the beginning of June, i.e., about two months later than the transition from the Southern to Northern Hemisphere summer monsoon. This transition takes place in an abrupt manner on the seasonal time scale.

Fig. 2 shows the time-latitude sections of the amplitude and phase of 200 mb U_1 (wavenumber 1, 40-50 day 200 mb, zonal winds; top), 850 mb U_1 (wavenumber 1, 40-50 day 850 mb zonal winds; middle) and OLR_1 (wavenumber 1, 40-50 day filtered, outgoing longwave radiation). Prior to day 44 (30 March), both 850 U_1 and OLR_1 perturbations are standing-wave character in the Southern Hemisphere around $15^{o}S$, while the standing character of 200 mb U_1 is evident in the Northern Hemisphere around $15^{o}N$. These features are of winter character. After day 67, 200 U_1, 850 U_1, and OLR_1 all show the summer character of eastward propagation which is most prominent between the equator and $20^{o}N$. In short, the nature of 40-50 day oscillations changes drastically during the transition from the Southern to Northern Hemisphere summer monsoon.

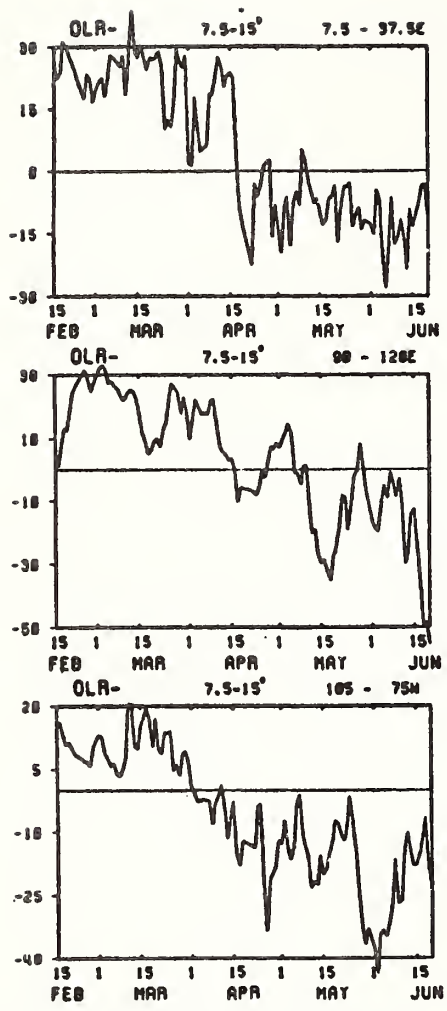

Fig. 1. Time series of $\overline{OLR}$ averaged over equatorial Africa (top: 7.5°-15°N-S, 7.5°-37.5°E), the maritime continent (middle: 7.5°-15°N-S, 90°-120°E), and Central America (bottom: 7.5°-15°N-S, 105°-75°W), during the transition period.

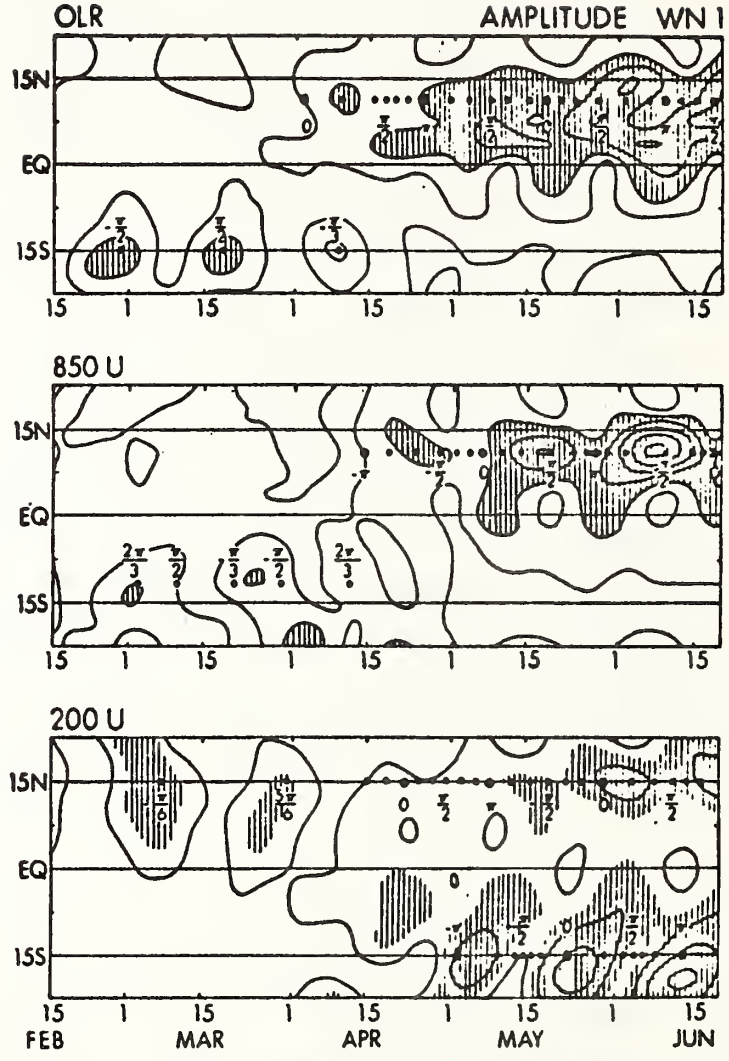

Fig. 2. Latitude-time section of wavenumber 1 amplitude (full lines) and phase (dots) for OLR (top), 850 mb u (middle), and 200 mb u (bottom) during the transition period.

Large-scale Variability in Indian Monsoon Rainfall Inferred from Satellite Data

Phillip A. Arkin, John E. Janowiak and William Replane
Climate Analysis Center
NOAA/NWS/NMC
Washington, D.C. 20233

The variations in rainfall which occur in the vicinity of the Indian subcontinent during the Northern Hemisphere summer are of significant interest to students of the general circulation as well as of practical significance to inhabitants of the region. Successful forecasts of monsoon rainfall will probably require that the large-scale spatial and temporal variability in rainfall in the region be better known than it has been to this point. Rainfall over the subcontinent is, in principle, relatively well defined by means of station observations. Rainfall over adjacent ocean areas, however, is much less well known. The object of this paper is to investigate the practicality of diagnosing rainfall variability by means of the indices constructed from the NOAA outgoing longwave radiation (OLR) data set.

Large-scale variations in tropical convective precipitation have been diagnosed from variations in OLR for some time. The underlying hypothesis is that, in the tropics, variations in OLR are primarily due to variations in the amount of convective cloud, with larger amounts of cloudiness resulting in lower values of OLR and, presumably, in greater rainfall. We have attempted to use the fraction of large areas covered by fluxes less than $240 Wm^{-2}$ averaged over periods of five days and over months to examine variations in monsoon rainfall. A set of more or less geographically homogenous areas between $60^{o}E$ and $100^{o}E$ (fig. 1) as well as the 10^{o} latitude bands in the same region extending from the equator to $40^{o}N$ were defined. We used time series of five day means to show intraseasonal variability and to determine objectively an "onset date" for each area and season. Time series of monthly means and standard deviations were used to compute standardized anomalies in the index values. Comparisons between the various areas and with other estimates of interannual variability in monsoon rainfall were made.

The principal conclusions drawn from this study were the following:

1. Indices using thresholds of $240 Wm^{-2}$ appeared to define the large-scale annual cycle in monsoon area rainfall reasonably well. It seems that an index using the mean flux would provide much of the same information.

2. Onset of the monsoon, defined as three consecutive five day periods with index values above 0.4, was observed in each area/year examined here.

3. Onset progressed from south to north in a regular fashion.

4. Onset occurred latest in the Indian and Arabian Sea index areas, with differing sequences in different years. It seems possible that onset occurs first in the Arabian Sea during years in which an "onset vortex" occurs.

5. Important features of the interannual variability in monsoon rainfall, such as the poor monsoon of 1979, were seen in the time series of standardized anomalies.

6. The drought of 1979 appears to have been a feature of the Indian and Arabian Sea index areas only, with index values above normal in the other areas.

7. On the other hand, the monsoon season of 1976 appears to have been relatively dry over the entire region.

8. The results obtained here are encouraging enough to warrant an effort to produce a precipitation index using INSAT imagery.

DATE OF ONSET

3 CONSECUTIVE 5-DAY PERIODS .4

	INDIA	ARABIAN SEA	ASSAM	BAY OF BENGAL
1974	34	36		
1975	34	33	25	20 (28)
1976	35	40	24	29 (35)
1977	33	25 (32)	27	25 (33)
1978				
1979	34	32	27	25 (31)
1980	31	34	28	20 (26)
1981	34	30	28	19 (26)
1982	33	28	27	22 (28)
1983	35	39	24	24
1984	32	30	26	19

Table 1. Dates of onset for the geographic index areas.

DATE OF ONSET

	0°-10°N	10°-20°N	20°-30°N	30°-40°N
1974		31	32	32
1975	28 (39)	29	29	31
1976	23 (35)	29	30	35
1977	24 (33)	25 (31)	26 (31)	31(33)
1978				
1979	17 (30)	31	33	33
1980	26	26	28	31
1981	16 (26)	19 (26)	30	31
1982	14 (22)(27)	28	29	30
1983	24 (32)	29	30	30
1984	18 (24)	21 (27)	29	30

Table 2. Dates of onset for the latitude band index areas.

STANDARDIZED ANOMALIES

	Arabian Sea	India	Assam	Bay of Bengal
Arabian Sea	1.00	0.57	0.17	0.42
India		1.00	0.20	0.44
Assam			1.00	0.34
Bay of Bengal				1.00

	0°-10°N	10°-20°N	20°-30°N	30°-40°N
0°-10°N	1.00	0.79	0.52	0.35
10°-20°N		1.00	0.84	0.53
20°-30°N			1.00	0.78
30°-40°N				1.00

Table 3. Linear correlations of the time series of standardized monthly anomaly among the various index areas.

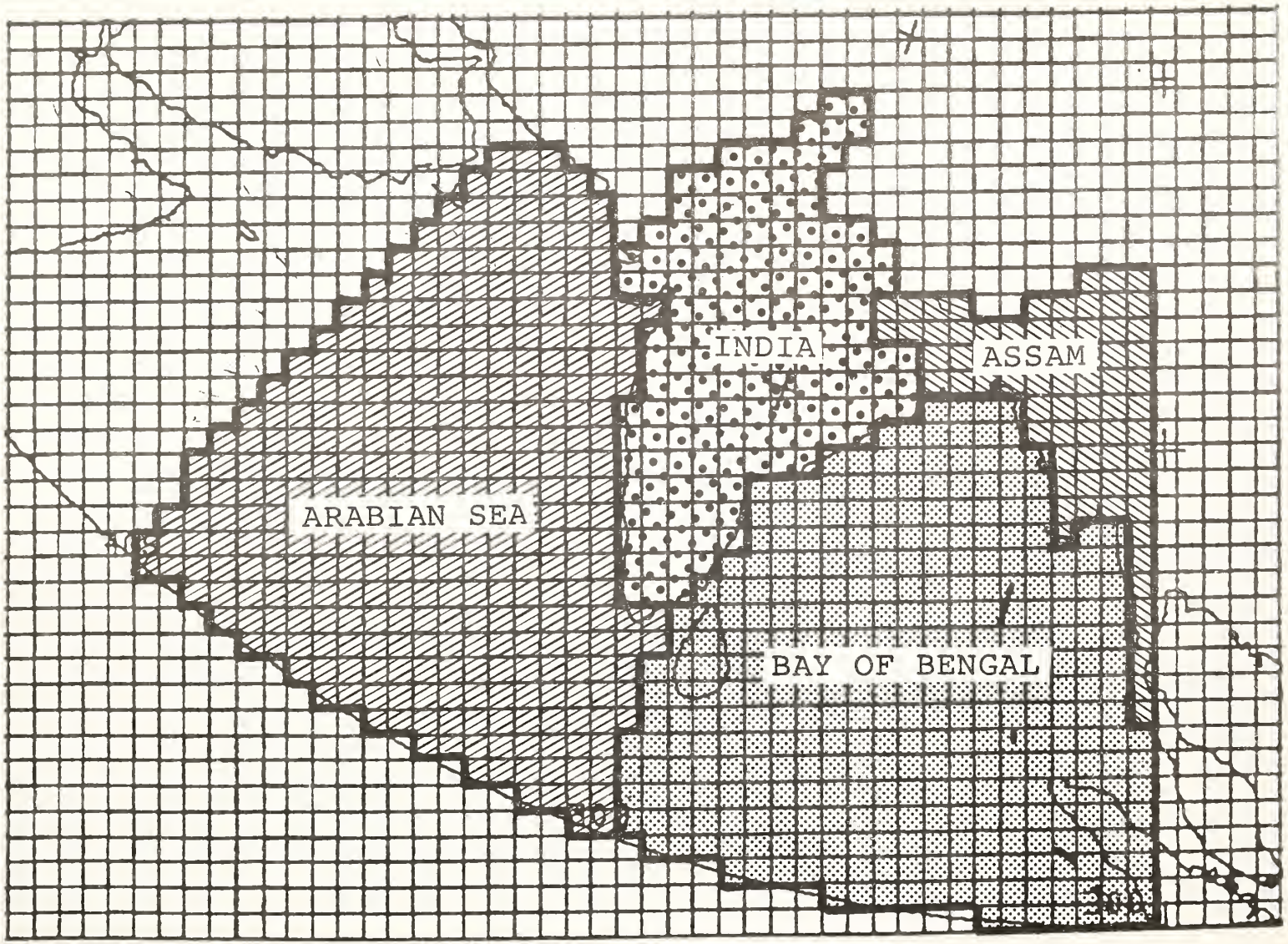

Figure 1. Areas for which the Arabian Sea, India, Assam and Bay of Bengal OLR indices were computed.

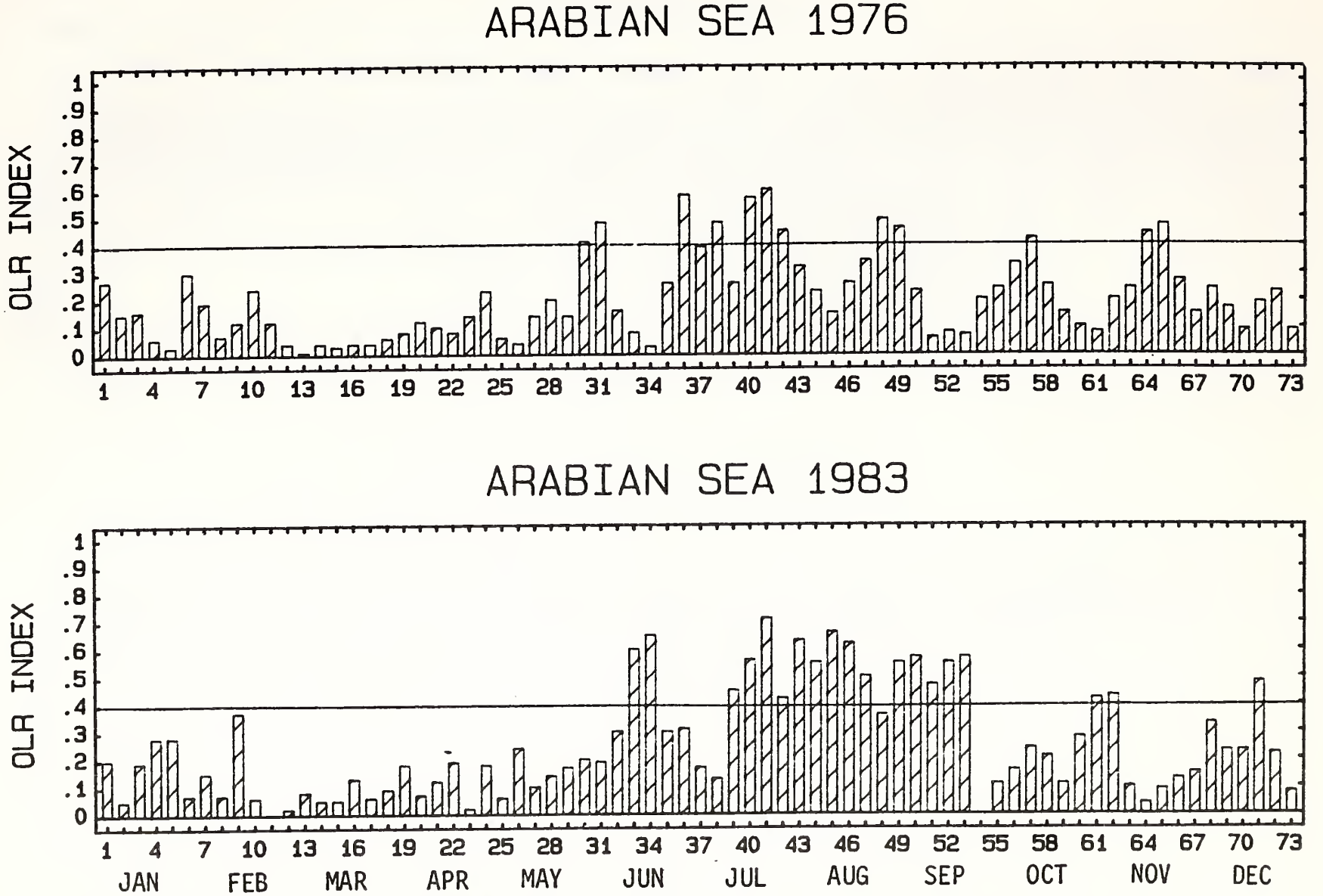

Figure 2. Arabian Sea indices (5 day means) for 1976 and 1983. Onset is defined as first of three consecutive pentads exceeding value of 0.4 (horizonal line).

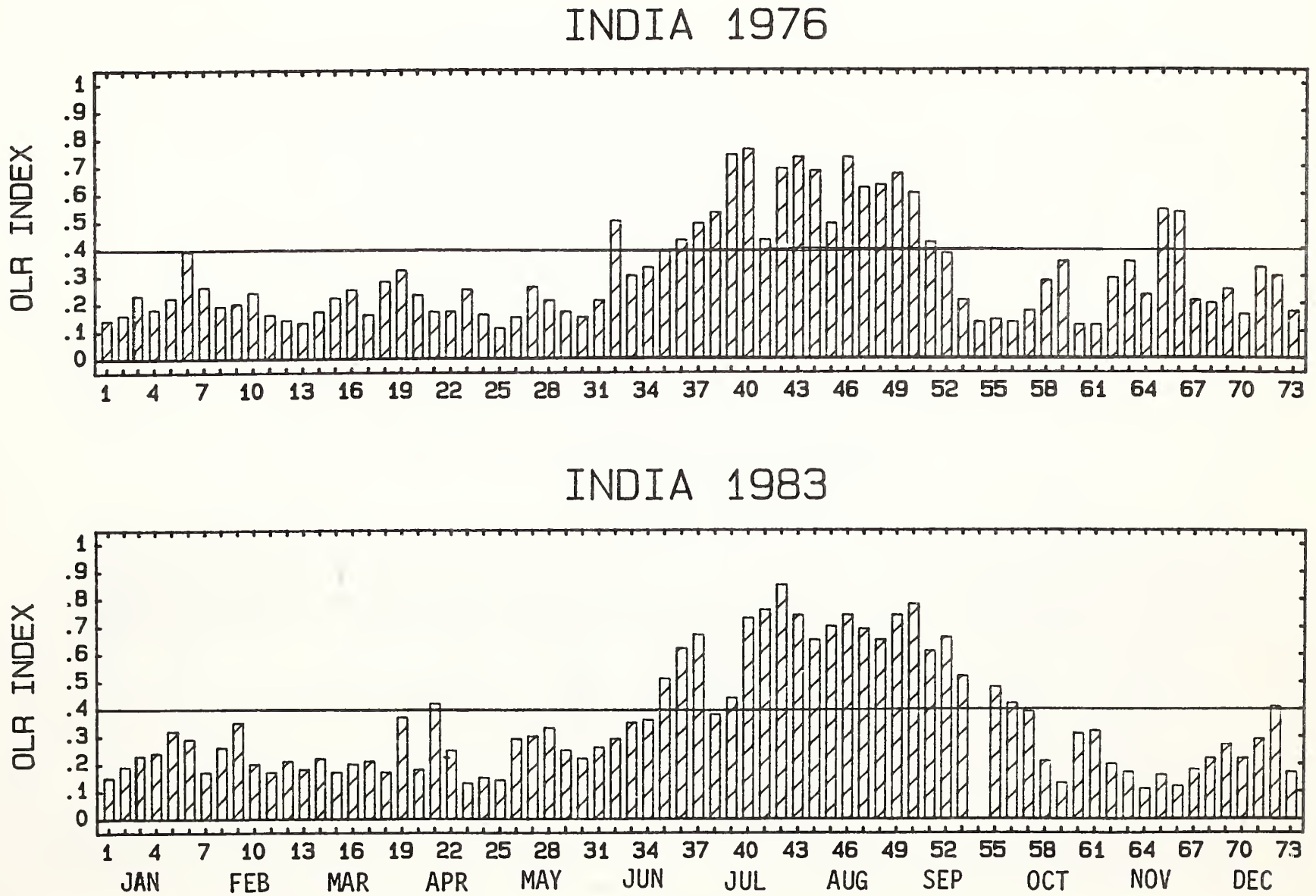

Figure 3. As in Fig. 2 except for India.

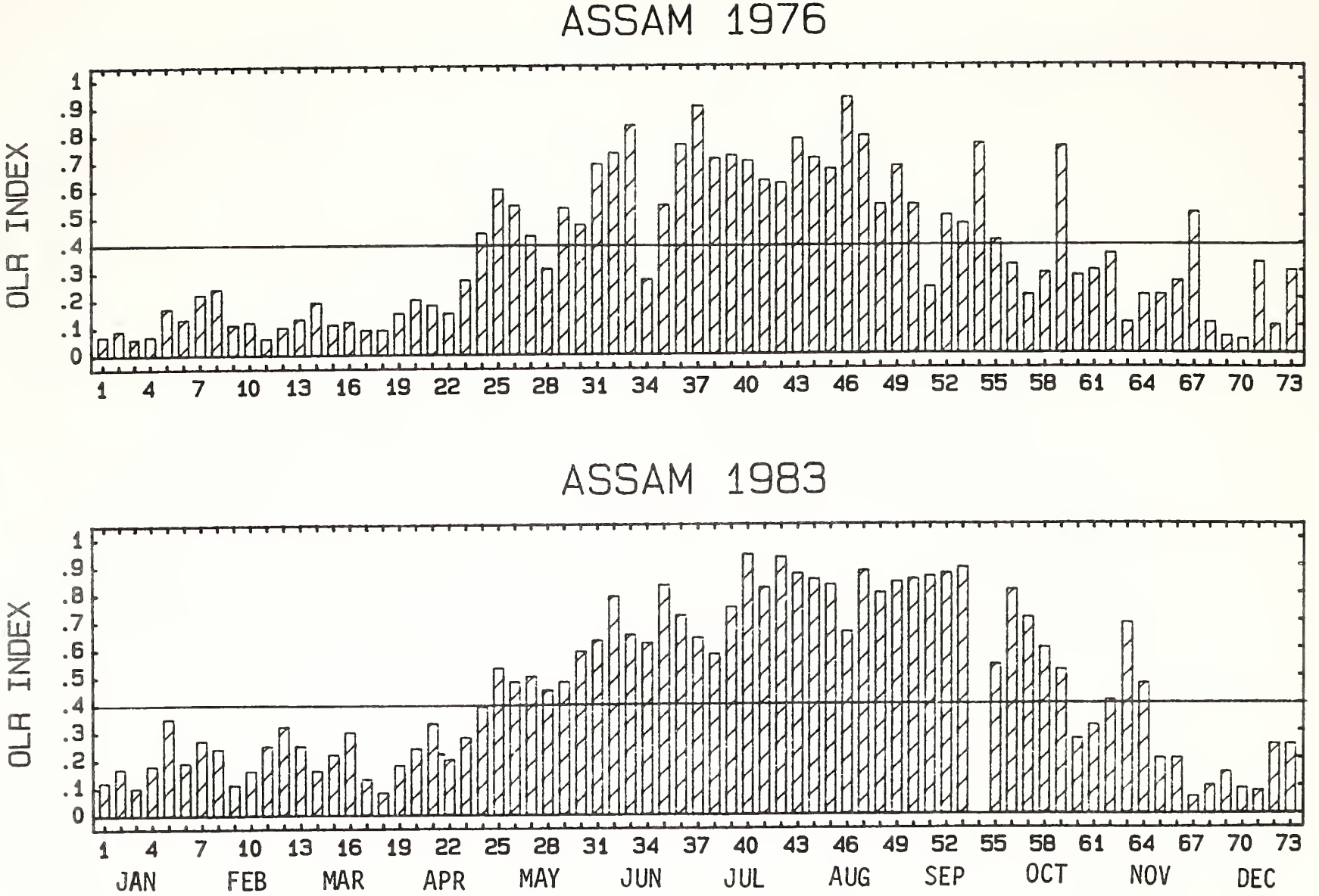

Figure 4. As in Fig. 2 except for Assam.

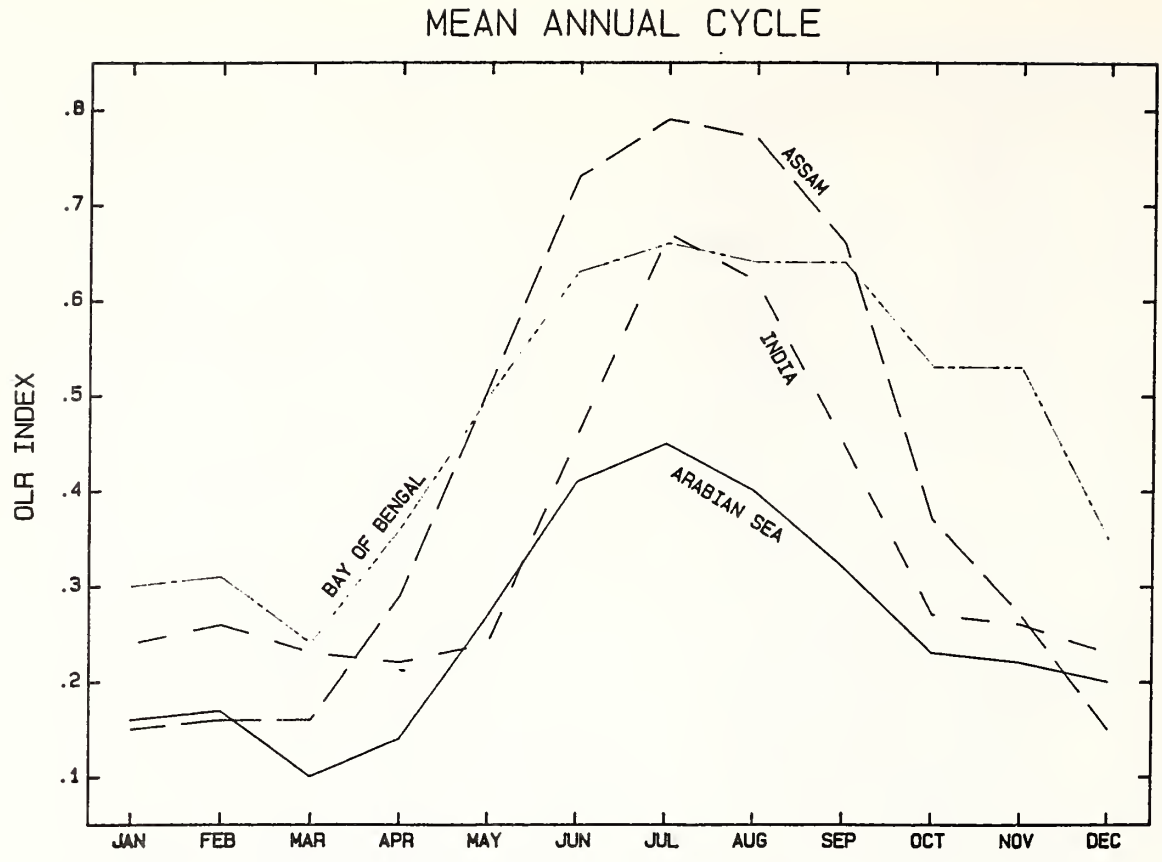

Figure 5. Mean annual cycle for Arabian Sea, India, Assam and Bay of Bengal.

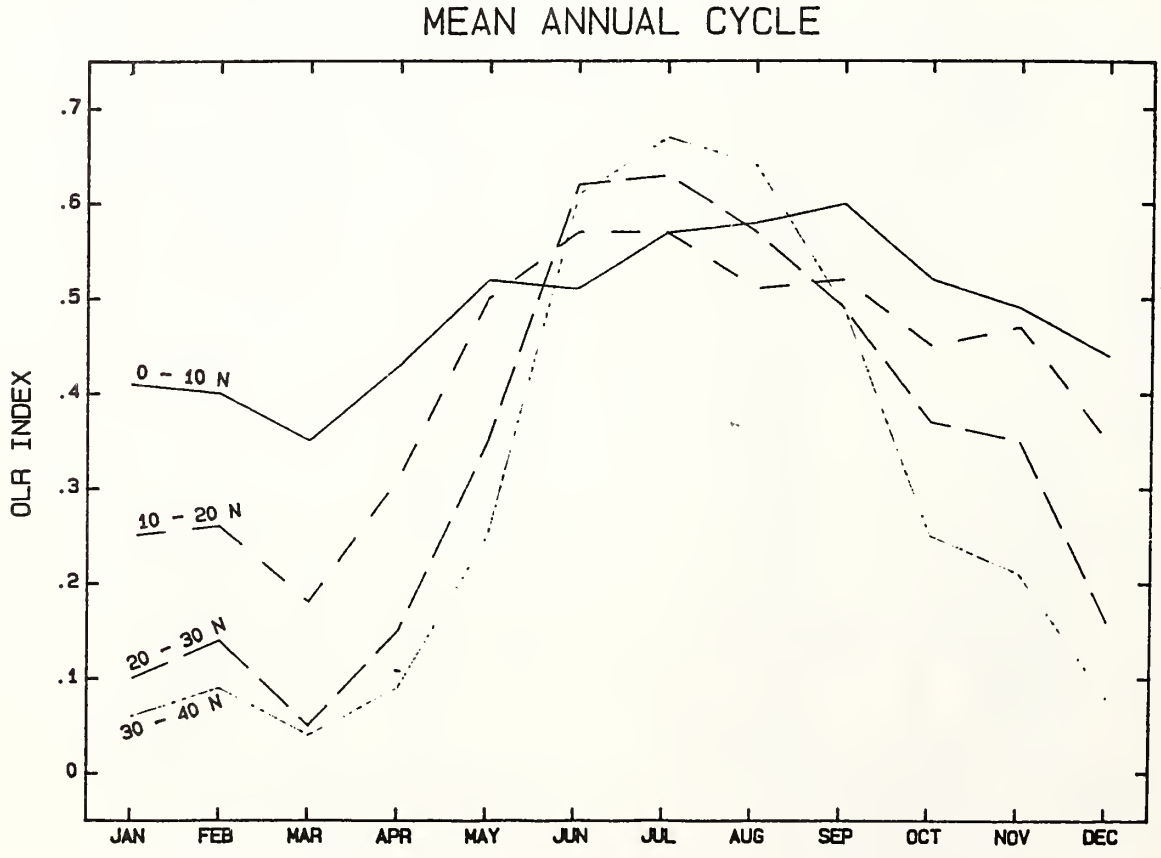

Figure 6. Mean annual cycle for 60°E-100°E and 0°-10°N, 10°N-20°N, 20°N-30°N and 30°N-40°N.

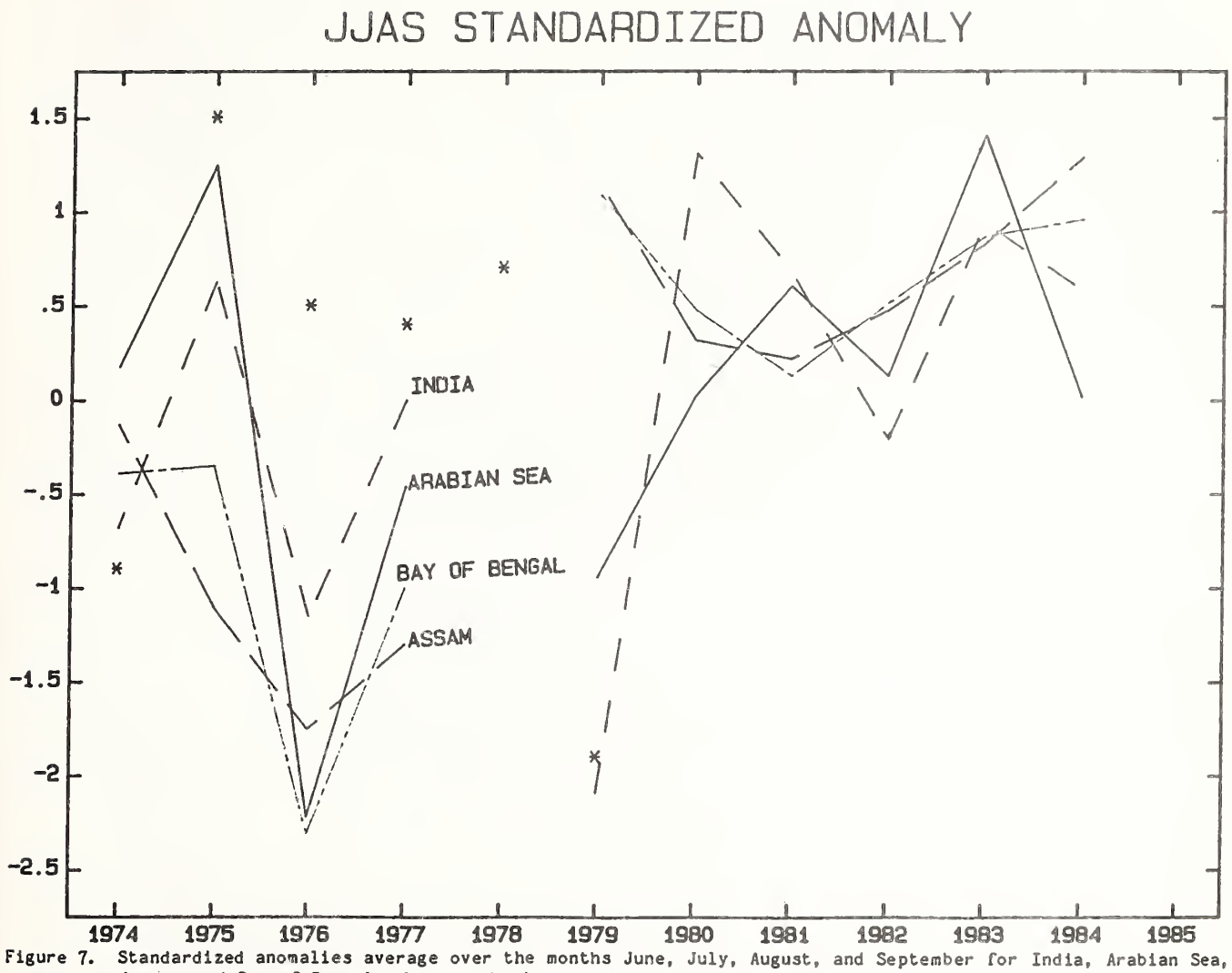

Figure 7. Standardized anomalies average over the months June, July, August, and September for India, Arabian Sea, Assam, and Bay of Bengal. Large asterix represent standardized anomalies for all of India taken from Rasmusson and Carpenter (MWR 1983).

TROPOSPHERIC STATIC STABILITY AND CENTRAL NORTH AMERICAN SUMMER RAINFALL DURING 1979

Peter J. Lamb[1] and Randy A. Peppler

Climate and Meteorology Section
Illinois State Water Survey
Champaign, Illinois 61820

The occurrence, rate, and duration of precipitation in a continental region are likely to be functions of the existence and strength of several atmospheric processes and conditions over the region itself and, in particular, the degree to which they are simultaneously favorable. We hypothesize that, in very general terms, such processes/conditions include the local presence and external supply of water vapor, and the troposphere's predisposition to providing the vertical motion necessary to produce the required condensation rates. One condition of potential importance in the latter regard is tropospheric static stability. This steady-state property indicates the likelihood of introduced vertical displacements or perturbations being thermodynamically damped, enhanced, or unchanged. The present preliminary study investigates the relation between tropospheric static stability and central North American summer (May-August) rainfall for 1979. It has two objectives. The first is to ascertain which of the many available methods of parameterizing static stability are most strongly related to the variation of the above rainfall. This seeks to provide a rational basis for the characterization of static stability in our intended later inquiry into the relative importance of all of the aforementioned processes/conditions for interannual and intraseasonal rainfall fluctuations. The second objective — to quantify the fraction of the 1979 rainfall variance that can be explained by static stability alone (i.e., by just one of the above processes/conditions) — was intended to provide an early check on the validity of the hypothesis given at the outset. As already intimated, that overall hypothesis is the subject of a more lengthy and ongoing investigation.

Many indices that quantitatively estimate tropospheric static stability have been proposed in the literature and/or incorporated into operational weather forecasting practice during the last 40 years. Most combine thermal and moisture values for the lower and middle troposphere and are purported to indicate the likelihood of convection. Unlike this investigation, the previous utilization of these indices has seldom related them to complete ranges of actual rainfall totals. There has instead been a strong emphasis on the relations between static stability and (a) the mere "yes/no" occurrence of measurable precipitation (e.g., in the MOS PoP statistical forecasting models) and (b) the incidence of thunderstorms and severe weather. Indeed, most stability indices were introduced for the explicit purpose of severe weather prediction. The earlier work linking stability to rainfall was not only limited, but also yielded relatively discouraging results. For example, stability indices were among the less important predictors of precipitation occurrence identified by the MOS PoP research (Lowry and Glahn, MWR, 1976), an endeaver that considered a wide range of atmospheric processes/conditions. Furthermore, in the few studies involving actual rainfall amounts, all of which were for restricted areas, stability indices accounted for no more than 9 percent of the rainfall

[1]Also affiliated with Department of Atmospheric Sciences, The University of Illinois.

variance (e.g., Achtemeier and Schickedanz, JAM, 1979; Burpee and Lahiff, MWR, 1984). Most of the previous research relating stability and rainfall also failed to consider a broad range of stability indices; those treated tended to be chosen on the basis of their originally-intended or traditional use, rather than empirically-demonstrated utility.

The present stability-rainfall study uses not only the full range of actual rainfall amounts, but also a comprehensive array of static stability indices and related thermodynamic parameters. The latter are summarized in Table 1. They include modified versions of several well known stability indices and variants of standard condensation levels, the full details of which will be provided elsewhere. All indices/parameters in Table 1 were evaluated twice daily (0000 and 1200 GMT) for May-August 1979 for the 38 rawinsonde stations shown in Fig. 1. This used standard and significant level data obtained from the National Climatic Data Center (Asheville, NC) and the Canadian Climate Centre (Toronto, Ont.). For each rawinsonde station, the values of each index/parameter for a given sounding time were then linearly correlated with the mean 12-hour rainfall accumulations (centered on the sounding time) for a circle of 100 mi. (161 km) radius centered on the station. Those circles appear in Fig. 1, along with the locations of the 854 recording raingauges whose data (obtained from the aforementioned sources) were used. A mean 12-hour rainfall accumulation for each circle was obtained by simply averaging all available individual gauge 12-hour totals (including zeros) for that area. When no gauge within a circle collected a measurable rainfall amount, the area-averaged accumulation was treated as zero. Experimentation with smaller (100 km radii) circles, 6-hour rainfall accumulations, and different area-averaging procedures (e.g., using only half of the available gauges; averaging only non-zero totals when at least one existed) did not appreciably alter the results presented below. The choice of 1979 for this preliminary study was made on the basis of Lamb and Richman's VARIMAX-rotated Principal Component regionalization of the study area for weekly summer rainfall (Proc. Second Int. Meeting on Stat. Clim., 1983; JCAM, submitted). This showed that 1979 received average-to-above-average rainfall in 8 of the 10 identified subregions for May, June, and August, but with pronounced variation on the scale of 1-2 weeks. The interspersing of periods of plentiful and deficient rainfall gave the wide range of area-averaged 12-hour rainfall accumulations needed for this investigation.

A selection of the results obtained appears in Figs. 2-4 and Table 2. Much fuller accounts of this work will be offered elsewhere in the near future. However, Fig. 2 does provide a concise summary of the entire effort. It indicates, for each sounding time, (a) which of the 40 static stability indices and thermodynamic parameters considered correlated most strongly with the area-averaged 12-hour rainfall accumulations for the 38 circles in Fig. 1, and (b) the magnitudes of those maximum correlations. The latter tend to be larger for the 12-hour period centered on 0000 GMT (i.e., noon to midnight, CST) than the one pertaining to 1200 GMT. This difference was detected for 30 of the 38 circles, with most of the exceptions being on the Great Plains of the United States. For the 1800-0600 GMT half-day, the maximum correlation magnitudes range from 0.34 (Moosonee, Ont.) to 0.70 (Jackson, Miss.) and have a mean of 0.47. The counterpart range for the 0600-1800 GMT half-day is 0.29 (Jackson, Miss.; Brownsville, Texas; Glasgow, Mont.) to 0.51 (Dayton, Ohio; Denver, Colo.), with a mean of 0.39. Particularly prominent among the 1800-0600 GMT results in Fig. 2 are the uniformly "high" maximum correlations in

the southeastern quadrant of the study region. These lie between 0.49-0.70 and indicate that 24-49 percent (often approximately 30 percent) of the rainfall variance was accounted for by some static stability index or thermodynamic parameter (generally the lifted condensation level, LCL). While the 1800-0600 GMT maximum correlations outside the above area tend to be smaller, a majority of them (evenly distributed) still exceed 0.41 and four (Edmonton, Alta; Denver, Colo.; International Falls and St. Cloud, Minn.) are as high as 0.51-0.62. Perhaps the most conspicuous feature of the 0600-1800 GMT maximum correlations (Fig. 2) is the relatively large size of all those in the northeastern quadrant (0.39-0.51). Those in the southeast for this time are much smaller than their 1800-0600 GMT counterparts.

The correlation coefficient magnitudes discussed above are all larger than those obtained in the aforementioned earlier work of this type, and generally by a substantial margin. Furthermore, the fact that the single atmospheric condition considered here accounted for as much as 20-50 percent of the rainfall variance in most of the study region during the 1800-0600 GMT half-day, and at least 15 percent for almost all areas in both 12-hour periods, offers considerable support for the hypothesis given at the outset. The validity of the latter is further enhanced by the nature of the stability indices and thermodynamic parameters that possessed the foregoing maximum correlations. Fig. 2 shows that the LCL was the index/parameter most strongly related to 1800-0600 GMT rainfall across the southern third of the study region and in the northwest. This suggests that low-level forced ascent and moisture availability — processes/conditions that also feature in the above hypothesis — are of considerable importance for "afternoon" rainfall production in those areas. Interestingly, the convective condensation level (CCL) and convective temperature (CON.T), parameters that emphasize the related roles of surface heating and free ascent, are much more weakly correlated (than the LCL) with the aforementioned southern rainfall everywhere except the three westernmost stations in Texas (not shown). For the latter, and also the western Great Plains stations to their immediate north (Dodge City, Kan.; Denver; North Platte, Neb.; Rapid City, S. Dak.; Fig. 2), the CCL, LCL, and CON.T have extremely similar correlations with "afternoon" rainfall. The fact that the K-index is most strongly related to such rainfall (or nearly so) over the Upper Midwest (Figs. 2 and 3) further reinforces the importance of low-level moisture availability. This area of relative pre-eminence of the K-index (including a modification thereof) is expanded both northward and southward for the remaining (i.e., 0600-1800 GMT) half-day (Figs. 2 and 3). The other indices/parameters most highly correlated with "morning" rainfall are the SWEAT index (extreme southeast), the CCL and CON.T (western Great Plains south of South Dakota and Canadian Prairies), the LCL (eastern Plains south of South Dakota), and a version of the Showalter Index (south Texas and Arkansas). Our final comment on Fig. 2 is that both its patterns (indices/parameters; correlation magnitudes) contain encouraging spatial coherence.

Table 2 and Fig. 3 supplement Fig. 2 by indicating the relative magnitudes of the correlations between selected stability indices/thermodynamic parameters and 12-hour rainfall accumulations for both individual circles (Fig. 1) and the entire domain. It is readily apparent from Table 2 that the correlation magnitudes span a wide range, particularly for 1800-0600 GMT. As already implied, the highest values tend to be for the condensation levels ("afternoon" half-day, especially) and the empirically-based stability indices

(e.g., K, modified K, Jefferson) that were originally designed for predicting air mass showers and non-severe thundershowers ("morning" half-day, especially). All of these indices/parameters incorporate the moisture as well as the thermal properties of the lower troposphere. Interestingly, the condensation levels have seldom been previously considered in this context. At the other extreme, very weak correlations were obtained for the stability indices that are entirely or predominantly dependent on the thermal lapse rate (e.g., Vertical Totals, Total Totals, modified Total Totals, various measures of the vertical gradient of potential temperature), for most of the indices intended for severe weather prediction (e.g., Lifted, Potential Wet-Bulb, Convective Instability, various buoyant energy parameters), and for the Rackliff index for (Western European) summer showers and thundershowers. Table 2 also reveals that the SWEAT index is much better correlated with rainfall amount than the other severe weather indices, and that the often used Showalter-type indices perform only moderately well in this regard. The spatial variations in the relative performance of the indices/parameters that Table 2 identified as being best related to rainfall for the region as a whole are documented in Fig. 3. They suggest that a K-type index is not informative for most of the Great Plains south of South Dakota (both half-days) and the extreme northwest of the study region (0600-1800 GMT). This may result from those areas' high station elevations making K-type indices structurally inappropriate. Fig. 3 also reveals that the LCL performed relatively poorly across most (parts) of the northern (southern) United States for the "morning" half-day, a situation that requires further investigation. Clearly, however, this research has provided valuable guidance as to which of the many available methods of parameterizing static stability are most strongly related to the variation of central North American summer rainfall.

Further information in that regard appears in Fig. 4. It documents the spatial variability of threshold values for the key indices/parameters treated in Fig. 3, beyond which (above for K-type, below for LCLs) the probability of occurrence of measurable rainfall exceeded that of nonoccurrence for 1979. The large spatial variation obtained strongly implies that single threshold values should not be used over wide areas, as seems to have previously been the case for the K-index. Our K-type threshold patterns, for instance, exhibit pronounced general northward or northeastward decreases, with the extreme station values varying by factors of 2-3. Although this reflects the substantial control that lower tropospheric temperature exerts on K-type indices, a more satisfying explanation is needed and will require further investigation. The LCL threshold patterns obtained, in contrast, are dominated by marked east-to-west increases. Their lowest values occur in the southeast and near the Great Lakes, and the maximum ones (more than double the former) are over the High Plains of the United States. More than anything else, this appears to reflect near-surface relative humidity. Fig. 4 thus provides important background information for our intended later inquiry into the role of static stability (among several atmospheric processes/conditions) for the interannual and intraseasonal rainfall fluctuations experienced in the various parts of the study region.

Acknowledgments

This study was supported by NSF Grant ATM 81-00158. We thank Dick Semonin and Gary Achtemeier for their interest and helpful comments, and Diane Portis for her computational assistance.

Table 1. Stability indices and thermodynamic parameters evaluated (40). They are categorized according to their originally-intended or traditional use.

A. For forecasting airmass showers/thundershowers, non-severe thundershowers:

1. K-index
2. Modified K-index of Charba
3. Jefferson index
4. Rackliff index
5. Adedokun indices (2)
6. Showalter index
7. Modified Showalter index of Curtis and Panofsky
8. Modified Showalter index of Hovanec and Horn

B. For forecasting strong thunderstorms and severe weather:

1. Cross, Vertical, Total Totals indices
2. Modified Total Totals index of Charba
3. Lifted index
4. Potential wet-bulb index
5. Convective instability indices (2)
6. SWEAT index
7. Total Energy index
8. Measures of parcel negative and positive buoyant energy (6)

C. For parameterizing static stability in numerical models and diagnostic studies:

1. $\frac{-T}{\Theta}\frac{\partial\Theta}{\partial p}$
2. $\frac{-1}{\Theta}\frac{\partial\Theta}{\partial p}$
3. $\frac{-\partial\Theta}{\partial p}$
4. $\frac{-\alpha}{\Theta}\frac{\partial\Theta}{\partial p}$
5. $\frac{-p}{\Theta}\frac{\partial\Theta}{\partial p}$
6. $\frac{-\rho}{\Theta}\frac{\partial\Theta}{\partial p}$

D. For estimating cloud base heights and critical surface convection temperatures (using different initial parcel states):

1. Lifted Condensation Levels (3)
2. Convective Condensation Levels (3)
3. Convective Temperatures (3)

Table 2. Selected correlation coefficient rankings (out of 40, except for Denver, out of 24) for 1800–0600 and 0600–1800 (parentheses) GMT half-days. Asterisk indicates not significant at 99% level according to one-tailed t-test. See Table 1 for information on the indices/parameters.

DENVER (N = 120)			PEORIA (N = 120)			JACKSON (N = 120)			ALL-STATION AVERAGE		
RANK	INDEX	r	RANK	INDEX	r	RANK	INDEX	r	RANK	INDEX	AVG. RANK
1 (2)	CCL (50 mb)	−0.62 (−0.49)	1 (22)	LCL (Sfc)	−0.54 (−0.22)	1 (35)	LCL (Sfc)	−0.70 (−0.05)*	1 (24)	LCL (Sfc)	2.5 (22.6)
2 (17)	LCL (50 mb)	−0.61 (−0.37)	2 (2)	K	+0.49 (+0.44)	2 (7)	LCL (50 mb)	−0.62 (−0.24)	2 (6)	LCL (50 mb)	3.6 (11.1)
3 (1)	CCL (100 mb)	−0.61 (−0.51)	3 (3)	JEFFERSON	+0.47 (+0.41)	3 (4)	LCL (100 mb)	−0.54 (−0.25)	3 (4)	LCL (100 mb)	5.7 (8.7)
4 (12)	LCL (100 mb)	−0.60 (−0.40)	7 (8)	MOD. SHOWALTER CP	−0.40 (−0.35)	4 (8)	MOD. SHOWALTER CP	−0.49 (−0.22)	4 (2)	K	6.6 (7.1)
5 (22)	LCL (Sfc)	−0.57 (−0.27)	8 (16)	CCL (50 mb)	−0.37 (−0.30)	5 (3)	K	+0.47 (+0.26)	5 (3)	JEFFERSON	6.9 (8.3)
6 (3)	CCL (Sfc)	−0.57 (−0.47)	9 (5)	SWEAT	+0.36 (+0.36)	7 (2)	CCL (Sfc)	−0.42 (−0.28)	6 (7)	CCL (Sfc)	8.8 (12.0)
7 (19)	$-p/\theta \cdot \partial\theta/\partial p$	+0.50 (+0.36)	12 (14)	SHOWALTER	−0.31 (−0.30)	12 (13)	$-T/\theta \cdot \partial\theta/\partial p$	+0.39 (+0.19)*	9 (1)	MODIFIED K	10.2 (6.1)
8 (5)	CONV. TEMP. (50 mb)	−0.50 (−0.46)	15 (19)	LIFTED	−0.30 (−0.23)	13 (24)	CCL (50 mb)	−0.35 (−0.10)*	10 (8)	SWEAT	11.8 (13.1)
9 (7)	CONV. TEMP. (Sfc)	−0.50 (−0.44)	16 (17)	CROSS TOTALS	+0.27 (+0.25)	17 (15)	SWEAT	+0.30 (+0.15)*	12 (13)	CROSS TOTALS	14.0 (17.0)
12 (15)	$-T/\theta \cdot \partial\theta/\partial p$	+0.49 (+0.38)	17 (25)	TOTAL TOTALS	+0.27 (+0.21)*	21 (28)	SHOWALTER	−0.23 (−0.09)*	13 (19)	SHOWALTER	17.8 (21.2)
16 (21)	CONV. INSTAB. I	−0.44 (−0.28)	20 (23)	POT. WET-BULB	−0.24 (−0.22)	23 (18)	CONV. INSTAB. II	+0.21 (+0.14)*	21 (30)	TOTAL TOTALS	23.0 (25.9)
17 (24)	LIFTED	+0.41 (+0.10)*	22 (32)	RACKLIFF	+0.23 (+0.14)*	25 (26)	CROSS TOTALS	+0.18* (+0.09)*	25 (27)	$-T/\theta \cdot \partial\theta/\partial p$	25.2 (23.3)
18 (23)	MOD. SHOWALTER HH	+0.36 (+0.22)	29 (6)	NEG. ENERGY	+0.15* (+0.36)	32 (19)	LIFTED	−0.09* (−0.13)*	27 (40)	LIFTED	27.0 (30.8)
22 (20)	NEG. ENERGY	−0.13* (+0.36)	33 (30)	$-T/\theta \cdot \partial\theta/\partial p$	+0.09* (+0.14)*	38 (37)	VERTICAL TOTALS	+0.01* (−0.02)*	34 (11)	NEG. ENERGY	29.3 (15.6)
24 (10)	POS. ENERGY	−0.06* (+0.40)	40 (31)	CONV. INSTAB. II	−0.04* (−0.14)*	39 (39)	TOTAL ENERGY	+0.00* (+0.01)*	37 (29)	VERTICAL TOTALS	29.7 (25.9)

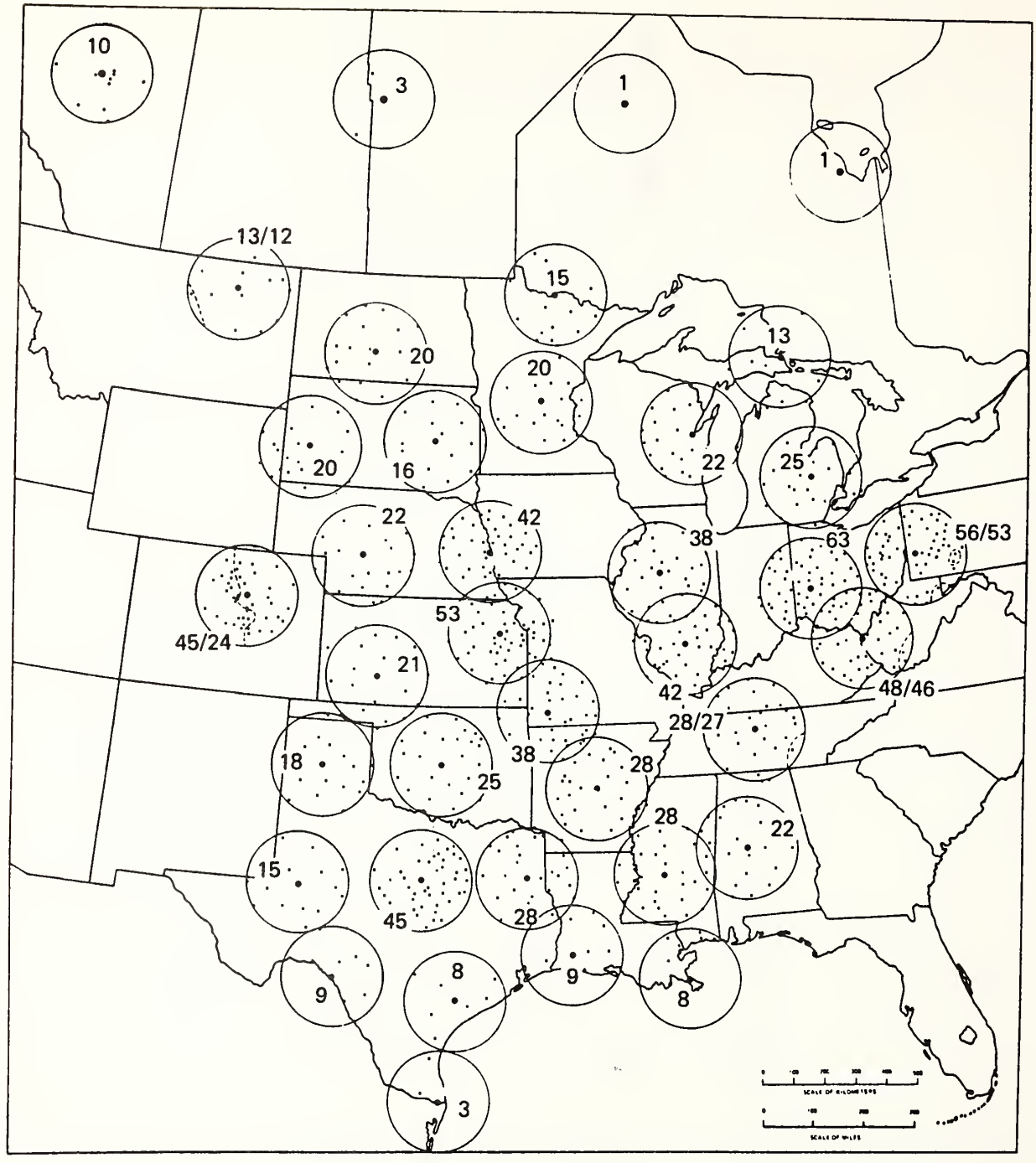

Figure 1: Data networks used. Large dots are rawinsonde stations (38) whose code letters appear in Fig. 2. Circles have 100 mi. (161 km) radii and are centered on rawinsonde stations. Small dots are hourly rainfall stations (854) that lie within or very close to those circles, the number pertaining to each circle being indicated. For five circles on the boundaries of the region, some of whose rainfall stations are in elevated areas (enclosed by broken lines), calculations were performed using both all available rainfall stations (total given by left-hand number) and only those at relatively low elevations (right-hand number). Results for the latter are given here; they differed little from those obtained using all rainfall data.

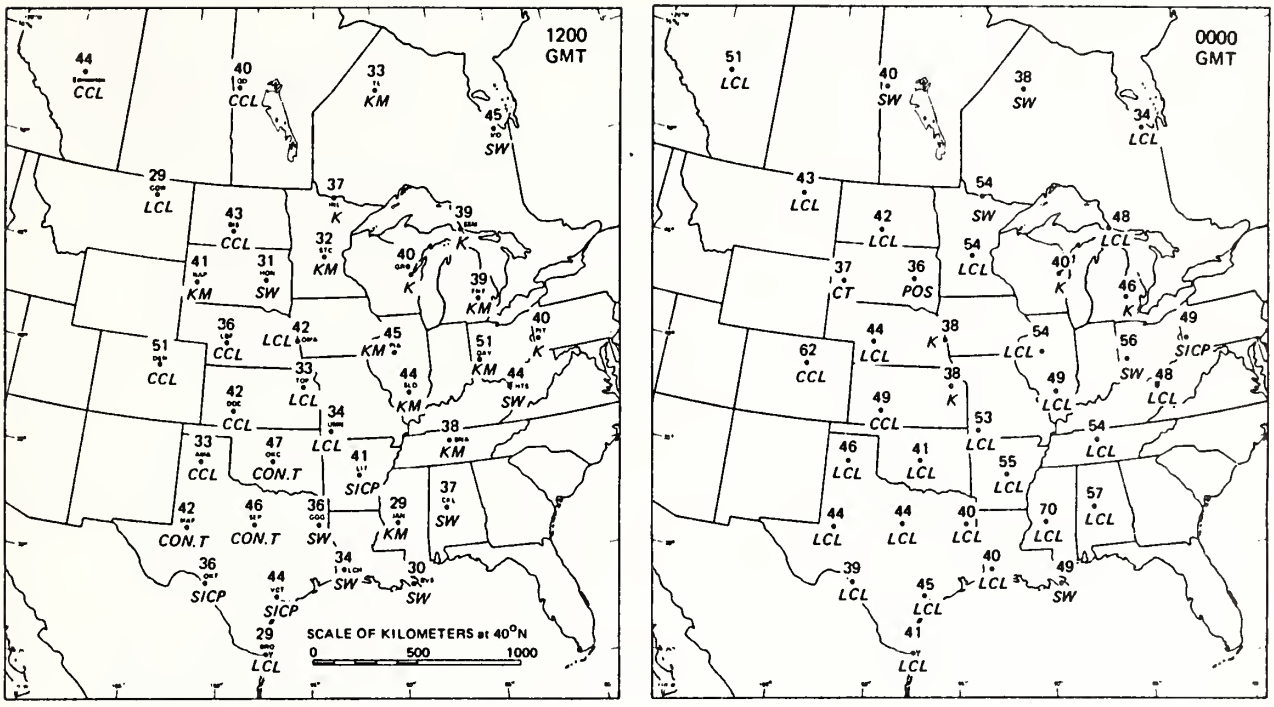

Figure 2: Results of linear correlation analyses for indicated sounding times between (a) values of static stability indices/thermodynamic parameters for the rawinsonde stations given in Fig. 1 and (b) area-averaged 12-hour rainfall accumulations (centered on sounding time) for the circles surrounding each station (Fig. 1). Small letters give rawinsonde station codes. Numbers are correlation coefficient magnitudes x 10^2. Large letters denote stability indices/thermodynamic parameters with the maximum correlation magnitudes: K is K-index, KM is modified K-index, CT is Cross Totals, SW is SWEAT, SICP is the modified Showalter index of Curtis and Panofsky, LCL is Lifted Condensation Level, CCL is Convective Condensation Level, CON.T is Convective Temperature, POS is Positive Buoyant Energy (see Table 1).

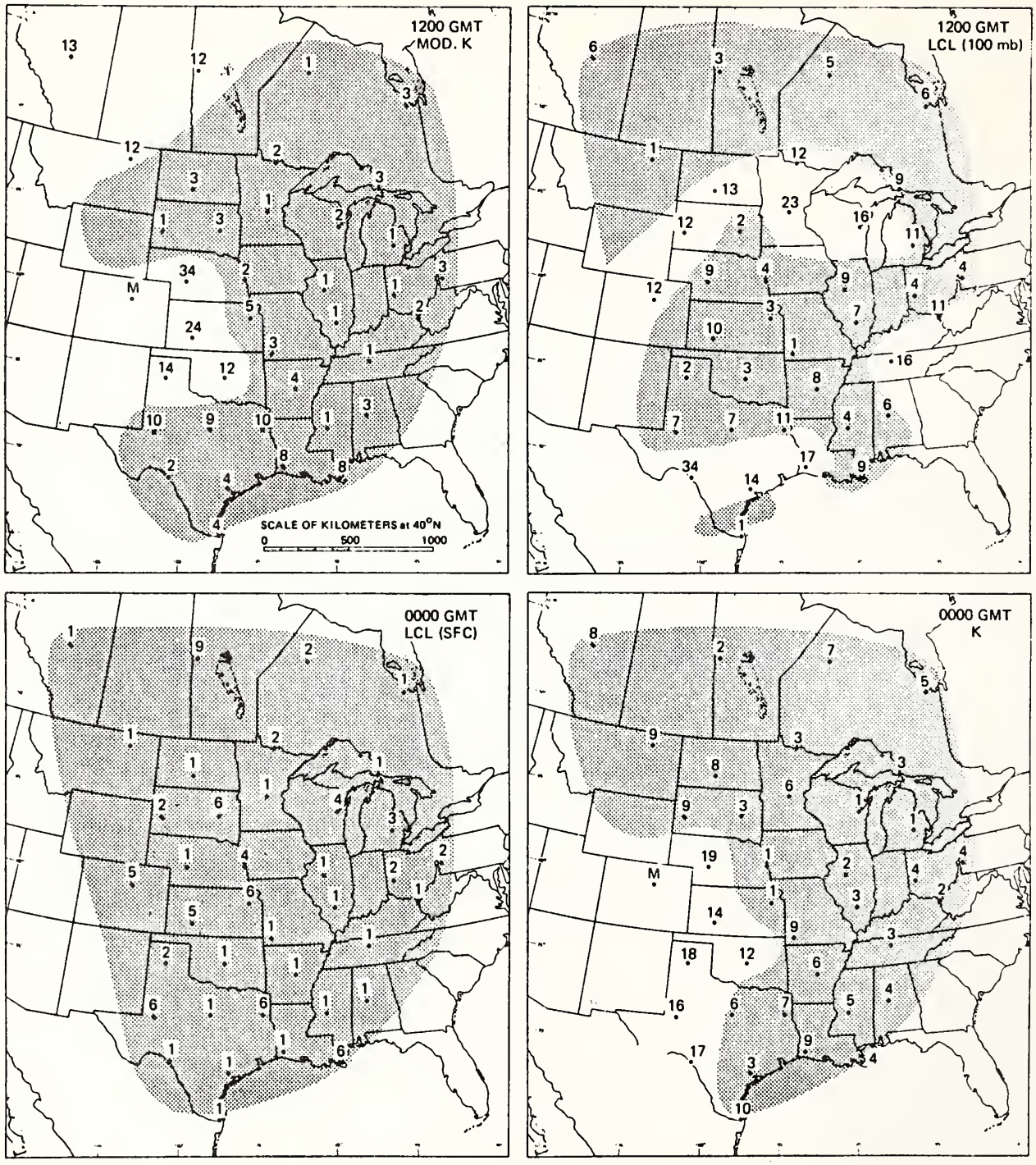

Figure 3: Individual station relative rankings (out of 40) of correlation coefficient magnitudes for the stability indices/thermodynamic parameters that Table 2 identified as being best related to rainfall for the region as a whole. Stippling covers stations for which rank was no worse than tenth. M indicates that an index/parameter could not be evaluated for that station.

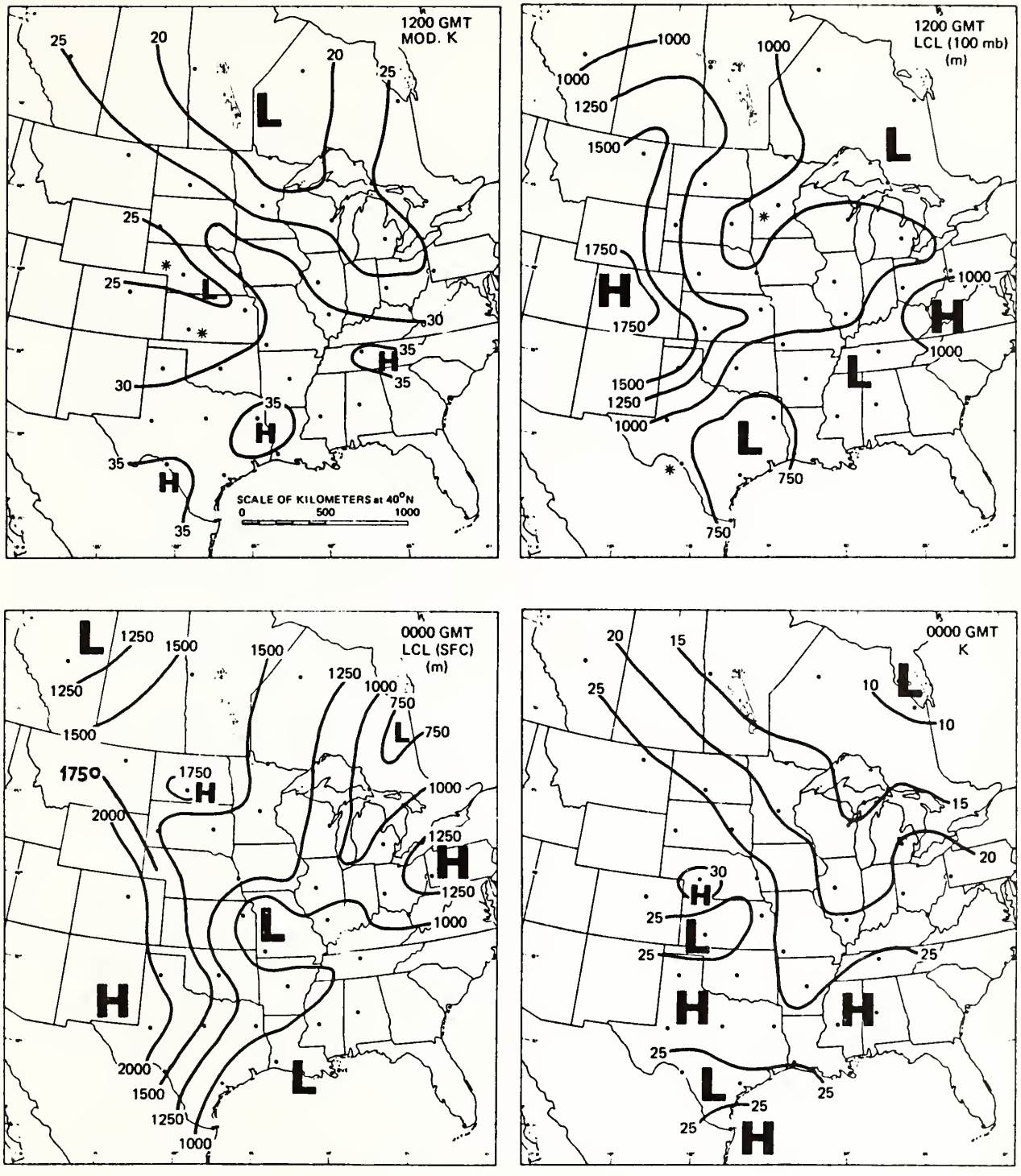

Figure 4: Threshold values of key indices/parameters treated in Fig. 3, beyond which (above for K-type; below for LCLs) the probability of occurrence of measurable rainfall exceeded that of nonoccurrence. Asterisk identifies stations for which the index/parameter was relatively poorly correlated with rainfall.

Meteorological Conditions during Drought Episodes in the United States Great Plains

Fong-Chiau Chang and John M. Wallace
Department of Atmospheric Sciences, AK-40
University of Washington
Seattle, WA 98195

Historical droughts over the central United States (1889-1980) and their associated large-scale circulation patterns and land-surface moisture conditions are investigated, using climatological monthly mean surface data, rawinsonde data, Palmer drought severity indices, 82 years of gridded monthly mean sea-level pressure data, and 30 years of gridded 5-day mean sea-level pressure and 500 mb height data. Surface station data include monthly mean surface pressure, maximum and minimum temperatures, temperature range, monthly total precipitation, dew point and relative humidity.

Anomalies in monthly mean surface air temperature at Kansas City were used as a basis for objectively ranking the 276 months in the 92 summers, 1889-1980 (Table 1). A striking feature that emerges is the concentration of drought months in the decades of the 1910's, 1930's, and 1950's. Many of the hot months exhibit negative anomalies in relative humidity, dew point, precipitation and Palmer drought severity index. The drought months during the 1930's were characterized by extreme negative relative humidity anomalies and very low Palmer drought severity indices. These results support the view, expressed by Namias (1960 a and b) and others, that soil moisture plays an important role in droughts.

Patterns of large-scale, low frequency circulation anomalies during the summer months were investigated, using one-point correlation maps analysis, based on sea-level pressure fields. The dominant pattern that emerged in the North America region involves a see-saw in sea-level pressure betweeen the climatological mean North Pacific anticyclone and the continental low over the Rockies. The positions of the centers of opposing sign in the strongest one-point correlation patterns for sea-level pressure are connected by arrows in Fig. 1 lower panel. The polarity and strength of this pattern can be represented by a summertime circulation index S1, defined as the difference in normalized sea-level pressure anomalies between these two "centers of action". Positive values of S1 denote an enhancement of the climatological mean, monsoonal circulation pattern over western North America. Correlation maps for the index S1 are represented in Fig. 2a. The composites (Fig. 2b) based on the 31 pentads (of the 570 pentads included in the 30 summer record) with the most positive values of S1 are associated with hot, dry conditions over the North America Great Plains. Fig. 2c show the composites with the most negative values of S1 which are associated with cool, wet conditions over the Great Plains.

Normalized monthly values of S1 (1899-1980) (listed in Table 1) were used to document the relationship between the Pacific Rockies pattern and historical drought episodes. In agreement with results of Klein (1952 a and b), Namias (1955) and others, it was found that drought conditions in the United States Great Plains tend to be associated with an enhanced monsoonal circulation: 11 out of the 25 hottest months at Kansas City were characterized by such conditions (see Table 2). However, it is evident that drought can occur even in the presence of a normal sea-level pressure field, provided that the soil is very dry, as it was, for example, during the 1930's "dust bowl" period. Table 3 lists the 15 months (of the 276 months of this study) that exhibited the lowest relative humidity at Kansas City. Ten of these 15 months are among the 25 hottest months at Kansas City, and all but two exhibited temperature well above normal. Conversely, we find that droughts can occur when the soil moisture is near or above normal, provided that an abnormally strong monsoonal circulation persists for an extended period. Of the 25 hottest summer months at Kansas City, 7 occurred in the absence of both of the above two conditions (Table 4).

References

Klein, W. H., 1952a: The weather and circulation of June 1952. Mon. Wea. Rev., 80, 99-104.

_____, 1952b: The early drought of 1952. weatherwise, 111, 111-113.

Namias, J., 1955: Some meteorological aspects of drought with special reference to the summers of 1952-1954 over the United States. Mon. Wea. Rev., 83, 199-205.

_____, 1960a: Factors in the initiation, perpetuation, and termination of drought. Extract of publ. No. 51 of the I. A. S. H. Commission of Surface Waters, 81-94.

_____, 1960b: Influences of abnormal surface heat sources and sinks on atmospheric behavior. Short Period Climatic Variations, Collected Works of J. Namias, 424-436.

Figure Captions

Fig. 1. Climatological mean 500 mb height field (top, contour interval 30 m) and sea level pressure (bottom, contour interval 2 mb) derived from the 570-pentad data set. Circles indicate a selection of base gridpoints along the Rockies which show interesting correlation patterns. The arrows are directed from the base gridpoint to the gridpoints with which they show the strongest negative correlation on their respective sea level pressure correlation maps and positive correlation on their respective 500 mb height correlation maps. The ±0.3 contours on the first mode of an eigenvector analysis (see Fig. 6) comprise the outline of the shading. The two individual base gridpoints discussed in the text are denoted by the heavier circles.

Fig. 2a. One point correlation maps showing correlation coefficients between 500 mb height (top), 1000-500 mb thickness (middle), and sea level pressure (bottom) over the hemisphere and the summertime circulation index S1 (the difference between normalized sea level pressure anomalies at grid-points (36°N,152°W) and (42°N,108°W)). Based on the same 570 pentad data set as Fig. 1. Contour interval 0.1

Fig. 2b. Composite charts for 500 mb height (top, contour interval 30 m), 1000-500 mb thickness (middle, contour interval 30 m) and sea level pressure (bottom, contour interval 2 mb). Based on the 31 pentads out of the 570-pentad data set with the summertime circulation index S1 above 1.2.

Fig. 2c. Composite charts for 500 mb height (top, contour interval 30 m), thickness (middle, contour interval 30 m) and sea level pressure (bottom, contour interval 2 mb). Based on the 45 pentads out of the 570-pentad data set with the summertime circulation index S1 more negative than -1.2.

Table 1. Selected data for the 25 hottest summer months at Kansas City (39°N,95°W) during the period 1889-1980, based on mean surface temperature anomalies. Parameters listed in Table include: mean maximum (Max.) and minimum (Min.), temperatures and temperature range (Range), mean temperature (T) and temperature anomaly (T Ano.), monthly precipitation anomaly (P Ano.), and mean dew point (DEW) and relative humidity (RH) anomalies - all as observed at Kansas City; temperature anomalies at the 500 mb level (T500), and mean lapse rates between the surface and 500 mb levels (Lapse) at Columbia, Missouri (39°N, 92°W); summertime circulation index (SI) defined as the difference between the normalized sea-level pressure anomalies at the gridpoints (36°N,150°W) and (42°N,108°W); temperature anomalies at Spokane (T SP); Palmer drought severity index (PDSI).

Rank	Year	Month	Max. °F	Min. °F	Range F	T °C	T Ano. °C	P Ano. IN	Dew °C	RH %	T500 C	Lapse	T SP °C	SI	PDSI
1	52	6	94	73	21	28.7	5.0	-1.1	2.2	- 8	2.5	33.1	-0.7	2.2	0.2
2	36	8	100	74	26	30.6	4.9	-3.7	-1.9	-18			1.4	0.3	-4.8
3	34	6	95	72	23	28.6	4.8	-3.1	0.0	-14			1.7	1.2	-4.7
4	34	7	102	75	27	31.3	4.8	-1.6	-3.0	-21			0.6	1.1	-5.5
5	36	7	101	74	27	31.0	4.4	-3.8	-3.0	-20			1.5	0.7	-3.7
6	47	8	97	76	21	30.1	4.4	0.4	2.0	- 7			-1.0	1.6	-1.4
7	53	6	94	72	22	28.1	4.4	-3.3	2.2	- 9	1.3	34.6	-2.9	1.2	-2.0
8	54	7	99	76	23	30.6	4.0	-2.9	-1.3	-16	1.7	34.6	-1.5	0.6	-4.6
9	01	7	98	76	22	30.6	4.0	-1.1	-1.9	-17			-1.4	1.8	
10	13	8	96	74	22	29.7	4.0	-3.0	-3.5	-22			0.0	-1.1	
11	33	6	92	71	21	27.7	3.9	-2.6	-2.2	-20			0.9	1.0	-1.7
12	35	7	98	76	22	30.4	3.9	-3.3	2.5	- 3			0.0	0.5	-1.2
13	11	6	91	71	20	27.1	3.4	-4.4	-1.7	-16			0.9	-0.1	
14	55	7	95	76	19	29.7	3.1	-2.9	2.0	- 5	1.3	32.6	-2.1	2.3	-2.2
15	37	8	94	73	21	28.8	3.1	-1.7	1.5	- 2			-1.3	1.6	-2.7
16	18	6	90	70	20	26.7	2.9	-3.3	-1.1	-10			3.3	-1.7	
17	80	7	97	73	24	29.4	2.9	-1.8	0.3	-10			-0.5	1.2	-2.5
18	18	8	95	73	22	28.5	2.8	-1.5	-1.9	-11			-1.5	0.2	
19	31	6	89	70	19	26.5	2.8	-3.3	0.5	- 8			0.9	-0.7	-1.7
20	39	7	96	74	22	29.3	2.7	-2.7	0.3	- 7			1.2	0.6	-2.3
21	38	8	94	72	22	28.3	2.7	2.9	1.5	- 1			-0.4	1.2	-1.8
22	34	8	96	71	25	28.3	2.7	-2.5	-3.0	-13			1.4	-0.6	-6.2
23	71	6	89	70	19	26.3	2.6	-1.6	2.8	- 1			-2.3	0.1	-1.1
24	63	6	89	70	19	26.3	2.5	-1.6	2.2	- 4	-0.4	29.2	-0.4	2.5	-1.6
25	54	6	89	70	19	26.2	2.5	-1.1	0.5	- 8	1.1	32.6	-2.9	0.3	-4.2

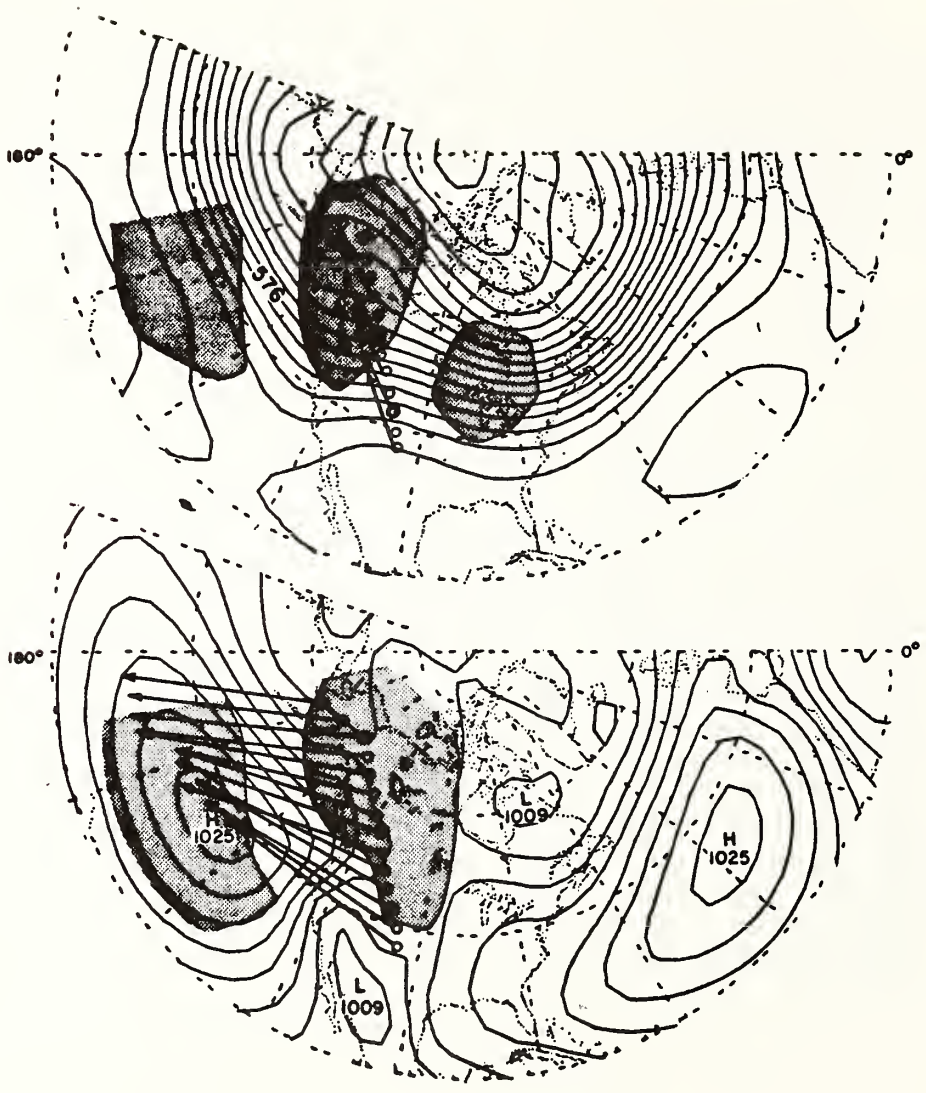

Fig. 1.

Fig. 2a.

Fig. 2b.

Fig. 2c.

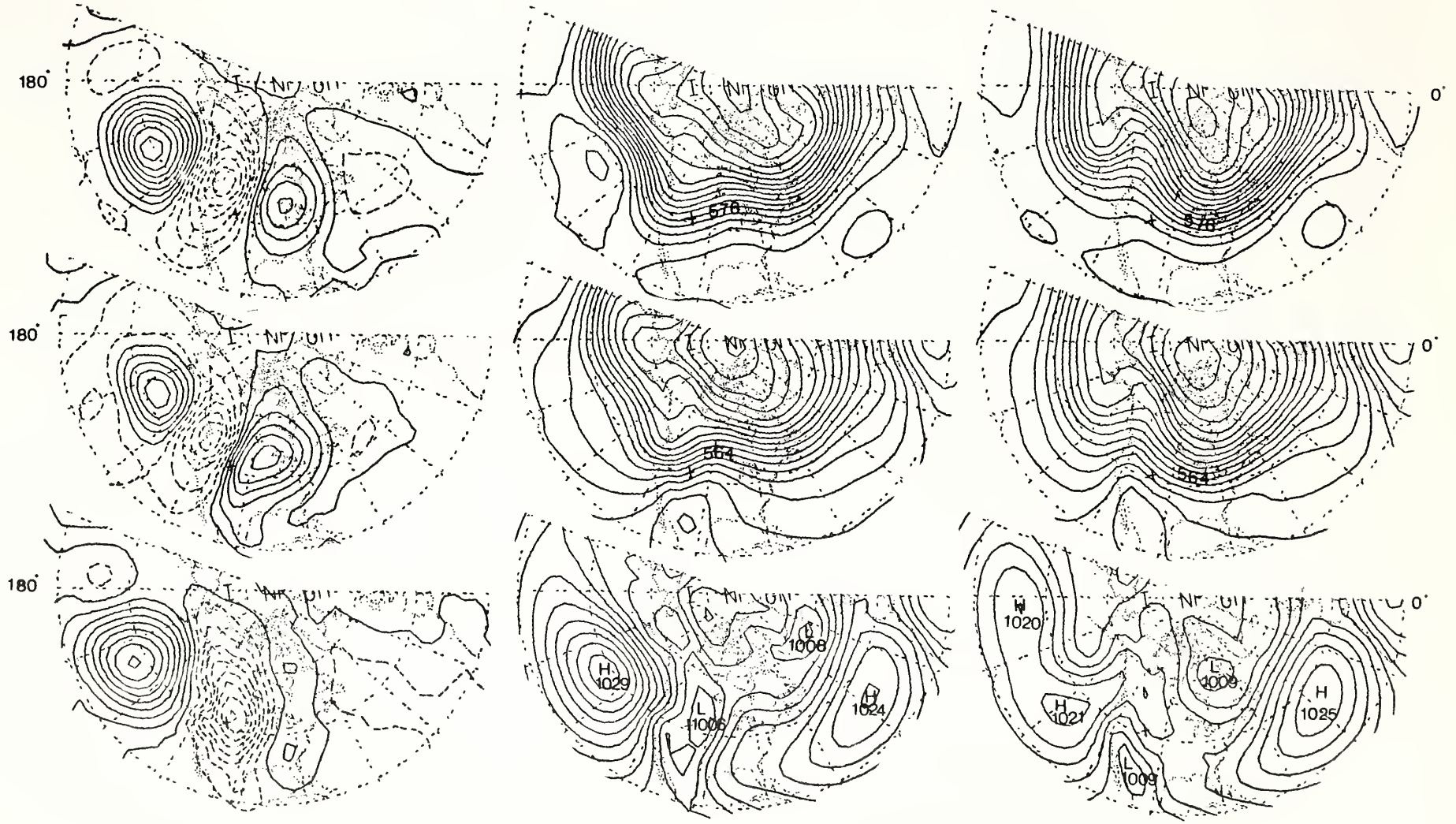

Table 2. The 11 months from among the 25 hottest months at Kansas City with summertime circulation index S1 > 1. T indicates temperature anomaly anomaly at Kansas City (KC). T SP indicates temperature anomaly at Spokane, Washington (48°N,118°W). RH indicates the relative humidity anomaly at Kansas City. PDSI indicates Palmer drought severity index in the six surrounding climatological subdivisions.

Month	Year	rank for KC T	T °C	S1	T SP °C	RH %	PDSI
June	1952	1	5.0	2.2	-0.7	- 8	0.2
June	1934	3	4.8	1.2	1.7	-14	-4.7
July	1934	4	4.8	1.1	0.6	-21	-5.5
August	1947	6	4.4	1.6	-1.0	- 7	-1.4
June	1953	7	4.4	1.2	-2.9	- 9	-2.0
July	1901	9	4.0	1.8	-1.4	-17	
July	1955	14	3.1	2.3	-2.1	- 5	-2.2
August	1937	15	3.1	1.6	-1.3	- 2	-2.7
July	1980	17	2.9	1.2	-0.5	-10	-2.5
August	1938	21	2.7	1.2	-0.4	- 1	-1.8
June	1963	24	2.5	2.5	-0.4	- 4	-1.6

Table 3. The 15 months with lowest relative humidity at Kansas City in the period 1889-1980. Dew indicates dew point temperature anomaly. Other abbreviations are the same as in Table 6.

Month	Year	RH %	Dew °C	rank for KC T	T °C	SI	PDSI
August	1913	-22	-3.5	10	4.0	-1.1	
July	1934	-21	-3.0	4	4.8	1.1	-5.5
June	1933	-20	-2.2	11	3.9	1.0	-1.7
July	1936	-20	-3.0	5	4.4	0.7	-3.7
August	1936	-18	-1.9	2	4.9	0.3	-4.8
August	1901	-18	-1.9		0.6	-0.1	
June	1936	-17	-3.3		2.0	-1.7	-2.6
July	1901	-17	-1.7	9	4.0	1.8	
June	1911	-16	-1.7	13	3.4	-0.1	
July	1954	-16	-1.3	8	4.0	0.6	-4.6
July	1930	-16	-3.6		1.7	-0.6	
June	1934	-14	0.0	3	4.8	1.2	-4.7
July	1974	-14	-2.5		1.2	0.1	-0.2
August	1934	-13	-3.0	22	2.7	-0.6	-6.2
July	1918	-13	-4.1		-0.6	-1.1	

Table 4. List of the 7 months from among the 25 hottest months at Kansas City in the period 1889-1980, which show in neither a large positive value of the summertime circulation index SI nor a particularly low relative humidity (i.e., those months that appear in neither of the two previous tables). The abbreviations are the same as in Table 6. Additional statistics for three months are available in Table 2.

Rank	Month	Year	T °C	SI	RH %	PDSI
12	July	1935	3.9	0.5	- 3	-1.2
16	June	1918	2.9	-1.7	-10	
18	August	1918	2.8	0.2	-11	
19	June	1931	2.8	-0.7	- 8	-1.7
20	July	1939	2.7	0.6	- 7	-2.3
23	June	1971	2.6	0.1	- 1	-1.1
25	June	1954	2.5	0.3	- 8	-4.2

Monthly forecast experiments with sea surface temperature anomaly forcings and envelope mountains: Preliminary results

by

J. Sirutis, K. Miyakoda, Y.-H. Lu, and J. Ploshay
Geophysical Fluid Dynamics Laboratory/NOAA
Princeton University
Princeton, New Jersey 08542

and

R. Reynolds
Climate Analysis Center/NMC/NWS/NOAA
Washington, D. C. 20233

A series of 30 day forecasts has been made for January 1983 to assess the impact of using observed sea surface temperature and envelope mountains on medium and long range forecasting. The basic model used in these studies is the GFDL global finite difference model. The model has a resolution of 1.875° in the north-south direction, and a variable resolution in the east-west direction, ranging from 1.875° in the tropics to 10° near the poles. The model has 9 sigma levels in the vertical.

A set of four experiments has been run with this model. They will be denoted as:

1) F - The control experiment using climatological sets and smooth topography.

2) FM - A forecast with envelope mountains which are steeper than those used in the control run.

3) FS - A forecast using the observed sets for January 1983.

4) FMS - A forecast using both observed sets and envelope mountains.

Each of these four experiments was run with two sets of initial conditions: one created from the NMC analysis, the other created from the ECMWF analysis.

Figure 1 shows the anomaly correlation coefficients and RMS error of the 10 day mean 500 mb geopotential height for the four forecasts made with the ECMWF initial conditions. The verification domain is the northern hemisphere

from north pole to 25°N. As can be seen, in the extra-tropics, the inclusion of the envelope mountains resulted in a slight improvement in the forecast, while the use of observed sets had a negative impact on the forecast.

Figure 2 shows the anomaly correlation coefficients and RMS error of the 10 day mean u component of the wind at 850 mb in the tropics (25°N to 25°S). Here, in contrast to what happened in the extra-tropics, the inclusion of the envelope mountains led to a slightly worse forecast while the use of the observed SST produced an improvement in the forecast.

The forecast precipitation patterns in the tropics (not shown here) for the control case and for the cases with the observed SSTs mimicked very closely the SST data used in the forecast with maxima in the precipitation corresponding to warm SST and minima in the precipitation corresponding to cool SST. However, the agreement between the forecast precipitation in the experiments using the observed SST data and the observed OLR pattern for January 1983 was poor. The reason for this is not clear.

Figure 3 shows the velocity potential at 200 mb computed from observed data and for the four forecasts made with the ECMWF initial conditions. In the observations the center of the negative area is located at 155°W and 20°S. In the two forecasts made with climatological SSTs, the center is located over Borneo. This is in agreement with observations. In the two forecasts made with observed SSTs, there is a slight eastward shift in the location of the minimum, but not enough to be in good agreement with observations. This defect in the forecast seems to be associated with the convective activity in the area of Borneo and northern Australia. In the forecasts it seems to be much stronger than is indicated by observations.

The results of the forecasts made with the NMC initial conditions are qualitatively the same as those for the forecasts made with the ECMWF initial conditions.

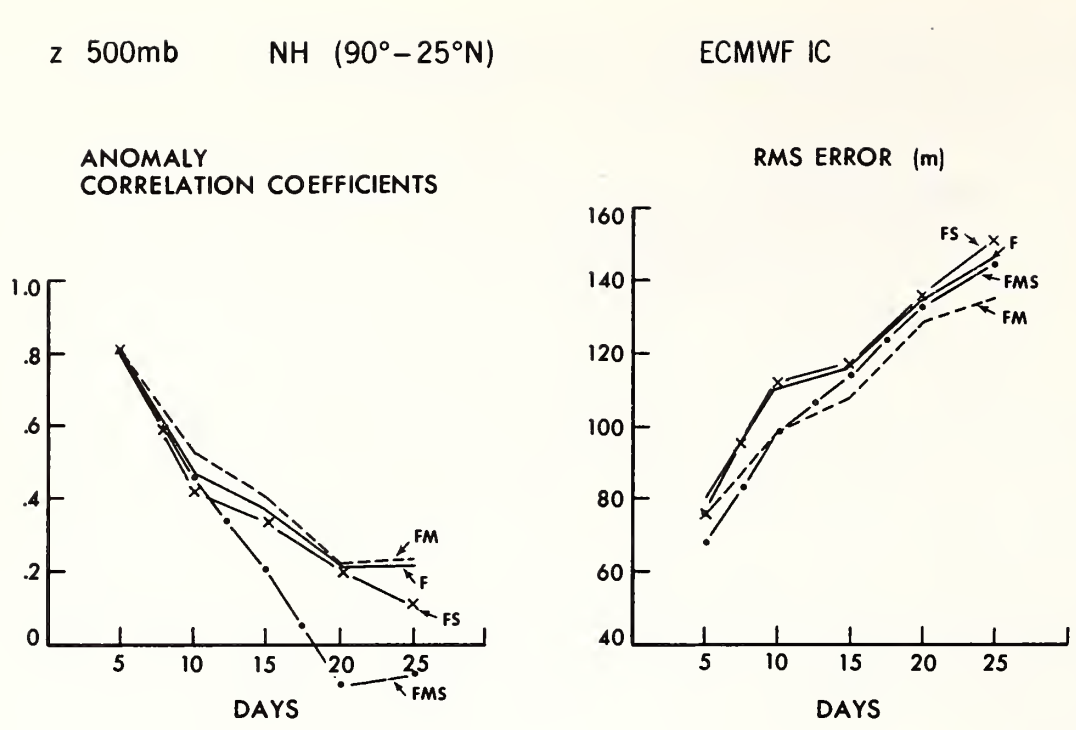

Figure 1. Anomaly correlation coefficients (left) and root mean square error(right) of 10 day mean 500 mb geopotential heights.

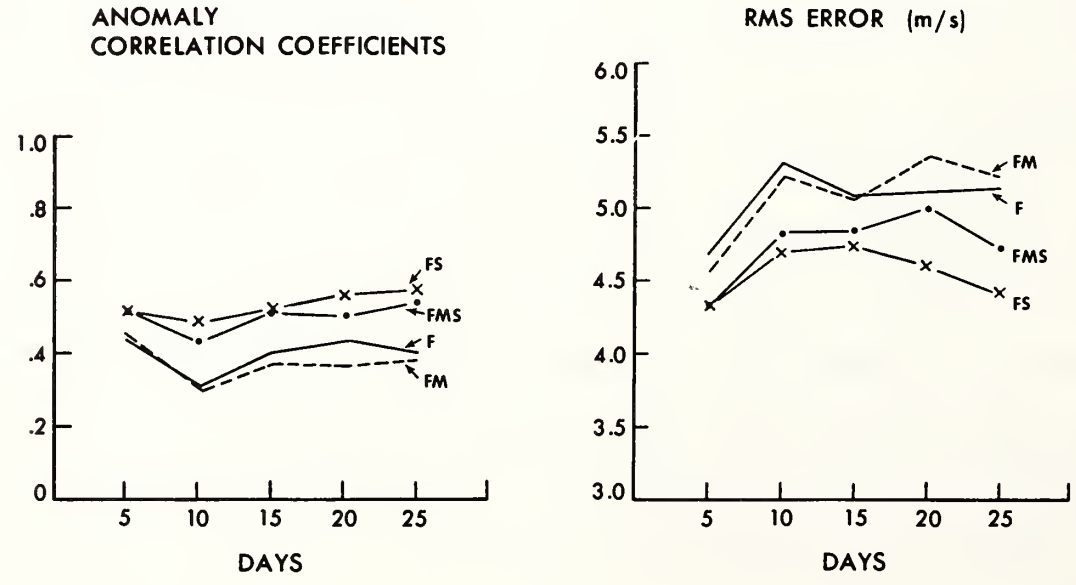

Figure 2. Anomaly correlation coefficients (left) and root mean square error (right) of 10 day mean u at 850 mb.

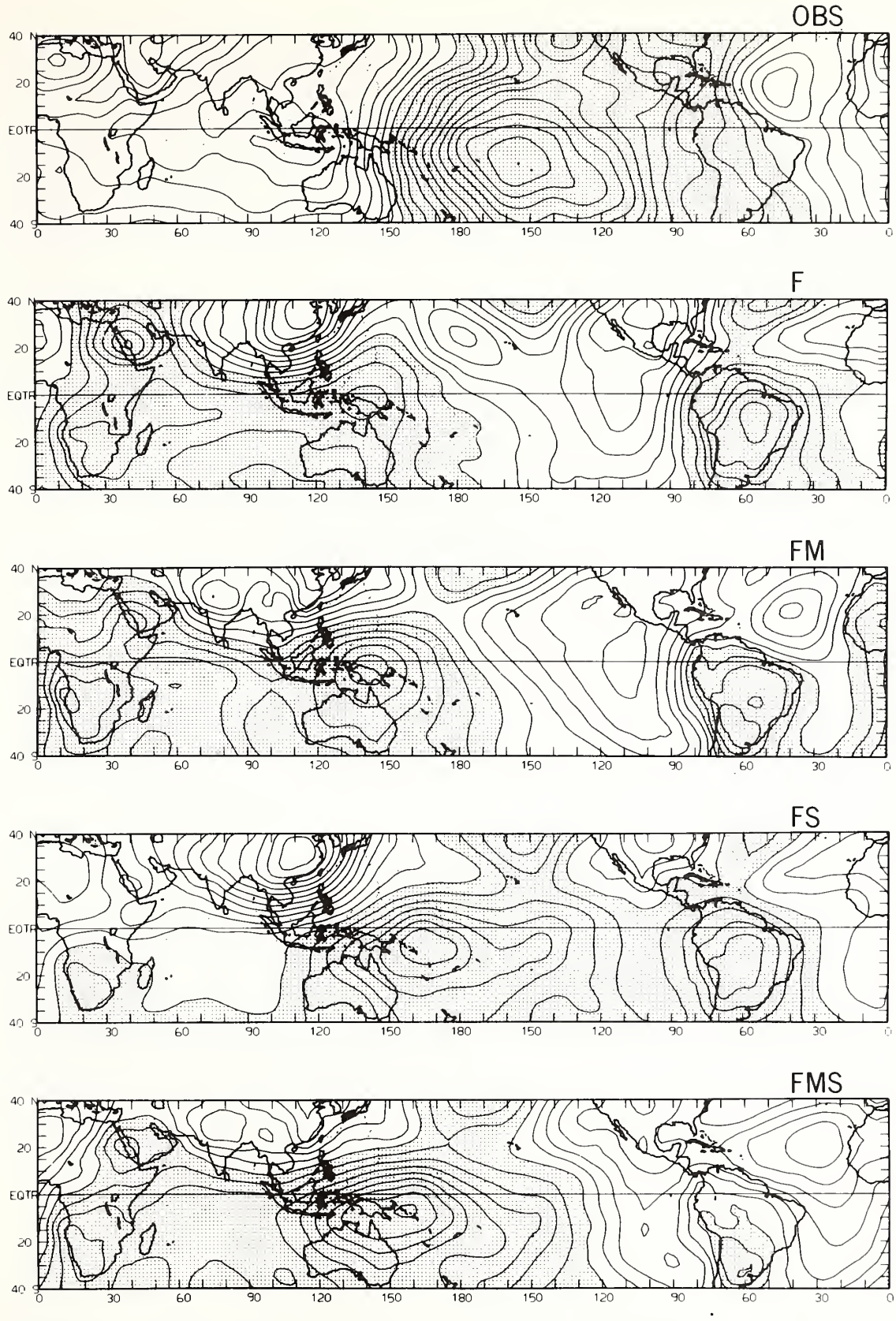

Figure 3. The velocity potential at 200 mb for the four forecasts made with the ECMWF initial conditions and for observations. The negative areas are shaded. The contour interval is 10^5 m^2/sec.

Spectral Statistical Forecasts of the 500 mb height field

by

John O. Roads

Tim P. Barnett

Scripps Institution of Oceanography

1. Introduction and Method

A simple dynamical model used to describe global weather variations is a model based upon damped propagating Rossby waves. For motions on the sphere, the solution is developed in terms of associated Legendre polynomials

$$\psi(\lambda,y) = \sum_n P^0_n(siny)\psi^0_{zn} + \sum_n^N \sum_{m=1}^n P^m_n(siny)\sqrt{2}(\psi^m_{cn}\cos m\lambda + \psi^m_{sn}\sin m\lambda)$$

In terms of a damped barotropic model linearized around solid body rotation for the nonzonal components, the solution can be found analytically and written in the form

$$\psi_{zp} = \psi_{zi}\ e^{-\gamma t}$$

$$\psi_{cp} = (\psi_{ci}\cos\omega t + \psi_{si}\sin\omega t)e^{-\gamma t}$$

$$\psi_{sp} = (\psi_{si}\cos\omega t - \psi_{ci}\sin\omega t)e^{-\gamma t}$$

where

$$\omega = \frac{m(1-(2-n(n+1))\psi^0_1)}{n(n+1)+\lambda^2}$$

$$\gamma = \frac{kn(n+1)}{n(n+1)+\lambda^2}$$

Here the subscript p refers to the variable at a future time t that results from the linear damped barotropic model acting on the initial value denoted ψ_i. Subscripts z, c, s refer to the zonal, cosine and sine components. Climatology is removed from this model and the nonlinear terms are implicitly assumed to be a stochastic process, i.e. "white" noise. γ is a frictional component that acts to damp out the initial perturbation. This damping is a function of scale and may be thought of simplistically as being due to surface friction. λ^2 is known as the divergence correction for a quasi-geostrophic model and takes on the values that give the best forecast. ω is the frequency of the Rossby waves which is dependent upon the two dimensional wavenumber n and divergence correction as well as the longitudinal wavenumber and the zonal flow, approximated here by solid body rotation.

For comparison to a statistical model we compress the functions of time into coefficients (a,b) where the correspondence to the cosine sine and exponential functions of time is obvious.

$$\psi_{zp} = a_z\ \psi_{zi}$$

$$\psi_{cp} = a_c\ \psi_{ci} + b_c\ \psi_{si}$$

$$\psi_{sp} = a_s\ \psi_{si} - b_s\ \psi_{ci}$$

To derive the best estimate for the free coefficients we used a data set consisting of twice daily spherical harmonics for the Northern Hemisphere 500 mb height field. Ten years of data were available. No attempt was made to convert from geopotential to streamfunction. Coefficients for the model were determined using least squares from the first 5 years and then the skill of the model was tested on the

independent data for the second 5 years. Similarly the second 5 years were used to derive coefficients which were then tested on the first 5 years.

The coefficients are shown in Figure 1. The cosine wave was solved separately from the sine wave and a measure of our Rossby wave concept was that the coefficients were about the same in each equation. The largest values of 'a' occur at low wavenumbers, both meridional and zonal. For the components 'b' there is a sign change with components at higher n being negative and components at smaller n being positive. These results mean that the larger waves propagate westward and the smaller waves propagate eastward. Furthermore, the period of the wave is shorter as the longitudinal wavenumber is increased.

Three measures of skill for the model are shown below.

$$\text{error} = < |(\psi_p - \psi_o)^2| >^{1/2}$$

$$\text{skill} = 1. - \frac{< |(\psi_p - \psi_o)^2| >}{< |\psi_o^2| >}$$

$$\text{pattern correlation} = < \frac{|\psi_p \psi_o| - |\psi_p||\psi_o|}{(|\psi_p^2| - |\psi_p|^2)^{1/2}(|\psi_o^2| - |\psi_o^2|)^{1/2}} >$$

where $< ... >$ denotes a time average and $|...|$ denotes a spatial average. Here ψ_p refers to the predicted value and ψ_o is the observed value.

2. Weather Forecasts

Figure 2 shows the error and skill in spectral space. The skill is highest for the lowest zonal wavenumbers and zonal flow which is equivalent to those waves with the largest period having the largest skill.

Figure 3 shows the error, skill and pattern correlation for the total field. The measures of error have been broken up into the zonal mean and waves for the error and skill measures. The pattern correlation incorporates both the zonal mean and the waves. Greater skill is found in the zonal component than in the wave components and at a time of 16 days, the skill is very close to zero. The pattern correlation shows also that there is a somewhat better correlation at short lead times using the derived model, but the results are not impressive. This indicated that the fitting of every single wave was only useful in the sense that we have a better physical understanding of the physical characteristics of the system. That is, the slowest moving Rossby waves, which indicate a tendency toward large zonal waves and intermediate scale two dimensional waves and the zonal flow, are the most predictable and may be usefully approximated by simple damped persistence models.

Can we improve this model? The answer to this was determined by examining the residual error characteristics of the error field. It was found that higher order models, i.e. consideration of the previous day might be helpful, especially in higher latitudes. In lower latitudes we discovered that a diurnal signal was present that we were not aware of initially, especially near the Himalayans and Sahara desert. For the most part, however, this improvement would probably be negligible.

3. Time Averaged Forecasts

Now suppose we want to make a forecast of the time averages, in particular we wanted to make monthly forecasts. From a damped model we have

$$|\psi_p|_{T_1} = a \{\psi_i\}_{T_2}$$

The usual way to find a predictive relationship is simply to use the same time averaging period for the predictor and predictand, i.e. use the previous monthly mean to predict a subsequent monthly mean. One justification for this is that time averaging will presumably remove random weather noise and allow the climate signal to emerge. On the other hand, for the damped barotropic model and any other envisioned dynamic model, all subsequent values including time averages depend only upon the initial state, not the previous time average. This dilemma led us to conduct a set of numerical experiments, the results of

which are shown in Table 1. The table is arranged in the form of the predictand averaging time moving left to right, i.e. the prediction of 1/2, 8, 16, 32 day averages and the predictor time average moving from the bottom to the top. From this table *we discovered that time averaging of a predictor will actually degrade the skill.* In fact it can be shown rigorously for a first order Markov process represented by Figure 4 that the best prediction of a time average is from the closest antecedent day. This suggests that prediction of monthly and seasonal forecasts might be immediately improved simply by using the first few antecedent days rather than the antecedent time average for those terms concerned with the persistent nature of the flow. This result probably depends heavily upon the predictand being well represented as a first order Markov process. For example, somewhat different results were found in another analysis presented by R. Harnack at this meeting (Ninth Climate Diagnostics Workshop proceedings).

The seasonal dependence of the monthly averaged skill (Fig. 5) is similar to those from other studies of persistence forecasts with the largest skill obtained during the winter and summer months and the smallest skill obtained during the transition seasons.

The physical picture of the skill is shown in Figure 6. The top panel averages the skill over the two independent cases. The two bottom panels show those regions where the skill is greater than 5% and 10% in both independent samples. The skill is marginal but probably significant in the regions near the eastern edges of the continents. The regions of high skill in high latitudes are also inversely correlated with those in low latitudes. We thus suggest that we have predicted via this model some of the regional variations known to be important on monthly time scales.

ACKNOWLEDGEMENTS

This work was supported in part by NSF Grant ATM-8213279, NSF Grant ATM-8210160 and NOAA Grant NA 81AA-D-0054. Further details can be found in Roads, J.O. and T.P. Barnett, 1984, *Mon. Wea. Rev., 112*, 1354-1369.

Figure and Table Legends

Figure 1. Persistence coefficients (X10) for the cosine (a_c) and sine (a_s) equations and wave coefficients (X10) for the cosine (b_c) and sine (b_s) equations for 1, 2, 4, 8 day weather predictions. n and m are the horizontal wavenumbers and stippled areas correspond to regions of negative skill.

Figure 2. Forecast error (m) and skill (%) in spectral space for 1, 2, 4, 8 day weather predictions. n and m are the horizontal wavenumbers and stippled areas correspond to regions of negative skill.

Figure 3. Forecast error, skill and pattern correlations for the zonal (z) and wave (w) modes as a function of lead times. Persistence (pz, pw), climatology (cz, cw) and statistical curves (SDZ, SDW) curves are shown. Shaded region indicates the separation between results for the two independent data sets (d) Error (m) (e) Skill (%) and (f) Pattern correlation for runs in which climatology is removed first. Also shown are results for the ECMWF (EC) numerical model.

Table 1. Error (m) and skill (%) for the zonal and wave components for various averaging times of the predictand T_1 and predictor T_2. Numbers in parentheses come from models derived from the second five years of data. Also shown are the pattern correlations P. Numbers in brackets are the values for persistence forecasts. Dashes indicate that these values were not calculated.

Figure 4. Theoretical error (m) and skill (%) for a first order Markov process in which various time averages are predicted from various independent time averages at zero lag. T_1 is the averaging time of the predicted quantity (predictand) and T_2 the averaging time of the initial state (predictor). The characteristic damping time is assumed to be $0.2 day^{-1}$. The error maps assume $< \psi_o^2 >^{1/2} = 70$ m.

Figure 5. Seasonal dependence of forecast skill (%) of 32-day averaged forecasts from previous day. Results for each 5-year independent test are shown separately.

Figure 6. (a) Average of forecast skill (%) for first 32-day average climate forecast from first and second 5-year independent data sets. (b) Regions (stippled) where skill is greater than 5% for both 5-year independent data sets. (c) Regions (stippled) where skill is greated than 10% for both 5-year independent data sets.

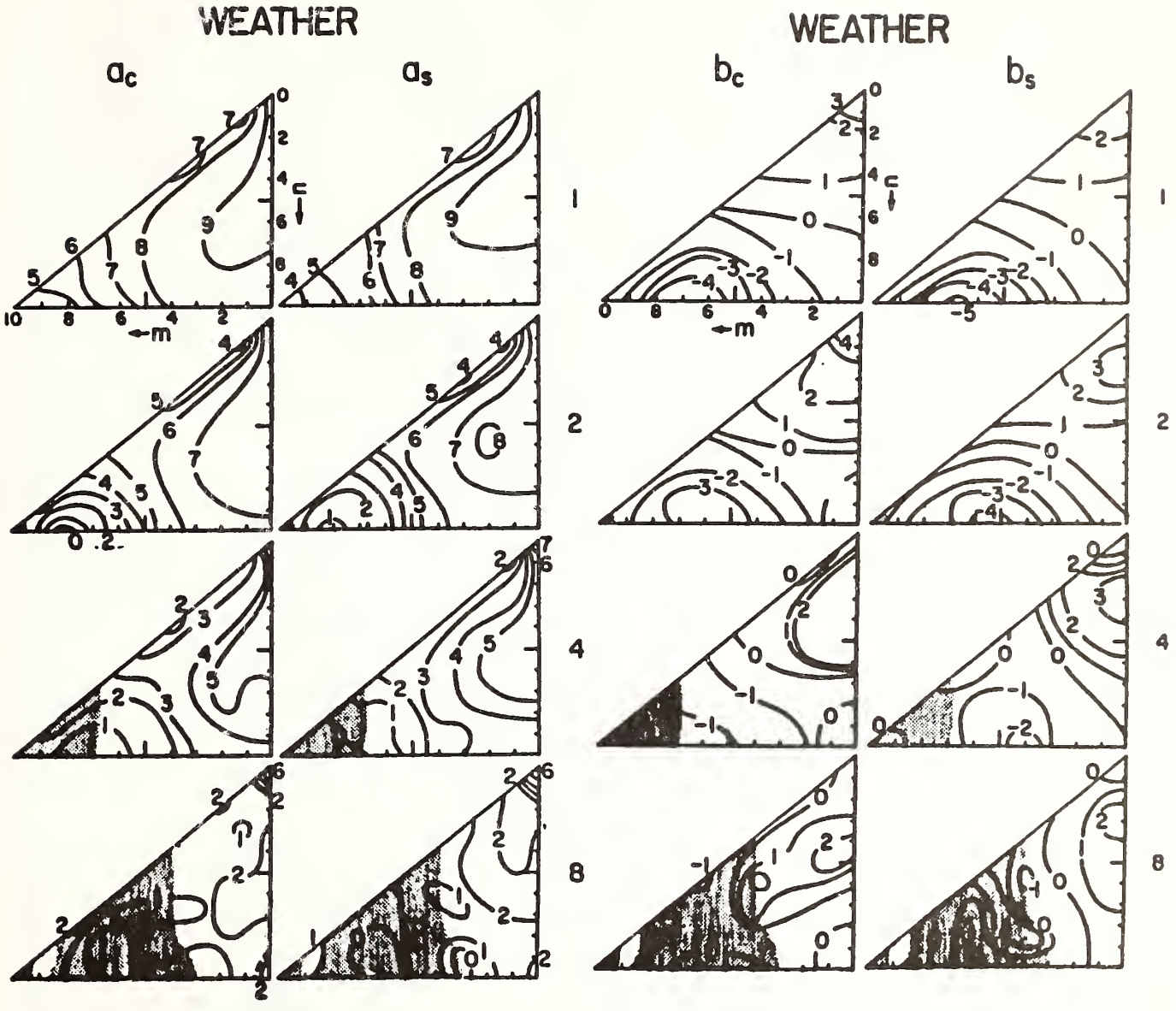

1

WEATHER

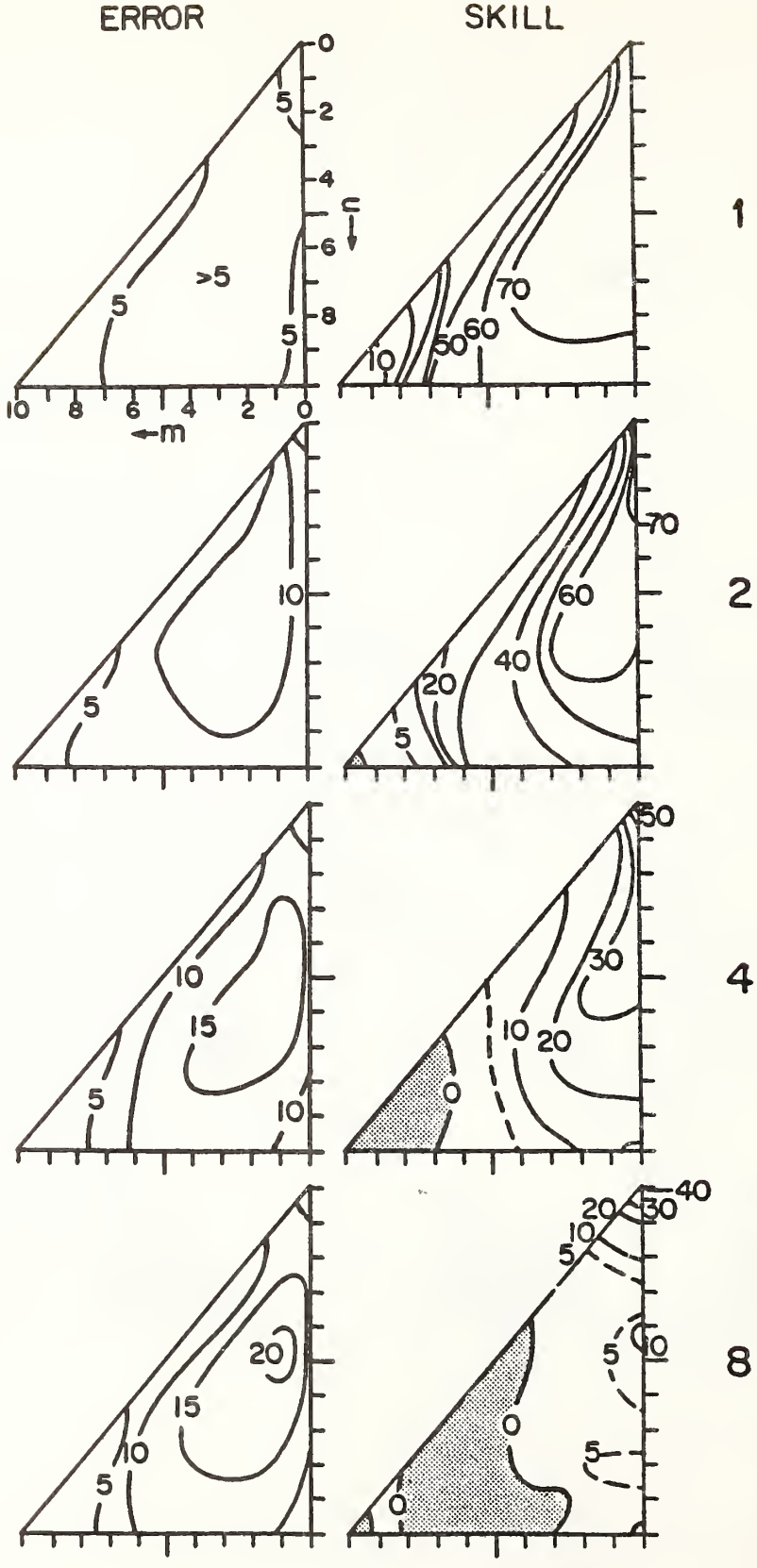
ERROR
SKILL
0
2
4
6
8
c
5
>5
5
5
10 8 6 4 2 0
m
1
10
5
70
60
50
10
2
70
60
40
20
5
10
5
4
50
30
10
20
0
10
15
5
10
8
40
30
20
10
5
5
10
20
15
10
5
0
5
0

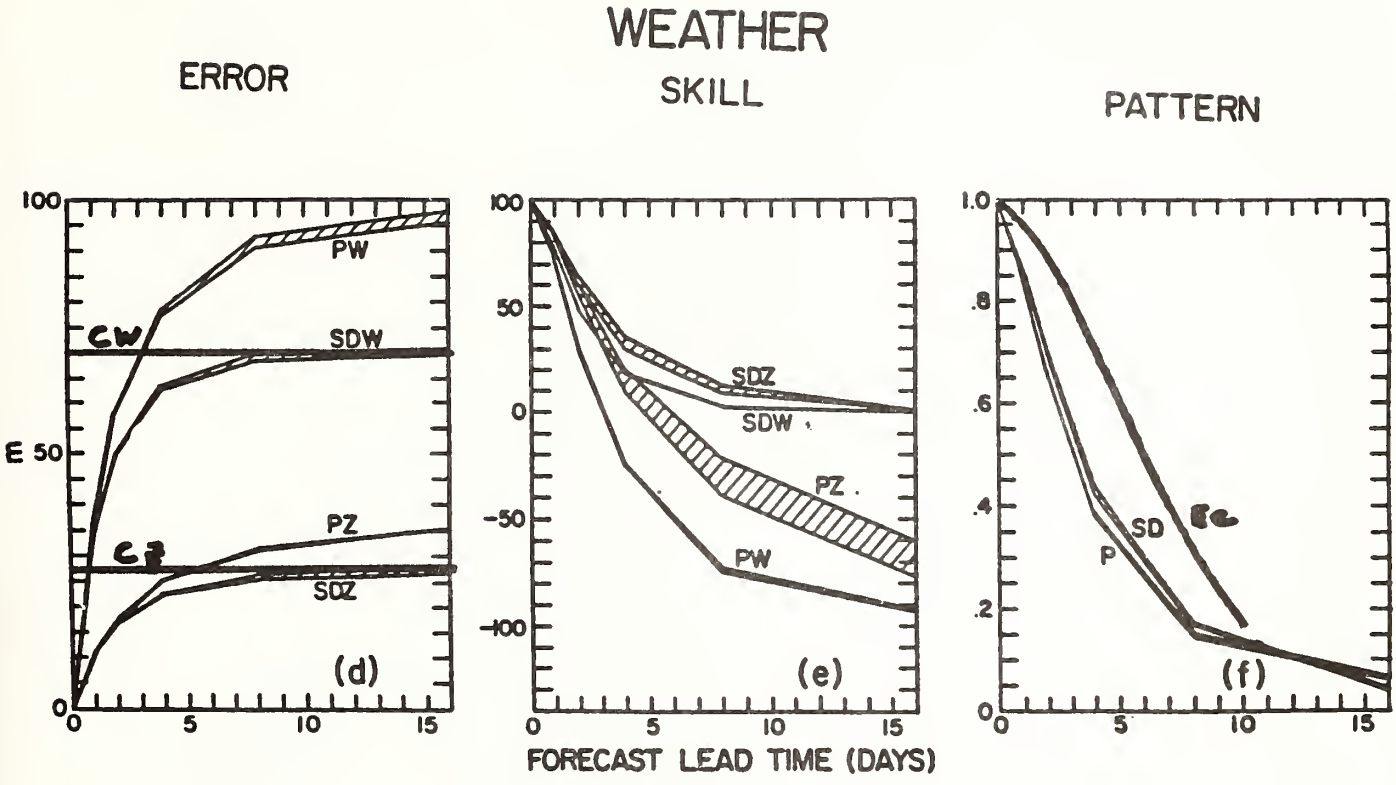
WEATHER
ERROR
SKILL
PATTERN
100
50
0
E 50
PW
CW
SDW
PZ
CZ
SDZ
(d)
0
5
10
15
100
50
0
-50
-100
SDZ
SDW
PZ
PW
(e)
FORECAST LEAD TIME (DAYS)
1.0
.8
.6
.4
.2
0
SD
P
Ec
(f)

3

T_2/T_1	1/2	8	16	32
		m zonal		
32	-	-	-	16.0
16	-	-	18.5	15.6
8	-	19.9	18.0	15.3
1/2	5.4 (5.5)	16.7 (17.2)	16.7 (18.1)	14.8 (16.8)
		m wave		
32	-	-	-	33.6
16	-	-	42.9	33.4
8	-	50.3	42.3	33.1
1/2	16.5 (1.65)	43.4 (44.2)	39.8 (40.3)	32.3 (32.3)
		% zonal		
32	-	-	-	2.2
16	-	-	9.9	5.9
8	-	22.5	14.2	9.0
1/2	91.7 (92.5)	45.4 (50.6)	26.3 (30.8)	15.2 (17.8)
		% wave		
32	-	-	-	-2.1
16	-	-	5.1	0.1
8	-	11.2	7.1	1.9
1/2	87.7 (89.0)	34.2 (33.9)	15.9 (15.1)	7.3 (7.2)
		Pattern correlation		
32	-	-	-	0.073 [0.192]
16	-	-	-	
8	-	0.331 [0.308]	-	.158 [.205]
1/2	0.934 (0.919) [0.919][(0.922)]	0.575 [0.540]	-	0.283 [0.270]

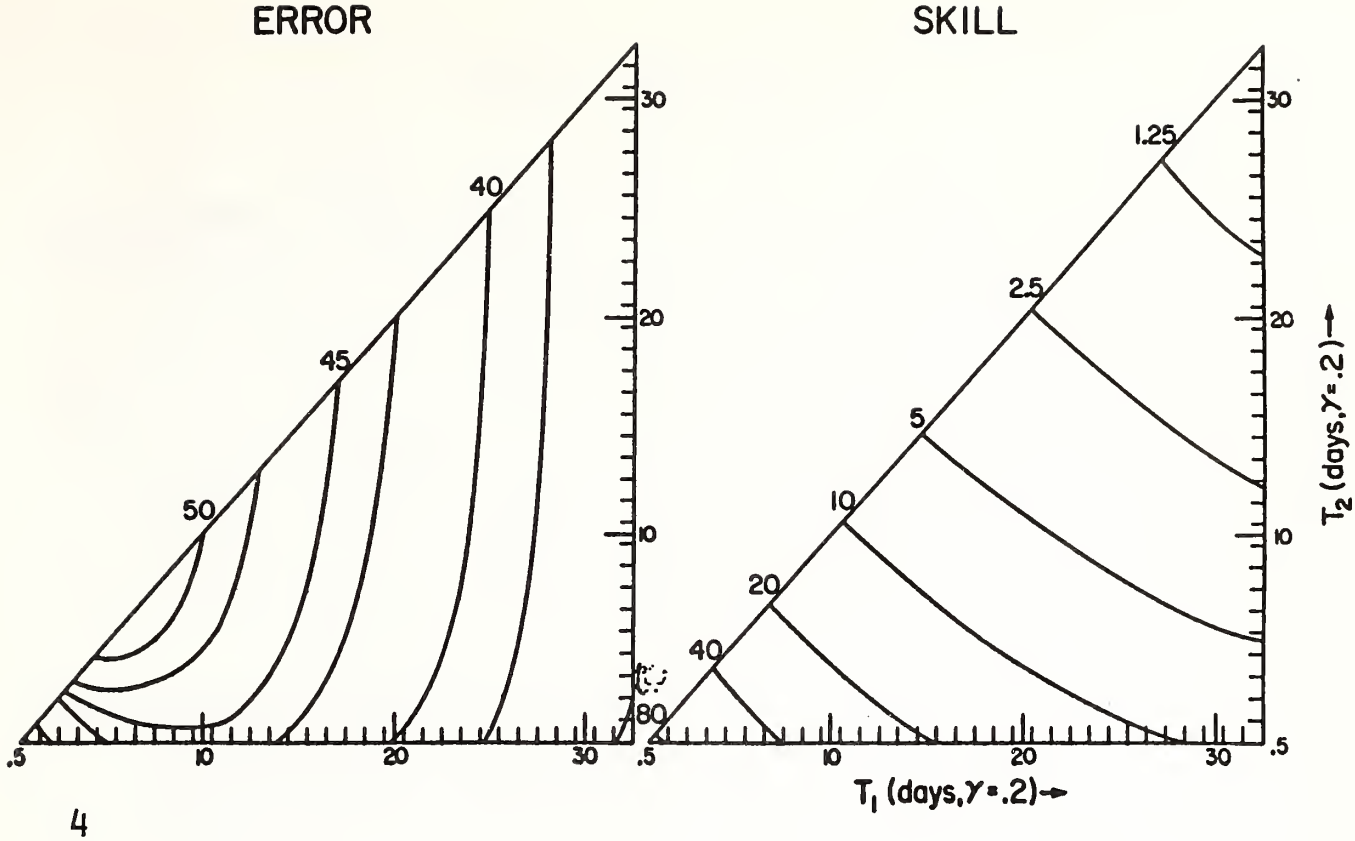
ERROR
SKILL
40
45
50
1.25
2.5
5
10
20
40
30
20
10
.5
10
20
30
T_1 (days, γ=.2)→
T_2 (days, γ=.2)→

4

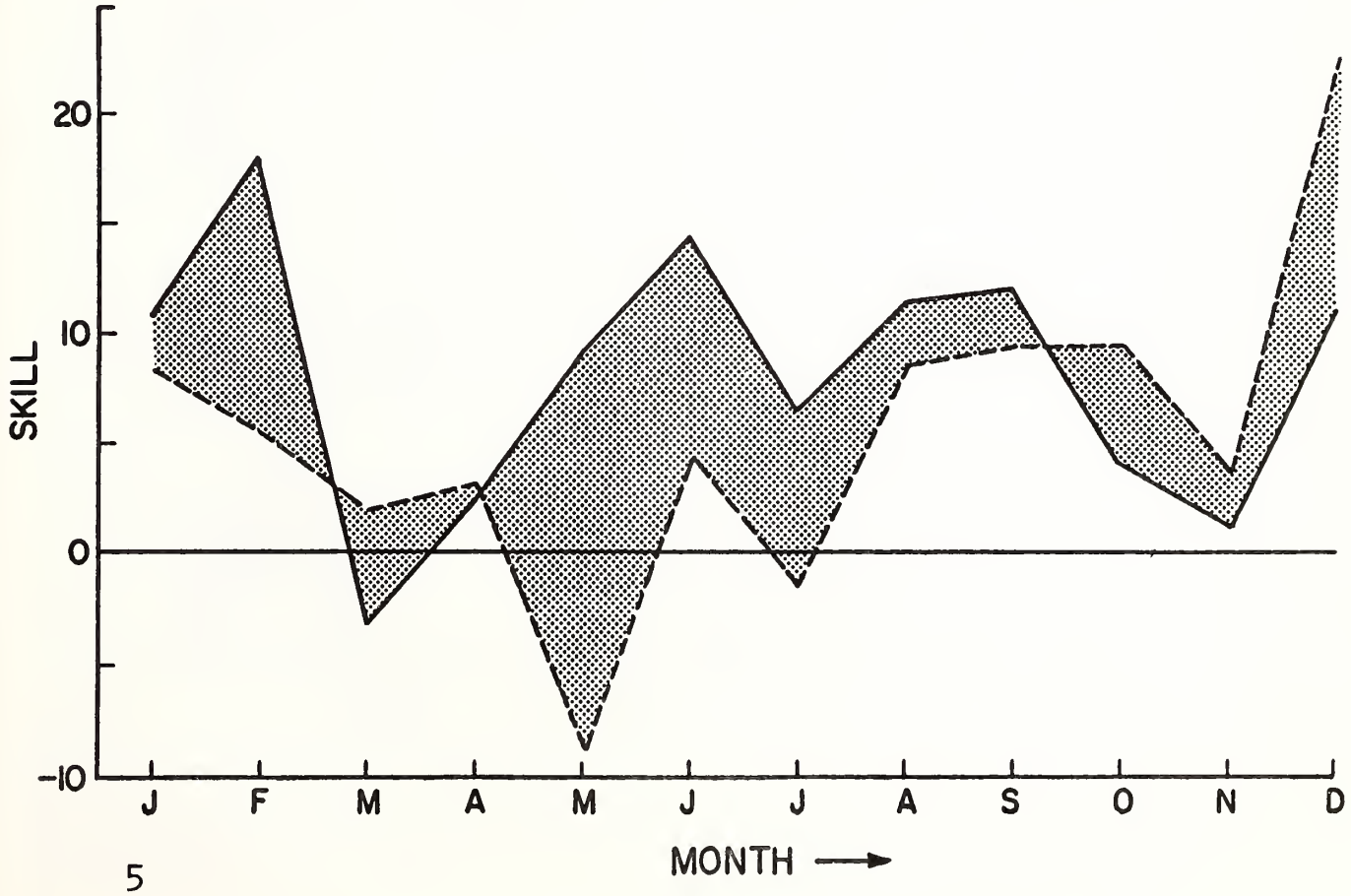
SKILL
20
10
0
-10
J
F
M
A
M
J
J
A
S
O
N
D
MONTH →

5

CLIMATE (32)

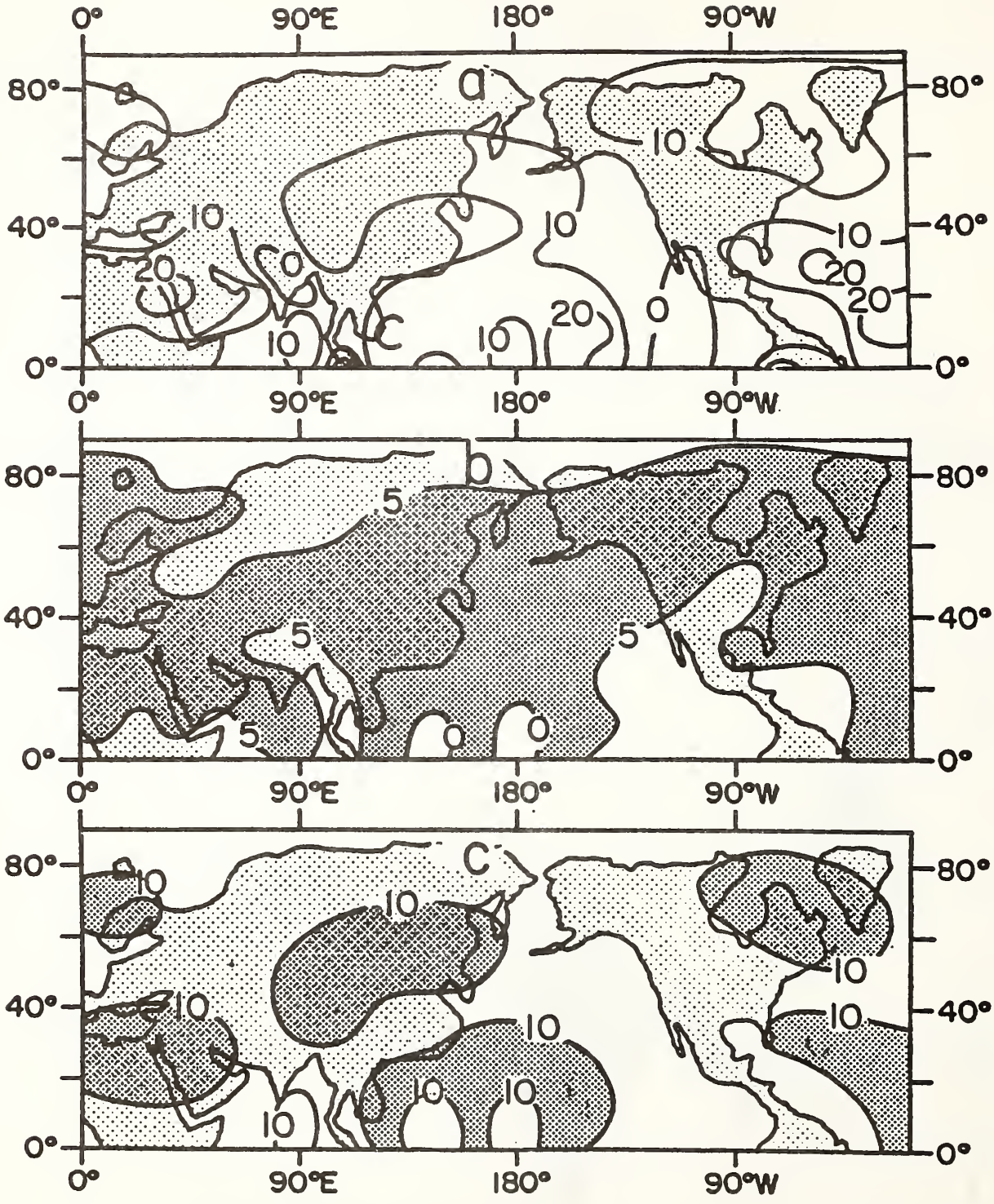
a
0°
90°E
180°
90°W
80°
40°
0°
10
20
0
10
10
10
20
20
20
10
b
5
5
5
0
0
c
10
10
10
10
10
10
10
10

6

Prediction of monthly 700 mb heights using antecedent and simulated prognostic height predictors

Robert Harnack[1], Charles Kluepfel[2], and Robert Livezey[3]

This study has two main parts. The first was the study of persistence relationships by computing pattern correlations between time-averaged Northern Hemisphere 700 mb height fields ending on the 28th of the month and monthly-averaged heights for the following month. The second portion of the study examines hindcast skill for monthly-mean 700 mb heights using antecedent heights, simulated prognostic heights, and a combination of both.

Raw data consisted of daily 700 mb heights in the period 1948-80 for the Northern Hemisphere from 25N to 75N. All analyses used standardized heights. Pattern correlations were computed between height fields consisting of time-averages for the last n days of an antecedent month on the one hand and the height field of the entire following (target) month on the other. n was set equal to each integer 1-10, 15, 20, and 28 in turn for computing correlations. All antecedent time averages were for the period ending on the 28th of the month, which is forecast day for the Climate Analysis Center. Results are presented as average pattern correlations for calendar month pairs (see Figs. 1-4). These show a general tendency for maximum correlations at small n in the spring, and intermediate or large n in other months especially in mid-winter and mid-summer. Table 1 summarizes these results and further indicates that higher maximum correlations are found in summer-early fall and lower values in the spring.

Simple linear regression was employed at each grid point using the local antecedent period height as the predictor and the following monthly mean height as the predictand. Analyses were seasonally-stratified by using three month pooled data and antecedent period lengths were set after examining the pattern correlation results (Table 2). The results are summarized in Table 3. Explained variances are quite modest on an area-averaged basis (ranging from 3.7 to 7.4%). Maps of explained variance for the best and worst seasons are shown in Figs. 5 and 6. The best hindcast skill was generally found in low latitudes.

If target month heights were perfectly known for the first 10 days of the month then pattern correlations between n-day averages at the beginning of the month and entire month average heights would increase with n as shown in Fig. 7. In order to simulate current operational model forecast performance for 700 mb heights, the historical standardized height data for each of the 10 days, beginning on the 28th of the antecedent month, were damped using an exponential function. The damping function is shown in Fig. 8. This function was subjectively determined so that diminishing, but positive skill (relative to climatology)

[1]Current affiliation: Department of Meteorology, Cook College-Rutgers University, PO Box 231, New Brunswick, NJ 08903
[2]Current affiliation: Science Systems and Applications, Inc., 10210 Greenbelt Rd. (Suite 640), Seabrook, MD 20706
[3]Current affiliation: Climate Analysis Center, NMC/NWS/NOAA, Washington, D.C. 20233

out to prog day 10, would be simulated. Pattern correlations, like those of Fig. 8, but using this simulated prognostic data, are illustrated in Fig. 9.

Hindcast skill using simple linear regression stratified by season, with 10-day period local simulated prog heights as predictors, is shown in Table 4. Area-averaged explained variances greatly exceed those for the antecedent predictor model that was shown in Table 3. Example maps of explained variance are shown in Figs. 10 and 11.

Table 5 summarizes all forecast experiments, including additional ones using Empirical Orthogonal Function (EOF) amplitude-time series as predictors. Also shown are the results for bivariate regression, in which the predictors are the local antecedent and local simulated prog height. In some regions, particularly at low latitudes in the warm season, antecedent height information makes a significant contribution to explained variance. An example of this situation is shown in Fig. 12.

Table 6 shows a comparison between National Weather Service operational 700 mb height forecast explained variance for the periods 1958-82 and 1978-82, and the explained variance of the simulated prog method described here. These indicate that if the simulated heights are at least as accurate as current operational numerical weather prediction models, such as the NMC spectral model, then operational 30-day 700 mb height forecasts could be improved significantly by heavily weighting numerical model height forecasts made on forecast day.

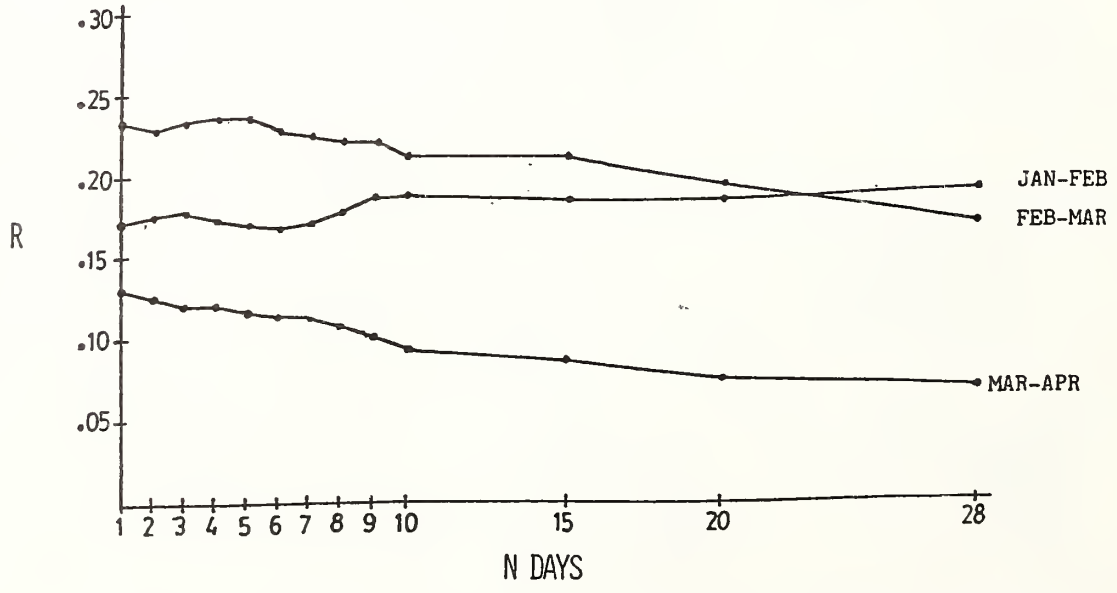

Figure 1 Pattern correlations between the last n days of the antecedent month and the entire target month. Curves are each labeled with antecedent and target month.

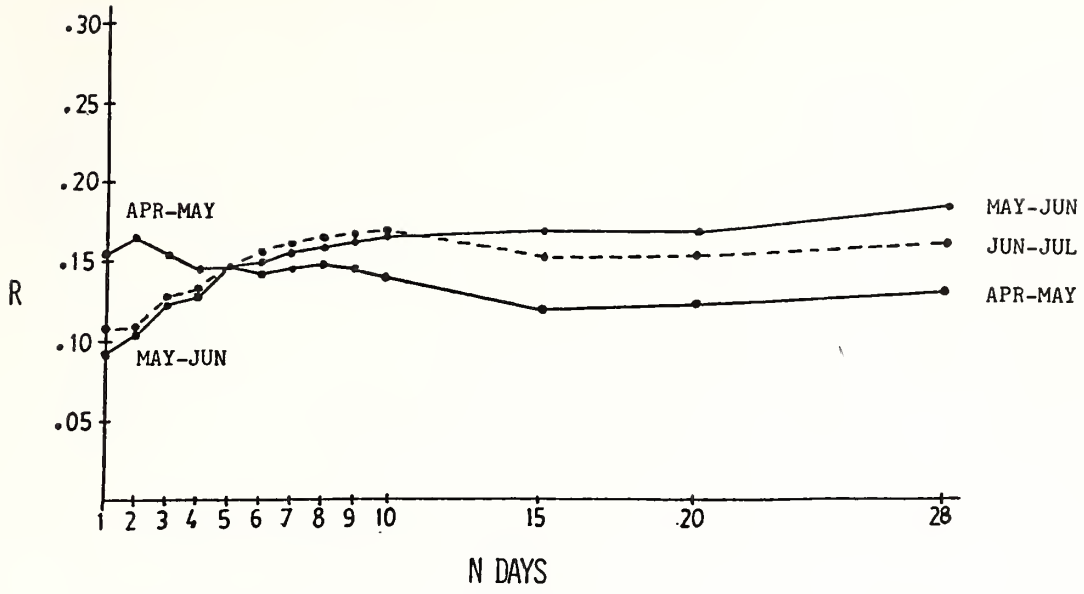

Figure 2 Pattern correlations between the last n days of the antecedent month and the entire target month. Curves are each labeled with antecedent and target month.

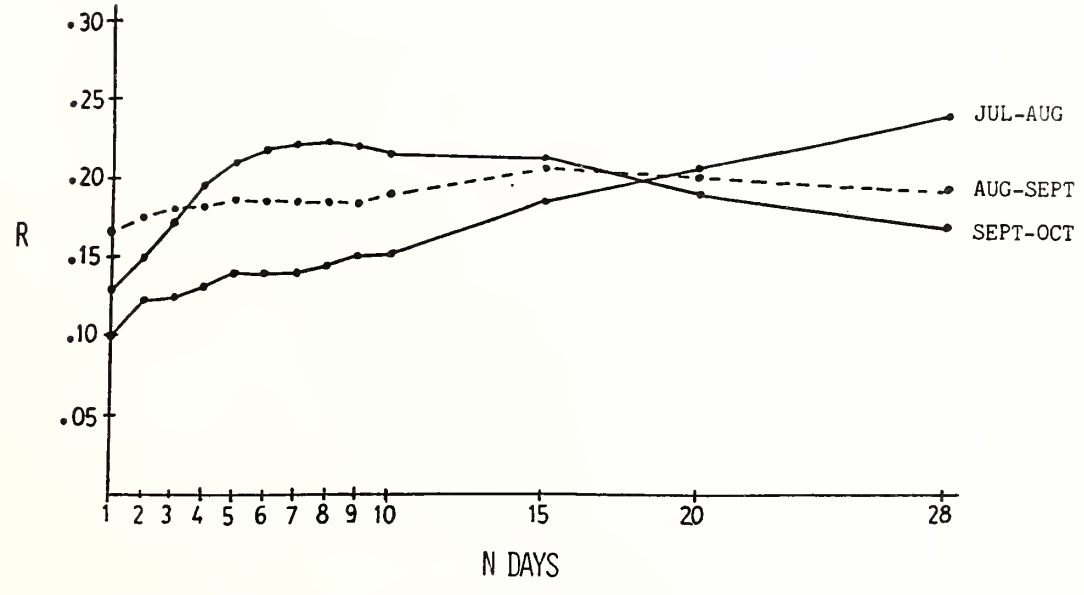

Figure 3 Pattern correlations between the last n days of the antecedent month and the entire target month. Curves are each labeled with antecedent and target month.

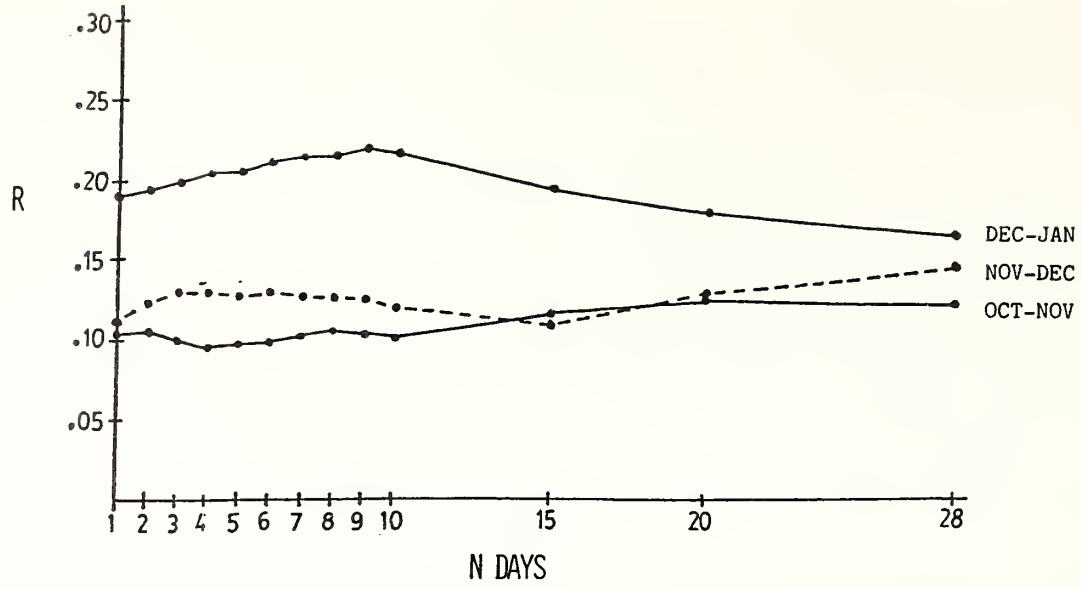

Figure 4 Pattern correlations between the last n days of the antecedent month and the entire target month. Curves are each labeled with antecedent and target month.

Month	n_{max}	r_{max}
DEC - JAN	9	.22
JAN - FEB	28	.19
FEB - MAR	5	.24
MAR - APR	1	.13
APR - MAY	2	.16
MAY - JUNE	28	.18
JUNE - JULY	10	.17
JULY - AUG	28	.24
AUG - SEPT	15	.21
SEPT - OCT	8	.22
OCT - NOV	20	.12
NOV - DEC	28	.14

Table 1. Period length (days) of maximum pattern correlation for 700 mb heights between the last n days of one month and the entire following month, given as n_{max}. The value of the maximum pattern correlation, r_{max} is also given.

Table 2. Period length (days) used to define antecedent predictors by season.

Season	Period Length
Dec - Feb	9
Jan - Mar	10
Feb - Apr	5
Mar - May	4
Apr - June	5
May - July	28
June - Aug	28
July - Sept	28
Aug - Oct	28
Sept - Nov	8
Oct - Dec	20
Nov - Jan	28

Table 3. Percentage of map area having local significance (% A_s) and range of grid point explained variance (R^2) achieved for each season. Also shown is area-averaged R^2.

MODEL TYPE: LOCAL ANTECEDENT HT. (UNIVARIATE)

POOL SIZE: 1

MODEL SIZE: 1

SEASON	% A_s	RANGE OF R^2	$\overline{R^2}$
DEC - FEB	28.4	0.0 - 16.9	4.8
JAN - MAR	37.8	0.0 - 19.3	5.7
FEB - APR	29.7	0.0 - 22.4	4.7
MAR - MAY	28.3	0.0 - 17.9	4.5
APR - JUNE	23.6	0.0 - 25.7	4.0
MAY - JULY	22.4	0.0 - 40.7	5.0
JUNE - AUG	28.4	0.0 - 46.8	6.1
JULY - SEPT	26.8	0.0 - 55.9	7.2
AUG - OCT	34.5	0.0 - 51.8	7.4
SEPT - NOV	20.6	0.0 - 37.5	4.9
OCT - DEC	20.3	0.0 - 29.5	4.1
NOV - JAN	21.4	0.0 - 21.7	3.7
AVERAGES	26.8	0.0 - 55.9	5.2

Fig. 5.

Map of explained variance (%) for simple regression, where the predictand is the monthly - mean 700 mb height and the predictor is the local mean height for the 28 day period ending on the 28th of the antecedent month. Predictand months August - October have been pooled to create the sample. Shading denotes local significance at the 95% confidence level.

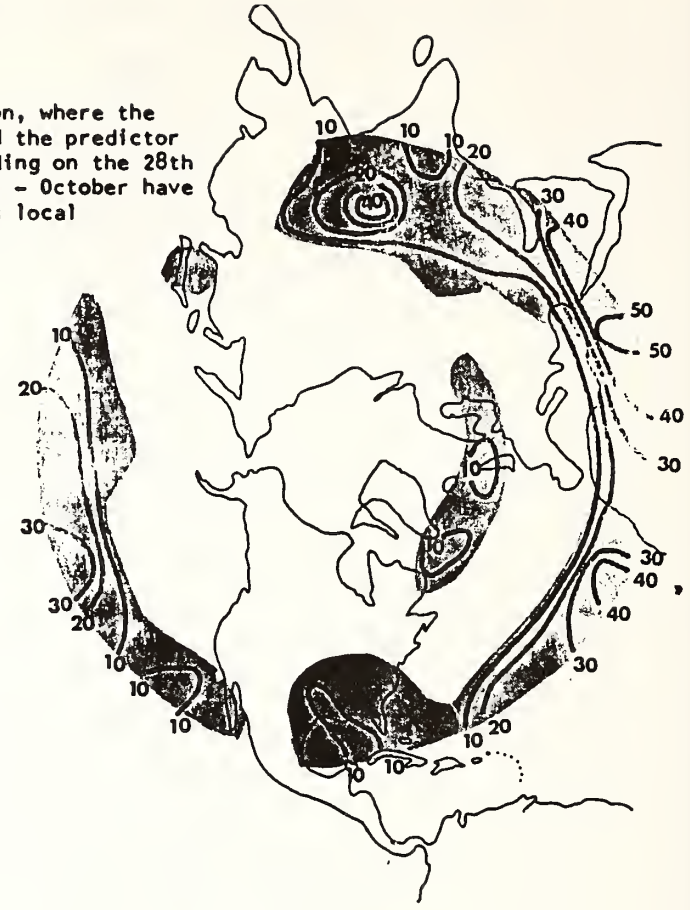

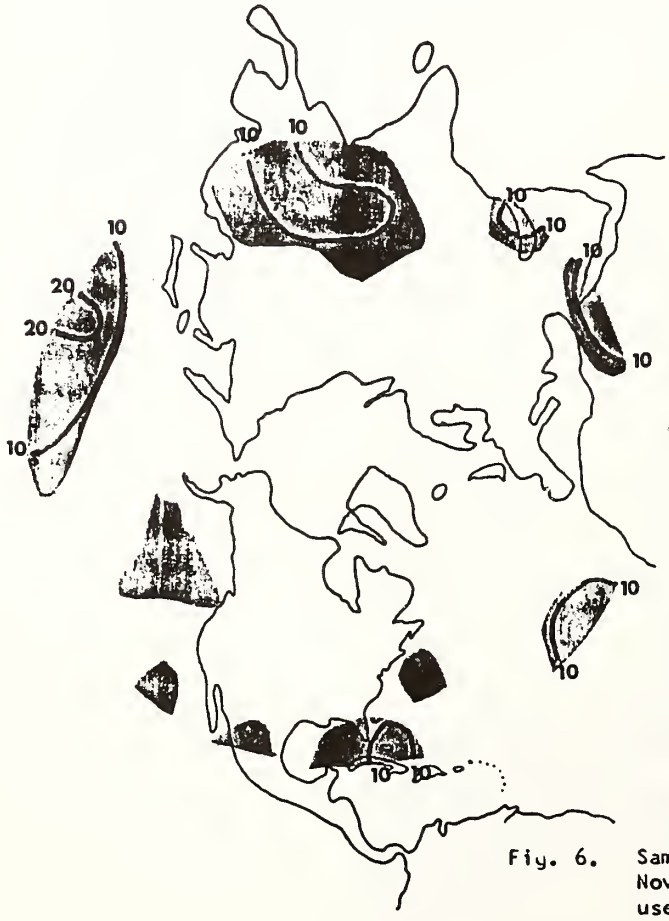

Fig. 6. Same as Figure 5 except the predictand months are November - January. The antecedent period length used to define predictors is 28 days.

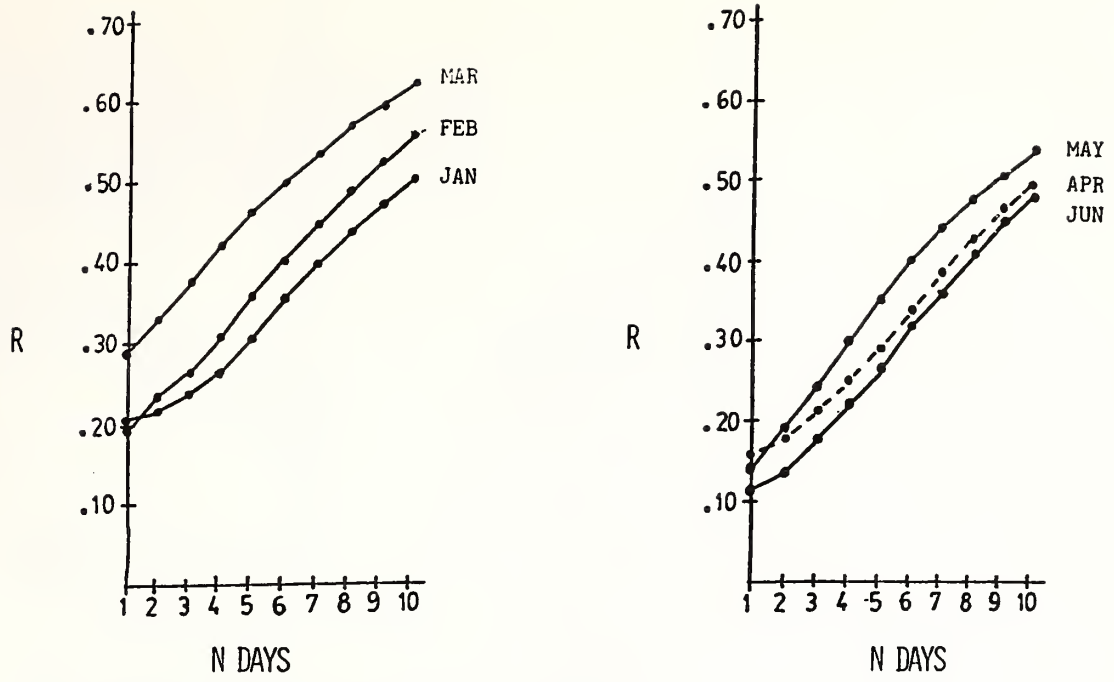

Figure 7. Pattern correlations are shown between the first n days of the target month and the entire target month. Each curve is labeled with the target month.

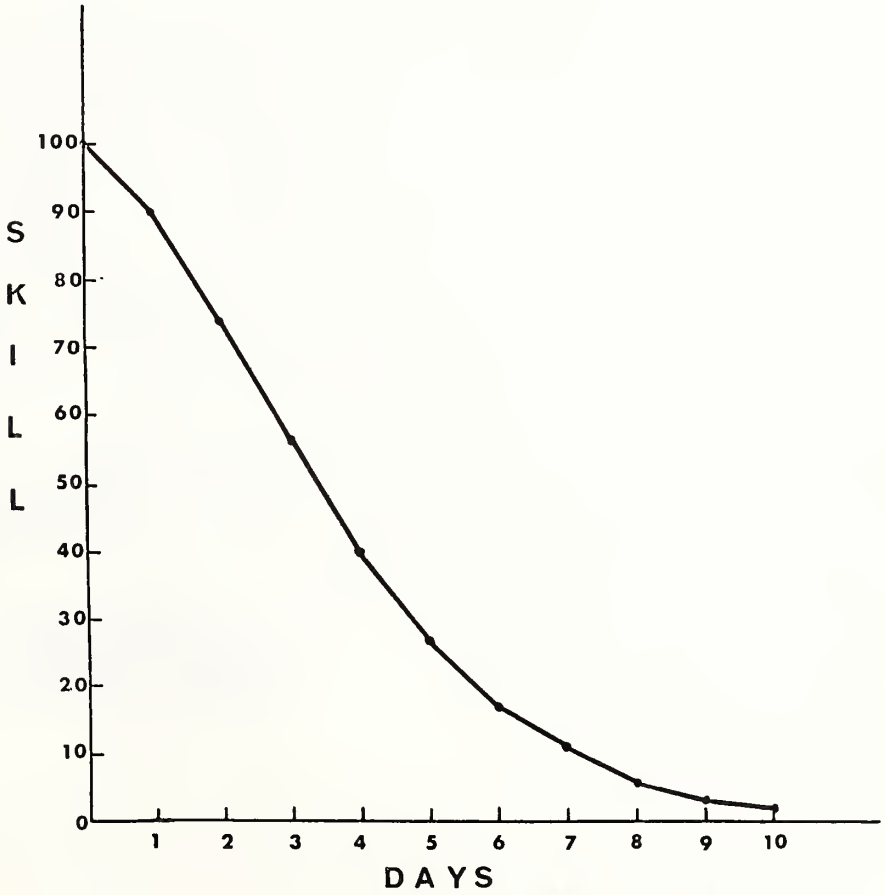

Fig. 8. Plot of the skill (% accuracy) versus time (days) of the simulated 700 mb height anomaly forecast at each grid point using the damping function exp ($-.1t^{1.6}$).

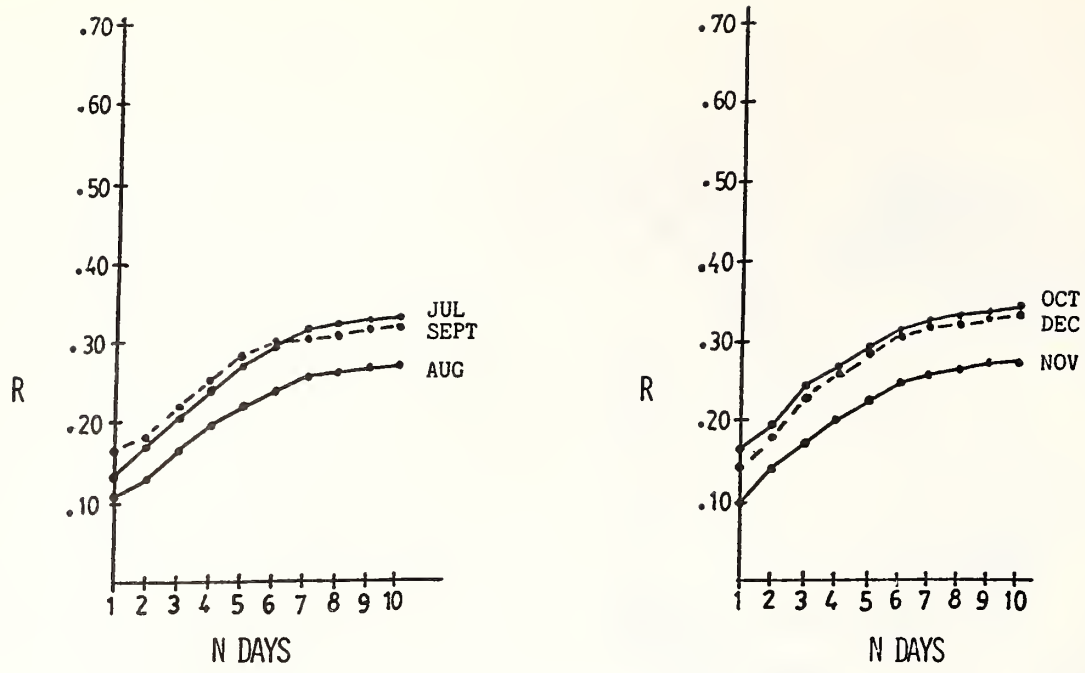

Figure 9. Pattern correlations of standardized 700-mb heights between the first n days of the target month and the entire target month are depicted. The daily heights for the first n days of the target month are multiplied by the exponential damper. Months are labeled on the graphs.

MODEL TYPE: LOCAL SIMULATED HT. (UNIVARIATE)

POOL SIZE: 1

MODEL SIZE: 1

SEASON	% A_s	RANGE OF R^2	$\overline{R^2}$
DEC - FEB	84.1	0.7 - 37.2	13.6
JAN - MAR	91.7	1.5 - 39.1	16.8
FEB - APR	89.7	2.9 - 39.3	16.0
MAR - MAY	89.4	2.3 - 33.0	16.0
APR - JUNE	74.7	0.7 - 37.9	11.5
MAY - JULY	78.3	0.7 - 41.1	13.8
JUNE - AUG	71.1	0.1 - 54.2	12.0
JULY - SEPT	74.1	0.4 - 56.2	12.7
AUG - OCT	73.7	0.6 - 61.8	13.0
SEPT - NOV	76.6	1.0 - 46.0	12.1
OCT - DEC	73.9	0.7 - 39.5	11.9
NOV - JAN	80.1	0.7 - 36.2	11.5
AVERAGES	79.8	0.1 - 61.8	13.4

Table 4. Percentage of map area having local significance (% A_s) and range of grid point explained variance (R^2) achieved for each season. Also shown is area-averaged R^2.

Fig. 10.

Map of explained variance (%) for simple regression, where the predictand is the monthly - mean 700 mb height and the predictor is the local simulated prog. height for the ten day period beginning on the 29th of the antecedent month. Predictand months January - March have been pooled to create the sample. Shading denotes local significance at 95% confidence level.

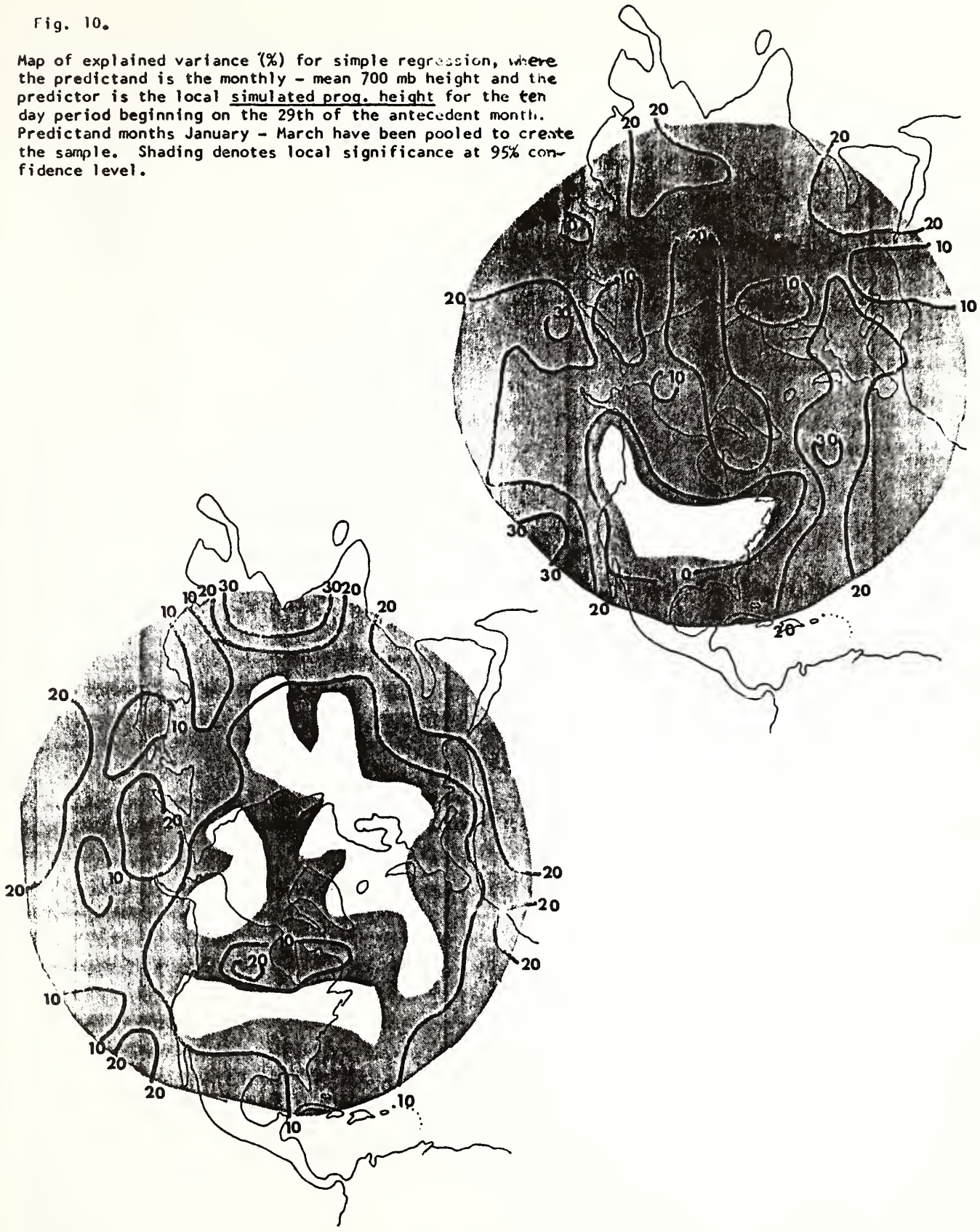

Fig. 11. Same as Figure 10 except pooled sample is for April - June.

MODEL TYPE	POOL SIZE	$\overline{\%\ A_s}$	RANGE OF R_2
LOCAL ANTECEDENT	1	26.8	0.0 - 55.9
NON-ROT.EOF, ANTECEDENT*	12-15	8.1	13.4 (1) - 51.4 (6)
ROT.EOF, ANTECEDENT*	4-7	12.5	11.2 (1) - 48.0 (2)
NON-ROT.EOF, SIMUL. PROG.*	13-18	17.7	13.3 (1) - 57.5 (8)
ROT.EOF, SIMUL. PROG.*	4-8	23.6	10.9 (1) - 49.5 (4)
LOCAL SIMUL. PROG.	1	79.8	0.1 - 61.8
LOCAL ANTECEDENT & SIMUL. PROG.	2	67.8	0.6 - 63.6

*Denotes screening regression.

Table 5. Summary of regression trials relating monthly-mean 700 mb heights (predictands) to antecedent or simulated prog heights (predictors). Results are for all months and grid points combined. The average percentage of map area with local significance ($\overline{\%\ A_s}$) and the range of explained variance (R^2) achieved are shown. Model size is in parentheses.

Fig. 12. Additional explained variance (%) achieved when antecedent height predictor is added to simulated prog predictor for July – Sept. month grouping.

Season	NWS All Years	NWS 1978-82	Simul. prog.
Dec - Feb	4.4	11.1	12.4
Jan - Mar	5.8	9.0	16.6
Feb - Apr	5.9	5.7	16.6
Mar - May	5.3	6.7	17.4
Apr - June	3.0	5.5	10.8
May - July	1.8	3.1	11.5
June - Aug	1.6	1.8	10.4
July - Sept	2.6	1.6	12.8
Aug - Oct	3.7	1.8	12.0
Sept - Nov	4.2	-1.6	10.4
Oct - Dec	4.1	4.9	9.4
Nov - Jan	4.1	9.5	9.9
Average	3.8	4.9	12.5

Table 6. Area-averaged explained variance (%) for monthly 700 mb height forecasts made by the National Weather Service (NWS) in the period 1958-82 (All Years) and in the period 1978-82, and by the simulated prog method.

Specification of Mean Surface Temperature Anomalies in Europe and Asia During the Fall Months

William H. Klein and Runhua Yang
Department of Meteorology
University of Maryland
College Park, MD 20742

This paper extends research for the United States and Canada reported previously (see Proceedings of 6th, 7th and 8th Annual Climate Diagnostics Workshops) to a network of 68 surface stations in the European sector and 47 in Asia (Fig. 1). Monthly mean air temperataure anomalies near the surface (MMATA) at each of these 115 stations have been screened as a function of the concurrent monthly mean 700 mb height anomalies (MMHA) at 134 grid points (Fig. 2), plus the previous month's local MMATA, for the 30-year period: Jan. 1951 - Dec. 1980. Here we present results for only the 90 fall months of Sept., Oct. and Nov.

Fig. 3a shows the correlation field for simultaneous values of MMATA at Madrid, Spain and MMHA at the 134 grid points. As in most of North America, the dominant feature is the large positive center near the reference station, showing that the lower troposphere tends to be equivalent barotropic. The maximum correlation (+.81) is the largest found for any city in Eurasia. The maximum negative correlation at any of the 115 stations was obtained for Irkutsk, Siberia (Fig. 3b). Here the center of -.74 about 2900 km northwest of the station exceeds the local positive correlation (+.55) in absolute value. A similar situation prevails in most of central North America, southern Asia and central Europe. The latter two regions are delineated by the shaded area in Fig. 4 which shows where the highest simple correlation coefficient for each of the 115 stations is negative. Over most of the map, however, the highest correlation (for the first variable selected by screening) is positive, with values ranging from over .8 in Spain to less than .3 near the Kamchatka peninsula.

The preceeding material indicates how well we could specify the MMATA from just one variable. Some results of examining the entire height field by stepwise multiple regression are illustrated in Table 1 for Madrid. Here the first variable selected, the MMHA near the .81 center in Fig. 3a, explains 65% of the variance of the MMATA. The next three variables indicate whether the anomalous flow is from a northerly or southerly direction, while the fifth is probably a remote teleconnection. The selection process was stopped at this point, with over 78% of the variance explained (RV) and a standard error of estimate of 0.7°C., because no other variable could add as much as 2% to the RV. Another type of specification equation is illustrated in Table 2 for Helsinki, Finland. Here simple persistence of the local MMATA adds 18% to the temperature variance explained by the first height selected (located near Helsinki), more than the amount added by any other MMHA. The selection process was

stopped after including two more heights (in the eastern Atlantic) because addition of the fifth variable would reduce the F-test probability level below 99%.

The reduction of variance (RV) in the final specification equations is shown in Fig. 5. Values range from over 75% in portions of the Atlantic coast and northern Siberia to less than 30% in extreme northeast Siberia and central China. Fig. 6 maps the standard error of estimate given by the specification equations. Values vary from less than 0.6°C along Atlantic, Mediterrean and Pacific coasts to more than 2°C in northern Siberia. As expected, the pattern resembles that for the standard deviation of MMATA (Fig. 7), but with values reduced by an amount proportional to the RV (Fig. 5).

Fig. 8 maps the one-month lag autocorrelation of MMATA. It shows that temperatures are persistent in most regions, except for a few areas (shaded) of zero or negative correlation in portions of the USSR, China, France and Iceland. Values are generally higher over maritime than inland regions, with maximum correlations (over .4) near the Baltic Sea, eastern Mediterrean, Barents Sea, and Sea of Japan. Fig. 9 is similar to Fig. 8 but for the percent of temperature variance added by the previous MMATA upon first entering the specification equation. This statistic reflects the persistence of local temperature after the effect of the 700 mb circulation has been removed. Values vary from over 15% in the eastern Mediterrean and southern Scandinavia to zero in large portions of the interior, where previous temperature was not chosen. As before, surface temperatures tend to persist more in coastal than inland regions.

On an overall basis, these results for Eurasia are similar to those obtained previously for North America during the fall months. One striking difference, however, is the relatively low value of RV in Asia, only 56% averaged over all stations east of 55°E, compared to mean values of 65% in the European sector, 68% for Canada and Alaska, and 67% for the continuous United States. These differences may be caused by greater frequency of boundary layer phenomena under anticyclonic circulation in Asia or by poorer quality of the basic data there.

Acknowledgment

This research was supported by the Climate Analysis Center, NOAA/Commerce Grant No. NA 83AA-D-00048A1.

Legends to Figures

1. Location and first 3 (or 4) letters of name of 115 surface stations for which monthly mean temperatures were available during 30-year period: 1951-80. The dashed line at 55°E separates European sector from Asia.

2. Network of 134 grid points used to delineate the field of 700 mb heights.

3. Field of simple linear correlation coefficients between concurrent monthly mean anomalies of surface temperature at a) Madrid, Spain and b) Irkutsk, Siberia (located by stars) and 700 mb height at grid points of Fig. 2 during 90 fall months from Sept. 1951 to Nov. 1980. The isopeths are drawn at intervals of 0.10, with zero lines dashed and central values interpolated.

4. The highest single correlation coefficient between monthly mean surface temperature anomaly at each of 115 stations and concurrent monthly mean anomalies of 700 mb height at 134 grid points of Fig. 2. The dashed line separates areas of positive and negative (shaded) correlations.

5. Percent of variance of monthly mean temperature anomaly explained by the specification equation for 90 fall months. High and low centers are marked H and L, respectively.

6. Standard error of estimate (°C) for monthly mean temperature anomaly specified by the regression equations for 90 fall months. High and low centers are marked H and L, respectively.

7. Standard deviation of observed monthly mean temperature anomaly (°C) for 90 fall months, with high and low centers marked H and L, respectively.

8. One-month lag autocorrelation coefficient of monthly mean surface temperature anomaly for 90 fall months. Centers of high and low correlation are labeled H and L, respectively, with negative values shaded.

9. Percent of variance of monthly mean surface temperature anomaly explained by previous month's temperature anomaly when first selected in specification equations for 90 fall months. Shading delineates areas where previous temperature was not chosen.

Table 1. Summary of the stepwise regression statistics obtained for Madrid, Spain (40°N, 4°W) during fall months. The final equation selected for use in specification is starred.

Step No.	Predictor selected	Reg. Coeff. upon entry	Probability (F-test)	Added RV(%)	Cumulative RV(%)	Standard error(°C)
0	0	0	0	0	0	1.48
1	40N,0	+.039	100.0	64.9	64.9	0.88
2	50N,20W	-.006	100.0	5.0	69.9	0.81
3	30N,20W	-.014	99.7	2.9	72.8	0.77
4	40N,10E	-.020	99.9	3.7	76.5	0.72
5*	40N,70E	-.020	99.4	2.1	78.5	0.69
6	30N,30W	+.017	99.5	1.9	80.5	0.66
7	70N,150W	-.007	99.4	1.8	82.2	0.63
8	Prev. temp.	+.112	98.2	1.2	83.4	0.60

Table 2. Summary of the stepwise regression statistics obtained for Helsinki, Finland (60°N, 25°E) during fall months. The final equation selected for use in specification is starred.

Step No.	Predictor selected	Reg. Coeff. upon entry	Probability (F-test)	Added RV(%)	Cumulative RV(%)	Standard error(°C)
0	0	0	0	0	0	1.83
1	50N,30E	+.037	100.0	42.7	42.7	1.38
2	Prev. temp.	+.479	100.0	17.8	60.6	1.15
3	40N,20W	+.014	100.0	6.1	66.6	1.06
4*	60N,0	-.007	99.4	2.9	69.5	1.01
5	30N,40E	-.022	98.6	2.1	71.6	0.97
6	50N,120E	-.013	99.3	2.4	74.0	0.93
7	20N,30E	+.021	99.2	2.2	76.2	0.89
8	50N,140E	+.010	95.5	1.2	77.3	0.87

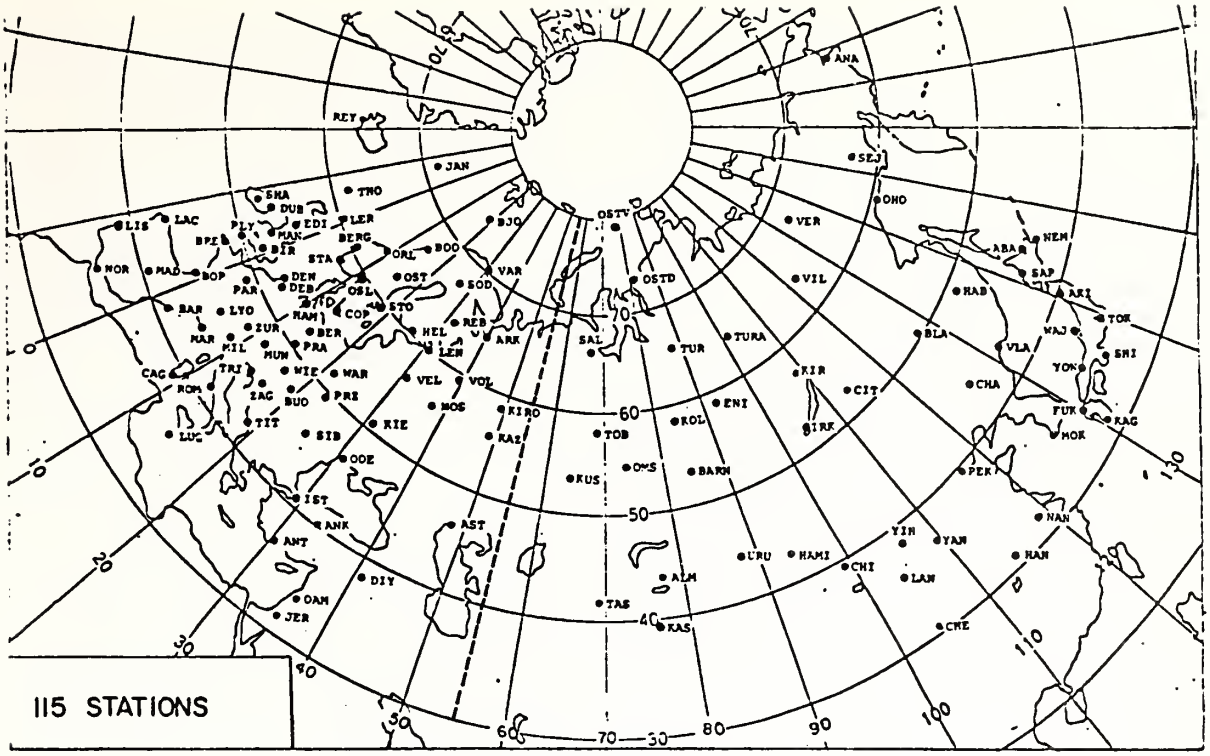

Fig. 1

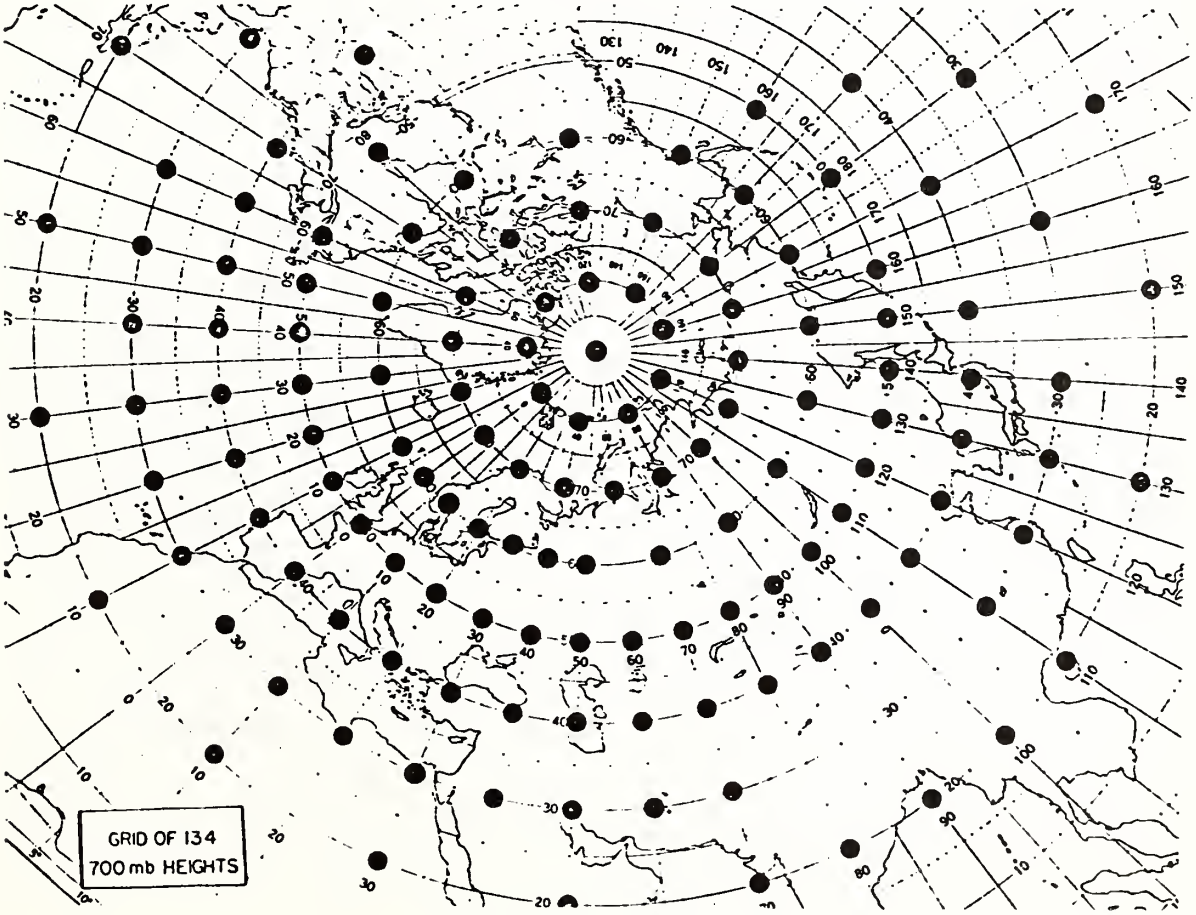

Fig. 2

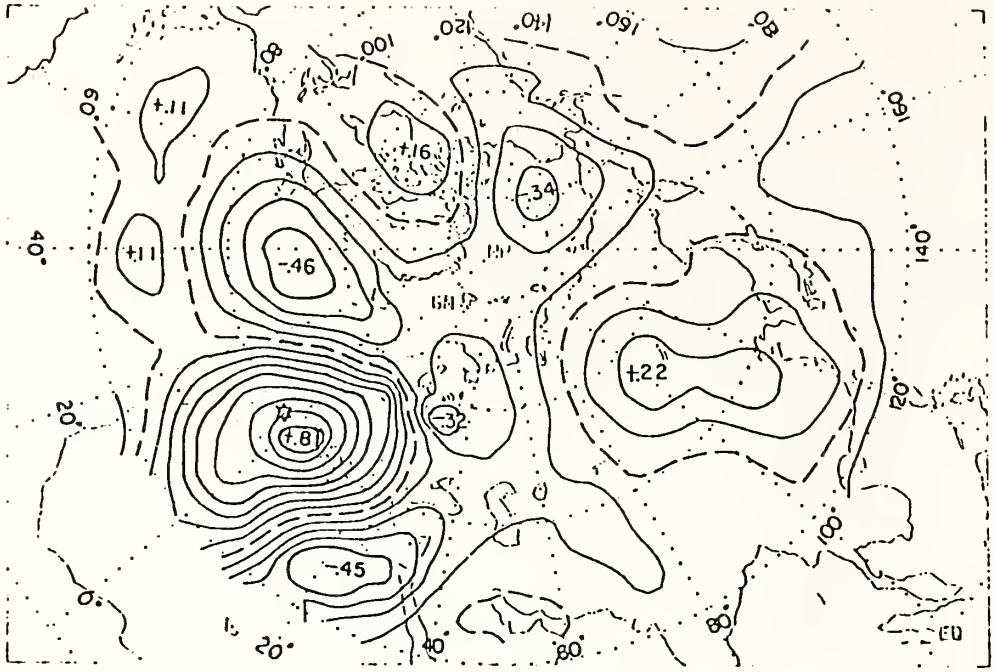

MADRID CORRELATIONS

SFC. TEMP. VS 700-MB. HT.

FALL MONTHS 1951 - 1980

Fig. 3a

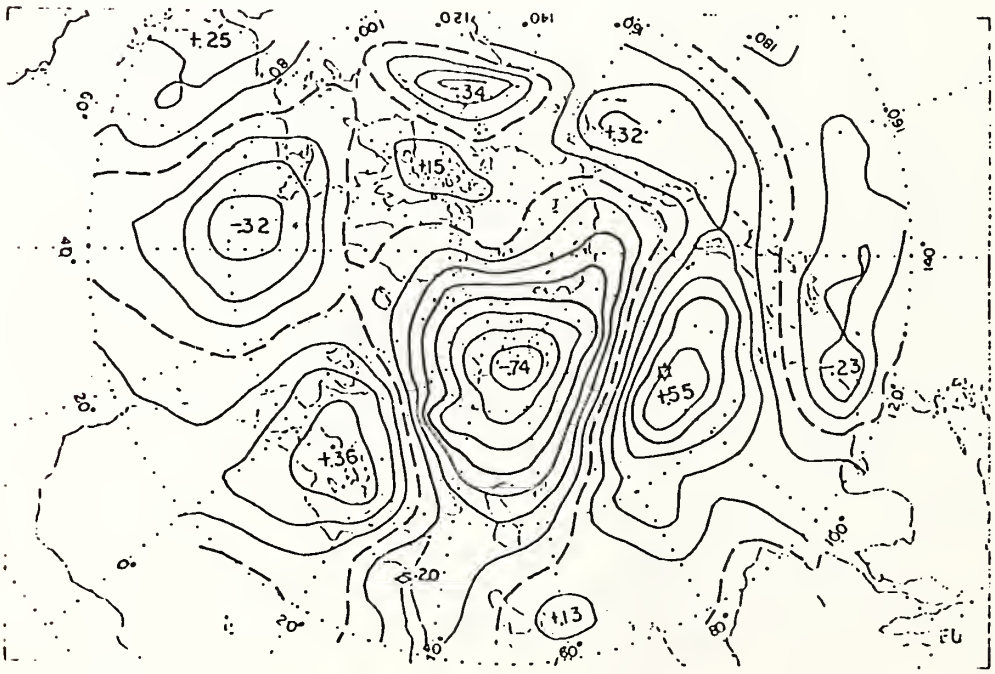

IRKUTSK CORRELATIONS

SFC. TEMP. VS 700-MB. HT.

FALL MONTHS 1951 - 1980

Fig. 3b

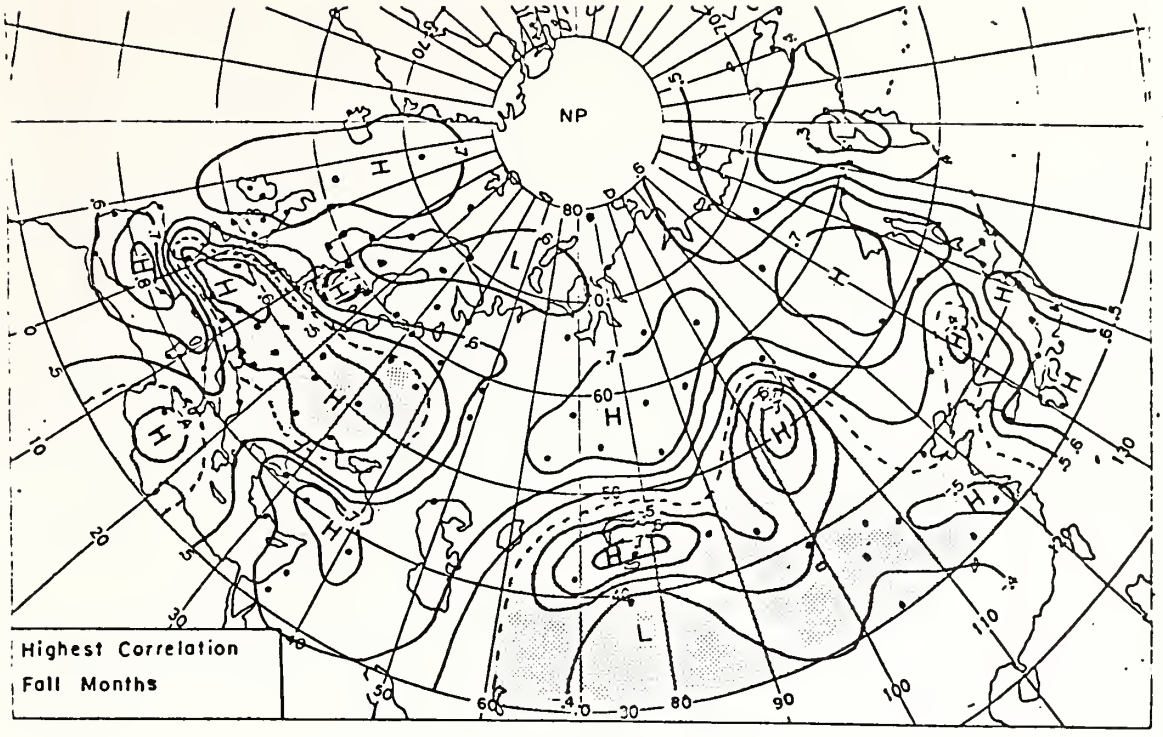
NP
Highest Correlation
Fall Months

Fig. 4

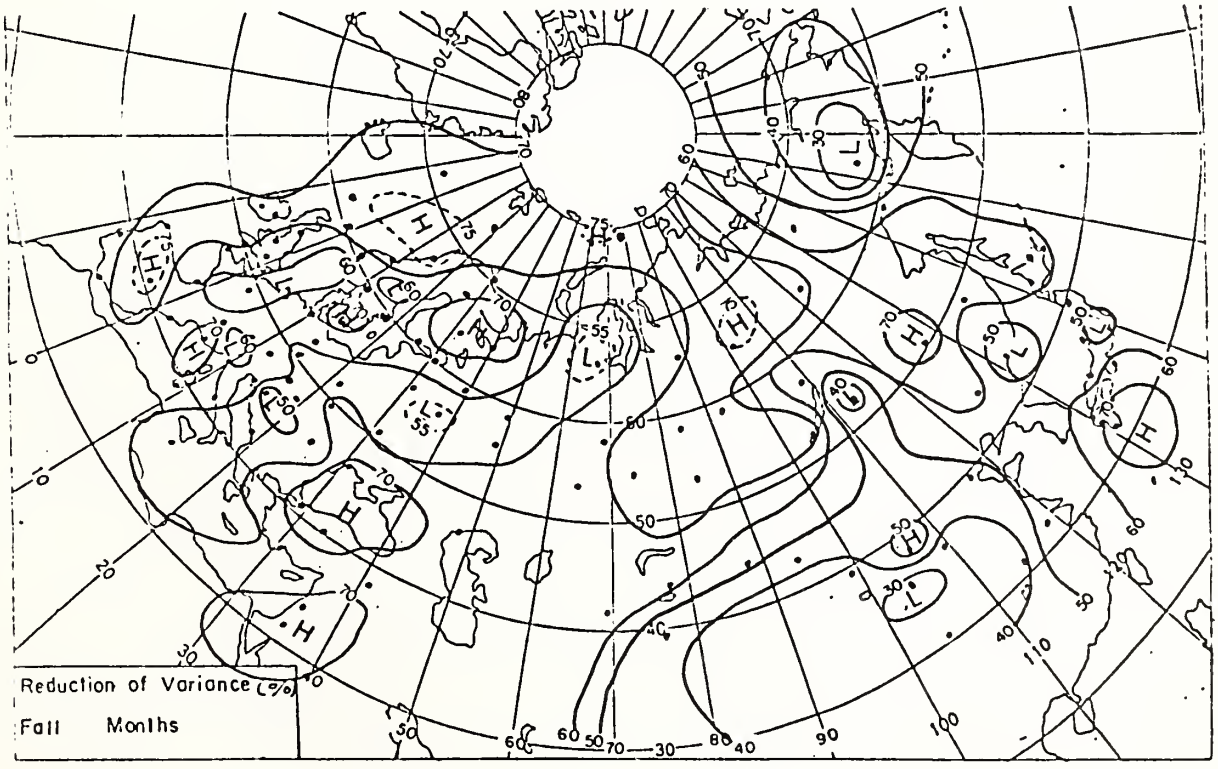
Reduction of Variance (%)
Fall Months

Fig. 5

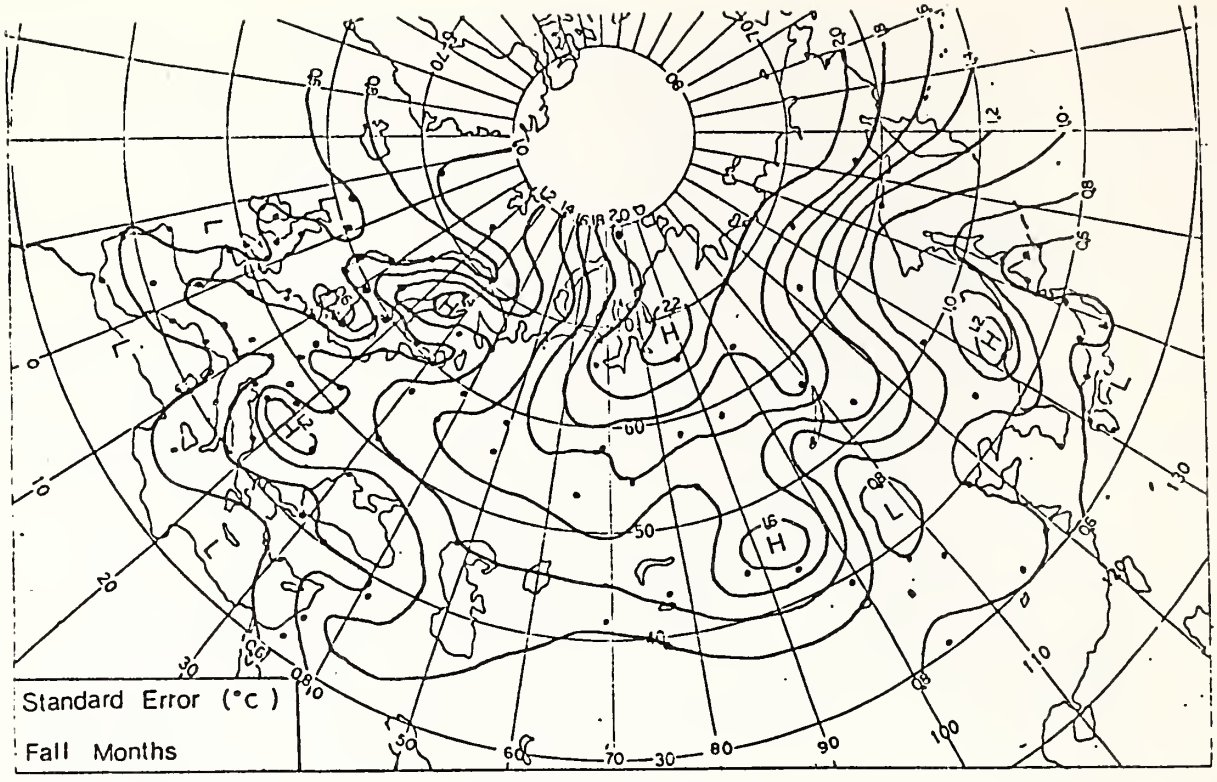
Standard Error (°c)
Fall Months

Fig. 6

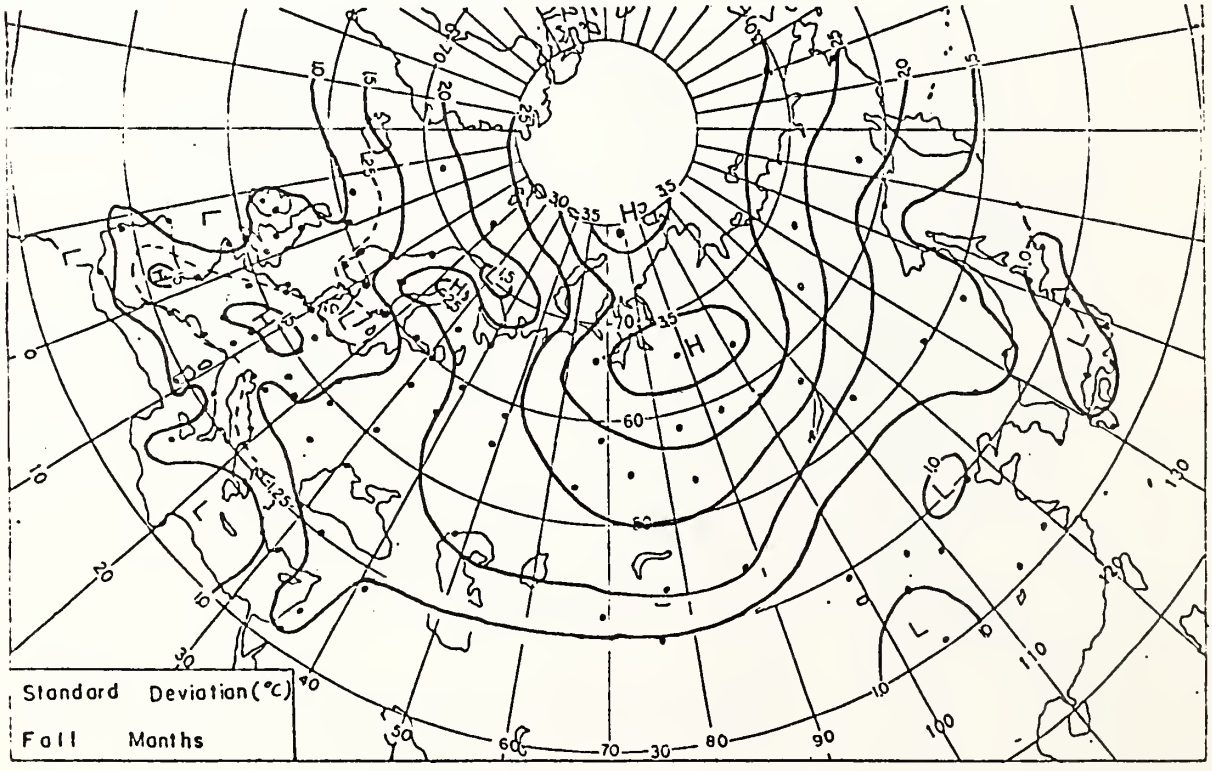
Standard Deviation (°C)
Fall Months

Fig. 7

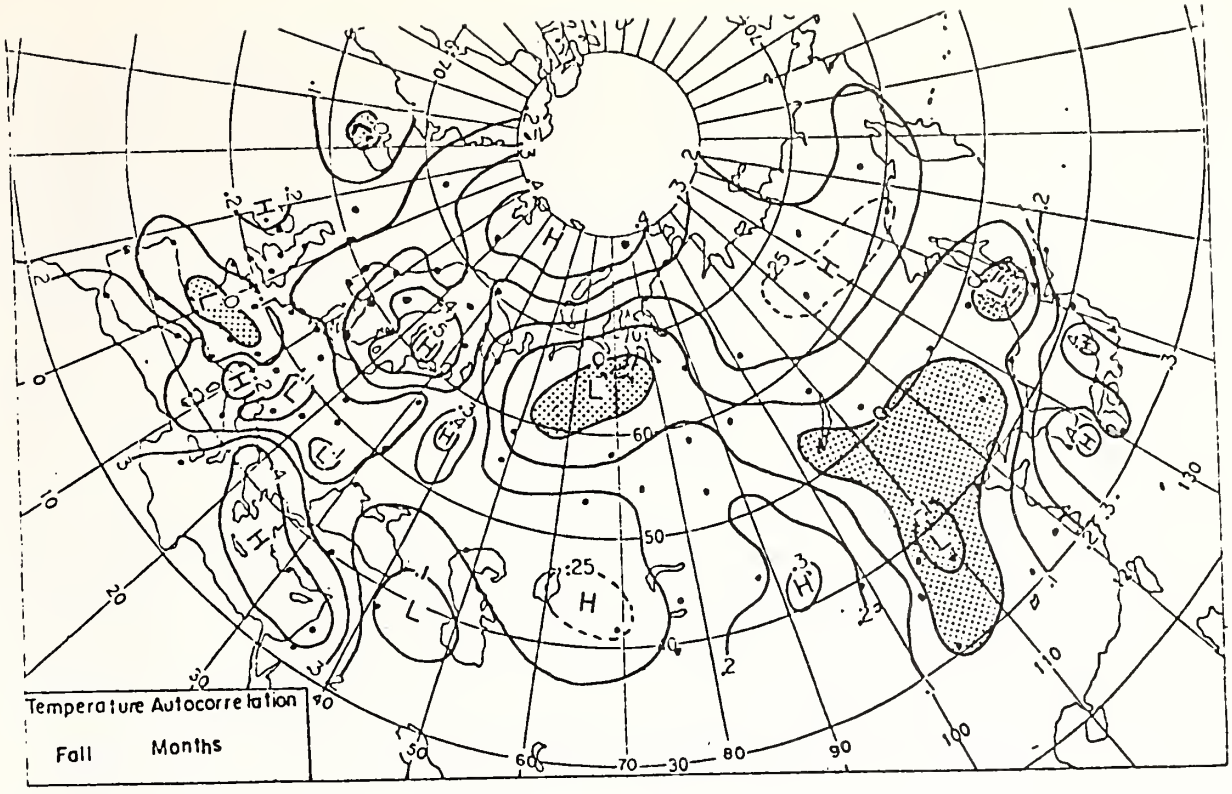
Temperature Autocorrelation
Fall Months

Fig. 8

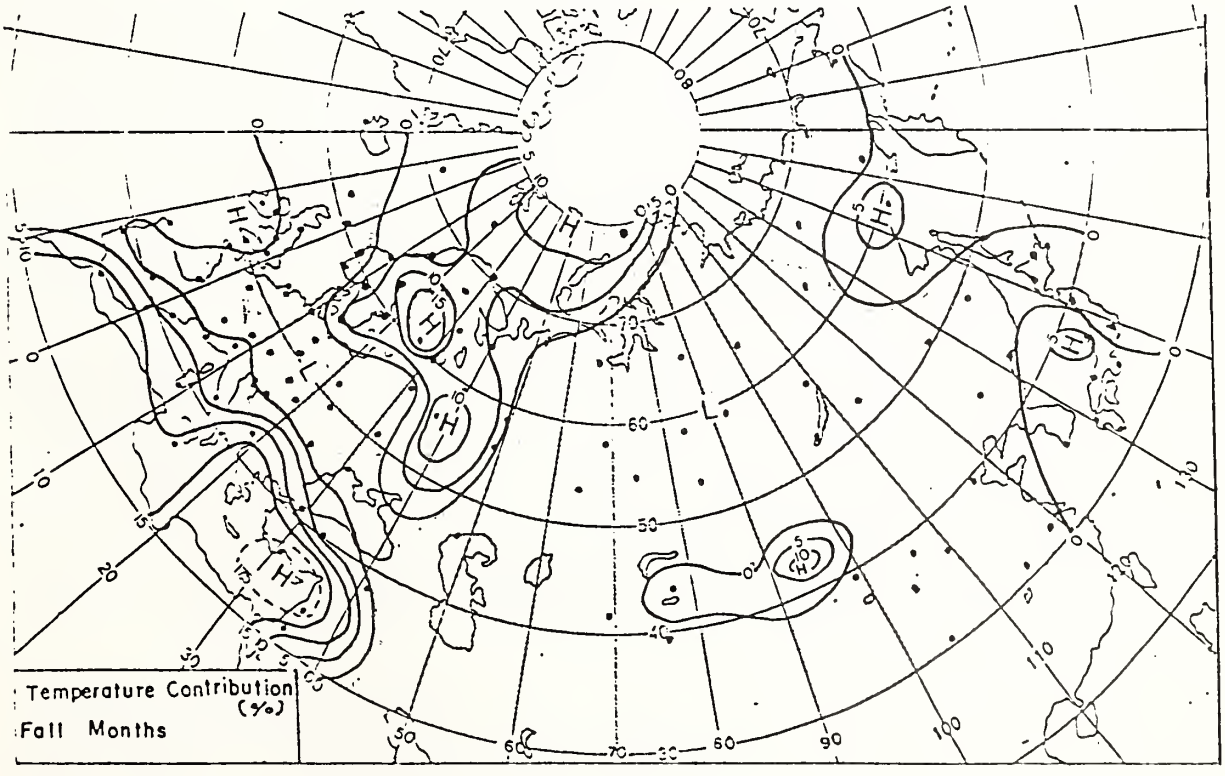
Temperature Contribution (%)
Fall Months

Fig. 9

LAND-SURFACE FLUCTUATIONS AND ASSOCIATED CLIMATIC VARIABILITY

John E. Walsh

University of Illinois
Urbana, IL 61801

and

William H. Jasperson

Control Data Corporation
Minneapolis, MN 55440

Land surface effects were examined by constructing specification equations for the monthly surface station temperatures over the United States and Eurasia. These equations were obtained by forward stepwise screening of monthly grids of 700 mb height. Each equation was truncated according to a 1% F-test criterion. The 700 mb grids contain 91 points in the domains bounded by 20°N, 80°N, and either 50°W and 180°W (U.S.) or 0°E and 150°E (Eurasia). The 700 mb grids for 34 years (1947-1980, inclusive) were used in the analysis. Monthly air temperatures for the same 34 years were obtained for 61 stations in the U.S. and 231 stations in Eurasia. Missing Eurasian temperatures were obtained from the temperature anomalies at nearby stations.

The snow data consisted of monthly snow cover (2.5 cm and 15.0 cm) at eleven longitudes in the U.S. (120°W, 115°W, ..., 70°W). The data were digitized from the Weekly Weather and Crop Bulletin. A monthly soil moisture index for each station was computed from the monthly temperatures and precipitation amounts using the Thornthwaite/Nappo parameterization scheme as modified by Fennessy and Sud (1983, NASA Tech. Memo. 85042). The computational scheme for soil moisture utilizes a temporally invariant field capacity of 15 cm at each station, and computes evapotranspiration and runoff with a daily timestep through the 34 years. The daily temperatures and precipitation amounts are assumed to be constant within each month.

The local impacts of snow cover and soil moisture were examined in terms of the errors in the 700 mb-derived specifications of monthly air temperatures. Briefly, the months were stratified according to the tercile of the local anomaly of snow cover or soil moisture. The errors of the specifications were then composited for the cases of above- or below-normal snow cover or soil moisture. The differences between the mean errors for the cases with positive and negative surface anomalies were tested for statistical significance with a t-test after allowance was made for the number of effectively independent cases in each subset of the sample.

Fig. 1a shows the fractions of the U.S. station temperature variance described by the height-derived specifications for January, February and March. Fig. 1b shows the differences between the algebraic mean errors for the subsets of months with positive and negative anomalies of snow cover at the nearest 5° meridian. The differences exceed 1°C in a broad

band extending from the western Great Plains to New England. The differences exceed 2°C in the Dakotas. The positive signs indicate that the equations tend to overestimate the temperatures in cases with above-normal snow cover and/or underestimate the temperatures in cases with below-normal snow cover. The differences thus provide quantitative support for a local suppression of air temperatures by snow cover.

Fig. 2a shows that the summertime specification equations generally describe 65-80% of the monthly temperature variance, although the percentages are considerably smaller along the coasts. According to Fig. 2b, the errors in the specifications are consistently more positive during months with wet soil than during months with dry soil. The magnitudes of the differences in Fig. 2b are smaller than the snow-derived differences of Fig. 1b, although the monthly temperatures themselves are considerably less variable in summer than in winter. Fig. 2b provides support for the hypothesis that larger fractions of the available energy are used for sensible heating under dry conditions, thereby favoring an underestimation of surface air temperatures if only the upper-air circulation is considered.

Many, of the composite differences in the central and western U.S. are statistically significant at the 5% level during the summer months (Fig. 3). However, the number of significant differences decreased systematically when the experiment was repeated for months closer to winter than to summer. The seasonality of the maximum significance (30 of 61 points in June-July-August) and the minimum significance (2 of 61 points in November-December-January) are quite suggestive of a role of soil moisture, since the soil moisture variability and the energy available for heating are both largest during the summer.

Finally, Fig. 4 shows for the Eurasian landmass the differences corresponding to Fig. 2b. (The soil moisture computations were performed for 231 Eurasian stations, which were grouped into the climatological regions indicated by the dashed lines in Fig. 4.) The soil moisture-derived differences for Eurasia are comparable to or larger than those for the U.S., especially in the interior regions of the Eurasian landmass. The spatial pattern in Fig. 4 provides further support for the hypothesized role of soil moisture, since alternative moisture sources (e.g., advection) can be expected to make smaller contributions to the local hydrology as the distance from the major oceans increases.

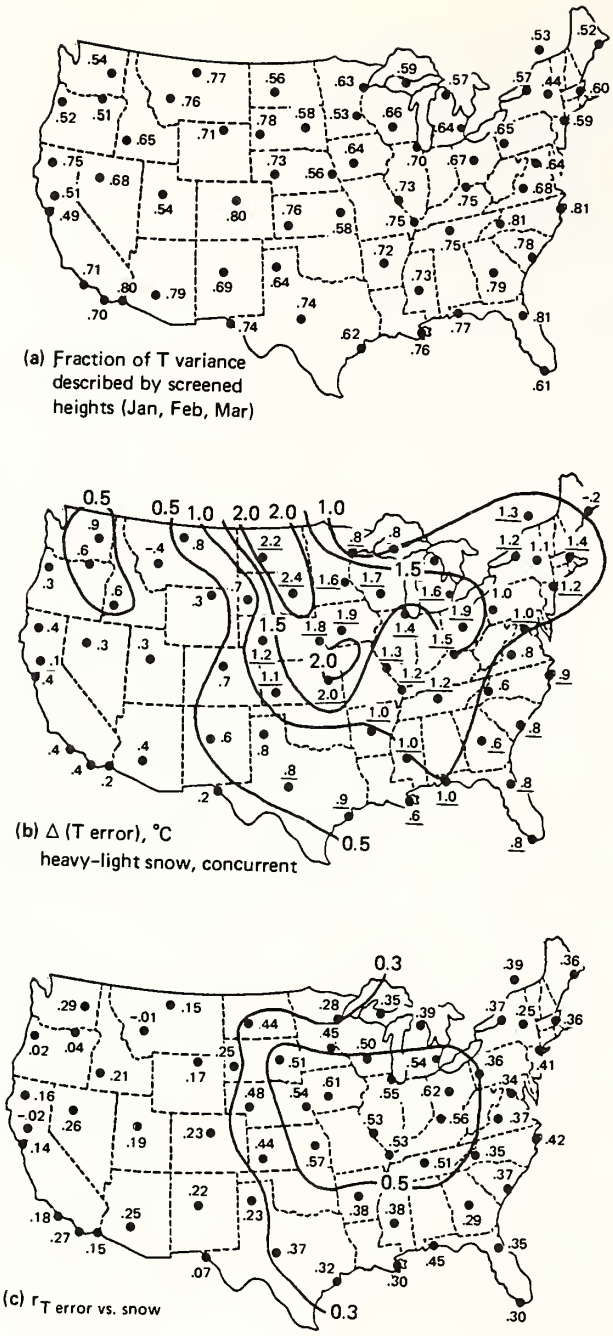
(a) Fraction of T variance described by screened heights (Jan, Feb, Mar)
(b) Δ (T error), °C heavy-light snow, concurrent
(c) $r_{T\ error\ vs.\ snow}$

Fig. 1. (a) Fractions of variance of monthly surface air temperature described by concurrent 700 mb height fields in January, February and March. (b) Composite differences of errors in objectively specified air temperatures (°C) during months when snow cover was above- or below-normal at nearest 5° longitudinal meridian; signs of errors correspond to months with above-normal snow cover; underlined values are statistically significant at 95% level.

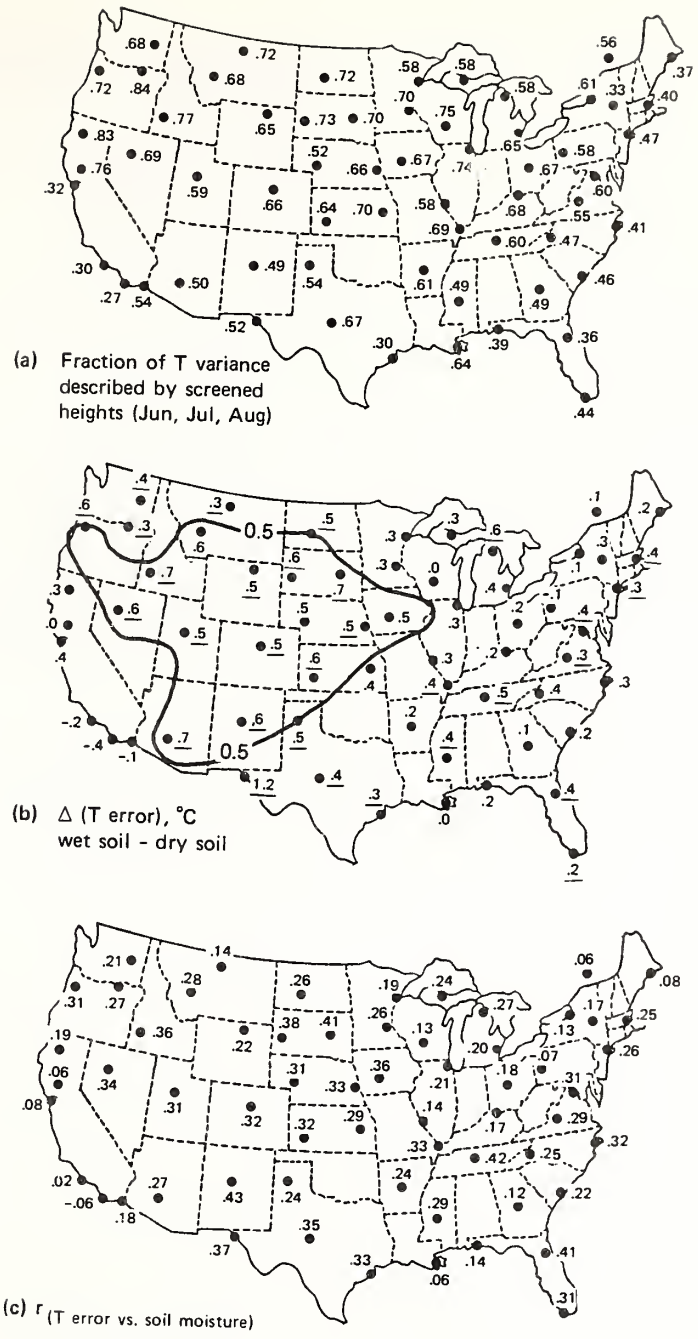
(a) Fraction of T variance described by screened heights (Jun, Jul, Aug)
(b) Δ (T error), °C wet soil - dry soil
0.5
0.5
(c) r (T error vs. soil moisture)

Fig. 2. (a) As in Fig. 1a except for temperatures of June, July and August. (b) As in Fig. 1b, except for temperature specification errors in months when local soil moisture was above- or below-normal; signs of errors correspond to months with above-normal soil moisture.

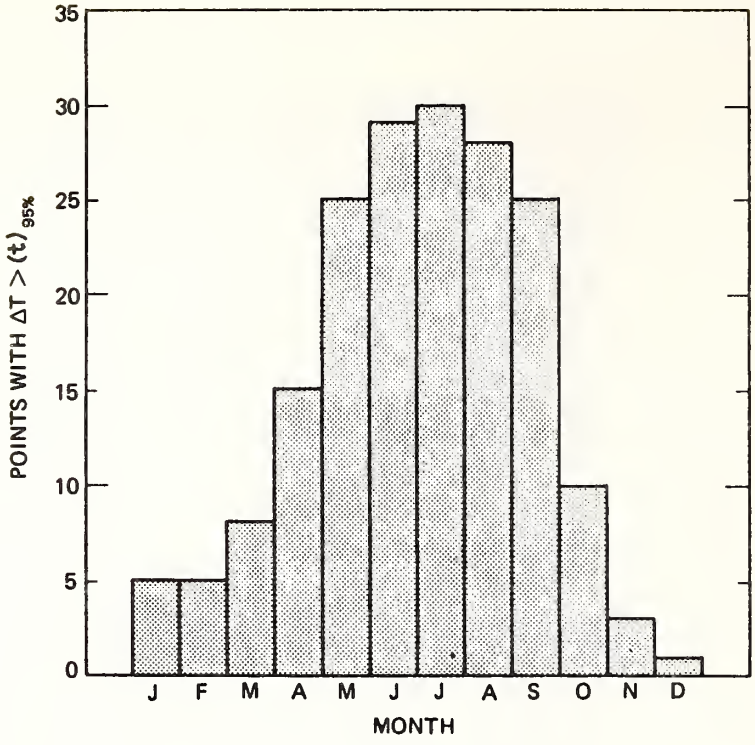

Fig. 3. Number of U.S. stations at which differences of composited mean specification errors are statistically significant at 5% level when composites are based on sign of soil moisture anomaly. Each bar corresponds to 3-month period centered on indicated month.

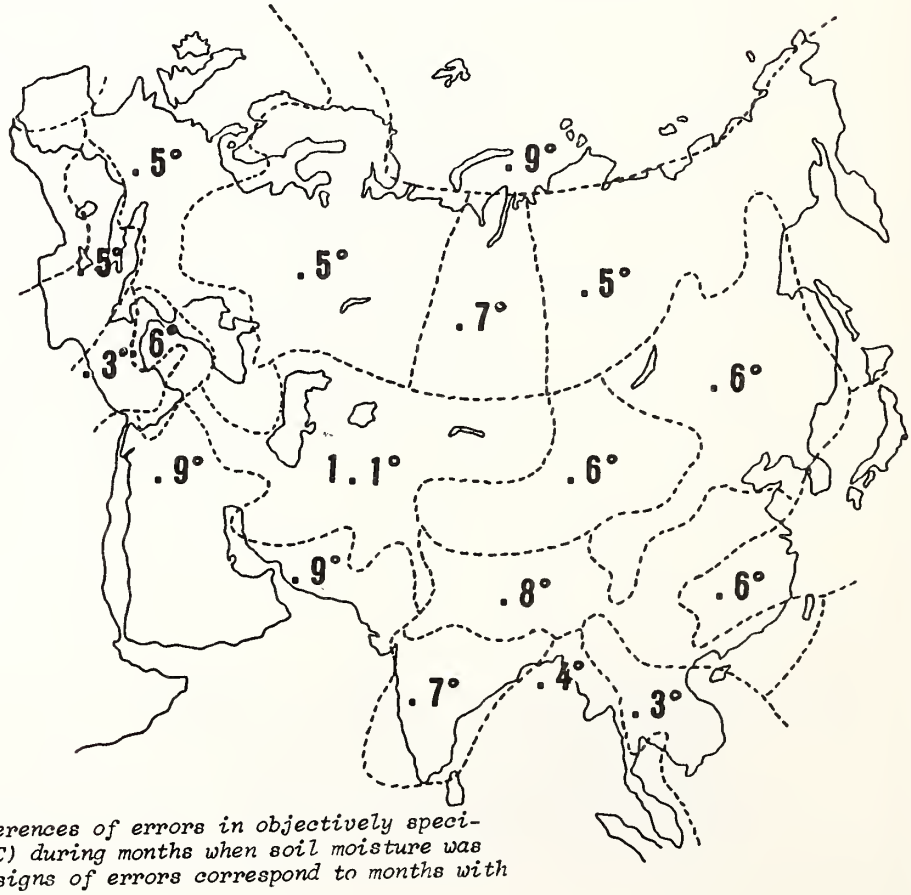

Fig. 4. Regionally averaged differences of errors in objectively specified air temperatures (°C) during months when soil moisture was above- or below-normal; signs of errors correspond to months with above-normal soil moisture.

Concurrent and Lagged Relationships between Precipitation Frequency and 700mb Heights

Arthur V. Douglas
Department of Atmospheric Sciences, Creighton University
Omaha, Nebraska 68178

Phillip J. Englehart
Midwest Research Institute
Kansas City, Missouri 64110

Experiments designed to specify monthly or seasonal precipitation from 700mb heights tend to be less successful than those for surface temperature. Precipitation specification is probably more difficult due to the smaller scale nature of precipitation patterns and the tendency for precipitation totals to be skewed (Figure 1). A better measure may be precipitation frequency (days with $\geq$0.10" precipitation), which shows less skewedness especially in the arid West (Figure 1). We have recently developed a new data set of precipitation frequency for 60 divisions in the United States. A description of this new data set and its properties will be published in JCAM sometime in 1985. This current report will focus on summer precipitation in two regions: The Southwest (combined data from 2 divisions in central and southeastern Arizona and one in northwest New Mexico); and the Central Plains (1 division each in central Kansas, central Nebraska, east central Colorado and southeast Wyoming.

The pattern correlation between southwestern precipitation frequency in summer and 700mb height anomalies is given in Figure 2. Only 10 grid points out of 82 are found to be significant and the overall field patterns are poorly organized. If the summer data (frequency and 700mb) are recalculated using data from the normally wet months of July and August, stronger relationships become apparent (Figure 3). This indicates that the June height data have little relationship with precipitation or subsequent height fields in July and August. If precipitation totals for the southwest region are related to 700mb heights instead of frequency, the observed correlation values tend to be lower, especially in the critical region of the central Rockies (Figure 4).

Individual monthly relationships for July and August are shown in Figures 5 and 6. In these months, heavy precipitation tends to occur when positive height anomalies develop over the northern Rockies. In Arizona the anomalous 700mb flow is from the east-southeast. The individual monthly fields tend to indicate a retrogression of the key positive

height anomalies from July to August. In addition, the development of increasingly negative correlations off Baja California are a reflection of warm-cold water regimes in the eastern tropical Pacific associated with El Niño or anti-El Niño conditions. During El Niños, positive heights become dominant off Baja California by August and this results in an anomalous dry westerly flow across the southwest (see last year's Diagnostic Workshop report).

The usefulness of regional frequency data can be seen when comparing Figures 6, 7 and 8. If a single station is used (Figure 8), the pattern correlations are generally less coherent. Even a single division (a composite of 16 stations) is still less effective than a regional time series from 3 divisions (48 stations) which show strong interdivisional coherence (Figures 6 and 7). A summary of these results is given in the following table:

Table 1. Summary of August specifications. Number of significant grid points out of 82.

Location	Number of Significant Points 95% Level
Tucson Frequency	11
Southeast Arizona Totals	12
Southeast Arizona Frequency	16
Southwest Totals	19
Southwest Frequency	24

A time series of the combined July and August precipitation frequency is given in Figure 9. Repeated periods of summer drought or wetness are typical and may last up to 9 years. An examination of the individual data for July and August indicates a strong tendency for reversals between July and August precipitation frequency. In Figure 10, the frequency anomalies (% normal) for August have been subtracted from those of July. From 1934 to 1947 there is a tendency for August to be wetter than July (negative values) while in the 1970's July tended to be the set month. However, long-term means for July and August frequency are very similar at 5.9 and 5.8 days/month respectively. June only averages 1.2 days/month.

If precipitation reversals are common between July and August, then they should be controlled in part by changes in the general circulation. This is evident in Figure 11 where the difference in July and August frequency is correlated with the difference in July and August 700mb height anomalies. Taken in the positive sense, the pattern correlation map in-

dicates that when wet Julys are followed by dry Augusts, 700mb height anomalies tend to be positive in July over the northern Rockies but negative by August. This makes synoptic sense in that the pattern correlation map suggests that the wet Julys are associated with anomalous southeast flow from out of Mexico, while dry Augusts are dominated by anomalous dry westerly air flow out of the North Pacific anticyclone. Teleconnection maps indicate that Rocky Mountain height anomalies show little relationship with height fields off Baja California (Figure 12). Thus, for an anomalous wet regime to develop in the Southwest, a unique combination of heights must develop with positive heights to the north and negative heights to the south.

The time series of precipitation frequency for the Central Plains is given in Figure 13. The well documented droughts of the 1930's, 1950's and 1970's are apparent in the plot. The pattern correlations between the time series and 700mb heights are given in Figure 14. Above normal precipitation frequency is associated with negative heights in the central North Pacific and in the upper Midwest. Surprisingly, correlation values are higher with grid points in the Pacific rather than with points near the frequency region. Lagged relationships between summer frequency and spring heights are given in Figure 15. A synoptic interpretation of the pattern suggests that wet summers are preceded by below normal heights in the subtropics and above normal heights in the Gulf of Alaska and Great Lakes. These lagged relationships give some hope that summer precipitation patterns in the Central Plains may be foreshadowed by 700mb height anomalies during the preceding spring.

Since 1970, there has been a strong tendency for precipitation frequency to be much higher than normal in spring and near or below normal in the subsequent summer (Figure 16). In recent years, precipitation frequency in July and August has tended to be much lower than normal and considerably below the frequency values of May and June. The pattern correlations between the 700mb heights of May and June and the difference in precipitation frequencies between May-June and July-August are given in Figure 17. A greater than normal drop in precipitation frequency from May and June to July and August is foreshadowed by negative heights in the western United States in May and June and positive heights in the eastern Great Lakes. The general correlation pattern observed in Figure 17 suggests that meridional circulation in May and June is typified by drier conditions during July and August.

FIGURE CAPTIONS

Figure 1. Geographical variations in percent of time that monthly sample distributions are non-normally distributed for precipitation frequency (A) and precipitation totals (B).

Figure 2. Correlation between Southwest precipitation frequency for summer and summer 700mb height anomalies. Summer is defined as June through August. Period of analysis 1951-80.

Figure 3. Correlation between July-August precipitation frequency for the Southwest and July-August 700mb height anomalies.

Figure 4. Correlation between July-August precipitation totals for the Southwest and July-August 700mb height anomalies.

Figure 5. Correlation between July precipitation frequency for the Southwest and July 700mb height anomalies.

Figure 6. Correlation between August precipitation frequency for the Southwest and 700mb height anomalies. Note the westward movement of the positive height correlation in the northern Rockies and the development of negative heights south of 25°N.

Figure 7. Correlation between August precipitation frequency for southeastern Arizona and August 700mb height anomalies.

Figure 8. Correlation between August precipitation frequency for Tucson and August 700mb height anomalies.

Figure 9. Time series showing the percent of normal precipitation frequency for the Southwest during July and August. Note the tendency towards decadal persistence of anomalies.

Figure 10. Time series depicting the difference between July and August precipitation frequency for the Southwest. Series was constructed by subtracting August % normal from July % normal.

Figure 11. Pattern correlation between the time series in Figure 10 and the July minus August 700mb height anomalies. Note the large number of significant points in the continental United States and a strong resemblance to Figures 5 and 6.

Figure 12. 700mb teleconnections for 20°N/120°W and 45°N/115°W. Note that the point at 20°N is not well correlated with height fields over the northern Rockies, while the point at 45°N does not indicate a tendency towards reversal in height fields to the south.

Figure 13. Time series of summer precipitation frequency for the Central Plains.

Figure 14. Pattern correlation between summer precipitation frequency in the Central Plains and 700mb height anomalies. Note that the best correlations are to the west in the Central Pacific and western Canada.

Figure 15. Lag correlation between spring 700mb height anomalies and subsequent precipitation in the Central Plains.

Figure 16. Time series depicting the difference between spring precipitation frequency (% normal) and summer precipitation frequency (% normal) for Kansas and Nebraska. Note that this time series employs state data and is derived from precipitation totals.

Figure 17. Correlation between the time series in Figure 16 and the 700mb height anomalies for May-June. When positive differences occur (wet May-June compared to dry July-August) negative height fields are expected in the Southwest during the May-June period.

Percentage of Months with Non-Normal Distributions

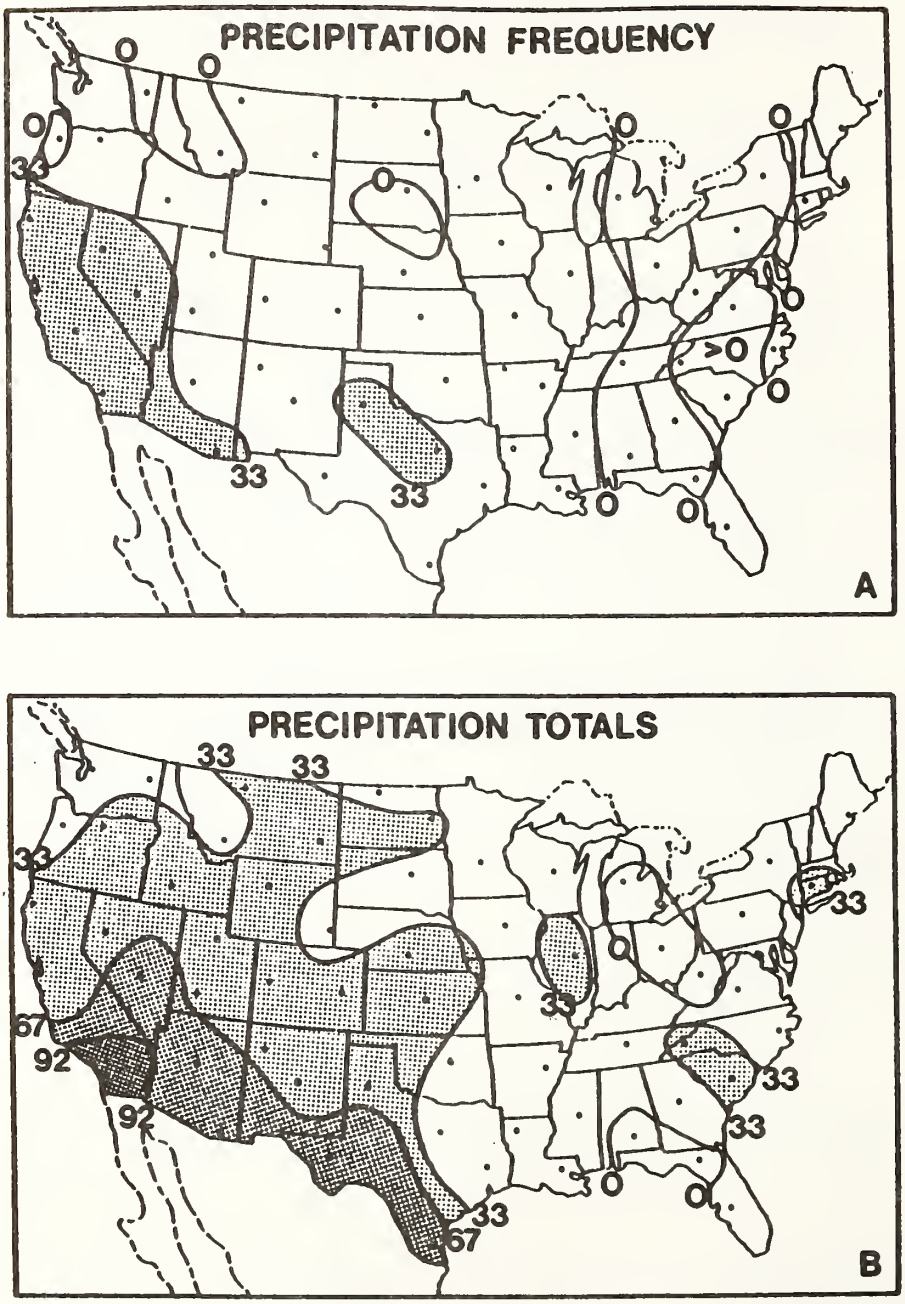

FIGURE 1

SUMMER FQ SOUTHWEST
vs
SUMMER 70 k Pa ANOMALIES

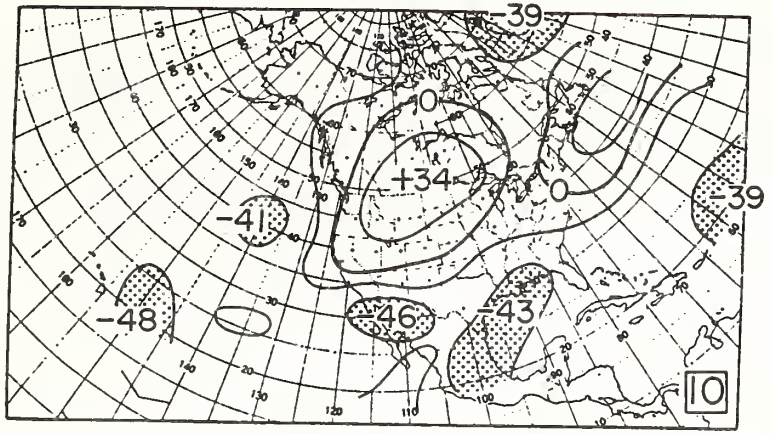

FIGURE 2

JULY AUGUST TOTALS SOUTHWEST
vs
JULY AUGUST 70 k Pa ANOMALIES

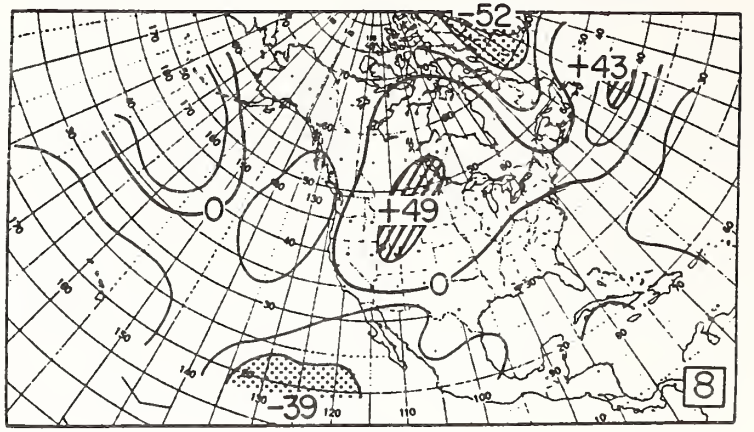

FIGURE 4

JULY AUGUST FQ SOUTHWEST
vs
JULY AUGUST 70 k Pa ANOMALIES

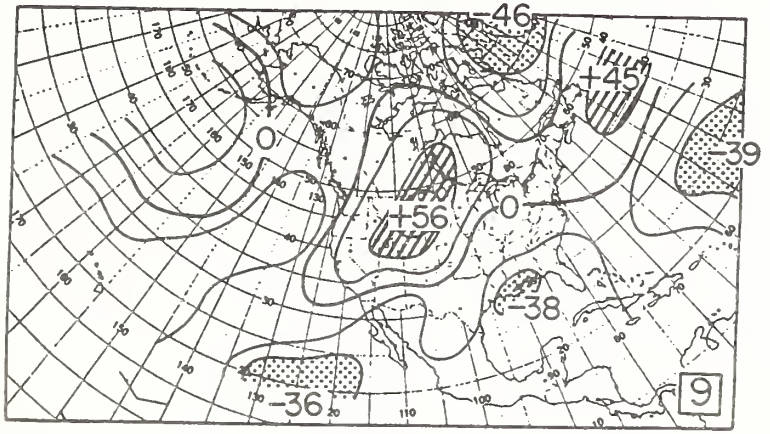

FIGURE 3

JULY FQ SOUTHWEST
vs
JULY 70 k Pa ANOMALIES

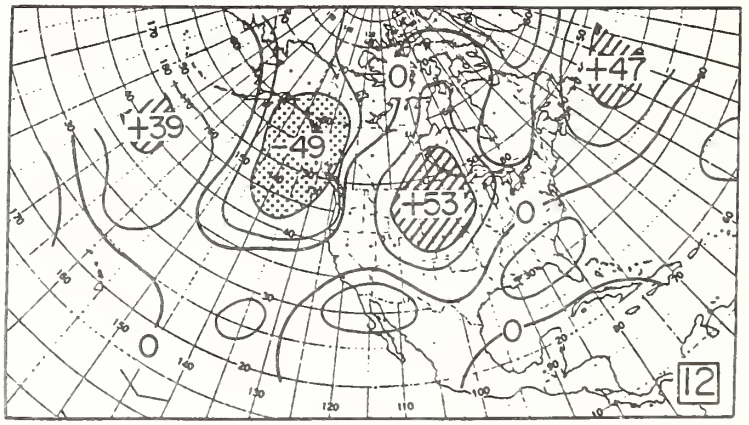

FIGURE 5

AUGUST FQ SOUTHWEST
vs
AUGUST 70kPa ANOMALIES

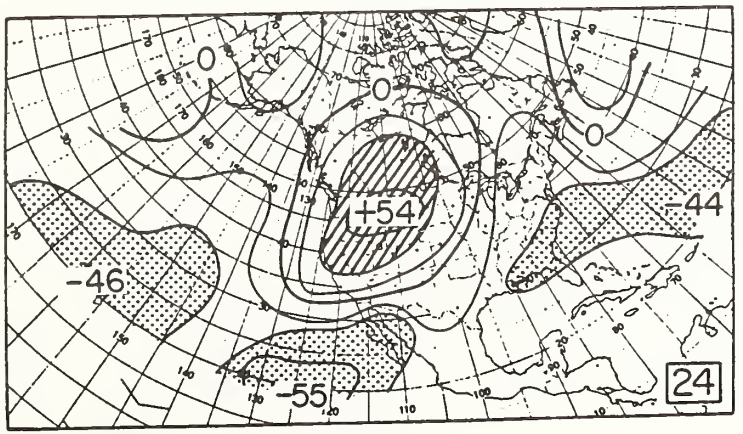

FIGURE 6

AUGUST FQ TUCSON
vs
AUGUST 70kPa ANOMALIES

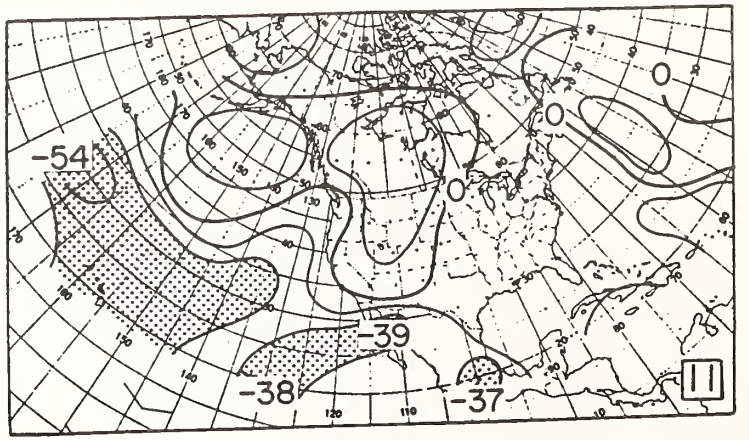

FIGURE 8

AUGUST FQ SE ARIZONA
vs
AUGUST 70kPa ANOMALIES

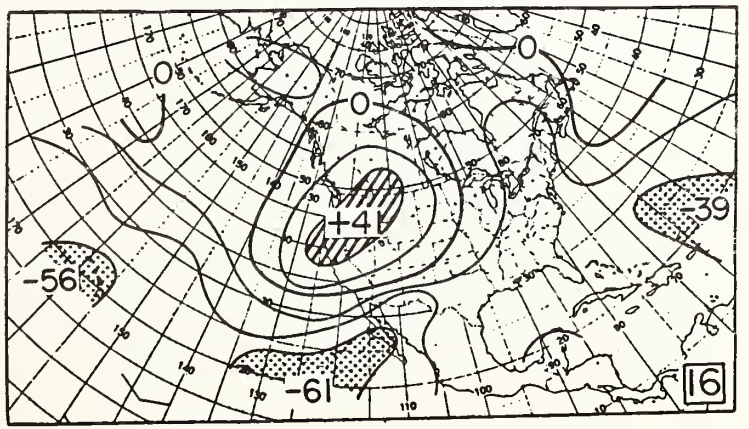

FIGURE 7

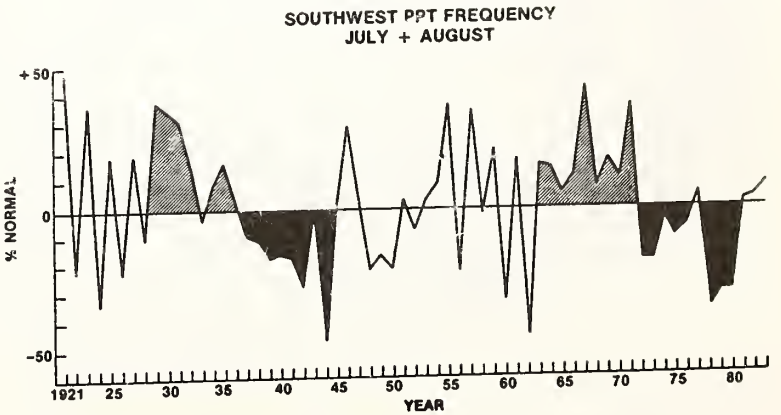

FIGURE 9

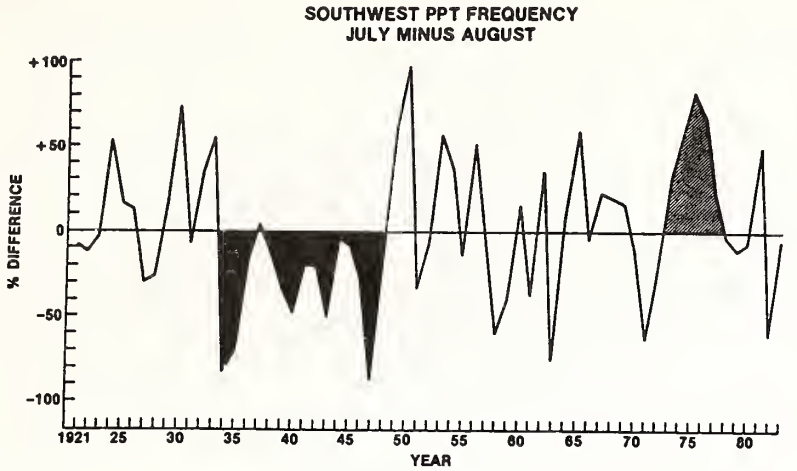

FIGURE 10

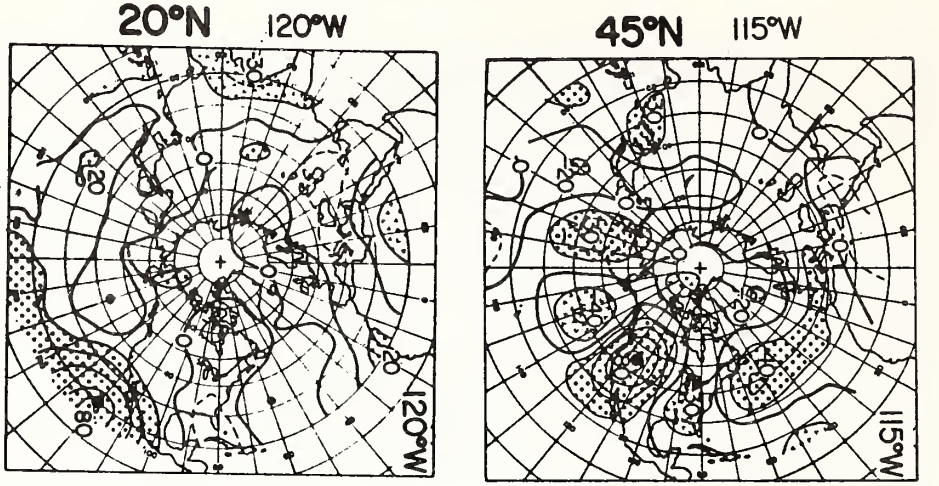

FIGURE 12

SOUTHWEST
JULY FQ MINUS AUGUST FQ
vs
JULY 70kPa MINUS AUGUST 70kPa ANOMALIES

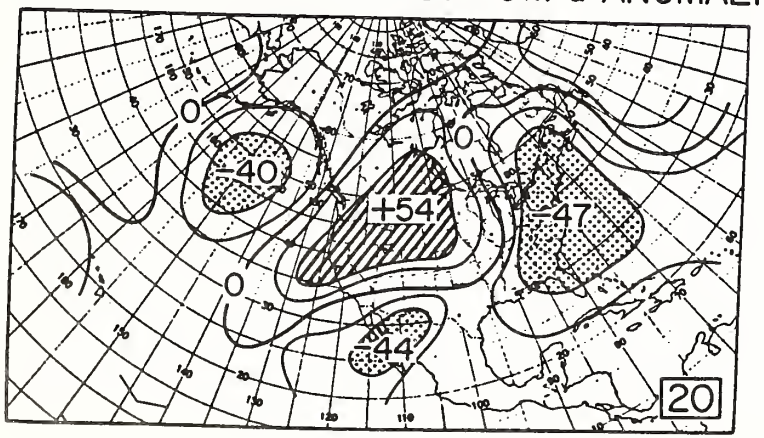

FIGURE 11

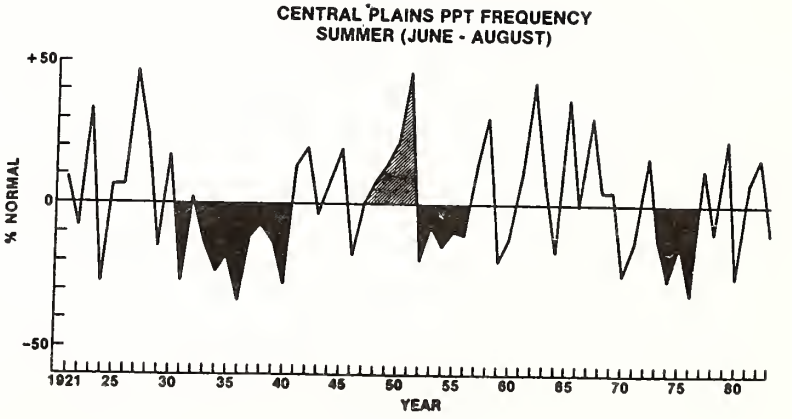

FIGURE 13

SUMMER FQ C. PLAINS
VS
SUMMER 70kPa ANOMALIES

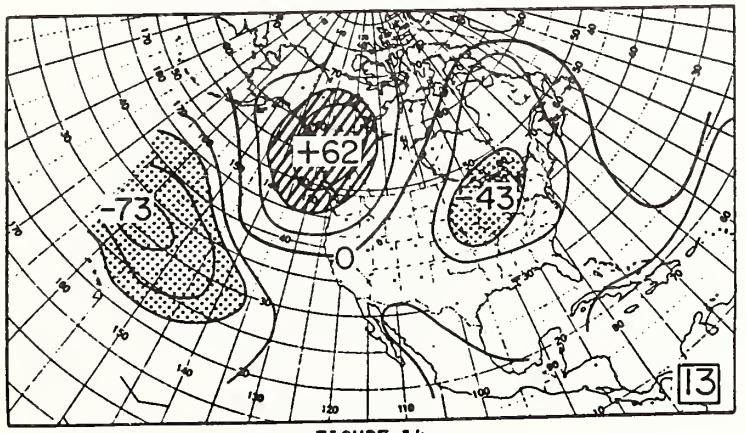

FIGURE 14

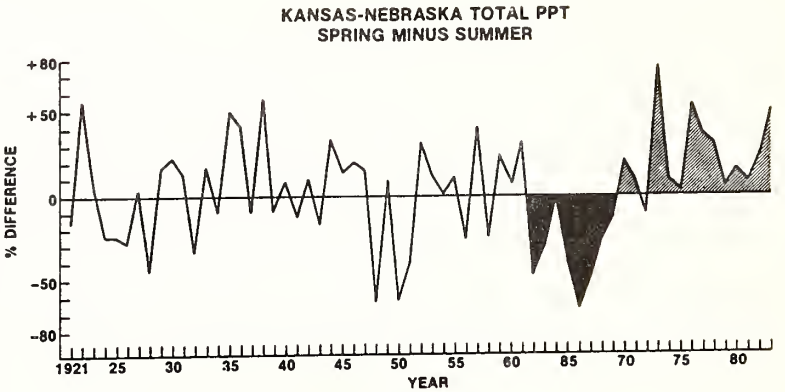

FIGURE 16

SUMMER FQ C. PLAINS
VS
SPRING 70 k Pa ANOMALIES

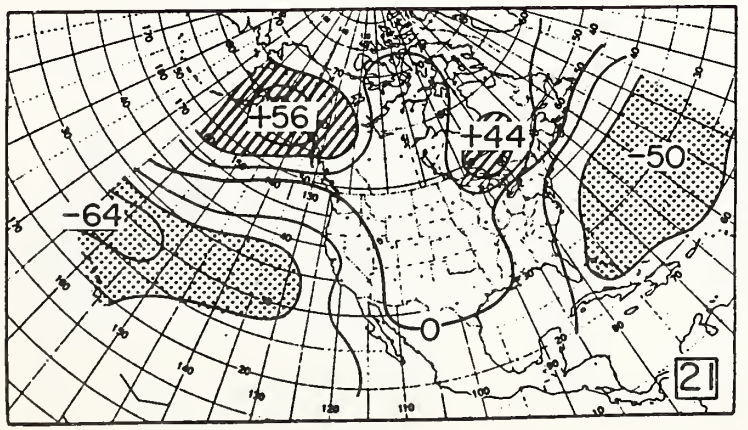

FIGURE 15

C. PLAINS
MAY JUNE FQ MINUS JULY AUGUST FQ
VS
MAY JUNE 70 k Pa ANOMALIES

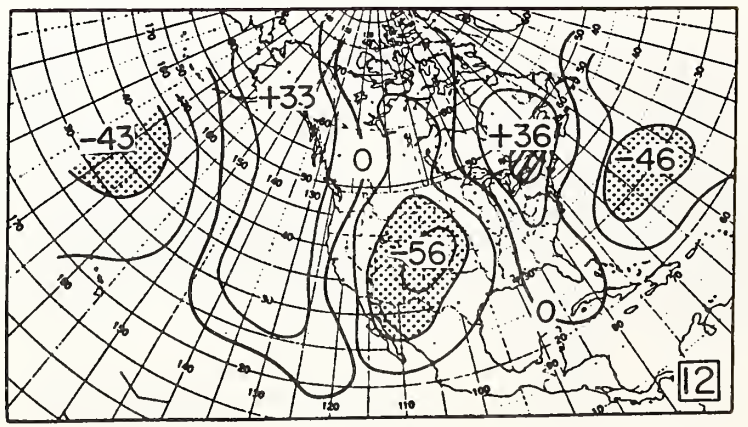

FIGURE 17

TROPICAL CONVECTION AND NORTH AMERICAN CYCLONES DURING THE 1982-83 EL NINO

Richard A. Keen

Cooperative Institute for Research in Environmental Sciences, (CIRES)
University of Colorado, Boulder CO 80309

Numerous theoretical and observational studies suggest that the planetary-scale wave pattern over North America can respond to changes in the location and intensity of convection in the tropical Pacific. During El Niño conditions, convection shifts eastward into the central and eastern Pacific; the indicated mid-latitude response to this shift is the so-called "Pacific-North America", or PNA, pattern. One feature of the PNA pattern is an enhanced subtropical jet stream (STJ) across southern North America. During 1982-83 jet stream wind velocities over the Gulf of Mexico were nearly twice their normal values. Such circulation anomalies are based on monthly or seasonal averages, and are indicative of the steady-state atmospheric response to persistent, large-scale tropical convection. However, the convection actually occurs in outbreaks lasting a few days to a week, and some modeling results (Paegle, 1978) suggest that the STJ can respond to transient convection within 1 or 2 days. If the STJ does respond to short-term convection, the enhanced jet over the Gulf of Mexico during 1982-83 should be associated with more and/or stronger synoptic-scale disturbances whose timing should be related to the timing of the convective outbreaks.

An increased number of surface cyclones over the Gulf of Mexico during 1982-83 is apparent in figure 1, which compares cyclone-days per five-degree grid square during that season (November through April) with a 40-year average. The area bounded by 80°- 100°W, 20°-30°N had nearly three times the long-term average number of cyclone-days, the greatest anomaly of any region on the map. In terms of cyclone numbers, rather than cyclone days, 25 cyclones formed south of 30° N between 70° and 140°W during 1982-83, compared to a 40-year average of 15. Examination of daily satellite imagery and 250-millibar and surface analyses shows that many of these low-latitude cyclones appear to follow transient tropical convection, with the intervening sequence of events shown schematically in figure 2. This sequence of events is frequently marked by the occurrence of cirrus streamers during stages 2 and 3. These streamers, which flow northeast from the area of the convection, appear to be a form of jet stream cirrus related to the sudden increase in wind speeds on the south fringe of the STJ.

The repeated occurrence of the convection-to-cyclone sequence of events over the eastern Pacific and southern North America during early 1983 is shown by a time-longitude plot of three selected parameters (figure 3). The three parameters are:

- *Near-equatorial convection.* The cross-hatched areas indicate longitudes with more than 15 percent coverage of Highly Reflective Clouds (HRC) between 10°N and 10°S. HRC's are

regions of intense convection seen on satellite imagery, and are described in detail by Garcia and Anderson (1984).

- *Strong southwesterly winds at 250 millibars.* The stippled areas indicate longitudes at which the product of the u and v components of the 250 millibar winds at 20 ° N exceeds 500 m^2/sec^2. This parameter has the multiple uses of locating strong northeastward convective outflow during stage 2, poleward westerly momentum transport during stage 3, and the leading edge of the trough (where surface cyclogenesis occurs) during stage 4.
- *Surface cyclones.* The heavy solid lines indicate the longitudes of surface cyclone centers south of 30 ° N (all are north of 20 ° N).

Readily apparent in figure 3 are frequent occurrences of intense convection between 135 ° W and 160 ° W and the characteristic durations and longitudinal extents of the individual outbreaks. Also apparent are the eastward-propagating 250 millibar troughs that induce low-latitude (south of 30 ° N) cyclones around 90 - 100 ° W. The thin dashed lines are subjective interpretations of the linkages between the convective outbreaks and the strong troughs and surface cyclones. The slopes of these dashed lines range from 12 to 18 degrees/day, and the entire sequence of events, from stage 1 through stage 4, lasts from 4 to 7 days. For those interested in synoptic forecasting, the onset of convection precedes cyclogenesis by 2 to 5 days.

Figure 3 shows all the cyclones that formed south of 30 ° N between 70 ° W and 140 ° W during the period 13 January through 1 March 1983. Of these 11 cyclones, 9 appear to be directly related to convective outbreaks over the eastern Pacific. For the entire 1982-83 season (November through April), 21 of the 25 low-latitude cyclones appear to be similarly linked to convection. It therefore seems likely that the exceptional cyclone activity around the Gulf of Mexico during 1982-83 is, to some extent, due to the equally exceptional amount of convection over the eastern Pacific, and that the timing of these cyclones is influenced by the timing of individual convective outbreaks. It should be noted that one of the factors affecting the timing of the convective outbreaks could be STJ disturbances arriving from the western Pacific; if this is the case, the mechanism discussed in this paper is more of a positive feedback mechanism (whereby a weak STJ disturbance is amplified by the convection) than a simple cause-effect mechanism (whereby the convection induces the STJ trough).

References

Garcia, O., and M. Anderson (1984). *Proc. of the Eighth Annual Climate Diagnostics Workshop,* Toronto, 122-128.

Paegle, J. (1978). *J. Atmos.Sci., 35,* 1678-1688.

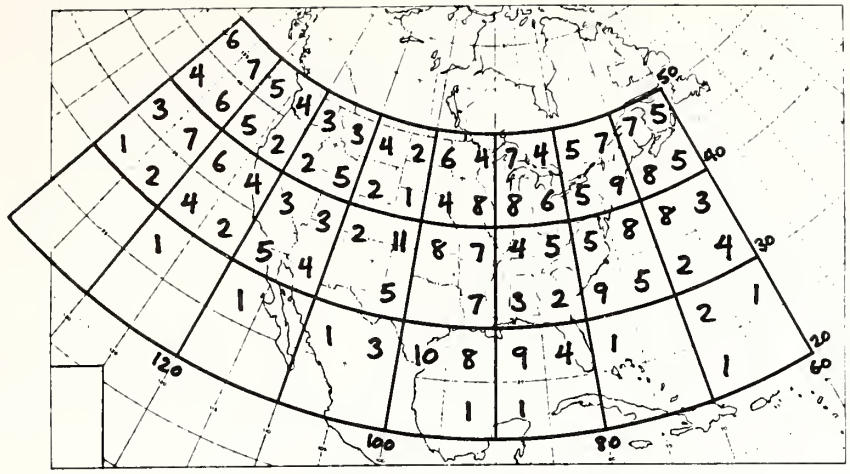

1982-83

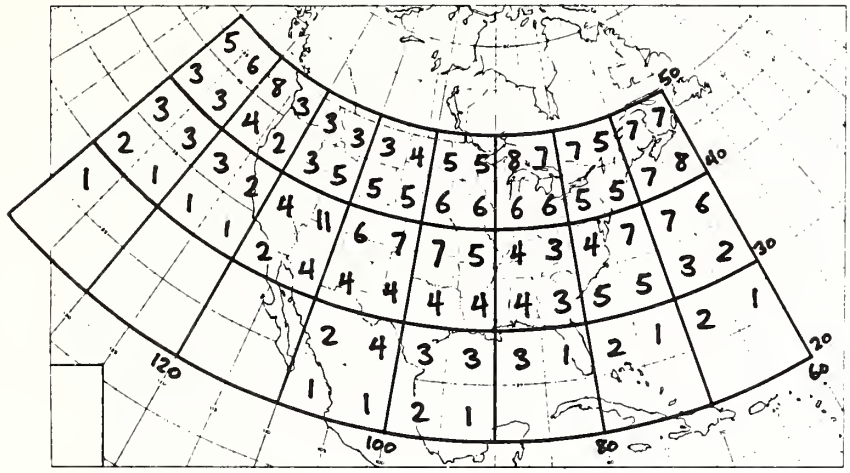

40-year average

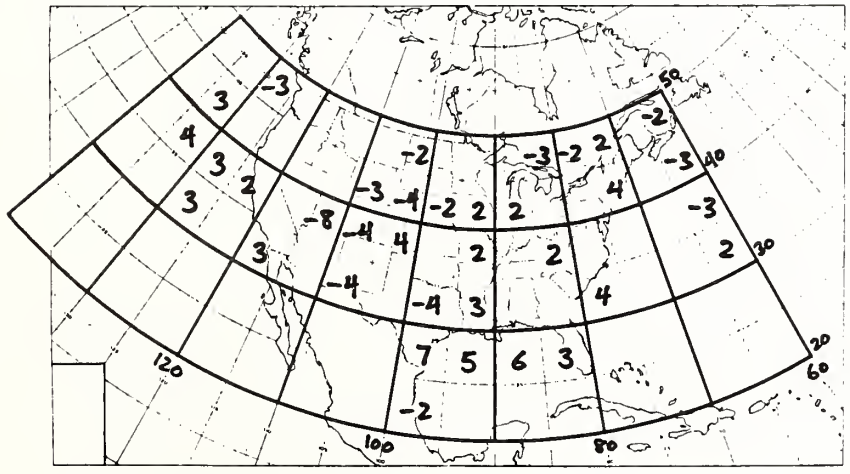

1982-83 minus 40-year average

Figure 1. Number of days during November through April with surface cyclone centers within 5^{o} by 5^{o} grid areas: 1982-83 (top), 40-year average (center), and difference (bottom; differences between 1 and -1 are omitted).

Figure 2. Atmospheric response to localized, transient outbreak of heavy convection (schematic).

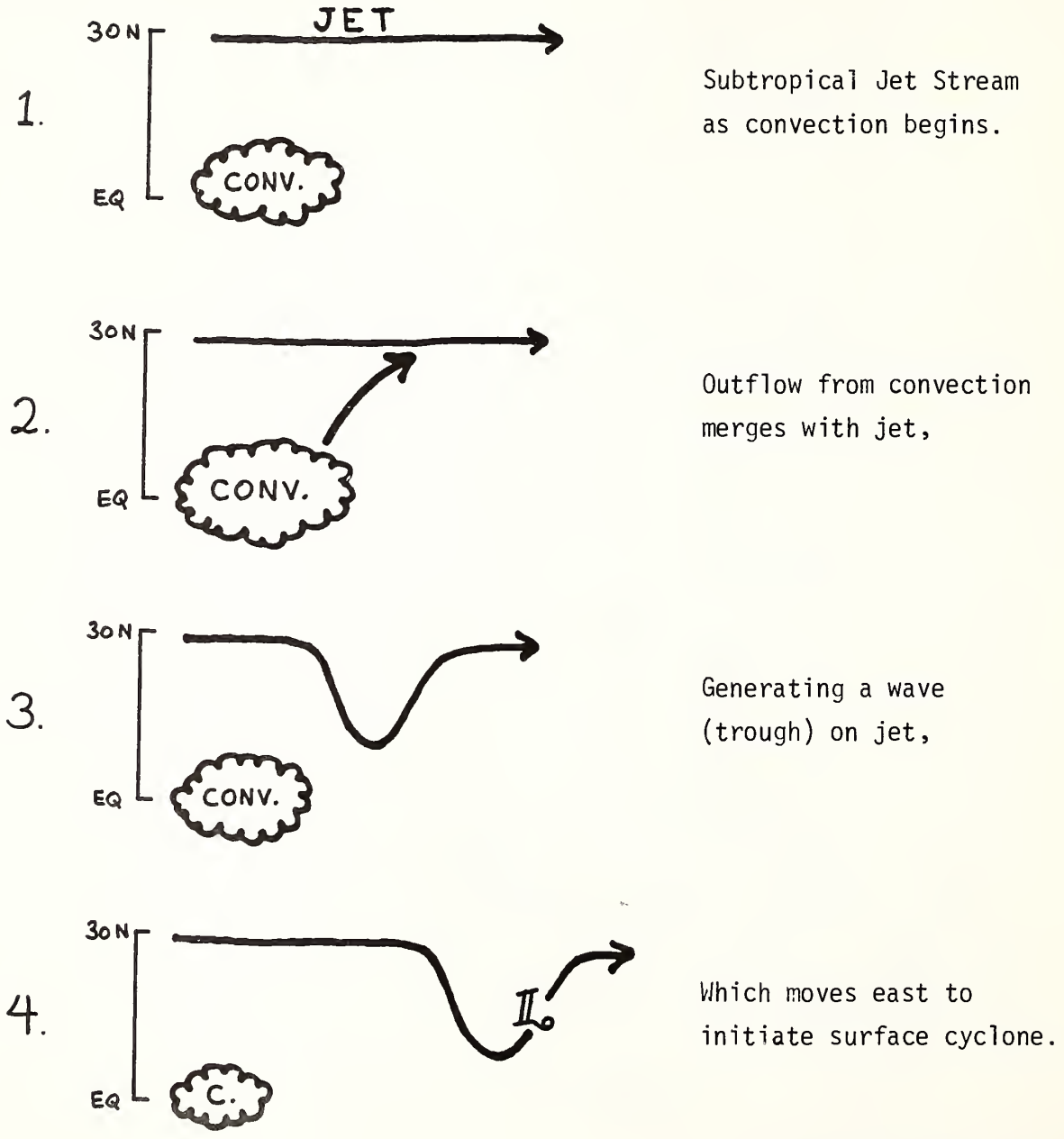

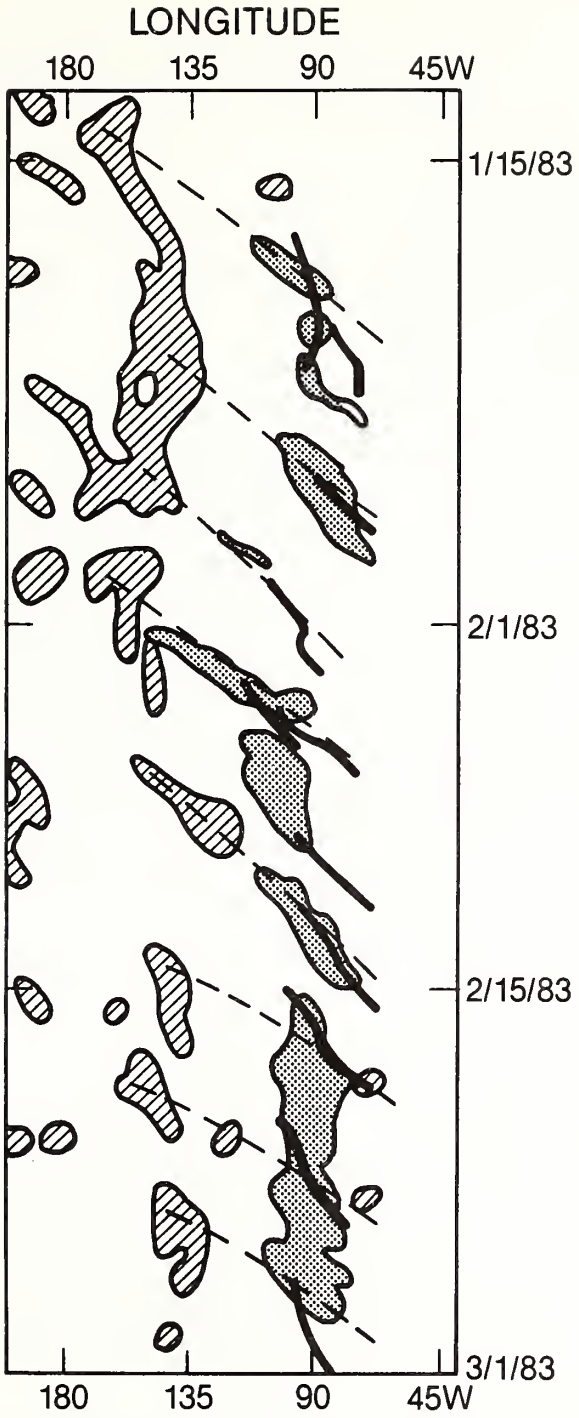

Figure 3. Time-longitude plot of transient activity over the Pacific - North American sector during early 1983: Near equatorial convection (cross-hatched), strong southwesterly 250 mb winds at 20°N (stippled), and low-latitude surface cyclones (heavy solid lines). The apparent linkages are noted by thin dashed lines.

An Observational Study of the Vertical Structure of Interannual Wind Fluctuations in the Tropics

David S. Gutzler
Center for Meteorology and Physical Oceanography
Massachusetts Institute of Technology
Cambridge, Massachusetts 02139

Time series of rawinsonde-derived monthly mean winds archived in Monthly Climatic Data for the World have been used to document and characterize the interannual variability of the tropical wind field with particular attention paid to the vertical structure of the observed fluctuations.

A network of 34 stations between 25°S and 25°N was found for which complete time series, typically 15-24 years long, were available. Six pressure levels ranging from 850 mb to 150 mb were used for the analysis.

For each pressure level at each station, seasonal means were formed from the monthly means. Seasonal climatology was calculated and then subtracted from each season's observed wind to form time series of seasonal anomalies. Empirical orthogonal functions of the vertical structure of interannual variability were then derived for each station and season for zonal and meridional wind components separately, by calculating the eigenvectors of a mass-weighted covariance matrix incorporating wind anomalies at all six levels, following the procedure used in Section 7 of Blackmon et al. (1979).

Examples of the results are shown in Figs. 1 and 2. At Johnston Island (lat. 17.0°N lon. 169.5°W) over 80% of the interannual variance of both summer (June-July-August) and winter (December-January-February) seasonal average zonal wind is described by a vertical mode representing wind anomalies of the same sign throughout the troposphere, the amplitude of the anomaly increasing with height up to 200 mb (Fig. 1). This "equivalent barotropic" signature is quite similar to that typically observed in middle latitudes in previous investigations (Blackmon et al., 1979). The majority of the residual variance is explained by a mode with a single sign change (node) occurring near 300 mb, which we shall denote as a "baroclinic" structure.

Nearer the equator at Truk (lat 7.5°N lon. 151.9°E) the signature is quite different (Fig. 2). The dominant vertical mode of winter interannual variability has an equivalent barotropic structure similar to that at Johnston, but a greater share of the variance is explained by the second mode with its baroclinic structure. In summer, the relative importance of these modes reverses, with the baroclinic mode dominating. This mode resembles the vertical structure associated with an idealized latent heat forced circulation modelled by Gill (1980).

With few exceptions, these two structures typified the first two modes of interannual variability for all stations and seasons. Together, this pair of modes universally explained at least 80% of the total variance, and generally 95% of the variance or more.

Fig. 3 displays the geographical distribution of the percentage of interannual variance explained by the dominant mode, and structure of the dominant mode, for Northern Hemisphere winter. In the subtropics, the vertical structure is typified by a single dominant mode with an equivalent barotropic structure. Near the equator, two modes are required to explain most of the variance and the dominant mode tends to have a baroclinic structure.

Fig. 4 provides an indication of the horizontal coherence of these modes. For Fig. 4(a), the winter time series of eigenvector coefficients of the dominant (equivalent barotropic) mode at Truk has been correlated with the time series associated with equivalent barotropic modes at the other stations (irregardless of whether they are the dominant or secondary modes). A plot of the analogous correlations for the baroclinic modes is shown in Fig. 4(b). Whereas the equivalent barotropic modes tend to fluctuate in phase throughout the tropics, the baroclinic modes for all stations in the tropical Pacific fluctuate out of phase with the baroclinic modes at stations in the Indonesian region and eastern Africa.

The correlation pattern in Fig. 4(a) is reminiscent of the zonally symmetric equatorial 200 mb geopotential height fluctuations documented by Horel and Wallace (1981), while the pattern in Fig. 4(b) associated with the baroclinic modes more closely resembles the 200 mb wind teleconnection pattern described by Arkin (1982).

REFERENCES

Arkin, P. A., 1982: The relationship between interannual variability in the 200 mb tropical wind field and the Southern Oscillation. Mon. Wea. Rev., 110, 1393-1404.

Blackmon, M. L., R. A. Madden, J. M. Wallace, and D. S. Gutzler, 1979: Geographical variations in the vertical structure of geopotential height disturbances over the Northern Hemisphere. J. Atmos. Sci., 36, 2450-2476.

Gill, A. E., 1980: Some simple solutions for heat-induced tropical circulations. Quart. J. Roy. Meteor. Soc., 106, 447-462.

Horel, J. D., and J. M. Wallace, 1981: Planetary-scale circulations associated with the Southern Oscillation. Mon. Wea. Rev., 109, 813-829.

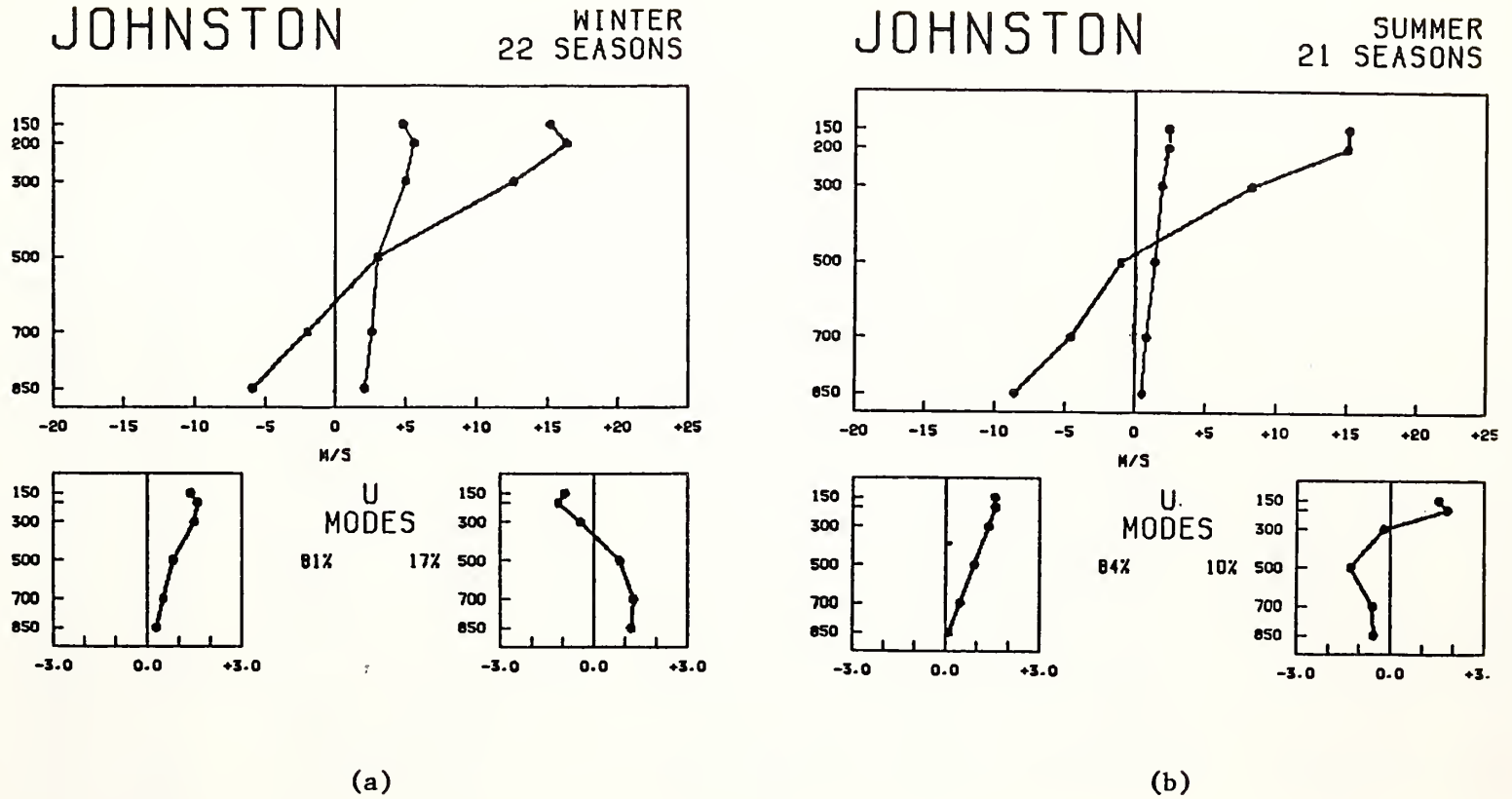

(a) (b)

Fig. 1. (a) Top panel: winter (Dec.-Jan.-Feb.) climatological zonal wind (thick line) and interannual standard deviation of seasonal departures from climatology (thin line) at Johnston Island (lat. 17.0°N, lon. 169.5°W).
Bottom panels: gravest two empirical orthogonal functions describing vertical structure of mass-weighted interannual variability, with percentage of variance explained by each mode.

(b) As in (a), but for summer (Jun.-Jul.-Aug.) zonal wind at Johnston.

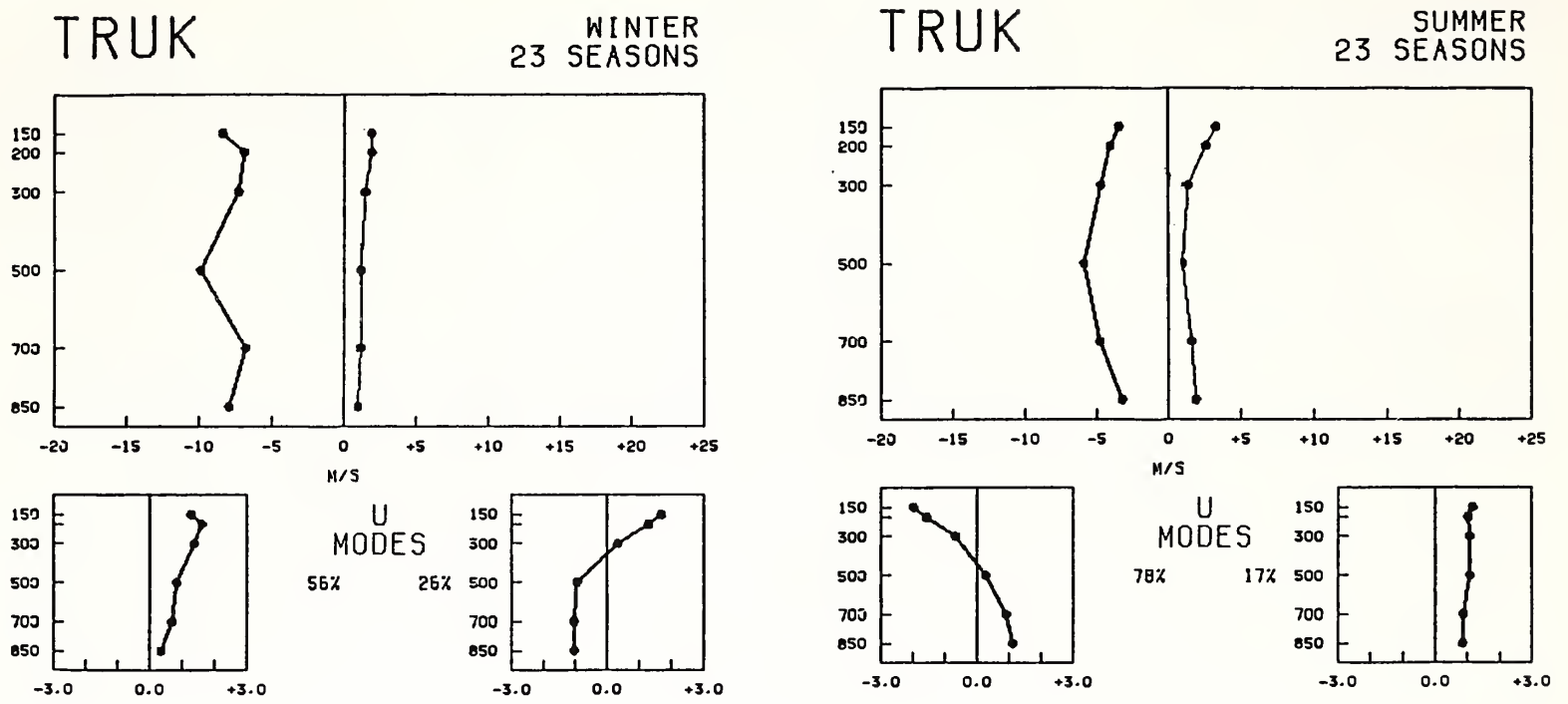

(a) (b)

Fig. 2. As in Fig. 1, but for Truk (lat 7.5°N, lon 151.9°E).

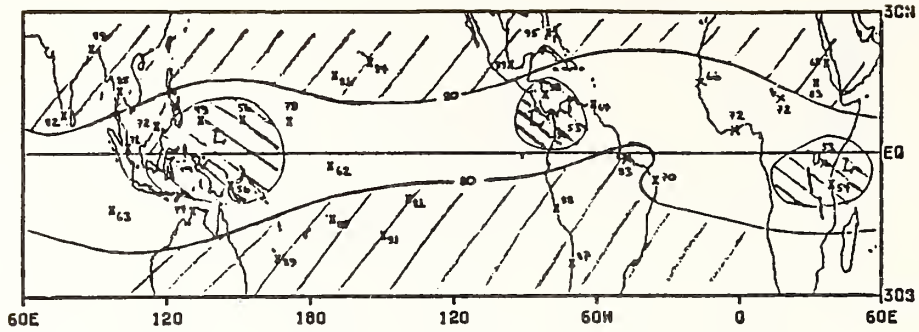

(a)

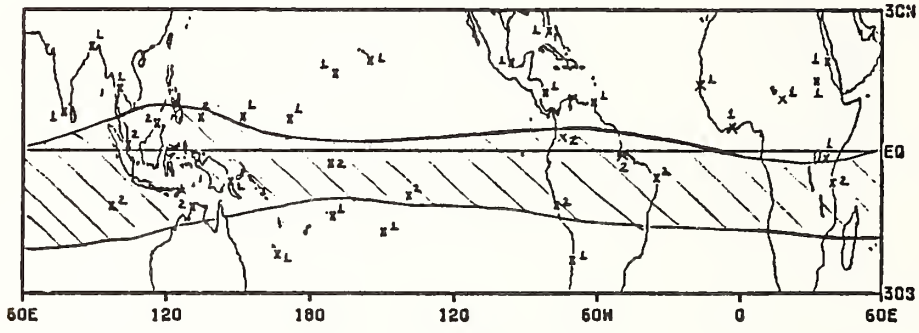

(b)

Fig. 3. (a) Percentage of winter interannual zonal wind variance explained by the dominant vertical mode at each station.

(b) Structure of the dominant winter vertical mode, expressed as (# nodes + 1) at each station. Hence, "1" represents an "equivalent barotropic" structure and "2" represents a "baroclinic" structure.

SW-NE hatching in (a) covers areas where the percentage is > 80%.
SE-NW hatching in (a) covers areas where the percentage is < 60%.

SE-NW hatching in (b) covers areas where the dominant mode has a "baroclinic" shape.
Areas in (b) where the dominant mode has an "equivalent barotropic" shape are unhatched.

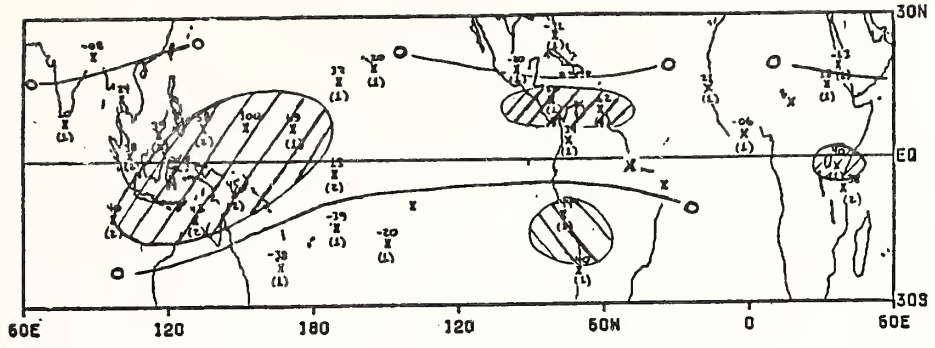

(a)

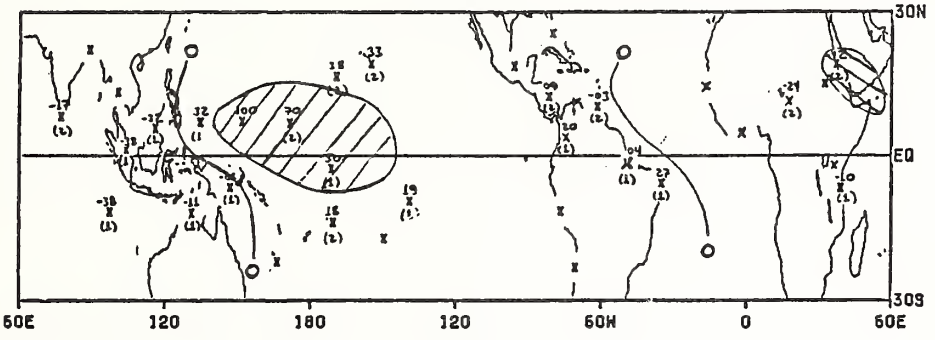

(b)

Fig. 4. (a) Correlation coefficients between the time series of eigenvector coefficients associated with winter mode 1 at Truk (see Fig. 2a) and coefficients associated with equivalent barotropic modes at other stations.

(b) As in (a), but for winter mode 2 at Truk correlated with winter baroclinic modes at other stations.

SW-NE hatching covers areas with correlations > +0.4.
SE-NW hatching covers areas with correlations < -0.4.

Low-frequency baroclinic features observed in the lee of major mountain ranges

Huang-Hsiung Hsu and John M. Wallace
Department of Atmospheric Sciences, AK-40
University of Washington
Seattle, Washington 98195

Much of the recent observational work on low-frequency variability has emphasized features with equivalent barotropic vertical structures with maximum amplitudes in the middle and upper troposphere [e.g. Wallace and Gutzler (1981); Esbensen(1983)]. Likewise, much of the theoretical and modeling work on this topic has emphasized the barotropic processes included in the models [e.g. Hoskins and Karoly (1981);Simmons et al (1983)]. The question of how much,if any, of the observed low-frequency variability is inherently baroclinic in nature has never been really adressed.

In the study of the geographical dependence of the vertical structure of the geopotential height field, Blackmon et al (1979) indicated the existence of the baroclinic vertical structure on the cold, or lee side of the major mountain ranges such as the Rockies and the Tibetan plateau in a wide frequency domain. The major purpose of this study is to investigate the role of the highly baroclinic patterns play in the low-frequency variability of the geopotential height field.

Results of orthogonal rotated principal component analysis to the wintertime, Northern Hemisphere, 5-day mean sea-level pressure field [for details, readers are referred to Hsu and Wallace (1984)] showed five modes which are of dynamical interest. One can be identified with the well known North Atlantic Oscillation and another with the Pacific/North American pattern. 1000mb and 500mb spatial patterns associated with three baroclinic modes are shown in Fig.1-3. Common properties of these patterns can be summarized as follows. First, the spatial scale of the features on the surface map is much larger than that of the corresponding 500mb features. Secondly, different types of vertical structure are present in the same modes. It is evident, indicated by changes of the polarity between surface and 500mb patterns, that baroclinic vertical structure are present and located in the lee side of the major mountain ranges. These baroclinic modes explain the regions of low or even negative 500/1000mb corrlation in Fig.1 of Blackmon et al (1979). Circulation patterns associated with positive (by our definition) polarities of the baroclinic patterns are related to cold air masses over the continental interiors while negative polarities are generally associated with more zonal flows. One example is shown in Fig. 4.

Time evolutions associated with baroclinic modes are presented in forms of lag-correlation statistics in Fig.5-7. Distinctly different patterns of time evolution are observed in the lower and middle troposphere. The 500mb patterns

evolve, but rather weak, in a manner consistent with the concept of Rossby wave dispersion while the sea-level pressure patterns exhibit a distinctive eastward and/or equatorward phase propagation, parallel to contours of surface elevation along the northern and/or eastern side of the mountain ranges. It is even evident that the baroclinity is enhanced in substantial area in the lee of the high terrain with the propagation of the surface pattern.

It is hypothesized here that the equatorward phase propagation of features in the sea-level pressure field is probably due, in part,to the equivalent-beta effect associated with the terrain slope. The effets of the terrain slope in inducing baroclinity and phase propagation in the low-frequency fluctuations are observed only near and downstream from the regions of sloping terrain, and are restricted to the lower troposphere. Hence it appears that barotropic processes still play the dominant role in the dispersion of low-frequency wave energy on a planetary scale; evidently, these baroclinic effects assume first-order important only locally. Similar patterns to these baroclinic modes have not been obtained in modeling results, perhaps due to the inappropriate incorporation of the mountain effects in the bottom boundary condition of the models.

Reference

Blackmon, M. L., R. A. Madden, J. M. Wallace, and D. S. Gutzler, 1979: Geographical variations in the vertical structure of geopotential height fluctuations. J. Atmos. Sci., 36, 2450-2466.

Esbensen, S. k., 1983: A comparison of intermonthly and interannually teleconnections in the 700mb geopotential height field during the Northern Hemisphere winter. Submitted to Mon. Wea. Rev.

Hoskins, B. J., and D. J. Karoly, 1981: The steady linear response of a spherical atmosphere to thermal and orographic forcing. J. Atmos. Sci., 38, 1117-1318.

Hsu, H. H., and J. M. Wallace, 1984: On the vertical structure of wintertime teleconnection patterns. Submitted to J. Atmos. Sci.

Simmons, A. J., J. M. Wallace, and G. W. Branstator, 1983: Barotropic wave propagation and instability and atmospheric teleconnection patterns. J. Atmos. Sci., 40, 1363-1392.

Wallace, J. M., and D. S. Gutzler, 1981: Teleconnections in the geopotential height field during the Northern Hemisphere winter. Mon. Wea. Rev., 109,784-812.

Figure Caption

Fig.1. Correlation coefficient between Component 2 and sea-level pressure (left) , 500mb height (right); contour interval 0.1. Negative contours are dashed. The percentage of variance of the sea-level pressure field explained by this component is indicated.

Fig.2. As in Fig.1 except for Component 3.

Fig.3. As in Fig.1 except for Component 4.

FIG.4. Composite 1000mb (left) and 500mb (right) height maps for the 29 pentads with Component 3 >1.96 (upper panel) and Component 3 < -1.76 (lower panel). Contour interval 20m for 1000mb height and 60m for 500mb height.

Fig.5. Lag-correlation between Component 2 and sea-level pressure (lower panel) and 500mb height (upper panel) for lags of -1 pentad (left) and +1 pentad (right); contour interval 0.1. Negative contours are dashed.

FIG.6. As in Fig.5 except for Component 3.

Fig.7. As in Fig.5 except for Component 4.

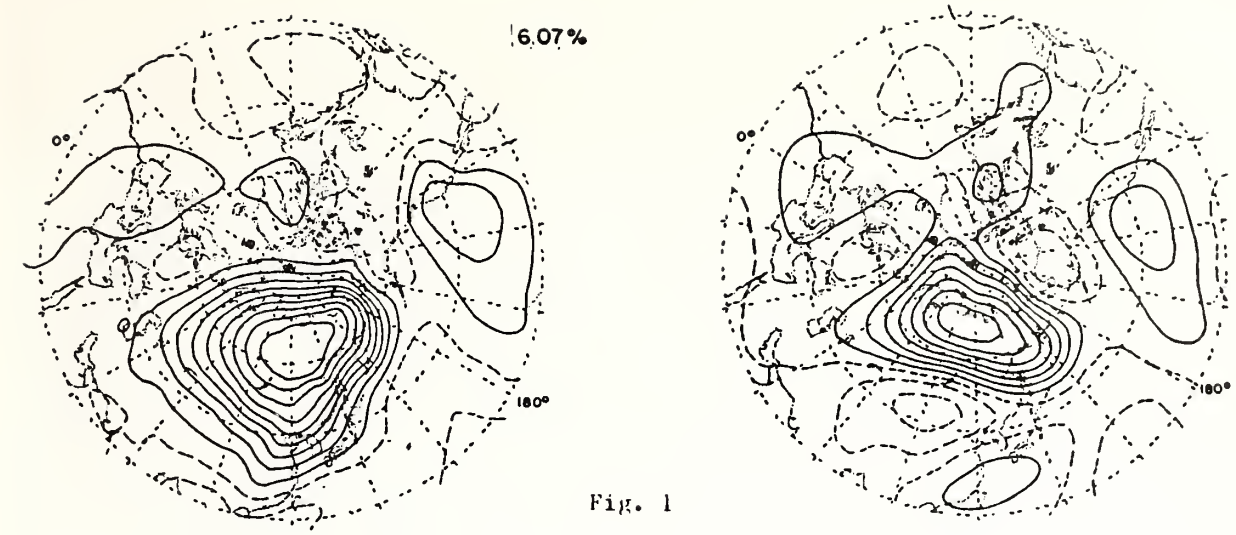

Fig. 1

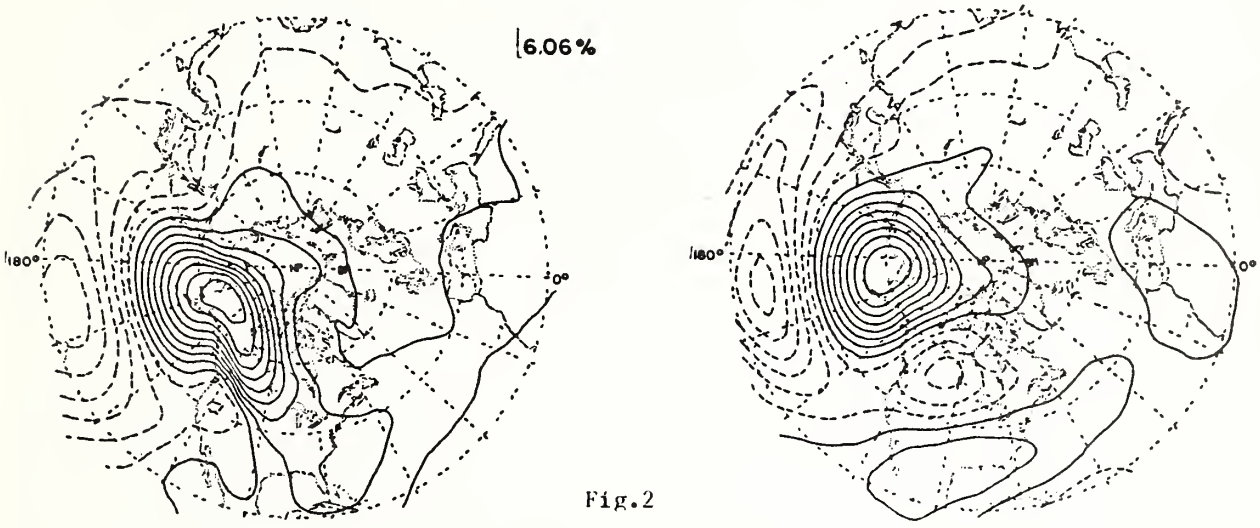

Fig.2

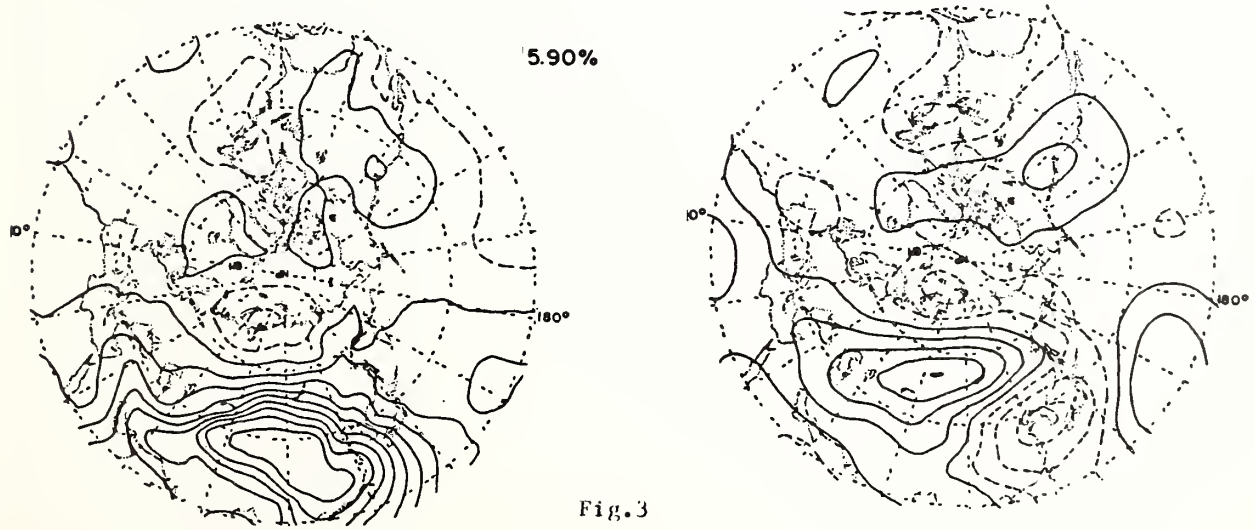

Fig.3

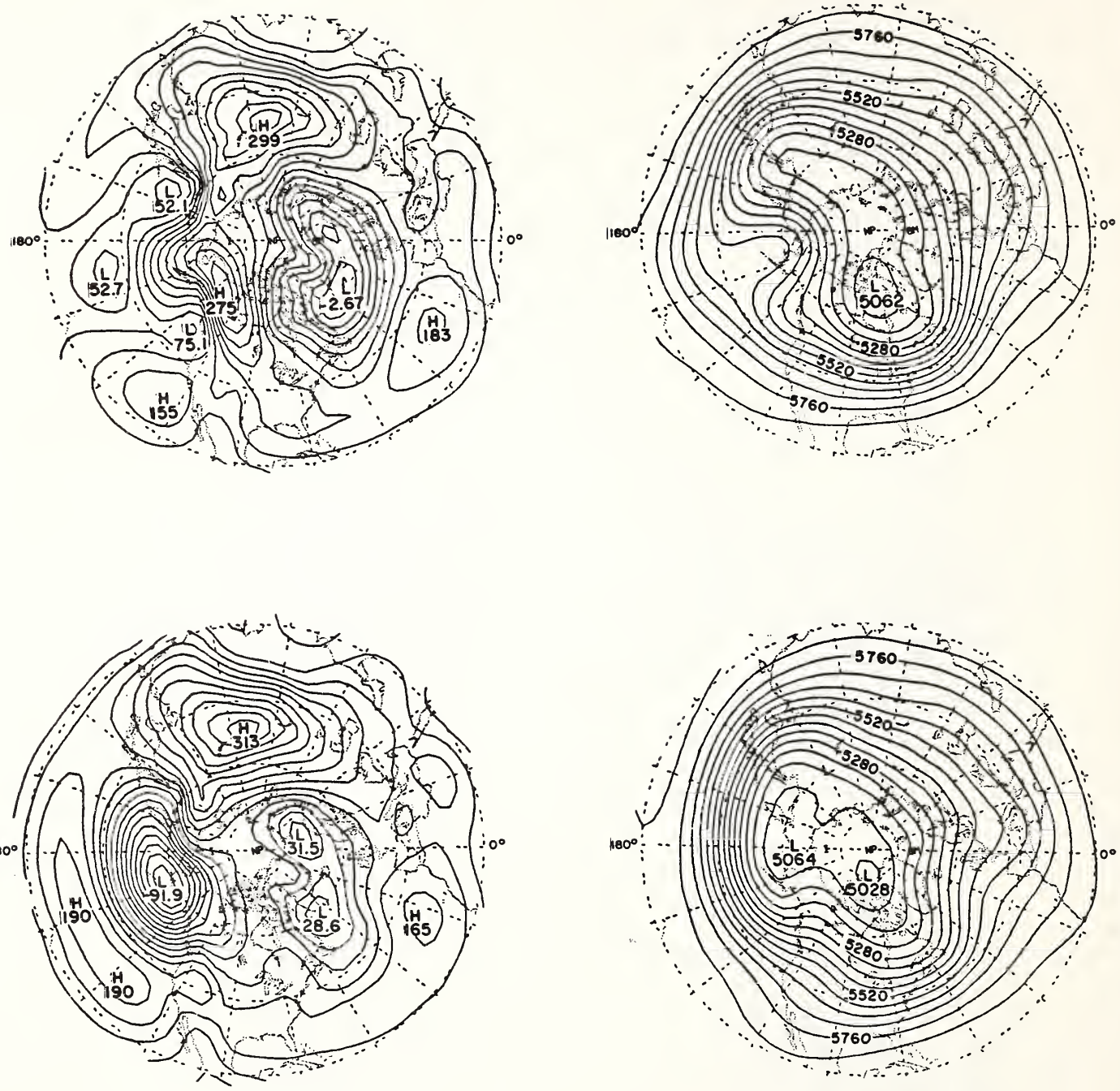
H
299
L
52.1
L
52.7
H
275
L
2.67
L
75.1
H
183
H
155
180°
0°
5760
5520
5280
L
5062
5280
5520
5760
H
313
L
31.5
L
91.9
H
190
L
28.6
H
165
H
190
180°
0°
5760
5520
5280
L
5064
L
5028
5280
5520
5760
180°
0°

Fig. 4

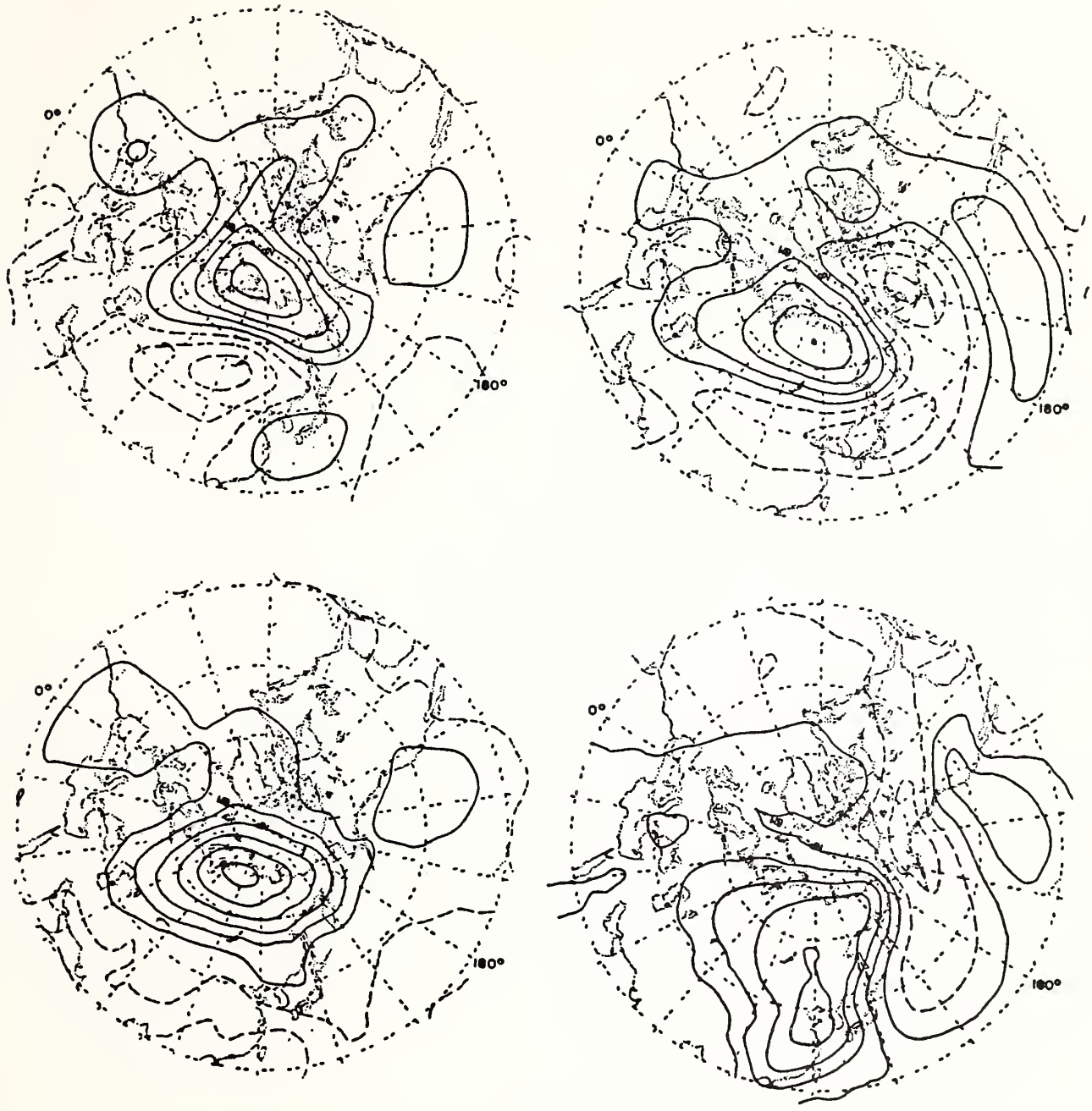

Fig. 5

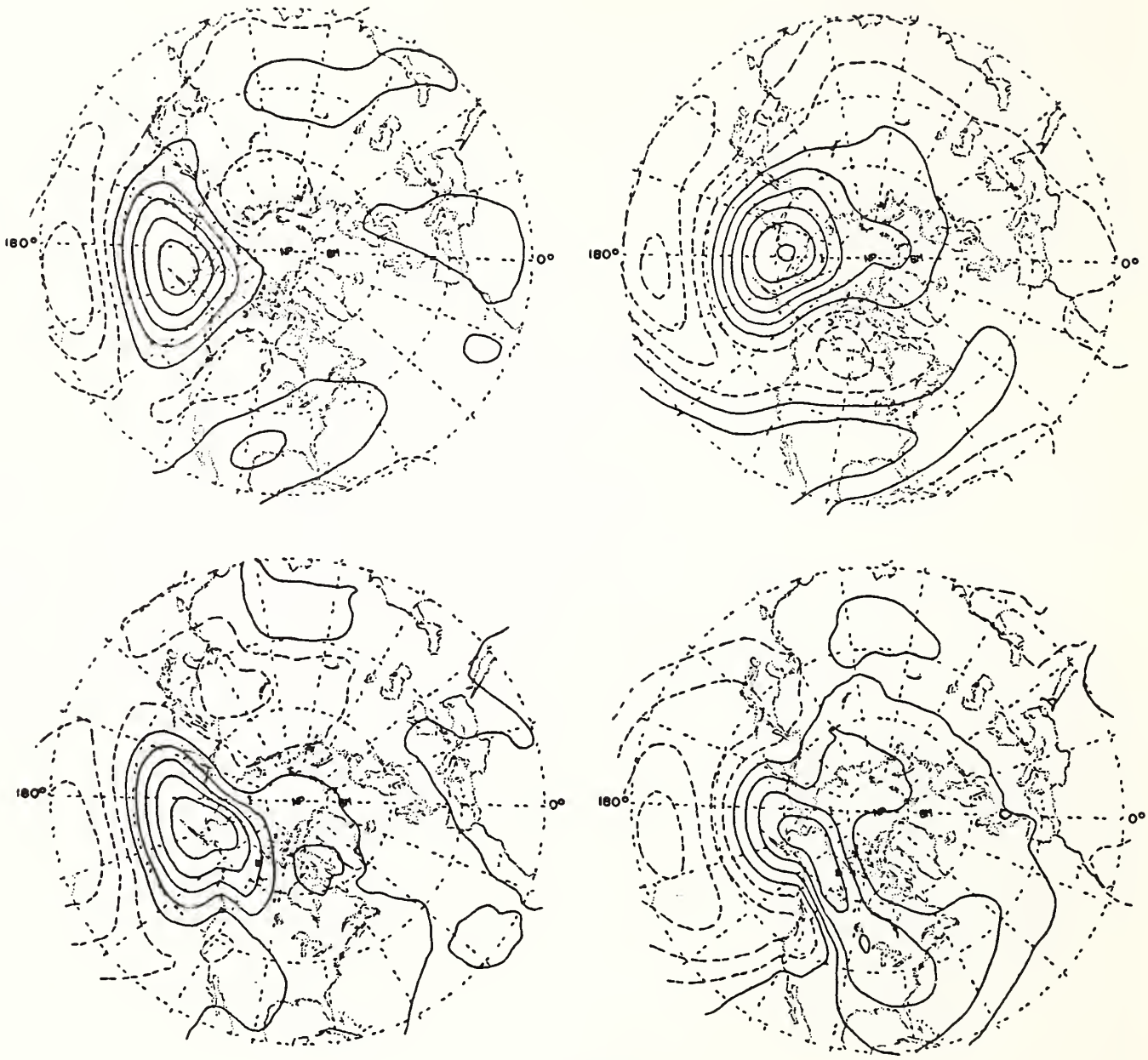

Fig. 6

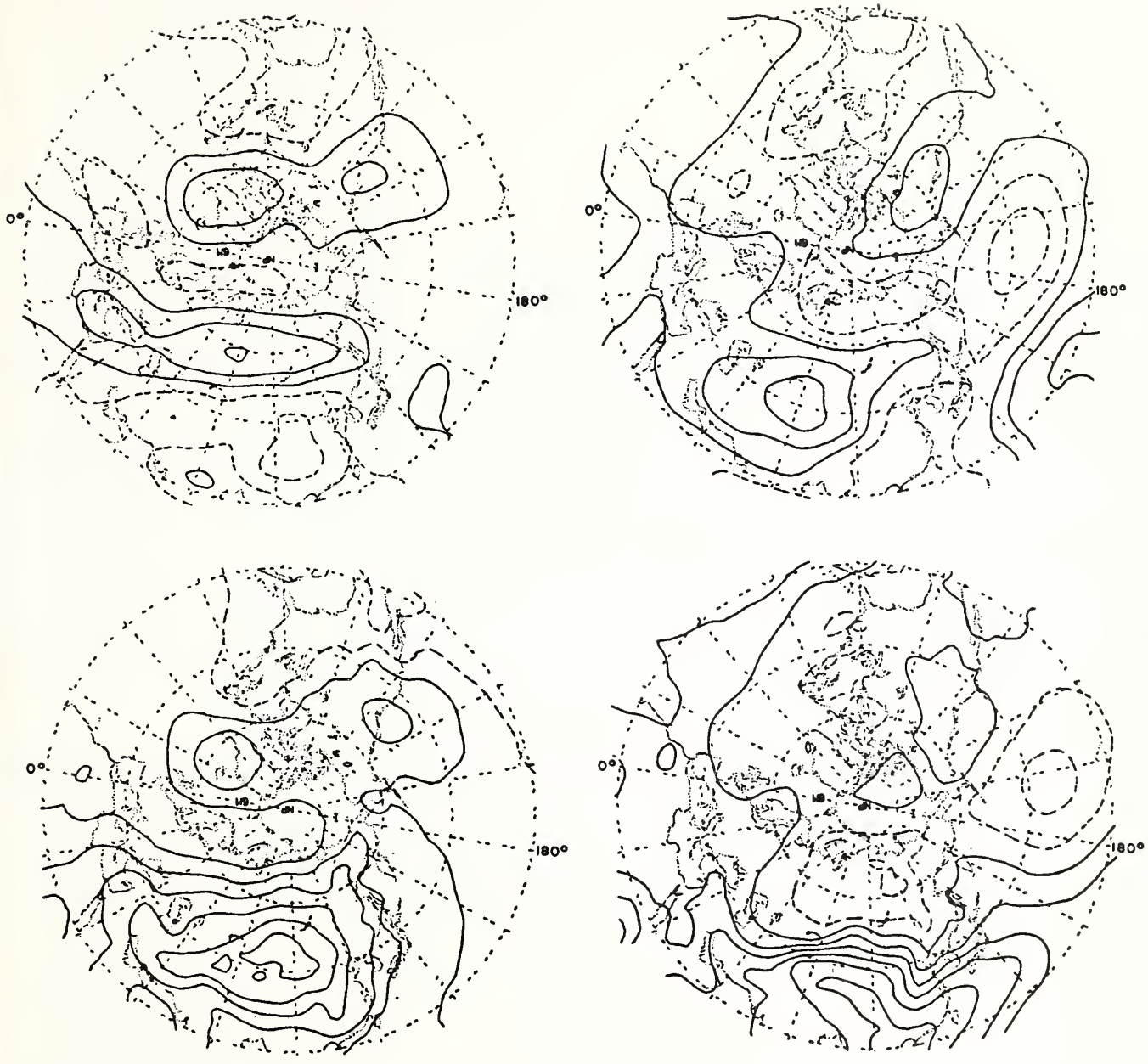

Fig. 7

SLOW FLUCTUATIONS OF THE TROPICAL CIRCULATION DURING THE FGGE YEAR

by

Rennie Selkirk

Department of Earth, Atmospheric & Planetary Science
Massachusetts Institute of Technology
Cambridge, MA 02139

This paper focuses on the fluctuations of the Walker circulation as reflected in the large scale divergent wind fields over the tropics and the subtropics during the FGGE Year, December 1978 through November 1979. Empirical orthogonal function (EOF) analysis is used to resolve the largest spatial and largest time scale variations in the fields of velocity potential at the 850 and 200mb levels computed from the analyzed winds of the ECMWF FGGE III-b data set. The EOF results presented here demonstrate that the 40-50 day time variations in both the Walker and Hadley cells are as important on the largest scale as the seasonal variability of the Hadley cell.

In this paper the term "Hadley Circulation" at a particular level will refer to the zonal mean of the meridional wind which can be derived from the meridional profile of the zonal mean velocity potential. The "Walker Circulation" is taken to refer to the divergent zonal wind derived from the asymmetric velocity potential. The FGGE 200mb mean velocity potential (waves 1-5) at the equator is shown in longitudinal profile in Figure 1, along with the mean divergent zonal wind field derived from it. Figure 1 clearly shows a strong Bjerknes-type Pacific Walker cell centered near 150°E, with eastward and westward directed branches encompassing nearly 3/4 of the equatorial zone; the weaker Atlantic cell is centered near 75°W.

Results from four separate semispectral EOF calculations are shown here, semispectral meaning that zonal Fourier coefficients on the latitudinal grid comprise the input fields. The velocity potential fields were derived from a 3.75° reduced-grid version of the ECMWF FGGE III-b data set prepared at NCAR. Each of the 730 twice-daily input fields were taken from Fourier decompositions of the derived global velocity potential fields along the 25 latitudes between 45° North and South; at each latitude only a low wave number truncation data subset was retained.

Figures 2 and 3 show the results of the first EOF calculation (EOF-a), in which the 200mb coefficients for waves 1-10 as well as the zonal mean were retained. The inclusion of the Hadley cell in these calculations is most apparent in the first mode which carries 32.6% of the variance. Both seasonal and intraseasonal variability is discernible in the time series of this mode. An additional 22.3% and 14.5% of the variance is contained in modes 2 and 3, which are clearly dominated by 40-50 day variability. For the most part, the spatial character of these two modes is wavenumber 1 and equatorially symmetric, and their EOF orthogonality places them roughly 90° out of phase; the time series are similarly out of phase.

The amplitude of mode 2 is slightly larger than that of mode 3, and with their approximate quadrature relationship in time and space, the combination of these modes produces a mixture of a standing oscillation and eastward wave propagation in the anomaly field. More on this later.

The second (EOF-b) and third (EOF-c) EOFs were performed on the 200 and 850mb velocity potential fields respectively for waves 1 through 5; the Hadley cell contributions were eliminated. Figures 4 and 5 show the spatial fields and time series for the 200mb azonal EOF and Figures 6 and 7 those for 850mb. Note the similarities between modes 2 and 3 of EOF-a and modes 1 and 2 of EOF-b. The restriction to Walker circulation variance effectively eliminates the variance due to the first mode of EOF-a as well as the seasonal variation and the small equatorial asymmetry of the next two modes in that calculation. What seasonal cycle remains in EOF-b is mostly contained in its third mode.

As in EOF-a, both the 200mb (EOF-b) and 850mb (EOF-c) calculations yield dominant modes whose time series and spatial functions are in approximate quadrature at wavenumber 1 and intraseasonal time scales. Figure 8 is a time lapse sequence which shows eastward propagation of divergent anomalies at 200mb on the equator. To obtain this figure the first and second modes from EOF-b, which in this calculation contain the overwhelming bulk of the 40-50 day variance, were band-passed with a filter centered at 40 days. The spatial functions along the equator of modes 1 and 2 were then weighed by the resultant time series and summed to obtain a velocity potential profile. From this a divergent wind anomaly profile was obtained by the usual derivative relationship:

$$U_d = \frac{1}{a\cos\phi} \frac{\partial \chi}{\partial \lambda}$$

A simple staggered finite difference approximation was used here. These wind anomalies were added to the mean wind profile to obtain the resultant wind. (It should be pointed out here that the EOF-b truncation after wave 5 smooths out some of the wind features revealed by higher truncations. Nonetheless, it does not change the eastward motion discussed below.

The wind anomalies shown in solid in the figure display an intermittent eastward propagation: negative (positive) anomalies appear over the Indian Ocean and amplify in place in the westward (Indian Ocean) branch of the Pacific Walker cell to as much as $\pm$ 2 meters/sec. As the Indian Ocean anomaly begins to decay, a second anomaly peak will begin to amplify in the center of the eastward branch of the Pacific Walker cell at 150°W. After it reaches its peak, the anomaly proceeds eastward into the Atlantic water, where weaker anomalies are found. The eastward propagation of anomalies can change the sign of the Walker circulation in some localities, but it is important to note that the eastward branch of the Pacific Walker cell never moves more than 5° from its maximum at 150°W.

The second important characteristic of the results in Figures 4-7 is the complementarity of the 850 and 200mb EOF modes: their spectral functions are extremely similar in shape with only a sign change and their time series are almost identical. The superposition of divergent regions of 200mb upon convergent regions at 850mb implies that the divergent circulations on large spatial and long-term scales are vertically phase locked by latent heating. As a further test on this result a fourth EOF (EOF-d) was done combining the

200 and 850mb variance from waves 0 through 5 together. The resultant modes 1 and 2 are shown in Figures 9a and 9b. There is little to distinguish between 850 and 200mb spatial functions for modes 1 and 2 in EOF-d from their counterparts in modes 1 and 2 of EOF-b and EOF-c.

In summary, the intraseasonal variability in the Walker circulation of the FGGE year as revealed in the ECMWF analysis is dominated by eastwardly moving anomalies on the 40-50 day time scale. There is evidence for this motion at both high and low levels; in fact, upper and lower level velocity potential variability is strongly coupled 180° out-of-phase.

Figure Captions

1. Longitudinal profile of the FGGE time mean (December 1, 1978 - November 30, 1979) 200mb velocity potential (dashed line) and divergent zonal wind (solid line) at the equator from ECMWF FGGE III-b. Velocity potential in units of 10^6meters^2/second, wind in meters/second. The velocity potential profile is comprised of waves 1-5 only.

2. Spatial functions for EOF-a, 200mb velocity potential, waves 0-10. From top, the mean field (December 1, 1978 - November 30, 1979), first, second and third EOFs. Negative contours dotted, bold contour interval $2x10^6$ m^2/s.

3. Time series associated with (from top) EOF modes 1, 2 and 3 from EOF-a. These time series are smoothed with a three-point binomial filter.

4. Spatial functions for EOF-b, 200mb azonal velocity potential, waves 1-5. Hadley cell fluctuations are not included. From top, the mean field (same time period as EOF-a), first, second and third EOF modes. Negative contours dotted, labelled contour at intervals of $1x10^6$ m^2/s.

5. Time series associated with (from top) EOF modes 1, 2, and 3 from EOF-b. These time series are not smoothed.

6. As in Fig. 4 but for EOF-c, 850mb.

7. As in Fig. 5 but for EOF-c, 850mb.

8. Time lapse sequence of Walker circulation fluctuations during the summer monsoon season. Starting with May 14 and reading across, each panel is a longitudinal profile at the equator as in Fig. 1 of the divergent zonal wind at 200mb at successive 5-day intervals starting May 14. Anomalies (solid lines) are the sum of modes 1 and 2 from EOF-b (waves 1-5) weighted by 40-day bandpassed versions of their corresponding time series. The mean profiles (dotted lines) are identical to the divergent wind profile in Fig. 1. The dashed lines are the sum of the anomaly and mean fields.

9a. Mode 1 from EOF-d, combined 850/200mb EOF with waves 1-5. From top, spatial function at 200mb, spatial function at 850mb, and time series.

9b. As in 9a, but for Mode 2 from EOF-d.

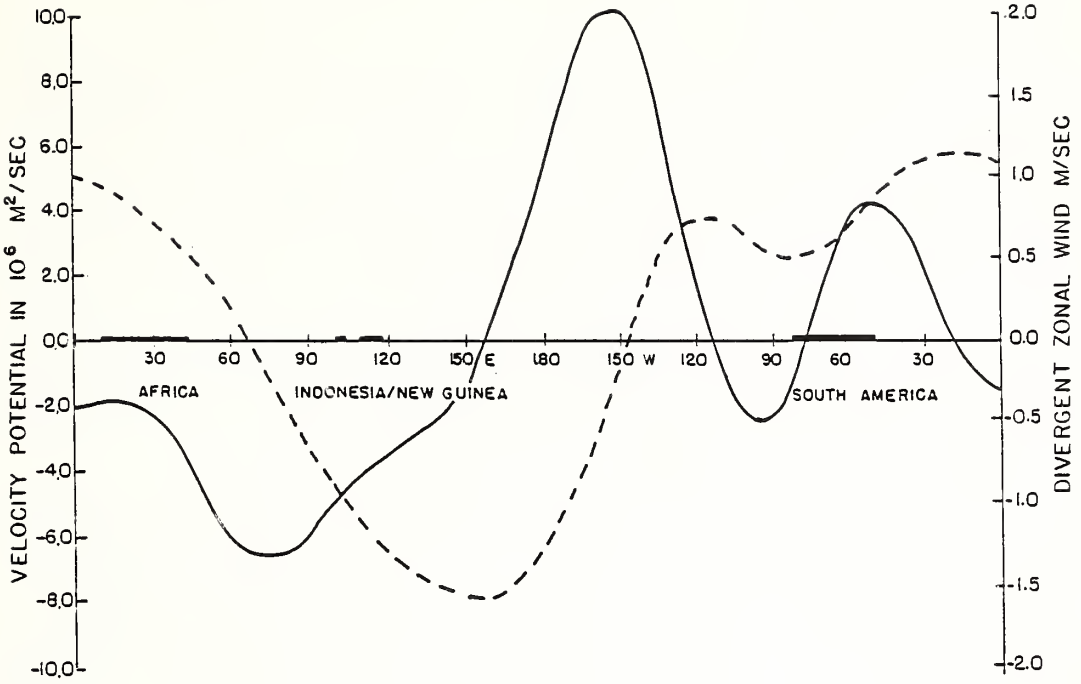
VELOCITY POTENTIAL IN 10^6 M^2/SEC
DIVERGENT ZONAL WIND M/SEC
10.0
8.0
6.0
4.0
2.0
0.0
-2.0
-4.0
-6.0
-8.0
-10.0
2.0
1.5
1.0
0.5
0.0
-0.5
-1.0
-1.5
-2.0
30
60
90
120
150 E
180
150 W
120
90
60
30
AFRICA
INDONESIA/NEW GUINEA
SOUTH AMERICA

Fig. 1

200 mb FGGE Velocity Potential EOF
Waves 1-10

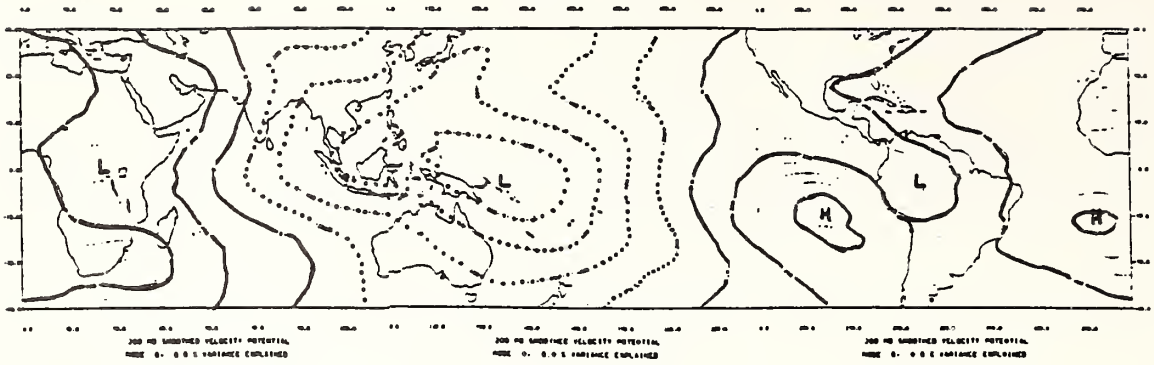

Mean Field

Mode 1
32.6%

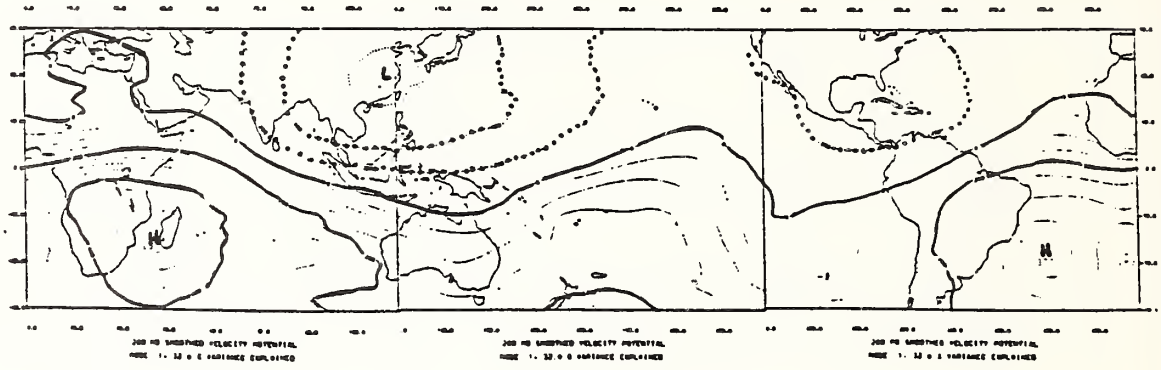

Mode 2
22.3%

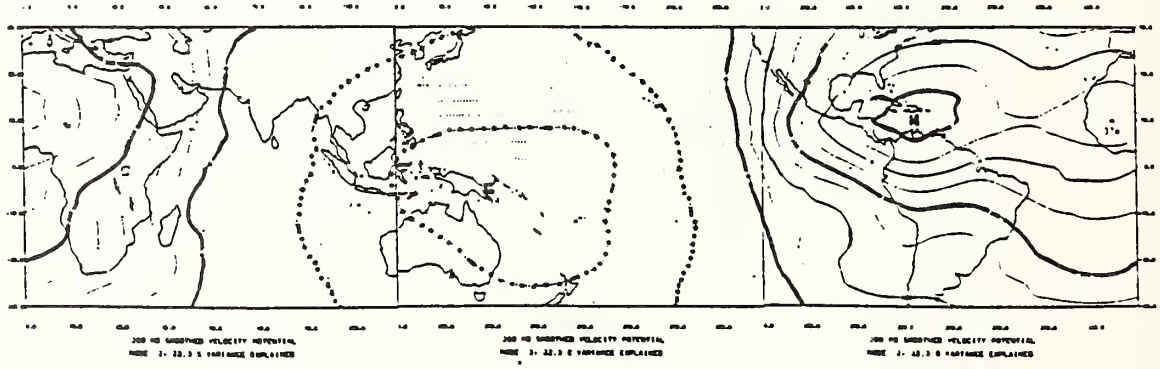

Mode 3
14.5%

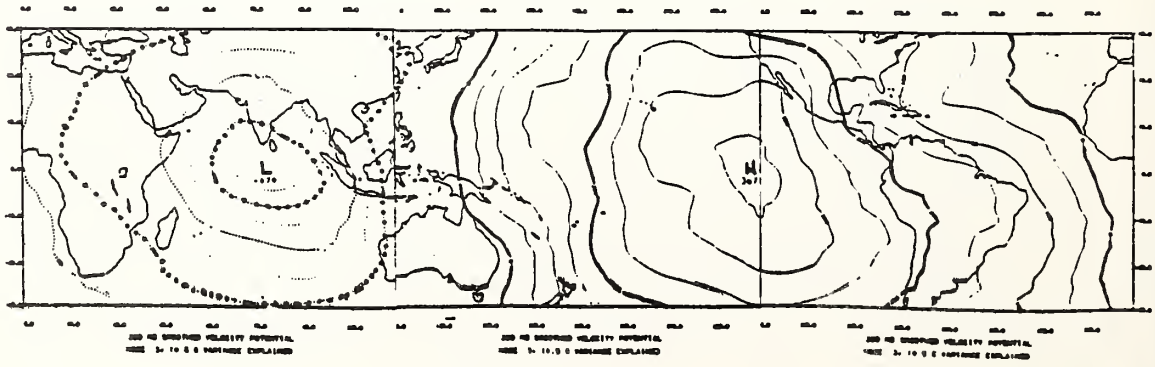

Fig. 2

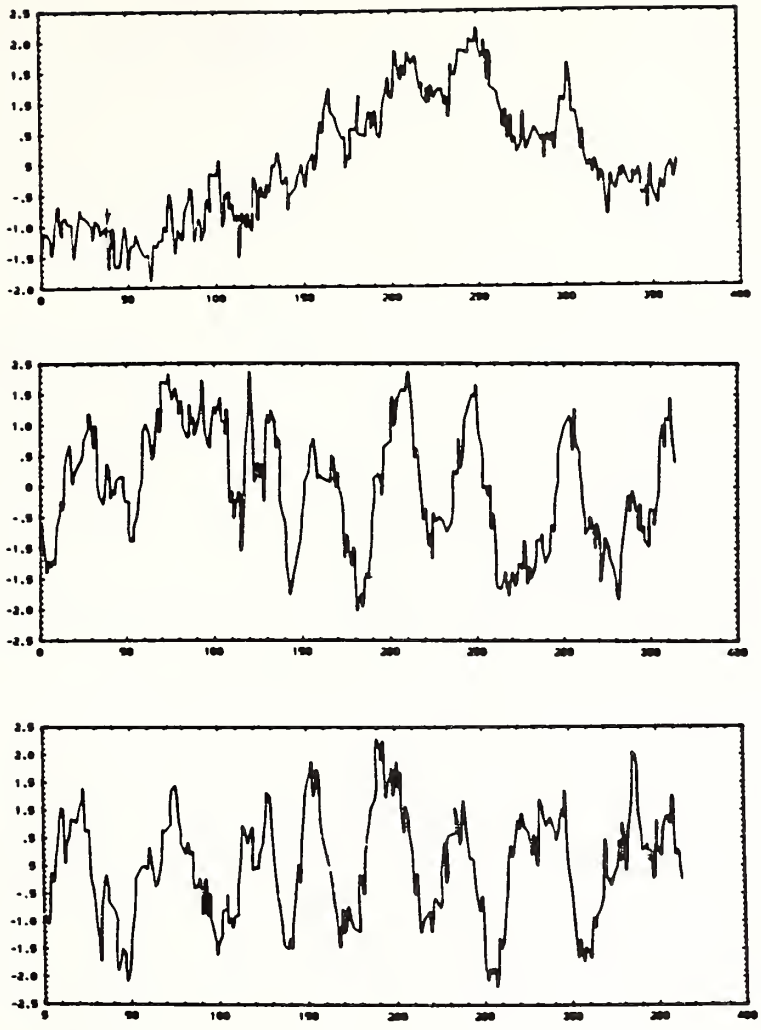

Fig. 3

200 mb Velocity Potential EOF
Waves 1-5

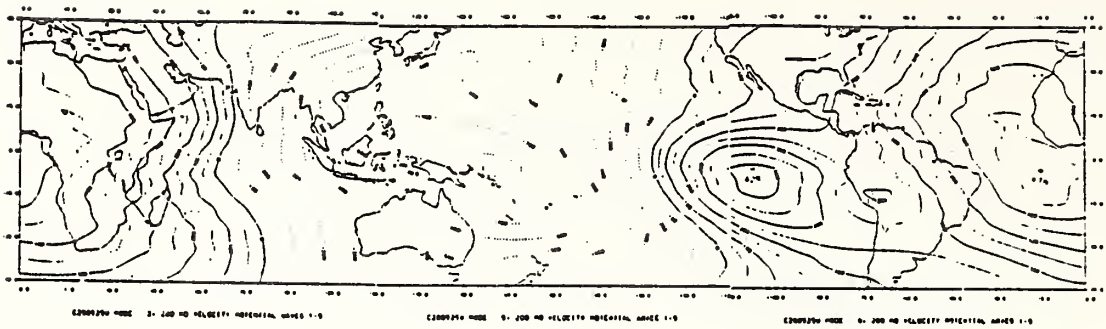

Mean Field

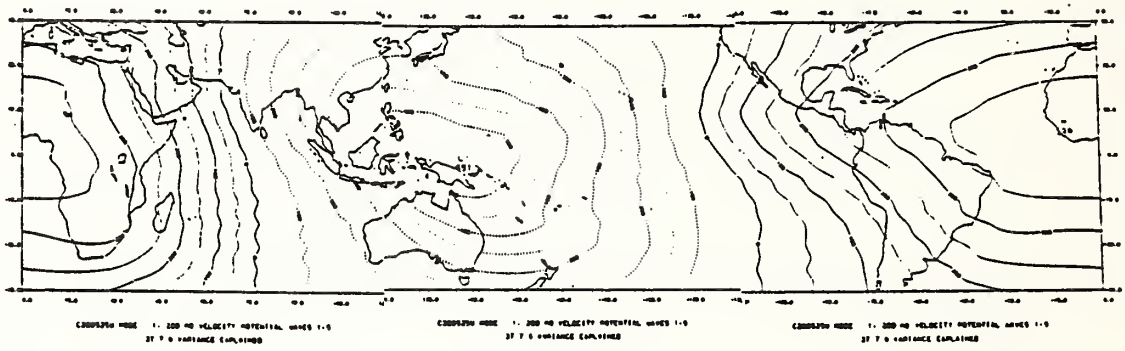

Mode 1
37.7 %

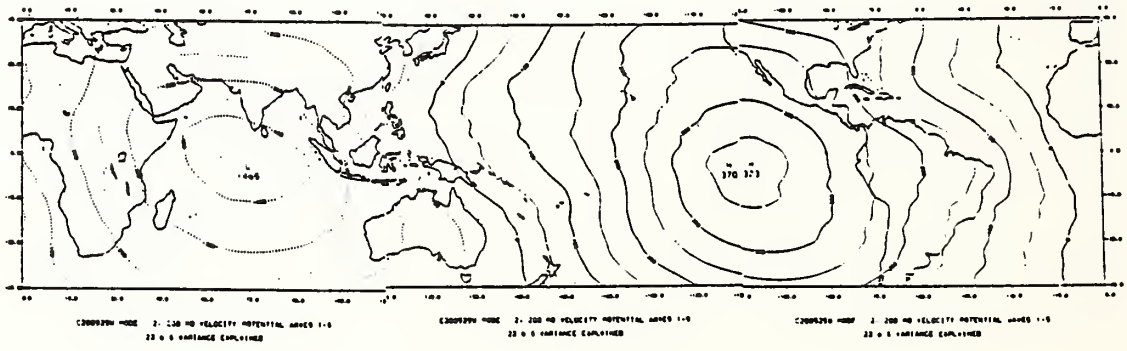

Mode 2
23.6 %

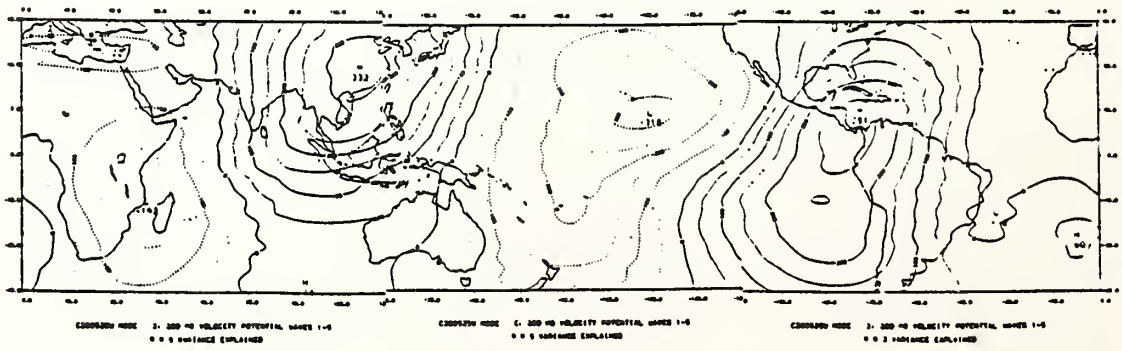

Mode 3
9.9 %

Fig. 4

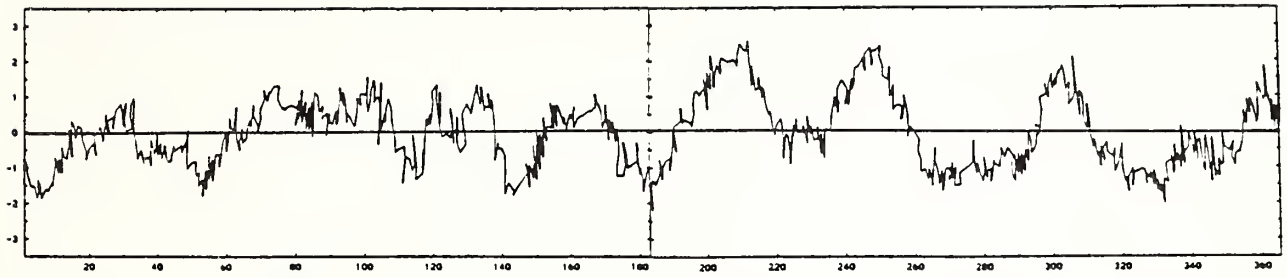

MODE 1 TIME SERIES DEC 1 78 - NOV 30 79

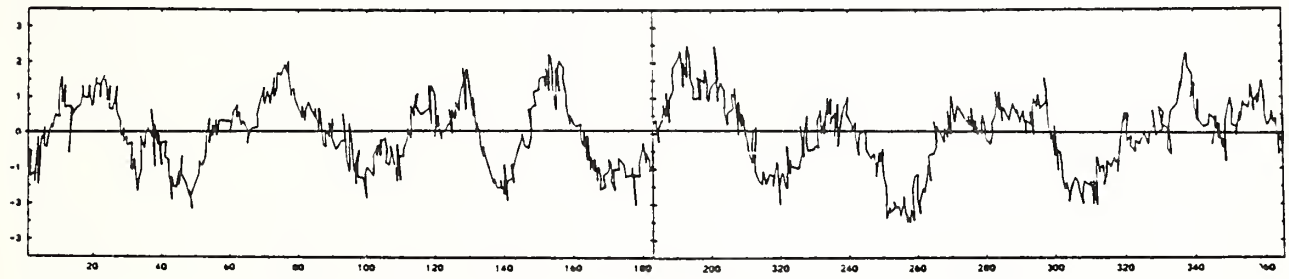

MODE 2 TIME SERIES DEC 1 78 - NOV 30 79

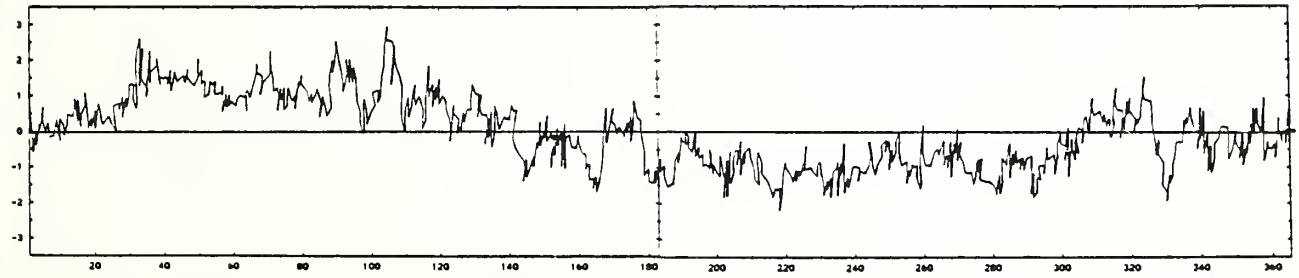

MODE 3 TIME SERIES DEC 1 78 - NOV 30 79

Fig. 5

850 mb Velocity Potential EOF
Waves 1-5

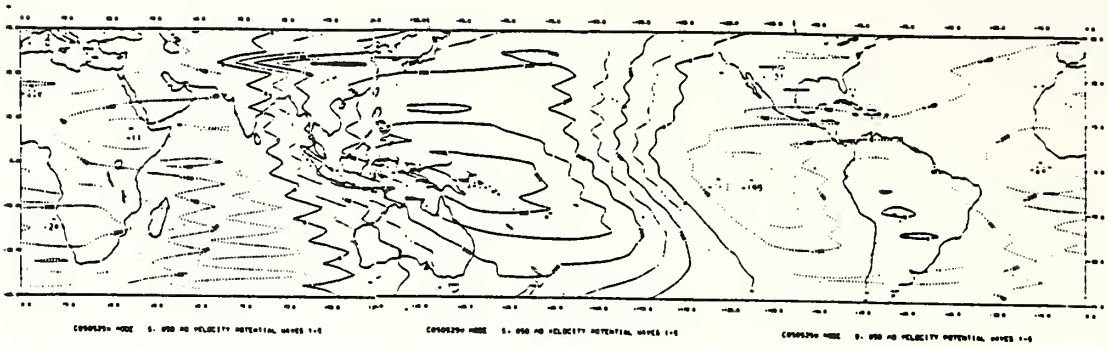

Mean Field

Mode 1
30.3 %

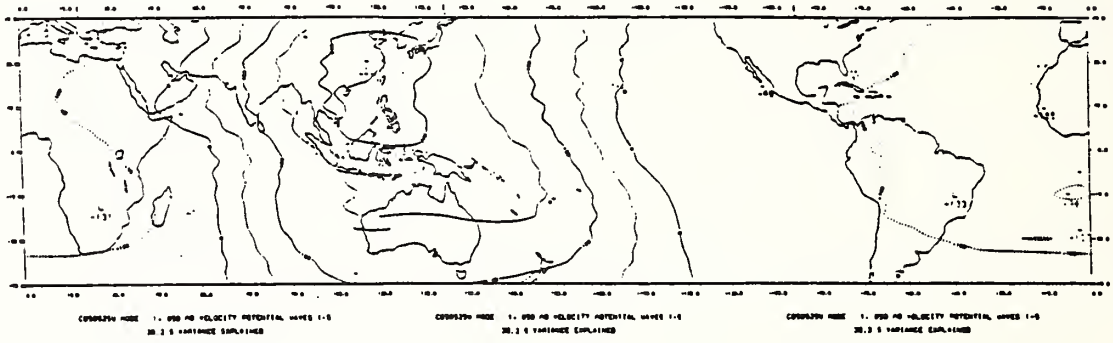

Mode 2
19.2 %

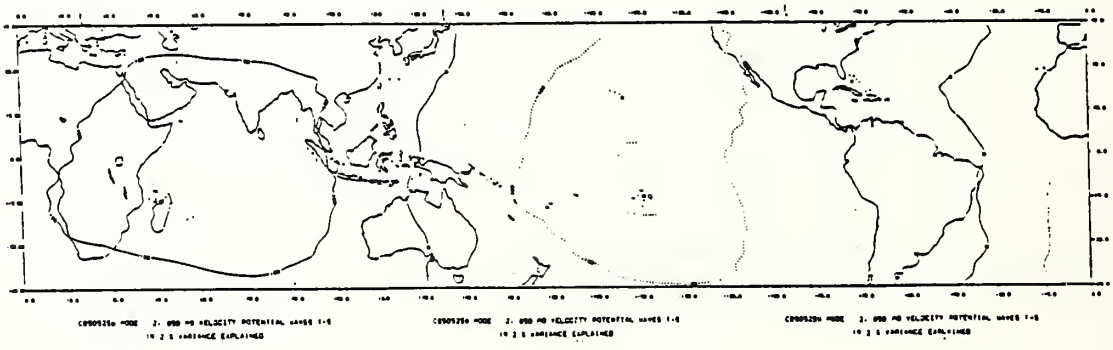

Mode 3
11.7 %

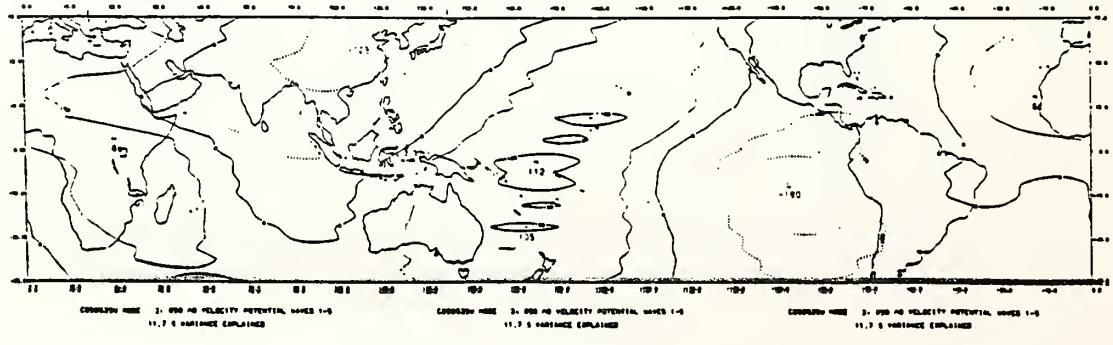

Fig. 6

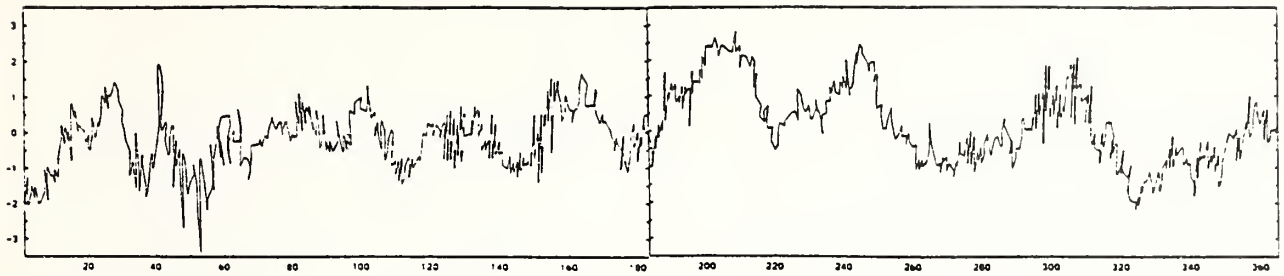

Mode 1

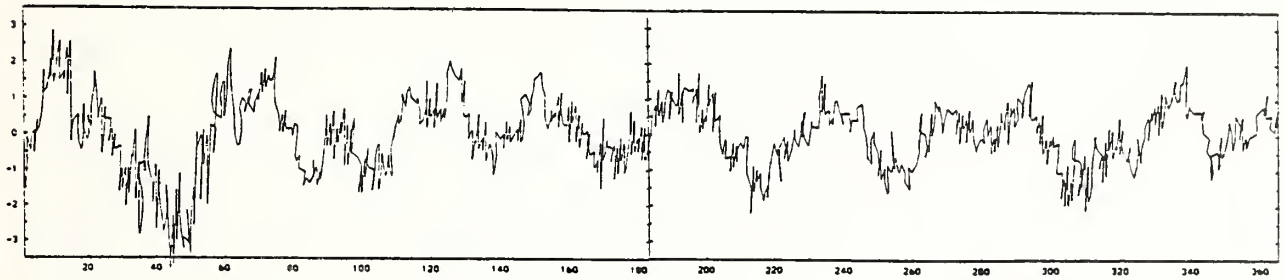

Mode 2

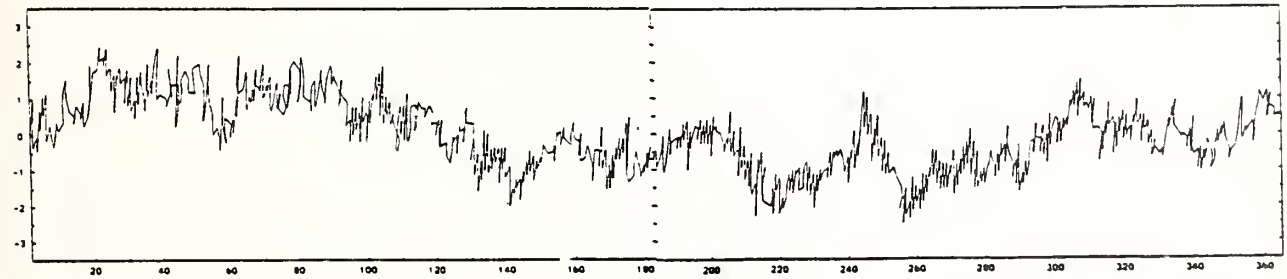

Mode 3

Fig. 7

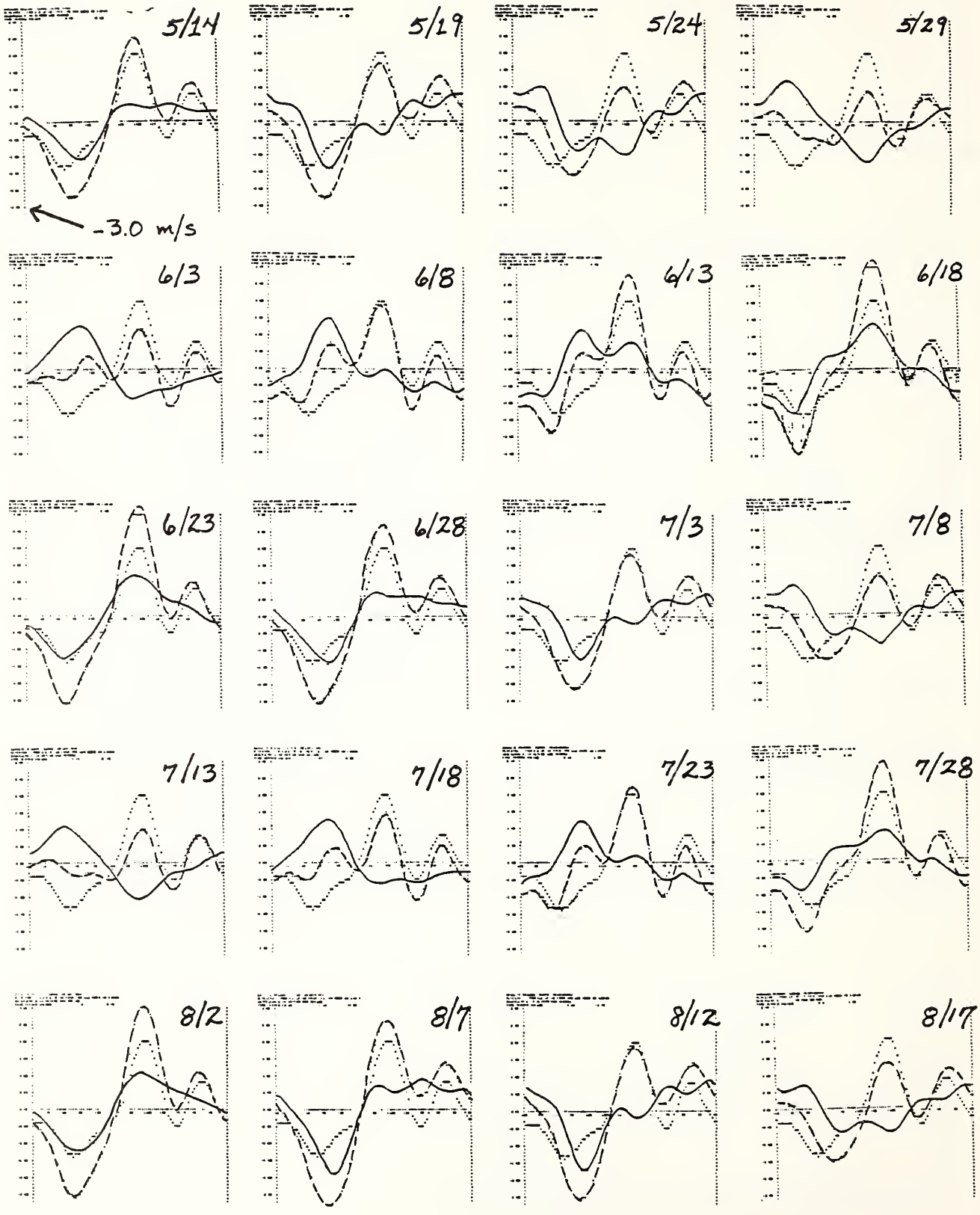
5/14
5/19
5/24
5/29
-3.0 m/s
6/3
6/8
6/13
6/18
6/23
6/28
7/3
7/8
7/13
7/18
7/23
7/28
8/2
8/7
8/12
8/17

Fig. 8

200/850 Combined Velocity Potential EOF

Waves 1-5

Mode 1

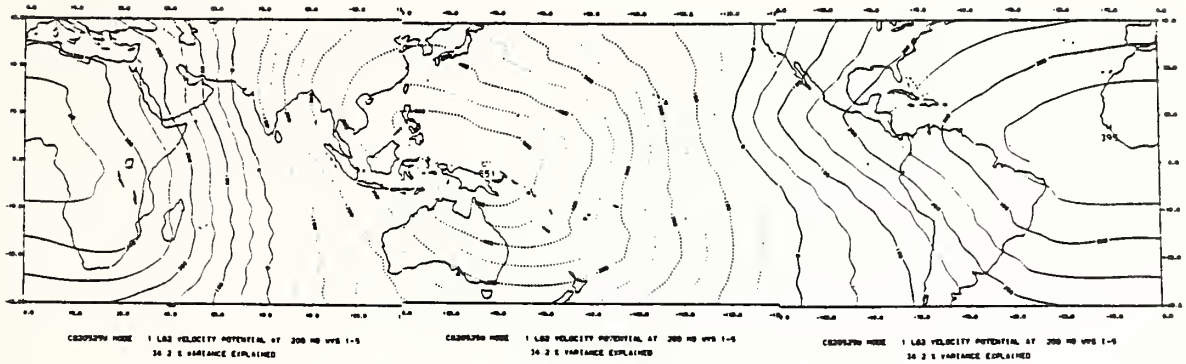

200 mb

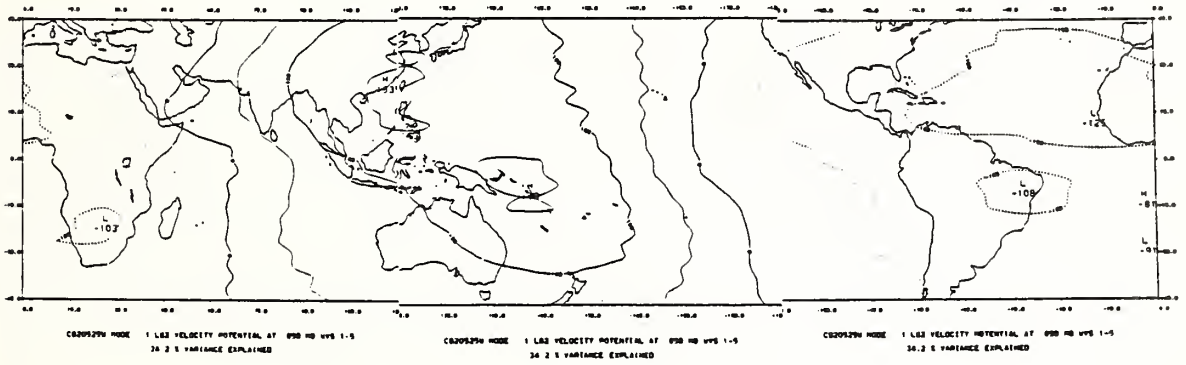

850 mb

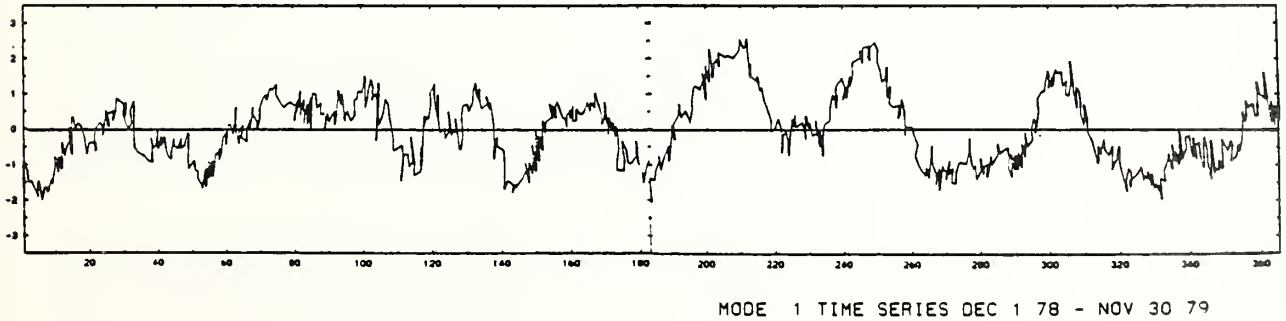

MODE 1 TIME SERIES DEC 1 78 - NOV 30 79

Fig. 9a

850/200 Combined Velocity Potential EOF

Waves 1-5
Mode 2

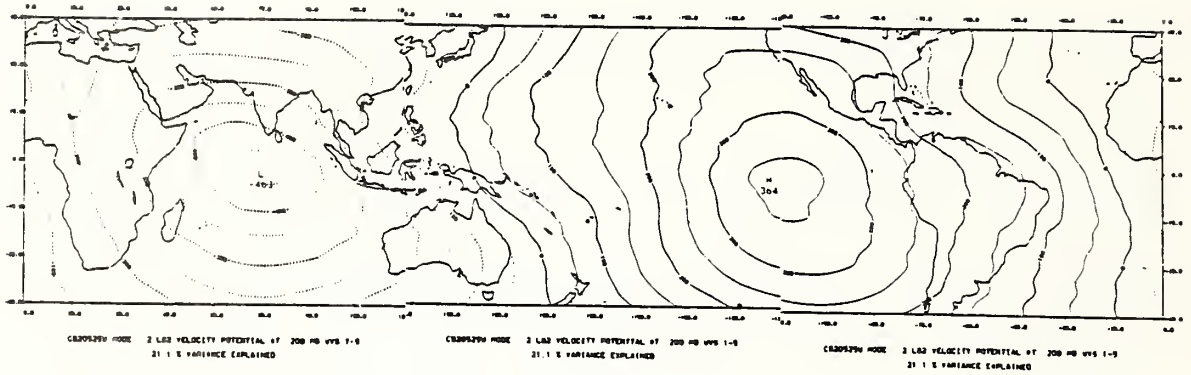

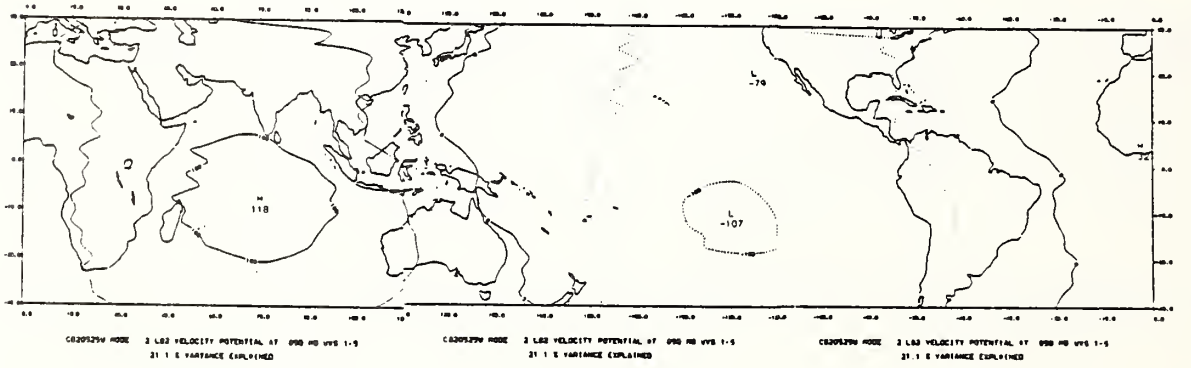

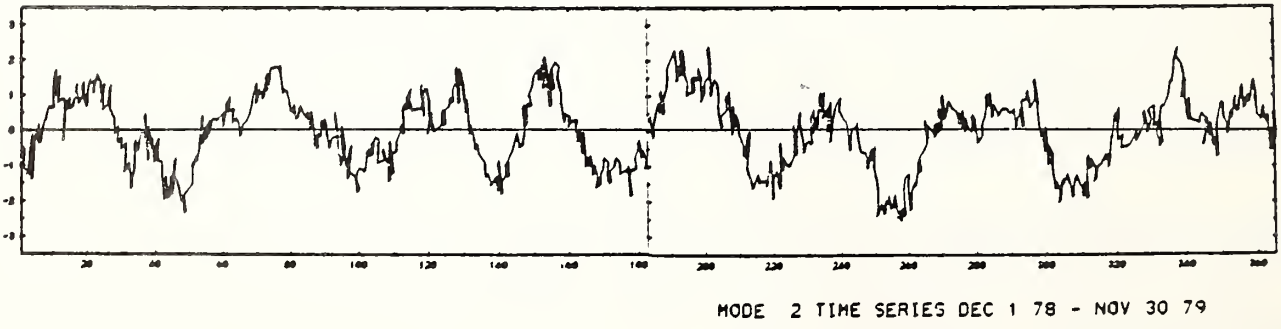

Fig. 9b

Very Anomalous Behavior of Outgoing Longwave Radiation in the Tropics in 1983-84: Aftermath of ENSO?

Jay S. Winston
Department of Meteorology
University of Maryland
College Park, MD 20742

The extreme anomalies of the outgoing longwave radiation (OLR) over the tropical Pacific during the 1982-83 ENSO event were discussed at last year's Workshop and in several papers describing this most unusual event. As sea surface temperatures, the Southern Oscillation index (SOI), and other circulation features returned to more normal conditions in the second half of 1983, OLR anomalies in the tropics also became less extreme. By winter 1983-84, however, strong OLR anomalies developed over the tropical Pacific and the Indian Ocean and generally persisted into spring 1984. These anomalies in tropical cloudiness and precipitation were accompanied by some pronounced anomalies of flow at 200 mb and 850 mb, but Pacific sea surface temperatures and the SOI exhibited values generally close to their normals.

The contrasts between the OLR anomaly patterns for the winters of 1982-83 and 1983-84 (Fig. 1) are quite striking over the tropical Pacific. In general the anomalous pattern reversed from 1982-83 to 1983-84, with the equatorial dry zone reasserting itself strongly, and cloudiness and precipitation becoming stronger than normal over the western Pacific. Anomalies in the South Pacific Convergence Zone also reversed from their positive values in 1982-83. Note, however, that the Indian Ocean anomalies were generally negative in both years, but became much stronger on the north side of the equator in 1983-84. The 200 mb anomalous tropical circulations of the two winters were generally very different (Fig. 2). Easterly anomalous flow dominated the tropics over the whole Eastern Hemisphere in 1983-84, while rather weak anomalous flow occurred over the Western Hemisphere. The usual association of negative OLR anomalies and anomalous easterlies at 200 mb held rather well over the western Pacific and the Indian Ocean in equatorial regions in 1983-84, but the positive anomalies over the central Pacific dry zone were generally not accompanied by the usual 200 mb anomalous westerlies.

The OLR anomaly charts for the springs of 1983 and 1984 (Fig. 3) both exhibit some very major, large-scale features over the tropics. In many regions the anomalies of 1984 were the opposite of those in 1983 (western Pacific, northern Indian Ocean, and the Atlantic), but some notable similarities of anomalies were observed at and north of the equator over the central Pacific and over the Indian Ocean south of the equator. Negative anomalies occurred in both years south of the equator over the east central Pacific, but these were much diminished in 1984 from the extraordinary values of 1983. As for the two winters, the 200 mb anomalous circulations over the tropics in

the two springs were also quite different (Fig. 4). In general there was much persistence in the 200 mb anomalous flow over the tropics from winter to spring in each of the years. Easterly anomalous flow again dominated equatorial regions over the Eastern Hemisphere in spring 1984, but the easterlies also extended across the entire Atlantic corresponding with the strong negative OLR anomalies observed across the Atlantic and into northern Brazil.

The time longitude evolution of monthly OLR anomalies for 1982-84 (as well as back to 1979) at the equator is shown in Fig. 5. The remarkable pattern over the Pacific in 1982-83, with its pronounced eastward shift over the central and eastern Pacific, has been discussed frequently by CAC staff and others. This pattern came to a rather rapid termination in the summer of 1983 and only minor anomalies were observed along the equator into autumn of 1983. By early winter the strong anomalous pattern of positives in the central Pacific and negatives in the western Pacific and Indian Oceans emerged and then generally persisted through April 1984. Note also the rapid development of negative anomalies over the Atlantic by early spring 1984. It is interesting that the patterns of 1982-83 and 1983-84 were not precisely out of phase over the Pacific region. Note the occurrence of strong positive anomalies near 160°E in the winters and springs of both years.

If one examines all of Fig. 5, including the years 1979-82, it is quite apparent that the strong and persistent patterns of 1982-83 and 1983-84 were not matched in the earlier years. The OLR anomalies in these years and also from June 1974 to February 1978 (not shown) exhibited smaller anomalies with considerable month-to-month and season-to-season variability. This is illustrated further for some selected grid points along the equator (for seasonal values only) in Figs. 6-9. Note that the most extreme OLR anomalies of each sign occurred at each of these grid points in the years 1982-83 and 1983-84 (except at 0°, 90°E in 1982-83). This is not quite the case for the anomalous zonal wind at 200 mb (also shown in Figs. 6-9), but in general there is good correspondence between the anomalous zonal wind and the OLR anomalies.

Fig. 10 sums up this anomalous behavior of the OLR anomalies along the equator since 1974 by showing the time variation of the spatial standard deviation of equatorial values of the seasonal OLR anomaly. The extreme variability in 1982-83 is most notable, of course. Although half as extreme as 1982-83, the standard deviations in 1983-84 are also far above any of the other standard deviations in all other years. Although the greatest standard deviations occurred in the winter and spring seasons in 1982-83 and 1983-84, autumn 1982 and summers 1982 and 1983 also exhibited greater variation at the equator than autumns or summers of any of the other years.

In conclusion, the very anomalous seasonal behavior of OLR and circulation in the tropics in both 1982-83 and 1983-84 raises some intriguing, but presently unanswerable questions: 1) Is the anomalous behavior of 1983-84 some sort of natural aftermath of the extreme ENSO event of 1982-83? and 2) Does the more anomalous behavior of the past few years signify the beginning of a new climatic regime of more extreme behavior in the tropics over the next several years as compared to much of the 1970's?

Acknowledgments

This material is based upon work supported by the National Science Foundation under Grant No. ATM-8215090. Compilations of data and some figures were supplied by the Climate Analysis Center.

Figure Legends

Fig. 1. Anomalies of outgoing longwave radiation (OLR) for winter 1982-83 (top) and winter 1983-84 (bottom). Anomaly isopleths are drawn at intervals of 15 Wm^{-2}; dashed lines for positive values, thin solid lines for negative values, and heavy solid lines for zero values. Anomalies are calculated relative to a base period extending from June 1974 through November 1983 (no data were available from March through December 1978). (See "Atlas of Outgoing Longwave Radiation Derived from NOAA Satellite Data" by Janowiak, Krueger, Arkin, and Gruber, NOAA Atlas No. 6, Silver Spring, Md., January 1985).

Fig. 2. Anomalies of 200 mb streamfunction for winter 1982-83 (top) and winter 1983-84 (bottom). Contour interval is $4x10^6$ m^2s^{-1}. Anomalies are calculated relative to a base period extending from March 1968 through February 1984.

Fig. 3. Anomalies of OLR for spring 1983 (top) and spring 1984 (bottom). See legend to Fig. 1.

Fig. 4. Anomalies of 200 mb streamfunction for spring 1983 (top) and spring 1984 (bottom). Contour interval for spring 1984 is $5x10^6m^2s^{-1}$. Otherwise legend to Fig. 2 applies.

Fig. 5. Longitude-time variation of monthly mean OLR anomalies at the equator from January 1979 at the top to April 1984 at the bottom. Longitude scale goes from 0° at the left margin eastward to 180° near the center and ends at 20°E on the right margin. Isopleths are drawn at intervals of 10 Wm^{-2}, solid lines for zero and positive values and dashed lines for negative values.

Fig. 6. Time variation of seasonal anomalies of OLR (dashed) and zonal wind (solid) at the equator and 150°W.

Fig. 7. Time variation of seasonal anomalies of OLR (dashed) and zonal wind (solid) at the equator and 120°E.

Fig. 8. Time variation of seasonal anomalies of OLR (dashed) and zonal wind (solid) at the equator and 90°E.

Fig. 9. Time variation of seasonal anomalies of OLR (dashed) and zonal wind (solid) at the equator and 40°W.

Fig. 10. Time variation of spatial standard deviation of seasonal OLR anomaly within the equatorial circle in Wm^{-2}.

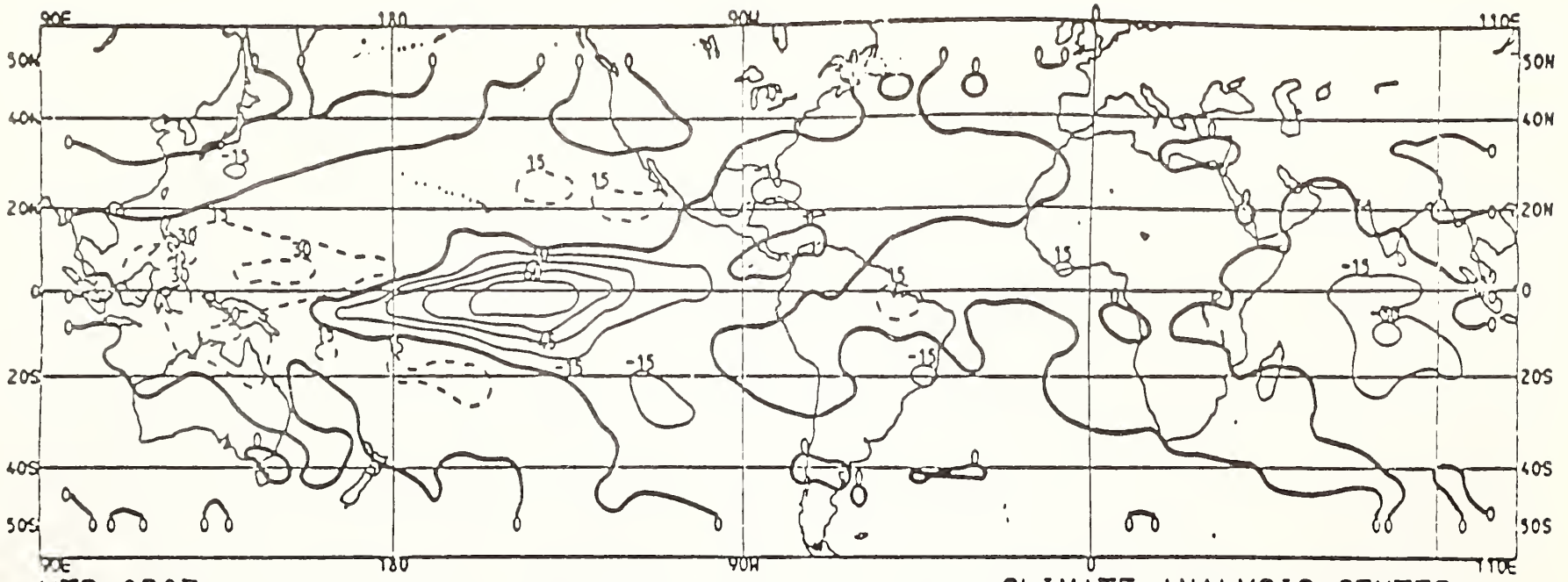
WTR 8283
ANOMALY
CLIMATE ANALYSIS CENTER

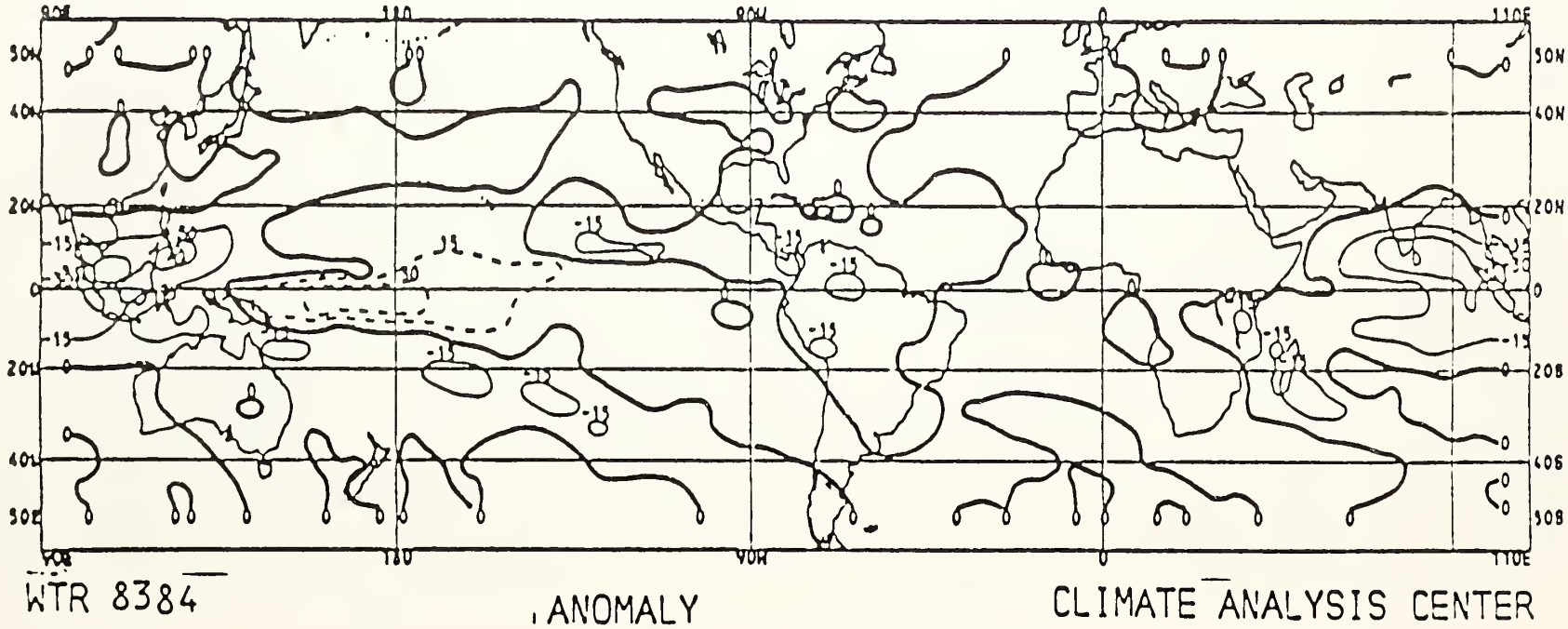
WTR 8384
ANOMALY
CLIMATE ANALYSIS CENTER

Fig. 1

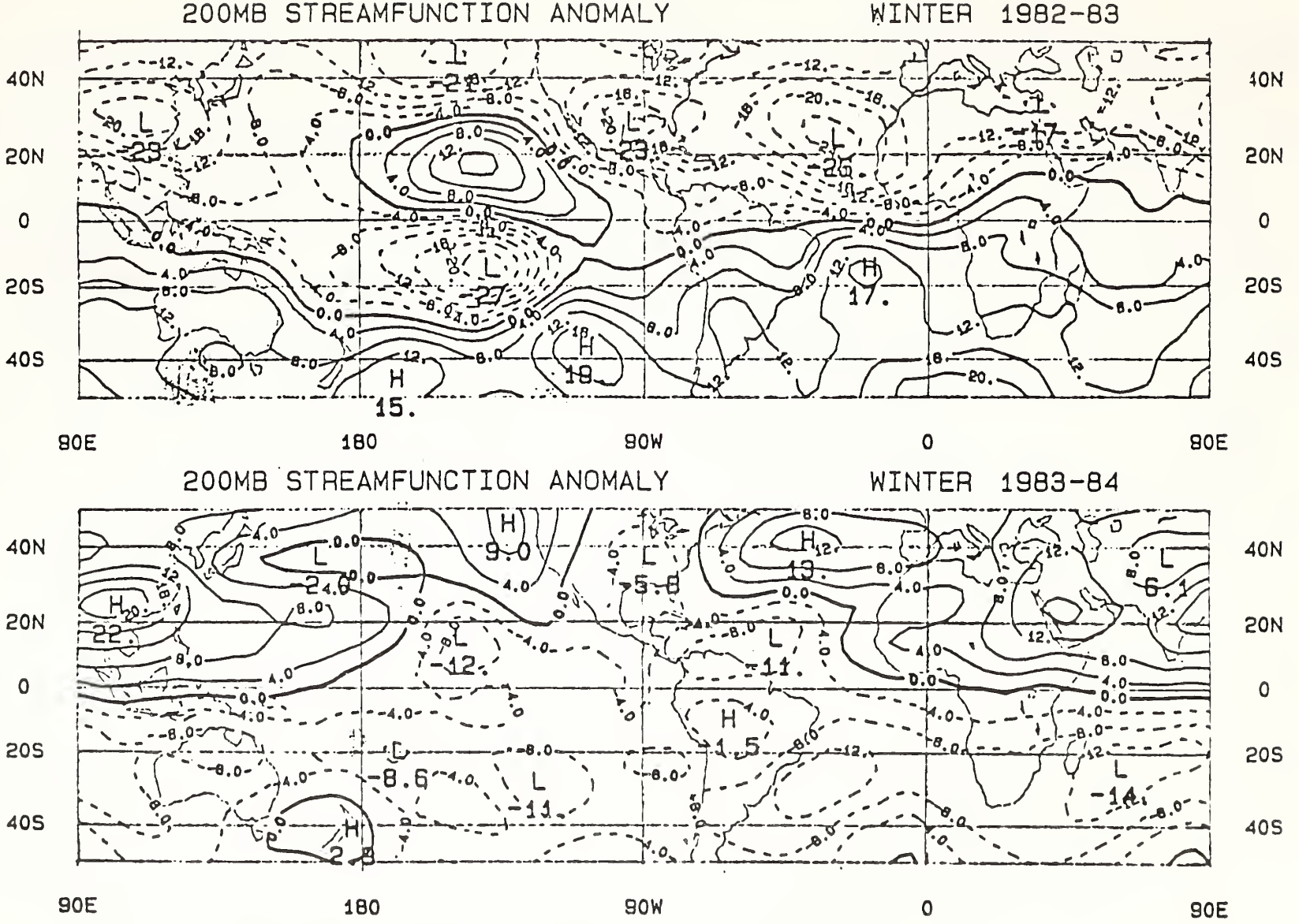
200MB STREAMFUNCTION ANOMALY
WINTER 1982-83
40N
20N
0
20S
40S
90E
180
90W
0
90E
200MB STREAMFUNCTION ANOMALY
WINTER 1983-84
40N
20N
0
20S
40S
90E
180
90W
0
90E

Fig. 2

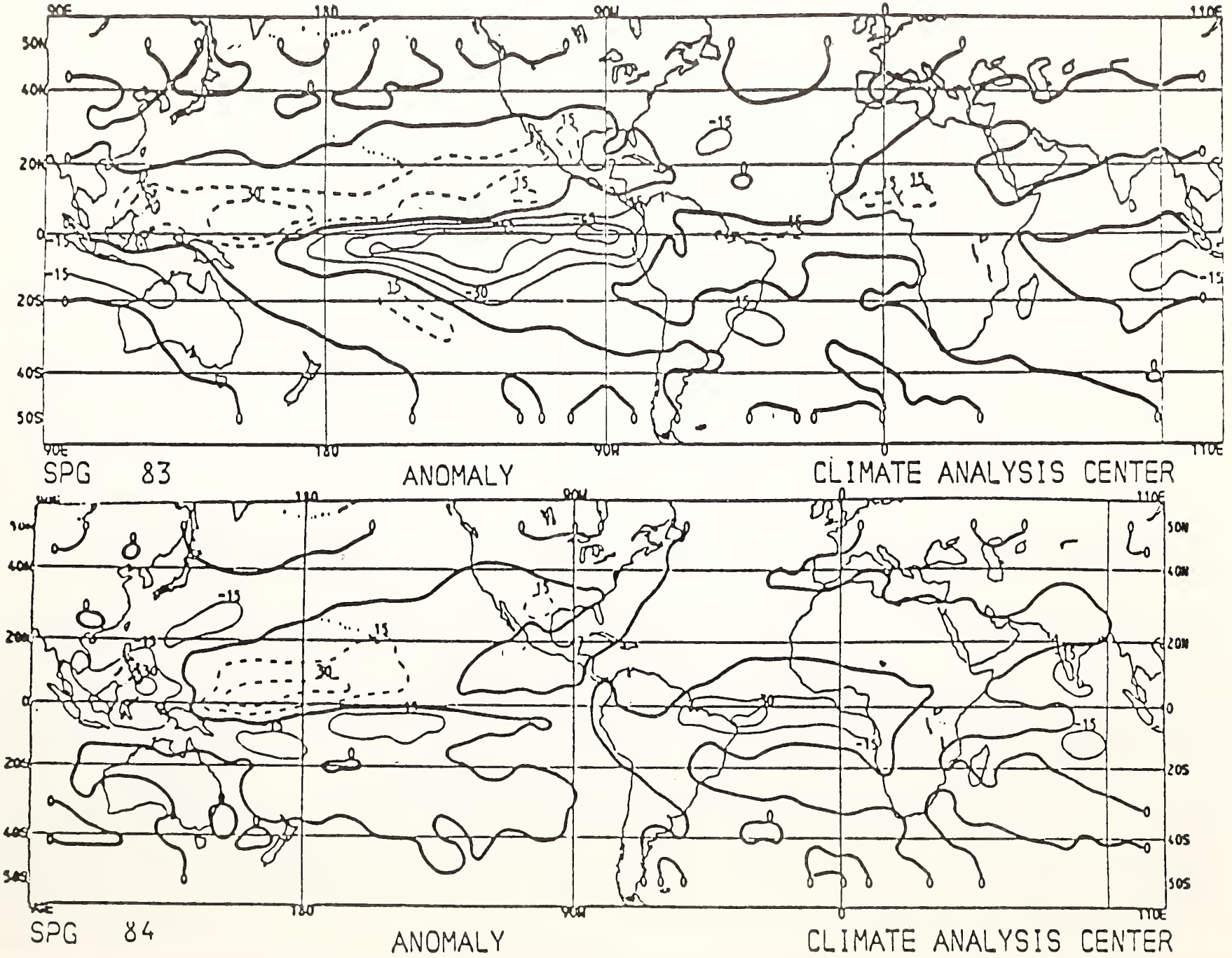
SPG 83
ANOMALY
CLIMATE ANALYSIS CENTER
SPG 84
ANOMALY
CLIMATE ANALYSIS CENTER

Fig. 3

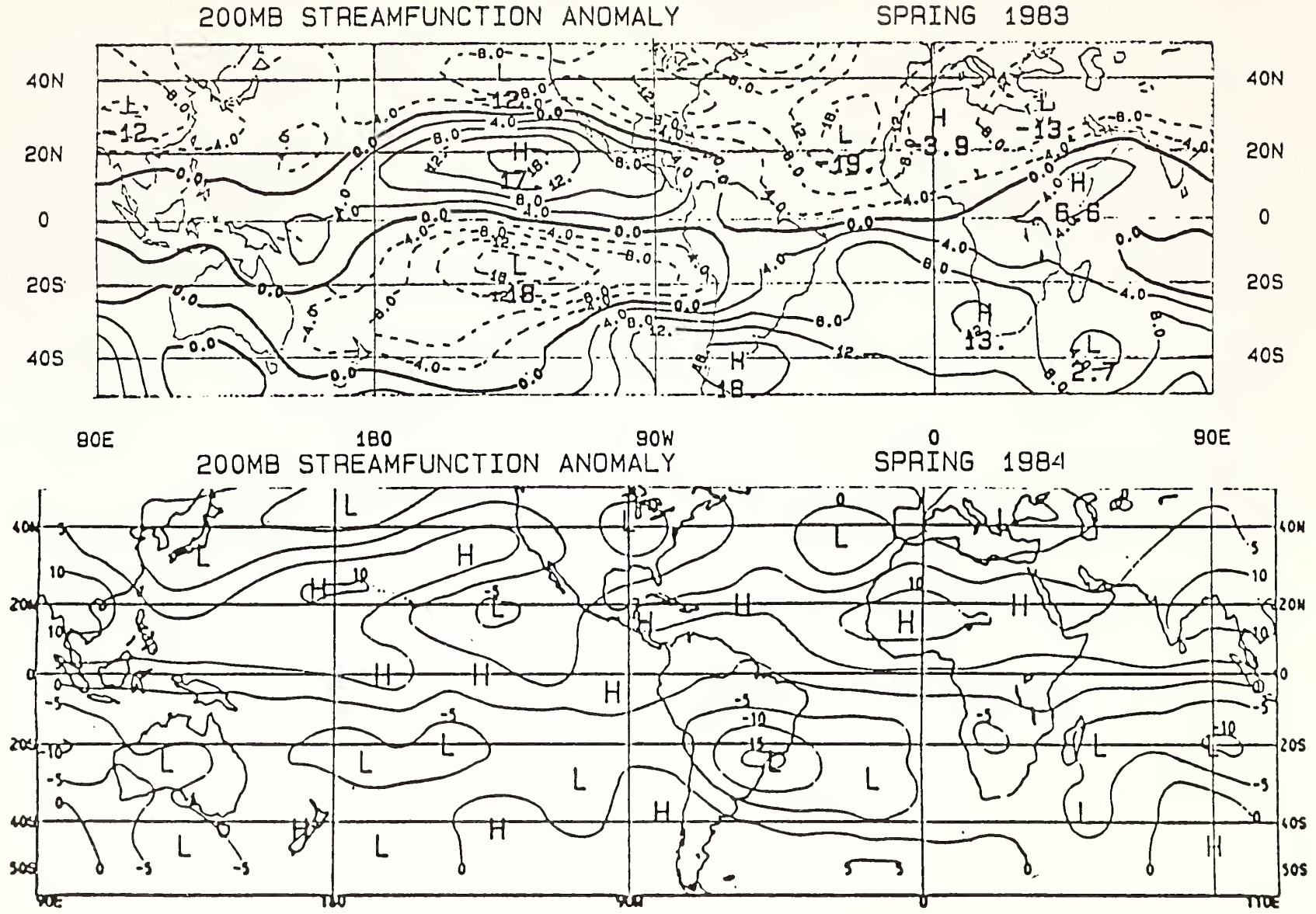
200MB STREAMFUNCTION ANOMALY
SPRING 1983
40N
20N
0
20S
40S
90E
180
90W
0
90E
200MB STREAMFUNCTION ANOMALY
SPRING 1984

Fig. 4

0 20E 40E 60E 80E 100E 120E 140E 160E 180 160W 140W 120W 100W 80W 60W 40W 20W 0 20E
JAN 79
APR
JUL
OCT
JAN 80
APR
JUL
OCT
JAN 81
APR
JUL
OCT
JAN 82
APR
JUL
OCT
JAN 83
APR
JUL
OCT
JAN 84
APR

Fig. 5

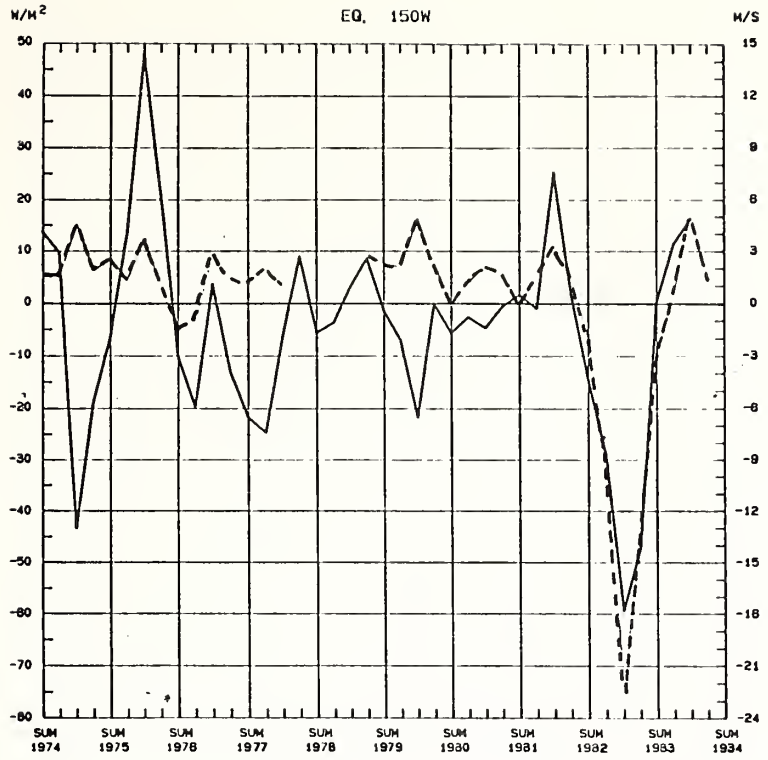
W/M²
EQ. 150W
M/S
50
40
30
20
10
0
-10
-20
-30
-40
-50
-60
-70
-80
15
12
9
6
3
0
-3
-6
-9
-12
-15
-18
-21
-24
SUM 1974
SUM 1975
SUM 1976
SUM 1977
SUM 1978
SUM 1979
SUM 1980
SUM 1981
SUM 1982
SUM 1983
SUM 1984
OLR ANOMALY
U ANOMALY

Fig. 6

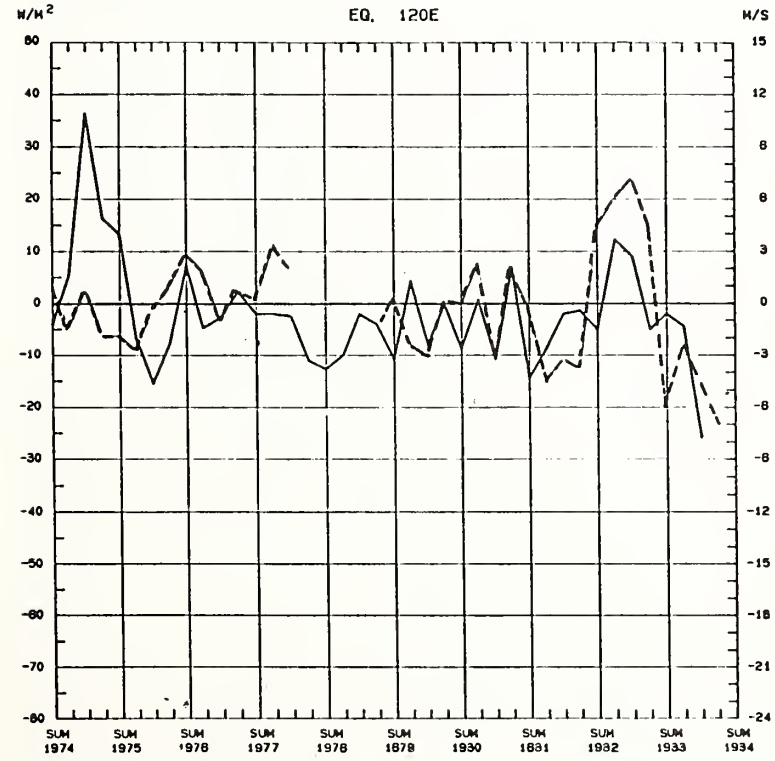
W/M²
EQ. 120E
M/S
60
40
30
20
10
0
-10
-20
-30
-40
-50
-60
-70
-80
15
12
9
6
3
0
-3
-6
-9
-12
-15
-18
-21
-24
SUM 1974
SUM 1975
SUM 1976
SUM 1977
SUM 1978
SUM 1979
SUM 1980
SUM 1981
SUM 1982
SUM 1983
SUM 1984
OLR ANOMALY
U ANOMALY

Fig. 7

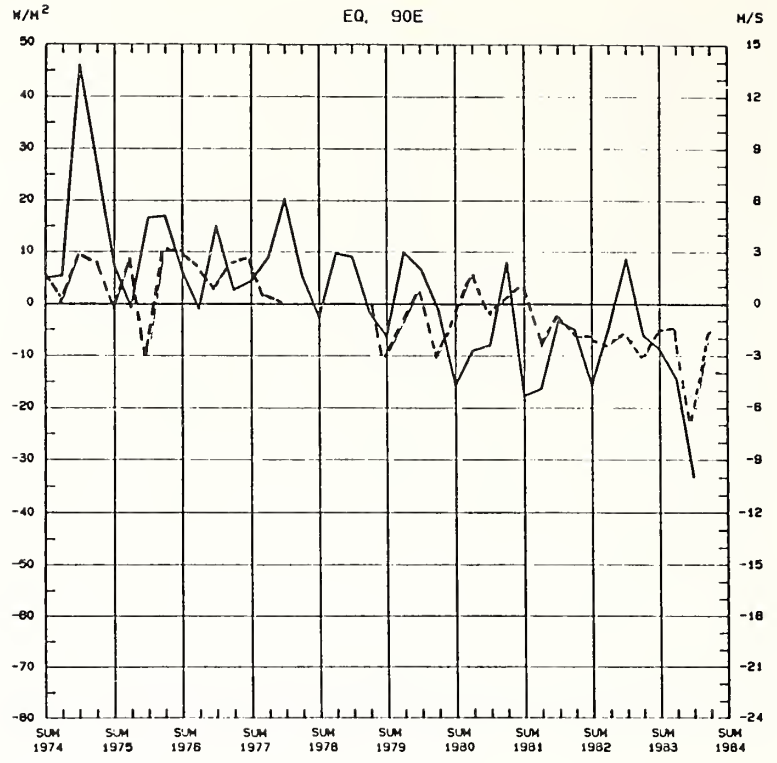
W/M²
EQ. 90E
M/S
50
40
30
20
10
0
-10
-20
-30
-40
-50
-60
-70
-80
15
12
9
6
3
0
-3
-6
-9
-12
-15
-18
-21
-24
SUM 1974
SUM 1975
SUM 1976
SUM 1977
SUM 1978
SUM 1979
SUM 1980
SUM 1981
SUM 1982
SUM 1983
SUM 1984
OLR ANOMALY
U ANOMALY

Fig. 8

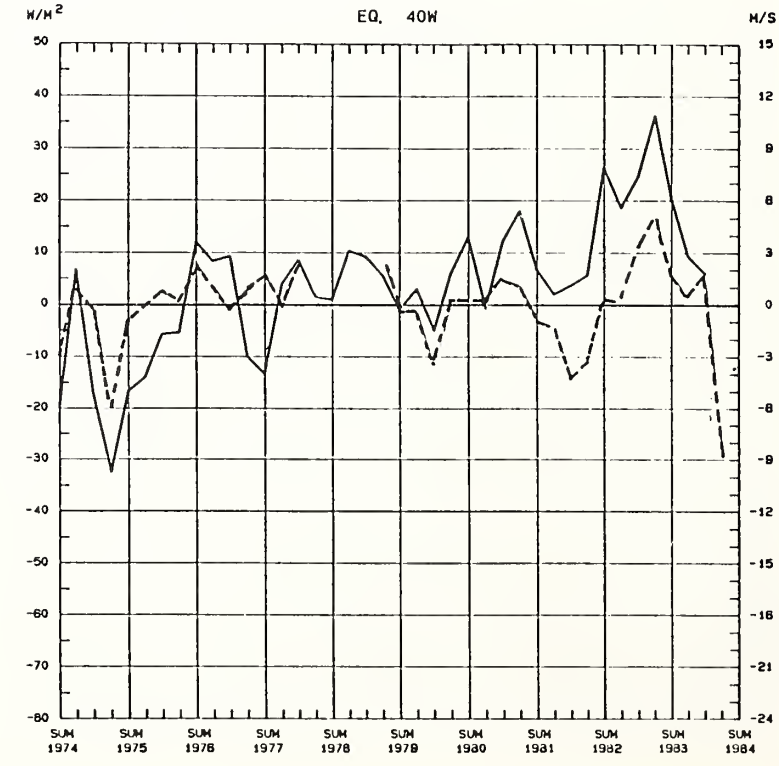
W/M²
EQ. 40W
M/S
50
40
30
20
10
0
-10
-20
-30
-40
-50
-60
-70
-80
15
12
9
6
3
0
-3
-6
-9
-12
-15
-18
-21
-24
SUM 1974
SUM 1975
SUM 1976
SUM 1977
SUM 1978
SUM 1979
SUM 1980
SUM 1981
SUM 1982
SUM 1983
SUM 1984
OLR ANOMALY
U ANOMALY

Fig. 9

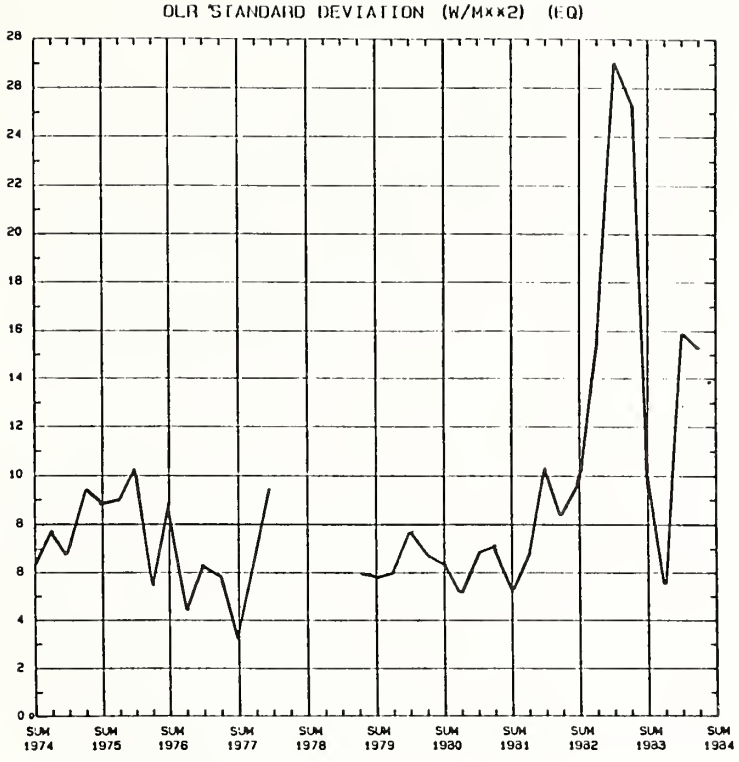
OLR STANDARD DEVIATION (W/M××2) (EQ)
28
28
24
22
20
18
16
14
12
10
8
8
4
2
0
SUM 1974
SUM 1975
SUM 1976
SUM 1977
SUM 1978
SUM 1979
SUM 1980
SUM 1981
SUM 1982
SUM 1983
SUM 1984

Fig. 10

CLIMATE SYSTEM FLUCTUATIONS, MONITORING

S. Unninayar
World Climate Programme Department
World Meteorological Organization
Geneva, Switzerland

1. INTRODUCTION

Climate fluctuations occur over an incredible range of time scales and are associated with a magnitude of impact which appears to be related to these time scales. Furthermore, the spatial extent of phenomena seems inextricably linked with their temporal characteristics. The cause of past climate fluctuations is still a profound question, and though the social need to predict climate is clear, the problem of successfully doing so is likely to challenge us for some years to come. Theoretical and numerical modelling research promises to bring us tantalizingly close to deterministic climate prediction in the near future, while proponents of "chaos" theories hint that prediction may be an illusive dream. Rapid advances in computer technology makes it possible to process enormous volumes of observational data and integrate models of greater and greater complexity. With the global deployment of satellite technology, observing systems have kept pace with the demand of models for more data, though in certain areas (e.g. oceanic) the availability of observations of certain variables/processes remains poor. Given adequate finances, an ideal, global observing system can, in theory, be implemented.

We must, however, ask the following questions: when is climate prediction going to improve?; and until it does what should we do now to better grasp climate system fluctuations in a comprehensible manner? Significantly extending the range of numerical forecasting and climate prediction in particular is expected to take at least 10 to 20 years. We can however approach the problem now in an empirical manner through judiciously monitoring the climate system taking advantage of existing observing systems and information that can be distilled from them. The multi-disciplinary nature of the atmosphere-ocean-cryosphere-land surface climate system requires a mechanism that promotes a cross-flow of information on the state of the system as a whole and on possible fluctuations (internally or externally driven) that are of regional and global consequence.

2. THE CLIMATE SYSTEM : FLUCTUATIONS AND EFFECTS

The following sections briefly summarize "climatic fluctuations" and consequences/effects to provide perspective to the types of climate system variability that we may need to deal with. Emphasis is placed on "abnormal" deviations based on the premise that the activities of human beings and other life forms have adjusted to "normal" conditions, be they good or bad. It is underscored that a linear separation of phenomena according to time-scale (for discussion purposes) does not preclude significant interaction between them. Slowly varying fluctuations can modulate higher frequency phenomena and vice-versa. Even classical mathematics shows that an impulse function (which could be interpreted as an abrupt change) is composed of a combination of periodic oscillations of substantially different frequency of time scales. In nature some of these oscillations are likely to be non-periodic, but the principle may apply.

- One day to a few weeks: weather, effects of which are immediately felt by people, is but a short-term atmospheric system fluctuation due to internal instability processes that aim to re-establish mass, momentum, or heat balance on certain space-time scales. Social and economic impact due to extreme weather events can be high but are usually localized (e.g. wind bursts, flash floods, tornadoes, hurricanes). On a synoptic scale atmospheric models can make predictions up to two weeks. Boundary conditions or coupling with the land surface, hydrology, cryosphere and ocean becomes important beyond the weekly time-scale. Partial longer-term atmospheric memory may exist, indirectly, through the positioning of long-wave systems in the atmosphere which are geographically determined for dynamic and thermodynamic reasons, and for example through the modulating effect of 30-60 day oscillations (Fig. 1).

- Months to one year: The annual cycle is strongest in this time-range, determined largely by the orbital position of the earth with respect to the sun. The change from summer to winter is due to the tilt of the earth's axis from its orbital plane, the climate system responds to this annual fluctuation in solar radiation (all well known facts). Predicting the severity (cold/ wet, hot or dry) of the next season, however, is not simple. Processes which integrate recent history (e.g. months to a year) with present system state need to be taken into account. Effects are larger (entire national economies can be affected) and the space scale is regional or global.

- One year to 10 years or more: Inter-annual variability involves more components and processes of the climate system. Atmosphere-ocean coupling is of particular significance (e.g. Warm Pacific SST anomalies and the occurence of El-Niño/Southern Oscillation (ENSO) Phenomena). Anomalies associated with ENSO can be persistent (12 to 18 months) and affect large areas of the world (Rasmussen & Carpenter, 1982, 1983) Figs. 1,3,4,5. The recurrence period of ENSO events is about 2-7 years. Phenomena such as the quasi-biennial oscillation (particularly its phase) may be of importance. Other fluctuations (of longer-time scales) and external influences may be significant through their modulating effect on atmospheric motion. For example there is evidence that solar activity, lunar effects (gravitational) are related to wet/ drought sequences of fairly long duration (Eddy, 1976 and Mitchell, 1976). The El-Niño signature is also apparent in changes in the earth's angular momentmum (rotation speed/day length) (Fig. 6). Atmosphere-cryosphere and atmosphere- vegetation/biomass/land surface interaction are likely to play a part in determining variability in the decadel time scale. Economic impact can be substantial (estimated at over 10 billion dollars for the 82-83 El-Niño event). Also of relevance may be mass transports within

the fluid core and coupling between the core and mantle which could affect the angular momentmum of the solid earth, assuming conservation of angular momentum, the atmosphere/ ocean could respond to compensate for changes in solid earth rotation speeds.

- 10 to 100 years: Changes in this time scale are usually designated as long-term climate trends - fluctuations here could be influenced by solar radiation variability (Figs. 7,8) increasing concentration of CO_2 and other radiatively active gases, aerosols (and the frequency of volcanic activity), interactions with the cryosphere (ice-albedo feedback), deep ocean circulation. Impacts are likely to be substantial - wide-spread disruption and dislocation of societies can occur if "anomalous" conditions persist for many years. The situation is further complicated by interaction between climate changes and social practice (e.g. overgrazing, deforestation, desertification) which could affect albedo, moisture recycling mechanisms, radiation balance and consequently climate. Ocean and ice interactions and ocean-atmosphere interactions are significant, as are solar and gravitational influence.

- 100-1000's of years: History documents rather drastic consequences of climatic fluctuations of this time scale. Entire civilizations have been forced to relocate or have been eliminated. Evidence points to major sea-level changes and large-scale floods. Thus the ice-ocean and ocean-atmosphere interaction processes appear to play a dominant role. CO_2, solar activity and orbital parameter fluctuations are also likely factors. Volcanic activity may also have played a role.

- Millions of years: Fossil and paleoclimatic records point to catastrophic changes approximately every 25-30 million years which were involved with the mass extinction of entire species on the earth. For example the Dinosaurs which existed for over 100 million years (mankind has thus far managed a mere 5 million years) were rather abruptly terminated. Several theories exist - most refer to impact with large comets or asteroids (detected by an abnormal enrichment in iridium or other noble metals) which caused an expulsion of terrestrial dust to such a scale that sunlight was blotted out, or that an unseen companion star to the sun (yet undetected black hole or brown dwarf, Marc Davio et al., 1984) in a highly eccentric orbit initiated intense comet showers. Some evidence (e.g. Mammoths which were instantly frozen and recently excavated in frozen, not fossilized, state) points to abrupt shifts of the earth's axis. A third scenario refers to the large rise and fall of sea level (along with changes in ice cover/extent) - supported by extensive black shale deposits, possibly through the extinction of biota by anoxia (A, Hallam, 1984).

Fluctuations of the order of millions and even thousands of years are generally difficult to grasp mentally. It is easy to assume that we do not need to be concerned about such time scales. However, it would be comforting to know this for a fact or consider monitoring some of the parameters (e.g. orbital) which may modulate/influence present climate. It would be most

uncomfortable to be frozen while having ones dinner - purportedly what happened to Mammoths in the Siberian area. Noteworthy is the fact that intervals as warm as the recent have occured for only about 10% of the time during the late Quaternary (T. Crowley, 1983). Also of significance is that the estimated change in average global temperature between non-glacial and full glacial worlds is only about 10°C over the last 100 million years, which means that relatively small variations can cause significant changes in the distribution of snow/ice, precipitation and weather which in many cases probably determined the fate of several species.

3. SOME COMMENTS ON THEORIES OF CLIMATE SYSTEM VARIABILITY

The climate system is coupled and interactive. The separation into atmosphere, ocean, cryosphere and land surface is in fact artificial and more a consequence of the history of scientific understanding and development than any profound scientific fact. This is also true of the distinction between weather and climate. It would have been most convenient if the climate system were linear. Linear theory allows several processes, influences and parameters to be eliminated as unimportant, i.e., small changes should have small effects and are thus unconsequential. However, the climate system is non-linear - small changes can grow and have large effects. Internal instability processes in the atmosphere (i.e. baroclinic, barotropic and convective) can explain variability from about one day to two weeks. Beyond this period the atmosphere is inherently unpredictable if interactive coupling and feed back with boundary conditions are not taken into account (i.e. the ocean, land surface, biosphere, cryosphere and upper atmospheric radiation balance). At present turbulence on any space or time scale can not be adequately modelled. Further, just as the synoptic scale modulates mesoscale weather, climate system fluctuations of longer time scales influence events of shorter temporal characteristics. This may mean that the type of models which are used and initialization schemes may need to be significantly changed.

External factors such as changes in solar radius or solar radiation (forced by orbital parameters) can not be neglected. Even though the direct thermal effects of solar fluctuations (decadel time scale) of about 0.2% are small, indirect effects could conceivably be substantive. In the north-east Atlantic the most severe interval of the Little Ice Age (Lamb, 1979) occured during the Maunder Sunspot Minimum between 1660 and 1710. Though the precise mechanism through which small changes in solar radiation flux affects climate is unknown, possible pathways are: (a) significant variation in solar UV output, (while total solar output remains nearly constant) which causes a UV induced differential production of O_3 (Callis et al., 1979, Ramanathan, 1982), (b) modulation of thunderstorm activity and tropical convection (atmospheric heating) through solar wind induced changes in ionospheric charge, and the ionospheric electric field which is a part of a global circuit (Markson, 1979, Markson & Muir, 1980), and (c) solar radiation fluctuations (forced by orbital parameters) which affect ice extent and CO_2 concentration and climate (N.G. Pisas et. al, 1984). The point of the above is that solar, gravitational and astronomical effects should probably not be ruled out even at interannual time scales. The potential climate predictive value of these influences are due to their relatively slowly varying nature.

Taken in a positive sense, "chaos", "intermittency" and "period-doubling" theories (Economist, September 8, 1984) may also provide insight into climate system variability. "Chaos" theory suggests that systems that fluctuate about a mean state could under certain circumstances (e.g. the continual increase of a critical control parameter) begin a cycle of fluctuations where-in the system returns to its original state approximately every 2, then 4, then 8 units of time. The ratio between two successive "period doublings" is about 4.6692 (Feigenbaum number) a new universal number. The system would eventually fluctuate into a chaotic state of apparently random fluctuation. The interesting feature of "chaos" theory is that it applies to a wide range of phenomena and/or systems unlike "turbulence" theory which strictly speaking applies only to fluids. The theory predicts the behaviour of a system en-route to chaos or random fluctuation. Intermittency theories refer to bursts of "chaos" separated by intervals of regular behaviour. While the atmosphere and oceans are fluids, climate and climate fluctuations are a consequence of a complex of interacting elements which include fluid, solid bodies, electromagnetic and gravitational and chemical energy transformations. Perhaps the climate system needs to be handled with the new perspectives into system behaviour provided by "chaos" and "intermittency" theories.

4. A PRELIMINARY HYPOTHESIS ON ENSO RECURRENCES

The El-Niño/Southern Oscillation (ENSO) is still unpredictable. Presently, the potential "prediction" value behind ENSO is due to the 18-24 month anomalous circulation (atmosphere and ocean) state which appears to manifest itself once an ENSO even has set in. The Tropical Ocean Global Atmosphere (TOGA) 10 year programme is an international undertaking of the World Climate Research Programme directed at studying ENSO.

Could ENSO be a result of "a system" on the margin of turbulence? Chaos and intermittency theories refer to the behaviour of systems en-route to randomness/chaos. Laboratory or model experiments through which "period doubling" was discovered, however, generally did not involve feed-back with the control paramters. Such feedback could, in principle, return the system to a quasi-equilibrium state after which it could drift once again in a predictably intermittent manner towards chaos.

The El-Niño record of the last 30 years may carry some such record. Note the following sequences (Ref. Table 1, and Fig. 2):

- An El-Niño, purportedly a big one, in 1940/41 followed by a period of quiesence;
- El-Niños in 1951, 1953, 1957/58 and 1963 with intervals of 2, 4 and 6 years;
- El-Niños in 1963, 1965, 1969 with intervals of 2 and 4 years.
- El-Niños in 1972/73, 1976, 1982/83 with intervals of approximately 4 and 6-7 years.

It is conceivable that since the 82/83 event was unusually strong, feed-back processes could have restored the system to a state of quasi-equilibrium. Should we then expect a quiescent phase after which a 2, 4 and possibly 8 year recurrence cycle begins again? Clearly there are other factors involved which modulate the intensity of El-Niños. The 1963 and 1969 events were relatively weak while others were strong ending with possibly the strongest thus far in 82/83.

El-Niño prediction is of considerable economic and social importance. If the above hypothesis is applicable at all, the following future scenarios are possible:

(i) An even bigger El-Niño (than the 82/83 event) occurs between 12 to 16 years from now, with a period of relative quiescence in between. (This is unlikely to occur based on historical evidence of the atmosphere-ocean system fluctuations);

(ii) A period of "normal" of undetermined length (possibly 5 to 10 years) followed by a repetition of a 2,4,... cycle until an extreme El-Niño occurs which forces feedback processes to kick the system back into a stable mode once again. The first El-Niño of this cycle can be of small to medium intensity.

(iii) The next El-Niño of moderate intensity in 2 to 3 years followed by a 2,4,8 year reccurrence cycle.

The key issue may be identifying the "control parameter". Could it be CO_2 or solar radiation fluctuations? Fig. 9 shows some evidence of frequency and possibly intensity modulation of El-Niño events by fluctuations in solar radiation (compare with Table 1). Other possibilities (e.g. lunar gravitation effects of 18.6 years time scale) exist - the juxtapositioning of the phases of signals of different time scales may provide a clearer picture (this analysis will be attempted in the future).

This initial look at a chaos theory of climate fluctuations should be investigated much more thoroughly to determine its applicability to our real climate. Until this or other theories of climate can significantly improve our prediction capabilities we should develop a useful procedure to monitor the climate system.

5. CLIMATE SYSTEM MONITORING

It is conceivable that the climate system meanders from time to time to a potentially unstable state at which time one of many small perturbations could trigger the system into a new state of quasi-equilibrium. We would need to identify such thresholds for monitoring purposes. Furthermore, the state of the climate system at any particular instant in time could be a consequence of the juxtapositioning of fluctuations of substantially different time scales. Thus it would be important to also keep track of "slowly varying" components of the system as well as their respective phase relationships. The following monitoring sub-set is proposed:

- atmospheric structure - large scale circulation
- large-scale overturning Walker & Hadley circulations
- temperature, precipitation and anomalies
- sea surface temperature, sea level pressure, sea level
- southern oscillation index, trade wind index
- outgoing long wave radiation
- ocean currents, depth of mixed layer (tropical)
- tropical 40-60 day waves (phase)
- quasi-biennial oscillation (phase)
- earth rotation (angular momentum/day length, changes)
- snow cover and sea ice boundaries
- planetary albedo (satellite derived)
- solar activity - double sun-spot number
- CO_2, O_3, radiatively active gases, aerosols
- lunar/tidal effects (phase of 18.6 year cycle of changing declination - gravitational effect)
- geomagnetic index (in case this could be an index of mass transports within the fluid core or an index of terrestrial and extra terrestrial interactions)
- ionospheric changes (index)
- orbital parameters - phase relationships.
- changes in ice sheets, glacier extent
- frequency of volcanic eruptions which deposit large volumes of dust or perturb the stratosphere in other ways

6. THE CLIMATE SYSTEM MONITORING (CSM) ACTIVITY OF THE WORLD CLIMATE DATA PROGRAMME (WCDP)

The monitoring and study of the climate system and associated interactive processes is complex and multidisciplinary. Accordingly it has been considered important that a mechanism be formulated to: (a) coordinate activities and (b) provide information to various specialists and specialized organizations involved so that significant events and changes are brought to their attention expeditiously and in a simple concise form. It is expected that this will foster a better awareness of climate and of research which must incorporate aspects of other disciplines outside the mainstream of each individual field of research and analyses.

Under the CSM project of the WCDP four types of activities and associated output products are envisaged:*

(i) The issue of a Monthly CSM Bulletin: This bulletin will contain as a standard feature (for the reference month) a global analysis of temperature and precipitation anomalies and statistics by region and country which indicate the persistence of hot/cold, wet/dry events. Aperiodically, other climate system features will be incorporated. Examples are: time series of indices (based on sea surface temperature, sea level pressure) showing the decay of the 82-83 El-Nino/Southern Oscillationj (ENSO) event - the time series should

---

* Additional time series information of parameters in Section 2 will be incorporated if scientific investigation proves them to be relevant.

cover several years to provide perspective. In this context it should be noted that while the monthly CSM bulletin will contain temperature/ precipitation information for the reference month, other insertions could refer to longer periods of time.

(ii) The issue of special advisories: Through monitoring the global climate system, if there are indications that a particular sequence of climatic events are likely to affect a particular country or countries in a region, a special advisory will be issued, contingent on the availability of relevant information and data analyses centres to prepare the necessary input. An example would be the onset of an El-Nino event - once established a special advisory could indicate the regions which are likely to be affected and how based on past occurences.

(iii) The issue of an Annual CSM Summary on the state of the climate system and significant large-scale anomalies. This should contain simple/concise text supported by a selection of standard products such as:

- globally analyzed fields (and anomalies) of surface temperature, sea level pressure, precipitation, surface and upper air (e.g. 500 mb, 200 mb) circulation/wind, sea surface temperature (SST) sea-level (sub-regions), satellite derived outgoing radiation/albedo/cloud, snow/ice cover, and as possible/available estimates of vegetation cover/biomass, changes in desert margins.

- time series of indices and area (key) averaged parameters of for example SST, sea level, snow cover, sea-ice, precipitation (selected areas e.g. drought prone), surface temperature (selected areas), trade wind index, zonal flow indices/blocking indices, aerosol, CO_2 and trace gases (selected stations), and as possible/desirable global angular momentum and earth rotation (day length changes), solar activity, geomagnetic index (if relevant),

- measures (preferably time series form) of proxy climate indicators (effects/impacts),

- statistics indicating the persistence of key climatic events (e.g. drought).

The annual issue will contain a combination of standard and non-standard products. For the reference year, globally analyzed fields and anomalies will generally pertain to seasonal averages (and deviations), e.g. summer/winter. Time series will cover several years to provide perspective to significant anomalies. Aperiodically, it is envisaged for inclusion special topic/event/climate-system-discipline reviews, prepared by specialized centres. Examples are effects of orbital parameter changes, paleoclimatology (tree ring/ ocean sediment based climate reconstructions - leading to present times), glaciology (glacier and ice sheet fluctuations and climate change - mini ice ages), past CO_2 fluctuations (reconstructions from proxy data) and apparent effects. These special articles would provide a reference to the state of the present climate system.

(iv) A biennial scientific review which comments on significant anomalies, causes/teleconnections, and consequences of social and economic significance.

The product ensuing from either (iii) or (iv) should, preferably, be in a form suitable for digestion by governmental/managerial decision makers - meaning that it should be simple and with colour graphics and pictures. Summaries of climate effects/impacts should be included to the extent feasible.

LIST OF REFERENCES

Callis, L.B. M. Natarajan, & J.E. Nealy, 1979: Ozone and Temperature Trends Associated with the 11-year Solar Cycle, Science, 204, 1303-1306, 1979

Carter, W.E., D.S. Robertson, J.E. Pettey, B.D. Tapley, B.E. Shutz, R.J. Eanes, Mia Lufeng, 1984: Variations in the Rotation of the Earth, Science, Vol. 224, 957-961

Crowley, T., 1983: The Geological Record of Climate Change, Rev. Geophysics and Space Physics, Vol. 21, No. 4, pp 828-877

Davis, M., P. Hut, R.A. Muller, 1984: Extinction of Species by Periodic Comet Showers, Nature, Vol. 308, 19, pp 715-717

Dyer, T.G.J. & J.M. Gosnell, 1978: Long-term Rainfall Trends in the South African Sugar Industry, Proceedings of the South African Sugar Technologists Association

Eddy, J.A., 1976: The Maunder Minimum, Science, 192, 1189-1202

Hallan, A., 1984: The Causes of Mass Extinction, Nature, Vol. 308 pp 686-687

Lorenc, A.C., 1983: The Evolution of Planetary Scale 200mb Divergence during the FGGE years, U.K. Meteorological Office, Tech. Note II/20

Markson, R., and M. Muir, 1980: Solar Wind Control in the Earth's Electric Field, Science, 208, 979-990, 1980

Mitchell, J.M., 1976: An Overview of Climatic Variability and its Casual Mechanisms, Quart. Res., 6, 481-493

Pestiaux, P., & A. Berger, 1982: Numerical Methods in search for periodicities and quasi-periodicities, Contribution No. 34 Georges Lemaitre Institute D'Astronomie et de Geophysique

Pisias, N.G., and N.J. Shackleton, 1984: Modelling the Global Climate Response to Orbital Forcing and Atmospheric Carbon Dioxide Changes, Nature, Vol. 310, pp 757-759, 30 Aug.

Ramanathan, V., 1979: Coupling Through Radiative and Chemical Processes; Solar Variability, Weather and Climate; pp 83-91, National Academy of Sciences, Washington, D.C.

Rasmusson, E.M.; El-Niño; 1984: The Ocean/Atmosphere Connection; Oceanus, Vol. 27, No. 2, Summer 1984

Rasmusson, E.M. & T.H. Carpenter; 1982: Variations in Tropical Sea Surface Temperature and Surface Wind Fields Associated with the Southern Oscillation/El-Niño. Mon. Wea. Rev., 110, 354-384

Science and Technology; 1984: The Mathematics of Mayhem; Economist, 8 Sept.

Shukla, J. & D.A. Paolino, 1983: The Southern Oscillation and Long-range Forecasting of the Summer Rainfall over India; Mon. Wea. Rev., 111, 1830-1837

Wang Shao-wu, Zhao Zong-ci & Zhen-hua; 1981: Reconstructions of Summer Rainfall Regime for the last 500 Years in China; Geo Journal, 5.2/1981, 517-521

Year	Event intensity	Key to source	Year	Event intensity	Key to source	Year	Event intensity	Key to source	Year	Event intensity	Key to source
1726	(3)	G	1852	2 (2)	B, PC	1896	(3)	PI, R	1943	(2)	G, T, R
1728	(4)	A, G	1854	2	B	1899	(4)	D, PI, R	1944	(2)	PI, T
1763	(4)	A	1855	(2)	PC	1900	(3)	PI, R	1946	(1)	PI, R
1770	(4)	A	1857	2 (2)	B, PC	1902	(3)	PI, R	1948	(1)	PI, T, R
1791	4 (4)	A, B	1862	2	B	1905	(3)	PI, R	1951	(2)	G, PI, T
1803	2	B	1864	4 (4)	A, B, PI	1911	(4)	F, E, PI	1953	(3)	G, E, T
1804	4 (4)	B	1866	2	B	1912	(3)	F, PI	1957	(4)	G, L, PI
1814	4 (4)	B	1868	1 (3)	B, C, PI	1914	(3)	G, PI, R	1958	(4)	G, L, PI
1817	3 (3)	B	1871	4 (3)	A, B, C	1917	(2)	H	1963	(1)	PI, R
1819	3 (3)	B	1873	(2)	PI	1918	(4)	C, D, PI	1965	(3)	M, PI, T
1821	3 (3)	B	1875	1 (1)	B, PC	1919	(3)	D, PI, R	1969	(2)	PI, T, R
1824	3 (3)	B	1877	4 (4)	A, B, PI	1923	(2)	H, PI	1972	(4)	N, O, PI
1828	4 (4)	A, B	1878	4 (4)	A, B, PI	1925	(4)	D, E, PI	1973	(4)	N, O, T
1829	1	B	1880	2 (3)	B, PI	1926	(4)	I, PI, T	1975	(1)	P, PI, T
1832	3 (3)	B	1884	4 (4)	A, B, PI	1929	(3)	G, I, PI	1976	(3)	Q, PI, T
1837	3 (3)	B	1885	(3)	PI	1930	(3)	G, PI, T	1982	(4)	S
1844	3 (2)	B, PC	1887	2 (3)	B, PI	1932	(2)	E, I, J	1983	(4)	S
1845	4 (4)	B, C, PC	1888	2 (3)	B, PI	1939	(3)	E, J, T			
1846	2 (3)	B, PC	1889	1 (1)	B, PI	1940	(2)	C, PI, T			
1850	2 (2)	B, PC	1891	(4)	D, E, PI	1941	(4)	E, K, T			

Key	Source	Key	Source	Key	Source
A	Frijlinck (1925)	H	Lavalle (1917, 1924)	O	Caviedes (1975)
B	Eguiguren (1894)	I	Shepard (1930, 1933)	P	Wyrtki et al. (1976)
C	Hutchinson (1950)	J	Mears (1944)	Q	Quinn (1976)
D	Murphy (1923, 1926)	K	Lnbell (1942)	R	Rainfall (equatorial and/or Peruvian)
E	Sears (1954)	L	Wooster (1960)	T	Sea-surface temperature off Peru
F	Forbes (1914)	M	Guillén (1967)	PC	Pressure component of Southern Oscillation index
G	Schweigger (1961)	N	Idyll (1973)	PI	Southern Oscillation pressure index
		S	Rasmusson (1982, 1983)		

Year of onset of El Niño type events, 1726–1983, as classified according to event intensity by Eguiguren (1894) (left, and the present authors, right (events below intensity 3 were not accepted prior to 1841 when pressure data became available). Numbers refer to event intensity: 1, very weak; 2, weak; 3, moderate; and 4, strong. (Adapted from W. H. Quinn and others, Fisheries Bulletin, Vol. 76, No. 3, 1978)

Table 1 : History of El-Nino Events (From E. Rasmusson, 1984)

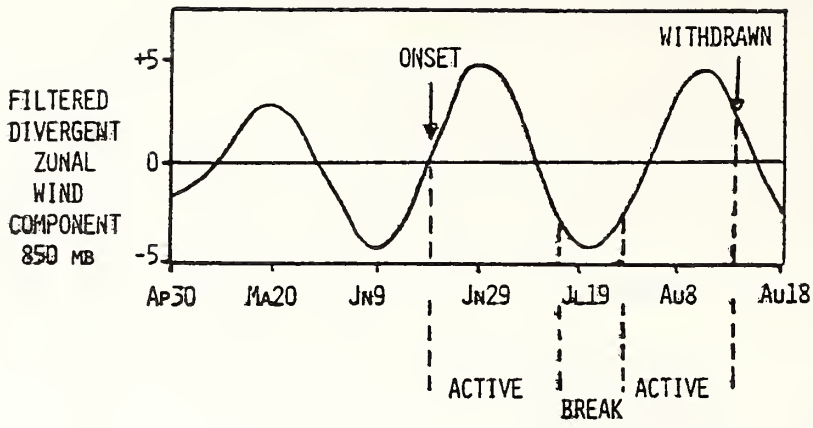

The zonal component of the divergent wint vector in the north Indian Ocean region. Postive values suggest an enhancement of the monsoon westerlies and negative values a weakening. Note that the "onset" appears to coincide with the change from divergent easterlies to westerlies (from Lorenc, 1983)

Fig. 1 : 30-60 day waves

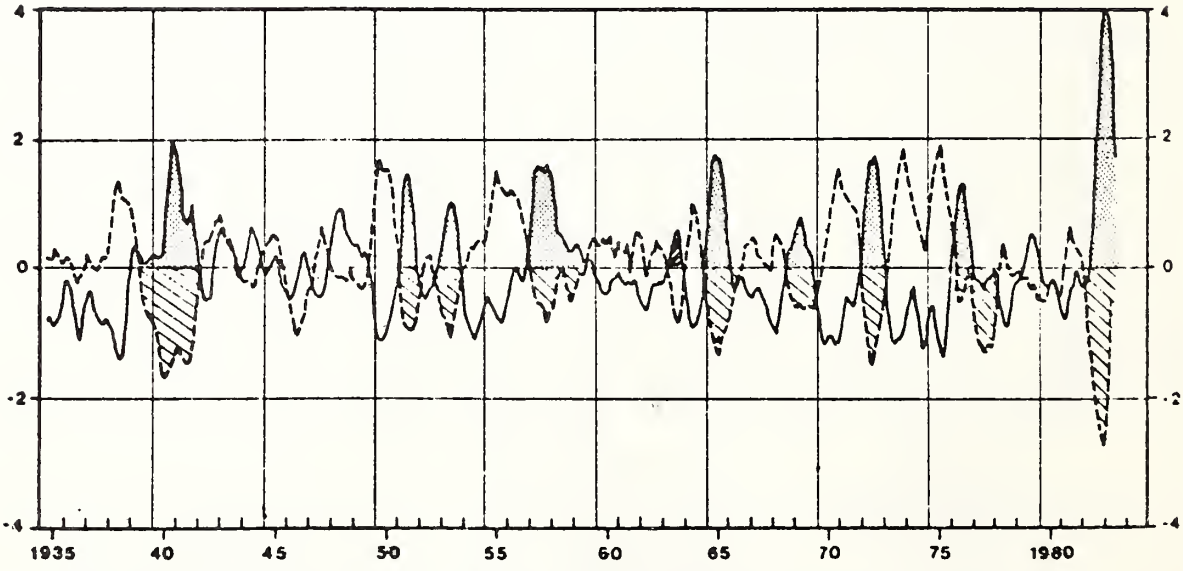

Curves for an index of El Niño (Puerto Chicama, Peru, sea-surface-temperature anomalies; solid line) and the Southern Oscillation (Tahiti-French Polynesia minus Darwin, Australia, surface-pressure-difference anomaly; dashed line). Values have been "standardized" by dividing the monthly anomaly values by their long-term standard deviation. Major ENSO events, which correspond to strong "negative" swings in the Southern Oscillation Index, and large positive sea-surface-temperature anomalies at Puerto Chicama are indicated by shading. Nine major episodes have occurred since 1935, with 1982-83 by far the most intense.

Fig. 2 : El-Nino events shaded (From E. Rasmusson, 1984)

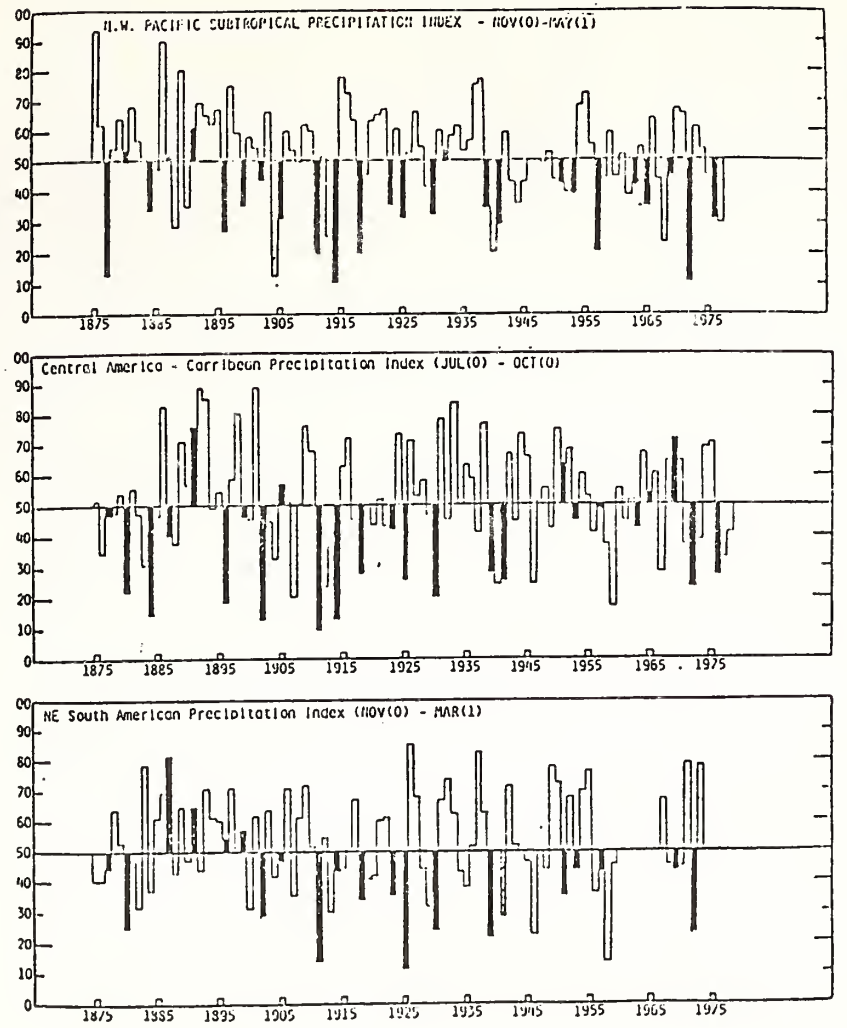

Fig. 3 : Time Series of Seasonally Averaged Precipitation
(From E. Rasmusson, personal communication, 1984)

Note: El-Niño years are indicated by solid/shaded bars.

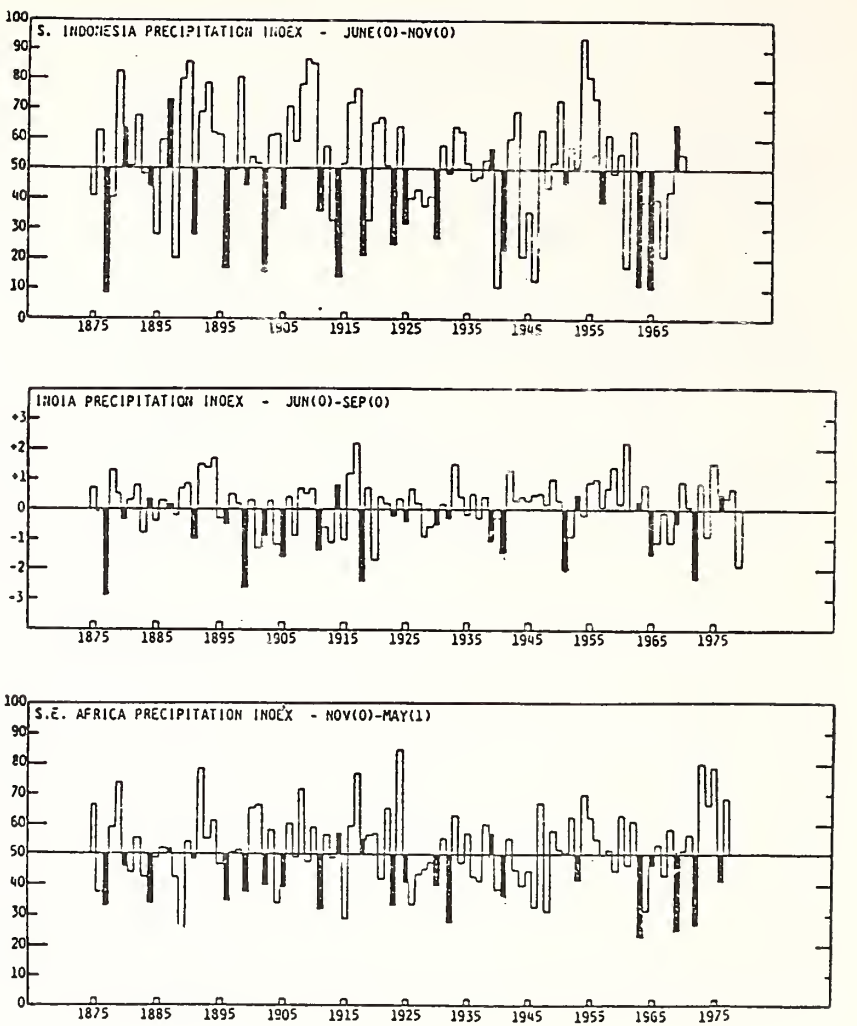

Fig. 4 : Time Series of Seasonally Averaged Precipitation
(From E. Rasmusson, personal communication, 1984)

Note: El-Niño years are indicated by solid/shaded bars.

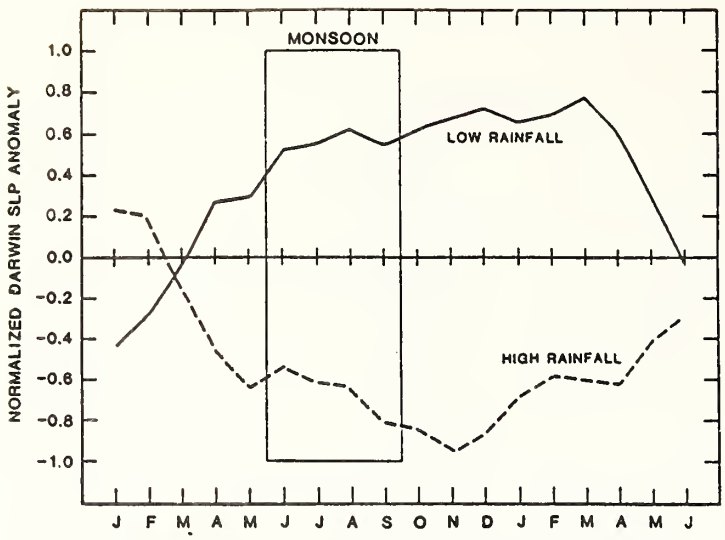

Composites of 3-month running mean of normalized Darwin pressure anomaly. Solid line: years of low rainfall in the Indian monsoon during June-September; dashed line: years of high monsoon rainfall (from Shukla and Paolino, 1983)

Fig. 5

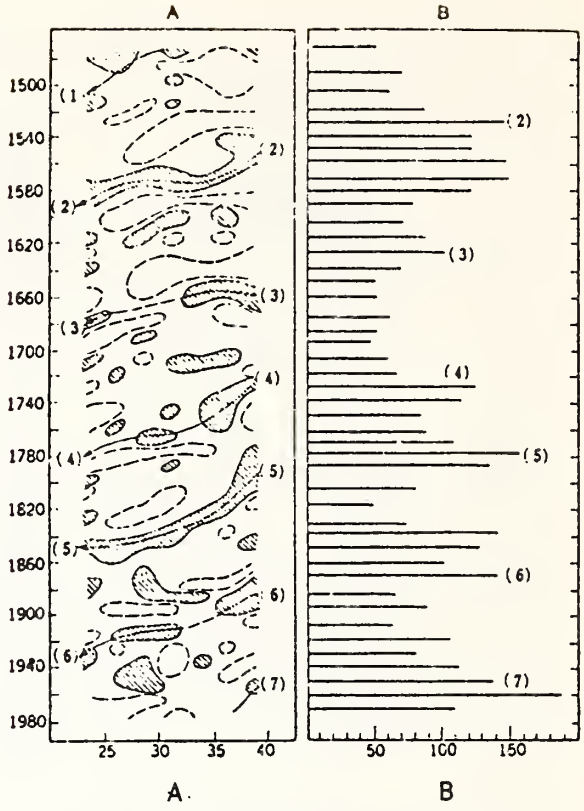

Fig. 7A : Latitude-time series of 10 yeor running means of reconstructed roinfoll onomalies overoged over 25 stotions (China) for 2.5 degree lotitude zones. Extensive flooding occurred 6 times in the lost 500 yeors numbered (2)-(7);
Fig. 7B : Moxima in the sunspot 11 yeor cycle - extremes ore numbered (2)-(7);

From Wang Shoo-wu et al., 1981.

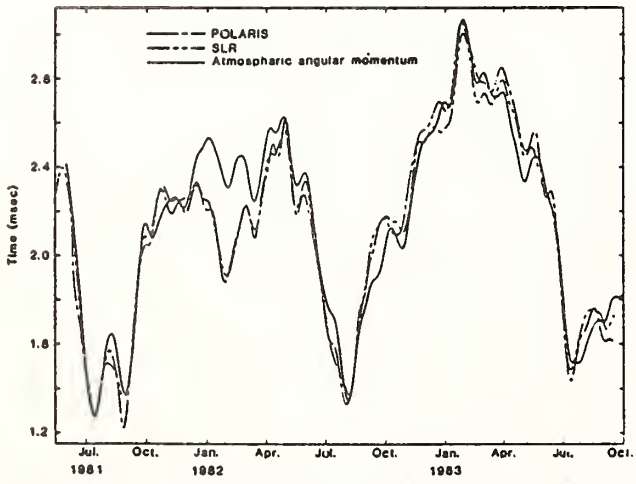

Excess length of day as measured by POLARIS VLBI and SLR observations and as inferred from observed changes in the global atmosphere angular momentum.

Fig. 6 (From Corter et al., 1984)

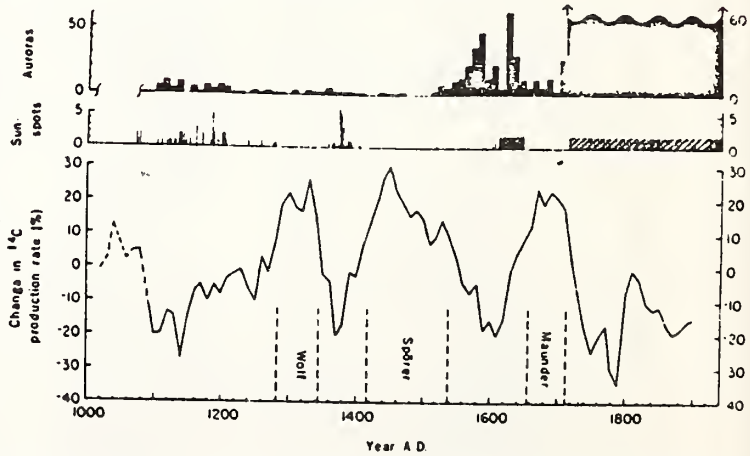

Evidence for ^{14}C changes attributable to a variable sun. Frequency of auroral observations, sunspots, and changes in ^{14}C production rate are calculated from a reservoir model. The number of naked eye sunspot observations per decade before 1610 is given by the vertical bars. The cross-hatched area denotes the existence of sunspots as observed by telescope (from *Stuiver and Quay*, 1980). (Copyright 1980 by the American Association for the Advancement of Science; reproduced with permission.)

Fig. 7C (From Crowley, 1983)

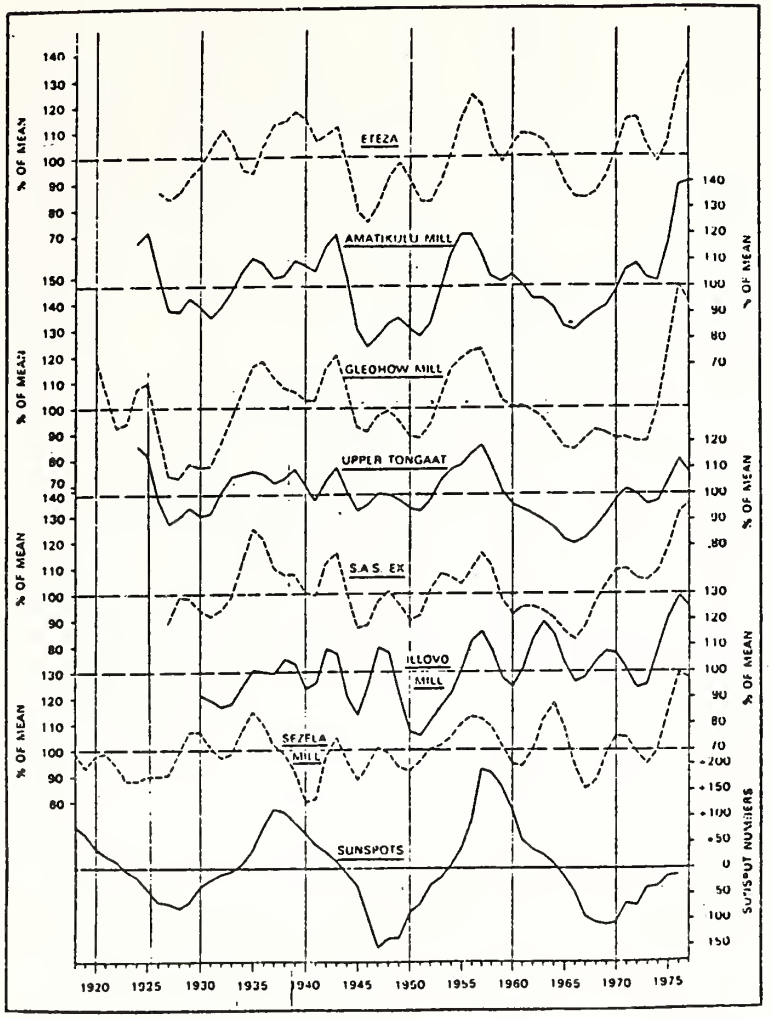

Filtered rainfall series of Eteza, Amatikulu Mill, Gledhow Mill, Upper Tongaat, S.A.S.Ex., Illovo Mill & Sezela Mill

Fig. 8 : Filtered rainfall time series (Southern Africa)
(From Dyer et al., 1978)

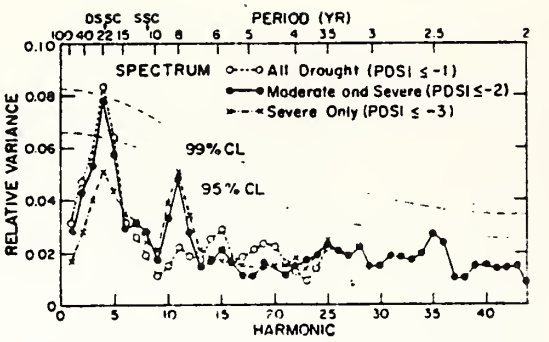

Fig. 49. Evidence for a 22-year drought rhythm in tree ring records from the western United States. Confidence limits are based on the assumption of first-order Markhov process as a generating function. Abbreviations are PDSI (Palmer drought severity index), SSC (sunspot cycle), and DSSC (double-sunspot cycle). Data are by *Mitchell et al.* [1979]. The figure is from *Roberts* [1979]. (Reproduced with the permission of D. Reidel.)

Fig. 9 (from Crowley, 1983)

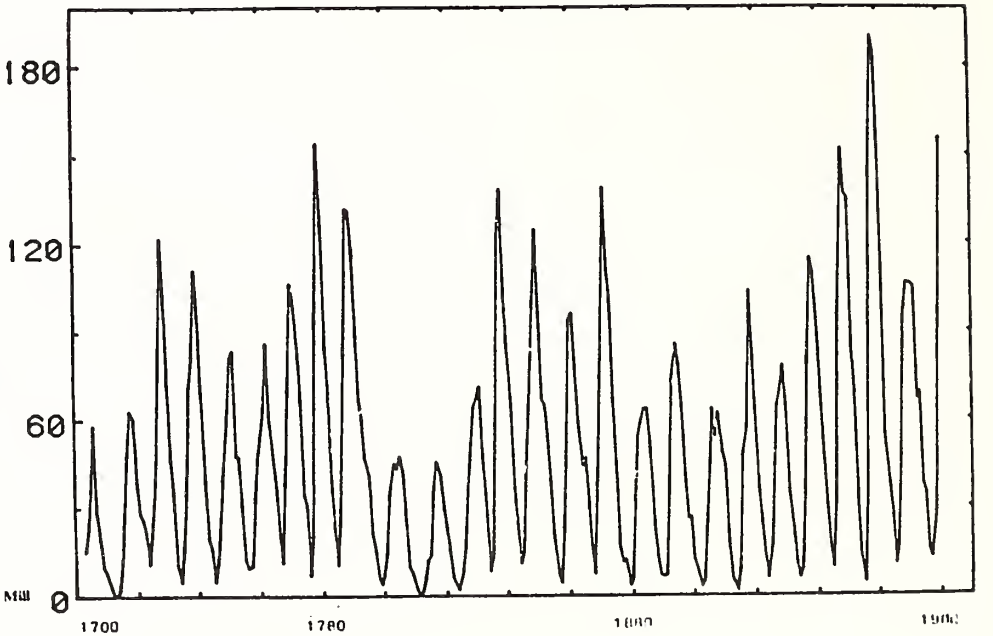

Fig. 10 : Yearly mean sunspot numbers from 1700 to 1979
(From P. Pestiaux and A. Berger, 1982)

The Status of the NOAA/NESDIS Radiation Budget Data Set

Arnold Gruber
Climate and Earth Sciences Laboratory
NOAA/NESDIS
Washington, D.C. 20233

Introduction

Estimates of the planetary albedo and outgoing longwave radiation have been obtained from NOAA polar orbiting operational spacecraft since June 1974. The record is however, not continuous. From June 1974 through February 1978 estimates were obtained from single satellite system, designated as NOAA SR. After a break of 10 months (March-December 1978) estimates of albedo and emitted radiation were again produced; this time from the TIROS-N series of satellites. This is a dual satellite system, one satellite having an equator crossing time at approximately 1430 LT and 0230 LT and the other at about 0730 and 1930 LT. As in the case of the NOAA SR, estimates of albedo were obtained from visible channel radiance and emitted flux were obtained from window channel (10-12 μm) measurements, however, from only one satellite on an alternating basis. Table 1 shows the period of time the satellites were in operation as well as the spectral width of the sensors.

Regression procedures are used to obtain the total broad band emitted flux from the window channel. These regression equations have undergone changes over the years in attempts to improve their accuracy. The most recent one was an empirical regression between simultaneous window data and broad band radiance observation from the Nimbus-7 ERB experiment (Ohring, Gruber and Ellingson, 1984). This was recently adopted as the most accurate equation for processing the data and all previous calculations have been adjusted to this new regression.

Outgoing Longwave Radiation (OLR)

An aspect of concern with the OLR from the two different satellite systems is their compatability. As previously mentioned the small variation of spectral response has been accounted for through a regression analysis relating the window channel to broad band flux values.

Figure 1 shows the monthly mean global average for the 4 different satellites, SR, TIROS-N, NOAA-6, NOAA-7. The SR data have been time averaged for the period June 1974-February 1978 and an estimate of their standard deviation has been provided. The important points to note on this figure are that the SR and TIROS-N results are higher than NOAA 6 and NOAA 7 but only by 2-3 Wm^{-2}. The times of maxima and minima are consistent with our expectations, that the N.H. with its larger amount of land rather than the S.H. would dominate the annual cycle. This will be seen more clearly when we compare TIROS-N results with Nimbus-7.

Factors that might have a bearing on the observed differences are natural year to year variablility, and the change in the equator crossing times, between satellites; that is, a diurnal variation effect. This is

believed to be a significant contribution to the differences between NOAA-6 and TIROS-N and NOAA-7 even though day and night observations are averaged. This is inferred from comparison of flux estimates from NOAA-7 (local times of 1500 and 0300) and NOAA-8 (local times 0730 and 1930; the same as NOAA-6) during the months December 1983 through April 1984 when data from both satellites were being processed. Figure 2, indicates a definite diurnal signal in the global and N.H. average with the day night average of NOAA-8, 2-4 Wm^{-2} less than NOAA-7 in the N.H. and 1-2 Wm^{-2} less than NOAA-7 on the global average. The S.H. with its greater extent of ocean exhibits only slight differences. A preliminary look at the regional character of the diurnal variability suggests that it is the subtropical deserts that dominate the diurnal signal, Figure 3.

Further insight into the compatability of the estimates of the emitted radiation is provided in Figure 4 which shows profiles of the annual zonal average. As shown the profiles track quite well with the largest variability occurring in the tropics and north of 60N.

These results suggests that the data are sufficiently compatible, so that new averages can be calculated for use in climate anomaly studies. Such calculations have recently been completed with my colleagues, J. Janowiak, A. Krueger and P. Arkin from the CAC and an atlas containing monthly, seasonal and annual means and standard deviations will be released soon. The averages will include data from the period June 1974 through November 1983. Figure 5 a, b are examples of the output of the atlas. Figure 6 shows a comparison of the monthly NOAA mean OLR with those produced from the Nimbus-7 ERB experiment. ERB, was specifically designed to measure the broad band (5-50 μm) outgoing longwave radiation. This figure indicates excellent agreement suggesting that the NOAA estimates provide an accurate measure of the planetary outgoing longwave radiation.

ALBEDO

The albedo is determined using several simplifying assumptions such as: visible channel albedo is the same as broad band albedo, the reflected energy is isotropic, and the albedo is independent of solar zenith angle. Depending on the reflecting surface, e.g. cloud, land, ocean etc., each of these assumptions can lead to inaccuracies in the determination of the albedo. Another complicating factor is that the albedo is determined from only 1 observation per day, thus, albedo estimates from different local times are more subject to diurnal variations, than the outgoing longwave radiation.

Figure 7 highlights some of these problems. Here we depict the zonal annual average albedo from the SR, TIROS-N, NOAA-6 and NOAA-7 satellites. While all exhibit similar shapes and variability, indicating that the large scale distributions of the planetary albedo is being captured, the magnitudes cover a rather large range; 27 to 33%. Notice that the highest albdeo is obtained from NOAA-6, the early morning satellite. We believe this is a solar zenith angle effect; the albedo tending to be high at large solar zenith angles. Other variations might be related to the slightly differing spectral intervals and the diurnal effect. We have not yet been able to separate the

various contributions satisfactorily. Clearly, such problems decrease the usefulness of these data as measures of the planetary albedo. However, since they do capture the large scale distributions it is possible that there is some use for these data as indices for large scale anomalies such as were associated with the 1982-83 El Nino/Southern Oscillation. In order to examine that possibility we have prepared a time-longitude anomaly chart of the absorbed solar radiation for the period September 1981 through August 1983, and compared it to the OLR anomaly prepared by CAC in their Quick Look Atlas, (Arkin et al., 1983) Figure 8. Note the obvious similarity in the patterns and propagation of the anomalies. Negative values of absorbed energy represent increased cloudiness similar to negative values of OLR.

Conclusion

1. The OLR from the NOAA SR and TIROS-N satellite system are compatible with each other and can be used to produce long term data sets.

2. The OLR also represents an accurate estimate of the planetary emission to space and can be used in radiation balance studies.

3. The albedo estimates are more uncertain, due to the restrictive assumptions used in obtaining them. However, if treated with care it can be used as an index for diagnosing large climate anomalies.

Acknowledgement

I would like to acknowledge Bob Ryan for drafting some of the figures, Cynthia Brown for typing the manuscript and Marylin Varnadore for programming support.

References

Ohring, G., A. Gruber and R. Ellingson, 1984: Satellite Determinations of the Relationship between Total Longwave Radiation Flux and Infrared Window Radiance. J. Clim. and Appli. Meteor. 23, 416-425

Arkin, P.A., J.D. Kopman and R.W. Reynolds, 1983: 1982-1983 El Nino/Southern Oscillation Event Quick Look Atlas. NOAA/National Wea. Soc., Nat. Meteor. Center, Climate Analysis Center, Washington, D.C. 20233.

Table 1: Characteristics of Satellites

	NOAA SR	TIROS N	NOAA 6	NOAA 7
Visible Spectrum (μm)	0.5-0.7	0.55-0.9	0.58-0.68	0.58-0.68
Infrared Window (μm)	10.5-12.5	10.5-11.5	10.5-11.5	11.5-12.5
Period of Record	6/74-2/78	1/79-1/80	2/80-7/81	9/81-
Equator Crossings (LT)	0900-2100	0300-1500	0730-1930	0230-1430
Instrument	SR	AVHRR	AVHRR	AVHRR/2

Figure Legends

Figure 1. Annual cycle of the globally averaged outgoing longwave radiation for SR, TIROS-N, NOAA-6, NOAA-7.

Figure 2. A comparison of outgoing longwave radiation from NOAA-7 (0230-1430LT) with NOAA-8 (0730, 1930LT).

Figure 3. Zonal average flux for (a) 0 - 117.5E and (b) 120E - 122.5W, for NOAA-7 and NOAA-8.

Figure 4. Zonal annual average of the outgoing longwave radiation for SR, TIROS-N, NOAA-6 and NOAA-7.

Figure 5. (a) Outgoing longwave radiation (b) Standard deviation, summer 1974-1983.

Figure 6. A comparison of outgoing longwave radiation derived from TIROS-N, NOAA-6 with Nimbus-7.

Figure 7. Annual average of the albedo estimates, SR, TIROS-N, NOAA-6, NOAA-7.

Figure 8. Time longitude anomaly at Eq-10S of (a) absorbed solar radiation (b) Outgoing longwave radiation. The anomalies are from averages over the period 1974-1983.

Global Average Outgoing Longwave Radiation

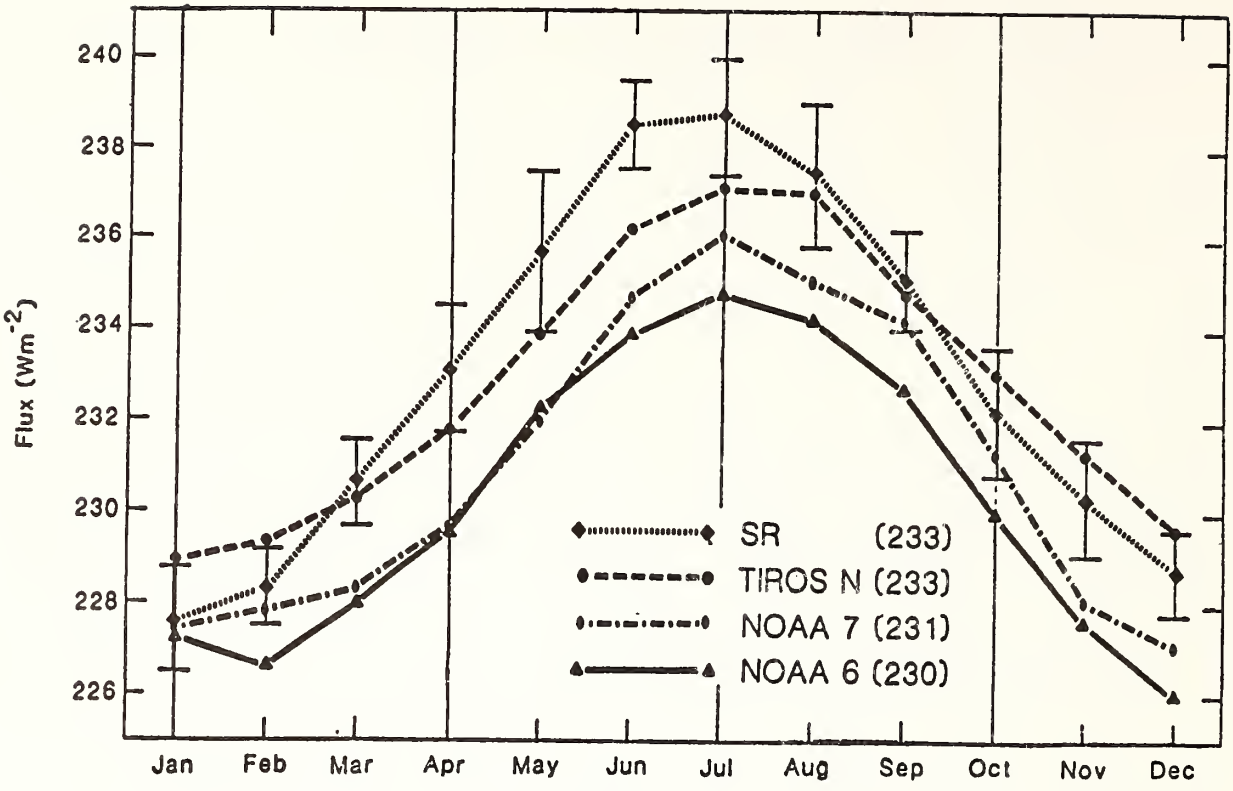

Figure 1

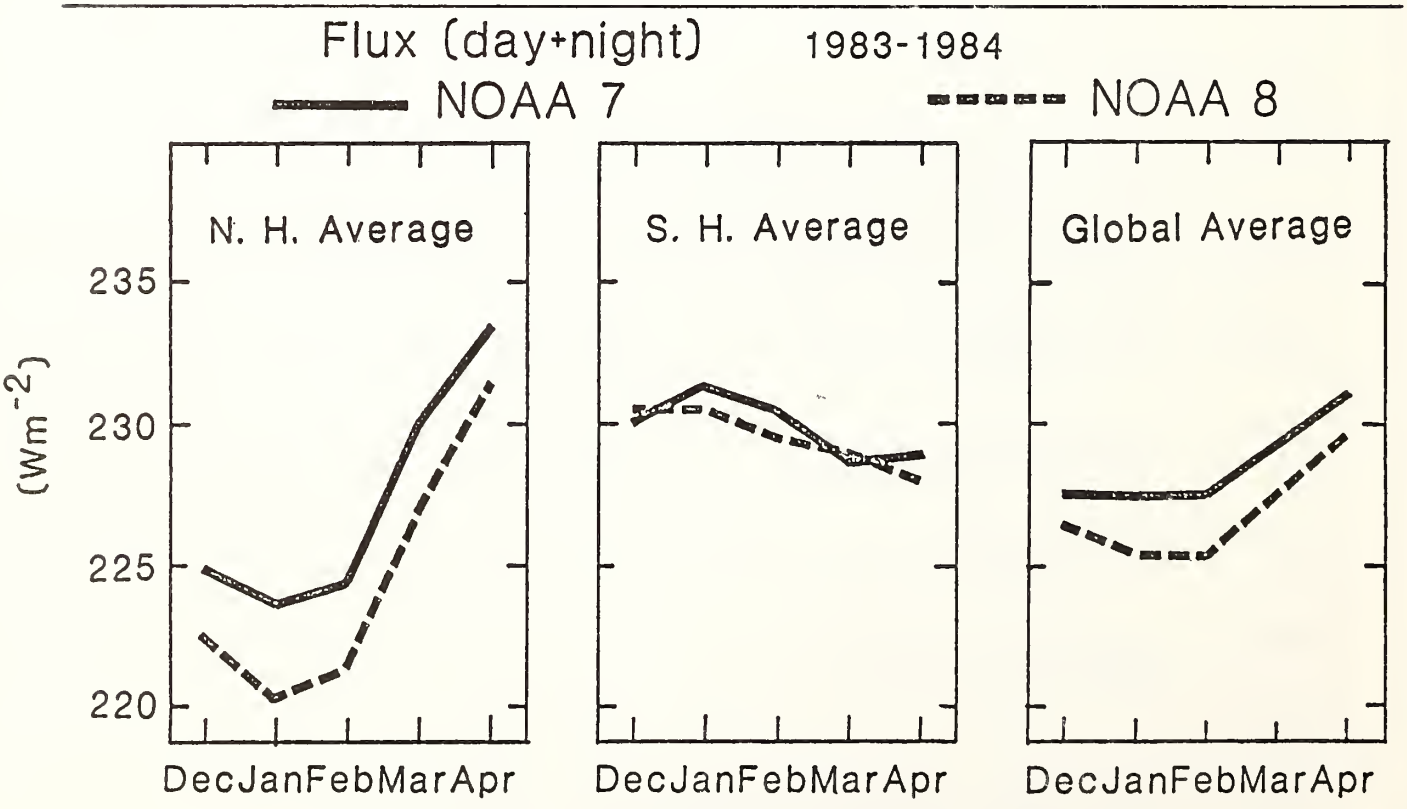

Figure 2

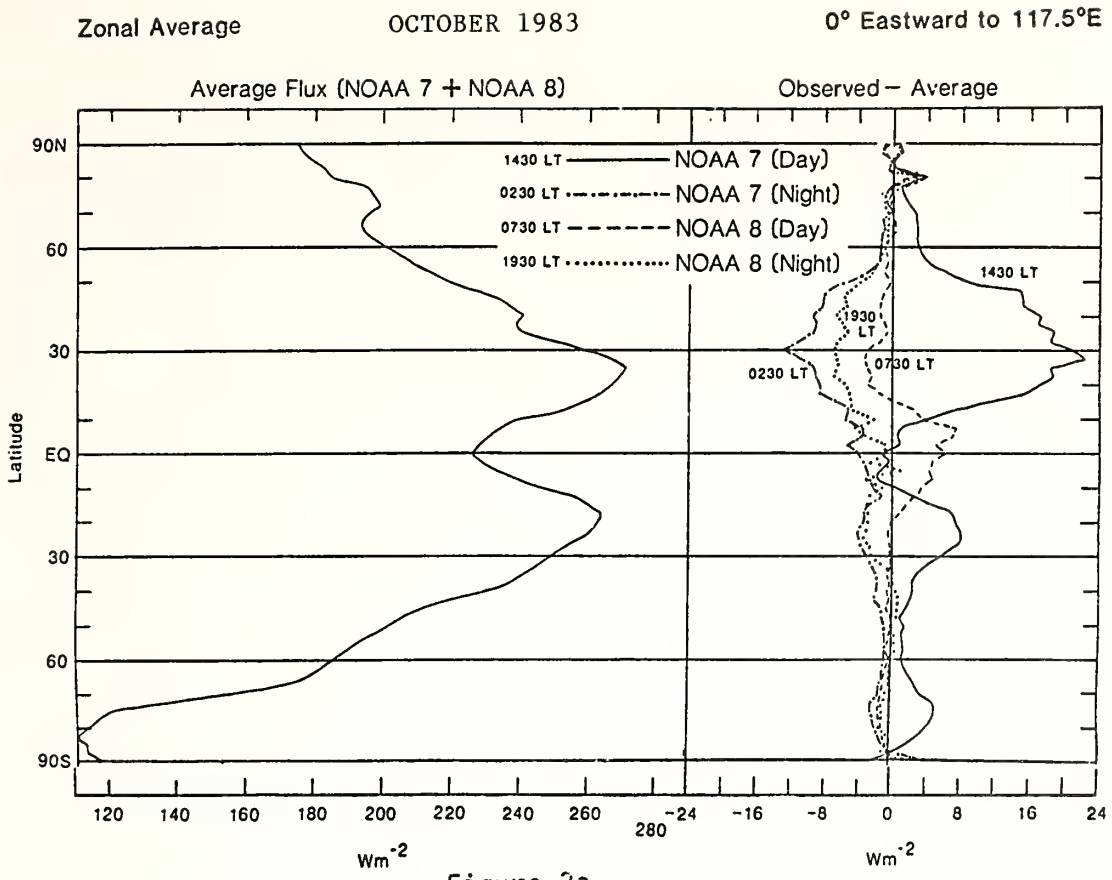

Figure 3a

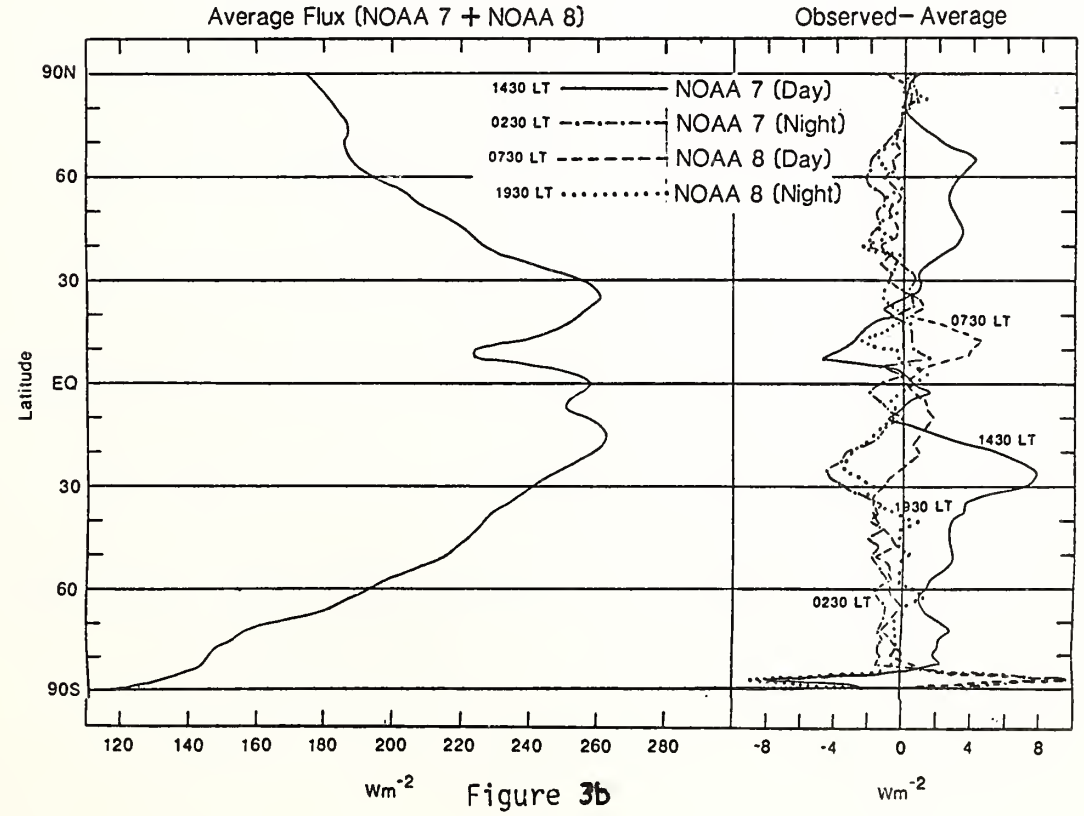

Figure 3b

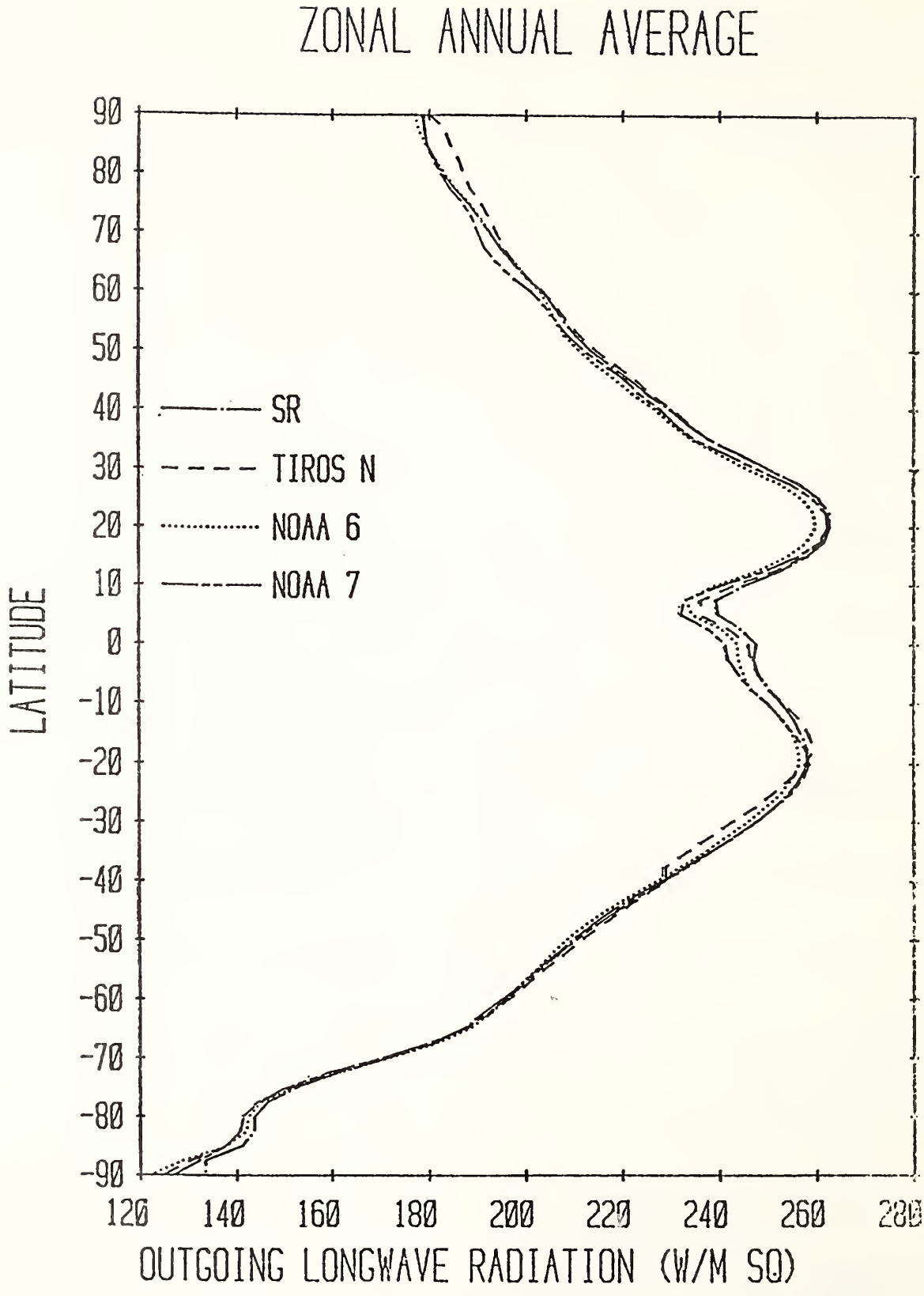
ZONAL ANNUAL AVERAGE
90
80
70
60
50
40
30
20
10
0
-10
-20
-30
-40
-50
-60
-70
-80
-90
LATITUDE
SR
TIROS N
NOAA 6
NOAA 7
120
140
160
180
200
220
240
260
280
OUTGOING LONGWAVE RADIATION (W/M SQ)

Figure 4

Figure 5a

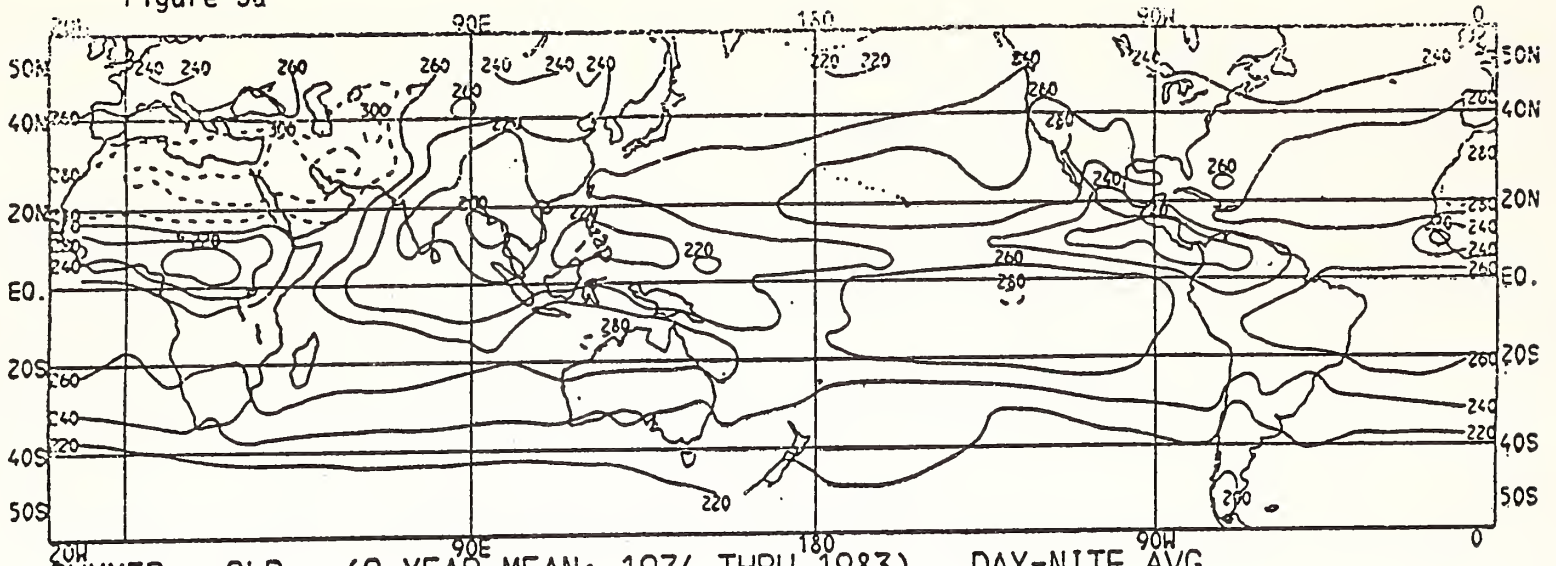

SUMMER OLR (9 YEAR MEAN: 1974 THRU 1983) DAY-NITE AVG

Figure 5b

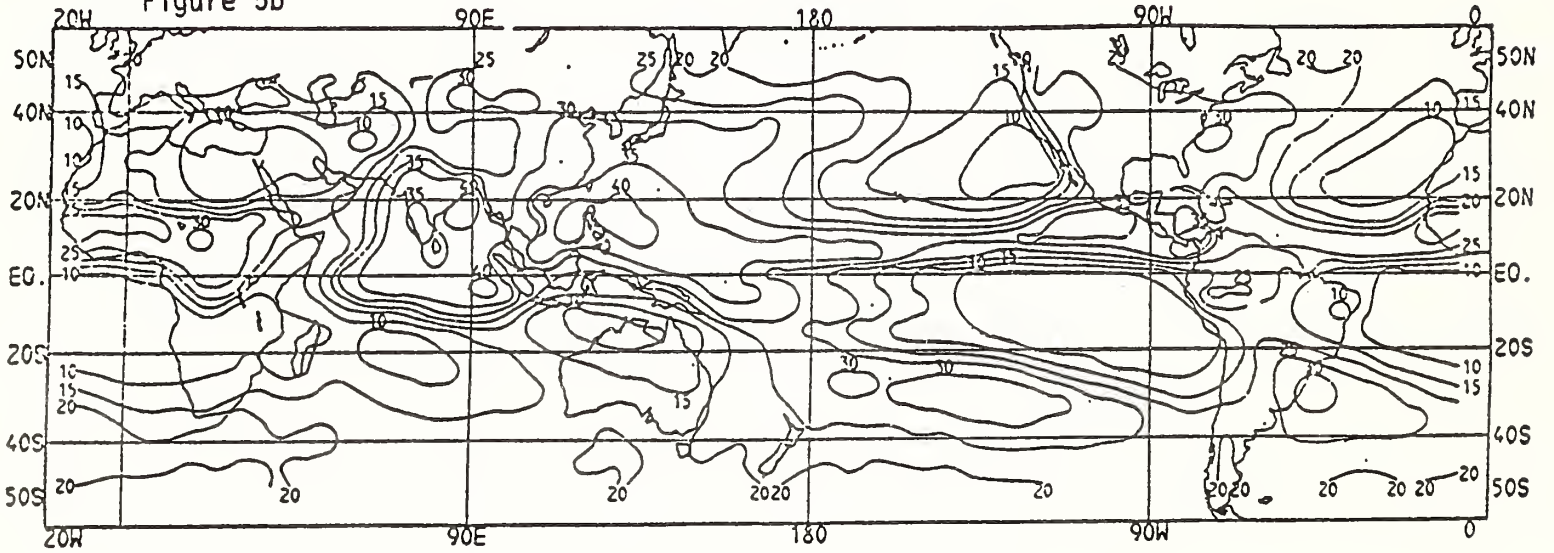

SUMMER AVG STD DEVIATIONS (1974 THRU 1983)

Figure 6

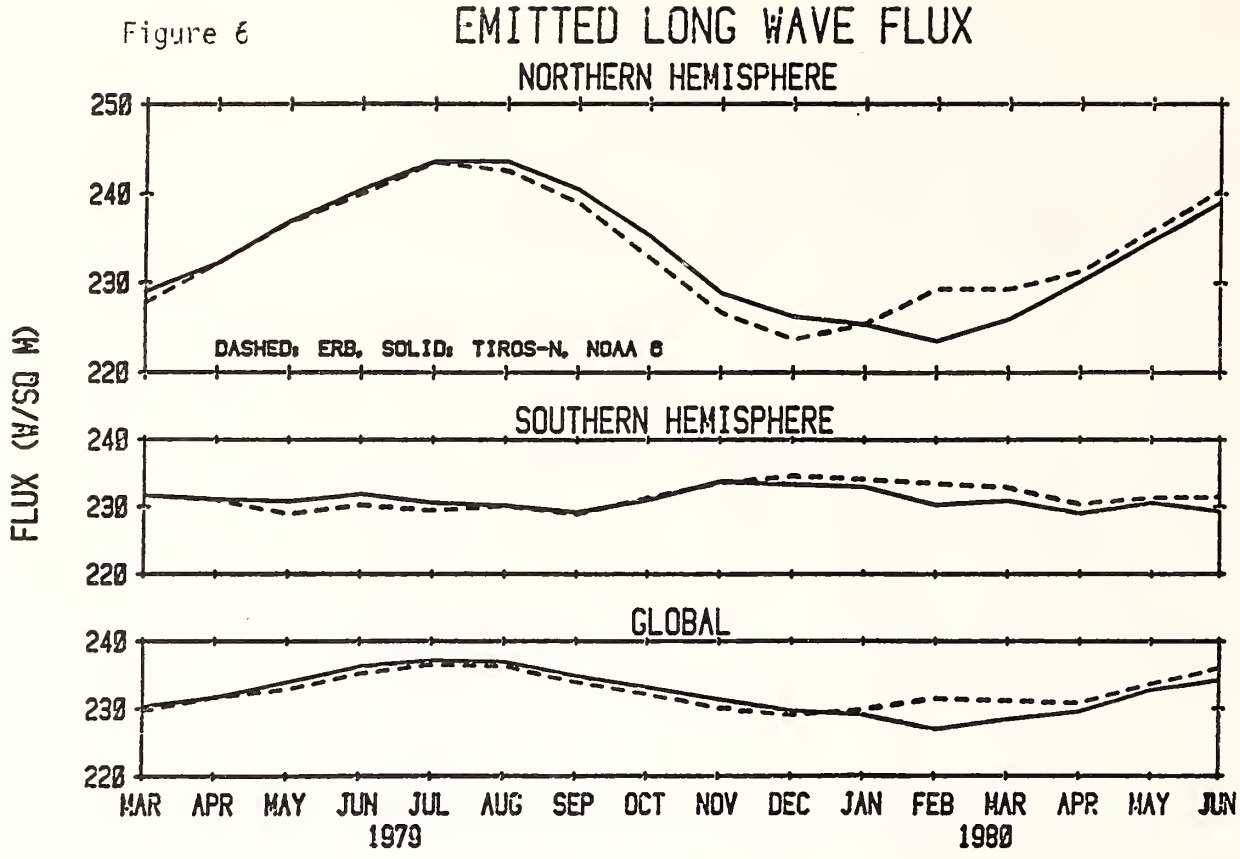

Zonal Annual Averages

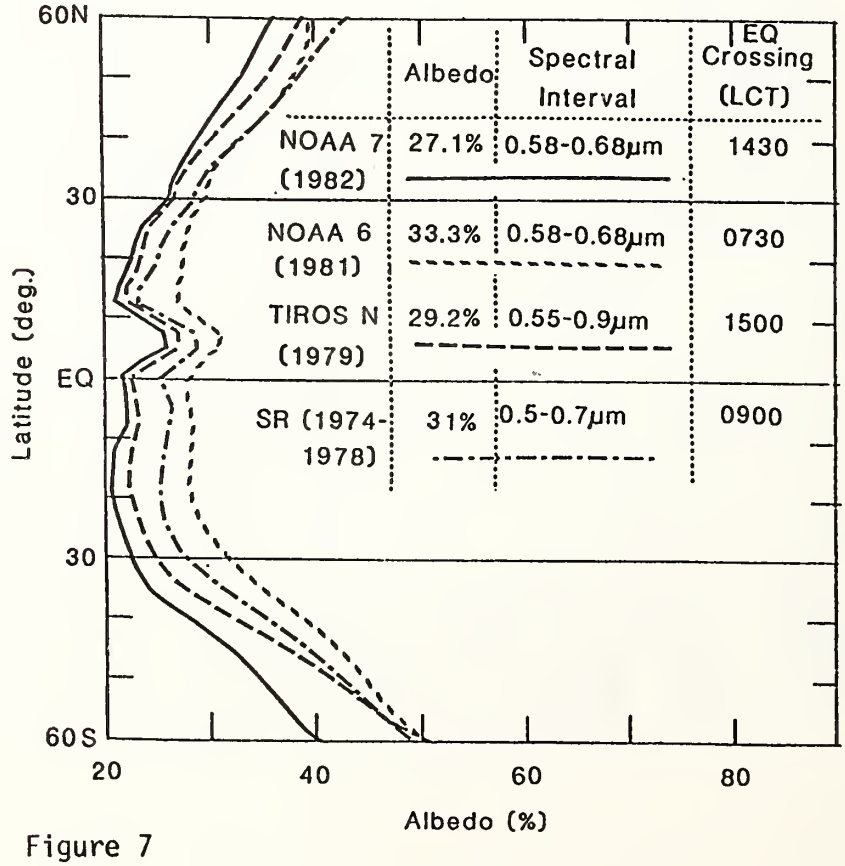

Figure 7

Figure 8a

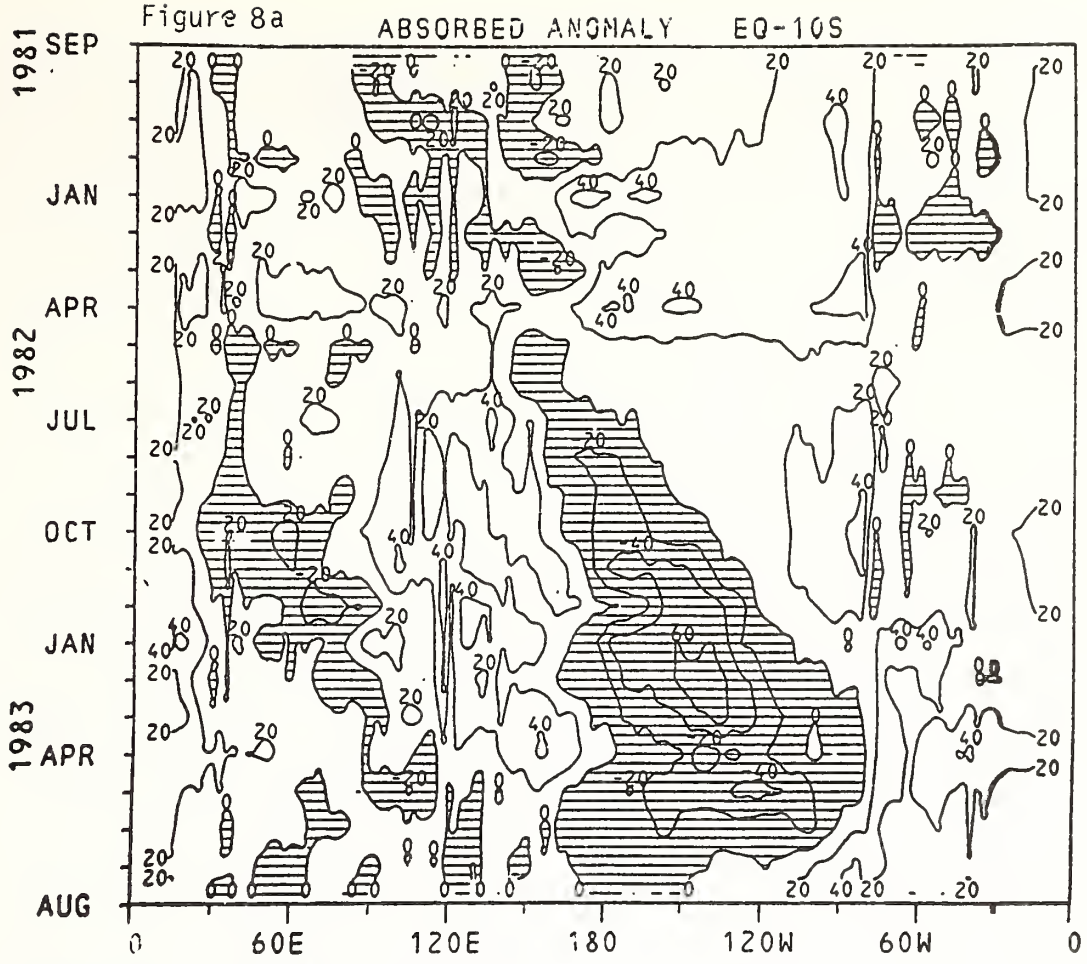

Figure 8b TIME/LONGITUDE CROSS SECTION OF TROPICAL OLR

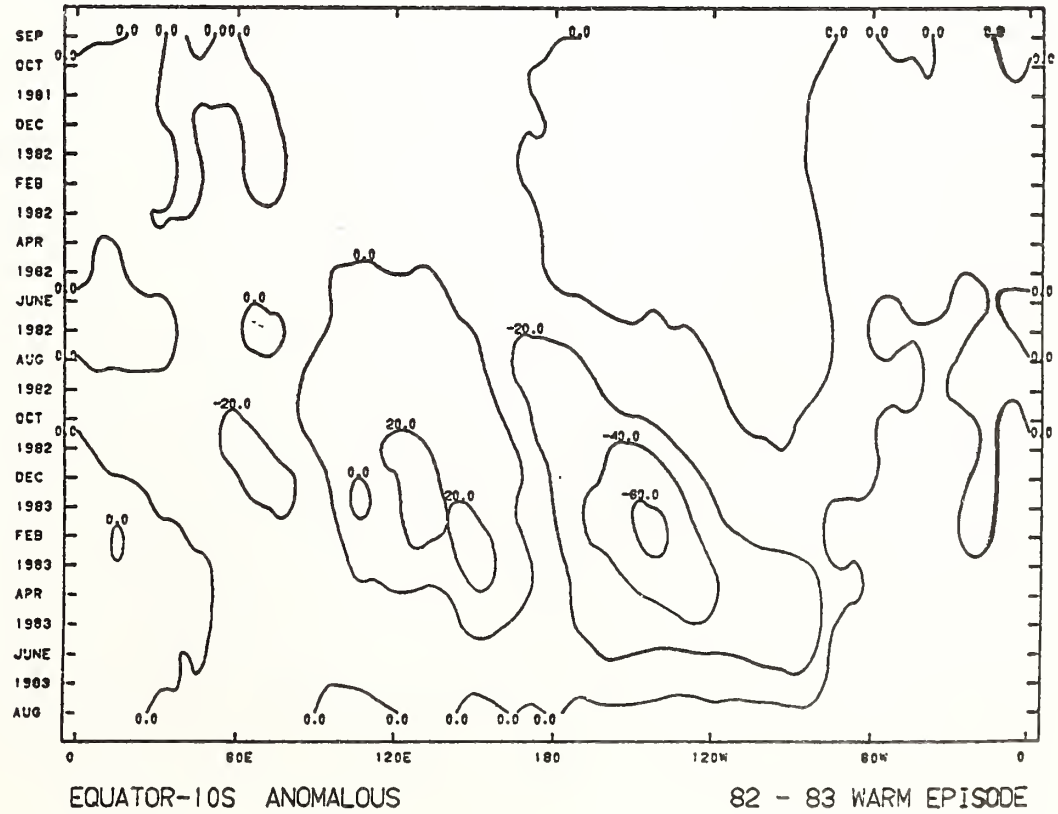

EQUATOR-10S ANOMALOUS 82 - 83 WARM EPISODE

A Sea Surface Temperature Analysis Based on In Situ and Satellite Data

Richard W. Reynolds
Climate Analysis Center
NMC/NWS/NOAA
Washington, D.C. 20233

and

William H. Gemmill
Ocean Products Center
NMC/NWS/NOAA
Washington, D.C. 20233

In an earlier paper (Reynolds and Gemmill, 1984) we described a monthly sea surface temperature (SST) analysis based on in situ (ship and buoy) data. These in situ data (mostly from ships) amount to approximately 100 to 120 thousand observations per month. The distribution of observations received via the Global Telecommunication System for July 1984 are shown in Figure 1. For the spatial scales described above, these data are adequate to describe the SST patterns between 60°N and 30°S except in the central and eastern tropical and southern Pacific. Unfortunately the tropical Pacific is of extreme climate importance because of the appearance of warm anomalies during Southern Oscillation/El Niño (ENSO) events and the large response of the climate to those anomalies. Also, the individual ship observations are subject to large errors in both temperature and postition. (Note the observations over land in the figure.) To extract the large-scale signal from the noise, the in situ data was initally screened using climatology averaged on a two-degree latitude and longitude grid for a month, and then analyzed with a non-linear spatial filter based on medians (see Rabiner, et al., 1975). The use of medians, rather than weighted means, results in the objective elimination of extreme values rather than smoothing their effects into the surrounding grid values. Because of this technique (see Figure 2) smaller scale features (less than 500 km) are not preserved. Although the larger-scale details are generally accurate, much of the smaller-scale variability in the tropical and southern Pacific is an unrealistic aspect of the limited amount of in situ data.

The use of satellite data can significantly improve this analysis. Figure 3 shows the monthly number of satellite SST retrievals over the globe. These retrievals are obtained from the multichannel techniques of McClain (1980) using Advanced Very High Resolution Radiometer (AVHRR). Generally the number of observations is much greater than the number of in situ observations and the satellite coverage is more uniform. However, the number of retrievals has varied from a low of 200 thousand to almost 3 million per month. The variation in the number of retrievals is due at times to satellite hardware problems but also to interpretation difficulties related to cloud cover and high level aerosols. Strong (1983) reported that the aerosols introduced into the atmosphere by the El Chichon eruptions in March-April 1982 resulted in cold biases sometimes exceeding 2°C in the satellite SST retrievals relative to in situ reports. Figure 4 shows the monthly satellite SST field for July 1984, a month with a high number of retrievals.

Comparison of Figures 2 and 4 shows that the overall patterns are similar but that there are important differences. The advantage of the use of the satellite data is clearly seen in the large-scale coherence which is shown in the tropical and southern Pacific in Figure 4 but not in 2. However large zonal differences in the Pacific are clearly evident. There are also smaller-scale differences where both types of data sources should be adequate. An example of this can be seen in the area off the coast of Japan near 40^{o}N and 150^{o}E were the satellite analysis is over 3^{o}C warmer than the in situ analysis.

To further illustrate these differences, Figure 5 shows time series of both analyses in an eastern Pacific equatorial and northern mid-latitude regions. Generally the satellite analysis is approximately 0.5^{o}C colder than the in situ analysis. However there are important reversals in these tendencies for several months. Figures 2, 4 and 5 demonstrate that the differences between the two analyses are not independent of time or position. Both analyses clearly show the warming signal of the 1982-83 ENSO event in the tropical Pacific.

Both types of data have clear advantages. The in situ data offer the advantage of direct measurement (i.e. ground truth) with independence of errors in observations from different platforms; the satellite data offer the advantage of expanded and more uniform data coverage. A method described here "blends" the two types of data by using the in situ data to define "benchmark" temperature values in regions of frequent in situ observations, and the satellite data to define the "shape" of the field between these points.

The two analyzed fields (as, for example, Figures 2 and 4) are used as input fields. These are blended together by solving Poison's equation with appropriate internal and external boundary conditions (see Oort and Rasmusson, 1971). The blended analysis, ϕ, is set equal to the in situ analysis in the region of frequent observations and ϕ is determined in the remaining regions by solving $\nabla^2\phi = \rho$. The forcing term, ρ, is defined by the Laplacian of the satellite analysis ($\nabla^2 S$). Note that the only Laplacian of S plays a role in this aspect of the analysis. The external boundary condition is specified by setting ϕ equal to the in situ analysis (in regions of frequent in situ observations) or to the satellite analysis at the poleward limits of all observations where ship data are infrequent. The resulting anomaly field is shown in Figure 6 where the stippled areas indicate regions where the SST field was fixed by the in situ analysis.

Comparison of the three analyses (Figures 2, 4 and 6) suggests that the blended analysis is an improvement over the fields obtained from in situ data only or satellite data only. Since the satellite data affect the field in the interior via its Laplacian, large scale biases or trends in the satellite data can only influence the final solution through the high latitude boundary conditions. In our example, any satellite bias could only impact the blended result south of 30^{o}S where the in situ data becomes sparse. Satellite features such as the coherent negative anomaly along the equator in the Pacific are maintained in the blended analysis although the size of the anomaly is slightly reduced by the in situ "benchmarks".

The blended analysis appears to be a useful way to utilize both in situ and satellite data. It is planned to monitor each blended field carefully using the individual in situ and satellite analyses as diagnostic tools. The blended analysis can be modified to reflect changes in either the in situ observations or the satellite retrievals.

REFERENCES

McClain, E.P., 1980: Multiple atmospheric-window techniques for satellite-derived sea surface temperatures. Oceanography from Space, edit. J.F.R. Gower, Plenum Press, New York, N.Y., 73-85.

Oort, A.H., and E.M. Rasmusson, 1971: Atmospheric circulation statistics, NOAA Professional Paper No. 5, U.S. Government Printing Office, Washington, D.C. 323 pp.

Rabiner, L.R., M.R. Sambar and C.E. Schmidt, 1975: Applications of a non-linear smoothing algorithm to speech processing. IEEE Trans. Acoust. Speech Signal Proc., ASSP-23, 552-557.

Reynolds, R.W., 1982: A monthly averaged climatology of sea surface temperatures. NOAA Tech. Rept. NWS 31, Washington, D.C., 33 pp.

Reynolds, R.W., and W.H. Gemmill, 1984: An objective global monthly mean sea surface temperature analysis. Tropical Ocean-Atmosphere Newsletter, No. 23, 4-5.

Strong, A.E., 1983: Satellite-derived sea surface temperture errors due to El Chichon aerosol cloud. Tropical Ocean-Atmosphere Newsletter, No. 18, 14-15.

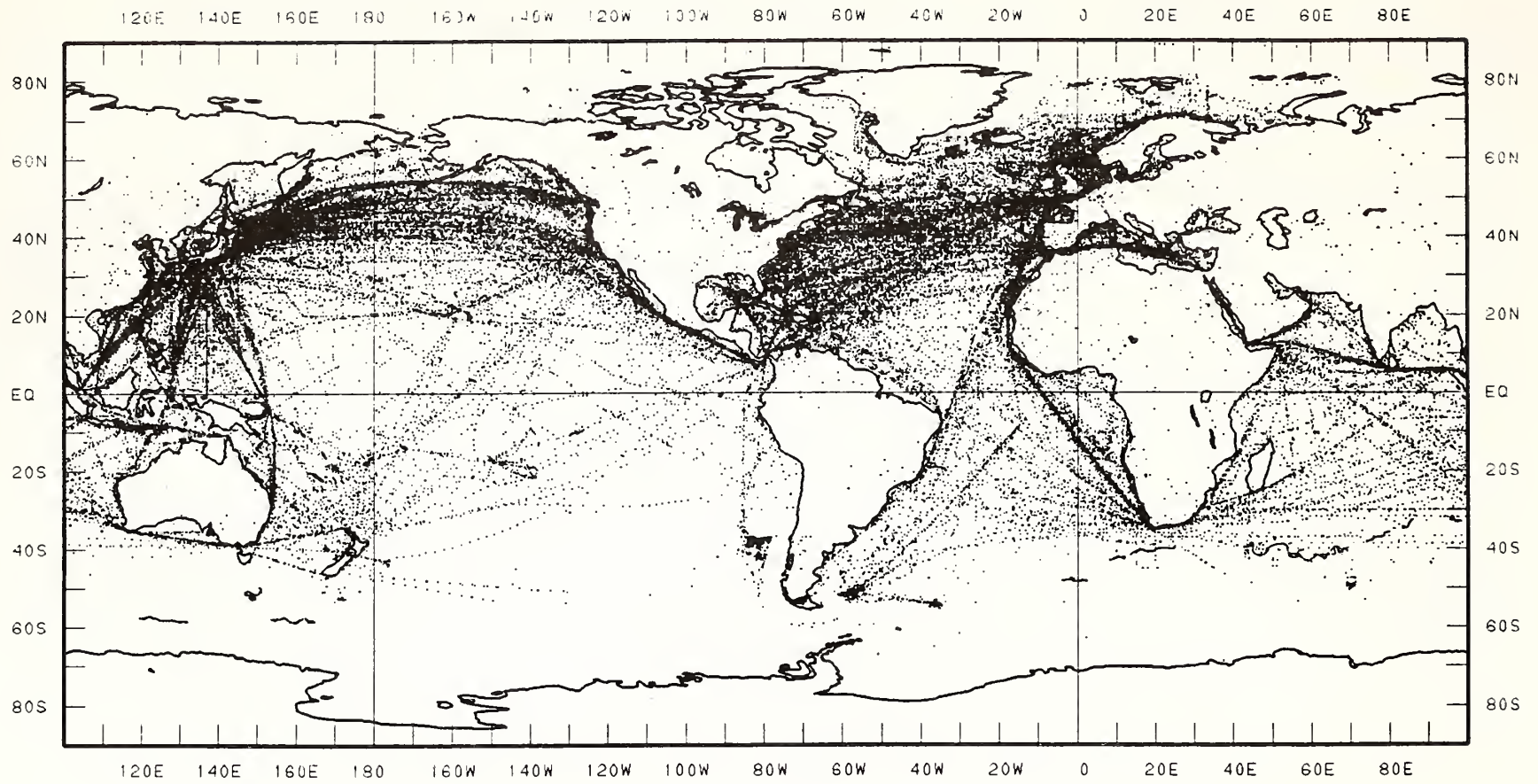

Fig. 1 - Distribution of in situ (ship and buoy) data received over the Global Telecommunication System for July 1984.

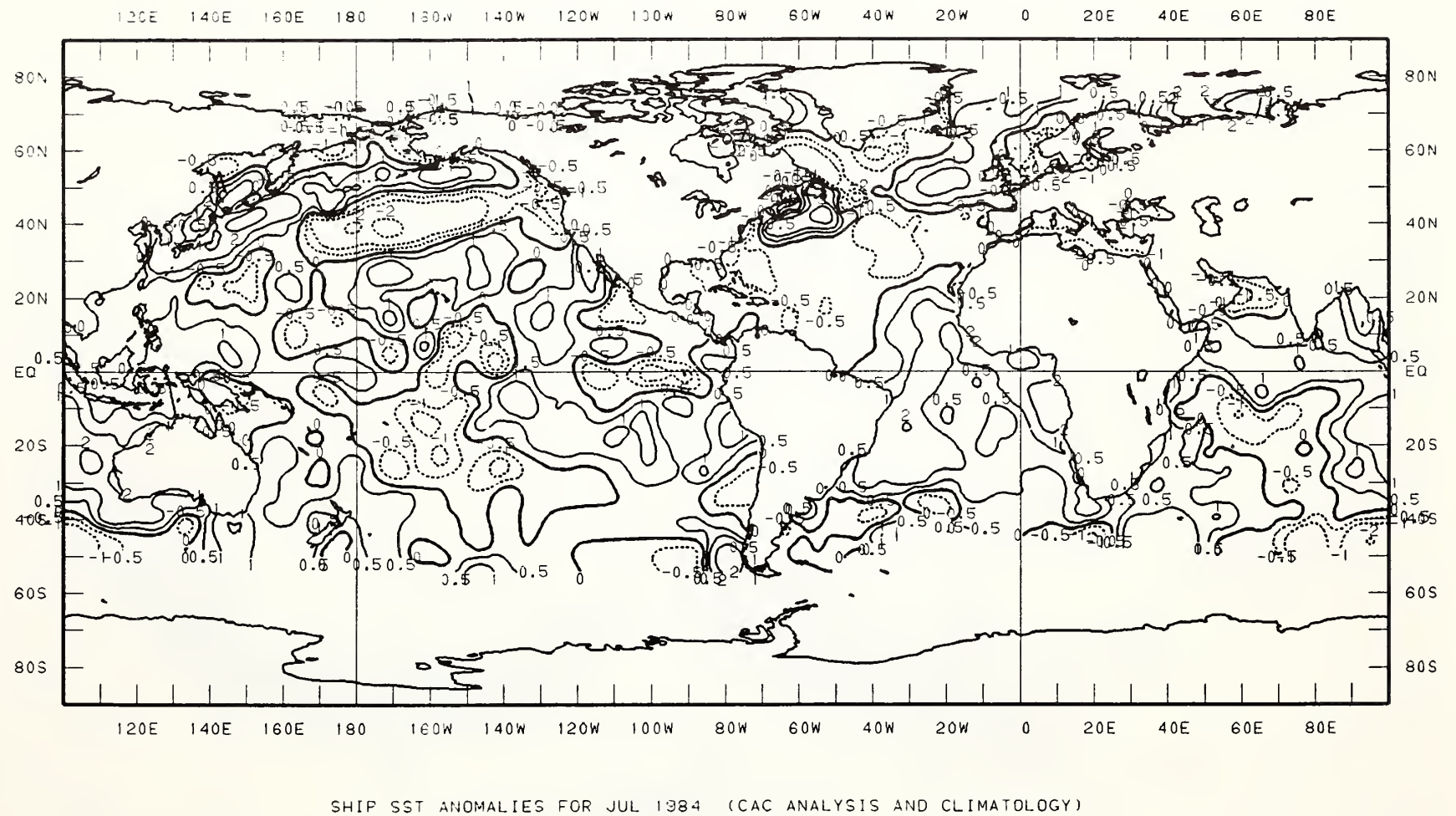

Fig. 2 - In situ SST anomalies for July 1984 on a 2° grid. Anomalies are computed from the climatology of Reynolds (1982). The contour interval is 0.5°C between ± 1°; otherwise the contour interval is 1°C; the negative anomalies are dashed.

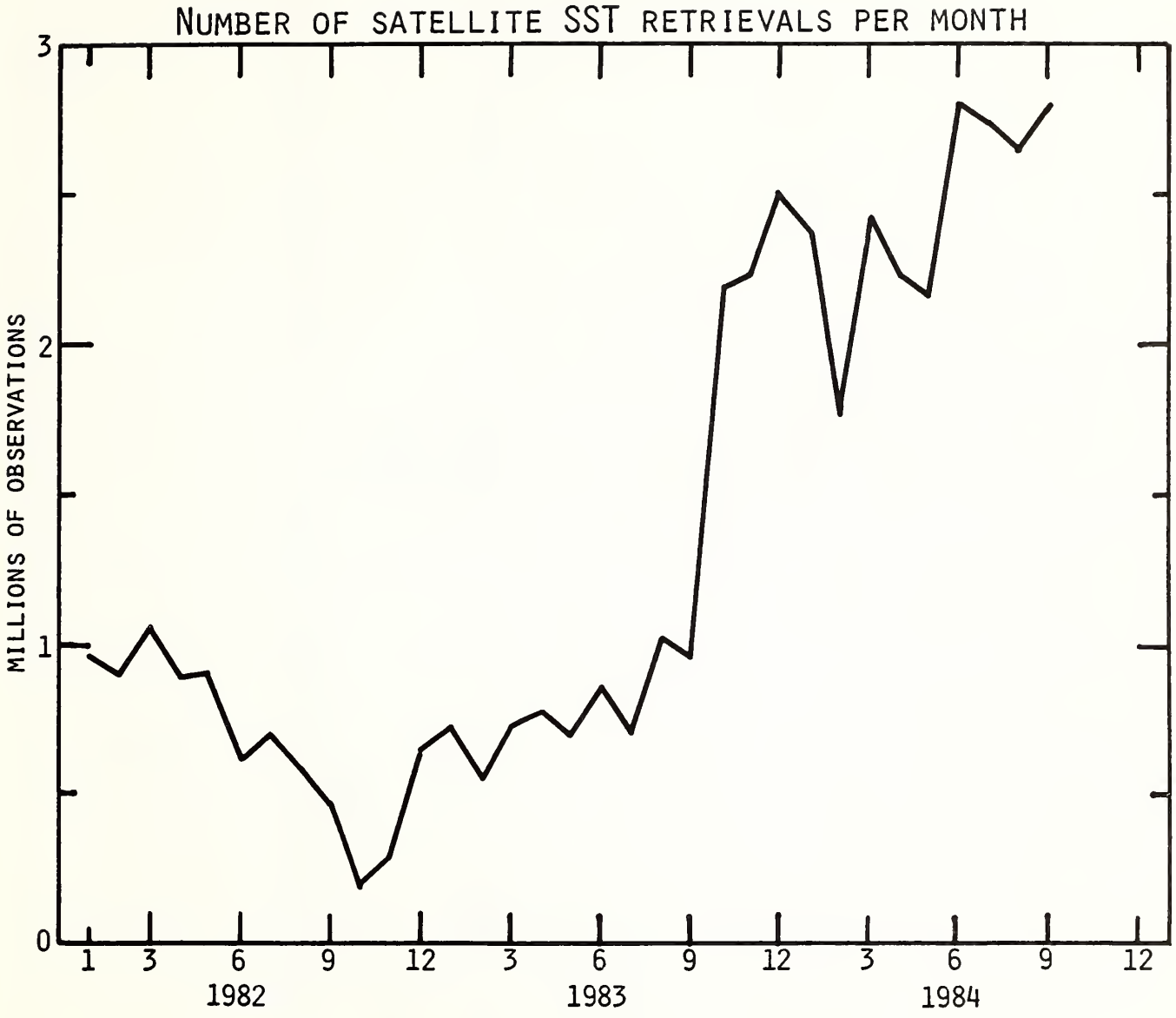

Fig. 3 - Number of global satellite AVHRR retrievals per month.

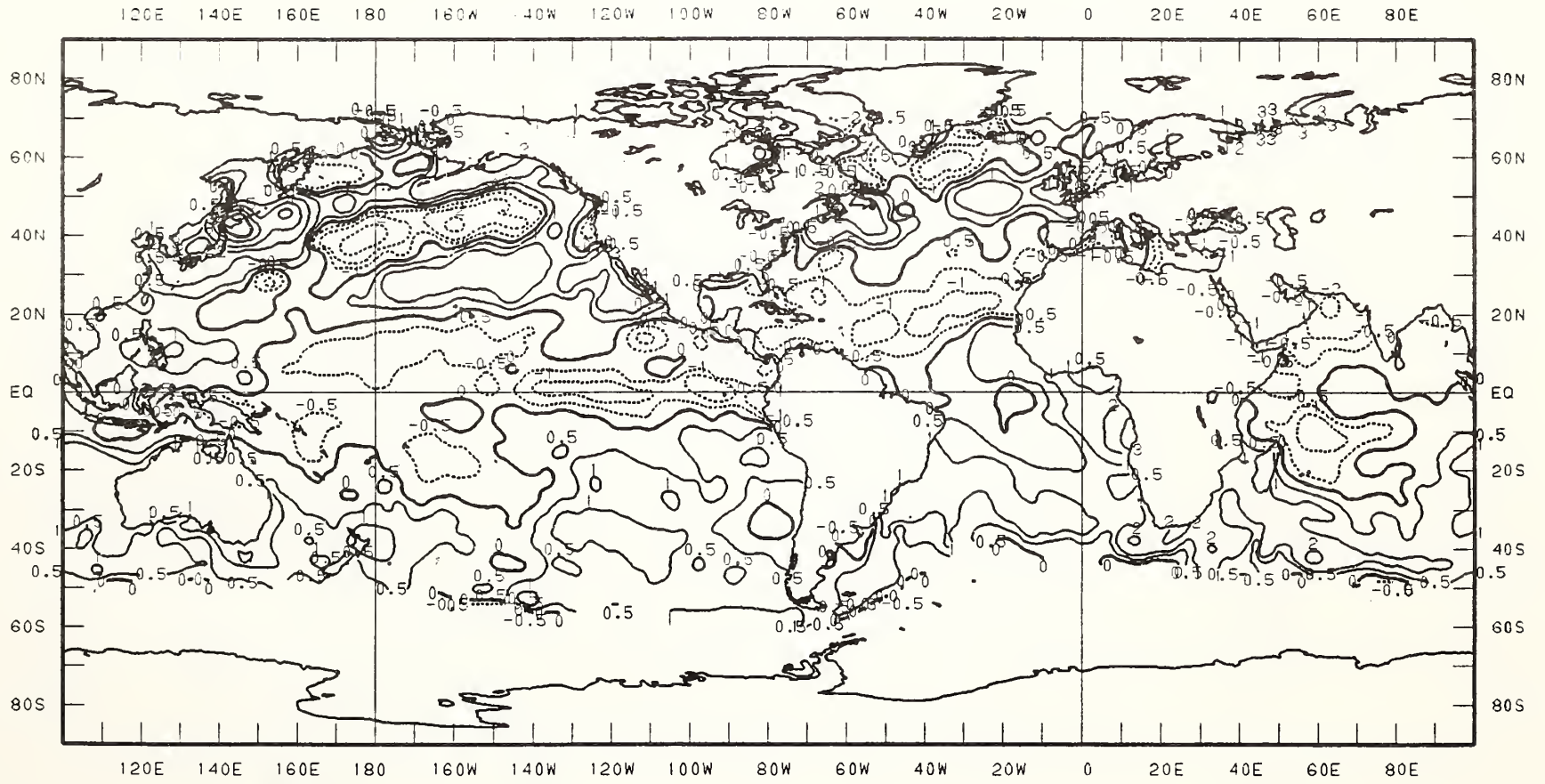

Fig. 4 - Satellite SST anomalies for July 1984. Otherwise as in Fig. 2.

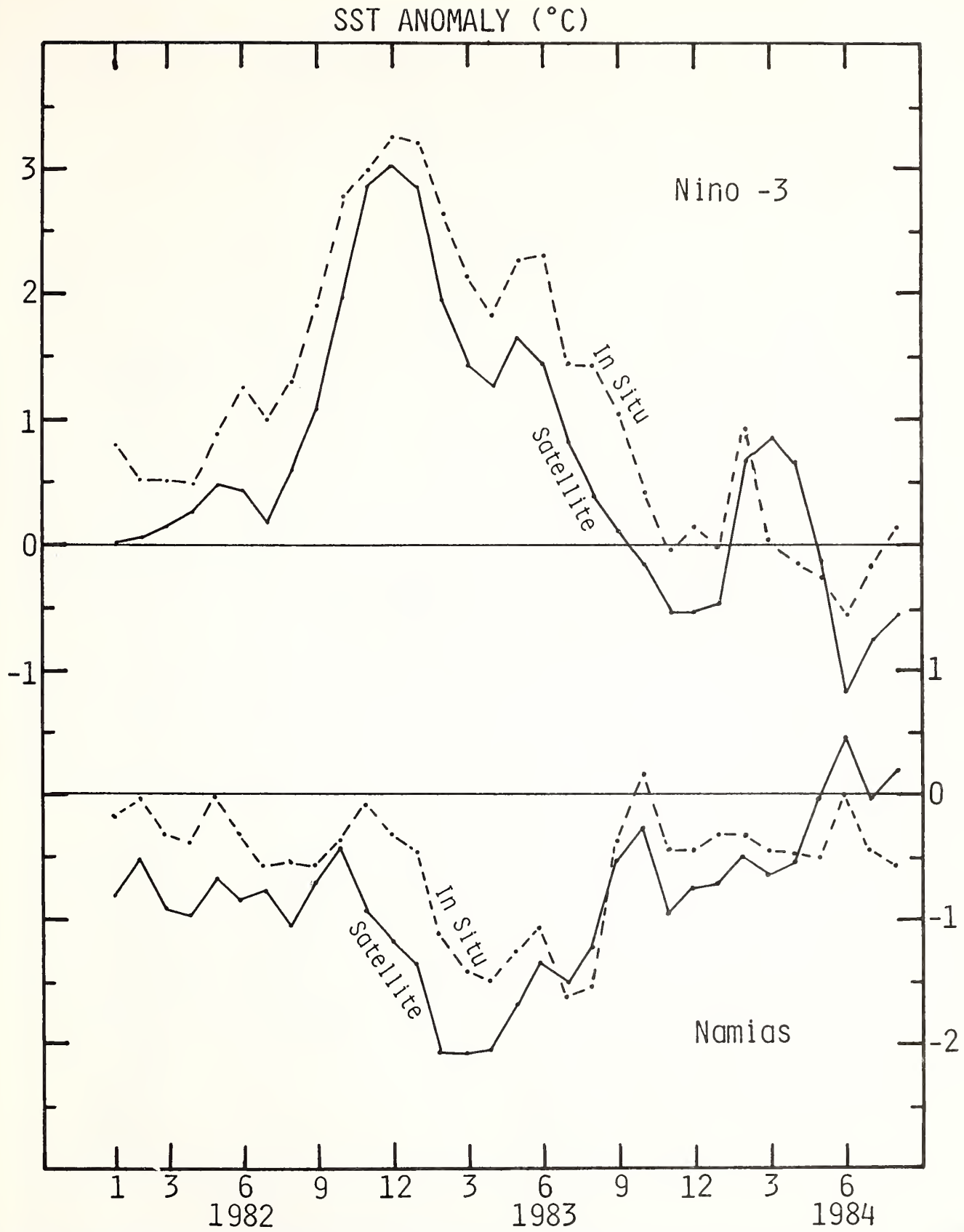

Fig. 5 - Time series of in situ and satellite SST anomalies. The Pacific regions are: Niño 3 (5°S-5°N, 90°W-150°W); Namias (30°N-50°N, 150°W-165°W)

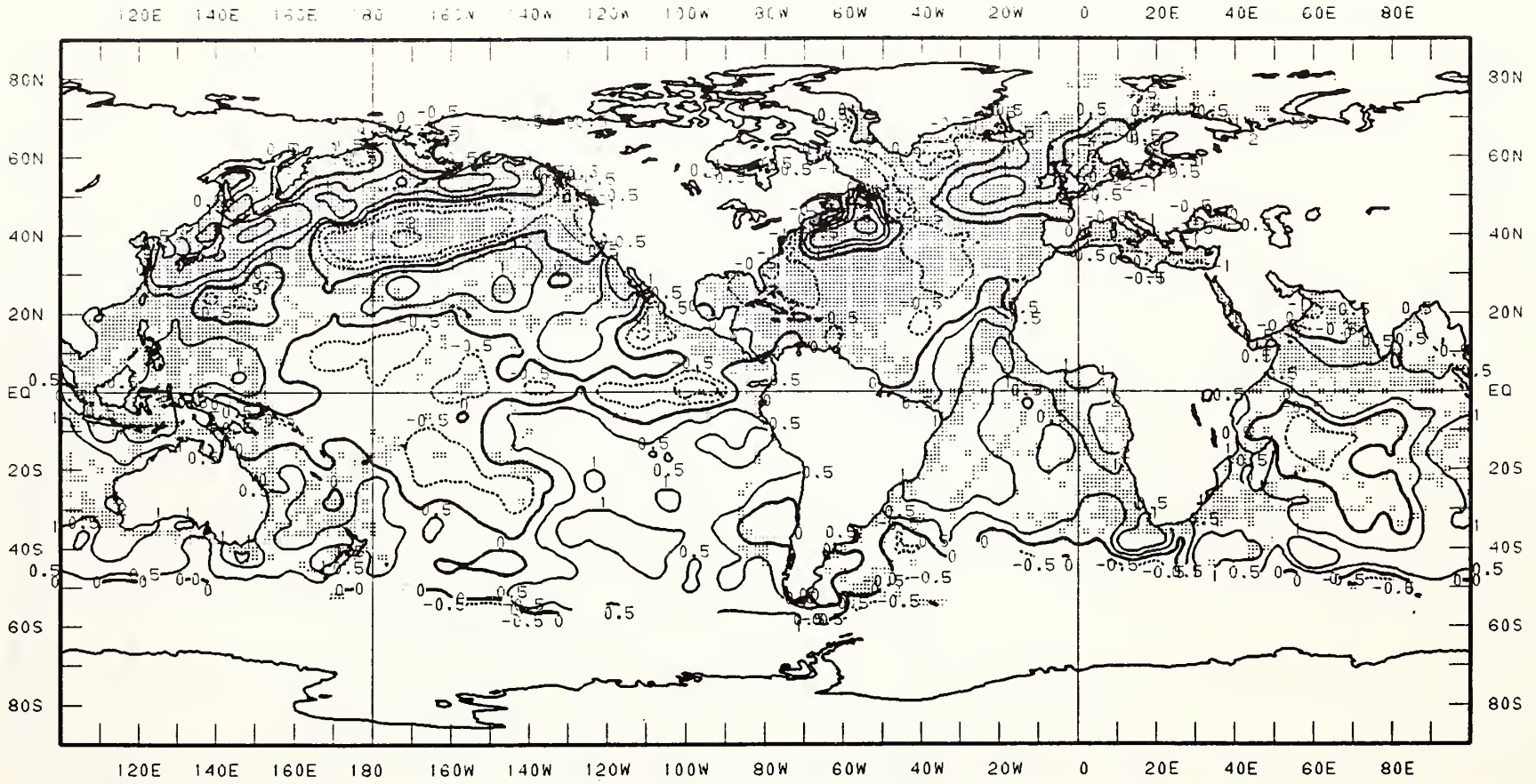

Fig. 6 - Blended (see text) SST anomalies for July 1984. As in Fig. 2, except that the stippling indicates regions where the blended field was defined by the in situ analysis.

Effect of Initialization on Diagnoses of Large-scale Circulation Statistics from NMC Analyses

Richard D. Rosen and David A. Salstein
Atmospheric and Environmental Research, Inc.
840 Memorial Drive, Cambridge, Massachusetts 02139

Analyses of the state of the atmosphere produced by operational weather centers such as NMC are finding increasing use in diagnostic studies of the large-scale circulation. It is important, therefore, to test the degree to which these analyses may be compromised for this purpose by their dependence on the methods used to generate them. Here we examine the effect of one element of the NMC global data assimilation system - namely, initialization - on calculation of circulation statistics.

Normally, the only NMC fields routinely archived and available to the scientific community are those that have undergone initialization. However, daily analyses that had been archived prior to the inititalization step were also made available to us for the months of January and July 1983, so that we could examine differences between statistics generated from these pre-initialized (PREI) analyses and the post-initialized (POSTI) ones. Although limited to a two month period, our results are more generally valid because the initialization scheme used by NMC remained unchanged during the entire period from about January 1981 through August 1984.

During this period, NMC utilized a non-linear normal mode initialization scheme that considered the atmosphere to be adiabatic. Previous studies have indicated that this assumption could affect the intensity of the tropical Hadley cell, and approaches which use a frequency cut-off criterion have been suggested to improve the situation. At NMC, gravity modes with periods beyond 48 hours are not initialized, but it is not obvious a priori what the impact of this choice of cut-off would be.

Cross sections of the mass streamfunction from the PREI and POSTI analyses for the two months studied here are contained in Fig. 1. It does appear that the initialization procedure has resulted in a weaker Hadley cell, although the effect is not especially large, perhaps in part because at NMC only four vertical modes are initialized and these do not have much structure in the lower troposphere. The impact of the initialization on other zonal mean fields is even smaller than that indicated in Fig. 1. Indeed, most differences between these other PREI and POSTI zonal mean fields are on the order of only 1%, an exception being the $[\overline{u'v'}]$ field shown in Fig. 2 in which differences of up to 5% are present near 40°S.

So far as the effect of NMC's initialization on regional scale features is concerned, Fig. 3 contains the 200 mb velocity potential field for January 1983 from PREI and POSTI analyses. The maximum in the difference plot is located near Indonesia, the nature of the difference implying generally weaker divergence in the POSTI analysis there. This region, along with most of the other tropical centers in the difference plots for January and June (not shown), appears to be an area of strong convective activity, as indicated by mean fields of outgoing longwave radiation for these months. This result

tends to support the conclusion that neglect of diabatic processes in initialization can be detrimental to the analysis of regional divergent motions. An examination of the monthly mean PREI and POSTI vertical motion fields (not shown) also reveals the damping effect of the initialization on this quantity. Indeed, the magnitudes of the extrema in the vertical motion field are often reduced significantly by the initialization.

The regional effects of initialization appear to be generally small for other fields, especially outside the tropics. For example, in Fig. 4 for $\bar{v}$ at 200 mb in July it is clear that the initialization has done very little to affect the train of cells strung along 40°N.

To provide a perspective on the importance of the impact of NMC's initialization on diagnostic calculations, it is useful to compare the NMC results with those generated independently by the ECMWF. In general, we have found that the NMC PREI and POSTI fields resemble each other more closely than either resembles the ECMWF fields. In this light, NMC's initialization procedure cannot, in itself, be viewed as a major factor contributing to the uncertainties in modern-day circulation statistics.

Mass streamfunctions from the ECMWF analyses for January and July 1983 are given in Fig. 5. These fields are somewhat weaker than NMC's both months, but the most striking difference is the presence of separate upper and lower tropospheric circulation cells within the Hadley regime of the ECMWF analyses but not in the NMC analyses. The unusual structure of the ECMWF Hadley cell may result from the inclusion of diabatic heating processes in their initialization procedure, but there are many other differences between the NMC and ECMWF data assimilation systems that could lead to the differences in Fig. 5.

Figure 6 contains cross sections of $[\bar{T}]$ for January 1983 from the ECMWF and NMC. The NMC PREI field has not been included in this figure because it is nearly identical to the NMC POSTI result. The same cannot be said of the ECMWF $[\bar{T}]$ field, however, which differs from the NMC analysis in several important areas. For example, the static stability of the region between the surface and 700 mb near the equator is significantly weaker in the ECMWF analysis. Moisture fields from the two centers (Fig. 7) are in generally good agreement outside the tropics, but the NMC analysis contains a number of peculiar features over the equatorial Pacific not seen in the ECMWF analysis.

Further study is needed to understand the differences between the NMC and ECMWF fields such as those shown above. In addition, future changes in the NMC initialization procedure, such as the introduction of a diabatic scheme in September 1984, should be accompanied by tests of the sort performed here.

Acknowledgments. We are very grateful to P. Arkin of the Climate Analysis Center for his efforts in providing us with the data sets used in this study and for his worthwhile suggestions. Members of the NMC Development Division were also especially helpful. The National Meteorological Center/NOAA provided funds for this research through contract NA-83-SAC-00738.

Mass Streamfunction, 10^{10} kg s^{-1} January 1983

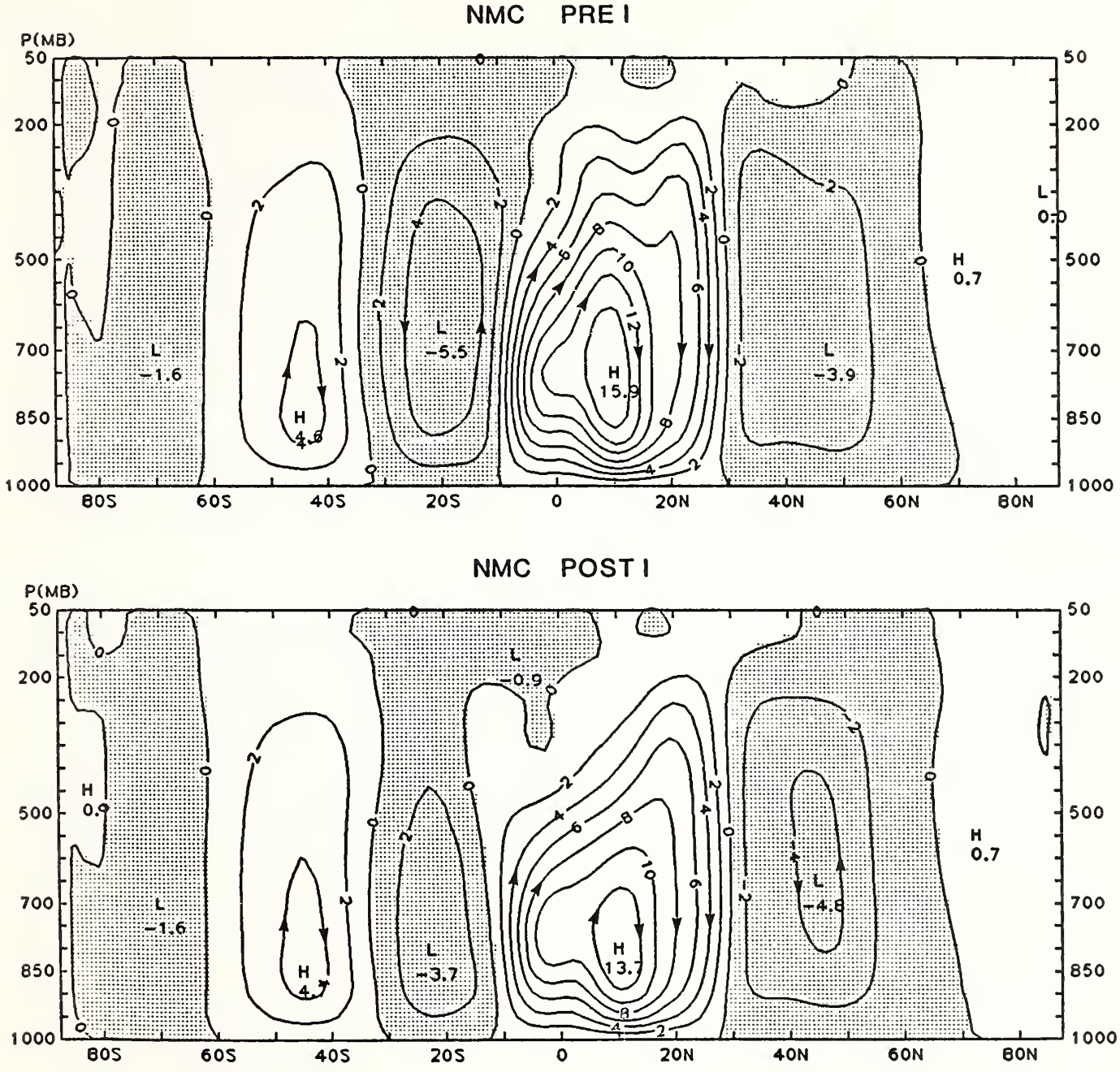

Fig. 1a. Cross sections of the mass streamfunction for the mean meridional circulation for January 1983 calculated from the NMC pre-initialized (PREI) and post-initialized (POSTI) analyses. Positive values indicate clockwise circulation.

Mass Streamfunction, 10^{10} kg s^{-1} July 1983

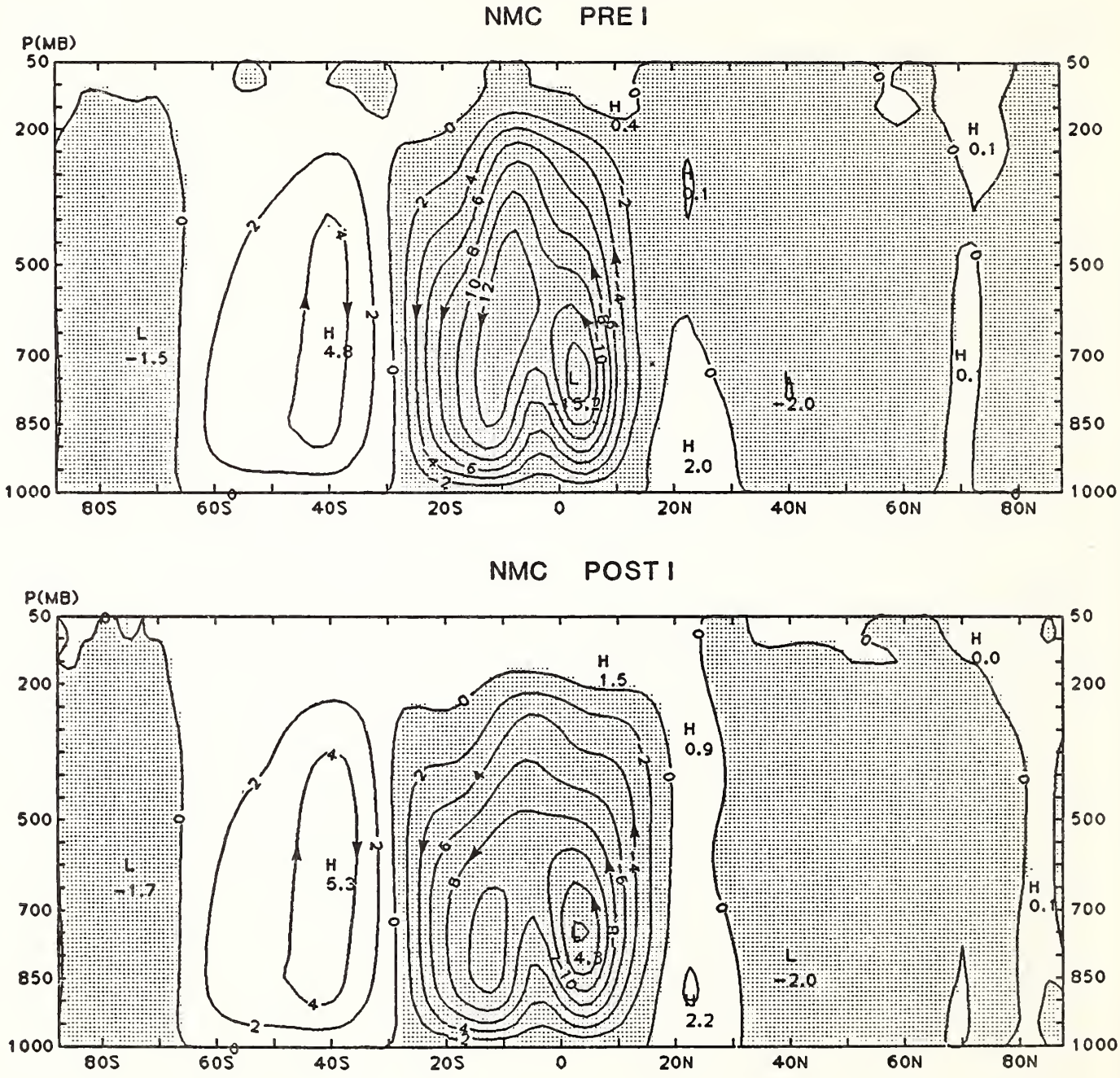

Fig. 1b. As in Fig. 1a, but for July 1983.

$\left[\overline{u'v'}\right]$, $m^2 s^{-2}$ July 1983

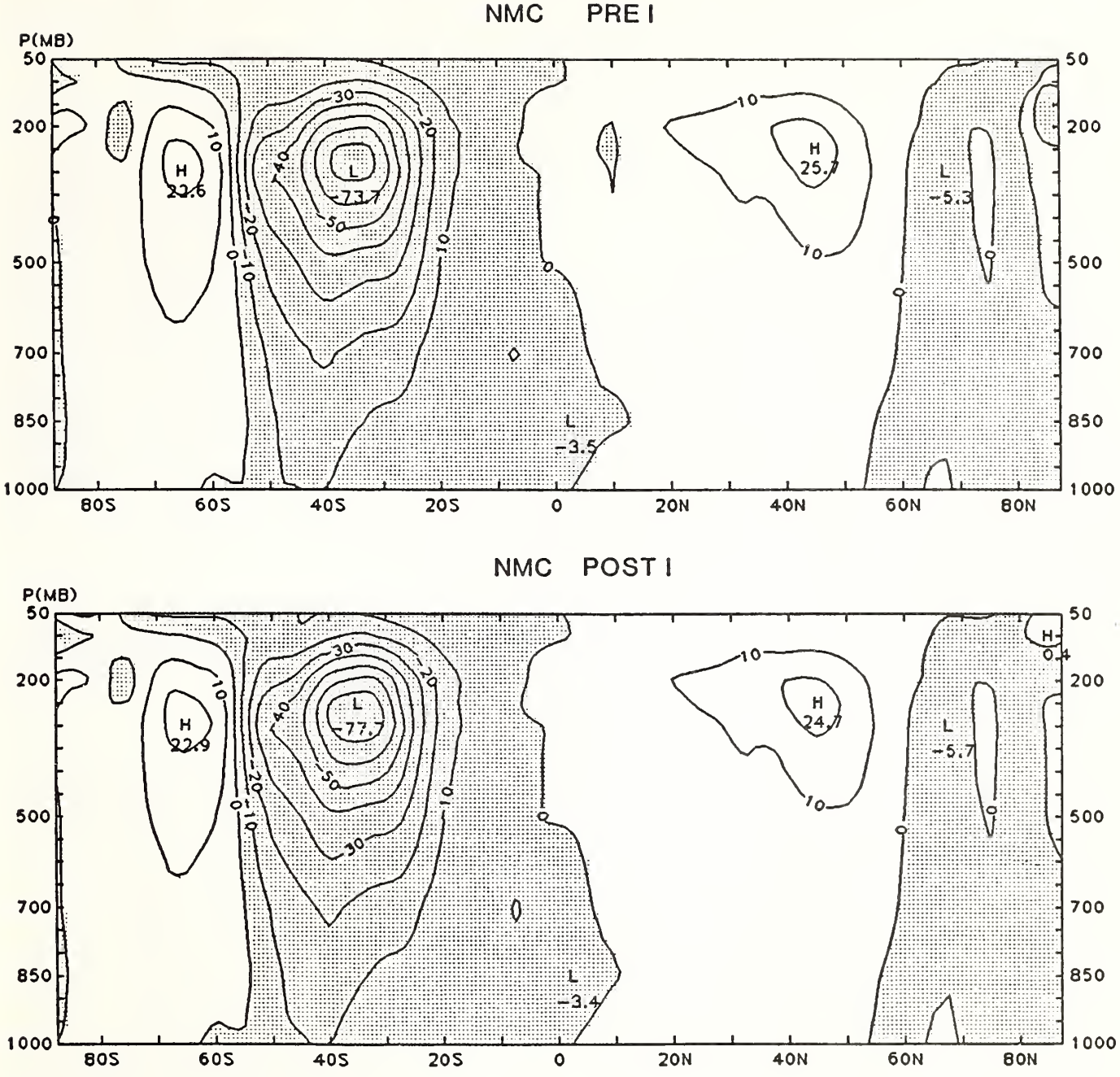

Fig. 2. Cross sections of the transient eddy flux of momentum for July 1983 calculated from the NMC pre-initialized (PREI) and post-initialized (POSTI) analyses. Negative values are shaded and indicate southward fluxes.

NMC PREI

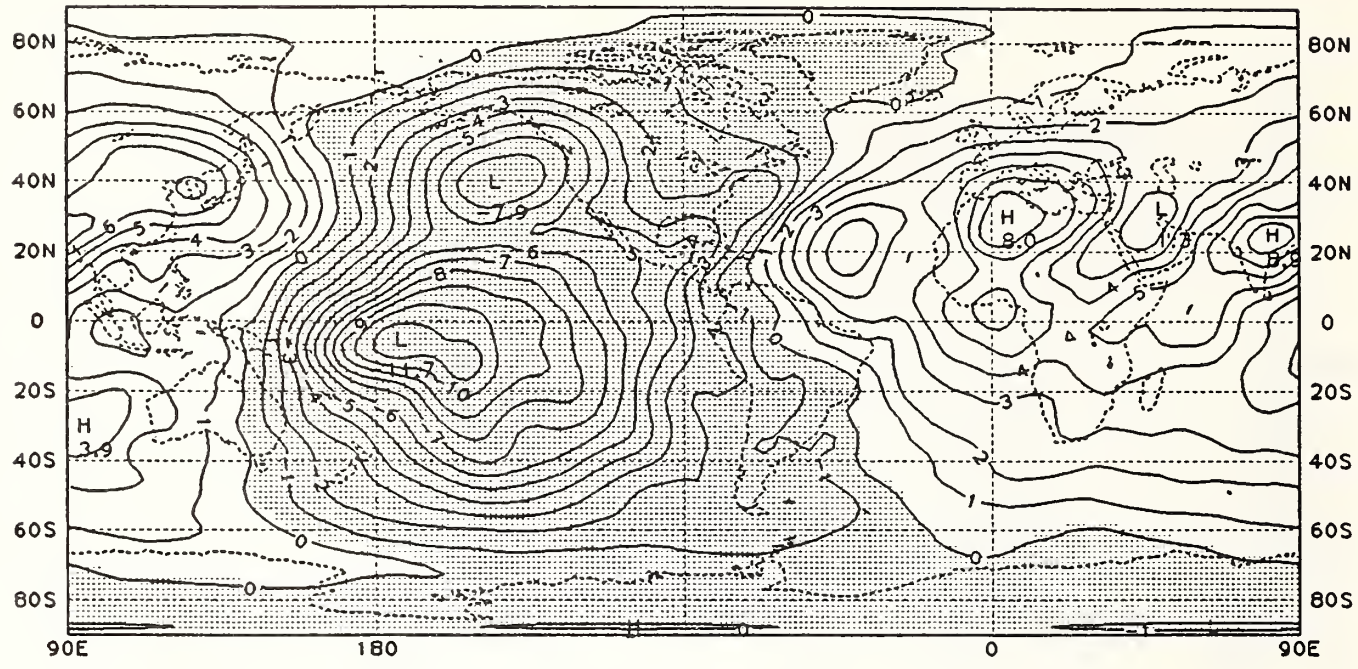

NMC POSTI

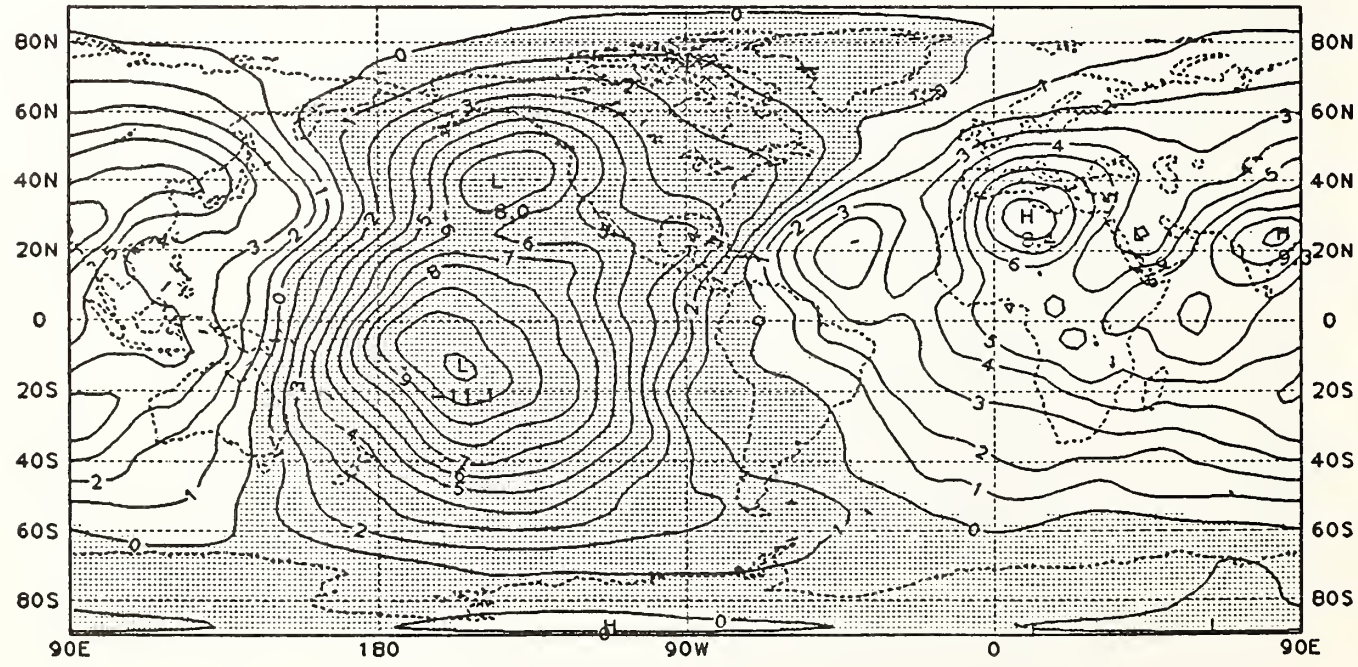

Fig. 3a. Global maps of the horizontal velocity potential at 200 mb for January 1983 calculated from the NMC pre-initialized (PREI) and post-initialized (POSTI) analyses. The sign convention is such that the divergent component of the wind is directed along the gradient of the potential from low to high values. Isolines are drawn at intervals of $10^6\ m^2s^{-1}$.

Velocity Potential, 10^6 m^2s^{-1} 200 mb January 1983

DIFFERENCE (POST I-PRE I)

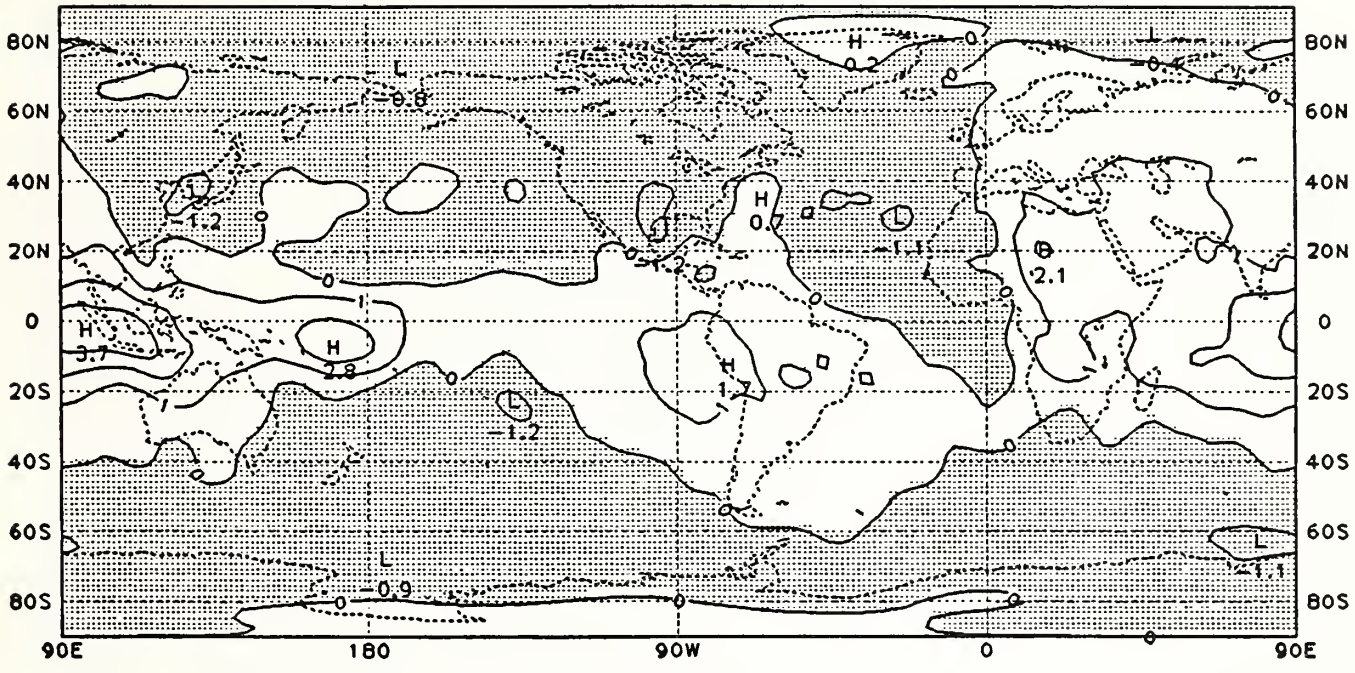

Fig 3b. The difference, POSTI minus PREI, of the two fields in part (a).

NMC PRE I

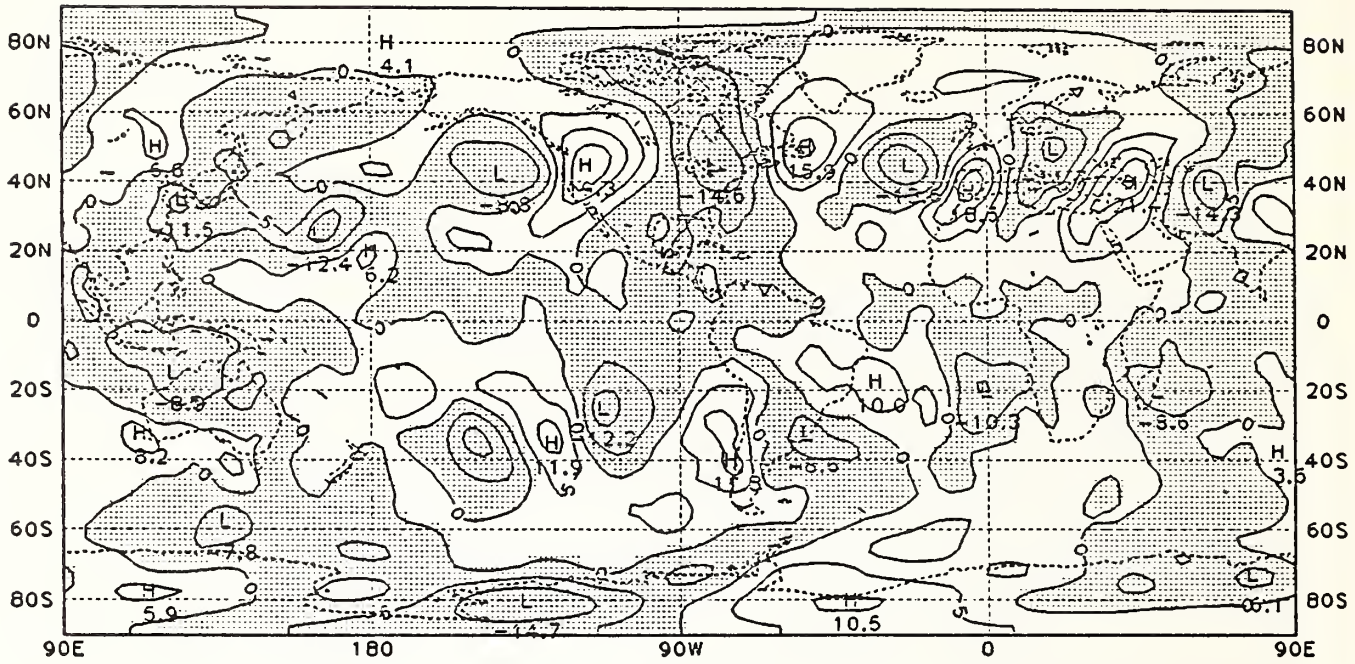

NMC POST I

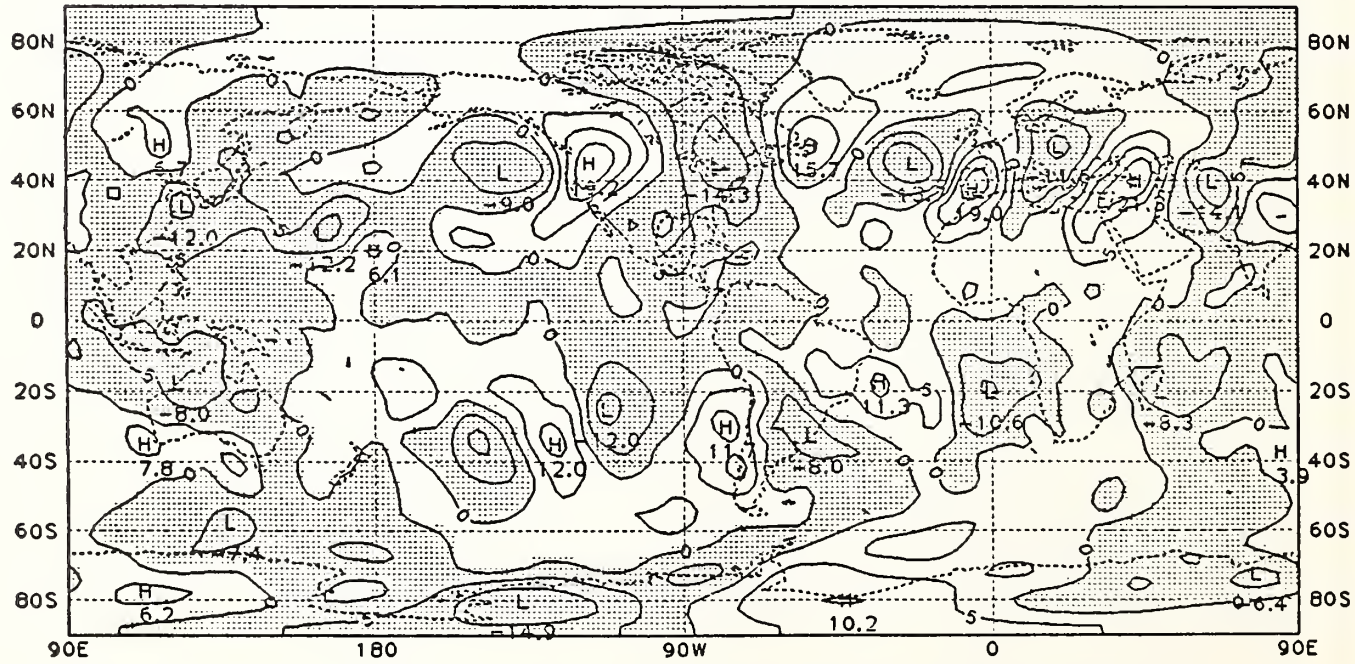

Fig. 4a. Global maps of the meridional velocity at 200 mb for July 1983 calculated from the NMC pre-initialized (PREI) and post-initialized (POSTI) analyses. Negative values are shaded and indicate southward motion. Isolines are drawn at intervals of 5 m s^{-1}.

$\bar{v}$, m s^{-1} 200 mb July 1983

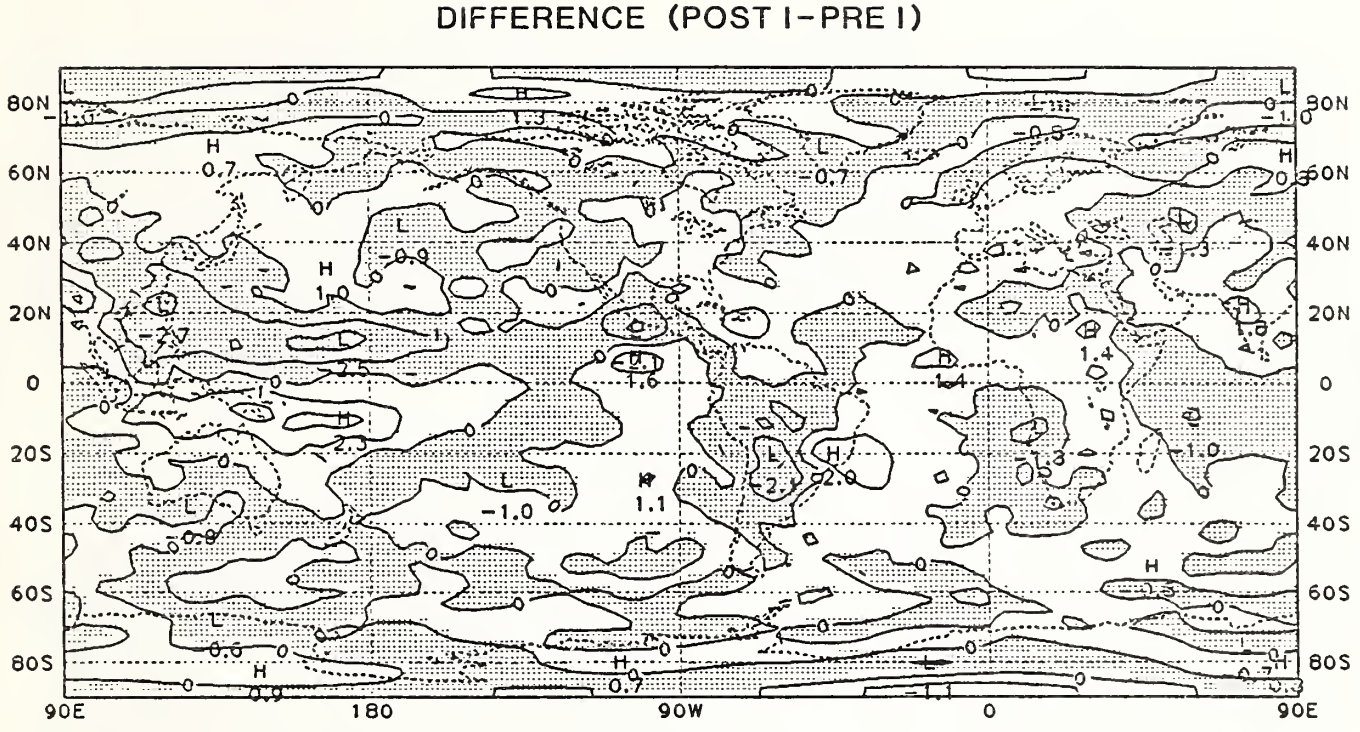

Fig. 4b. The difference, POSTI minus PREI, of the two fields in part (a). Isolines are drawn at intervals of 1 m s^{-1}.

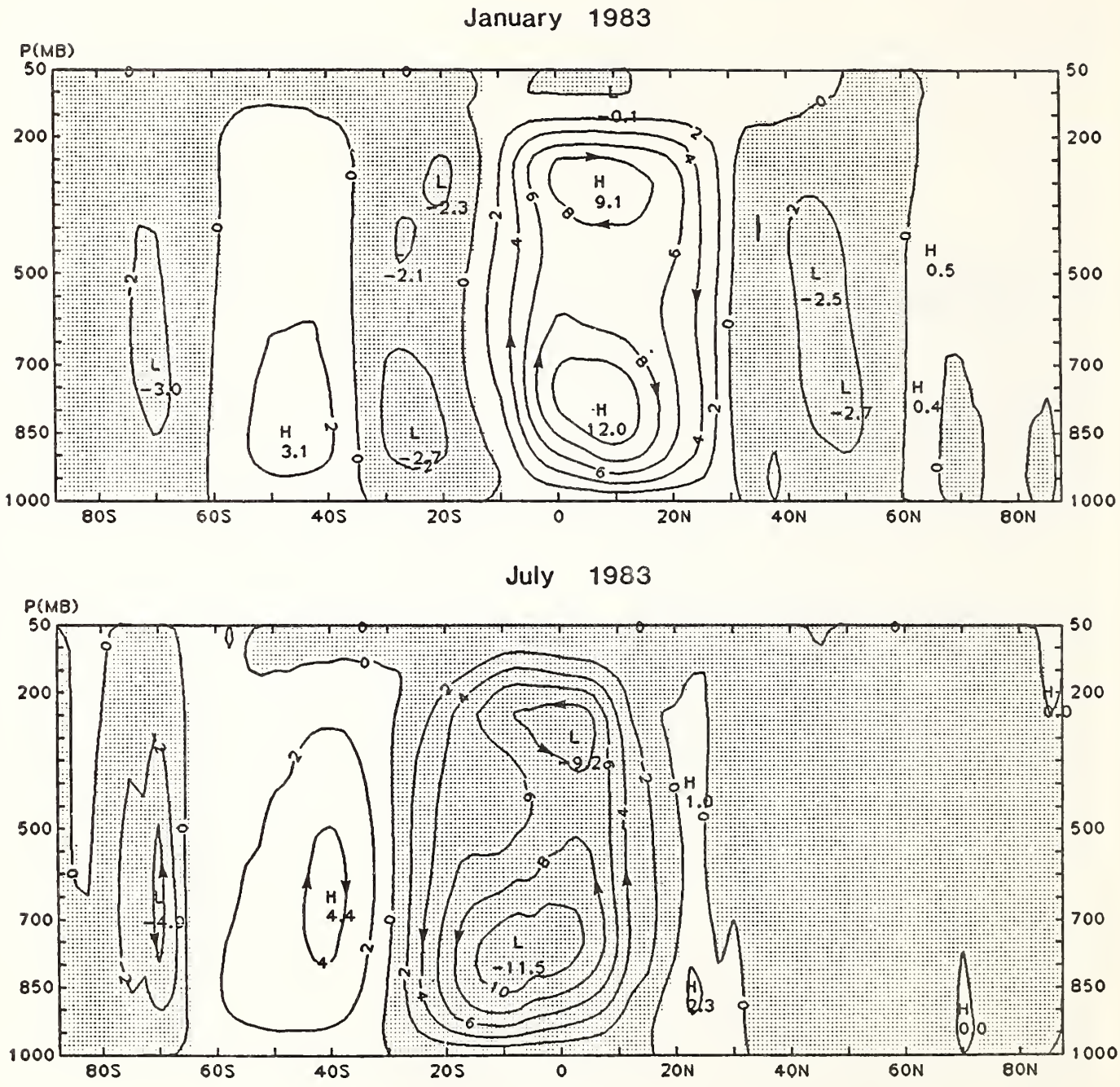

Fig. 5. Cross section of the mass streamfunction for the mean meridional circulation for January and July 1983 calculated from ECMWF analyses.

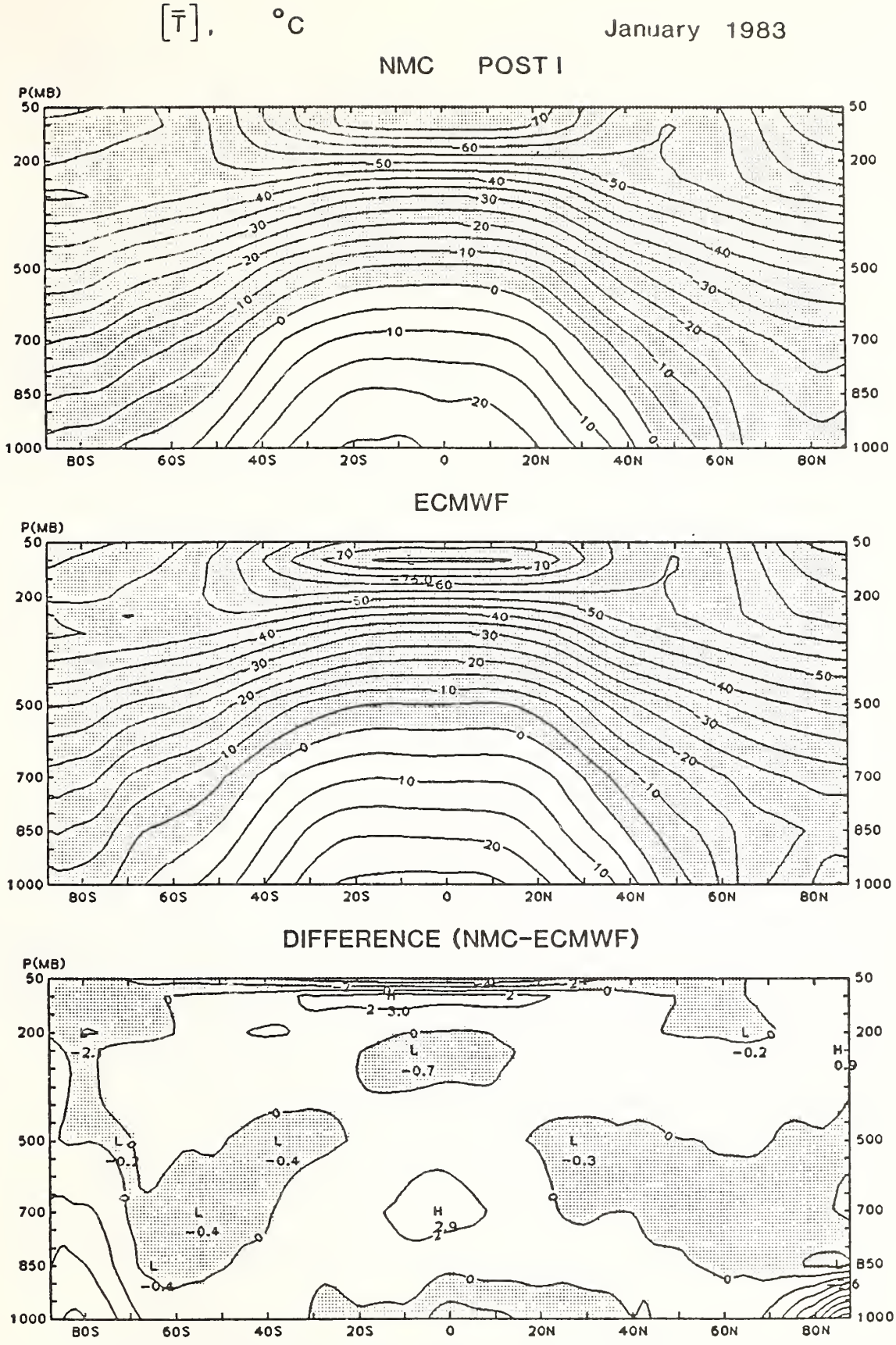

Fig. 6. Cross sections of the temperature for January 1983 calculated from the NMC post-initialized and the ECMWF analyses; and their difference, NMC POSTI minus ECMWF.

$\bar{q}$, g kg^{-1} 850 mb July 1983

NMC POST I

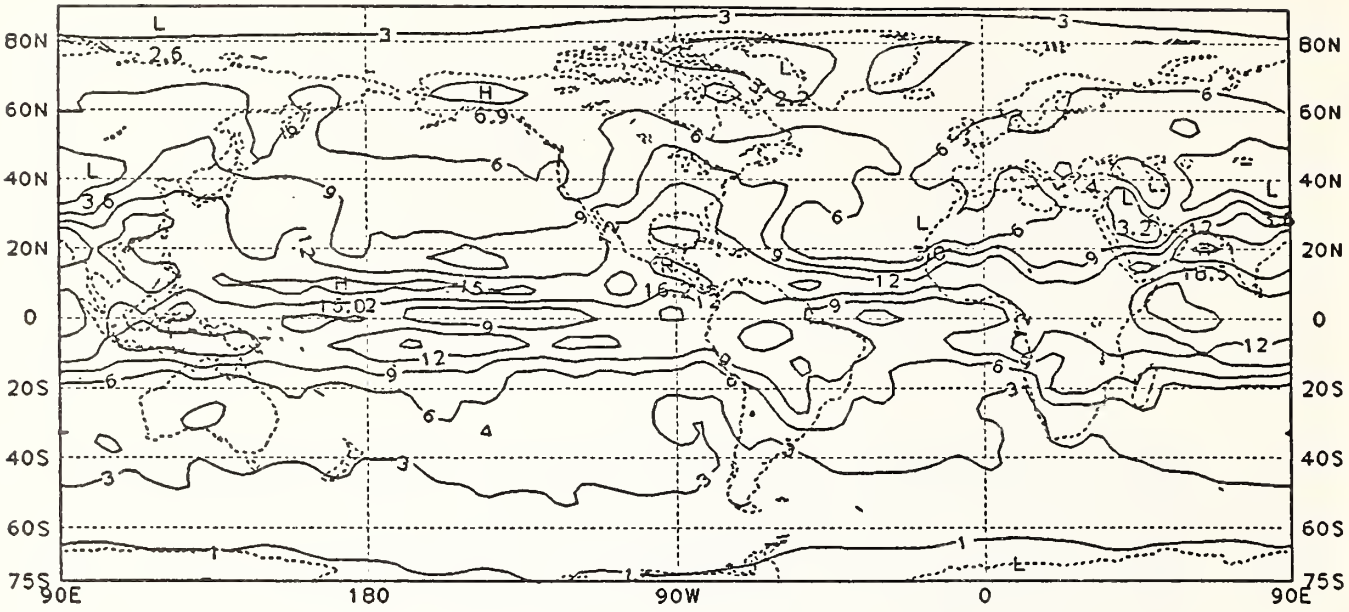

ECMWF

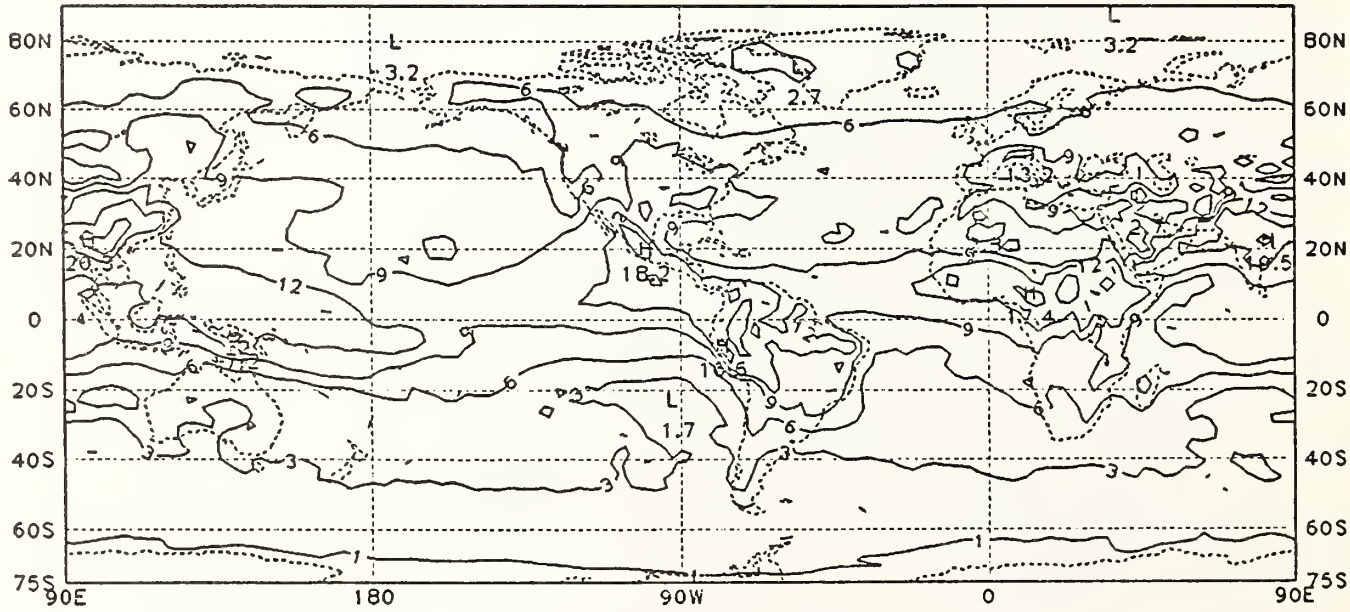

Fig. 7. Global maps of the specific humidity at 850 mb for July 1983 calculated from the NMC post-initialized and the ECMWF analyses. Isolines are drawn at intervals of 3 g kg^{-1}.

Observing the Eastern Pacific Hadley Circulation

James P. McGuirk, Aylmer H. Thompson, and Neil R. Smith
Department of Meteorology
Texas A&M University
College Station, Texas 77843

Some aspects of the tropical Eastern Pacific mean meridional circulation (MMC) can be interpreted in terms of the mean behavior of a synoptic event called a "moisture burst". This event is documented by McGuirk et al., 1984 (8th Climate Diagnostics Workshop). Three different aspects of the interaction of moisture bursts and the Hadley cell are described herein.

1. El Niño Behavior.

A distribution of moisture bursts during the 1982-83 El Niño cool season was prepared from NOAA 7 photo-mosaics (fig. 1). It shows:

(A) During El Niño moisture bursts do not occur in the region of strong ITCZ convection; that is, east of Australia and to the west of the eastern edge of the outgoing longwave radiation (OLR) minimum.

(B) The central Pacific deficit of bursts is more than 5 standard deviations below climatological expectations.

2. Mean Meridional Wind Behavior.

Calculations were performed on a nine-day gridded wind set (FGGE III (b) analysis during the January Special Observing Period). "Zonal averaging" was performed across the sector from the dateline to 112.5°W (7500 km) and from 20°S to 30°N. Meridional sections of the mean meridional wind component are shown for the 9-day average (fig. 2) and for selected days (fig. 3). The time average differs significantly from previous climatologies of the region.

(C) A thermally-direct MMC may be inferred. Climatology has this indirect in the eastern Pacific.

(D) A two-celled MMC appears in the vertical, with stronger southerlies centered at 600 mb and a weaker southerly maximum at the climatologically expected position at 200 mb.

The time sequence (fig. 3) shows large variations in the zonally-averaged meridional winds on a day-to-day basis.

(E) At the peak of the moisture burst on the 23rd and 25th (fig. 3b and 3c), meridional confluence into the ITCZ below 800 mb is intense.

(F) Except on the 27th (fig. 3d), the strongest southerlies are at, or even below, 500 mb, and the flow at tropopause level is two times stronger into the southern hemisphere.

(G) The only "classical" Hadley cell flow appears at the end of the moisture burst period on the 27th (fig. 3d).

(H) The weakest Hadley cell, as measured by low-level meridional confluence, occurs on the 21st, when no moisture bursts were present.

Based on (A), (C), (E), (H), and existing climatology, we tentatively introduce the following speculation. In the absence of synoptic or convective tropical forcing, the Pacific Hadley cell is weak, and may even switch directions, with tropical subsidence. With synoptic forcing, a Hadley cell develops, and its characteristics result as a statistical composite of a number of synoptic events (moisture bursts). This MMC appears primarily in the lower half of the troposphere. With strong convective forcing, moisture bursts do not form, and a strong, deep Hadley cell results--the classical picture.

3. Data Quality (FGGE SOP)

In spite of the intense observational coverage during FGGE, the study area remained data-sparse. The following results are restricted to the boundary layer (below 800 mb) and pertain to analyzed wind (FGGE), satellite winds (SAT), and surface ship and island observations (SFC). Fig. 4 shows the distribution of SAT and total nine-day observation frequency.

(I) Many regions in the equatorial band have no observations.

(J) SAT is synoptically biased, with a sparsity of data, particularly, in the moisture burst region.

(K) Low-level ITCZ convergence calculations are based on SAT at 10°N and west of 150°W, and at 3°N and east of 135°W.

(L) In most regions, simultaneous SFC and SAT observations are not available, making vertical extrapolation tenuous.

Hovmöller-type diagrams of low-level zonally-averaged meridional winds in a time-latitude section appear in fig. 5; the three representations show analysis of SFC only, SAT only, and FGGE data. Analysis assumptions require that these fields present the same signal (in particular, FGGE is derived from SAT and SFC). Clearly, they do not.

(M) FGGE presents considerably fewer southerlies, and weaker southerly amplitudes than either SAT or SFC; it also shows more northerlies at 15°N then either SAT or SFC.

(N) Even where SAT and SFC are consistent, FGGE may "disagree" (at 10°S from the 22nd to the 24th, or 25°N on the 27th and 28th).

(O) There are significant regions of disagreement between the two sets of observations (SFC detects more southerlies; SAT predicts stronger meridional confluence at the ITCZ; SAT is less coherent, both temporally and meridionally).

(P) Similar sections of zonal winds (not shown) yield similar inconsistencies; FGGE shows fewer equatorial westerlies than SAT, but also less variability than SFC.

In an effort to resolve the inconsistencies between FGGE, SAT, and SFC, additional analyses and intercomparisons were performed.

(Q) Examination of the 1000-850 mb wind shear of 50 ship soundings between 9°N and 9°S showed a mean shear of only 1 m/sec but a standard deviation of 7 m/sec with shear direction varying over 360°; in other words there should be little ability to extrapolate synoptic signals upward or downward in the tropical boundary layer.

(R) Fig. 6 shows FGGE 1000-850 mb shear in the equatorial belt. Four regions are identified: I and II with surface winds increasing strength with height; IV with easterlies shifting to westerlies with height; and III, with the trades turning cyclonically with height in the moisture burst region. It is unclear how accurately optimal interpolation represents these regimes in data-sparse regions.

(S) Shear magnitude is not well-related to surface speed.

Finally, an effective analysis error was computed between SAT and FGGE at 850 mb. "Effective" is included because no attempt was made to account for SAT observational errors or differences between observation and analysis times and positions. Two histograms of analysis error are presented in fig. 7 for a single time, comparing FGGE with two SAT sets: GOES (West) and GOES (Indian Ocean). The GOES (Indian Ocean) represents an erroneous calculation; the positions of observations are erroneously located in °W longitude on the World Data Center archive tape, so they were accidentally placed in the eastern Pacific for the analysis-error calculation.

(T) Although there is larger analysis error for the erroneous data, figs. 7a and 7b are quantitatively similar. Correct data show rms analysis errors of 3.6 m/sec whereas the "random data", correct in latitude, but moved from the Indian Ocean to the Pacific, show rms errors of only 4.2 m/sec. Could it be that SAT possesses only about 0.6 m/sec signal in the lower atmosphere?

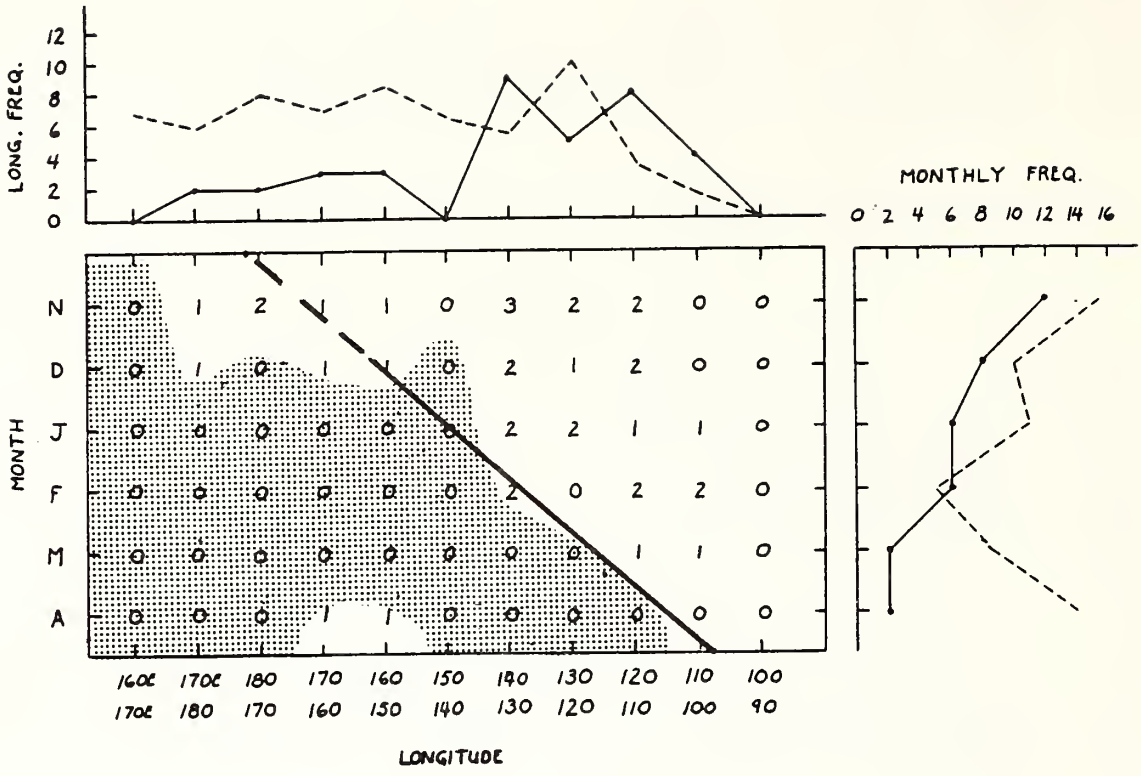

Fig. 1. Distribution of the occurrence of moisture bursts during the 82-83 El Niño as a function of month and longitude of origin. Dashed lines give non-El Niño climatology; heavy line gives approximate position of the eastern edge of the OLR minimum associated with El Niño. Shading emphasizes burst-void region.

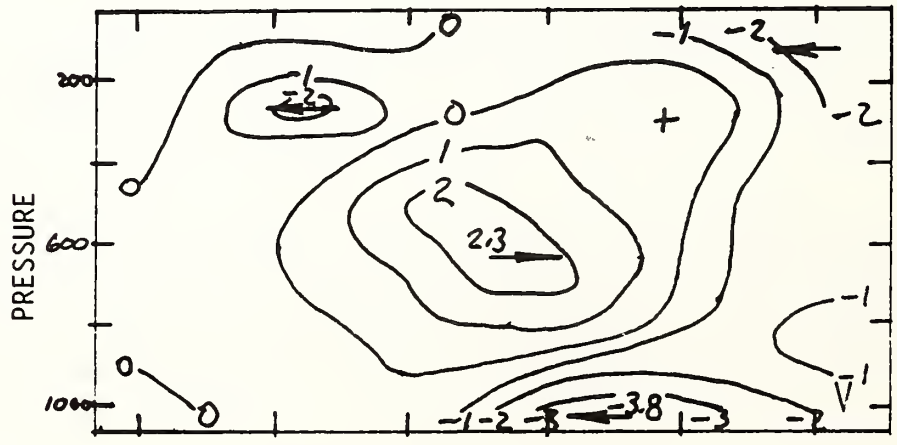

Fig. 2. Meridional section of the temporally (9 days) and zonally (180-112°W) averaged meridional winds. Units of m/sec.

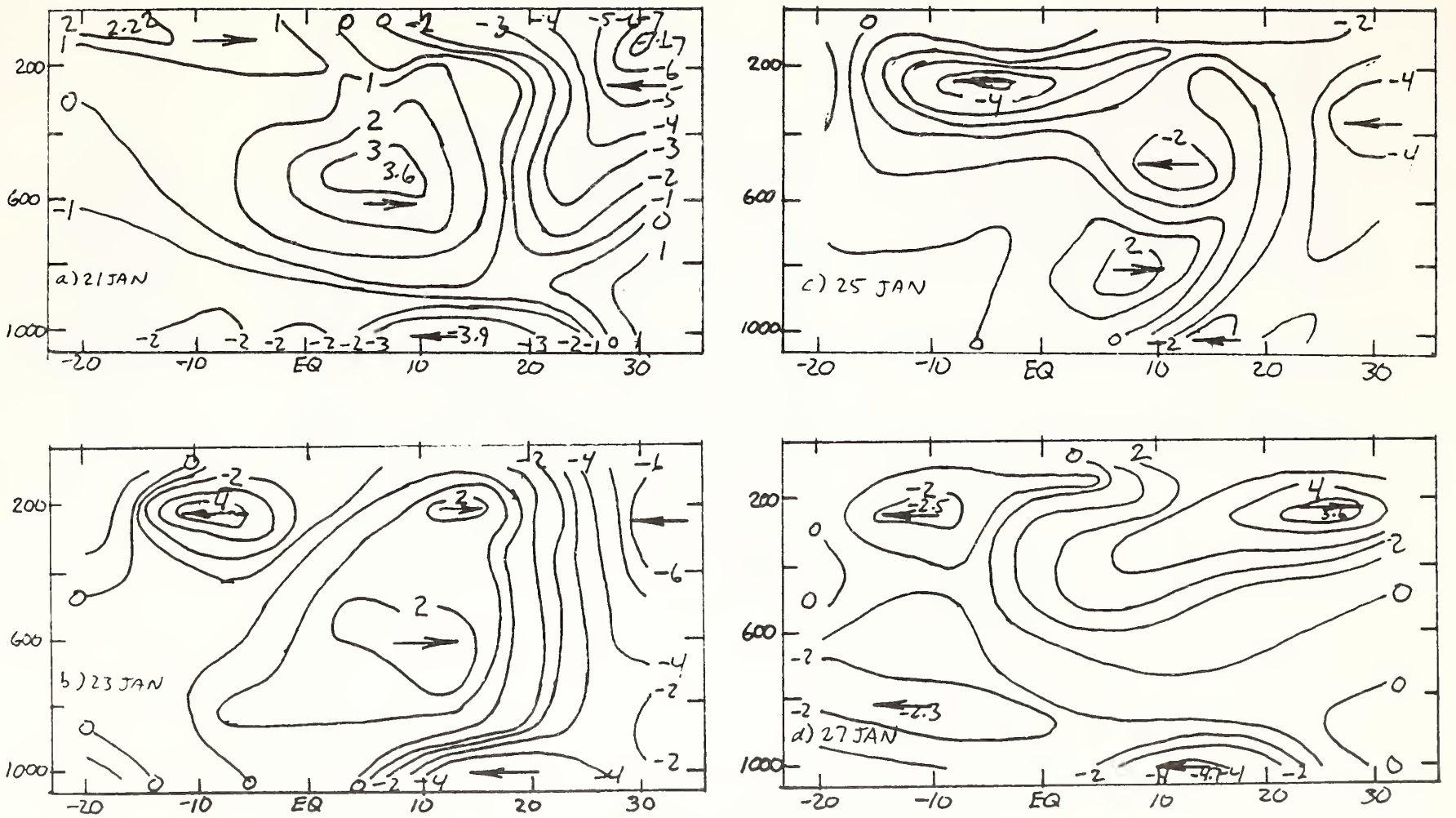

Fig. 3. As in fig. 2 except for individual days.

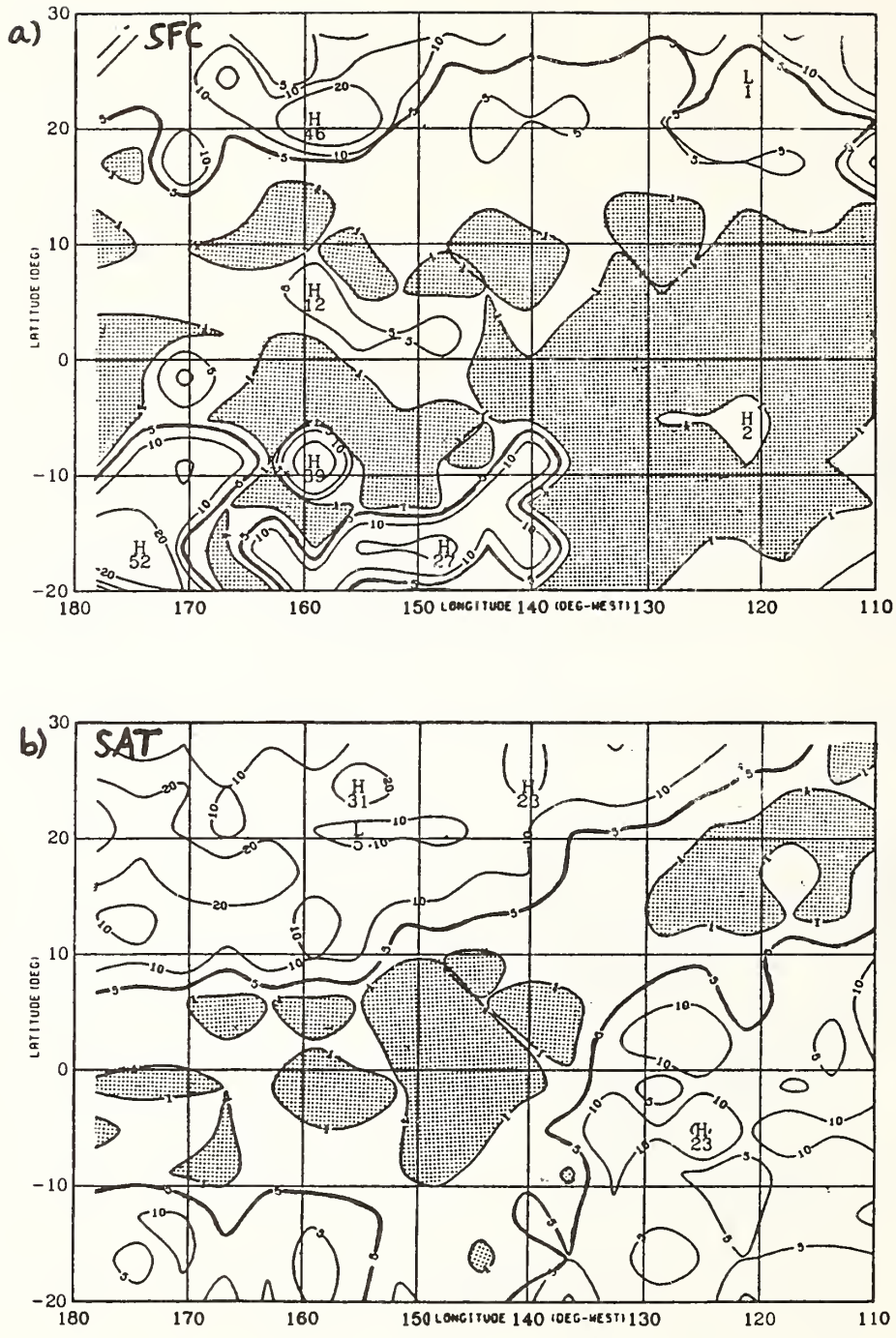

Fig. 4. Number of wind observations per 3.75 X 3.75° lat/lon box for the entire 9-day period. Isopleths are 1 (shaded), 5 (highlighted), 10 and 20 observations. a) Surface (SFC) observations; b) low-level satellite (SAT) observations.

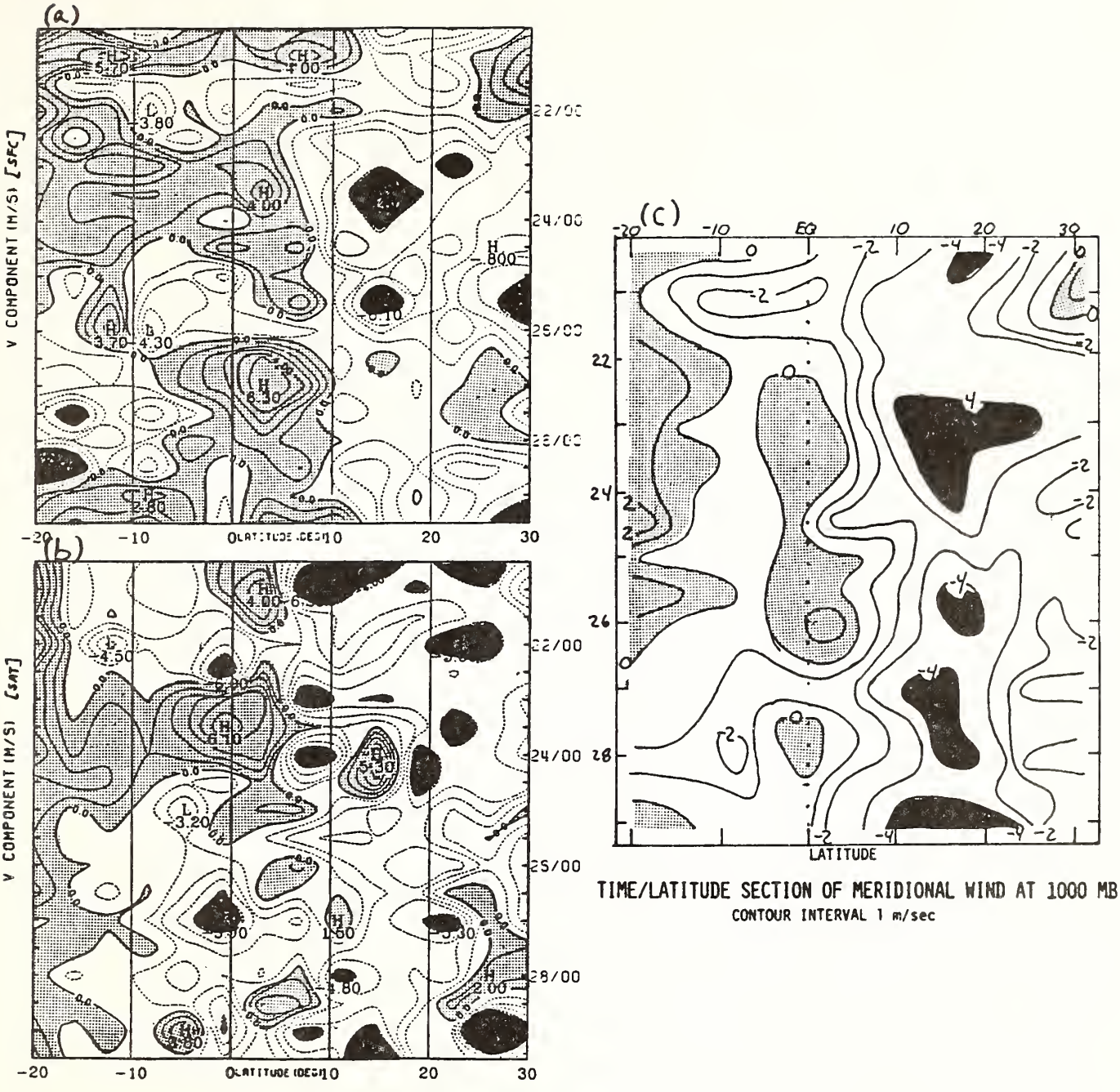

Fig. 5. Time-latitude sections of the zonally-averaged meridional wind between 180 and 112°W. Light shading gives southerlies; heavy shading gives northerlies greater than 4 m/sec. a) SFC observations; b) SAT observations; c) 1000 mb FGGE analysis. Contour interval is 1 m/sec.

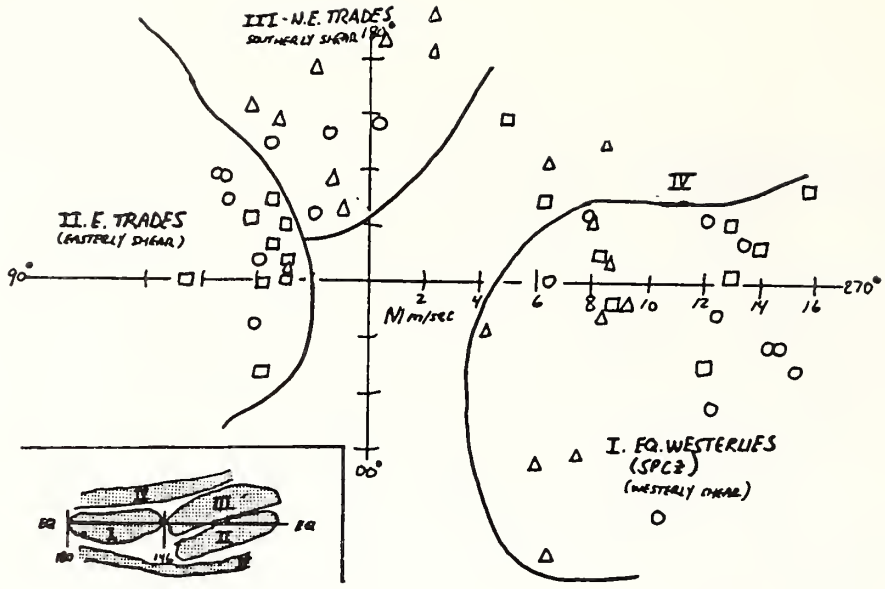

Fig. 6. 850-1000 mb wind shear in the equatorial belt from FGGE analysis. Wind vector from origin to data point gives speed and direction of shear. Data are clustered by surface wind direction, with associated geographical region shown in the inset at the lower left.

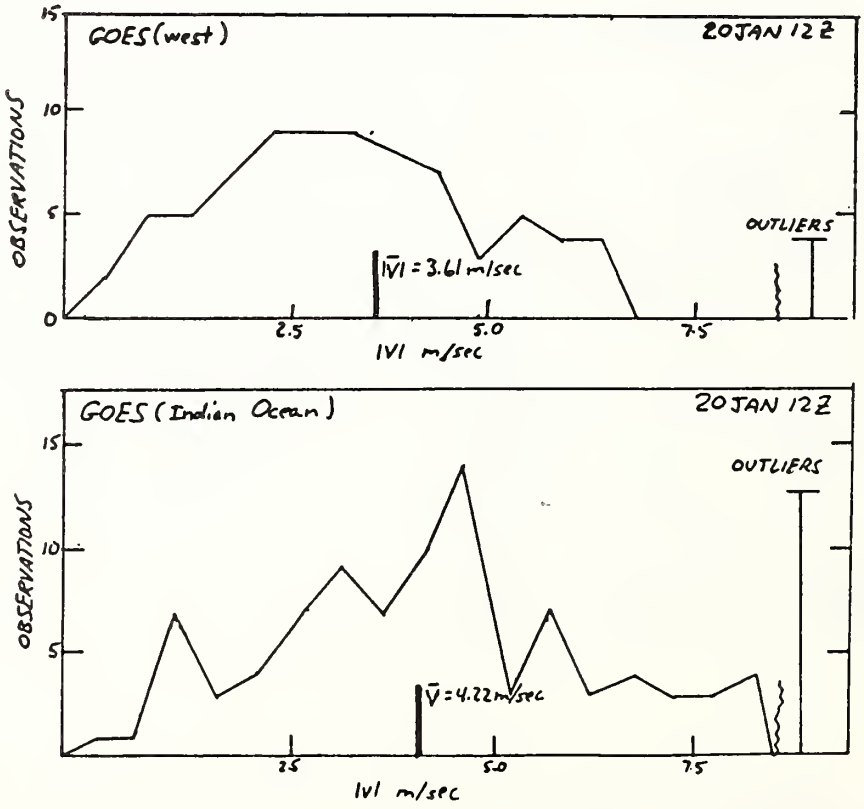

Fig. 7. Histograms of the distribution of effective analysis error between the 850 mb FGGE analysis and colocated SAT observations. a) GOES (west); b) GOES (Indian Ocean), which is erroneous because the data were improperly located in the eastern Pacific. Heavy vertical bars give sample means; vertical lines to right give flagged outliers.

PENN STATE UNIVERSITY LIBRARIES
A00007202247 4